UCLA
UCLA Electronic Theses and Dissertations

Title

The Dynamical Origins and mHz Gravitational Wave Signatures of Eccentric Compact Object Binaries

Permalink

https://escholarship.org/uc/item/4m19k20z

ISBN

9798186342427

Author

Xuan, Zeyuan

Publication Date

2026-08-11

Peer reviewed|Thesis/dissertation

eScholarship.org Powered by the California Digital Library
University of California

UNIVERSITY OF CALIFORNIA

Los Angeles

The Dynamical Origins and mHz Gravitational Wave Signatures of Eccentric Compact Object Binaries

A dissertation submitted in partial satisfaction
of the requirements for the degree of
Doctor of Philosophy
in Physics

by

Zeyuan Xuan

2026

© Copyright by

Zeyuan Xuan

2026

ABSTRACT OF THE DISSERTATION

The Dynamical Origins and mHz Gravitational Wave Signatures
of Eccentric Compact Object Binaries

by

Zeyuan Xuan

Doctor of Philosophy in Physics

University of California, Los Angeles, 2026

Professor Smadar Naoz, Chair

The detection of gravitational waves (GWs) has opened a new window beyond traditional electromagnetic (EM) observations, vastly expanding the observable compact-object population and revealing some of the Universe's most energetic and exotic processes. In this thesis, I focus on one defining property of GW sources: *eccentricity*. Specifically, I investigate the population and GW signatures of eccentric compact object binaries across a variety of astrophysical environments. Combining dynamical simulations and waveform analysis, I demonstrate that highly eccentric binaries can dominate the mHz GW source population in the local Universe and produce distinctive "repeated-burst" GW signals. These signatures can significantly improve binary parameter measurements and provide direct probes of their host environments. Furthermore, I show that eccentric systems can generate a substantial stochastic GW background and produce multimessenger counterparts such as ultracompact X-ray binaries (UCXBs). I also develop a public software package (`LEAP`) for the population and waveform analysis of eccentric sources. These results establish eccentric compact binaries as a prevalent and promising population for multimessenger observations, enabling them to be accurately modeled and fully utilized in the era of GW astronomy.

The dissertation of Zeyuan Xuan is approved.

Tuan H. Do

Mikhail Pil Solon

Tommaso L. Treu

Smadar Naoz, Committee Chair

University of California, Los Angeles

2026

DEDICATION

致我的母亲

TABLE OF CONTENTS

Page

LIST OF FIGURES **x**

LIST OF TABLES **xliii**

ACKNOWLEDGMENTS **xliv**

VITA **xlvi**

LIST OF PUBLICATIONS **xlvii**

ABSTRACT OF THE DISSERTATION **1**

1 Introduction **1**

2 Detecting Accelerating Eccentric Binaries in the LISA Band **6**

2.1 Introduction 7

2.2 Analytical Consideration 11

2.2.1 Mass-Acceleration Degeneracy in GW Data Analysis 12

2.2.2 Disentangling the Signatures of Accelerating Eccentric GW Sources - Analytical Approach 16

2.2.3 Measuring the Acceleration of Eccentric Compact Binaries - Analytical Approach 27

2.3 Numerical Approach 32

2.3.1 Waveform Template . . . 32
2.3.2 Matched Filtering and Criteria for Distinguishing the Acceleration . . 33
2.3.3 Fisher Matrix Analysis and Measurement Accuracy . . . 36
2.4 Examples and Results . . . 37
2.4.1 Distinguishing the Acceleration - Numerical Approach . . . 37
2.4.2 Measuring the Acceleration - Numerical Approach . . . 42
2.5 Discussion . . . 46
2.6 Acknowledgments . . . 48

3 Detecting Gravitational Wave Bursts From Stellar-Mass Binaries in the Milli-hertz Band 49

3.1 Introduction . . . 50
3.2 Repeated Bursts for Eccentric Sources in the Milli-hertz Band . . . 53
3.2.1 Burst Definition . . . 53
3.2.2 Detectability of Bursting Sources in the Milli-hertz Band . . . 56
3.2.3 Lifetime of Bursting Sources in the Milli-Hertz Band . . . 64
3.3 Population Estimation and Astrophysical Consequences . . . 70
3.3.1 General Considerations . . . 70
3.3.2 Steady-State Approximation and Constraints from LVK . . . 71
3.3.3 BBHs in the Field . . . 74
3.3.4 BBHs in Globular Clusters . . . 75
3.3.5 BBHs in the Galactic Nucleus . . . 76
3.3.6 EMRIs . . . 79
3.4 Discussion . . . 81
3.5 Acknowledgments . . . 83
3.6 Appendix . . . 83
3.6.1 Details of Numerical Simulations . . . 83
3.6.2 Numerical Approach to Calculate the SNR of Highly Eccentric Binaries 91

4 Stochastic Gravitational Wave Background from Highly-Eccentric Stellar-Mass Binaries in the Milli-hertz Band **94**

4.1 Introduction . . . 95

4.2 Theoretical Consideration . . . 99

4.2.1 The Properties of GW Bursts from Highly Eccentric Binaries . . . 99

4.2.2 Stochastic GW Background from Bursting Sources . . . 104

4.2.3 Stochastic Background Calculation . . . 107

4.3 Simulations of Different Bursting Galactic Sources . . . 114

4.3.1 Configuration of the Simulations . . . 114

4.3.2 Stochastic Background from the Simulations' Results . . . 116

4.4 Discussion . . . 123

4.5 Acknowledgments . . . 127

5 Extracting Astrophysical Information of Highly-Eccentric Binaries in the Millihertz Gravitational Wave Band **128**

5.1 Introduction . . . 129

5.2 Astrophysical Properties and Waveform Modeling . . . 133

5.2.1 Astrophysical Properties . . . 133

5.2.2 Waveform Model . . . 138

5.3 Source Identification and Parameter Extraction . . . 145

5.3.1 Fisher Matrix Analysis . . . 145

5.3.2 Matched Filtering . . . 157

5.4 An Example of Mock Data Analysis . . . 159

5.4.1 The Difference Between a Bursting and Non-Bursting Data Analysis . 159

5.4.2 Population Model and Waveform Generation . . . 160

5.4.3 Matched Filtering and Mock Observation Results . . . 163

5.5 Discussion . . . 168

5.6 Acknowledgments . . . 172

5.7 Appendix . . . 172
5.7.1 Time Domain Estimation of the Inner Product . . . 172
5.7.2 Analytical Estimation of the Fisher Matrix . . . 173
5.7.3 Computing the Major and Minor Axes of Sky Error Ellipsoids . . . 182

6 Localizing Dynamically-Formed Black Hole Binaries in Milky Way Globular Clusters with LISA 187
6.1 Introduction . . . 188
6.2 Creating a Mock Galactic Sample . . . 192
6.3 Source Localization and Astrophysical Implications . . . 196
6.3.1 Detectability and Eccentricity Distribution . . . 196
6.3.2 The Location of Gravitational Wave Sources . . . 199
6.3.3 Astrophysical Implication . . . 200
6.3.4 Further Validation of BBH Localization Using Bayesian Analysis . . . 209
6.4 Discussion . . . 214
6.5 Acknowledgments . . . 218
6.6 Appendix . . . 218

7 Eccentric Stellar-mass Binary Black Holes: Population, Detectability, and Waveform Analysis in the LISA and LIGO Era 221
7.1 Introduction . . . 222
7.2 Key Aspects of Eccentric GW Sources in the Millihertz Band . . . 226
7.2.1 Basic Properties . . . 226
7.2.2 Characteristic Strain Representations . . . 231
7.3 Simulated Eccentric BBH Population . . . 236
7.3.1 Creating a mock BBH Catalog . . . 236
7.3.2 Astrophysical Implication . . . 243
7.3.3 BBHs at Cosmological Distances . . . 249

7.4 Eccentric BBHs in the LISA Global Fit . . . 254
7.5 Waveform Generation and Validation . . . 262
7.6 Discussion . . . 269
7.7 Acknowledgments . . . 273
7.8 Appendix . . . 274
7.8.1 Eccentric GW signal analysis . . . 274

8 From Wide Triples to UCXBs: Multimessenger Signatures of Dynamically-formed Black Hole-White Dwarf Systems in the LISA Band 288

8.1 Introduction . . . 289
8.2 Simulation Setup . . . 293
8.2.1 Generating the Initial BH-WD Population . . . 293
8.2.2 Evolution of BH-WDs in Triples and the Inclusion of Dynamical Tides 295
8.2.3 Evolution of Mass-transfer BH-WDs . . . 301
8.3 Results and Discussion . . . 304
8.3.1 Triple Path of UCXB Formation . . . 304
8.3.2 UCXB Detectability and Expected Population . . . 306
8.3.3 Discussion . . . 310
8.4 Conclusions . . . 314
8.5 Acknowledgments . . . 315
8.6 Appendix . . . 316
8.6.1 Initial Conditions . . . 316
8.6.2 An Analytical Approximation of WD Dynamical Tides . . . 316
8.6.3 X-ray Detectable Time of UCXBs . . . 322

Bibliography 324

LIST OF FIGURES

Page

2.1 **The frequency spectrum of GW signals from two eccentric BBHs systems with the same chirp mass but different total mass.** For the first system (blue line) $m_1 = 8$ $M_\odot$, $m_2 = 40$ $M_\odot$, $e = 0.3$; For the second system (red line) $m_1 = m_2 = 16.867$ $M_\odot$, $e = 0.3$. Both of these systems have the same chirp mass $\mathcal{M}_c \sim 14.684$ $M_\odot$, but as depicted the difference in total mass results in a different position of the harmonics. The initial period of radial motion for the first systems is 1.5mHz, but its GW frequency of each harmonic is not the integer multiple of 1.5mHz because of the shift induced by GR precession (Δf). For the second system, its GR precession shifts the position of each harmonic by a different value. For illustration purposes, we adjust the initial radial frequency of the second system to be slightly different from 1.5mHz, so that we compensate for the difference in Δf and make its GW's 2nd harmonic having the same initial frequency as the first system's. . 17

2.2 **A flowchart of the proposed strategy, as the reason why the eccentricity can help us disentangle the acceleration in template fitting**. The GW signal from accelerating eccentric sources has the signatures of GR precession (Δf) and chirp waveform ($\dot{f}_o$), which contribute differently to the result of template fitting. *Left branch* describes that Δf primarily constrains the fitted total mass $M_{\rm tot}$, for either accelerating or non-accelerating templates. Since the total mass $M_{\rm tot}$ and the chirp mass $\mathcal{M}_c$ can be related to each other (See Eq.(2.12)), GR precession signatures in the waveform eventually put a constraint on the chirp mass $\mathcal{M}_c$ in template fitting. *Middle branch* shows the case when we use non-accelerating GW templates. In this case, the acceleration distorts the chirp rate ($\dot{f}_o \neq \dot{f}_e$) and yields an inaccurate chirp mass $\mathcal{M}_o$ in template fitting. However, the $\mathcal{M}_c$ from *left branch* (GR precession signature's constraint) is not affected by acceleration, thus will not agree with $\mathcal{M}_o$. Such a discrepancy between two waveform signatures means we can hardly find a good match in the non-accelerating templates family. It reminds us to include acceleration in the GW templates (i.e., shift to the *Right branch*). In the *Right branch*, we use GW templates with acceleration to fit both $\dot{f}_e$ and $\dot{f}_{\rm acc}$. Since the GR precession (from *left branch*) can constrain the intrinsic chirp rate $\dot{f}_e$, it disentangles $\dot{f}_e$ from $\dot{f}_{acc}$ and further help with improving the acceleration measurement accuracy. 19

2.3 **The measured chirp mass $\mathcal{M}_o$ as a function of binary's acceleration.** We show a DWD system with $m_1 = 0.25\mathrm{M}_\odot, \mathrm{m}_2 = 0.5\mathrm{M}_\odot$, $e = 0.1$, $f_e^{j=2} =$ 3mHz, on a circular orbit around a SMBH with $M_{\mathrm{SMBH}} = 4\times10^6$ $\mathrm{M}_\odot$ at different distances. We choose the phase angle such that line-of-sight acceleration caused by the SMBH gravitational pull is maximized and pointing toward the observer. The chirp mass one measures using non-accelerating GW templates is depicted as a function of DWD's acceleration/ distance from the SMBH. As is shown in Section 2.2.2.2, GR precession pattern will put a constraint on the maximum possible value of chirp mass: $\mathcal{M}_c \leqslant 0.25^{3/5} M_{\mathrm{total}}$. The figure shows that when the DWD system is close to the SMBH ($\sim$ 1pc), acceleration becomes large enough ($a > a_{\mathrm{max}}$) to make $\mathcal{M}_o$ exceed the upper bound $\mathcal{M}_{\mathrm{max}}$, enabling us to find the discrepancy between $\mathcal{M}_o$ and M_{total}, thus distinguishing the acceleration. Note that the acceleration in this Figure increases to the left. 25

2.4 **The measured acceleration as a function of the uncertainty in measured symmetric mass ratio** $\nu_{\rm uncert}$ Here we place a binary at 0.04 pc from a $4 \times 10^6 M_\odot$ SMBH and choose the phase angle so that the line-of-sight acceleration is maximized. *Upper Panel* shows a binary WD composed of: $m_1 = 0.35$ $M_\odot$, $m_2 = 0.4$ $M_\odot$, $e = 0.1$, with the frequency of second harmonic $f_2 = 2, 3, 4, 5$ and 6 mHz, bottom to top. *Middle Panel* depicts a BH binary composed of: $m_1 = 15$ $M_\odot$, $m_2 = 20$ $M_\odot$, $e = 0.1$. *Bottom Panel* is the same as the top and middle panel, but shows the comparison between DWDs and BBHs for $f_2 = 3$mHz to scale. The solid lines represent the measured acceleration as a function of measured ν, (see Eq. (2.22)). The dashed lines correspond to the magnitude of peculiar acceleration at the labeled distances from the SMBH. As noted in the text, the measurement of the symmetric mass ratio can be uncertain, depicted here in the x-axis by $\nu_{\rm uncert}$ (all the possible values of ν).The intrinsic symmetric mass ratio $\nu_{\rm int}$ of the binary is marked on the plot for reference. 30

2.5 **The mismatch between an accelerating DWD's GW and its optimal fit within non-accelerating templates (1 − FF), as a function of the DWDs' peculiar acceleration.** We show a DWD system with $m_1 = 0.35 M_\odot, m_2 = 0.4 M_\odot$, $e = 0.1$, $f_e^{j=2} = 3$mHz, on a circular orbit around a SMBH with $M_{\rm SMBH} = 4 \times 10^6$ $M_\odot$ at different distances. The observation duration is set to be 4 years. Adopting the proposed methodology of future observations, we apply matched filtering method (Finn, 1992; Cutler and Flanagan, 1994) to find the best fit in templates without considering acceleration. 1 − FF is plotted as a function of DWD's acceleration/ distance from the SMBH. The black lines mark the critical value of 1 − FF for the detection of acceleration, providing different SNR in observation (see Eq. (7.22), $D = 10$ for this example). Note that the acceleration in this Figure increases to the left. 38

2.6 **The mismatch between an accelerating BBH's GW and its optimal fit within non-accelerating templates ($1-\mathrm{FF}$), as a function of the BBH's eccentricity.** Here we place a BBH system with $m_1 = 15\mathrm{M}_\odot, m_2 = 20\mathrm{M}_\odot$, $f_e^{j=2} = 3\mathrm{mHz}$ at 0.1 pc from a $4\times10^6\mathrm{M}_\odot$ SMBH, set the observational time $\tau_{\mathrm{obs}} = 4\mathrm{yrs}$. Following the same steps as Figure 2.5, we apply matched filtering method to find the best fit in templates without considering acceleration and plot $1-\mathrm{FF}$ as a function of BBH's eccentricity. As is shown in the figure, $1-\mathrm{FF}$ becomes larger and the acceleration is more likely to be detected for higher eccentricity. 39

2.7 **Relative error of acceleration measurement as a function of the compact binary's eccentricity.** Here we place a compact binary system at 0.4 pc from a $4\times10^6\mathrm{M}_\odot$ SMBH, set the initial GW frequency $f_e^{j=2} = 3\mathrm{mHz}$, observational time $\tau_{\mathrm{obs}} = 4\mathrm{yrs}$ and SNR= 20. We plot the relative error of acceleration measurement, as a result of the fisher matrix analysis (see text), as a function of binary's initial eccentricity. Red line shows a DWD system with $m_1 = 0.35\mathrm{M}_\odot, m_2 = 0.4\mathrm{M}_\odot$, while blue line represents a BBH system with $m_1 = 15\mathrm{M}_\odot, m_2 = 20\mathrm{M}_\odot$. Note that the amplitude of peculiar acceleration is $a_0 \sim 3.5\times10^{-6} m\cdot s^{-2}$ for this configuration. 41

2.8 **Absolute error of acceleration measurement as a function of BBHs' eccentricity for different observation durations.** Here we take the same BBH as in Figure 2.7, but compare the absolute error of acceleration measurement for different observation durations (2yrs/ 4yrs /10yrs). The initial frequency of GW is $f_e^{j=2} = 3\mathrm{mHz}$ and SNR is set to be 20 for all the cases. . 43

2.9 **Critical eccentricity, for the measurement accuracy of acceleration to reach given thresholds, as a function of the binary's peculiar acceleration.** For each line in the two panels, we set a targeted accuracy of peculiar acceleration measurement (i.e., 30%, 10%, and 3%, from left to right), and show the critical eccentricity of the binary for GW measurement to reach such accuracy as a function of the binary's acceleration. The solid lines represent a BBH ($m_1 = 15\mathrm{M}_\odot, m_2 = 20\mathrm{M}_\odot$), and the dashed lines represent a DWD ($m_1 = 0.35\mathrm{M}_\odot, m_2 = 0.4\mathrm{M}_\odot$). Both systems have the initial GW frequency $f_e^{j=2} = 3\mathrm{mHz}$. As explained in the text, the acceleration measurement can be applied to a wide range of tertiaries. Here, as an example we consider a $4 \times 10^6 \mathrm{M}_\odot$ SMBH case (*Left Panel*), and a $1\mathrm{M}_\odot$ star case (*Right Panel*). We set the observation duration as 4 yrs and SNR to be 20, compute the absolute error of acceleration measurement for a fixed distance from the tertiary ($r = 0.4pc$ for the SMBH case, $r = 100au$ for the star case), and analytically generalize the results to get the relative error for the different magnitude of a (distance to the tertiary). The acceleration measurement exceeds the targeted accuracy in the region to the right of each line, where we darken the background color to highlight the difference. For illustration purposes, we translate the acceleration into the binary's distance to the tertiary and mark it on the top of each panel. This figure highlights that higher eccentricity can extend the parameter space where acceleration can be accurately measured. 45

3.1 **The GW waveforms of a BBH system with the same orbital frequency but different eccentricities.** We show a BBH system with $m_1 = m_2 = 20$ $M_\odot$, orbital frequency $f_{\rm orb} = 1.8 \times 10^{-5}$ Hz, luminosity distance $D_l = 8$ kpc, and $e = 0.001, 0.4, 0.9$, respectively. As explained in the text, when the binary's orbital eccentricity increases, its GW energy emission will concentrate near each pericenter passage, turning the GW signal from a sinusoidal wave ($e \sim 0$ case) into a "burst-like" waveform ($e = 0.9$ case). 55

3.2 **The signal-to-noise ratio of a single GW burst, as a function of the source's pericenter distance.** We show a BBH system with $m_1 = m_2 = 10$ $M_\odot$, placed at $D_l = 1, 8, 50, 765$ kpc, respectively. The SNR of a single GW burst is plotted as a function of the binary's pericenter distance $a(1-e)$, and the corresponding GW burst frequency is plotted on the top x-axis. We note that repeated burst sources can have multiple bursts detected during the observation, and the overall SNR can be higher than the single burst case of this figure. See Figure 3.4 for the repeated burst case. 60

3.3 **Comparison between the GW signal of a bursting BBH and a near-circular DWD, both with the same signal-to-noise ratio** SNR ~ 12**.** We show a BBH system (blue line) with $m_1 = m_2 = 20$ $M_\odot$, $a = 4.43$ au, $e = 0.999$ and a DWD system (green line) with $m_1 = m_2 = 0.5$ $M_\odot$, $a = 0.001$ au, $e = 0.01$, both of them are placed at $D_l = 8$ kpc, and observed for $T_{\rm obs} = 4$ yr. These parameters are chosen such that these sources will have SNR $= 12$. *Upper Panel* shows the characteristic strain (Eq. 3.28) compared with the LISA noise curve ($\sqrt{fS_n(f)}$) (red line), *Middle Panel* and *Bottom Panel* show the time-domain waveforms. This plot highlights that bursting signals in the milli-hertz band can have significant amplitude in the time domain (thousands of times greater than a circular source with the same SNR), even if their averaged SNR is limited. 63

3.4 **The Dependence of the (RB) compact binary's detectability on its semi-major axis and eccentricity.** Here we show a BBH system (*Left Panel*) with $m_1 = m_2 = 10$ $M_\odot$, and a DWD system (*Right Panel*) with $m_1 = m_2 = 0.75$ $M_\odot$, placed at $D_l = 8$ kpc and observed for 4 yr with LISA. The color represents the compact binary's signal-to-noise ratio as a function of its semi-major axis a and eccentricity $1 - e$. As a proof of concept, we depict an example system's evolution (purple line with star and arrows) for both parameter spaces and plot the corresponding orbital time on the top x-axis. The solid lines with color represent the merger timescale $\tau_{\rm merger}$ for a given (a, e) configuration of the binary. In other words, when the evolution track of the binary gets into the colored region and gets across a given merger timescale, we can estimate the remaining time for it to emit detectable GW bursts before the merger. We note that the signal-to-noise ratio is suppressed in the region below the dashed lines ($t_{\rm merger} < T_{\rm obs}$) because the binary will merge during the observation, thus having less observational time than the total LISA mission time. Therefore, when calculating the SNR for these binaries following Equation. (7.34), we replaced the $T_{\rm obs}$ with $t_{\rm merger}$. 66

3.5 **The maximum detectable distance of the (RB) compact binary.** Here we consider the same systems as in Figure 3.4, but choose different values of luminosity distance D_l, and show the equal signal-to-noise ratio (SNR = 5) contours for a 4 yr LISA observation. The left (right) panel shows the BBHs (DWDs) system. The detectability of bursting sources increases at the top-left part of the plot. 69

3.6 **The number of bursting sources and bursts detected per year, assuming a 10-yr LISA mission and detection threshold** SNR = 5**.** The figure depicts the estimation results of bursting BBHs for different channels, with the error bars reflecting the theoretical uncertainties. Specifically, we show the number of detectable bursting sources from each channel (x-axis) and their contribution to the number of bursts detected per year (y-axis). For details of the simulation, see Appendix 3.6.1. Note that the number of detectable bursting sources is roughly proportional to the observational time. The solid points represent the population with convincing evidence of existence, while the hollow points are for the potentially existing population of bursting sources. We emphasize that if future detection does not show evidence of the population marked in hollow points, it serves as a strong constraint on the corresponding formation channels. 72

3.7 **Number of detectable bursting sources in the galactic nucleus YNC, as a function of their age.** Here we show the expectation of observable bursting systems in the Milky Way center young nuclear cluster, as a function of the cluster's age. The deep blue line stands for a LISA observational period $T_{\rm obs} = 10$ yr while the light blue line represents $T_{\rm obs} = 4$ yr. The YNC's age is constrained by observation to be $2 \sim 8$ Myr. 78

3.8 **An example of the repeated burst phase and inspiral phase during the evolution of an EKL merger.** We show a BBH system with $m_1 = 57.7\ \mathrm{M}_\odot, \mathrm{m}_2 = 51.9\ \mathrm{M}_\odot$, $a_1 = 1.97$ au, $e_1 = 0.38$, placed near a SMBH with $\mathrm{M} = 4 \times 10^6\ \mathrm{M}_\odot$, $a_2 = 4706$ au, $e_2 = 0.97$, $i = 88°$, $D_l = 8$ kpc . *Upper Panel* shows the signal-to-noise ratio of this source, for the observational time 4 yr. *Middle Panel* and *Bottom Panel* show its eccentricity and semi-major axis evolution as functions of time. As is shown in the figure, this example system undergoes strong EKL oscillation because of the SMBH. It spends a significant fraction of time in the repeated burst phase, bursting detectable GW signal via highly eccentric orbit, before finally reaching the inspiral phase with moderate eccentricity. 84

3.9 **Number of detectable bursts during LISA mission, as a function of the YNC's age.** Here we show the simulation result of observable bursts in the Milky Way center young nuclear cluster, as a function of the cluster's age. The deep blue line assumes the LISA observational period $\tau_{\rm obs} = 10$ yr while the light blue line represents $\tau_{\rm obs} = 4$ yr. The large fluctuation of the light blue line is caused by the limited number of systems in the simulation. . . . 90

4.1 **GW background from bursting BBHs within the Milky Way globular clusters.** Here we generate the bursting BBHs population using the methodology described in Section 8.2, and calculate their collective GW signals observed by LISA. *Upper panel* shows the detector's Michelson response (Cutler, 1998; Cornish and Rubbo, 2003), $s_1(t)$, over a 1-yr period. *Lower panel* shows a zoom-in of the signal. In the *upper panel*, the modulation of the GW background is a result of the detector's annual motion around the sun. 106

4.2 **Total GW background from bursting BBHs in Globular Clusters and Galactic Field.** Here we show (in dashed lines) the maximum collective GW power spectrum, $\sqrt{fS_n(f)}$, corresponding to bursting BBHs in the GCs (*Left Panel*) and Galactic Field (*Right Panel*) of Milky Way, M31, M33, and cosmological sources. The blue-colored region shows the total GW background from all four channels mentioned above, with its boundary representing the upper and lower limits. For comparison purposes, we also plot the LISA noise curve (N2A5 configuration (Klein et al., 2016a; Robson et al., 2019a), in the solid red line). 117

4.3 **Total GW background from bursting BBHs in the Galactic Nuclei.** Here we show the same GW background results as in Figure 4.2, but for the case of bursting BBHs in the galactic nuclei. We exclude the case of M33 in this figure since it does not have a SMBH in the galactic center. For a detailed explanation of the populations shown in the figure, see Section 4.3.2.3. . . . 121

4.4 **Summary of the stochastic GW backgrounds from bursting BBHs.** Here, we show the upper limit of the GW background, $\sqrt{fS_n(f)}$, corresponding to highly eccentric BBHs from the Globular Clusters (blue dashed lines), Galactic Field (green dashed lines), and Galactic Nuclei (brown dash-dotted lines) in the universe. *Upper Panel* shows the maximum level of total GW background from bursting BBHs. *Bottom Panel* represents the unresolvable GW noise background from bursting sources with SNR < 8 for a 4 yr LISA mission. For demonstration purposes, we sum the contribution of the three channels mentioned above and show the collective background in the solid red lines, and plot the LISA noise curve (N2A5 configuration (Klein et al., 2016a; Robson et al., 2019a), in orange). 125

5.1 **Bursting GW waveform from a wide, highly eccentric BBH system.** Here we show the strain amplitude (h_+) of a BBH system with $m_1 = 15\ \mathrm{M}_\odot$, $m_2 = 10\ \mathrm{M}_\odot, a = 0.100148\mathrm{au}, e = 0.99, \Theta = \Phi = \pi/4$, placed at $R = 8$ kpc and observed for 3 years (see Section 5.2.2 for detailed definitions of Θ, Φ). The time domain waveform is generated using the x-model as described in Section 5.2.2. *Upper Panel* shows the entire 3-year-long signal, which is made up of ~ 473 GW bursts (clustering in the black-colored region). Furthermore, the amplitude modulation in the *Upper Panel* is caused by general relativistic precession of the binary's orbit (precession period ~ 11.8 yr). *Middle Panel* is a zoom-in of the signal for a ~ 10 days period, and *Bottom Panel* illustrates the details of waveform near a single GW burst. Note that in this example, we do not include the detector's response, otherwise, the LISA's annual motion around the sun will induce another long-term modulation on the amplitude and phase of the bursting signal. 137

5.2 **The definition of $\Theta, \Phi, \theta, \phi$ and R (not to scale).** Here we show an example compact object binary, which is emitting GW signal and being detected by LISA, to illustrate the definition of angular parameters in Section 5.2.2. The coordinate system (X, Y, Z) is the non-rotating, comoving frame of the compact object binary, with the Z axis parallel to the orbital angular momentum vector and the X axis pointing in the direction of the (initial) pericenter. Θ, Φ represent the spherical polar angles of the source's orientation relative to the observer (i.e., the propagation direction of the GW signal viewed in the source's non-rotating, comoving frame). The coordinate system (x, y, z) is the comoving frame of the Sun, with θ, ϕ representing the sky location of the GW source. R is the distance between the compact binary system and the Sun. 142

5.3 **The dependence of a compact binary's parameter measurement error on its semi-major axis and eccentricity, computed using the Fisher matrix analysis (for 1-yr observation).** Here we show a BBH system with $m_1 = 15\ \mathrm{M}_\odot$, $m_2 = 10\ \mathrm{M}_\odot$, (i.e., $M = 25\ \mathrm{M}_\odot$, $q = 3/2$), placed at $R = 8$ kpc and observed for 1 yr with LISA. In this example, we set $\Phi = \Theta = \theta = \phi = \pi/4$ for simplicity and map the compact binary's relative parameter measurement error as a function of its initial semi-major axis a_0 and eccentricity $1 - e_0$ (see different colors in the figure). In each panel, the dashed lines represent equal signal-to-noise ratio contours (analytically calculated using Eq. 17 in Ref. (Xuan et al., 2024a)), with SNR = 8, 100, 1000 from right to left. We exclude the parameter space where the binary has an orbital period $T_{\rm orb} > 1\,\mathrm{yr}$ (since their GW signal is not repeated bursts during the observation), or has a short merger timescale $\tau_{\rm merger} < 100\,\mathrm{yr}$ (since these short-living systems may have negligible number expectation in future detection). We note that the Fisher matrix analysis is computed for ten parameters $(f_{\rm orb}, 1 - e_0, M, q, \cos\Theta, \Phi, \cos\theta, \phi, R, \psi)$, while here we only show nine of them. This is because the last parameter ψ, which represents the polarization angle of the GW beam relative to the observer, is less relevant to the astrophysical inference, and we put its estimation in the appendix to avoid clutter. Also, we convert the measurement accuracy of the source orientation, $\{\cos\Theta, \Phi\}$, and sky location, $\{\cos\theta, \phi\}$, into the major and minor axes of the sky error ellipsoids, $\{2A_s, 2B_s\}$, $\{2a_s, 2b_s\}$, respectively. See Appendix 5.7.3 for more details. Additionally, the green dotted lines in panel (e) of Figure 5.3 mark the parameter space that is later presented in Figure 5.4, for comparison.147

5.4 **The dependence of a compact binary's parameter measurement error on its initial pericenter distance, $r_p = a_0(1-e_0)$, and eccentricity e_0 (for 5-yr observation).** Here, we consider the same systems as in Figure 5.3, but re-parameterize the x-axis using $r_p = a_0(1-e_0)$ and zoom in to highlight the parameter space where we expect to detect most of the stellar mass bursting BBHs (Xuan et al., 2024a,b), i.e., SNR $\sim 8-1000$. Additionally, we changed the observation time from 1 year to 5 years to show an optimistic estimation of measurement accuracy (for the 1-year case, see Figure 5.7 in Appendix), and mark the parameter space of this figure with green dotted lines in panel (e) of Figure 5.3 for comparison purposes. 152

5.5 **An example of the intrinsic parameters of highly eccentric BBHs used in our mock LISA observation.** Here, we adopt the simulation result of the compact binary population in the Milky Way's nuclear star cluster (see Section 3.5 in Ref. (Xuan et al., 2024a)) and show the parameters of highly eccentric BBHs in black dots. The x-axis represents the binary's semi-major axis a, and the y-axis represents one minus the binary's eccentricity $(1-e)$. We estimate the overall signal-to-noise ratio of the BBH system during a 4-yr LISA observation, depicted in different colors. The dashed lines represent equal signal-to-noise ratio contours for SNR = 1000, 100, 8, and 1, from left to right. Here, the SNR is analytically calculated using Equation (5.4), assuming $m_1 = m_2 = 10$ $M_\odot$ and $R = 8$ kpc for simplicity. However, we note that the mass of BBHs in the mock data analysis is generated from the stellar evolution model and may slightly differ from ~ 10 $M_\odot$. Therefore, the numerical SNR is expected to vary slightly from the analytical calculation. For demonstration purposes, we enlarge the size of dots for the detectable BBH systems based on the SNR. 162

5.6 **The matched filtering output in the mock LISA data analysis of highly eccentric BBHs.** Here we fit the mock LISA data with different bursting GW templates and plot the optimal signal-to-noise ratio, $\mathrm{SNR_m}$, in different colors, as a function of $f_{\rm orb}$ and $1-e_0$ of the template (see Sections 5.2.2 and 5.4 for more details). Specifically, the optimal SNR is calculated numerically, using matched filtering as described in Section 5.4 (note that $\mathrm{SNR_m}$ represents the realistic fitting result, and is different from the analytical estimation of SNR in Equation (5.4) and Figures 5.3 - 8.3). *Left Panel* shows the fitting results for all the potential GW sources with an orbital frequency of $f_{\rm orb} \sim 4\times10^{-7} - 2\times10^{-5}$ Hz and eccentricity $e \sim 0.9 - 0.997$, while the *Right Panel* shows a zoom-in of the region near the parameters of a "real" GW source that appears in the mock data (i.e., the detection case). For demonstration purposes, we mark, in stars, the intrinsic parameters of the GW sources and highlight the region where we successfully fit these signals with high $\mathrm{SNR_m}$ (see the rectangular boxes in light blue). We note that, in some regions of *Left Panel*, numerical artifacts cause the fitted $\mathrm{SNR_m}$ to exceed the detection threshold of 8, while there are no astrophysical sources (see Section 5.4 for a more detailed discussion). 163

5.7 **The dependence of a compact binary's parameter measurement error on its initial pericenter distance, $r_p = a_0(1-e_0)$, and eccentricity e_0. (1-yr observation)** Here we consider the same systems as in Figure 5.3, but re-parameterize the x-axis using $r_p = a_0(1-e_0)$. We exclude the grey-colored region at the bottom of each panel since here the binary's orbital period is longer than the observation time (1 year). 184

5.8 **The dependence of a compact binary's polarization angle measurement error on its semi-major axis and eccentricity, computed using the Fisher matrix analysis. (1-yr observation)** Here we consider the same systems as in Figure 5.3, but show the result according to parameter ψ for completeness. 185

5.9 **Comparison between the analytical and numerical estimation of $f_{\rm orb}$ measurement error.** Here we consider the same systems as shown in Figure 5.3, but calculate the relative $f_{\rm orb}$ measurement error using Equation (5.18) (*Upper Panel*), and compare it with the numerical results from Fisher matrix analysis (*Bottom Panel*). As shown in the figure, the analytical approach provides an accurate estimation of $f_{\rm orb}$ measurement error in the moderate SNR region (i.e., close to the dashed line of SNR = 8). However, its performance is limited when the binary has a short merger timescale (to the bottom left of each panel) and becomes inconsistent with the Fisher matrix analysis. 186

6.1 **An example of simulated BBHs population in Milky Way GCs.** Here, we plot the orbital frequency and peak GW frequency of BBH systems from a single realization of our simulated Milky Way GCs (see Equation (7.2)). The SNR of each BBH, estimated analytically using Equation (7.33) for a 5-year LISA observation, is represented by different colors. Detectable BBHs, based on their SNR, are highlighted with enlarged dots. Dashed lines indicate the eccentricity of BBHs in different regions, with $e = 0.99, 0.97, 0.9, 0.7, 0.2, 0$, from left to right. The simulated BBHs have an average component mass of $m_1 = 15.56\ {\rm M}_\odot$, $m_2 = 15.21\ {\rm M}_\odot$ for in-cluster BBHs and $m_1 = 20.73\ {\rm M}_\odot$, $m_2 = 20.46\ {\rm M}_\odot$ for ejected BBHs, but the mass of individual systems may vary. . . 195

6.2 **Properties of Milky Way globular clusters likely to host detectable BBHs in the mHz GW band.** Here we adopt the simulation results of the BBH population in the Milky Way GCs, based on 10 realizations of in-cluster sources. The size of solid dots represents the expected probability for a cluster to host a BBH system with SNR > 1, $P(\mathrm{SNR} > 1)$, and the color represents the maximum SNR of detectable BBHs, assuming a 10-year observation. *Left Panel* plots the distance R (x-axis) against the ratio of the core radius to the half-light radius, r_c/r_h (y-axis); *Right Panel* plots the distance R (x-axis) against the estimated total mass $M_{\rm GC}$ of each globular cluster. The largest dot corresponds to the GC hosting 9 BBHs with SNR > 1 across the 10 realizations (i.e., an expected probability of $\sim 90\%$), while the smallest dots represent GCs hosting 1 BBH system with SNR > 1 (expected probability $\sim 10\%$). Solid blue dots represent GCs with no detectable BBHs (maximum SNR < 1), and hollow gray dots represent GCs without any BBHs in the simulation. We highlight the names of the top 8 GCs most likely to host detectable BBHs. 198

6.3 **The population of BBHs from simulated Milky Way GCs, and their estimated parameter measurement error as a function of semi-major axis and eccentricity (for 5-yr observation).** Here, we adopt the simulation result of the compact binary population in the Milky Way globular clusters (see Section 8.2, note that here we show a single realization of the in-cluster and ejected BBHs from Milky Way GCs), and plot the semi-major axis and eccentricity (as $1-e$) of each BBH system (see the white stars). The background color maps the compact binary's parameter measurement error, for the orbital frequency ($\delta f_{\rm orb}/f_{\rm orb}$, *Panel a*), eccentricity ($\delta e/e$, *Panel b*), total mass ($\delta M/M$, *Panel c*), and sky location (major axis of sky error ellipsoid, $2a_s$, *Panel d*). We note that, in reality, the BBHs can have different mass, inclination, and sky locations, which affects their parameter measurement. However, for simplicity, here we assume a fixed intrinsic parameter of $m_1 = 10\ {\rm M}_\odot$, $m_2 = 15\ {\rm M}_\odot$, $R = 8$ kpc and $\Phi = \Theta = \theta = \phi = \psi = \pi/4$ when estimating the Fisher matrix and mapping the parameter measurement accuracy. In each panel, the dashed lines represent equal signal-to-noise ratio contours (analytically calculated using Equation (7.33)), with SNR = 1, 5, 20, 100 from right to left. We exclude the parameter space where the binary has a pericenter distance smaller than $a(1-e) < 2\times10^{-3}\,{\rm au}$, since they have a short merger timescale and negligible number expectation in our simulation. 203

6.4 **Parameter Measurement error of the detectable BBHs in simulated Milky Way GCs, estimated using Fisher matrix analysis.** Here we adopt the simulation results of BBHs population in Milky Way GCs, with a total of 10 realizations. Each point in the figure represents a BBH system in the simulation, with the color showing the SNR of its GW signal (assuming a 5-year observation) and the shape showing the eccentricity of the orbit ($e > 0.7$, plotted in triangles; $e < 0.7$, plotted in circles). *Upper Panel* shows the relative error of orbital frequency and eccentricity measurement. *Middle Panel* shows the relative error of total mass and mass ratio measurement. In *Bottom Panel*, we show the absolute error of the BBHs' distance measurement (x-axis), and their sky localization accuracy (as the major axis of the sky error ellipsoids, $2a_s$, on the y-axis). We exclude the parameter space where measurement accuracy is insufficient to help with the astrophysical interpretation, as marked using grey-shaded regions. 206

6.5 **Parameter Measurement error of an example BBH system in Milky Way Globular Clusters, estimated using Bayesian analysis (for 5-yr observation).** Here we consider a BBH system with $m_1 = 23.3\ \mathrm{M}_\odot$, $m_2 = 18.6\ \mathrm{M}_\odot$, $f_{\rm orb} = 1.2877164 \times 10^{-5}$ Hz, $e = 0.897$, $R = 4.9$ kpc, $\Phi = 158.7°$, $\Theta = 141.4°$, $\phi = 219.9°$, $\theta = 125.2°$, $\psi = 153.9°$. (Note that this system has SNR ~ 77, and we keep 8 significant digits of $f_{\rm orb}$ to highlight its realistic measurement accuracy.) The color maps show the marginal posterior density of the binary's observed parameters, assuming a flat, 10-dimensional hyperrectangular prior and stationary Gaussian LISA noise. We use the star in each panel to indicate the system's intrinsic parameters, and plot 68%, 95%, and 99.7% credible regions for the marginal posterior densities (i.e, $1-3\,\sigma$ level sets defined analogously to a bivariate Gaussian density). To avoid clutter, we plot the results for the binary's intrinsic parameters $f_{\rm orb}$, e, M; distance R; and sky location ϕ, θ, which are mostly relevant to its astrophysical inference. Additionally, the peak of posterior density exhibits a small offset from some parameters' intrinsic value (typically within 1σ level), which is caused by the random fluctuation of time-domain LISA noise and the limit of numerical accuracy for highly eccentric binary waveforms. 208

6.6 **Histogram of Milky Way GC angular diameters and their hosted BBH counts.** Here we show the distribution of GC angular diameters (left), taken from the Milky Way Star Clusters Catalog (Kharchenko et al., 2012, 2013; Schmeja et al., 2014; Scholz et al., 2015), and the number of hosted BBH systems with SNR > 1 in each GC diameter bin (right), based on 10 realizations from the `CMC Cluster Catalog`. The difference between the left and right panels arises because detectable BBH systems tend to be hosted by more massive and nearby GCs, which also have a larger angular size. 219

6.7 **Parameter Measurement error of an example BBH system in Milky Way Globular Clusters.** Here we adopt the same method as Figure 6.5, but consider a different BBH system with $m_1 = 17.6$ $M_\odot$, $m_2 = 16.5$ $M_\odot$, $f_{\rm orb} = 1.572852 \times 10^{-6}$ Hz, $e = 0.9668$, $R = 10$ kpc, $\Phi = 329.2°$, $\Theta = 64.5°$, $\phi = 341.4°$, $\theta = 149.8°$, $\psi = 14.8°$ (SNR ~ 9). 220

7.1 **GW waveforms and corresponding characteristic strains for BBHs with different eccentricities.** We show the GW signals (plus polarization) from BBH systems with $m_1 = 25$ $M_\odot$, $m_2 = 20$ $M_\odot$, placed at 8 kpc and observed for 0.5 yrs. Blue curves represent a highly eccentric BBH with $f_{\rm orb} = 2 \times 10^{-5}$ Hz, $e = 0.9$, Red curves represent a quasi-circular BBH with $f_{\rm orb} = 3 \times 10^{-4}$ Hz, $e = 10^{-6}$. These parameters are chosen such that both BBHs will have SNR ~ 120 for a 0.5-year observation. *Upper Panel* shows a zoom-in view of their time-domain waveforms, $h(t)$; *Bottom Panel* shows their characteristic strains (*numerical spectrum*, $h_{\rm c,num}$, see Appendix 7.8.1.3 for details), compared with the LISA noise curve ($\sqrt{fS_n(f)}$, black line). The signals are numerically generated using a post-Newtonian waveform model (see Section 7.5). 229

7.2 **Comparison of three different characteristic strain representations for the same eccentric BBH source.** The plot displays the individual harmonic representation ($h_{c,n}$, scatter points), the smoothed spectrum representation ($h_{\rm c,env}$, solid envelope), and the numerical spectrum representation ($h_{\rm c,num}$, oscillatory curve) for the characteristic strain of a BBH system with $m_1 = 15M_\odot$, $m_2 = 10M_\odot$, $f_{\rm orb} = 10^{-5}$ Hz, $e = 0.95$, $T_{\rm obs} = 0.5$ yr, and $D_l = 8$ kpc. In the non-evolving limit ($\dot{f} \to 0$), the peak heights of the numerical spectrum coincide with the individual harmonics, and differ from the smoothed spectrum envelope by a factor of $\sqrt{f_{\rm orb}/f}$. This system has an overall SNR of ~ 60. 234

7.3 **Dynamically-formed BBHs in a mock realization of the Milky Way.** We plot the orbital parameter distribution $(a, 1-e)$ of simulated BBHs in a mock realization of the Milky Way. Different formation channels are indicated by marker shapes: Galactic nucleus (GN; stars), globular clusters (GC; circles), and the Galactic field (triangles). Marker colors and sizes represent the expected GW signal-to-noise ratio, assuming a 4-year LISA observation. Diagonal dashed and dotted lines show contours of constant merger timescale ($t_{\rm merger} = 10^{10}, 10^{7}$, and $10^{4}\,{\rm yr}$) for an example BBH mass of $10\,M_\odot + 10\,M_\odot$. We further illustrate the evolutionary pathways using arrows. In particular, dynamical perturbations excite eccentricity (blue arrow) until GW emission becomes strong enough to decouple the system from the environment ($t_{\rm merger} \sim 10^{4} - 10^{10}\,{\rm yr}$), which further shrinks and circularizes the orbit (purple arrow). We note that a cutoff at $a = 100\,{\rm au}$ is artificially imposed on the wide field population for conservative purposes. In addition, most of the detectable BBH systems cluster near the $t_{\rm merger} \sim 10^{7}\,{\rm yr}$ contour, which is because contours of constant signal-to-noise ratio (e.g., SNR = 8) are approximately parallel to those of constant $t_{\rm merger}$ in this regime, see Sections 7.3.1 and 7.3.2 for details. 241

7.4 **Orbital parameter distributions of simulated Milky Way BBHs across different dynamical formation channels.** The four columns correspond to the Galactic Field, Galactic Nuclei, GC In-cluster, and GC Ejected BBH population, respectively. *Top panels* show the 2D probability density distributions in the a and $1-e$ plane, for systems with SNR > 0.1 for a 4-yr LISA observation. The top and right sub-panels show the marginalized 1D probability density projections ($\mathrm{d}P/\mathrm{d}\log a$ and $\mathrm{d}P/\mathrm{d}\log(1-e)$). Vertical and horizontal lines indicate the 50% (red solid), 10% and 90% (blue dashed), and 1% and 99% (green dash-dotted) percentiles of the distributions. *Bottom panels* show zoomed-in views of the regions containing the SNR > 0.1 populations, with the semi-transparent grey squares representing the underlying background population. Note that this figure assumes a local Milky Way snapshot. For populations at larger cosmological distances, the observable distribution would shift toward the upper-left region of the parameter space. 244

7.5 **Expected number of dynamically-formed Milky Way BBHs in each SNR bin.** The histograms display the differential probability distribution $\mathrm{d}P/\mathrm{d}\log(\mathrm{SNR})$ for all the simulated systems with an expected SNR > 0.1 in a 4-yr LISA observation. Vertical lines denote the 50% (red solid), top 10% (blue dashed), and top 1% (green dash-dotted) percentiles of the population in SNR distribution. The shaded region marks systems below the nominal detectability threshold, SNR < 8, while the unshaded region corresponds to detectable sources. The black dashed lines illustrate the analytically derived power-law scaling, for comparison. Notably, the highly eccentric Field population follows a shallower slope ($\sim \mathrm{SNR}^{-2/3}$), whereas the GN and GC populations exhibit a steeper slope ($\sim \mathrm{SNR}^{-0.93}$). For a detailed analysis of these power-law dependencies, see Section 7.3.2. 246

7.6 **Eccentricity distribution of dynamically-formed BBHs in the LIGO band.** The plot compares the cumulative distribution functions (CDFs) of eccentricities at $f_{\rm GW} = 10\,{\rm Hz}$, for BBH mergers formed via Galactic Field fly-bys (black dot-dashed line), Galactic Nucleus EKL-driven mergers (red dashed line), and two Globular Cluster populations (in-cluster mergers as the teal dotted line, and ejected mergers as the blue dotted line). The GC distributions are adapted from Martinez et al. (2020). The in-cluster GC curve shown here combines contributions from the KL and non-KL triple channels, few-body and single-single capture channels, and the in-cluster binary channel, following their fig. 4. This figure provides a unified comparison of the eccentricity distributions of dynamically formed BBHs at the final merger stage, combining previously published GC results with new predictions for the eccentricity distribution of Galactic Field fly-by and Galactic Nucleus EKL-induced merger channels. 250

7.7 **Orbital properties and number of mHz eccentric BBHs at different luminosity distances.** All panels assume a 4-year LISA observation and a SNR threshold of 8. The *bottom-left panel* shows the 2D probability density distribution of the detectable dynamically-formed BBH population in the a – $(1-e)$ parameter space. Overlaid contours indicate the 99% percentiles for populations placed at different luminosity distances: 10 kpc (blue dotted), 765 kpc (green dashed), 10 Mpc (purple dot-dashed), and 100 Mpc (red solid). The *top-left* and *center vertical* panels display the corresponding 1D marginal distributions for the semi-major axis ($\mathrm{d}P/\mathrm{d}\log a$) and eccentricity ($\mathrm{d}P/\mathrm{d}\log(1-e)$), respectively. The *top-right panel* illustrates the cumulative number of expected BBHs as a function of distance, starting from the Milky Way local contribution to the extragalactic population. The *bottom-right panel* presents the 1-D eccentricity distribution (10% to 90% percentiles, with black median ticks) at different D_l, with highlighted color bars directly matching the populations in the left panels. The vertical orange dot-dashed line across the right panels marks the maximum detectable distance ($D_{l,\mathrm{max}} \sim 1\,\mathrm{Gpc}$) for a fiducial binary mass of $100 + 100\,M_\odot$. As distance increases, the observable BBH population systematically shifts toward tighter and more circular orbits due to the selection effect. 251

7.8 **Individual GW harmonics of dynamically-formed BBHs in one realization of the Milky Way.** The plot shows the characteristic strain for dynamically-formed BBHs in a single realization of the Milky Way (*individual harmonic representation* $h_{c,n}$, see Equation 7.8). The red markers highlight GW harmonics that have an individual SNR > 5. The blue points represent the background harmonics from all GW sources with a total SNR ≥ 0.1 for a 4-yr LISA observation, and the yellow points represent BBHs with total SNR (summing over all harmonics) greater than 8, but individual harmonic SNR smaller than 5. For comparison, we also plotted the Galactic double white dwarf population (grey point, see, e.g., Lamberts et al., 2018) and extra-galactic circular BBHs (green curves, see, e.g., Amaro-Seoane et al., 2022). 255

7.9 **Distribution of individual GW harmonics in each SNR bin, for BBHs in the Milky Way.** The histogram displays the average number of individual GW harmonics per Milky Way realization as a function of their single-harmonic SNR. The purple bars represent the expected count of harmonics within each log-uniform SNR bin, derived by averaging over 100 realizations of the Galactic population. The shaded region marks harmonics below the nominal detectability threshold, SNR < 8, while the unshaded region corresponds to detectable harmonics. The distribution highlights the relative abundance of sub-threshold harmonics versus individually resolvable harmonics for a 4-yr LISA observation. 257

7.10 **Apparent chirp mass bias for highly eccentric sources.** The curve demonstrates the ratio of the inferred apparent chirp mass $\mathcal{M}_c'$ to the true chirp mass $\mathcal{M}_{c,0}$ when the peak radiating harmonic of an eccentric binary is mistakenly fitted with a quasi-circular waveform template. As the eccentricity approaches unity, the apparent mass significantly underestimates the true system mass. 260

7.11 **Characteristic strain spectrum and collective GW background of highly eccentric BBHs in the Milky Way.** The plot shows the characteristic strain for BBH sources with $e > 0.9$ in the Milky Way (*smoothed spectrum representation* $h_{c,\mathrm{env}}$, see Equation 7.9). The thin blue curves represent the characteristic strains of dynamically formed BBHs, compiled from 50 realizations of our mock Galactic catalog, assuming a 4-year LISA observation. The thick red dashed curve illustrates the average stochastic GW background produced by this highly eccentric subpopulation in a single MW realization, calculated following eq.19 in Xuan et al. (2024b). For reference, the solid black curve denotes the nominal LISA instrumental noise. 261

7.12 **Parameter spaces for post-Newtonian waveforms to converge well in eccentric GW data analysis.** The colormaps show the critical signal-to-noise ratio (SNR_c) required to distinguish between waveforms generated using 2PN and 3PN expansions over a 1-year observation, computed numerically using waveform fitting methods (Equation 7.24). The red hatched regions ("Poor PN convergence") indicate parameter spaces where the PN expansion may break down ($\mathrm{SNR}_c \lesssim 100$), making it inadequate for data analysis (see also Khalil et al., 2022, note that their fig.1 compares PN with PM expansion, whereas we focus on the *intrinsic* convergence of PN expansion.). *Left Panel:* SNR_c as a function of periastron distance r_p and eccentricity e for a fixed binary mass of $20 + 25\,M_\odot$. The horizontal dashed lines mark constant GW peak frequencies of 1 mHz and 10 mHz. As shown, PN waveforms are highly accurate for stellar-mass systems with high eccentricities, provided $f_\mathrm{GW} \lesssim 10\,\mathrm{mHz}$. *Right Panel:* SNR_c as a function of f_GW and total mass M, assuming an equal-mass binary with $e = 0.9$. The solid gray region is excluded because the periastron distance falls below the innermost stable circular orbit ($r_\mathrm{p} < r_\mathrm{ISCO}$, in which $r_\mathrm{ISCO} = 6M$ for a Schwarzschild BH). It demonstrates that as total mass increases, PN waveforms can only converge at lower frequencies for mHz GW data analysis. 263

7.13 **Regime of validity for PN waveforms with different binary orbital frequencies, eccentricities, and masses.** We plot the boundary of parameter space where 2PN and 3PN waveforms converge well in data analysis ($\mathcal{O}(h_{\rm 2PN}, h_{\rm 3PN}) > 0.9995$, corresponding to $\mathrm{SNR}_c > 100$) over a 1-year LISA observation. *Left Panel* shows the boundaries for equal-mass binaries ranging from $1.4{+}1.4\,M_\odot$ to $5000{+}5000\,M_\odot$. *Right Panel* shows unequal-mass systems ranging from $1 + 10\,M_\odot$ to $10 + 10^5\,M_\odot$. For a given mass, the region to the upper-left of the dashed contour, as indicated by the dark grey arrow, represents the high-accuracy regime where the PN waveforms are safe to use. The green shaded area represents the LISA sensitive band (0.1 mHz – 0.1 Hz). We note that the minor "wiggles" along the contours are computational artifacts caused by numerical fluctuations and the discrete parameter grid sampling in the overlap integrals (see Equation 7.19). 267

7.14 **Comparison between different SNR calculation methods.** Here we compute the analytical SNR approximation, $\mathrm{SNR}_{\rm approx}$, Equation (8.19), and the strictly computed SNR, $\mathrm{SNR}_{\rm strict}$, Equation (7.35) for a $10{+}10\,M_\odot$ binary with different orbital parameters. *Left panel:* The numerical ratio of $\mathrm{SNR}_{\rm approx}$ to $\mathrm{SNR}_{\rm strict}$. The green region highlights where the ratio is close to unity. *Right panel:* The relative deviation percentage between the two calculations. The region bounded by the white dashed lines represents the LISA sensitivity band (0.1 mHz to 10 mHz). Within this band, the analytical approximation is consistent with the strict calculation, with the relative deviation generally below 60%. 279

8.1 **Comparison between the energy transfer rate of dynamical tides and GW radiation, for a highly eccentric BH–WD system.** Here we consider a 10–0.6 $M_\odot$ BH–WD binary with $e = 0.95$, WD radius $R_2 = 5.3 \times 10^{-5}$ au, and WD dimensionless tidal torque $\hat{F}(\omega) \sim 150\omega^5$. The energy transfer rates from WD dynamical tides and from GW radiation are plotted as functions of the binary's pericenter distance r_p. We show two cases for dynamical tides: the zero-spin case (red solid line, fixing $\Omega_s = 0$) and the synchronized-spin case (blue dashed line, when Ω_s synchronizes with pericenter frequency and satisfies $\dot{J}_{\rm tide} = 0$). The energy loss due to GW radiation is shown as the grey dash-dotted line. We note that when eccentricity is nonzero, there will be a residual tidal heating rate (blue dashed line) even when there is no net torque on the WD. This rate will vanish in the circular limit. . . . 298

8.2 **Time evolution of an example BH-WD system that undergoes strong EKL oscillations during the dynamical formation stage (left column) and transitions into a mass-transferring UCXB (right column).** Here we show the time evolution of a representative BH-WD system from our simulation, with initial mass $m_1 = 10$ $M_\odot$, $m_2 = 0.6$ $M_\odot$, orbit separation $a_0 = 95.3$ au, eccentricity $e_0 = 0.199$. This binary is orbited by a tertiary companion with mass $m_3 = 0.836$ $M_\odot$, outer orbit separation $a_2 = 4997$ au, eccentricity $e_2 = 0.602$, and mutual inclination $i = 91.8°$ to the inner binary. We define t_c as the time when the BH–WD binary becomes fully circularized ($e < 0.01$). The system's evolution during the dynamical formation stage is shown in the left column as a function of $t_c - t$ (log-scale), while its post-circularization evolution is shown in the right column as a function of $t - t_c$. The first row shows the inner binary's orbital eccentricity, as $1-e$. The second row shows the inner orbital separation (red solid line, a), the WD–BH mass ratio (blue dash-dotted line, m_2/m_1), the Roche lobe radius (black dashed line, $R_{\rm lobe}$, see, e.g., eq.28 in Ye et al. (2023)), and the WD radius (black dotted line, R_2). The third row plots two ratios: the tidal energy dissipation rate (red solid line, see Equation (8.4)) to the GW radiation power (see, e.g., eq. 5.4 in Peters (1964)), and the WD spin angular frequency Ω_s to the binary's pericenter frequency $\Omega_p = \Omega(1-e)^{-3/2}$ (blue dash-dotted line). The bottom row shows the expected gravitational wave SNR at distance $D_l = 8$ kpc (red solid line) for a 4-year LISA observation, and the binary's X-ray luminosity L_X (blue dash-dotted line), normalized by 0.1% of the BH Eddington luminosity, $L_0 = 10^{-3} L_{\rm Edd} \sim 1.26 \times 10^{36}$erg s^{-1}. 300

8.3 **The population of BH-WD systems from simulated Milky Way Galactic field, and their estimated GW SNR as a function of semi-major axis and eccentricity (for a 4-yr LISA observation).** Here, we plot the semi-major axis, a, and eccentricity, as $1-e$, of each simulated BH-WD system (see the white stars). The *Left Panel* shows the initial conditions, while the *Right Panel* represents the final state of each system, either when its dynamical evolution ends at the Hubble time or when the orbit separation shrinks to $\lesssim 10^{-3}$ au and triggers the mass transfer. The background color maps the binary's expected gravitational wave SNR, assuming a fixed distance $D_l = 8$ kpc and a 4-yr LISA observation. In the *Right Panel*, we also plot intermediate evolutionary stages (pink dots) for binaries that eventually evolve into UCXBs. These dots represent the evolution track of UCXBs formed via the wide triple channel, and highlight the region of parameter space where they may become detectable. 305

8.4 **Parameters of detached BH-WD systems in triples after main sequence evolution.** Here we plot the semimajor axis of inner (a_1) and outer orbits (a_2) for the BH–WD binaries and their tertiary companions, immediately after the inner binary has evolved into a BH–WD configuration. Red circles represent all systems, while blue triangles indicate those that later form UCXBs in our simulations. The dashed line indicates $a_2/a_1 = 1$. 317

8.5 **Comparison between tidal angular momentum and energy transfer rate, $\dot{J}_{\rm tide}$ and $\dot{E}_{\rm tide}$, as functions of the WD spin.** Here we consider a $10-0.6$ M$_\odot$ BH-WD system with $e = 0.9$, $r_p = 3\times10^{-3}$ au, $\hat{F}(\omega) = 150\omega^5$, and plot $\dot{J}_{\rm tide}$ and $\dot{E}_{\rm tide}$ as functions of the ratio between the WD spin angular frequency, Ω_s, and orbital pericenter frequency, Ω_p. 320

8.6 **The X-ray detectable time of a representative UCXB source, as a function of its distance.** Here we consider a mass-transferring BH-WD system with initial mass $m_1 = 10$ $M_\odot$, $m_2 = 0.6$ $M_\odot$, and computed its total detectable lifetime in X-ray, assuming a detector sensitivity of $F_{\rm X,crit} = 10^{-15}$, 10^{-14}, 10^{-13} erg cm^{-2} s^{-1}, respectively (from left to right). 323

LIST OF TABLES

Page

6.1 Sky location and distance measurement accuracy of representative systems in the mock Milky Way GC catalog, compared with their host cluster size (5-yr observation) 219

7.1 Typical Orbital Parameters and Lifetimes of Dynamically-Formed, Stellar-mass BBHs at Different Evolutionary Stages 236

7.2 Expected Number of Dynamically-formed BBHs in the MW, for Different SNR Thresholds. 239

ACKNOWLEDGMENTS

First and foremost, I am deeply grateful to my PhD advisor, Smadar Naoz. Smadar, you guided me through my most difficult days as an international student navigating a new country during the pandemic. Over the past five years at UCLA, your patience and support have helped me grow into an independent scientist. Beyond specific research skills, I have learned from you a profound passion for academia and teaching, a broad curiosity across diverse fields, and a rigorous, grounded approach to research. Thank you for setting such an inspiring standard of excellence, and for giving me the confidence to reach for it.

This thesis has also benefited from the support and collaboration of many researchers. I am especially grateful to Bence Kocsis, Kyle Kremer, Erez Michaely, Xian Chen, Cheyanne Shariat, Alvin K.Y. Li, Erik Petigura, Alan M. Knee, Jess McIver, Michael L. Katz, and Will M. Farr for the many helpful conversations and suggestions they provided throughout these projects. Over the years, I have also been fortunate to interact with many other researchers who deeply influenced me. Even without direct collaboration, the discussions, encouragement, and perspectives you shared have shaped both my scientific work and the way I think about research.

Throughout my PhD journey, I have been especially grateful for the support of my girlfriend. Despite the miles that often separated us, your understanding, encouragement, and constant presence have been my greatest source of strength and motivation. I am also thankful to my family and to the incredible friends who walked alongside me in the US. Your companionship and encouragement ensured this journey was never lonely. Lastly, thank you to everyone in Smadar's group, for the memorable moments we experienced as a team.

This dissertation incorporates material from previously published articles. Chapters 2, 3, and 4 are reprinted from Physical Review D (Xuan et al., 2023, 2024b, 2025b), with permission from the American Physical Society (© 2023–2025). Chapters 5, 6, and 7 are reprinted

from The Astrophysical Journal and The Astrophysical Journal Letters (Xuan et al., 2024a, 2025a,c), with permission from the American Astronomical Society (© 2024–2025).

This work is supported by the UCLA Graduate Division Dissertation Year Fellowship, the Mani L. Bhaumik Graduate Fellowship in Theoretical Physics, and the UCLA Hoffman2 Cluster.

VITA

Zeyuan Xuan

EDUCATION

M.S. – Physics **2021-2022**

University of California, Los Angeles *Los Angeles, CA*

B.S. – Physics **2017-2021**

Peking University *Beijing, China*

ACADEMIC EXPERIENCE

Graduate Student Researcher **2022–2026**

University of California, Los Angeles *Los Angeles, CA*

Teaching Assistant **2021–2026**

University of California, Los Angeles *Los Angeles, CA*

HONORS AND AWARDS

Dissertation Year Award **2025-2026**

University of California, Los Angeles

Raynor L. Duncombe Student Research Prize **2025**

American Astronomical Society, Division on Dynamical Astronomy

Mani L. Bhaumik Fellowship in Theoretical Physics **2022–2025**

University of California, Los Angeles

PUBLICATIONS

1. Xuan, Z., Naoz, S., Kremer, K., Katz, M. L., Kocsis, B., and Michaely, E. (2026). Eccentric Stellar-mass Binary Black Holes: Population, Detectability, and Waveform Analysis in the LISA and LIGO Era. *arXiv:2605.15265*

2. Xuan, Z., Shariat, C., and Naoz, S. (2025c). From Wide Triples to Ultracompact X-ray Binaries: Multimessenger Signatures of Dynamically Formed Black Hole-White Dwarf Systems in the LISA Band. *ApJ*, 995(1):27

3. Xuan, Z., Kremer, K., and Naoz, S. (2025a). Localizing Dynamically Formed Black Hole Binaries in Milky Way Globular Clusters with LISA. *ApJ Lett.*, 985(2):L42

4. Xuan, Z., Naoz, S., Li, A. K. Y., Kocsis, B., Petigura, E., Knee, A. M., McIver, J., Kremer, K., and Farr, W. M. (2025b). Extracting astrophysical information of highly eccentric binaries in the millihertz gravitational wave band. *Phys. Rev. D*, 111(4):043018

5. Xuan, Z., Naoz, S., Kocsis, B., and Michaely, E. (2024b). Stochastic gravitational wave background from highly-eccentric stellar-mass binaries in the millihertz band. *Phys. Rev. D*, 110(2):023020

6. Xuan, Z., Naoz, S., Kocsis, B., and Michaely, E. (2024a). Detecting Gravitational Wave Bursts from Stellar-mass Binaries in the mHz Band. *ApJ*, 965(2):148

7. Xuan, Z., Naoz, S., and Chen, X. (2023). Detecting accelerating eccentric binaries in the LISA band. *Phys. Rev. D*, 107(4):043009

8. Xuan, Z., Peng, P., and Chen, X. (2021). Degeneracy between mass and peculiar acceleration for the double white dwarfs in the LISA band. *MNRAS*, 502(3):4199–4209

9. Chen, X., Xuan, Z.-Y., and Peng, P. (2020a). Fake Massive Black Holes in the Milli-Hertz Gravitational-wave Band. *ApJ*, 896(2):171

10. Sharpe, C., Ginat, Y. B., Xuan, Z., and Kocsis, B. (2026). Resonant locking between binary systems induced by gravitational waves. *Phys. Rev. D*, 113(2):023040

11. Torres-Orjuela, A., Amaro Seoane, P., Xuan, Z., Chua, A. J. K., Rosell, M. J. B., and Chen, X. (2021). Exciting Modes due to the Aberration of Gravitational Waves: Measurability for Extreme-Mass-Ratio Inspirals. *Phys. Rev. Lett.*, 127(4):041102

Chapter 1

Introduction

The detection of gravitational waves (GWs) by the LIGO/Virgo/KAGRA (LVK) collaboration has opened a new observational window beyond traditional electromagnetic astronomy (see, e.g., Abbott et al., 2016; The LIGO Scientific Collaboration et al., 2021; Abbott et al., 2023a). Most GW sources detected to date originate from compact object binaries composed of black holes (BHs) or neutron stars (NSs), which form through the evolution of massive stars. As two compact objects orbit each other, they generate gravitational waves that carry away orbital energy and angular momentum, causing the binary to inspiral and eventually merge. The LVK collaboration has observed hundreds of compact object sources in the high-frequency band ($\sim$ 100 Hz), corresponding to the late inspiral phase shortly before merger. However, most observed systems show no evidence of orbital eccentricity (e.g., Abbott et al., 2019, 2021; Abbott et al., 2023a), primarily because gravitational wave radiation efficiently circularizes the orbit, rendering eccentricity negligible at these late stages (see, e.g., Peters, 1964; Lenon et al., 2020; Romero-Shaw et al., 2020; Zevin et al., 2021; Gayathri et al., 2022).

In contrast, space-borne detectors such as LISA, TianQin, and Taiji will probe the mHz GW band (see, e.g., Amaro-Seoane et al., 2023; Luo et al., 2016; Ruan et al., 2020). Due

to their sensitivity to lower-frequency GWs, these observatories will access compact binaries at earlier evolutionary stages, before significant circularization has occurred. As a result, a large population of eccentric GW sources is expected to populate the mHz data stream.

The study of GW signals from eccentric compact object binaries plays an important role in GW astronomy and provides valuable insights into their formation channels and surrounding environments. Broadly, compact binary formation channels fall into two major categories: *isolated* and *dynamical*. In the isolated channel, binaries are born in proximity during their main-sequence stage and subsequently evolve through complex phases such as mass transfer and common-envelope (see, e.g., Mandel and de Mink, 2016; Mandel and Broekgaarden, 2022). A fraction of these systems survive as close compact object binaries, which further inspiral under gravitational wave emission and eventually merge. Due to strong tidal interactions and long-term orbital shrinkage, binaries formed via isolated channels are expected to be fully circularized by the time they enter the mHz GW band (Broekgaarden and Berger, 2021). In contrast, eccentric GW sources are primarily expected to form through dynamical channels, which involve environmental perturbations, such as scatterings, flybys, and three-body interactions, that bring initially distant compact objects into proximity. These close encounters significantly enhance the binary's GW emission, rapidly dissipating orbital energy until the system merges. For example, BBHs assembled dynamically in star clusters can undergo frequent external perturbations, including scatterings and GW captures (O'Leary et al., 2009a; Kocsis and Levin, 2012; Breivik et al., 2016; Rodriguez et al., 2016; D'Orazio and Samsing, 2018), which efficiently excite their orbital eccentricities and lead to eccentric mergers (Kremer et al., 2019b; Zevin et al., 2019; Samsing et al., 2019; Martinez et al., 2020; Antonini and Gieles, 2020; Winter-Granić et al., 2023; Xuan et al., 2025a). BBHs in hierarchical triple systems, particularly those near supermassive black holes (SMBH) in galactic nuclei, can undergo significant eccentricity oscillations driven by the eccentric Kozai-Lidov (EKL) mechanism (Kozai, 1962; Lidov, 1962; Naoz, 2016), potentially leading to observable mergers (Hoang et al., 2018; Stephan et al., 2019; Randall and Xianyu, 2019b; Bub and

Petrovich, 2020; Deme et al., 2020; Wang et al., 2021; Xuan et al., 2024a; Knee et al., 2024; Grishin et al., 2017). In addition, fly-by interactions and galactic tides in the field (e.g., Michaely and Perets, 2019, 2020; Michaely and Naoz, 2022; Stegmann et al., 2024), as well as interactions within active galactic nucleus (AGN) accretion disks (Tagawa et al., 2021; Peng and Chen, 2021; Samsing et al., 2022; Muñoz et al., 2022; Gautham Bhaskar et al., 2023), can also provide significant contributions to the population of eccentric mHz GW sources. Because different formation channels produce distinct eccentricity distributions, observations of eccentric GW sources will play a crucial role in distinguishing between competing formation scenarios and in constraining the evolutionary histories of compact object binaries.

Despite these astrophysical implications, research on eccentric GW data analysis and source demographics remains limited, primarily due to the complexity of highly eccentric waveforms and the uncertainties in their underlying population models. In the highly eccentric regime, GW emission is dominated by radiation near pericenter, where the orbital separation $r_p = a(1-e)$ becomes small (Peters, 1964). As a result, the signal takes the form of repeated, short-duration bursts (Kocsis and Levin, 2012; Tai et al., 2014; Loutrel and Yunes, 2017; Loutrel, 2020; Romero-Shaw et al., 2023; Xuan et al., 2024a, 2025b). These burst-like morphologies are qualitatively different from the continuous quasi-circular inspirals targeted by standard GW search pipelines. Consequently, quasi-circular templates are both morphologically mismatched and computationally inefficient for detecting such signals, potentially limiting future observational sensitivity Xuan et al. (2025b). Moreover, current LVK observations provide limited constraints on the progenitor population of eccentric mergers, since most systems circularize before entering the LIGO band. This observational limitation underscores the need for a fully self-consistent simulation framework capable of predicting the properties of eccentric GW sources across different formation channels.

Motivated by these challenges, this thesis develops a set of complementary approaches to

characterize the population, detectability, and parameter inference of eccentric compact binaries in the mHz GW band. Combining numerical simulations of compact object dynamics with observational constraints and waveform modeling, I demonstrate that highly eccentric binaries can make a dominant contribution to the mHz GW source population in the local Universe (Xuan et al., 2024a). At the level of individual sources, I perform mock data analyses based on realistic eccentric waveforms and develop robust strategies for identifying their repeated-burst GW signals in noisy data (Xuan et al., 2025b). These analyses show that eccentricity can significantly improve binary parameter estimation (Xuan et al., 2023, 2025a), providing accurate probes of the dynamical environments in which these systems form. At the population level, I show that unresolved eccentric binaries generate a substantial stochastic gravitational-wave background in the mHz band (Xuan et al., 2024b). In addition, certain evolutionary channels produce multimessenger counterparts, including ultracompact X-ray binaries (UCXBs), thereby linking gravitational-wave and electromagnetic observations within a unified dynamical framework (Xuan et al., 2025c).

This thesis is organized as follows. Chapter 2 demonstrates the advantages of eccentric gravitational wave signals in source parameter estimation, showing that general relativistic pericenter precession of an eccentric GW source can break degeneracies in GW waveform analysis, improving the measurement accuracy of a binary's peculiar acceleration by one to two orders of magnitude. Chapter 3 initiates a series of studies focused on highly eccentric systems, predicting the detectability of stellar-mass binaries in the mHz gravitational wave band, and showing that their long lifetimes lead to a substantial, detectable population in the local Universe. Chapters 4 and 5 address the observational consequences of these highly eccentric GW signals. In particular, Chapter 4 shows that the superposition of unresolved eccentric sources can generate a stochastic GW background that significantly contributes to the LISA noise. Chapter 5 shows that individual bursting signals can be realistically extracted and used to recover accurate orbital parameters. Moving toward astrophysical applications, Chapter 6 studies the spatial distribution of dynamically formed

BBHs in Milky Way globular clusters using N-body simulations, demonstrating that high-SNR eccentric sources can be localized to specific angular regions on the sky, allowing for direct association with their host clusters and providing observational tests of cluster-driven formation channels. Chapter 7 synthesizes the results in Chapters 2 - 6, and extends the eccentric GW source modeling to cosmological distances. It also presents a ready-to-use mock catalog and introduces the open-source waveform and population analysis package (`LEAP`, https://github.com/zeyuanxuan/lisa-leap/), enabling the incorporation of eccentric GW signals into LISA global-fit analyses. Finally, Chapter 8 extends the scope to multi-messenger sources, showing that wide black hole–white dwarf (BH–WD) triples can undergo eccentric Kozai-Lidov evolution, which drives them into mass-transferring ultracompact X-ray binaries (UCXBs) and produces joint X-ray and mHz GW signals. Together, these results establish eccentric compact binaries as a key population for multimessenger gravitational wave astronomy, enabling their systematic modeling and full exploitation in the era of space-based GW observations.

Chapter 2

Detecting Accelerating Eccentric Binaries in the LISA Band

A version of this chapter was previously published in *Physical Review D* (Xuan et al., 2023, Phys. Rev. D 107, 043009).

Abstract

Many gravitational wave (GW) sources in the LISA band are expected to have non-negligible eccentricity. Furthermore, many of them can undergo acceleration because they reside in the presence of a tertiary. Here we develop analytical and numerical methods to quantify how the compact binary's eccentricity enhances the detection of its peculiar acceleration. We show that the general relativistic precession pattern can disentangle the binary's acceleration-induced frequency shift from the chirp-mass-induced frequency shift in GW template fitting, thus relaxing the signal-to-noise ratio requirement for distinguishing the acceleration by a factor of $10 \sim 100$. Moreover, by adopting the GW templates of the accelerating eccentric

compact binaries, we can enhance the acceleration measurement accuracy by a factor of ~ 100, compared to the zero-eccentricity case, and detect the source's acceleration even if it does not change during the observational time. For example, a stellar-mass binary black hole (BBH) with moderate eccentricity in the LISA band yields an error of the acceleration measurement $\sim 10^{-7} m \cdot s^{-2}$ for SNR $= 20$ and observational time of 4 yrs. In this example, we can measure the BBHs' peculiar acceleration even when it is $\sim$ 1pc away from a $4 \times 10^6 M_\odot$ SMBH. Our results highlight the importance of eccentricity to the LISA-band sources and show the necessity of developing GW templates for accelerating eccentric compact binaries.

2.1 Introduction

The detection of gravitational wave (GW) by LIGO and Virgo (Abbott et al., 2021; The LIGO Scientific Collaboration et al., 2021) has greatly enhanced our understanding of the properties of compact objects in the Universe. In the future, the Laser Interferometer Space Antenna (LISA) (Amaro-Seoane et al., 2017b) would broaden the scope of GW astronomy by detecting GW signals in a lower frequency band ($10^{-4} - 10^{-1}$ Hz), where GW signal in the LISA band may last for years (Amaro-Seoane et al., 2022), potentially having signatures of compact binary's long-term evolution long before they merge. Therefore, LISA detection can shed light on compact object binary's formation channel and surrounding environment.

Among all the parameters that can be measured using LISA, the GW source's acceleration is of great importance, because it carries the signature of the binary's environment. Several studies suggested that accelerating compact object binaries may significantly contribute to the population observed by LISA (Pribulla and Rucinski, 2006; Tokovinin et al., 2008; Raghavan et al., 2010; Sana and Evans, 2011; Sana et al., 2012; Moe and Di Stefano, 2017; Naoz et al., 2013a; Naoz and Fabrycky, 2014; Hamers and Portegies Zwart, 2016; Hamers, 2018, 2020; Rose et al., 2019; Hamers et al., 2013; Toonen et al., 2016, 2018, 2017; Perpinyà-

Vallès et al., 2019; Lagos et al., 2020; O'Leary et al., 2009a; Antonini and Perets, 2012; Antonini et al., 2014; Stephan et al., 2016a, 2019; Hoang et al., 2018; Wang et al., 2021). For example, observational endeavors shows that stars often reside in binaries, and high mass stars reside in higher multiples (Pribulla and Rucinski, 2006; Tokovinin et al., 2008; Raghavan et al., 2010; Sana and Evans, 2011; Sana et al., 2012; Moe and Di Stefano, 2017). According to long term stability arguments, the spatial separation of these multiples is likely to evolve into one tight inner binary with tertiary in wide outer orbit(s) (Naoz et al., 2013a; Naoz and Fabrycky, 2014; Hamers and Portegies Zwart, 2016; Hamers, 2018, 2020; Rose et al., 2019). Stellar evolution of such systems may result in compact object binaries that host at least a tertiary companion (Hamers et al., 2013; Toonen et al., 2016, 2018). The observation of white dwarfs (WDs) also directly suggests that many WDs binaries reside in a triple configuration (Toonen et al., 2017; Perpinyà-Vallès et al., 2019; Lagos et al., 2020). These compact object binaries can undergo non-negligible acceleration in the triple system, thus leaving an imprint of acceleration on the GW signal.

Additionally, many binaries and compact object binaries are supposed to reside in the center of galaxies (O'Leary et al., 2009a; Antonini and Perets, 2012; Antonini et al., 2014; Stephan et al., 2016a, 2019; Naoz et al., 2018; Hoang et al., 2018; Wang et al., 2021). Already a few stellar binaries were detected in the inner ~ 0.1 pc of our galactic center (Pfuhl et al., 2014a). Moreover, the number of compact binaries visible in the LISA band within the inner parsec of our galactic center is estimated to be $14-150$ WD-WD, $0-2$ neutron star (NS) - black hole (BH), $0.2-4$ NS-NS, $0.3-20$ BH-BH, and the results are of the same order for other galaxies (Wang et al., 2021). These systems mentioned above can undergo non-negligible acceleration caused by the gravitational potential of the supermassive black hole (SMBH) in the galactic center.

Measuring the acceleration will give us direct evidence about the GW source's dynamic environment. For example, a binary black hole (BBH) orbiting the SMBH on a close configuration

will undergo a time-dependent Doppler shift induced by acceleration, which is potentially detectable (Inayoshi et al., 2017; Meiron et al., 2017; Robson et al., 2018a; Randall and Xianyu, 2019a; Wong et al., 2019; Gupta et al., 2020; Tamanini et al., 2020a). Additionally, an acceleration signature on GW signal may help detect double WDs (DWDs) accompanied by a star or a planet (Seto, 2008; Bonvin et al., 2017; Robson et al., 2018a; Steffen et al., 2018; Tamanini and Danielski, 2019; Danielski et al., 2019). Further, eccentricity oscillations due to the Eccentric Kozai Lidov mechanism (e.g., Kozai, 1962; Lidov, 1962; Naoz, 2016), can induce a time-changing characteristic strain profile in the LISA band (Hoang et al., 2019; Randall and Xianyu, 2019b; Deme et al., 2020; Emami and Loeb, 2020), thus imprinting a signature on a binary in the presence of a tertiary. However, the effect of acceleration on the GW signal is not always distinguishable and measurable. Sometimes it may degenerate with the measurement of other parameters and yield a misleading interpretation of the physics behind the GW sources (Robson et al., 2018a; Tamanini et al., 2020a; Chen, 2020; Xuan et al., 2021).

Consider a circular compact object binary as an example. When its evolution is dominated by GW radiation and the observer is in the rest frame of the source, the intrinsic GW frequency f_e will increase with time. The frequency shift rate $\dot{f}_e$ is proportional to the "chirp mass" as: $\dot{f}_e \sim \mathcal{M}_c^{5/3}$, where $\mathcal{M}_c \equiv (m_1 m_2)^{3/5}/(m_1+m_2)^{1/5}$, and m_1 and m_2 are masses of the two compact objects (Cutler and Flanagan, 1994). But if the GW source is accelerating, the peculiar acceleration also leads to an extra frequency shift rate $\dot{f}_{\rm acc}$ by changing the peculiar velocity of the GW source and inducing a time-dependent Doppler shift. Therefore, the detected GW signal has two components that contribute to the observed frequency shift rate, one from the GW emission that shrinks and circularizes the orbit, and the other from the acceleration of the system. In other words, there is a degeneracy between the chirp mass and peculiar acceleration since they both contribute to the frequency shift rate in the GW signal for the leading order.

Such kind of degeneracy makes it harder to measure peculiar acceleration. Some studies suggested that GW source with measurable acceleration may be limited to the cases when the compact binary is very close to the tertiary and the period of the outer orbit is short enough (Robson et al., 2018a; Tamanini et al., 2020a). Further, for DWDs in the Milky Way, there is a significant parameter space where acceleration is large enough to cause a non-negligible $\dot{f}_{\rm acc}$ yet still not distinguishable (degenerate with other parameters) in GW template fitting (Xuan et al., 2021).

However, there can be a different story when the eccentricity of the GW source is detected. In fact, several studies suggest that many eccentric compact binaries are in the LISA band (O'Leary et al., 2009a; Samsing, 2018; Hoang et al., 2019; Fragione et al., 2019; Breivik et al., 2020; Naoz et al., 2020; Wang et al., 2021; Zhang et al., 2021). And in some dynamical channels, the existence of a tertiary is supposed to directly produce LISA-band sources by exciting the eccentricity of inner orbit and accelerating the merger (Thompson, 2011; Antognini et al., 2014; Hoang et al., 2018; Stephan et al., 2019; Martinez et al., 2020; Hoang et al., 2020; Naoz et al., 2020; Stephan et al., 2019; Wang et al., 2021). Thus, we expect binaries in an accelerating environment to be eccentric.

If the binary has non-zero eccentricity, the general relativistic (GR) precession will induce a triplet waveform, which in turn changes the frequency-peak position of each harmonic. This signature can be used to extract the binary's total mass independently of the frequency shift rate (Seto, 2001; Mikóczi et al., 2012a), making it possible to break the degeneracy between peculiar acceleration and the chirp-mass-induced frequency shift.

Here we propose a strategy aimed to break this degeneracy by considering the GR precession signature of the accelerating eccentric binary. In Section 2.2, we present analytical methods yielding an overall understanding of how eccentricity can disentangle the acceleration feature from the chirp-mass-induced frequency shift. In Section 2.3, we introduce the numerical tools used to simulate LISA event waveforms (§2.3.1), analyze the waveform (§2.3.2), and

estimating the error of parameter measurements (§2.3.3). Section 2.4 shows the application of numerical methods. In particular, in this section, we map the parameter space where the GW signal from accelerating sources can be distinguished from non-accelerating GW templates and quantify the effect of eccentricity on the accuracy of peculiar acceleration measurement. Finally, in Section 2.5, we offer our discussion and conclude that eccentric binaries have a clear signature on the GW form when it is undergoing peculiar acceleration. Specifically, the acceleration measurement enhanced by eccentricity can shed light on the GW source's environment.

2.2 Analytical Consideration

We begin with establishing the effects of acceleration on the GW signal (§2.2.1). This effect causes a degeneracy between the peculiar acceleration and the chirp-mass-induced frequency shift. We suggest that eccentricity can be used to disentangle this degeneracy. The role of eccentricity in detecting compact binaries' peculiar acceleration can be divided into two parts.

1. *Ignoring the possible contribution of acceleration in the signal.* In this case, consider using GW templates, in the data analysis, that do not include the binary's peculiar acceleration. Below (§2.2.2), we show that eccentricity can help distinguish an accelerating eccentric compact binary from non-accelerating ones.

2. *Including the possible contribution of acceleration in the signal.* In this case, the data analysis uses the GW templates with accelerating features, making it possible to measure the binary's acceleration. Below (§2.2.3), we show how the measurement of acceleration depends on the eccentricity of the binary. Later, using numerical analysis, we demonstrate that the eccentricity can increase the acceleration measurement accuracy

(§2.4.2).

2.2.1 Mass-Acceleration Degeneracy in GW Data Analysis

Consider a compact object binary with a semi-major axis a, eccentricity e, and the two components' masses m_1 and m_2. Its energy is dissipated by the GW radiation, which results in the decrease of the orbital period P_b. The average changing rate of the semi-major axis, a is (Peters, 1964):

$$\left\langle \frac{da}{dt} \right\rangle = -\frac{64}{5} \frac{G^3 m_1 m_2 \left(m_1 + m_2\right)}{c^5 a^3 \left(1 - e^2\right)^{7/2}} \left(1 + \frac{73}{24} e^2 + \frac{37}{96} e^4\right) \ , \tag{2.1}$$

where G is the gravitational constant and c is the speed of light.

When the binary has a non-zero eccentricity, the GW signal is made up of multiple harmonics. The frequency of GW's n-th harmonic is related to the binary's orbital period as $f_e^{j=n} \approx n/P_b$, where the subscript "e" denotes quantities in the rest frame of the source. Note that since the orbital period is shrinking, the frequency of the GW signal will increase with time. This phenomenon is known as the "chirp signal" of a GW source.

GW data analysis studies often focus on the second harmonic of the GW signal, which is the dominant signal for circular and low eccentricities orbits. Thus, here we will take $f_e^{j=2}$ as an example to demonstrate the commonly used method for estimating the mass of the GW source. It should be noted that GW data analysis methodology often proposes to fit the numerical template for the parameter estimation of GW sources (Finn, 1992; Cutler and Flanagan, 1994), while the analysis presented here aims to explain different factors' contribution to the result of the numerical fitting and give an analytical estimation of the acceleration measurement accuracy in different cases.

The time derivative of the 2nd harmonic is uniquely determined by the frequency of the GW

signal, eccentricity, and the mass of the GW source for the leading order:

$$\dot{f}_e^{j=2} = \frac{96\pi^{8/3}}{5}\left(\mathcal{M}_c\frac{G}{c^3}\right)^{5/3}\left(f_e^{j=2}\right)^{11/3}F(e)\ , \tag{2.2}$$

We emphasize that $\mathcal{M}_c$ is the intrinsic chirp mass of the binary as a GW source, which only depends on the mass of the compact binary's components; The observed chirp mass, $\mathcal{M}_o$, can be different from $\mathcal{M}_c$ because the observed GW signal can be distorted. $F(e)$ is a function of the compact binary's eccentricity (the enhancement function)(Peters and Mathews, 1963):

$$F(e) \equiv \frac{1+\frac{73}{24}e^2+\frac{37}{96}e^4}{(1-e^2)^{7/2}}\ . \tag{2.3}$$

Thus, we can estimate the intrinsic chirp mass $\mathcal{M}_c$ of compact binaries based on two observables, the frequency f_e and its time derivative $\dot{f}_e$. For the circular binary case, the details of this method can be found in Cutler and Flanagan (1994). On the other hand, for an eccentric binary, the amplitude profile of different harmonics is related to the eccentricity (Moreno-Garrido et al., 1995; Gopakumar and Iyer, 2002; Barack and Cutler, 2004b). It can enable us to measure the eccentricity in template fitting (Cornish and Rubbo, 2003). In this way, the results of (Cutler and Flanagan, 1994) can be generalized by plugging in $f_e, \dot{f}_e$, and e into Eq. (5.34) and finding the intrinsic chirp mass of the source :

$$\mathcal{M}_c = \left(\frac{5c^5}{96\pi^{8/3}G^{5/3}}\right)^{3/5}(f_e^{j=2})^{-11/5}(\dot{f}_e^{j=2})^{3/5}F(e)^{-3/5}\ . \tag{2.4}$$

When the GW source is moving relative to the observer with a velocity v, the frequency of GW's each harmonic will be shifted because of the Doppler effect. In the observer frame, the frequency, f_o, is then (Meiron et al., 2017; Inayoshi et al., 2017; Robson et al., 2018a; Chen et al., 2019a):

$$f_o^{j=n} = f_e^{j=n}\frac{\sqrt{1-\beta^2}}{1+\beta\cos\theta} = f_e^{j=n}(1+z_{\rm dop})^{-1}\,, \tag{2.5}$$

where $\beta = v/c$, θ is the angle between the velocity vector and the line of sight, and $z_{\rm dop}$ is the Doppler coefficient.

We are interested in the case when the GW source is accelerating, which means that the peculiar velocity and Doppler shift factor are changing with time. Thus, from Eq. (2.5) it is straightforward to find the time derivative of the observed frequency (Chen et al., 2019b), i.e.,

$$\frac{d}{dt} f_o^{j=n} = \frac{\dot{f}_e^{j=n}}{(1+z_{dop})^2} + f_e^{j=n} \frac{d}{dt}\left(\frac{\sqrt{1-\beta^2}}{1+\beta\cos\theta}\right) \ , \tag{2.6}$$

where the power 2 factor on the Doppler coefficient comes due to the transformation from the observed frames to the source frame. The last term of Eq. (2.6), represents the line of sight acceleration $a_{//}/c$. In other words :

$$\frac{a_{//}}{c} = \frac{d}{dt}\left(\frac{\sqrt{1-\beta^2}}{1+\beta\cos\theta}\right) \ . \tag{2.7}$$

Equivalently, from Eq. (2.6), this acceleration relates to the difference between the time derivative of frequency in the observer's frame and the rest frame of the GW source. Such difference is directly caused by the change of peculiar velocity, thus can be used to constrain the line of sight acceleration $a_{//}$, i.e.,

$$\frac{a_{//}}{c} = \frac{\dot{f}_o - \dot{f}_e(1+z_{\rm dop})^{-2}}{f_e} \ . \tag{2.8}$$

However, we cannot directly measure the frequency (f_e) and its time derivative ($\dot{f}_e$) in the source frame. Instead, the observed quantities are f_o and $\dot{f}_o$ in the observer frame. As mentioned above, even when $a_{//} = 0$, constant peculiar velocity and cosmological redshift can cause a significant difference between f_o and f_e and distorts the parameters of the GW source. This phenomenon is known as "mass-redshift degeneracy," (e.g., Sathyaprakash and Schutz, 2009; Broadhurst et al., 2018; Smith et al., 2018; Chen et al., 2019a). Because of the scale-

free property of gravity, the effect of mass-redshift degeneracy can be exactly canceled out by making the measured chirp mass the "redshifted chirp mass" and the measured distance of the source the luminosity distance (Broadhurst et al., 2018) while keeping other parameters the same. Thus, for simplicity, we will focus on the effect of acceleration and limit the discussion to the cases when cosmological and gravitational redshift can be neglected, i.e., $z \ll 1$. In particular, we assume $z_{\rm dop} \ll a_{//} f_e / 2c\dot{f}_e$, and simplify Eq. (2.8) to be:

$$\dot{f}_o \approx \dot{f}_e + f_e \frac{a_{//}}{c} \ . \tag{2.9}$$

The complete result for arbitrarily large redshift can be recovered by replacing all the $\mathcal{M}_c$ in the following discussion to be the redshifted chirp-mass $\mathcal{M}_c(1+z)$.

Most of the proposed LISA mission strategies are to search for a signal using non-accelerating compact binary's GW templates. (e.g. Cornish and Rubbo, 2003; Littenberg et al., 2020) However, as discussed above we expect a degeneracy between $\mathcal{M}_c$ and $a_{//}$ since they both contribute to the frequency shift rate $\dot{f}_o$ in the leading order. For the case of a compact object binary with no or negligible eccentricity, only the 2nd harmonic of the GW signal dominates. In the LISA band, such kind of signal is a nearly-monochromatic sinusoidal wave with slowly increasing frequency. Since the waveform does not have other significant features except for f_o and $\dot{f}_o$, neglecting the acceleration's contribution can lead to a biased estimation of the chirp mass. In particular, if one assumes $\dot{f}_o \approx \dot{f}_e + f_e a_{//}/c$ (see Eq. (2.9)) as the intrinsic frequency shift rate $\dot{f}_e$ in template fitting, the resultant chirp mass will differ from the "true" chirp mass. This can be seen by combining Eq. (2.4) and (2.9), which yields

an observed chirp mass with the following expression:

$$\begin{aligned}\mathcal{M}_o &= \left(\frac{5c^5}{96\pi^{8/3}G^{5/3}F(e)}\right)^{3/5}(f_o^{j=2})^{-11/5}(\dot{f}_o^{j=2})^{3/5} \\ &= \left(\frac{5c^5}{96\pi^{8/3}G^{5/3}F(e)}\right)^{3/5}(f_o^{j=2})^{-11/5}(\dot{f}_e^{j=2} + a_{//}/c)^{3/5} \\ &\neq \mathcal{M}_c \ . \end{aligned} \tag{2.10}$$

Thus, there is a degeneracy between the binary's acceleration and mass in GW data analysis. In other words, the acceleration can significantly bias the chirp mass estimation if the compact binary has small or zero eccentricity and only the 2nd harmonic is detected.

2.2.2 Disentangling the Signatures of Accelerating Eccentric GW Sources - Analytical Approach

For a GW source with peculiar acceleration, the chirp mass measurement without considering an accelerating template can lead to erroneous results (see examples above). However, when the source has non-negligible eccentricity and detectable multiple harmonics, the GR precession creates a unique signature in the GW signal and disentangles the acceleration from the bias on the chirp mass. As a result, the accelerating GW signal will be different from any of the non-accelerating GW templates, thus can be identified.

Here we detailed the steps of this strategy. In particular, Section 2.2.2.1 describes how the GR precession pattern of the eccentric compact binary leaves a signature on the GW waveform, thus differentiating the accelerating GW signal from the non-accelerating one. Section 2.2.2.2 estimates the critical acceleration for distinguishing accelerating GW sources in data analysis.

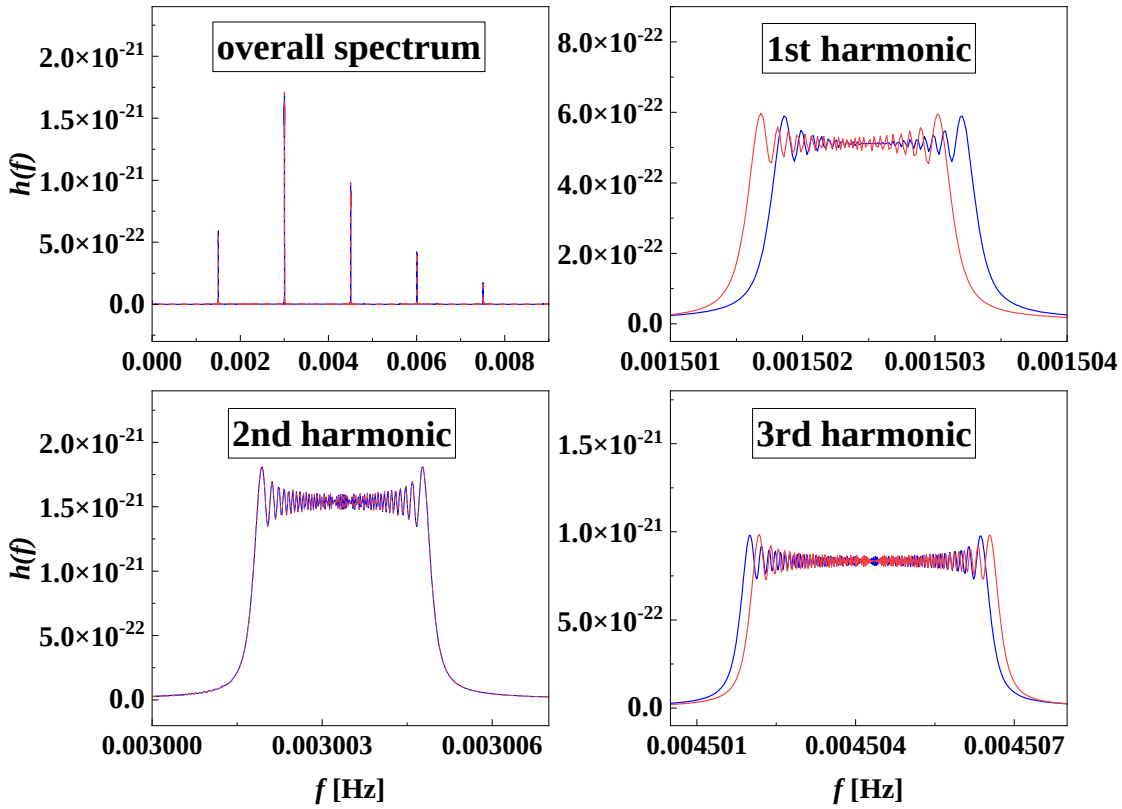


Figure 2.1: **The frequency spectrum of GW signals from two eccentric BBHs systems with the same chirp mass but different total mass.** For the first system (blue line) $m_1 = 8\ \mathrm{M}_\odot$, $m_2 = 40\ \mathrm{M}_\odot$, $e = 0.3$; For the second system (red line) $m_1 = m_2 = 16.867\ \mathrm{M}_\odot$, $e = 0.3$. Both of these systems have the same chirp mass $\mathcal{M}_c \sim 14.684\ \mathrm{M}_\odot$, but as depicted the difference in total mass results in a different position of the harmonics. The initial period of radial motion for the first systems is 1.5mHz, but its GW frequency of each harmonic is not the integer multiple of 1.5mHz because of the shift induced by GR precession (Δf). For the second system, its GR precession shifts the position of each harmonic by a different value. For illustration purposes, we adjust the initial radial frequency of the second system to be slightly different from 1.5mHz, so that we compensate for the difference in Δf and make its GW's 2nd harmonic having the same initial frequency as the first system's. The observation duration is set to be two years.

2.2.2.1 Eccentricity as Means to Disentangle the Mass-Acceleration Degeneracy

The GR precession of an eccentric orbit shifts the periastron by an angle $\delta\phi_0$ for each period Misner et al. (1973). Thus, the frequency of GW's n-th harmonic will split into a triplet $(nf - \Delta f, nf, nf + \Delta f)$ (Seto, 2001; Moreno-Garrido et al., 1995), in which

$$\Delta f = \frac{6(2\pi G)^{2/3}}{(1-e^2)c^2} M_{\rm total}^{2/3} (P_b)^{-5/3} \ , \tag{2.11}$$

where $M_{\rm total}$ is the total mass of compact binary system, P_b is the orbital period, and f equals $1/P_b$. For small eccentricity, coefficients of some terms in the triplet waveform are negligible, and the dominant component is $nf + \Delta f$. Therefore, the position of each GW's harmonic will be shifted by Δf in the frequency domain.

Δf is independent of the harmonic number because it is a feature of the GR dynamic of the orbit. Thus, all the harmonics will be shifted by the same value Δf. This feature allows us to disentangle Δf and extract the total mass of the system, $M_{\rm total}$ (Seto, 2001).

Figure 2.1 demonstrates this feature of the GR precession pattern. In this figure, we adopt the x-model (Hinder et al., 2010) to generate the GW signal from eccentric compact object binaries (see Section 2.3.1 for detailed information) and show the frequency spectrum of the GW signals from two different compact binary systems. They have the same chirp mass $\mathcal{M}_c$, which means that for each harmonic the time derivative of frequency (width of the peak in the frequency domain) is the same. But because of their different mass ratio, their total mass, $M_{\rm total}$, is different. Such difference in $M_{\rm total}$ yield a different Δf (see Eq. (2.11)). Thus, even if we choose the special case when their GW's 2nd harmonic has the same initial frequency/frequency shift rate (position/width), there will be a position displacement for their 1st and 3rd harmonics, which enables us to estimate their different $M_{\rm total}$. However, if their eccentricity is zero, only the 2nd harmonic is present, and we cannot distinguish such kind of precession pattern.

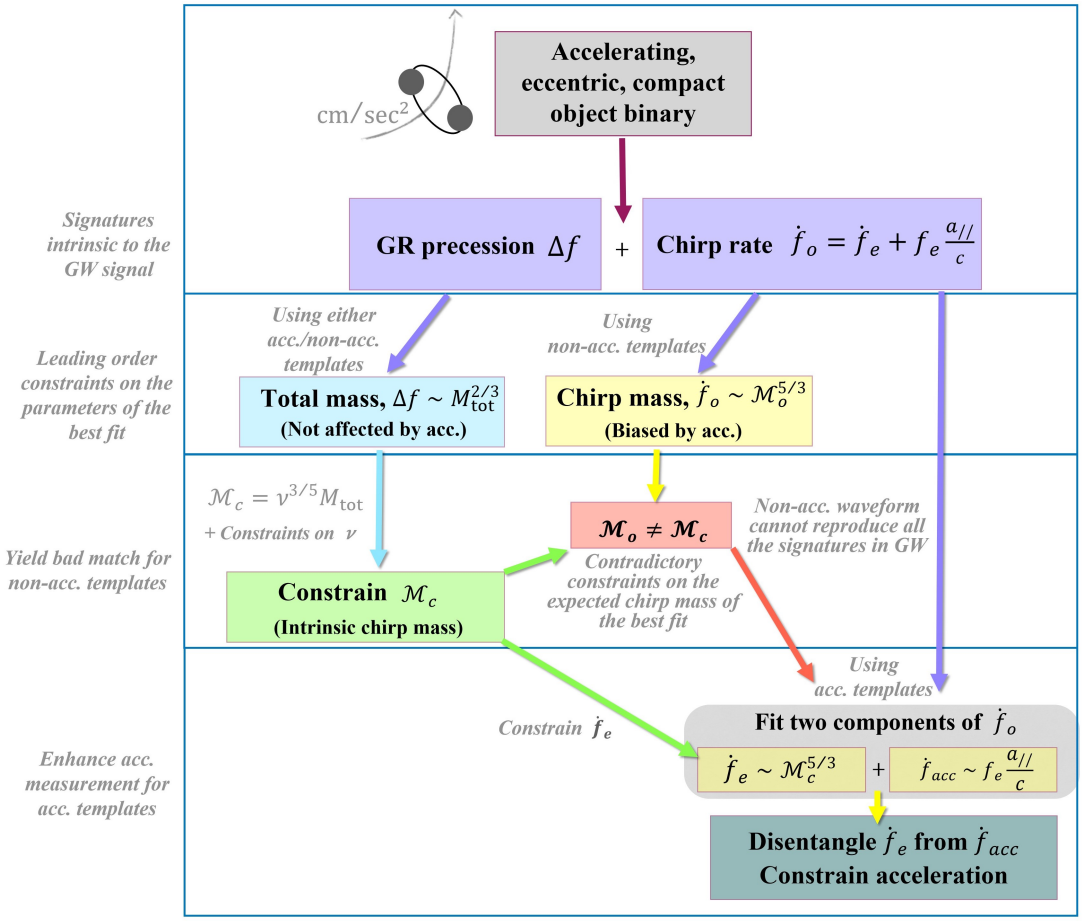


Figure 2.2: **A flowchart of the proposed strategy, as the reason why the eccentricity can help us disentangle the acceleration in template fitting**. The GW signal from accelerating eccentric sources has the signatures of GR precession (Δf) and chirp waveform ($\dot{f}_o$), which contribute differently to the result of template fitting. *Left branch* describes that Δf primarily constrains the fitted total mass $M_{\rm tot}$, for either accelerating or non-accelerating templates. Since the total mass $M_{\rm tot}$ and the chirp mass $\mathcal{M}_c$ can be related to each other (See Eq.(2.12)), GR precession signatures in the waveform eventually put a constraint on the chirp mass $\mathcal{M}_c$ in template fitting. *Middle branch* shows the case when we use non-accelerating GW templates. In this case, the acceleration distorts the chirp rate ($\dot{f}_o \neq \dot{f}_e$) and yields an inaccurate chirp mass $\mathcal{M}_o$ in template fitting. However, the $\mathcal{M}_c$ from *left branch* (GR precession signature's constraint) is not affected by acceleration, thus will not agree with $\mathcal{M}_o$. Such a discrepancy between two waveform signatures means we can hardly find a good match in the non-accelerating templates family. It reminds us to include acceleration in the GW templates (i.e., shift to the *Right branch*). In the *Right branch*, we use GW templates with acceleration to fit both $\dot{f}_e$ and $\dot{f}_{\rm acc}$. Since the GR precession (from *left branch*) can constrain the intrinsic chirp rate $\dot{f}_e$, it disentangles $\dot{f}_e$ from $\dot{f}_{acc}$ and further help with improving the acceleration measurement accuracy.

As shown in Section 2.2.1, the acceleration can yield a degeneracy between $\mathcal{M}_c$ and $a_{//}$ (see Eqs. (2.8) and (2.10)). This phenomenon is due to the degeneracy in the level of observed frequency time derivative $\dot{f}_o$. However, estimating $M_{\rm total}$ from the Δf caused by GR precession, only relies on the value of f, instead of its time derivative, (see Eq. (2.11)). Thus, the total mass derived from the precession pattern is not affected by the degeneracy in the level of $\dot{f}$, therefore independent of the source's peculiar acceleration.

Thus, we propose that the acceleration signature can be disentangled from the GW signal for an eccentric source. Further, we suggest that a higher eccentricity can yield a higher sensitivity in the detection of acceleration.

This strategy is described in Figure 2.2. In particular, we firstly introduce the symmetric mass ratio that connects the chirp mass to the total mass in the following way:

$$\mathcal{M}_c = \nu^{3/5} M_{total} \ , \tag{2.12}$$

in which ν is the symmetric mass ratio:

$$\nu = \frac{m_1 m_2}{(m_1 + m_2)^2} \ . \tag{2.13}$$

The symmetric mass ratio always satisfies $\nu \leq 1/4$, and the value of ν is often constrained in GW template fitting.

As illustrated in Figure 2.2, given an accelerating, eccentric compact object binary, its GW signal has the signatures of GR precession and GW emission. We can use templates (with/ without including the sources' peculiar acceleration) to fit the parameters of the source. In either case, the GR precession pattern (Δf) in the signal will constrain the total mass $M_{\rm total}$, which is not biased by the acceleration according to the reasons mentioned above. Thus, Eq. (2.12), combined with the limits on ν, places constraints on the intrinsic chirp mass $\mathcal{M}_c$

(see left branch in Figure 2.2). The limits on $\mathcal{M}_c$ can be used to constrain the intrinsic frequency shift rate $\dot{f}_e$ via Eq. (5.34) ("Constrain $\dot{f}_e$" sub-branch).

On the other hand, the observed waveform has the information of both the frequency and its time derivative, i.e., f_o and $\dot{f}_o$ (see the middle and right branch in Figure 2.2). Moreover, $\dot{f}_o$ has two components, one due to the intrinsic GW emission decay, and another caused by the peculiar acceleration. The former is $\dot{f}_e$, while the latter is $\dot{f}_{acc} \propto f_o \times a_{//}$ (see Eqs. (2.6) and (2.7)). If we use non-accelerating GW templates to fit the signal (middle branch), the distorted $\dot{f}_o$ will result in a distorted chirp mass $\mathcal{M}_o$ (see Eq. (2.10)). Therefore, the constraints of $\mathcal{M}_c$ we get from the GR precession signature in the left branch of Figure 2.2 contradicts the $\mathcal{M}_o$ we get from the GW emission signature. In the template fitting, such a discrepancy means that two different signatures in the signal require contradictory parameters in the fitting result. In other words, in the parameter space of the non-accelerating templates there is no such a parameter set that can recover the signatures of both GR precession and GW emission. The bad match for non-accelerating templates may help us distinguish the acceleration.

In the right branch, we use templates with acceleration to fit the signal. The constraints on $\dot{f}_e$ (from the left branch's GR precession signature) allow for disentangling the intrinsic frequency shift rate $\dot{f}_e$ from the observed quantity $\dot{f}_o$, thus yields constraints on the acceleration-induced frequency shift rate ($\dot{f}_{\rm acc} = \dot{f}_o - \dot{f}_e$). Therefore, the strategy in Figure 2.2 overall explains why the eccentricity can help us distinguish (measure) the binary's acceleration when using GW templates without (with) acceleration.

We emphasize that here we adopt a simple case of one source signal. In practice, LISA may detect multiple sources simultaneously (e.g., Amaro-Seoane et al., 2017a), which can considerably add to the noise and confusion. However, the strategy we outlined here demonstrates that the GR precession signature in the signal disentangles the peculiar acceleration from the chirp-mass-induced frequency shift. In other words, the eccentricity can cause the

accelerating GW signal to differ from any non-accelerating GW template and constrains the acceleration-induced frequency shift rate, even when multiple sources are detected.

Below, we estimate the critical detection threshold that differentiate between the accelerating and non-accelerating GW sources.

2.2.2.2 Analytical Analysis of the Detection Threshold

Let us consider a LISA-band GW waveform that is generated by an accelerating compact binary with non-negligible eccentricity (e.g., DWDs, initially $f_e^{j=2} = 3\text{mHz}$, $e > 0.1$). In the cases that we consider, multiple harmonics of the waveform should be detected. For simplicity, below we neglect the constant redshift by assuming $z \ll 1$.

In this subsection we consider the implications of using non-accelerating GW templates to fit the GW signal. In particular, the GR precession pattern (Δf) constrains the intrinsic total mass of the system in template fitting. As outlined in Section 2.2.2.1, one can use Eq. (2.11) to extract the total mass, which is not affected by the extra $\dot{f}$ caused by $a_{//}$ since the measurement only depends on f_e and Δf. However, the measured chirp mass $\mathcal{M}_o$ is different from the intrinsic chirp mass $\mathcal{M}_c$ for an accelerating source, because the acceleration changes the frequency shift rate $\dot{f}_o$ of the signal (i.e., Eq. (2.10)).

We can relate the intrinsic M_{total} with the intrinsic $\mathcal{M}_c$ via the symmetry mass ratio ν (see Eq.(2.14)). But as mentioned above, in the template fitting of accelerating GW sources, the M_{total} remains its intrinsic value while the $\mathcal{M}_o$ is biased. Thus, instead of being its intrinsic value (ν_{int}), the fitted symmetric mass ratio has to be biased ($\nu^{'}$) to make $\mathcal{M}_o$ and M_{total} agree with each other:

$$\mathcal{M}_o = (\nu^{'})^{3/5} M_{\text{total}} \ . \tag{2.14}$$

In other words, the acceleration distorts the GW signal by changing the $\dot{f}_o$ (width of each

harmonic in the frequency domain) but keeping the Δf (the position displacement of each harmonic) unchanged. We can create a similar signature with non-accelerating waveforms by changing the symmetric mass ratio. Thus, sometimes it is still possible to find a non-accelerating GW template that fits the accelerating GW signal for the leading order. However, when the amplitude of acceleration increases, such degeneracy will eventually break.

In particular, since the symmetric mass ratio ν (and also $\nu^{'}$) has an upper bound of 0.25, the observed chirp mass has a clear limit for a given total mass, i.e., $\mathcal{M}_o \leq 0.25^{3/5} M_{\rm total}$. This limit can then be translated to a maximum acceleration $a_{\rm max}$ for which the observed chirp mass reaches $0.25^{3/5} M_{\rm total}$. In other words, when the acceleration exceeds $a_{\rm max}$, $\mathcal{M}_o > 0.25^{3/5} M_{\rm total}$, we cannot find a proper match in non-accelerating GW templates to fit both the $\mathcal{M}_c$ ($\dot{f}_o$) and the $M_{\rm total}$ (Δf).

This relationship is depicted in Figure 2.3, where we consider an example of a DWD system at varying distances, and thus with varying acceleration, from a SMBH. As seen in the Figure, neglecting the contribution of acceleration in the template fitting can yield an observed chirp mass $\mathcal{M}_o$ which is larger than the allowed limit. Thus, implying that the binary exists in an accelerating environment.

We now derive the expression of $a_{\rm max}$. As outlined in Section 2.2.1, comparing the difference between the intrinsic and observed GW frequency shift rate can be used to constrain the binary's peculiar acceleration. Using Eqs. (2.4), (2.8), and (2.10) we have:

$$\begin{aligned} \frac{a_{//}}{c} &\approx \frac{\dot{f}_o - \dot{f}_e}{f_e} \\ &= \frac{1}{f_e^{j=2}} \frac{96\pi^{\frac{8}{3}}}{5} \left(\frac{G}{c^3}\right)^{5/3} (f_e^{j=2})^{11/3} F(e) \left(\mathcal{M}_o^{5/3} - \mathcal{M}_c^{5/3}\right) \ , \end{aligned} \tag{2.15}$$

which describes the dependency of the observed acceleration on the difference between the observed ($\mathcal{M}_o$) and intrinsic ($\mathcal{M}_c$) chirp mass.

As seen in Figure 2.3, the maximum acceleration is reached when the observed chirp mass $\mathcal{M}_o$ reaches it upper limit $\mathcal{M}_{\rm max}$:

$$\mathcal{M}_{\rm max} = 0.25^{3/5} M_{\rm total} = (\frac{0.25}{\nu_{\rm int}})^{3/5} \mathcal{M}_c \ . \tag{2.16}$$

Plug Eq. (2.16) into Eq. (2.15), we can get:

$$\begin{aligned} \frac{a_{\rm max}}{c} &= \frac{F(e)}{f_e^{j=2}} \frac{96\pi^{8/3}}{5} (\frac{G}{c^3})^{5/3} (f_e^{j=2})^{11/3} \mathcal{M}_c^{5/3} \left(\frac{0.25}{\nu_{\rm int}} - 1 \right) \\ &= \frac{\dot{f}_e^{j=2}}{f_e^{j=2}} \left(\frac{0.25}{\nu_{\rm int}} - 1 \right) \ , \end{aligned} \tag{2.17}$$

which is shown as the dashed vertical line in Figure 2.3. Thus, this maximum acceleration can help us estimate the detectability of the acceleration for eccentric GW sources.

Additionally, in realistic observation there is noise. Thus, to distinguish the accelerating GW signal, the actual critical acceleration will need to be higher than the maximum acceleration $a_{\rm max}$ by a factor of δa:

$$a_{\rm crit} = \delta a + a_{\rm max} \ . \tag{2.18}$$

We can get δa via the following reasoning: In general, to distinguish the acceleration, two conditions need to take place. First, the acceleration amplitude needs to be higher than $a_{\rm max}$, and second, the acceleration creates a significant difference in the waveform, which is larger than the noise.

When $a < a_{\rm max}$ (right-hand side on Figure 2.3), the acceleration's signature can still be compensated for by changing the parameters of non-accelerating templates, and thus, harder to detect. On the other hand, for $a > a_{\rm max}$, we can no longer find a fit in the non-accelerating templates. However, due to the noise, the minimal acceleration that causes a fail fit in non-accelerating templates should be larger, see Eq. (2.18). Therefore, the observed chirp mass will be larger than its original critical value when there is no noise. Using Eq. (2.15), once

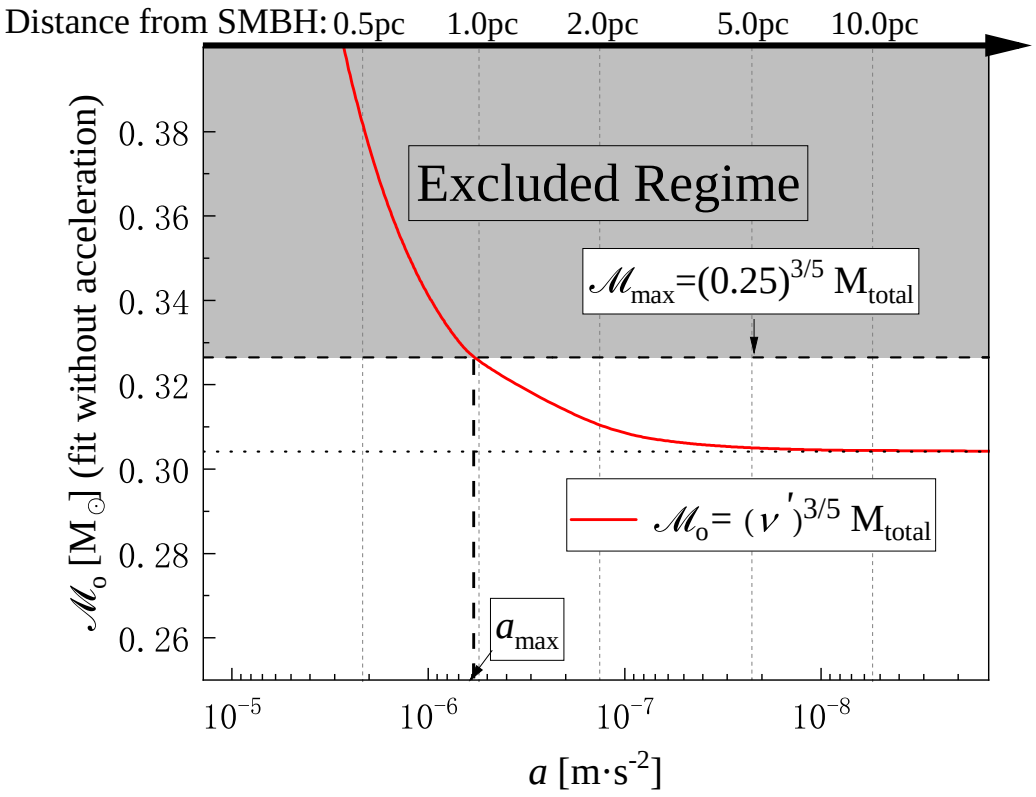


Figure 2.3: **The measured chirp mass $\mathcal{M}_o$ as a function of binary's acceleration.** We show a DWD system with $m_1 = 0.25\mathrm{M}_\odot, \mathrm{m}_2 = 0.5\mathrm{M}_\odot$, $e = 0.1, f_e^{j=2} = 3\mathrm{mHz}$, on a circular orbit around a SMBH with $M_{\mathrm{SMBH}} = 4 \times 10^6$ $\mathrm{M}_\odot$ at different distances. We choose the phase angle such that line-of-sight acceleration caused by the SMBH gravitational pull is maximized and pointing toward the observer. The chirp mass one measures using non-accelerating GW templates is depicted as a function of DWD's acceleration/ distance from the SMBH. As is shown in Section 2.2.2.2, GR precession pattern will put a constraint on the maximum possible value of chirp mass: $\mathcal{M}_c \leqslant 0.25^{3/5} M_{\mathrm{total}}$. The figure shows that when the DWD system is close to the SMBH ($\sim$ 1pc), acceleration becomes large enough ($a > a_{\mathrm{max}}$) to make $\mathcal{M}_o$ exceed the upper bound $\mathcal{M}_{\mathrm{max}}$, enabling us to find the discrepancy between $\mathcal{M}_o$ and M_{total}, thus distinguishing the acceleration. Note that the acceleration in this Figure increases to the left.

for $a_{\rm crit}$, and once for $a_{\rm max}$, we can express this higher chirp mass as follow:

$$\begin{aligned}\mathcal{M}^{'} &= \left(\mathcal{M}_{\rm max}^{5/3} + \frac{\delta a}{\frac{96}{5}\pi^{8/3}(f_e^{j=2})^{8/3}F(e)}\left(\frac{c^3}{G}\right)^{5/3}\right)^{3/5} \\ &= 0.25^{3/5}M_{\rm total}^{'} \\ &> 0.25^{3/5}M_{\rm total}\ .\end{aligned} \tag{2.19}$$

Since $\nu^{'}$ has reached its maximum value of 0.25, the total mass $M_{\rm total}^{'}$ in the template fitting has to be larger to be consistent with this new, and higher, chirp mass $\mathcal{M}^{'}$. Thus, the fitted template will have a larger shift for the frequency ($\Delta f^{'}$), due to the GR precession, than the shift that is observed (Δf). If the difference between $\Delta f^{'}$ and Δf is larger than the frequency resolution of GW detector (Takahashi and Seto, 2002a), we will have a clear signature of the acceleration. In other words, if

$$\Delta f^{'} - \Delta f > \frac{4\sqrt{3}}{\pi}\frac{\tau_{\rm obs}^{-1}}{\rm SNR}\ , \tag{2.20}$$

where $\tau_{\rm obs}$ is the duration of observation, and SNR is the signal-to-noise ratio, the acceleration may result in a fail fit for a non-accelerating template.

Using the Equations above, we can find the minimum magnitude of the acceleration ($a_{\rm crit}$) required to detect a signature of accelerating eccentric binary. In particular, we plug Eq. (2.16) into Eq. (2.19) to get the $M_{\rm total}^{'}$ as a function of $M_{\rm total}$. Then we use Eq. (2.11) to get Δf and $\Delta f^{'}$. We thus can use Eq. (2.20) to relate δa with $M_{\rm total}$ and SNR. Using the relationship between $a_{\rm crit}$ and $a_{\rm max}$ (Eq. (2.18)), we finally get:

$$\begin{aligned}\frac{a_{\rm crit}}{c} \approx\ & \frac{\dot{f}_e^{j=2}}{f_e^{j=2}}\frac{10\sqrt{3}(1-e^2)}{3\pi^{5/3}}\frac{\tau_{\rm obs}^{-1}}{\rm SNR}(f_e^{j=2})^{-5/3}\left(\frac{G}{c^3}M_{\rm total}\right)^{-2/3} \\ &+ \frac{\dot{f}_e^{j=2}}{f_e^{j=2}}\left(\frac{0.25}{\nu_{\rm int}} - 1\right)\ .\end{aligned} \tag{2.21}$$

This analytical expression of the critical acceleration is useful for estimating whether the GW signal from accelerating eccentric sources can be distinguished from non-accelerating GW templates, providing that more than one harmonic is detected with a signal-to-noise ratio above a certain SNR. In other words, if the acceleration of the GW source is larger than the critical acceleration in Eq.(2.21), we can distinguish between the accelerating signal and non-accelerating templates in observation.

Additionally, this criteria is suitable for analyzing a wide range of sources, in particular, double white dwarfs and double neutron stars (DNSs). However, the GW frequency of BBHs can change significantly during the observation because of their higher mass. This significant change of frequency contributes extra sensitivity in GW data analysis, thus limiting the potential usage of Eq. (2.21). Below, we will use numerical results to discuss the case of accelerating BBHs. We do emphasize that a dense place, such as the galactic center, is expected to host a high abundance of DWDs and potentially DNSs (e.g., Stephan et al., 2019; Wang et al., 2021).

2.2.3 Measuring the Acceleration of Eccentric Compact Binaries - Analytical Approach

Here we assume that an accelerating template for eccentric binaries is used in the data analysis. As mentioned before, the precession pattern can assist in distinguishing the eccentric binary's peculiar acceleration when we use non-accelerating GW templates to fit the signal. Thus, it is also possible that such a pattern can enhance the accuracy of acceleration measurement when we include the acceleration in the template. In this section, we derive an analytical expression for the eccentric binary's measured acceleration and use it to estimate the accuracy of acceleration measurement for different kinds of compact binaries.

In particular, consider an accelerating eccentric compact binary system, for which the GR

precession is detected so the total mass $M_{\rm total}$ can be extracted. As shown in Section 2.2.2, the measured frequency shift $\dot{f}_o$ has two parts: intrinsic frequency shift $\dot{f}_e$ caused by GW radiation, and an extra term caused by the acceleration. In order to determine the extra term and measure the acceleration, we need to subtract $\dot{f}_e$ from $\dot{f}_o$ (see Eq. (2.15)). However, $\dot{f}_e$ is a function of the intrinsic chirp mass $\mathcal{M}_c$, while we can only extract the $M_{\rm total}$ from the precession pattern. In fact, $\mathcal{M}_c$ depends on both $M_{\rm total}$ and ν (see Eq. (2.12)). Thus, an eccentric binary with a total mass measured from its GR precession will still have uncertainty on its acceleration measurement, which is coupled to the symmetric mass ratio ν.

The acceleration has straightforward dependence on the symmetric mass ratio ν. Thus, for a range of possible ν, the line of sight acceleration $a_{//}$ can be expressed as:

$$\frac{a_{//}}{c} \approx \frac{\dot{f}_o^{j=2}}{f_o^{j=2}} - \frac{96\pi}{5}(\Delta f_o)^{5/2}(f_o^{j=2})^{-3/2}\left(\frac{1-e^2}{3}\right)^{5/2} F(e)\nu \ , \tag{2.22}$$

$f_o^{j=2}$ ($\dot{f}_o^{j=2}$) is the observed frequency (the observed frequency shift) of GW's second harmonic; Δf_o is the observed frequency difference caused by precession; e is the eccentricity of binary, which can be got by comparing the relative amplitude of each harmonic. Eq. (2.22) was derived by using Eqs. (5.34), (2.6) and (2.11), and substitute $\mathcal{M}_c$ with $\nu^{3/5}M_{\rm total}$. We have also assumed that the redshift of the binary is small.

All the other quantities on the right side of Eq. (2.22) can be directly found by measuring the frequency, frequency evolution, and amplitude for different harmonics of the GW waveform, except for ν. Thus, the only unknown, in this case, is ν, for considering the leading order features of the GW signal. However, since ν will affect the frequency evolution in higher order, it can be constrained using template fitting in the data analysis. The error of the measured ν and its influence on acceleration measurement can be different, depending on the specific parameters of the GW source. Thus, we will adopt DWDs/BBHs as examples in the following discussion.

DWDs typically have a smaller chirp mass than BBHs, which means their intrinsic frequency shift rate of GW ("chirp rate" hereafter) is smaller. In other words, DWDs behave like monochromatic GW sources. As mentioned above, the lack of intrinsic frequency evolution renders an under-constrained ν for DWDs. However, since $\Delta f \propto M_{\rm total}^{2/3}$, the coefficient before ν is also smaller for DWDs in Eq. (2.22). Therefore acceleration measurement of DWDs has a weaker dependency on ν compared to the BBHs case. Thus, even if DWDs' ν is highly uncertain, we can still establish an accurate acceleration measurement in the observation.

This behavior is depicted in the upper panel of Figure 2.4, where we show the acceleration as a function of the symmetric mass ratio ν (see Eq. (2.22)). To highlight that the symmetric mass ratio is not constrained, we denote it in the Figure as "uncert," i.e., $\nu_{\rm uncert}$. As seen in the Figure, because the DWDs' chirp rate ($\dot{f}_e$) is relatively small, the frequency shift we observe mostly comes from the source's peculiar acceleration ("$f_e a_{///}/c$" in Eq. (2.9)). Thus, the DWDs have a small error of acceleration measurement and a clear signature of the accelerating environment. Even for a highly under-constrained symmetric mass ratio, the accuracy of acceleration measurement is still promising, about $0.5-10\%$ from the lowest to highest frequency (compared to the dashed line in the Figure, and also see the bottom panel).

On the other hand, BBHs' chirp rate is relatively large, enabling us to determine ν better. But the acceleration measurement of BBHs highly depends on ν because of their large total mass. Therefore, an inaccurate ν in the GW data analysis of BBHs can induce an extremely large error in the acceleration measurement. For example, in the middle and lower panel of Fig. 2.4, error of acceleration measurement is over 100% for a BBH system with the frequency of the 2nd harmonic $2-4$ mHz, which is not acceptable in the observation.

To conclude, DWDs' acceleration measurement accuracy is promising even if there is no constraint on the symmetric mass ratio ν in observation. Thus, it can be estimated analytically. However, the estimation of BBHs' acceleration measurement error requires the

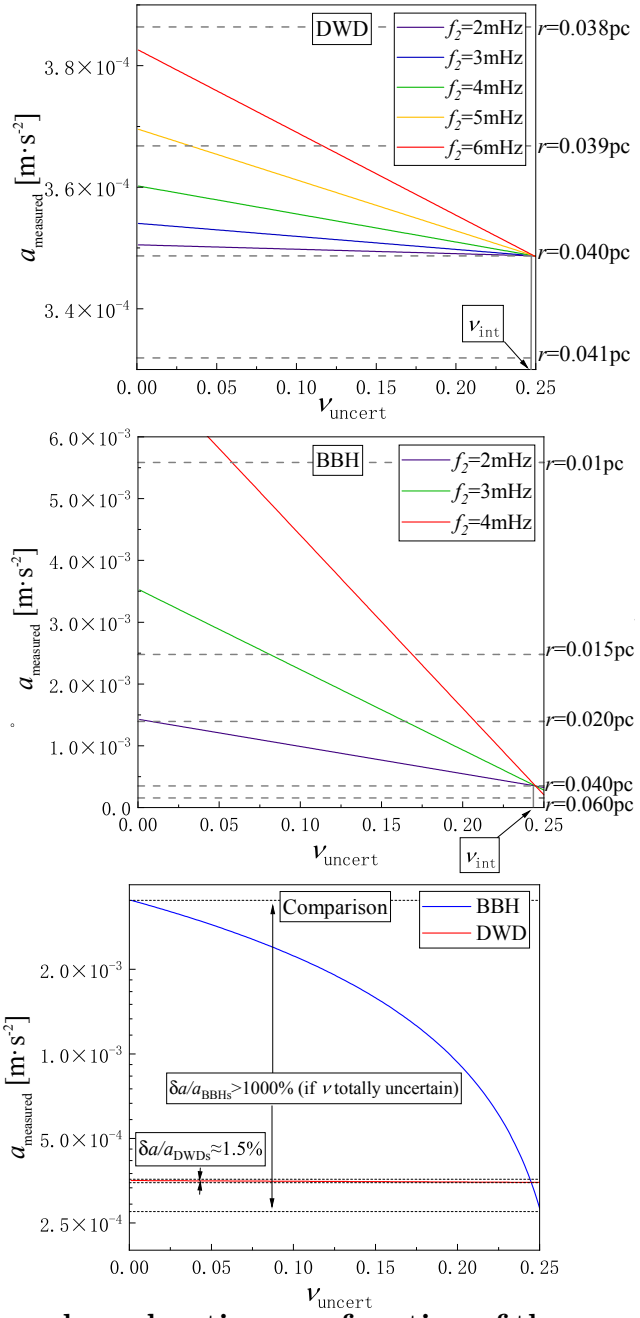


Figure 2.4: **The measured acceleration as a function of the uncertainty in measured symmetric mass ratio** $\nu_{\rm uncert}$ Here we place a binary at 0.04 pc from a $4 \times 10^6 M_\odot$ SMBH and choose the phase angle so that the line-of-sight acceleration is maximized. *Upper Panel* shows a binary WD composed of: $m_1 = 0.35\ M_\odot$, $m_2 = 0.4\ M_\odot$, $e = 0.1$, with the frequency of second harmonic $f_2 = 2, 3, 4, 5$ and 6 mHz, bottom to top. *Middle Panel* depicts a BH binary composed of: $m_1 = 15\ M_\odot$, $m_2 = 20\ M_\odot$, $e = 0.1$. *Bottom Panel* is the same as the top and middle panel, but shows the comparison between DWDs and BBHs for $f_2 = 3$mHz to scale. The solid lines represent the measured acceleration as a function of measured ν, (see Eq. (2.22)). The dashed lines correspond to the magnitude of peculiar acceleration at the labeled distances from the SMBH. As noted in the text, the measurement of the symmetric mass ratio can be uncertain, depicted here in the x-axis by $\nu_{\rm uncert}$ (all the possible values of ν).The intrinsic symmetric mass ratio $\nu_{\rm int}$ of the binary is marked on the plot for reference.

numerical GW template fitting, in which we analyze the higher-order frequency evolution and determine the accuracy of ν measurement. We address this issue for the case of BBHs using the numerical method in Section 2.4.2.

For a binary at the center of a galaxy, other physical processes may also affect its evolution. In particular, the Eccentric Kozai-Lidov (EKL, e.g., Kozai, 1962; Lidov, 1962; Naoz, 2016), can excite eccentricities and enhance the compact objects merger rate (e.g., Hoang et al., 2018; Stephan et al., 2019; Wang et al., 2021). However, in our case, we focus on binaries that will appear in the LISA band (i.e., in the mHz frequencies), in other words, hard binaries, where the EKL timescale is very long. For example, a 3 mHz GW signal for a 35 $M_\odot$ circular binary system corresponds to a binary separation of ~ 0.0025au. Specifically,

$$\begin{aligned} T_{\rm LK} &\sim \frac{P_{\rm SMBH}^2}{P_b}(1-e^2)^{3/2} \\ &\sim 2\times 10^{10}{\rm yr} \\ &\times \left(\frac{m_{\rm SMBH}}{4\times 10^6 M_\odot}\right)^{-1}\left(\frac{f_e^{j=2}}{3{\rm mHz}}\right)\left(\frac{r}{0.1{\rm pc}}\right)^3(1-e^2)^{3/2}\ , \end{aligned} \tag{2.23}$$

where $P_{\rm SMBH}$ is the period of the binary around the SMBH. Therefore, for these hard binaries, EKL effects can be neglected [1]. Similarly, the interactions with flying neighbors will only tend to harden the binary (e.g., Heggie, 1975). Moreover, two-body relaxation may allow the binary to migrate in a diffusive manner over time, however, this process is also much longer than the observational timescale and thus can be neglected (e.g., Sari and Fragione, 2019; Rose et al., 2020).

We emphasize that the peculiar acceleration and the velocity of the binary are still relatively small here ($\sim 10^2\ km\cdot s^{-1}$ in this example), thus do not require any special relativity corrections. Additionally, when measuring the acceleration of the eccentric compact binaries, other factors can contribute differently to the precession pattern in the GW signal (e.g., spin

[1] Note that for the binaries that are in close proximity to the SMBH, the EKL mechanism can still result in eccentricity excitations for hard binaries that are potentially detectable in LISA (Hoang et al., 2019).

effect and tidal effect, the latter can be important for DWDs and BNSs (Lau et al., 2022)). The full inclusion of these effects is beyond the scope of this paper. Moreover, unlike the previous studies of circular binary's acceleration (Seto, 2008; Robson et al., 2018a; Tamanini et al., 2020a, e.g.,), the acceleration of eccentric compact binaries is measurable even when they are distant from the tertiary, up to $\sim$ 1pc for a BBH system around a $4\times10^6 M_\odot$ SMBH, with the orbital period ($\sim 10^3$ yrs) much longer than the observation duration.

2.3 Numerical Approach

2.3.1 Waveform Template

For the generation of the accelerating eccentric compact binaries' GW templates, we adopt the x-model developed in Ref. (Hinder et al., 2010) and add the effect of peculiar acceleration by including the time-dependent doppler effect in waveform modulation.

The x-model is a time-domain, post-Newtonian (pN)-based waveform family, which captures all the critical features that eccentricity introduces to non-spinning binary (Huerta et al., 2014). The binary orbit is given in the Keplerian parameterization to 3 pN order and the conservative evolution is given to 3 pN order as well. In the x-model, the loss of energy and angular momentum is mapped to the change of orbital eccentricity e and the pN expansion parameter $x \equiv (\omega M_{\rm total})^{2/3}$, in which ω is the mean Keplerian orbital frequency. These two parameters are evolved according to 2 pN equations.

The equations in the x-model can be numerically solved, and thus can be used to generate eccentric GW templates in the time domain. The results have been validated against numerical relativity for the case of equal mass BBHs, $e = 0.1$, 21 circles before the merger. The x-model also reduces to some well-studied template families in the GW data analysis

for the zero-eccentricity case (Brown and Zimmerman, 2010).

We remind the reader that here, as a proof of concept, we focus on the acceleration-induced, time-dependent doppler effect. For demonstration purposes, in the following examples, the tertiary is placed in a circular orbit, and the phase angle is set to make the line-of-sight acceleration towards the detector maximized. However, we emphasize that different phase angles can lead to different signatures of acceleration in the GW waveform, and the specific value of acceleration measurement accuracy also varies.

2.3.2 Matched Filtering and Criteria for Distinguishing the Acceleration

To numerically verify whether the acceleration can be identified or not, we need to introduce some standard definitions in the GW data analysis. Here we use a numerical technique called "matched filtering", which is commonly adopted in the GW data analysis to estimate the GW sources' parameters (Thorne et al., 1987; Finn, 1992; Cutler and Flanagan, 1994).

For our purpose, we use this technique to quantify the similarity between two different waveforms. In particular, we will first transform the GW signal from an accelerating eccentric compact binary into the frequency domain (denoted as h_1 hereafter), then use a set of non-accelerating GW templates, h_2, to fit the detected signal h_1. We treat the waveforms as vectors in a Hilbert space (Helstrom, 2013), and define the noise-weighted inner product between h_1 and h_2 as:

$$\langle h_1 \mid h_2 \rangle = 2 \int_0^\infty \frac{\tilde{h}_1(f)\tilde{h}_2^*(f) + \tilde{h}_1^*(f)\tilde{h}_2(f)}{S_{\rm n}(f)} {\rm d}f \ , \tag{2.24}$$

in which $\tilde{h}_j$ (with $j = 1, 2$) means a Fourier transformation of the waveform, the star stands for the complex conjugate, and $S_n(f)$ is the one-sided noise power spectral density of LISA

(Thorne, 1987; Klein et al., 2016b).

The similarity between h_1 and h_2 can be estimated by the Match between them (e.g., see Section IV of Ref.(Afle et al., 2018) for a summary). First, define the normalized overlap as:

$$\mathcal{O}(h_1, h_2) = \langle \hat{h}_1 | \hat{h}_2 \rangle = \frac{\langle h_1 | h_2 \rangle}{\sqrt{\langle h_1 | h_1 \rangle \langle h_2 | h_2 \rangle}} \ . \tag{2.25}$$

The Match between h_1 and h_2 is defined as the maximized overlap over the signal's arrival time t_0 and phase Φ_0:

$$\mathrm{Match}(\mathrm{h}_1, \mathrm{h}_2) = \max_{\mathrm{t}_0, \Phi_0} \mathcal{O}(\mathrm{h}_1, \mathrm{h}_2) \ . \tag{2.26}$$

For a given h_1, we will generate a set of non-accelerating waveforms h_2, with different values of template parameters, to match h_1. The maximized Match over all the template parameters of h_2 is called the fitting factor (FF):

$$\mathrm{FF} = \max_{\boldsymbol{\lambda}} \{ \mathrm{Match}(\mathrm{h}_1, \mathrm{h}_2) \} \ , \tag{2.27}$$

in which $\boldsymbol{\lambda}$ represents the parameters of the GW template. (e.g., chirp mass $\mathcal{M}_c$, symmetric mass ratio ν, etc.)

In general, the absolute value of FF varies from 0 to 1, and a perfect match between two waveforms would give FF = 1.

Additionally, we need to consider the strength of the signal, which is quantified by the signal-to-noise ratio (SNR). For a given SNR level, there should exist a region in the parameter space where we cannot tell between two similar GW templates because of the noise in observation. The stronger the signal is (i.e., larger SNR), the smaller the confusion region will be. Since FF evaluates the similarity between two GW waveforms, we can compare the FF with SNR and derive a rule-of-thumb criterion for the two waveforms to be indistinguishable in the GW data analysis: (Lindblom et al., 2008; Chatziioannou et al., 2017; Takahashi and

Seto, 2002b; Cutler and Vallisneri, 2007):

$$\mathrm{FF} > 1 - (D-1)/(2\ \mathrm{SNR}^2)\ , \tag{2.28}$$

in which D represents the dimension of parameter space where the matched filtering is carried out (~ 10 for LISA-band sources, depending on the template. In our case, the parameters include mass for the components of binary m_1, m_2; eccentricity e; orbital frequency f; the distance of the source d; the angular position of the source ϕ_S, θ_S; orientation of the source ϕ_L, θ_L; and the line-of-sight acceleration $a_{//}$).

To conclude, we generate a set of non-accelerating GW waveforms h_2, with different parameters, then compute the match between an accelerating GW signal, h_1, with h_2, using Eq (7.21). Denoting the value of the optimal match as FF, it represents how similar the accelerating GW signal can be to the non-accelerating waveforms. Thus, in the observation, if FF is below the threshold given by the right side of Eq (7.22), it means the accelerating GW source's signal is distinguishable from any non-accelerating GW templates, i.e., strong enough for us to find the signature of acceleration in GW data analysis.

For demonstration purposes, in this paper, we will plot the quantity $1 - \mathrm{FF}$ instead of FF to highlight the difference between the two waveforms. Since FF is the maximized Match over all the template parameters, $1 - \mathrm{FF}$ represents the minimized Mismatch ($1 - \mathrm{Match}$) between a GW signal and its optimal fit. Similar to the criteria mentioned above, if this minimized mismatch becomes large enough, i.e., $1 - \mathrm{FF} > (\mathrm{D} - 1)/(2\ \mathrm{SNR}^2)$, there will be a distinguishable difference between the accelerating and non-accelerating waveforms.

2.3.3 Fisher Matrix Analysis and Measurement Accuracy

Adopting the GW templates with acceleration, we can measure the value of compact binaries' peculiar acceleration in the data analysis. In this case, the accuracy of acceleration measurement can be evaluated using the Fisher Matrix Analysis (Coe, 2009; Cutler and Flanagan, 1994), which is commonly used as a linearized estimation for the measurement error in the high SNR limit.

Representing the parameters of a GW source as a vector $\boldsymbol{\lambda}$, the GW waveform h can be expressed as $h(\boldsymbol{\lambda})$. The Fisher Matrix is defined as:

$$F_{ij} = \left\langle \frac{\partial h(\boldsymbol{\lambda})}{\partial \lambda_i}, \frac{\partial h(\boldsymbol{\lambda})}{\partial \lambda_j} \right\rangle . \tag{2.29}$$

We define C as the inverse of the Fisher matrix, $C = F^{-1}$. It approximates the sample covariance matrix of the Bayesian posterior distribution for the GW source's parameters. In other words, we can use the following equation to estimate the error of parameter measurement in our work:

$$\delta\lambda_i = \sqrt{\left\langle (\Delta\lambda_i)^2 \right\rangle} = \sqrt{C_{ii}} \tag{2.30}$$

In a nutshell, when estimating the accuracy of acceleration measurement, the waveform templates are generated numerically according to the method mentioned in Section 2.3.1, including the peculiar acceleration in the parameter set. We then adopt Fisher Matrix Analysis to calculate the error of the acceleration measurement for different kinds of GW sources.

2.4 Examples and Results

Here we provide several examples to highlight the usefulness and application of the methods in Section 2.3. We emphasize that the measurement accuracy of acceleration is only valid if we distinguish the accelerating GW sources from the non-accelerating ones. Thus, adopting non-accelerating GW templates in search of GW signals can suppress us from identifying some accelerating GW sources. As mentioned in Section 2.3.3 and 2.3.2, these sources can have good acceleration measurement accuracy but are misidentified because they fail to meet the criteria for distinguishing the acceleration. However, we can overcome this drawback by using the accelerating GW templates when searching for the GW signal.

In other words, the criteria in Section 2.3.2 and the examples in this Section 2.4.1 are for the cases when we merely use non-accelerating templates in search of GW signals, thus being more stringent. However, the analysis of Section 2.3.3 and examples of Section 2.4.2 assume that the acceleration has been identified and included in the GW template fitting. Thus, their results represent the maximum capability of LISA to measure the acceleration of eccentric compact binaries.

2.4.1 Distinguishing the Acceleration - Numerical Approach

In Section 2.2.2.2, we derived the criteria for distinguishing the acceleration (Eq. (2.21)). This equation is valid when the mass of a compact binary is small and the curvature of frequency evolution is hard to measure (e.g., DWDs). Here we compare this Equation with numerical results as well as expand it to other cases, such as BBHs.

The first example is depicted in Figure 2.5, where we consider a DWD system orbiting around a SMBH. Note that we expect a high abundance of DWDs to reside in the vicinity of our own SMBH (Stephan et al., 2019; Wang et al., 2021). This Figure shows $1 - \mathrm{FF}$, the mismatch

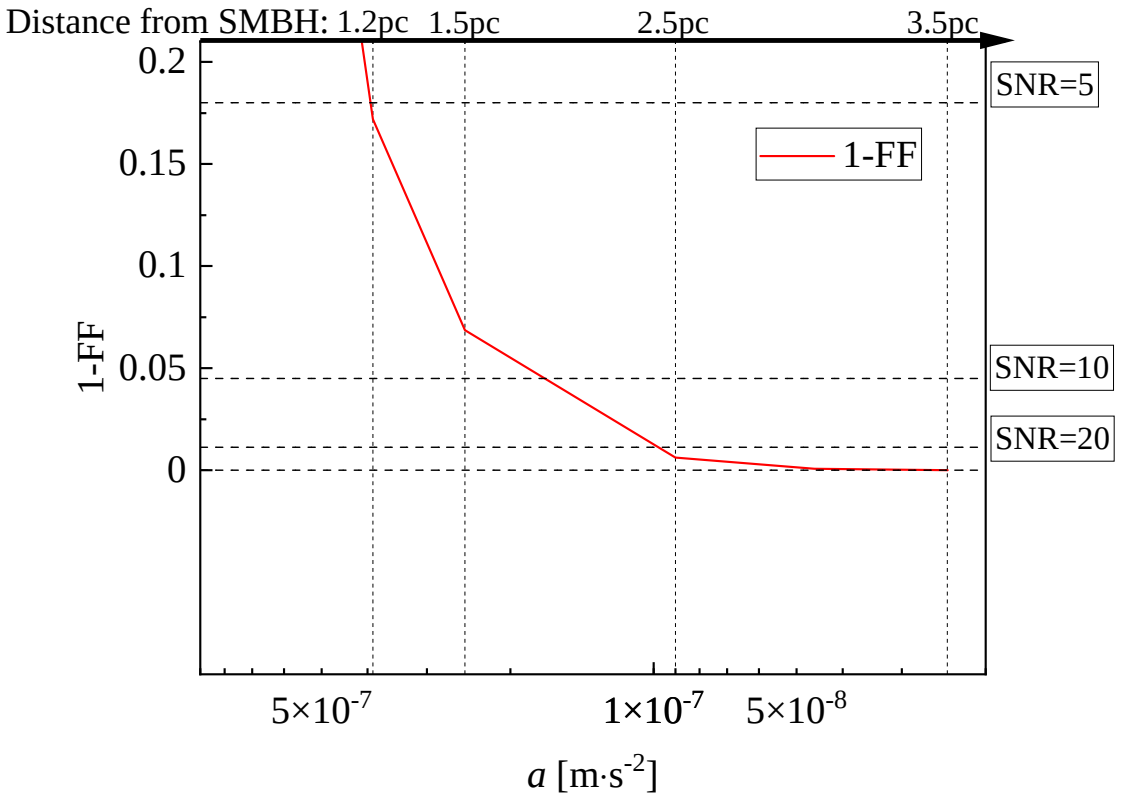


Figure 2.5: **The mismatch between an accelerating DWD's GW and its optimal fit within non-accelerating templates $(1-\mathrm{FF})$, as a function of the DWDs' peculiar acceleration.** We show a DWD system with $m_1 = 0.35\mathrm{M}_\odot, \mathrm{m}_2 = 0.4\mathrm{M}_\odot$, $e = 0.1$, $f_e^{j=2} = 3\mathrm{mHz}$, on a circular orbit around a SMBH with $M_{\mathrm{SMBH}} = 4\times10^6\ \mathrm{M}_\odot$ at different distances. The observation duration is set to be 4 years. Adopting the proposed methodology of future observations, we apply matched filtering method (Finn, 1992; Cutler and Flanagan, 1994) to find the best fit in templates without considering acceleration. $1-\mathrm{FF}$ is plotted as a function of DWD's acceleration/ distance from the SMBH. The black lines mark the critical value of $1-\mathrm{FF}$ for the detection of acceleration, providing different SNR in observation (see Eq. (7.22), $D = 10$ for this example). Note that the acceleration in this Figure increases to the left.

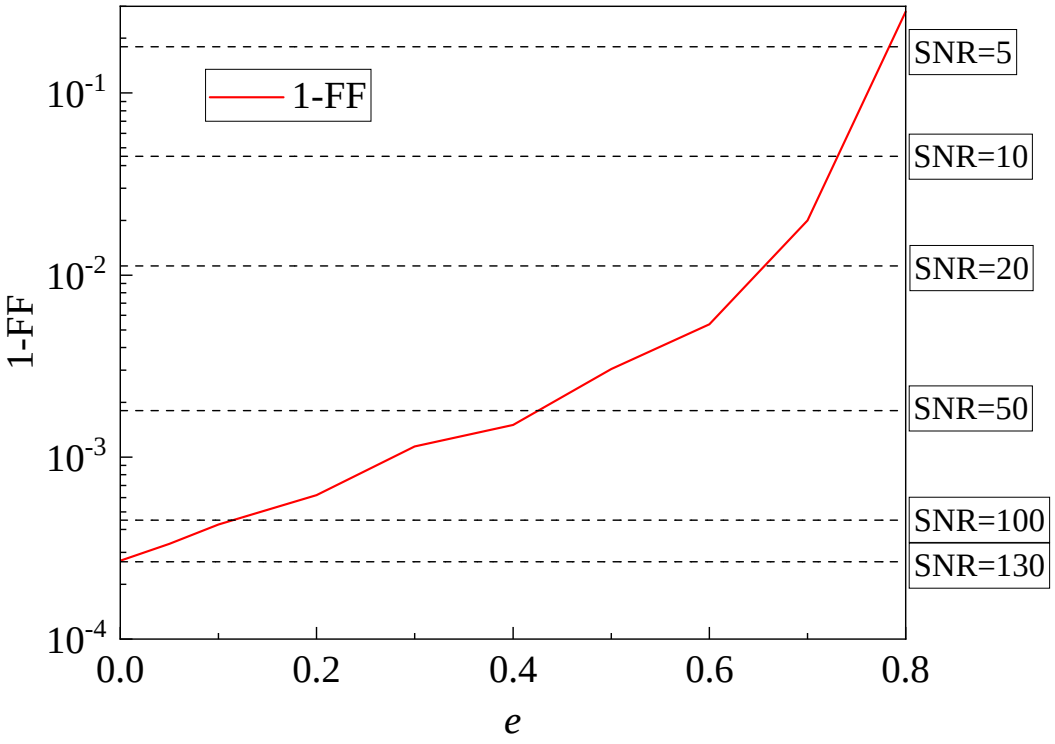


Figure 2.6: **The mismatch between an accelerating BBH's GW and its optimal fit within non-accelerating templates $(1-\mathrm{FF})$, as a function of the BBH's eccentricity.** Here we place a BBH system with $m_1 = 15\mathrm{M}_\odot, m_2 = 20\mathrm{M}_\odot, f_e^{j=2} = 3\mathrm{mHz}$ at 0.1 pc from a $4 \times 10^6 \mathrm{M}_\odot$ SMBH, set the observational time $\tau_{\mathrm{obs}} = 4\mathrm{yrs}$. Following the same steps as Figure 2.5, we apply matched filtering method to find the best fit in templates without considering acceleration and plot $1 - \mathrm{FF}$ as a function of BBH's eccentricity. As is shown in the figure, $1 - \mathrm{FF}$ becomes larger and the acceleration is more likely to be detected for higher eccentricity.

between the accelerating signal and its optimal fit within non-accelerating templates, as a function of the source's acceleration. As shown in the Figure, larger acceleration values yield a larger mismatch between the accelerating signal and non-accelerating templates. Comparing Figure 2.5 with Figure 2.3, while the y-axis is different in these two Figures, we recover a similar trend as in the analytical estimation.

In particular, when $1 - \mathrm{FF}$ exceeds each dashed black line in Figure 2.5, we can distinguish the acceleration of the GW source for the corresponding SNR level. For the configuration in this Figure, the mismatch becomes large enough for us to distinguish the acceleration when the DWD's distance to the SMBH is $2.4\mathrm{pc}, 1.9\mathrm{pc}, 1.2\mathrm{pc}$ (for the $\mathrm{SNR} = 20, 10, 5$, respectively). This result is consistent with the analytical estimation in Figure 2.3, where the chirp mass measurement significantly deviates from the intrinsic chirp mass and exceeds the upper bound given by the precession pattern at around $1 \sim 2\mathrm{pc}$.

Figure 2.5 highlights that the critical distance for distinguishing the acceleration is much larger than the estimation of former works (Robson et al., 2018a; Tamanini et al., 2020a). This difference is because we allowed for a non-negligible, though still small, eccentricity, $e = 0.1$, in our example.

Next (Figure 2.6) we consider a BBH system orbiting around a SMBH. As mentioned in Section 2.2.2.2, since the BBH system has a larger chirp mass than DWD and DNS systems, its intrinsic chirp rate changes significantly during the observation (See Eq. (5.34)). The varying chirp rate makes it hard to estimate analytically if the acceleration is distinguishable. However, the numerical analysis (see Section 2.3.2) is still valid and can be used to estimate if we can distinguish an accelerating signal from a non-accelerating signal in this case.

In Figure 2.6, we fix the BBHs' distance to the SMBH as 0.1pc and vary the eccentricity of the BBH system. As shown in this Figure, the mismatch between the accelerating GW signal and its optimal fit in non-accelerating templates grows with eccentricity. In particular,

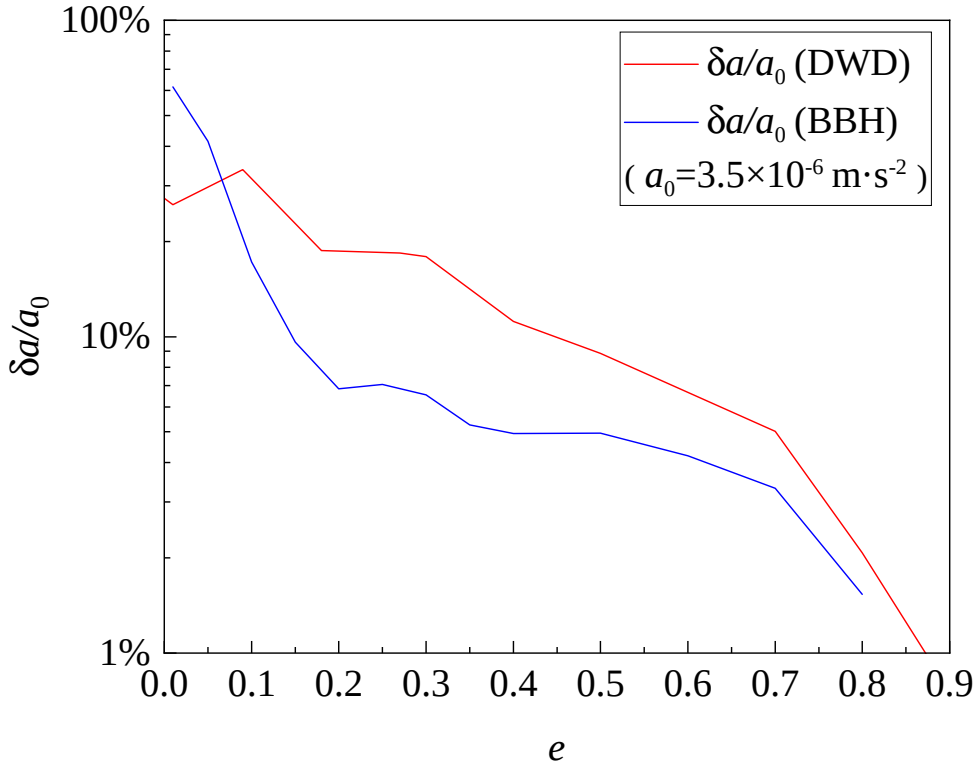


Figure 2.7: **Relative error of acceleration measurement as a function of the compact binary's eccentricity.** Here we place a compact binary system at 0.4 pc from a $4\times10^6\mathrm{M}_\odot$ SMBH, set the initial GW frequency $f_e^{j=2}=3\mathrm{mHz}$, observational time $\tau_{\mathrm{obs}}=4\mathrm{yrs}$ and SNR= 20. We plot the relative error of acceleration measurement, as a result of the fisher matrix analysis (see text), as a function of binary's initial eccentricity. Red line shows a DWD system with $m_1=0.35\mathrm{M}_\odot, m_2=0.4\mathrm{M}_\odot$, while blue line represents a BBH system with $m_1=15\mathrm{M}_\odot, m_2=20\mathrm{M}_\odot$. Note that the amplitude of peculiar acceleration is $a_0\sim3.5\times10^{-6}m\cdot s^{-2}$ for this configuration.

the signal-to-noise ratio requirement for distinguishing the acceleration drops from 130 to 10 as the eccentricity increases from 0 to 0.7. This Figure is also a proof of concept that distinguishing an accelerating GW source from a non-accelerating one can be done for an eccentric system with a large chirp mass, i.e., BBH.

2.4.2 Measuring the Acceleration - Numerical Approach

With the help of Fisher Matrix Analysis (See Section 2.3.3), we can give a numerical estimation of the acceleration measurement accuracy, providing that GW templates with acceleration are adopted in the parameter extraction. Figure 2.7 demonstrates how the relative error of acceleration measurement ($\delta a/a_0$, where a_0 is the intrinsic acceleration) decreases with increasing eccentricity. As a proof of concept, we fix the signal-to-noise ratio (SNR = 20), observation duration ($\tau_{\rm obs} = 4yrs$), and the acceleration ($a = 3.5 \times 10^{-6} m \cdot s^{-2}$). As shown in the Figure, the error of acceleration measurement is quite large ($\sim 100\%$) when the orbit eccentricity is zero. However, the error sharply drops to $\sim 5\%$ for moderate eccentricity and is lower than 1% when the eccentricity is over 0.8. This sharp decrease happens because the multiple harmonics in the GW signal can be detected even when the binary's eccentricity is ~ 0.1. This feature enables us to detect the eccentric GR precession pattern and disentangle the acceleration from the chirp mass measurement.

Additionally, the acceleration measurement accuracy's dependence on eccentricity varies for different kinds of compact binaries. In particular, BBHs have a larger error of acceleration measurement than DWDs when their eccentricity is negligible. However, the error drops more sharply along with the increase of BBHs' eccentricity. This fact is consistent with the analysis in Section 2.2.3: the large chirp mass of BBHs renders its large intrinsic chirp rate $\dot{f}_e$. Therefore, because of the degeneracy between the acceleration and the chirp mass ($\dot{f}_{acc}$ and $\dot{f}_e$), BBHs will have larger uncertainty of acceleration if the eccentric precession pattern

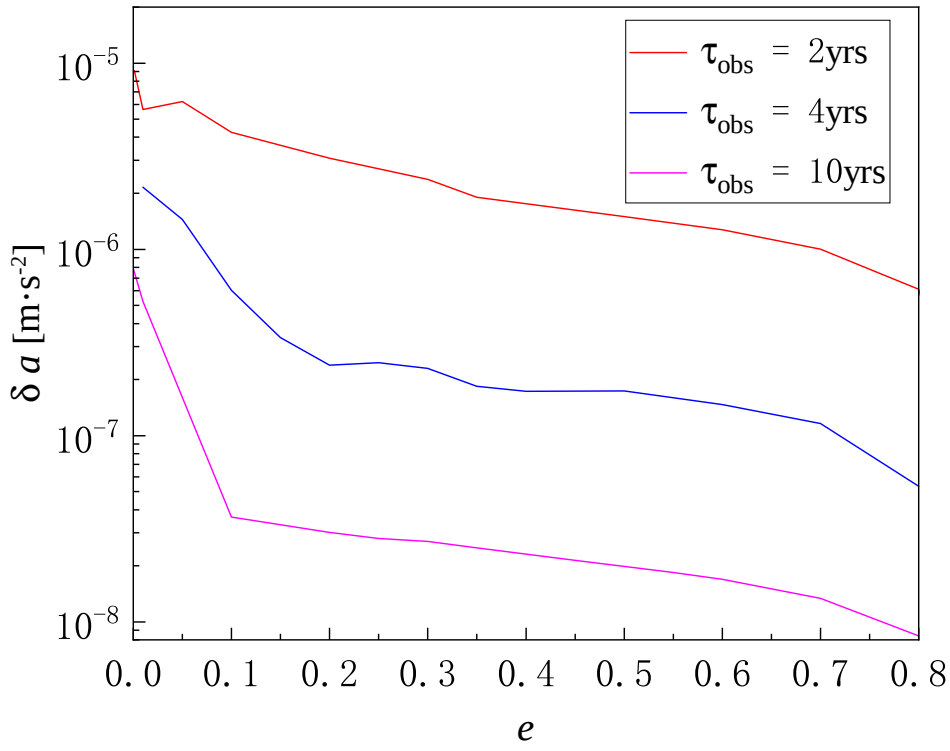


Figure 2.8: **Absolute error of acceleration measurement as a function of BBHs' eccentricity for different observation durations.** Here we take the same BBH as in Figure 2.7, but compare the absolute error of acceleration measurement for different observation durations (2yrs/ 4yrs /10yrs). The initial frequency of GW is $f_e^{j=2} = 3$mHz and SNR is set to be 20 for all the cases.

is not detected and $\dot{f}_e$ is not disentangled. However, when the eccentricity increases and the precession pattern helps us disentangle the acceleration, the large chirp rate of BBH enables us to get a higher measurement accuracy of the source's parameters, including acceleration.

Figure 2.8 demonstrates the effect of the observation duration on the acceleration measurement accuracy. Here we focus on the case of an eccentric BBH system around a SMBH and adopt the same configuration as in Figure 2.7 to quantify LISA's ability of acceleration measurement. The signal-to-noise ratio is set to be 20, and we consider three characteristic observation duration ($\tau_{\rm obs} = 2, 4$ and 10 years, from top to bottom, respectively). For a stellar mass BBH system like the one in Figure 2.8, the accuracy of acceleration measurement is around $\sim 10^{-7} m \cdot s^{-2}$ for a 4-year mission, and can be $\sim 10^{-8} m \cdot s^{-2}$ for a 10-year mission.

We emphasize that the period of the outer orbit ($\sim 10^5 yrs$) is much longer than the observation duration ($\sim 4 yrs$) in Figure 2.8. Thus, the results of this figure can be generalized to other cases when the acceleration is almost constant during the observation. Figure 2.9 maps the parameter space where we can accurately measure the binary's peculiar acceleration. In particular, the left panel corresponds to a compact binary orbiting around the $4 \times 10^6 M_\odot$ SMBH, and the right panel demonstrates the case when the tertiary is a $1 M_\odot$ star. Setting the x-axis as the amplitude of acceleration (distance to the tertiary) and the y-axis as the eccentricity of the inner binary, we plot the boundary of the regimes where the acceleration measurement accuracy is higher than the given values. The result shows that LISA can measure an eccentric compact binary's peculiar acceleration when it is within $\sim 10^0$pc from a $4 \times 10^6 \mathrm{M}_\odot$ SMBH, or $\sim 10^2$AU from a stellar-mass tertiary.

As shown in Figure 2.9, the existence of eccentricity extends the parameter space where the binary's acceleration can be measured, allowing us to identify more distant tertiaries (up to $\sim$ 10 times the distance when the inner binary is circular). Moreover, when the binary's eccentricity is small, DWDs have a higher accuracy of acceleration measurement than BBHs. However, the increase in eccentricity can enhance the BBHs' acceleration measurement more

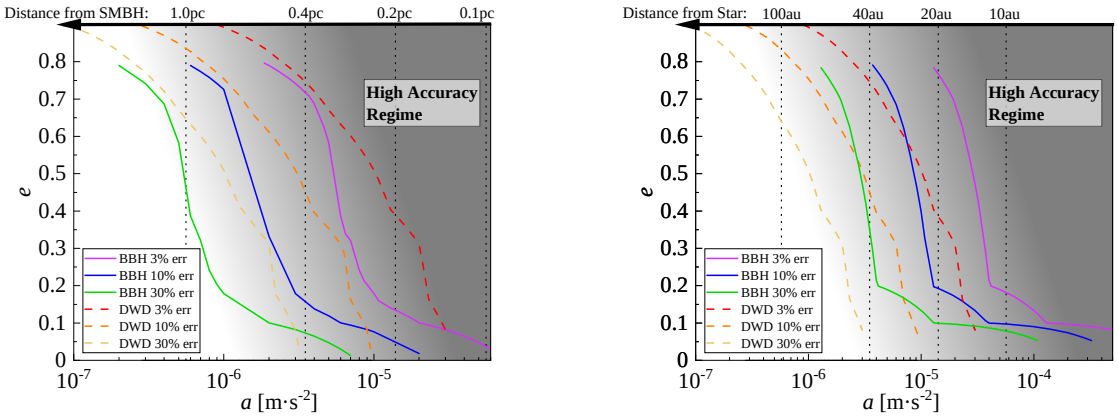


Figure 2.9: **Critical eccentricity, for the measurement accuracy of acceleration to reach given thresholds, as a function of the binary's peculiar acceleration.** For each line in the two panels, we set a targeted accuracy of peculiar acceleration measurement (i.e., 30%, 10%, and 3%, from left to right), and show the critical eccentricity of the binary for GW measurement to reach such accuracy as a function of the binary's acceleration. The solid lines represent a BBH ($m_1 = 15\mathrm{M}_\odot, m_2 = 20\mathrm{M}_\odot$), and the dashed lines represent a DWD ($m_1 = 0.35\mathrm{M}_\odot, m_2 = 0.4\mathrm{M}_\odot$). Both systems have the initial GW frequency $f_e^{j=2} = 3\mathrm{mHz}$. As explained in the text, the acceleration measurement can be applied to a wide range of tertiaries. Here, as an example we consider a $4 \times 10^6\mathrm{M}_\odot$ SMBH case (*Left Panel*), and a $1\mathrm{M}_\odot$ star case (*Right Panel*). We set the observation duration as 4 yrs and SNR to be 20, compute the absolute error of acceleration measurement for a fixed distance from the tertiary ($r = 0.4pc$ for the SMBH case, $r = 100au$ for the star case), and analytically generalize the results to get the relative error for the different magnitude of a (distance to the tertiary). The acceleration measurement exceeds the targeted accuracy in the region to the right of each line, where we darken the background color to highlight the difference. For illustration purposes, we translate the acceleration into the binary's distance to the tertiary and mark it on the top of each panel. This figure highlights that higher eccentricity can extend the parameter space where acceleration can be accurately measured.

significantly, which is consistent with our analysis of Figure 2.7.

2.5 Discussion

Many LISA-band compact object binaries have non-negligible acceleration caused by the gravitational pull of either a nearby stellar-mass tertiary or a SMBH in the galactic center (e.g., Antognini et al., 2014; Antognini and Thompson, 2016; Hoang et al., 2018; Stephan et al., 2016a, 2019; Wang et al., 2021; Rose et al., 2020). Moreover, these accelerating GW sources are likely to have eccentricity in the millihertz band (O'Leary et al., 2009a; Samsing, 2018; Hoang et al., 2019; Fragione et al., 2019; Breivik et al., 2020; Naoz et al., 2020; Wang et al., 2021; Zhang et al., 2021). In particular, in some dynamical channels, the existence of a tertiary can directly produce LISA-band sources by exciting the eccentricity of inner orbit and accelerating the merger (Thompson, 2011; Antognini et al., 2014; Hoang et al., 2018; Stephan et al., 2019; Martinez et al., 2020; Hoang et al., 2020; Naoz et al., 2020; Stephan et al., 2019; Wang et al., 2021). Thus, we expect the accelerating eccentric binaries to be a common feature in the future GW observation.

However, it may be difficult to ascertain the properties of these sources because a degeneracy exists between the chirp-mass-induced frequency shift and acceleration-induced frequency shift (Robson et al., 2018a; Tamanini et al., 2020a; Chen, 2020; Xuan et al., 2021). This degeneracy happens because both the chirp mass and the peculiar acceleration contribute to the frequency shift rate in the GW signal for the leading order, making it hard to disentangle chirp mass from acceleration in data analysis.

In this work, we explored the detection of peculiar acceleration for eccentric compact binaries in the LISA band, taking into account the effect of GR precession pattern. We find that the eccentric GR precession pattern can break the degeneracy between the compact bi-

nary's acceleration and chirp mass (See the flowchart in Figure 2.2 for our overall approach). Therefore, it can be much easier to detect the acceleration of eccentric GW sources than circular ones.

By deriving analytical formulas, we quantified how eccentricity helps with distinguishing the accelerating GW sources from non-accelerating GW templates (see Eq.(2.21)). Furthermore, we demonstrated that the existence of eccentricity can improve the measurement accuracy of acceleration. Analytically, we constrained such accuracy for DWDs in Figure 2.4.

The analytical results are verified numerically, and the ability of LISA to detect the peculiar acceleration of eccentric GW sources is estimated. For example, we find that the critical distance to distinguish the acceleration is $\sim$ 2pc for the case of a DWD system orbiting around a $4 \times 10^6 \mathrm{M}_\odot$ SMBH, with $e = 0.1$ and SNR ~ 20 (i.e., Figure 2.5). Additionally, we find that the critical SNR for distinguishing the acceleration of a stellar-mass BBH system can drop from 130 to 10 when the eccentricity rises from 0 to 0.7 (for example, as highlighted in Figure 2.6). Moreover, by adopting the GW templates with acceleration, we can improve the accuracy of acceleration measurement by a factor of $10 \sim 100$ for GW sources with moderate eccentricity, compared with the zero-eccentricity cases (see Figure 2.7).

During a 4-year LISA mission, the accuracy of acceleration measurement can be $\sim 10^{-7} m \cdot s^{-2}$ when SNR = 20 for an eccentric stellar-mass BBH system orbiting around a SMBH. Such accuracy enables us to measure the binary's acceleration when it is $\sim$ 1pc from a $4 \times 10^6 \mathrm{M}_\odot$ SMBH. Moreover, the accuracy of acceleration measurement for eccentric compact object binaries can be even higher when the observation duration is longer (see Figure 2.8), or if the eccentricity of the GW source is higher (as depicted in Figure 2.9).

Our results highlight the importance of eccentricity in GW astronomy, as it can disentangle the compact binary's parameters and significantly enhance acceleration measurement. In future GW data analysis, adopting GW templates that include both eccentricity and accel-

eration can be meaningful to our understanding of the environment of the GW sources.

2.6 Acknowledgments

ZY acknowledges the partial support from the Mani L. Bhaumik Institute for Theoretical Physics summer fellowship and a partial support of the UCLA's Summer Mentored Research Fellowship (SMRF). SN acknowledges the partial support from NASA ATP 80NSSC20K0505, NSF through grant No. 2206428, and thanks Howard and Astrid Preston for their generous support. XC is supported by the Chinese National Science Foundation through grant No. 11873022.

Chapter 3

Detecting Gravitational Wave Bursts From Stellar-Mass Binaries in the Milli-hertz Band

A version of this chapter was previously published in *The Astrophysical Journal* (Xuan et al., 2024a, ApJ 965 148).

Abstract

The dynamical formation channels of gravitational wave (GW) sources typically involve a stage when the compact object binary source interacts with the environment, which may excite its eccentricity, yielding efficient GW emission. For the wide eccentric compact object binaries, the GW emission happens mostly near the pericenter passage, creating a unique, burst-like signature in the waveform. This work examines the possibility of stellar-mass bursting sources in the mHz band for future LISA detections. Because of their long lifetime

($\sim 10^7$ yr) and promising detectability, the number of mHz bursting sources can be large in the local universe. For example, based on our estimates, there will be $\sim 3-45$ bursting binary black holes in the Milky Way, with $\sim 10^2 - 10^4$ bursts detected during the LISA mission. Moreover, we find that the number of bursting sources strongly depends on their formation history. If certain regions undergo active formation of compact object binaries in the recent few million years, there will be a significantly higher bursting source fraction. Thus, the detection of mHz GW bursts not only serves as a clue for distinguishing different formation channels, but also helps us understand the star formation history in different regions of the Milky Way.

3.1 Introduction

Gravitational wave bursts are expected to be a natural consequence of wide, eccentric compact object binaries' GW emission. In particular, for highly eccentric binaries, the GW emission happens mostly near the pericenter passage, creating a unique, pulse-like signature that lasts much shorter than the orbital period (see, e.g., Kocsis et al., 2006a; O'Leary et al., 2009a; Gould, 2011; Kocsis and Levin, 2012; Seto, 2013). Most of the burst emission does not yield a merger immediately; therefore, if the GW sources have an orbital period that is smaller than the observational time, the bursting signal will appear as *repeated bursts* (RB).

As the source of GW bursts, eccentric compact object binaries are often expected to form via dynamical channels, during which the binary's interaction with the environment excites its eccentricity e, reduces the pericenter distance, and causes effective GW radiation. Generally, several dynamical mechanisms involve a highly eccentric stage during the GW source's evolution. For example, in a hierarchical triple system (a tight binary orbiting a third body on a much wider "outer orbit"), the inner binary can undergo large eccentricity oscillations due to gravitational perturbations from the tertiary. This so-called eccentric Kozai-Lidov

(EKL) mechanism (Kozai, 1962; Lidov, 1962; Naoz, 2016) may potentially contribute to the overall merger rate of stellar mass compact objects at significant levels (e.g., Wen, 2003; Hoang et al., 2018; Hamers, 2018; Stephan et al., 2019; Bub and Petrovich, 2020; Deme et al., 2020; Wang et al., 2021). Additionally, wide compact object binaries in the galactic field may interact with the surrounding environment, which can excite the binary's eccentricity (e.g., Michaely and Perets, 2019, 2020; Michaely and Naoz, 2022), resulting in merger events that are potentially observable. Moreover, a variety of dynamical mechanisms, such as GW capture, binary-single, and binary-binary scattering interaction, can take place in dense star clusters, producing compact object binaries with non-negligible eccentricity (e.g., O'Leary et al., 2009a; Thompson, 2011; Aarseth, 2012; Kocsis and Levin, 2012; Breivik et al., 2016; D'Orazio and Samsing, 2018; Zevin et al., 2019; Samsing et al., 2019; Martinez et al., 2020; Antonini and Gieles, 2020; Kremer et al., 2020; Winter-Granić et al., 2023). Furthermore, dynamical interactions in a flattened black hole distribution, such as in a stellar disk or an active galactic nucleus accretion disk, may also lead to highly eccentric mergers (Tagawa et al., 2021; Samsing et al., 2022; Muñoz et al., 2022; Gautham Bhaskar et al., 2023).

The detection of repeated bursts can greatly enhance our understanding of the GW sources' dynamical formation. In particular, with the corresponding data analysis methods (e.g., Tai et al., 2014; Loutrel and Yunes, 2017; Bécsy et al., 2020), the LIGO-VIRGO-KAGRA (LVK) detectors may detect the residual eccentricity of highly eccentric sources, thus helping with identifying the fraction of GW sources formed in a variety of dynamical channels (e.g., East et al., 2013; Samsing et al., 2014; Coughlin et al., 2015; Gondán et al., 2018b,a; Zevin et al., 2021). Furthermore, as one of the main targets of the future space-based gravitational wave detectors, the extreme mass ratio inspirals (EMRIs) are expected to have high eccentricity in the mHz band, emitting detectable GW bursts at a cosmological distance (e.g., Glampedakis, 2005; Hopman and Alexander, 2006; Rubbo et al., 2006; Amaro-Seoane et al., 2007; Barack, 2009; Berry and Gair, 2013; Chen and Han, 2018; Fan et al., 2022; Oliver et al., 2023; Naoz et al., 2022; Naoz and Haiman, 2023). With the unique signature of highly-eccentric orbit,

we can even enhance the peculiar acceleration measurement of the GW source by a factor of ~ 100 (Xuan et al., 2024a) and probe the gravitational potential surrounding these bursting systems (Zhang et al., 2021; Romero-Shaw et al., 2023).

In this work, we focus on stellar-mass compact object binaries that are bursting in the mHz band. These sources will typically have a semi-major axis $a \gtrsim 0.1$ au, up to $\sim 10^5$ au, with the pericenter distance $a(1-e) \sim 10^{-3}$ au, which makes the peak frequency of GW emission in the milli-hertz band. Although the GWs from these sources may be weaker because of their light mass (compared with EMRIs) and larger orbital separation (compared with bursting sources in the LIGO band, see, e.g., Randall et al., 2022), they are expected to have a much longer lifetime and therefore a larger number of systems in the mHz band (e.g., Fang et al., 2019). Furthermore, since the mHz bursting sources have not undergone significant orbital shrinkage, their eccentricity is more likely to be extreme, and their evolution is less rapid. These features can be used to extract relevant information about compact object binaries' surrounding environment, as well as their formation history.

This paper is organized as follows. We first specify the definition of bursting GW sources in Section 3.2.1, then quantify their detectability (Section 8.3.2) and lifetime (Section 3.2.3). In Section 7.3, we constrain the population of bursting sources from the observational results of LIGO (Section 3.3.2), then carry out numerical simulations to predict the number of detectable bursts for LISA. We show the results separately, for the field (Section 4.3.2.2), globular clusters (Section 4.3.2.1), and the galactic nucleus (Section 3.3.5) of the Milky Way. In Section 7.6, the properties of stellar-mass bursting sources are summarized and the implications are discussed.

Unless otherwise specified, we set $G = c = 1$.

3.2 Repeated Bursts for Eccentric Sources in the Millihertz Band

3.2.1 Burst Definition

Heuristically, a burst is defined as a situation in which a significant amount of energy is emitted in a short amount of time compared to the orbital period. In particular, for eccentric binary sources, the pericenter time is usually defined with the orbital separation, velocity, and eccentricity, (r_p, v_p, e) as (e.g., O'Leary et al., 2009a)

$$T_{\rm p} \sim \frac{r_p}{v_p} \sim (1-e)^{3/2} T_{\rm orb} \ , \tag{3.1}$$

where $T_{\rm orb} = 2\pi a^{3/2} m_{\rm bin}^{-1/2}$ is the period of a binary with a mass $m_{\rm bin}$ and semi-major axis a. Note that there is an order unity factor of $(1+e)^{-1/2}$ that we omit here.

As a proof of concept, consider a source with $e > 0.9$, we demonstrate below that, in this case, more than 88% of the GW energy emission is emitted in less than 1% of the orbital period during pericenter passage, regardless of its masses and semi-major axis.

The fraction of GW energy emitted during a burst can be estimated by integrating the power of GW emission, P, over the orbital true anomaly ψ. Particularly, $P(\psi)$ is given by (Peters and Mathews, 1963):

$$\begin{aligned} P(\psi) &= \frac{8}{15} \frac{m_1^2 m_2^2 \left(m_1+m_2\right)}{a^5 \left(1-e^2\right)^5} (1+e\cos\psi)^4 \\ &\quad \times \left[12(1+e\cos\psi)^2 + e^2 \sin^2\psi\right] \ , \end{aligned} \tag{3.2}$$

in which m_1, m_2 are the mass of the binary's components.

Throughout the paper, as a proof of concept, we adopt 1% as the fraction of burst time rela-

tive to the orbital period (note that other bursting fractions are straightforward to analyze.) In this case, the corresponding change in the orbital phase, $\delta\psi$, can be solved by integrating the Keplerian motion of the binary near the pericenter passage, $\psi \sim 0$, and require that $T_{\rm burst}/T_{\rm orb} = 1\%$:

$$\frac{T_{\rm burst}}{T_{\rm orb}} = \frac{1}{T_{\rm orb}} \int_{-\frac{1}{2}\delta\psi}^{\frac{1}{2}\delta\psi} \frac{d\psi}{\dot{\psi}} = \frac{1}{2\pi} \int_{-\frac{1}{2}\delta\psi}^{\frac{1}{2}\delta\psi} \frac{(1-e^2)^{\frac{3}{2}}}{(1+e\cos\psi)^2} d\psi \ , \tag{3.3}$$

where $\dot{\psi}$ is the time derivative of the orbital true anomaly:

$$\dot{\psi} = \frac{\sqrt{(m_1+m_2)\,a\,(1-e^2)}}{d^2} \ , \tag{3.4}$$

with $d = a\,(1-e^2)\,/(1+e\cos\psi)$.

The fraction of energy emitted in the burst, compared with the total energy loss during one orbital period, is given by:

$$\mathcal{F}(e) = \frac{1}{\langle P \rangle T_{\rm orb}} \int_{-\delta\psi/2}^{\delta\psi/2} P(\psi) \frac{d\psi}{\dot{\psi}} \ , \tag{3.5}$$

where $\langle P \rangle$ is the orbit-averaged GW energy emission power, given by Peters and Mathews (1963):

$$\langle P \rangle = \frac{32}{5} \frac{m_1^2 m_2^2\,(m_1+m_2)}{a^5\,(1-e^2)^{7/2}} \left(1 + \frac{73}{24}e^2 + \frac{37}{96}e^4\right) \ . \tag{3.6}$$

We note that the fraction shown in Equation (3.5) is a function of the orbital eccentricity, as e will affect both the GW emission waveform (Eq. 3.2) and the Keplerian motion, resulting in different $\delta\psi$ (Eq. 3.3). Therefore, higher eccentricity values will yield a higher fraction of energy loss around the pericenter passage, making GW emission look more and more like bursts (see, e.g., Figure 3.1. The waveform in this case is calculated numerically using the x-model (see, e.g., eq.(1)-(13), (A1)-(A36) in Hinder et al., 2010)).

Adopting $\mathcal{F}(e) \sim 90\%$ and $T_{\rm burst}/T_{\rm orb} = 1\%$, we can solve for the corresponding eccentricity threshold and find that a bursting source should have $e > 0.9$, regardless of its masses and semi-major axis.

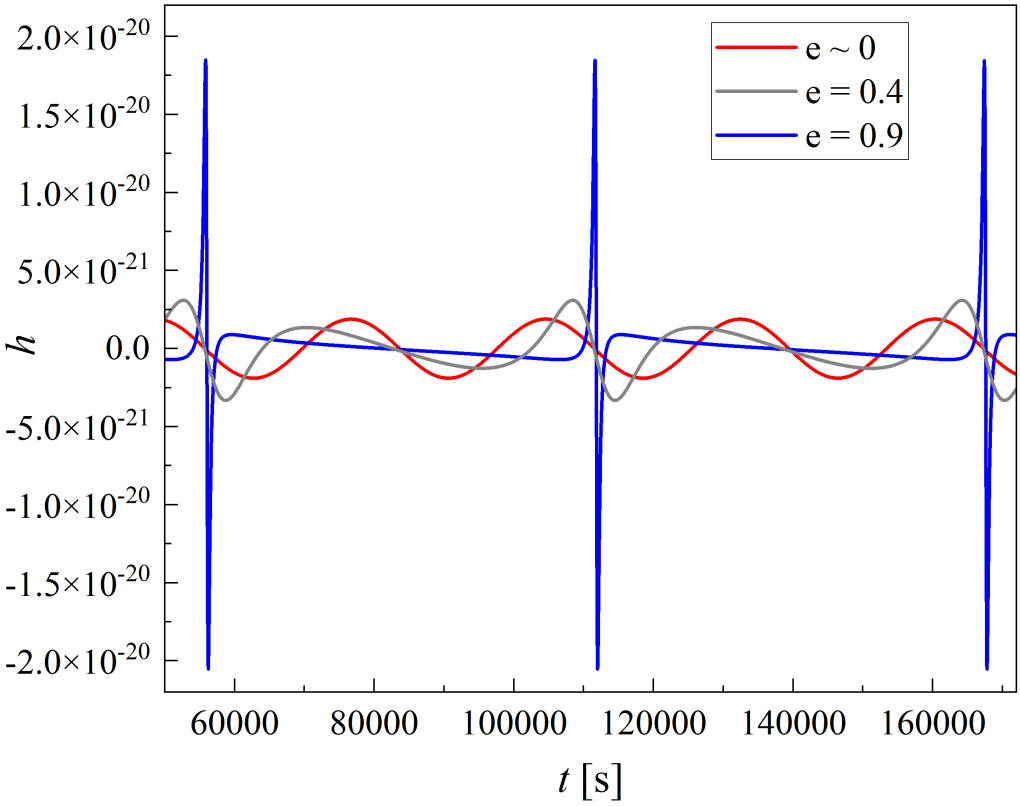


Figure 3.1: **The GW waveforms of a BBH system with the same orbital frequency but different eccentricities.** We show a BBH system with $m_1 = m_2 = 20$ $\mathrm{M}_\odot$, orbital frequency $f_{\rm orb} = 1.8 \times 10^{-5}$ Hz, luminosity distance $D_l = 8$ kpc, and $e = 0.001, 0.4, 0.9$, respectively. As explained in the text, when the binary's orbital eccentricity increases, its GW energy emission will concentrate near each pericenter passage, turning the GW signal from a sinusoidal wave ($e \sim 0$ case) into a "burst-like" waveform ($e = 0.9$ case).

3.2.2 Detectability of Bursting Sources in the Milli-hertz Band

The detection of GW bursts from highly eccentric sources is quite different from that of quasi-circular sources. In particular, when the binary's eccentricity is small (e.g., $e \sim 0.001$ in Figure 3.1), the GW signal can be well approximated by a near-monochromatic, sinusoidal wave. Therefore, the GW templates of these sources are relatively straightforward to construct, which enables us to adopt the matched filtering method in the template fitting (Thorne et al., 1987; Finn, 1992; Cutler and Flanagan, 1994) and measure the source's parameters accurately.

On the other hand, when the source's eccentricity increases (e.g., $e = 0.4, e = 0.9$ in Figure 3.1), its GW emission will become stronger upon each pericenter passage, turning the signal into a burst-like waveform. For example, mHz bursting sources typically emit a bright GW signal during a period of $10^2 \sim 10^3$ s. However, for the rest of the orbital time (which is typically much longer than the signal time and can be days, months, or even years), the emission is suppressed. The transient nature of bursting sources makes them hard to detect, mostly because it adds to the computational expense of the template fitting and reduces their average signal-to-noise ratio.

Note that the transient nature of bursting sources can also lead to their long lifetime. Since the bursting sources spend a small amount of time emitting GW during each orbit (near the pericenter passage), the average power of orbital energy loss is small when compared with a circular binary with the same GW frequency as the eccentric bursting source's peak frequency. This means their orbit will shrink on a longer timescale. Therefore, bursting sources potentially have more significant numbers in future mHz GW detection. In the following sections, we will quantify how this feature enhances their detectability.

The signal-to-noise ratio (SNR) of a bursting source can be estimated analytically[1]. In

[1]Here we focus on giving a simple and direct estimation by comparing the system to a circular orbit with

particular, the energy loss of a bursting source mostly takes place near the pericenter passage; thus, consider a circular binary with the orbital radius the same as the bursting source's pericenter distance, $r_c = a(1-e)$, then such a circular binary's GW emission power should be on the same order of magnitude as the "bursting power" of the bursting source.

This approximation is consistent with the nature of GW radiation, since the strain amplitude is proportional to the second-order time derivative of the binary's mass-quadrupole moment, while the peak GW frequency depends on the angular velocity at pericenter passage. Thus, a circular and eccentric binary with a similar radius/periapsis and velocity have a similar GW strain amplitude and frequency.

The bursting source has similar GW amplitude and frequency as the corresponding circular binary enclosed by the pericenter distance. The effective GW burst duration can be written as:

$$T_{\rm burst} \sim T_p \sim T_{\rm orb}(1-e)^{\frac{3}{2}} \ , \tag{3.7}$$

Note that this expression also describes the period of the corresponding circular orbit.

Moreover, highly eccentric sources emit GW emission in a wide range of frequencies, which peak at $f_{\rm peak} \sim f_{\rm orb}(1-e)^{-3/2}$ (Peters and Mathews, 1963). In the approximation that the GW burst emission from a highly-eccentric source has a similar frequency as the circular orbit with $r_c \sim a(1-e)$, the peak frequency is approximately[2]:

$$f_{\rm burst} \sim f_{\rm circ,GW} = \frac{2}{T_{\rm circ}(r_c)} \ , \tag{3.8}$$

in which $f_{\rm circ,GW}$ is the GW frequency of the corresponding circular orbit, and $T_{\rm circ}$ is the period of the circular orbit.

the radius of the pericenter distance. A more detailed analysis of the signal-to-noise ratio may be found in e.g. Kocsis et al. (2006b); O'Leary et al. (2009a); Randall et al. (2022).

[2]The peak frequency is often estimated as $f_{\rm peak} = f_{\rm orb}(1+e)^{1/2}(1-e)^{-3/2}$ (O'Leary et al., 2009a). For consistency with other definitions in our treatment above, we adopt $f_{\rm circ,GW}$, which differs by an order of unity.

Similarly, the strain amplitude of a burst can be estimated by considering the circular orbit enclosed within the pericenter distance (Peters and Mathews, 1963; Kocsis and Levin, 2012), i.e.,

$$
\begin{aligned}
h_{\rm burst} &\sim \sqrt{\frac{32}{5}}\frac{m_1 m_2}{D_l r_c} \sim \sqrt{\frac{32}{5}}\frac{m_1 m_2}{D_l a(1-e)} \\
&\sim 5.54\times 10^{-21}\eta_s \left(\frac{m}{10\,{\rm M}_\odot}\right)^{\frac{5}{3}} \left(\frac{T_{\rm burst}}{1000\,{\rm s}}\right)^{-\frac{2}{3}} \left(\frac{D_l}{8\,{\rm kpc}}\right)^{-1} ,
\end{aligned}
\tag{3.9}
$$

here D_l is the luminosity distance of the binary, and the constant coefficient comes from the average of strain amplitude over the binary's orientation. Furthermore, $m = (m_1 + m_2)/2$ is the average component mass, $\eta_s = 4m_1m_2/(m_1+m_2)^2 = 4q/(1+q)^2$ is unity for equal mass sources where $q = m_1/m_2$.

The analytical expression of signal-to-noise ratio (SNR), for a monochromatic source, is given by (see, e.g., Seto, 2002a):

$$
{\rm SNR} = \frac{h_A\sqrt{fT}}{\sqrt{fS_{\rm n}(f)}} , \tag{3.10}
$$

in which h_A is the (time-domain) strain amplitude of the GW signal, $\sqrt{fT}$ is the number of observed cycles, and $S_{\rm n}(f)$ is the spectral noise density of LISA evaluated at GW frequency f (we adopt the LISA-N2A5 noise model, see, e.g., Klein et al., 2016a; Robson et al., 2019a)[3], $\sqrt{fS_n(f)}$ is the dimensionless spectral noise amplitude per logarithmic frequency bin. The numerator in Eq. (3.10) defines h_c, the characteristic strain for a monochromatic source.

Note that T in Equation (3.10) stands for the time of observation when the signal is present, thus is different from the total observational time of LISA, $T_{\rm obs}$. For bursting sources, we sum over the pericenter passage time when they are emitting GW with significant amplitude (comparable with the corresponding circular source enclosed by the pericenter distance) to get T. For example, in a four-year LISA mission, if a bursting source bursts n times, then

[3]In this work, we do not take into account the potential stochastic GW background created by astrophysical bursting sources when evaluating the LISA noise curve, but they may have a significant contribution to the noise level (see, e.g., Naoz and Haiman, 2023).

we have $T = nT_{\rm burst}$, while $T_{\rm obs} = nT_{\rm orb} = 4$ yr.

Plugging in Equation (3.7), (3.8), and (7.5) into Equation (3.10), then take into account the small amount of time when the source is bursting ($T = nT_{\rm burst} = T_{\rm obs}/T_{\rm orb} \times T_{\rm burst}$ if $T_{\rm obs}/T_{\rm orb} = n \geq 1$, otherwise $T = T_{\rm burst}$ if $T_{\rm obs} \leq T_{\rm orb}$), we can get an estimate of the bursting source's detectability:

$$\begin{aligned} {\rm SNR}_{\rm burst} &\sim \frac{h_{\rm burst}\sqrt{f_{\rm burst}T}}{\sqrt{f_{\rm burst}S_n\left(f_{\rm burst}\right)}} \\ &\sim \begin{cases} \dfrac{h_{\rm burst}\sqrt{f_{\rm burst}T_{\rm obs}(1-e)^{3/2}}}{\sqrt{f_{\rm burst}S_n(f_{\rm burst})}} & \text{if } T_{\rm obs} \geq T_{\rm orb} \\ \dfrac{h_{\rm burst}}{\sqrt{f_{\rm burst}S_n(f_{\rm burst})}} & \text{if } T_{\rm obs} \leq T_{\rm orb} \end{cases} \end{aligned} \tag{3.11}$$

Note that for the first case ($T_{\rm obs} \geq T_{\rm orb}$) in Equation (5.4), the SNR can also be expressed as:

$${\rm SNR}_{\rm burst} \sim \frac{h_{\rm burst}}{\sqrt{S_n\left(f_{\rm burst}\right)}}\sqrt{T_{\rm obs}\left(1-e\right)^{3/2}} \text{if } T_{\rm obs} \geq T_{\rm orb}, \tag{3.12}$$

which shows the dependency of (repeated) bursting sources' SNR on the eccentricity.

Equation (8.19) estimates the RB sources' SNR. Furthermore, it can be verified against the numerical results of eccentric binaries' detectability (e.g., Kocsis and Levin, 2012; Hoang et al., 2019). For example, the SNR of a bursting BBH system with $m_1 = m_2 = 10$ M$_\odot$, $a = 1$ au, $e = 0.999$ is estimated to be ~ 200 in the Milky Way center, and ~ 2 at the distance of the Andromeda. Therefore, Equation (8.19) implies that stellar-mass mHz bursting sources can be detected in the Milky Way, and are marginally detectable in nearby galaxies.

For the second case ($T_{\rm obs} \leq T_{\rm orb}$) in Equation (5.4), the binary can only undergo one pericenter passage during the observation. Therefore, the signal-to-noise ratio represents a single GW burst's detectability. We show in Figure 3.2 that such SNR of a single burst can be

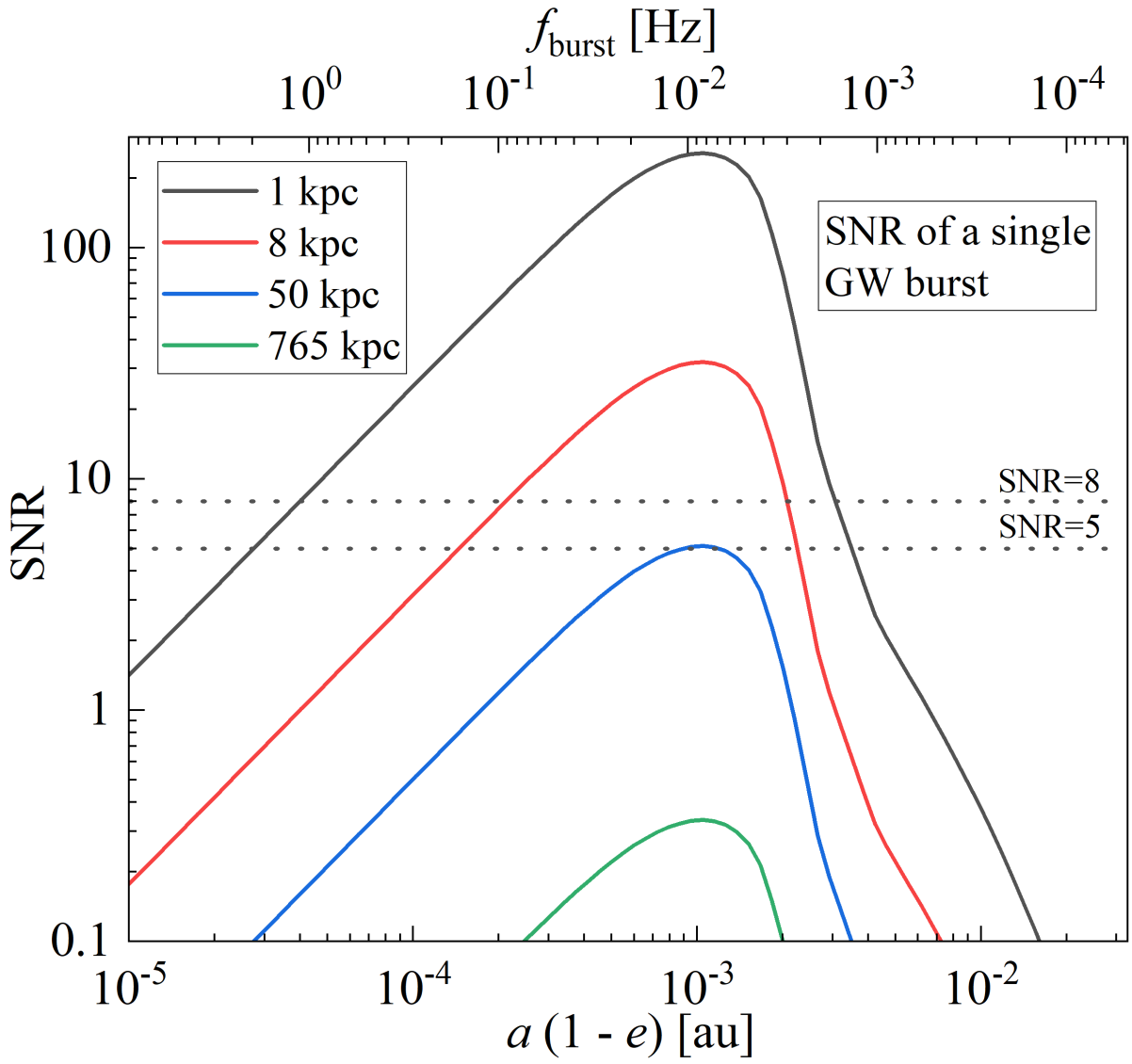


Figure 3.2: **The signal-to-noise ratio of a single GW burst, as a function of the source's pericenter distance.** We show a BBH system with $m_1 = m_2 = 10$ $M_\odot$, placed at $D_l = 1, 8, 50, 765$ kpc, respectively. The SNR of a single GW burst is plotted as a function of the binary's pericenter distance $a(1-e)$, and the corresponding GW burst frequency is plotted on the top x-axis. We note that repeated burst sources can have multiple bursts detected during the observation, and the overall SNR can be higher than the single burst case of this figure. See Figure 3.4 for the repeated burst case.

expressed as a function of the binary's pericenter distance, and for stellar-mass binaries, the distance of single burst detection is mostly limited to the Milky Way. The SNR peaks at a burst frequency of about 6 mHz, the minimum of the LISA sensitivity curve, corresponding to a pericenter distance of $\sim 10^{-3}$ au.

We emphasize that, the expression of SNR in Equation (5.4) are based on the average GW emission power, and thus may not describe the full detectability of bursting sources. For example, Figure 3.3 shows the comparison of time and frequency domain waveforms of a bursting BBH and a circular double white dwarf (DWD), calculated numerically using the x-model (Hinder et al., 2010).[4] For a comprehensive comparison, we adjust their parameters to have the same SNR ~ 12. As shown in the figure, even if the bursting BBH system has the same SNR as the circular DWDs, its time-domain GW amplitude is thousands of times greater than the latter one. In other words, with the same SNR, the time-domain strain amplitude of a mHz "burst" is much greater than that of a continuous GW. Therefore, we may use this signature to enhance the bursting sources' detectability (e.g., East et al., 2013; Tai et al., 2014; Loutrel, 2020; Wu et al., 2023).

We note, however, that the transient nature of bursting sources also adds to the difficulty of data analysis. In particular, the typical strategy for detecting GWs uses matched filtering (Finn, 1992; Cutler and Flanagan, 1994), which heavily relies on the accurate model of GW signal and is not well-suited for searching for discrete bursts localized in time and frequency (see, e.g., Tai et al., 2014; Loutrel and Yunes, 2017; Loutrel, 2020). In the context of LIGO data analysis, extensive efforts were made to identify transient events using time-frequency methods, such as power stacking (East et al., 2013), the TFCLUSTER algorithm (Sylvestre, 2002), wavelet decomposition (Klimenko and Mitselmakher, 2004), and the Q-transform (Bassetti et al., 2005; Tai et al., 2014). These methods may lead to a lower SNR relative

[4]We note that the Fourier transform of highly eccentric sources' GW signal can be made up of millions of harmonics, in the *Upper Panel* of Figure 3.3 we only plot their spectrum density for simplicity. A detailed discussion can be found in Kocsis and Levin (2012).

to the matched filtering but are robust to different kinds of transients and can combine the information from multiple bursts from a single source. For LISA data analysis, burst detection methods for stellar mass binaries are still underdeveloped, but some efforts have been made to detect highly eccentric EMRIs (see, e.g., Barack and Cutler, 2004b; Cornish and Rubbo, 2003; Hopman et al., 2007; Porter and Sesana, 2010; Mikóczi et al., 2012b) and burst from scattering of black holes (Kocsis and Levin, 2012).

Moreover, the detection of bursts with the LIGO-VIRGO-KAGRA network has the advantage that the source may be more precisely localized in the sky, given the ability to measure the GW arrival time difference at different detector sites. In contrast, for persistent inspiraling sources in the LISA band, their localization depends on the modulation of the signal caused by the annual motion of the LISA satellite constellation along its orbit. While "time delay interferometry" (see, e.g., Tinto et al., 2002; Tinto and Dhurandhar, 2021) may be utilized to identify unmodeled astrophysical GW sources with LISA, corresponding mock data analysis methods are currently unavailable for cases with only a small number of bursts in the observational period. Thus, it is currently not known how accurately the source may be localized in the sky, if at all in this case. Additionally, distance information may also be unavailable, as it degenerates with the total mass of the source and the separation at the closest approach. Thus, confusion of several distinct binaries with repeating single GW bursts may be a major uncertainty for these types of sources. It remains unclear how many repeated bursting sources (with what SNR) are needed for secure detection. For conservative purposes, in this paper, we adopt the average SNR as the criteria for evaluating the bursting sources' detectability. This approach represents the power of the GW signal and provides an optimistic estimate of bursting sources' detectability in the LISA band with current data analysis methods.

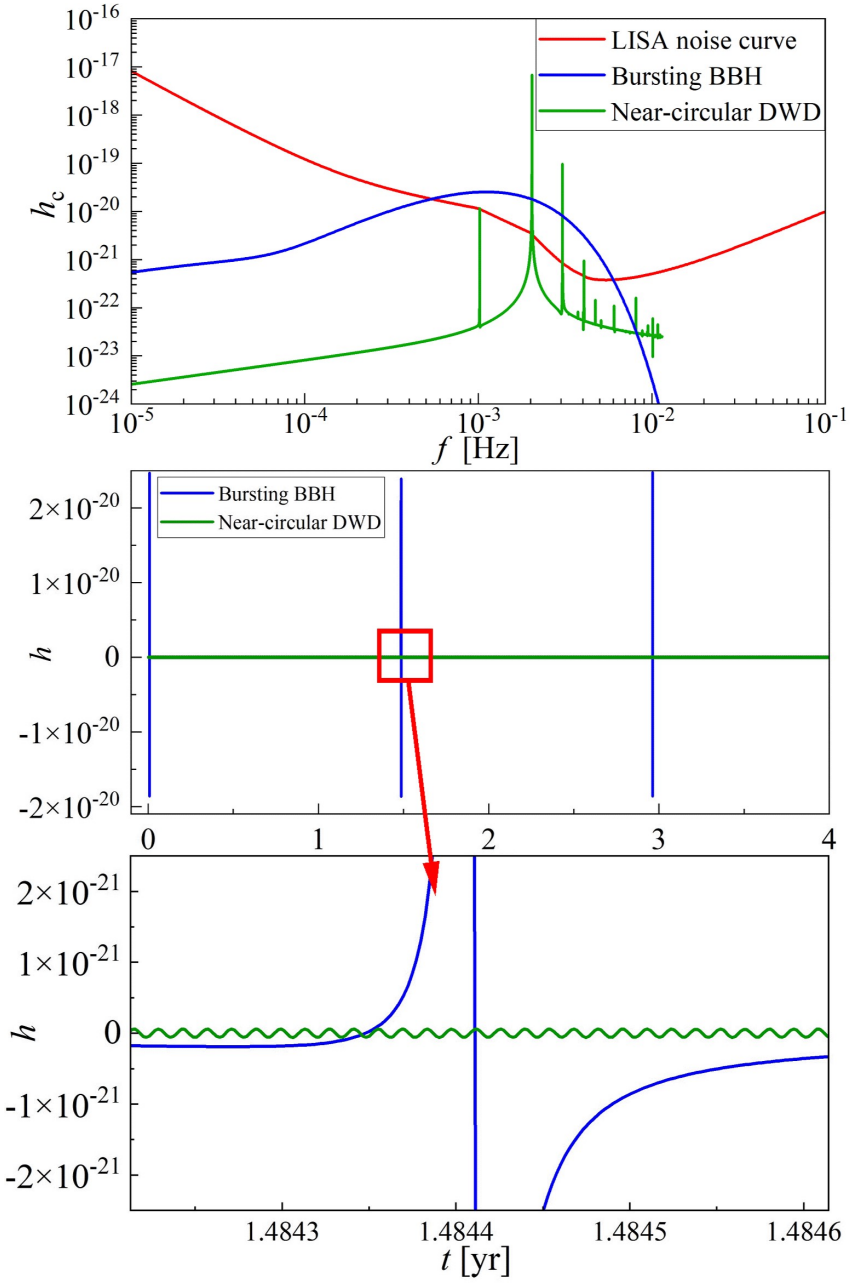


Figure 3.3: **Comparison between the GW signal of a bursting BBH and a near-circular DWD, both with the same signal-to-noise ratio** SNR ~ 12**.** We show a BBH system (blue line) with $m_1 = m_2 = 20$ $M_\odot$, $a = 4.43$ au, $e = 0.999$ and a DWD system (green line) with $m_1 = m_2 = 0.5$ $M_\odot$, $a = 0.001$ au, $e = 0.01$, both of them are placed at $D_l = 8$ kpc, and observed for $T_{\rm obs} = 4$ yr. These parameters are chosen such that these sources will have SNR = 12. *Upper Panel* shows the characteristic strain (Eq. 3.28) compared with the LISA noise curve ($\sqrt{fS_n(f)}$) (red line), *Middle Panel* and *Bottom Panel* show the time-domain waveforms. This plot highlights that bursting signals in the milli-hertz band can have significant amplitude in the time domain (thousands of times greater than a circular source with the same SNR), even if their averaged SNR is limited.

3.2.3 Lifetime of Bursting Sources in the Milli-Hertz Band

Most of the stellar-mass bursting sources start their evolution from a wide configuration. These systems undergo some dynamical interaction, such as EKL, fly-by, or a strong encounter, resulting in a highly eccentric configuration. At this stage, the system undergoes repeated GW bursts. Following this RB stage, the binary's orbit shrinks, and if GW emission dominates the evolution, it becomes circularized, yielding a merged system (e.g., see Figure 3.8). Particularly, an RB source's lifetime, $\tau_{\rm RB}$, can be estimated using the merger timescale for binaries with extreme eccentricity (Peters, 1964):

$$\tau_{\rm RB} \sim \frac{3}{85\mu M^2} a^4 \left(1-e^2\right)^{7/2} \sim 1.12\times10^7 {\rm yr} \times \\ \frac{2}{q(1+q)} \left(\frac{m}{10{\rm M}_\odot}\right)^{-\frac{5}{3}} \left(\frac{f_{\rm burst}}{1{\rm mHz}}\right)^{-\frac{8}{3}} \left(\frac{1-e}{0.01}\right)^{-\frac{1}{2}}, \tag{3.13}$$

where $\mu = m_1 m_2/(m_1+m_2)$, and $M = m_1 + m_2$.

Equation (7.1) describes the isolated evolution of bursting binaries. However, some bursting sources that undergo dynamical interaction can have eccentricity oscillation throughout their evolution (e.g., EKL merger systems Hoang et al., 2019; Randall and Xianyu, 2019b; Deme et al., 2020; Emami and Loeb, 2020; Chandramouli and Yunes, 2022). In this case, we adopt the maximum eccentricity during the oscillation, $e_{\rm max}$, as the value of e in Equation (7.1), which yields a lower limit of the timescale for a source to burst.

We are interested in comparing the length of a bursting system's RB stage with its latter stage of evolution (inspiral with moderate eccentricity). Thus, for simplicity, we assume that the binary circularizes and shrinks to a radius $r_c \sim a(1-e)$ after the RB evolution. Such systems are well described in EKL systems or captured systems (e.g., see Kocsis and Levin, 2012; Naoz, 2016). Further, this approximation is consistent with the concept that

the pericenter of a highly eccentric GW source remains nearly the same (in the absence of dynamical evolution, see for details Peters and Mathews, 1963; Peters, 1964).

Thus, under this notion, when the bursting binary's eccentricity drops to a moderate value, its remaining inspiral time, $\tau_{\rm inspiral}$, can be estimated as (Peters, 1964):

$$\begin{aligned}\tau_{\rm inspiral} &\sim \frac{5}{256\mu M^2} r_c^4 \sim \frac{5}{256\mu M^2} a^4 (1-e)^4 \\ &\sim 5.5\times 10^4 {\rm yr}\, \eta_s \left(\frac{m}{10\,{\rm M}_\odot}\right)^{-\frac{5}{3}} \left(\frac{f_{\rm burst}}{1\,{\rm mHz}}\right)^{-\frac{8}{3}} . \end{aligned} \tag{3.14}$$

We note that Equation (7.3) also serves as a general estimate of millihertz circular BBHs' merger timescale (if we replace $f_{\rm burst}$ in the equation with $f_{\rm circ,GW}$). Therefore, the equation implies that a stellar mass circular binary will stay in the mHz band, in particular $f_{\rm circ,GW} \gtrsim$ 1mHz, for $\sim 10^3 - 10^5$ yr (e.g., Chen et al., 2020a).

As can be seen from Equation (7.1) and (7.3), the timescale for a highly-eccentric source's RB stage is longer than the following inspiral stage with moderate eccentricity:

$$\tau_{\rm RB} \sim 20(1-e)^{-\frac{1}{2}} \tau_{\rm inspiral} \ , \tag{3.15}$$

which reflects the fact that in the RB stage, the eccentric binary will spend most of its time at large separation, yielding a lower GW emission and orbital energy loss compared to a circular orbit with a separation $a(1-e)$. For example, the EKL mergers of BBHs in the galactic nucleus are expected to have $e \gtrsim 0.999$, induced by the supermassive black (SMBH) via the EK mechanism (Naoz, 2016; Hoang et al., 2018; Hoang et al., 2019). Thus, Equation (4.8) means the RB stage of EKL mergers will be hundreds of times longer than their inspiral time with moderate eccentricity and the same $a(1-e)$.

Figure 3.4 shows the lifetime (Eq. 4.8) and detectability of RB sources with a more detailed

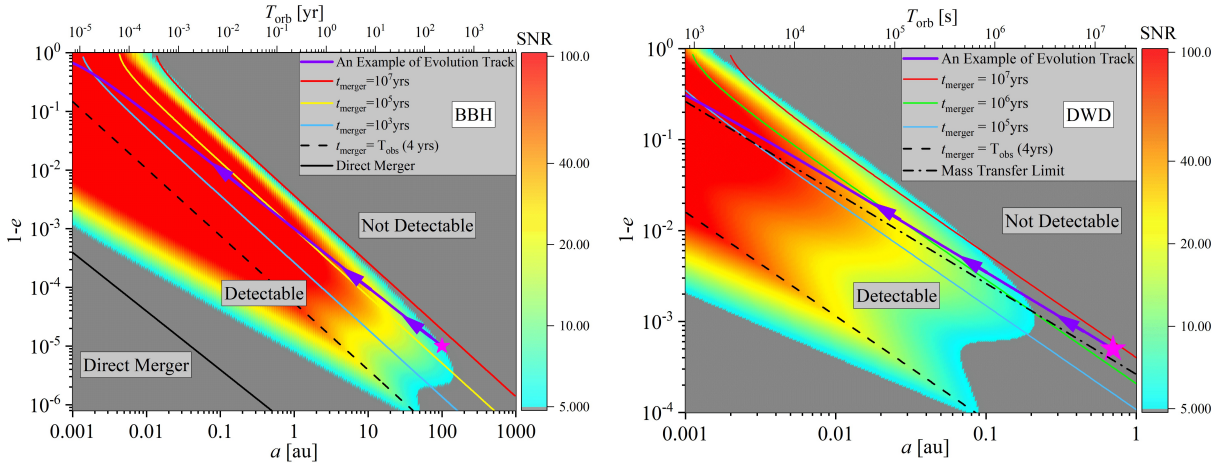


Figure 3.4: **The Dependence of the (RB) compact binary's detectability on its semi-major axis and eccentricity.** Here we show a BBH system (*Left Panel*) with $m_1 = m_2 = 10$ M$_\odot$, and a DWD system (*Right Panel*) with $m_1 = m_2 = 0.75$ M$_\odot$, placed at $D_l = 8$ kpc and observed for 4 yr with LISA. The color represents the compact binary's signal-to-noise ratio as a function of its semi-major axis a and eccentricity $1 - e$. As a proof of concept, we depict an example system's evolution (purple line with star and arrows) for both parameter spaces and plot the corresponding orbital time on the top x-axis. The solid lines with color represent the merger timescale $\tau_{\rm merger}$ for a given (a, e) configuration of the binary. In other words, when the evolution track of the binary gets into the colored region and gets across a given merger timescale, we can estimate the remaining time for it to emit detectable GW bursts before the merger. We note that the signal-to-noise ratio is suppressed in the region below the dashed lines ($t_{\rm merger} < T_{\rm obs}$) because the binary will merge during the observation, thus having less observational time than the total LISA mission time. Therefore, when calculating the SNR for these binaries following Equation. (7.34), we replaced the $T_{\rm obs}$ with $t_{\rm merger}$.

calculation for the SNR than in Equation (5.4), as depicted in Appendix 3.6.2. Particularly, we consider equal mass 10 $M_\odot$ BBH systems (left panel), and equal mass 0.75 $M_\odot$ DWD systems (right panel) at a luminosity distance $D_l = 8$ kpc from the detector. The Figure shows the GW signal-to-noise ratio, as a color map of the binary's semi-major axis a and e. The detectable regions are labeled on the map.

We also over-plot, in Figure 3.4, the merger timescales for isolated binaries in each panel (thin solid lines in the figure). For comparison purposes, in the left panel, we further show the direct merger limit for BBHs (black solid line at the bottom). In the right panel, we show the Roche limit for DWD in the black dash-dotted line (which is the limit that DWDs will undergo mass transfer).

Overplotted in Figure 3.4 is a representative example. Specifically, starting from a given initial condition, the RB source will evolve in the $a-e$ parameter space following the changes in its semi-major axis and eccentricity due to the GW emission (Peters, 1964):

$$\left\langle \frac{da}{de} \right\rangle = \frac{12}{19} \frac{a}{e} \frac{[1 + (73/24)e^2 + (37/96)e^4]}{(1 - e^2)\,[1 + (121/304)e^2]} \,. \tag{3.16}$$

Using these equations, we plot the evolutionary track (the solid lines with arrows) on each panel in the absence of further dynamical evolution.

Consider, for example, the evolutionary track in the right panel. This DWD system began in the undetectable regime; however, as it evolves, it becomes detectable via RB, with SNRs corresponding to the color on the map. When the system crosses the lifetime line, it will merge within that time, thus undergoing repeated bursts for that remaining time. In particular, the DWD example crosses the 10^6 yr mark with $a \sim 0.03$ au and $e \sim 0.99$, which means it will survive for an additional 10^6 years as a detectable repeated burst source.

As can be seen in Figure 3.4, the lifetime of a detectable RB source in the Milky Way can

be as much as $\sim 10^7$ yr, since the edge of the detectable region roughly coincides with the line of merger timescale $t_{\rm merger} = 10^7$ yr for both BBHs and DWDs. This phenomenon can be explained using Equation (8.19) and (7.1). Particularly, for extreme eccentricity cases, the merger timescale lines follow $a^4(1-e)^{7/2} =$ constant in the a-e parameters space (see Equation (7.1)), while the edge of the detectable region (SNR=5 line) follows $h_{\rm burst}(1-e)^{3/4}(S_n(f_{\rm burst}))^{-1/2} =$ constant (see Equation (8.19)). For the expression of the constant SNR contour, we can substitute $h_{\rm burst} \sim a^{-1}(1-e)^{-1}$ (see Equation (7.5)) and $f_{\rm burst} \sim a^{-3/2}(1-e)^{-3/2}$ (see Equation (3.8)), then take into account the frequency dependence of the LISA noise curve (e.g., for N2A5 configuration, dominant term $S_n(f) \sim 20/3 f^{-4.4} \times 10^{-50.92}$ in the millihertz band (Klein et al., 2016b)) and get that $a^{-4.3}(1-e)^{-3.55} \sim$ constant. Therefore, in Figure 3.4, the constant $t_{\rm merger}$ lines ($\log_{10}a + 0.88\log_{10}(1-e) \sim$ constant) nearly follow the same $a-e$ dependence as the constant SNR lines ($\log_{10}a + 0.83\log_{10}(1-e) \sim$ constant), indicating that each SNR level roughly corresponds to a given merger timescale. In our example, the specific values of SNR=5 and $t_{\rm merger} = 10^7$ yr are coincidental. If certain dynamical formation channel creates compact binaries that evolve and get across this region, they will become long-lived mHz GW sources ($\tau_{\rm RB} \sim 10^6 - 10^7$ yr, see Equation (7.1)) with a detectable time much longer than the circular inspirals within the same frequency band ($\tau_{\rm inspiral} \sim 10^3 - 10^5$ yr, see Equation (7.3)).

We note that in Figure 3.4, another population of BBHs potentially exists, which is characterized by moderate eccentricity ($e \sim 0$) and long lifetime ($t_{\rm merger} \sim 10^7$ yr). However, these systems exhibit a much lower GW frequency (~ 0.1mHz) compared to the bursting sources considered in this paper ($\gtrsim 1$mHz). For example, a BBH system with $e \sim 0, a \sim 0.03$ au would be detectable in the Milky Way (~ 10kpc) for 10^7 yr, with an orbital period of $T_{\rm orb} \sim 10^4$ s and GW frequency $f_{\rm circ,GW} \sim 10^{-4}$ Hz. Note that because we expect a large population of circular DWDs in the sub-millihertz band (see, e.g., Nissanke et al., 2012a; Lamberts et al., 2018; Xuan et al., 2021), the identification of the near-circular, low-frequency BBHs is beyond the scope of this study. Thus, in this paper, we focus on the dynamically

formed, highly-eccentric bursting sources, with $f_{\rm GW} \gtrsim 1$mHz.

For comparison purposes, we show in Figure 3.5 the maximum detectable distance of RB sources, assuming a 4 yr LISA mission and a detection threshold of SNR = 5. As shown in the figure, the detection of bursting BBHs can be promising within the distance of nearby galaxies, while the detection of bursting DWDs is limited to the Milky Way. This result is consistent with the estimation in Section 8.3.2 (see, Equations (5.4), (8.19) and Figure 3.2).

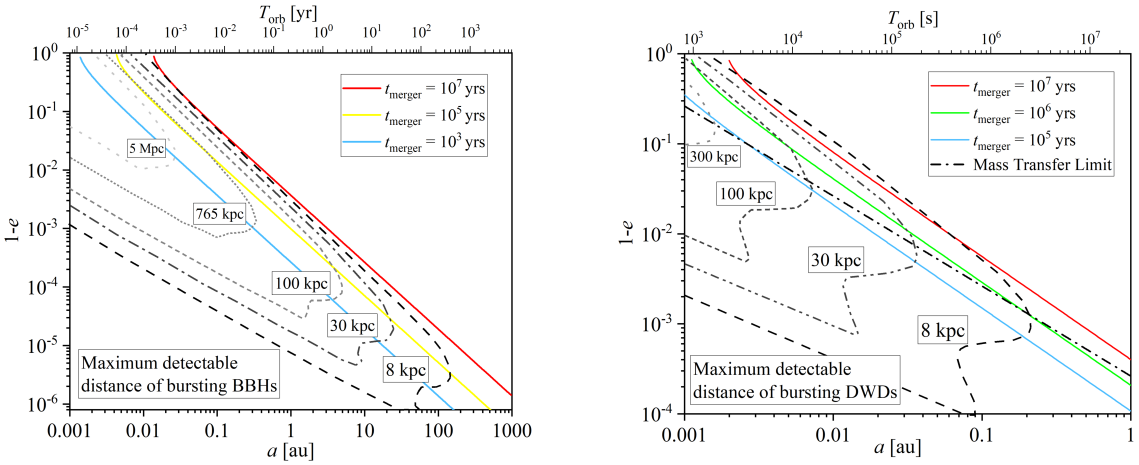


Figure 3.5: **The maximum detectable distance of the (RB) compact binary.** Here we consider the same systems as in Figure 3.4, but choose different values of luminosity distance D_l, and show the equal signal-to-noise ratio (SNR = 5) contours for a 4 yr LISA observation. The left (right) panel shows the BBHs (DWDs) system. The detectability of bursting sources increases at the top-left part of the plot.

One important caveat is that the estimation of SNR in Figure 3.4 and 3.5 is based on the averaged power of the GW signal, where for a binary with $T_{\rm orb}$ larger than $T_{\rm obs}$, the number of bursts we expect to detect during the observation is smaller than one. In this case, the average SNR in Figure 3.4 is smaller than the SNR of detected bursts because we detect only a fraction of such bursting sources, only having a probability of less than one for detection. However, for these non-repeated bursting sources, a single burst falling within the observational window will be brighter than shown in the Figure according to Eq. (8.19), and hence can still be bright enough to detect with LISA. Moreover, in the region below the dashed black line of Figure 3.4, the merger timescale of a GW source is shorter than

the observational duration, which means the fast-merging sources in this region will not be observed for the whole LISA mission, thus having lower SNR. Therefore, we can further include these facts and finally get:

$$\mathrm{SNR} \sim \frac{h_{\mathrm{burst}} \sqrt{\max\{\min(\tau_{\mathrm{insp}}, T_{\mathrm{obs}}), T_{\mathrm{orb}}\}(1-e)^{3/2}}}{\sqrt{S_n\left(f_{\mathrm{burst}}\right)}}. \tag{3.17}$$

in which τ_{insp} is the binary's remaining inspiral time.

Equation (3.17) gives the full detectability of (both repeated and non-repeated) burst sources, providing that at least one burst takes place during the observation. The suppression of SNR caused by τ_{insp} is taken into account in the numerical results of this paper.

3.3 Population Estimation and Astrophysical Consequences

3.3.1 General Considerations

As shown in Section. 3.2, the RB stage of a stellar-mass GW source is well detectable within $\lesssim 10$ kpc, and lasts longer than the inspiral stage with moderate eccentricity. Therefore, the population of bursting sources can have a significant contribution to the detection of dynamically formed GW sources, especially in the Milky Way.

As a proof of concept, we heuristically estimate the expected populations of bursting BBHs. Due to the large uncertainties of star formation and detailed dynamical evolution, we focus on the expected order of magnitude of the bursts. We consider three regimes that are expected to have eccentric sources, namely: Galactic Field, Globular Clusters (GCs), and Galactic Nucleus (GN), and show the results in Figure 8.3. For comparison purposes, we also present the number estimation of GW bursts from the EMRIs in the universe.

For other kinds of bursting sources, such as DWDs, their number, parameter distribution, and evolution is less understood, mostly due to the uncertainty in the formation scenario and the complexity of tidal effects in extreme eccentricity cases. Therefore, we will leave these populations for future work.

Before providing the estimation for bursting sources in the three regions mentioned above, we first describe a general estimate agnostic to the astrophysical formation channel of the source.

3.3.2 Steady-State Approximation and Constraints from LVK

Motivated by LVK observations, we first estimate the number of RB sources under the assumption that LVK represents a steady-state population. In particular, assume there is a continuous birth and death of compact object binaries in the Milky Way, keeping the total number of systems unchanged. In this case, the replenishing rate of a GW source is balanced by its merger rate. In other words,

$$\Gamma_{\rm rep} = \Gamma_{\rm merger} \ . \tag{3.18}$$

For GW sources formed through dynamical interaction, the expected number of systems in the RB stage, $N_{\rm RB}$, is found by multiplying the average lifetime of the RB stage (Eq. (7.1)) with the formation rate of the source:

$$N_{\rm RB} = \tau_{\rm RB}\Gamma_{\rm rep,RB} = \tau_{\rm RB}\Gamma_{\rm merger,RB} \ , \tag{3.19}$$

which is also applicable to other evolutionary stages, such as the inspiral with moderate eccentricity.

The LVK observations indicate that BBHs merge at a rate of $15^{\smile}38\,{\rm Gpc}^{\smile 3}{\rm yr}^{-1}$ (Abbott et al.,

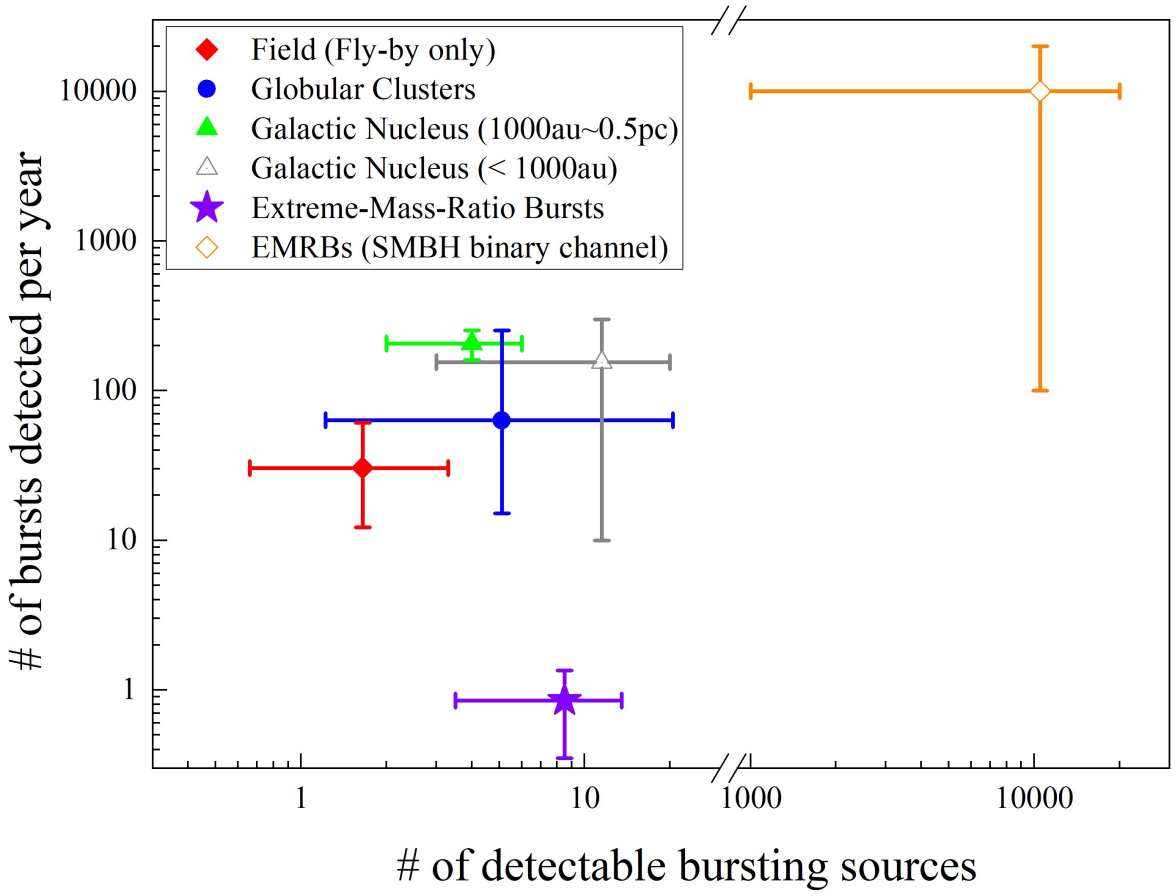


Figure 3.6: **The number of bursting sources and bursts detected per year, assuming a 10-yr LISA mission and detection threshold** SNR = 5**.** The figure depicts the estimation results of bursting BBHs for different channels, with the error bars reflecting the theoretical uncertainties. Specifically, we show the number of detectable bursting sources from each channel (x-axis) and their contribution to the number of bursts detected per year (y-axis). For details of the simulation, see Appendix 3.6.1. Note that the number of detectable bursting sources is roughly proportional to the observational time. The solid points represent the population with convincing evidence of existence, while the hollow points are for the potentially existing population of bursting sources. We emphasize that if future detection does not show evidence of the population marked in hollow points, it serves as a strong constraint on the corresponding formation channels.

2021). Therefore, we can estimate the BBHs merger rate per galaxy by dividing the galaxy number density. Adopting the galaxy number density of 0.02 Mpc^{-3} (Conselice et al., 2005), the merger rate of BBHs in an averaged galaxy is estimated as:

$$\Gamma_{\mathrm{merger,avg}} \sim 10^{-6}\,\mathrm{yr}^{-1}\ . \tag{3.20}$$

Thus, plugging Equation (3.20) into Equation (8.15) places a constraint on the number of bursting BBHs we can detect locally. For example, bursting GW sources can spend up to a few 10^7 yr in the detectable regime (Figure 3.4). Therefore, the upper bound of RB BBHs' number, from the steady-state approximation and LIGO's constraint, is on the order of $N_{\mathrm{RB}} \sim 10^7\,\mathrm{yr}\,10^{-6}\,\mathrm{yr}^{-1} \sim 10$ sources in the Milky Way. Below we use this approach to place constraints on different formation channels.

We emphasize that this constraint only serves as a rough estimation of bursting BBHs' number. It can be well-exceeded if taking into account the non-equilibrium formation history of compact binaries. For example, different regions in a galaxy may undergo starbursts while others have a quiescence phase, making the number of bursting sources fluctuate in a wide range. (See Section 3.3.5 for a detailed analysis.) Further, assuming that the observed rate of mergers all form at mHz or smaller frequencies[5] due to their long lifetime, bursting binaries could be the dominant source in the local mHz BBHs population (see Equation (8.15)). For example, consider the lifetime of circular (non-bursting) BBHs in the mHz band, $\tau_{\mathrm{inspiral}} \sim 10^3 - 10^5$ yr (see Equation (7.3)). Provided that both bursting and non-bursting sources are detectable within the Milky Way, the shorter lifetime of circular sources results in their small number in the local population, $N_{\mathrm{circ,BBHs}} \lesssim 10^5\,\mathrm{yr}\,10^{-6}\,\mathrm{yr}^{-1} \sim 0.1$ in the mHz band, while bursting sources represent the majority of mHz sources ($\mathrm{N_{RB}} \sim 10$).

Below, we consider three characteristic BBHs formation channels and provide heuristic esti-

[5]Note that if all sources form at higher frequencies during close encounters, e.g. at 0.01Hz, it is in principle also possible not to have any mHz sources without violating the LIGO/VIRGO merger rate.

mations for their bursting properties.

3.3.3 BBHs in the Field

Isolated stellar binaries in the galactic field have been proposed as a possible channel explaining the LVK observations (e.g., de Mink and Belczynski, 2015; Dominik et al., 2015; Belczynski et al., 2016; Eldridge et al., 2017; Giacobbo et al., 2018; Olejak et al., 2020). However, in the context of bursting systems, we focus on wide binaries in the field, which are less likely to be seen with LVK without external perturbations. Providing that external perturbations such as flybys or galactic tides will affect their evolution, these wide-field binaries can be driven to extreme eccentricity, emit bursting GW signals, and become mergers in the end.

We adopt the model proposed in Michaely and Naoz (2022), as well as the steady-state approximation, to calculate the eccentricity and semi-major axis distribution for the BBH mergers in the disk of the Milky Way. In particular, following Michaely and Perets (2019), the merger rate from the wide-binaries field channel can be within the range of $5^{+5}_{-3}\mathrm{Gpc}^{-3}\mathrm{yr}^{-1}$ in the local universe (up to $50\mathrm{Gpc}^{-3}\mathrm{yr}^{-1}$ if taking elliptical galaxies into account, see Michaely et al. in prep). Based on this rate estimate, assuming an optimistic LISA observation timescale $T_{\mathrm{LISA,obs}} = 10$ yr and detection threshold SNR$= 5$, we find that the minimum (maximum) number of detectable bursting BBHs in the MW, induced by fly-by interaction, is 0.7 (3.3), and they are expected to emit 12 (61) GW bursts per year. In these bursting sources, we identified the lower (upper) bound of the repeated burst sources number as 0.4 (1.8), and 0.3 (1.5) for non-repeated burst sources. However, because of the long orbital period of non-repeated burst sources, the chance that we will observe GW bursts during their pericenter passage is small. Thus, the number expectation of non-repeated bursts is negligible (~ 0.1). This is consistent with the estimate in Kocsis et al. (2006a). See

Appendix 3.6.1.1 for more details.

3.3.4 BBHs in Globular Clusters

BBHs formed through dynamical interactions in globular clusters are suggested to be one of the main sources of GW mergers (e.g., D'Orazio and Samsing, 2018; Samsing, 2018; Antonini and Gieles, 2020; Fragione et al., 2019; Martinez et al., 2020; Kremer et al., 2020). Thus, given the $\sim$ 150 Milky Way's GCs (e.g., Harris, 1996; Baumgardt and Hilker, 2018), we expect a significant number of bursting sources from GCs. Furthermore, it was recently pointed out that BBHs in GCs can have non-negligible eccentricity (even potential detected by LVK D'Orazio and Samsing, 2018; Antonini and Gieles, 2020; Zevin et al., 2019; Samsing et al., 2019; Martinez et al., 2020; Kremer et al., 2020).

Here, we adopt the eccentricity distribution of BBHs in Martinez et al. (2020, see their figure 4) and the spatial distribution of GCs in the Milky Way from Arakelyan et al. (2018). Since we are interested in the RB stage where BBHs are in a wide configuration with low GW frequency ($\sim$ mHz), we evolve the systems shown in Martinez et al. (2020), which is in a higher frequency band, back to the former RB stage. The bursting time of these sources is calculated by counting the time difference between the point when they become detectable and the point when their eccentricity drops below 0.9 (see the example tracks in Figure 3.4). In the simulation, we use steady-state approximation to calculate the expectation of bursting sources number (For detailed information, see Appendix 3.6.1.2).

We adopt the BBH merger rate in GCs to be: $\mathcal{R}_0 = 7.2^{+21.5}_{-5.5}\mathrm{Gpc}^{-3}\mathrm{yr}^{-1}$ (e.g., Rodriguez et al., 2016; Kremer et al., 2020; Antonini and Gieles, 2020). Assuming $T_{\mathrm{LISA,obs}} = 10$ yr and SNR=5, we find that the minimum (maximum) number of detectable bursting sources in the Milky Way GCs is 1.2 (20.1), which corresponds to a number of GW bursts 15.2 (253) per year. Among these sources, the minimum (maximum) number of repeated burst sources

is 0.34 (5.7), while the minimum (maximum) number of non-repeated burst sources is 0.85 (14.4).

3.3.5 BBHs in the Galactic Nucleus

The Milky Way's galactic nucleus offers a natural place for the formation of bursting BBHs (see, e.g., Kocsis and Levin, 2012; Hoang et al., 2019; Stephan et al., 2019; Arca Sedda et al., 2023; Zhang and Chen, 2024a). In particular, BBHs orbiting around the supermassive black hole in the galactic nucleus will undergo eccentricity excitation via the EKL mechanism, resulting in the bursting signatures on their GW signal.

The orbital evolution of BBHs in the GN is quite different from the isolated binaries (e.g., Equation (3.16)) since they are strongly affected by the gravitational perturbation from the SMBH tertiary. Thus, to get the bursting properties of these sources, we carried our detailed simulations of hierarchical triple systems, including the secular equations up to the octupole level of approximation (Naoz et al., 2013a), general relativity precession (e.g., Naoz et al., 2013b), and GW emission (Peters, 1964; Zwick et al., 2020). These calculations follow a similar approach to Hoang et al. (2018).

We first present the results under the steady-state approximation (see details in Appendix 3.6.1.3). This approximation can well-describe the main population of stars in the GN (old population, aged $2 \sim 8$ Gyr Chen et al., 2023). Assuming a 10 yr LISA observation with the signal-to-noise ratio threshold 5, we got the expectation of EKL induced, bursting BBHs number ~ 1 in the mHz band, with the number of detectable bursts ~ 100 per year. All the bursting sources in the simulation are repeated burst sources, which is consistent with the fact that wide binaries will evaporate quickly in the active dynamical environment of GN. The result is calibrated using the $m - \sigma$ relation (Merritt, 1999; Kormendy and Ho, 2013) and observational results of the Milky Way center.

However, unlike the previous channels (i.e., in the field and GCs), we go beyond the steady state approximation because observations suggest a recent ($2 \sim 8$ Myr) star formation occurred in the GN (Paumard et al., 2006; Lu et al., 2008; Do et al., 2013; Chen et al., 2023). Specifically, this recent star formation may have formed a young nuclear star cluster (YNC) within 0.5 pc from the central SMBH, with a total mass of $\sim (1.4 - 3.7) \times 10^4 M_\odot$ and a top-heavy mass distribution (Lu et al., 2008). Therefore, it can hold $\sim 100 - 400$ BHs as a result of the stellar evolution. Furthermore, since stars often reside in binaries, and high-mass stars reside in higher multiples (Pribulla and Rucinski, 2006; Tokovinin et al., 2008; Raghavan et al., 2010; Sana and Evans, 2011; Sana et al., 2012; Moe and Di Stefano, 2017), we expect these black holes to form ~ 100 BBH systems in the YNC. This expectation is supported by myriad observational and theoretical arguments (e.g., Ott et al., 1999; Martins et al., 2006; Rafelski et al., 2007; Pfuhl et al., 2014a; Alexander and Pfuhl, 2014; Naoz et al., 2018; Gautam et al., 2019; Chu et al., 2023). For the newly-born BBHs, we carried out Monte-Carlo simulations to get the evolution of RB sources' number as a function of the age of YNC (see Figure 3.7), as well as the number of bursts in the Appendix (see Figure 3.9). As is shown by the simulation, although the YNC has a relatively small mass ($M \sim 10^4$ $M_\odot$), there can be $2 \sim 4$ RB sources with $60 \sim 150$ bursts detected per year. These numbers are larger than the expectation of bursting systems from the old population of stars under the steady-state approximation, even if the latter one has a much larger total mass of stars ($\sim 10^7$ $M_\odot$).

Combining the simulation results of bursting BBHs in the old population of stars with those in the YNC, we get the number estimation of detectable bursting BBHs in the inner 1000 au ~ 0.5 pc of the galactic center as $2 \sim 6$. These sources will contribute to $160 \sim 254$ bursts per year.

Furthermore, observations suggest that inwards of S0-2's orbit ($\lesssim 1000$ au) there is a hidden mass of ~ 3000 $M_\odot$ (e.g., Do et al., 2019; GRAVITY Collaboration et al., 2020). This is

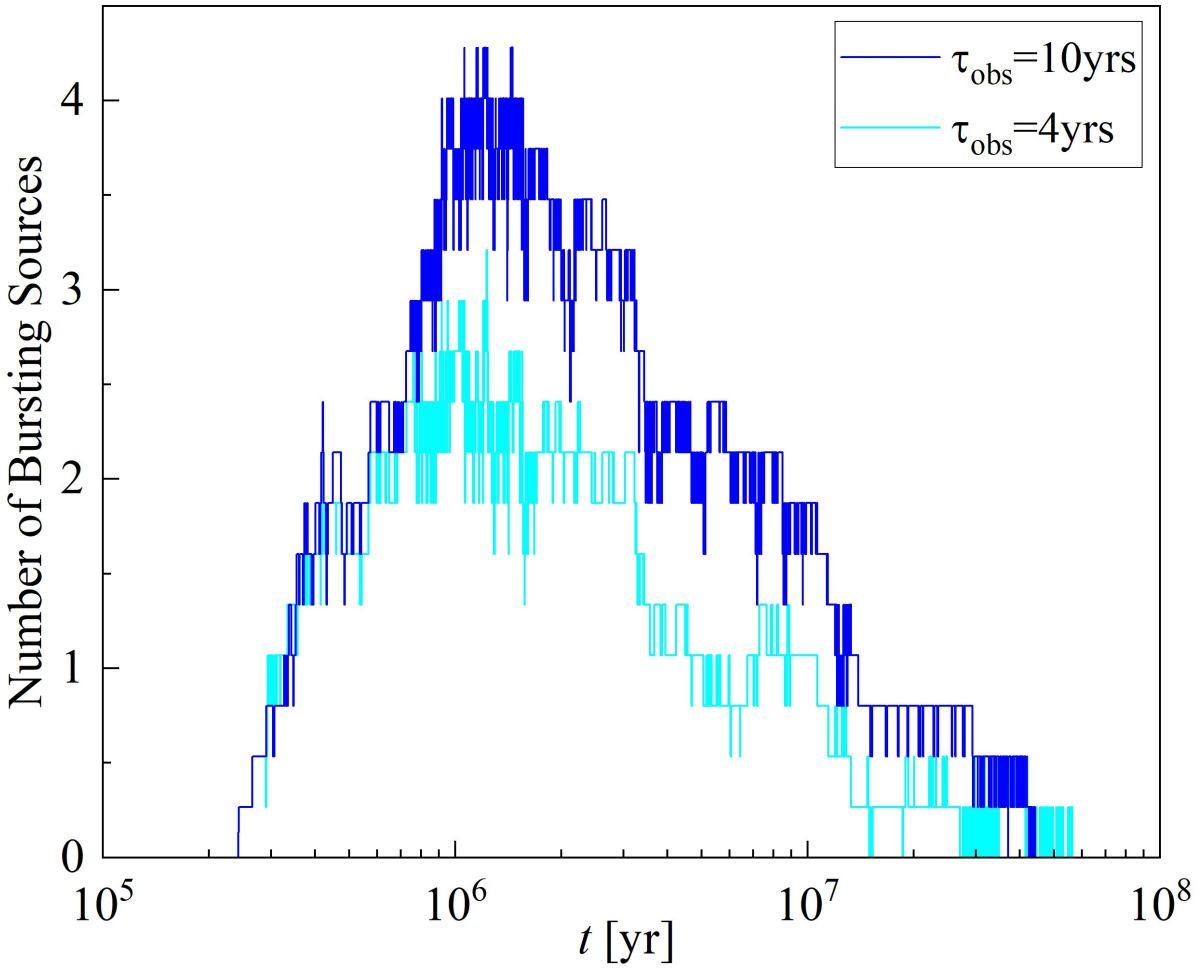


Figure 3.7: **Number of detectable bursting sources in the galactic nucleus YNC, as a function of their age.** Here we show the expectation of observable bursting systems in the Milky Way center young nuclear cluster, as a function of the cluster's age. The deep blue line stands for a LISA observational period $T_{\rm obs} = 10$ yr while the light blue line represents $T_{\rm obs} = 4$ yr. The YNC's age is constrained by observation to be $2 \sim 8$ Myr.

supported by theoretical arguments of the stability of S0-2, (e.g., Naoz et al., 2020; Zhang et al., 2023b; Will et al., 2023). We, thus, explored the possibility that these unidentified objects are all stellar-mass BHs binaries formed within the recent 10^7 yr, and find that there can be $\sim 3-20$ detectable RB sources with $\sim 10-300$ bursts per year under this assumption (see the grey data point in Figure 8.3). We note that the existence of BBHs in the inner 1000 au is highly uncertain, but any potential population in this region can have a significantly high fraction of bursting systems. Therefore, GW burst detection in the future will serve as a strong constraint on the number of BBHs in the inner 1000 au of the GN. For more details, see Appendix 3.6.1.3.

These results highlight the close relationship between the number of bursting BBHs and their formation history. In the young population of BBHs, RB systems will remain detectable up to $\sim 10^7$ yr after being driven to extreme eccentricity by the SMBH, which is longer than the YNC's age. However, despite the large total mass of the old population, they are likely to reach a steady state because of the low formation rate of BBHs. Therefore the young population will appear to have a much higher RB source fraction than the average value, as depicted in Figure 3.7.

In other words, RB sources can serve as a tracer of active star formation and dynamical evolution of compact object binaries in the recent $\sim 10^7$ yr history of the central Milky Way. We speculate that excess detection of bursting sources in certain regions of the Milky Way may indicate a recent episode of compact object formation.

3.3.6 EMRIs

EMRIs occur when a stellar-mass BH merges with an SMBH, emitting GW in the process. One of the popular formation channels for EMRIs is based on weak gravitational interactions between neighboring objects in the dense environment surrounding SMBHs, known as

two body relaxation/lose cone dynamics (e.g., Merritt, 2010; Binney and Tremaine, 2008; Hopman et al., 2007; Hopman and Alexander, 2006; Alexander and Hopman, 2009; Sari and Fragione, 2019; Berry and Gair, 2013; Fan et al., 2022). In Figure 8.3, we depict the expected number of GW bursts from EMRIs (i.e., EMRBs) following Hopman et al. (2007); Berry and Gair (2013); Fan et al. (2022), as well as the EMRBs rate assuming a significant fraction of SMBH binary existing in the universe (see, e.g., Naoz et al., 2022; Naoz and Haiman, 2023).

In particular, Naoz and Haiman (2023) estimate that there can be as much as $100 \sim 2000$ EMRIs detected per year if there is a significant fraction of galaxies holding an SMBH binary at their galactic center. Their simulation shows that most of the detectable EMRIs via SMBH binary channel are in a highly eccentric configuration, with the orbital period in the range of $\sim 1 - 10$ yr. Therefore, we estimate the number of detectable bursting sources and bursts per year by multiplying the EMRIs number with their orbital frequency ($\sim 0.1 - 1\ \mathrm{yr}^{-1}$). It turns out that under the assumption of Naoz and Haiman (2023), there can be $\sim 1000 - 20000$ bursting EMRIs detected during the LISA mission, which contribute to $\sim 100 - 20000$ GW bursts per year.

We emphasize that, similar to the case of bursting BBHs in the inner 1000 au of the Milky Way (see Section 3.3.5), the existence of SMBH binaries in the universe is poorly constrained. Therefore, in Figure 8.3, we use a hollow diamond to highlight the uncertainty of EMRI bursting sources formed via the SMBH binary channel. Similar to the arguments in Naoz and Haiman (2023), whether or not we will detect a large number of bursting sources as expected by this channel can strongly constrain the fraction of SMBH binaries in the universe.

3.4 Discussion

Many dynamically formed GW sources are expected to undergo an evolutionary stage at which the compact object binary is driven to extreme eccentricity. Such a system will emit GW bursts effectively upon each pericenter passage (see, for example, Figure 3.1), creating a pulse-like pattern in the signal before finally losing enough orbital energy and becoming a merger. Therefore, GW bursts from highly eccentric compact object binaries can be a promising tracer of their dynamical formation.

In Section 3.2, we estimate the detectability and lifetime of these sources analytically (see Eqs. (7.1)-(3.17)) and compare the results to numerical calculations (see Figure 3.4). Particularly, we show that stellar-mass bursting sources should be detectable in the Milky Way ($\sim$ 10kpc), with a much longer lifetime than other mHz sources (up to 10^7 yr). Moreover, a bursting source yields a larger strain amplitude than a low eccentricity source with the same average signal-to-noise ratio (see Figure 3.3). Considering this feature, we can potentially enhance these sources' detectability and parameter extraction in future data analysis.

Notably, BBH systems in many different regimes, such as in the field, globular clusters, and galactic nuclei, can naturally form bursting GW sources in the mHz band. For example, in Section 7.3, we show that bursting sources can dominate the population of mHz BBHs in the Milky Way since their longer lifetime (Equation (4.8)) results in a larger number expectation (Equation (8.15)). Adopting the constraints from LIGO's observation, we estimate $\sim$ 10 bursting BBHs detectable for the future LISA mission under the steady-state approximation (see Section 3.3.2).

In Figure 8.3, we present the estimated number of bursts as a function of bursting sources for different formation environments. In particular, we consider stellar-mass BHs in the galactic field, the globular clusters, and the galactic nucleus. We find that these channels can contribute to the number of detectable stellar-mass bursting BBHs in a range of $3 \sim 45$,

with $10^2 \sim 10^4$ mHz GW bursts observed during the LISA mission.

We highlight that the number of detectable bursting sources can well exceed the steady-state value since the formation history of bursting sources significantly affects their number in the mHz band. In particular, the Milky Way is expected to be a star-forming galaxy. Therefore, in Section 3.3.5, we go beyond the steady-state approximations and simulate the time evolution of bursting sources in the galactic center Young Nuclear Star Cluster, which is expected to form $\sim 2-8$ Myr ago. The simulation result supports that long-living bursting sources can remain detectable for $\sim 10^7$ yr. This region, with an active star formation in the recent few million years, will have a much higher fraction of bursting sources ($2 \sim 4$ bursting sources out of ~ 100 BBHs) than those old ones (~ 1 bursting sources out of ~ 1500 BBHs). In future observation, the distribution of bursting sources, as well as their actual number, can serve as a valuable tool to probe the GW sources' creation time in different regions of the Milky Way.

To conclude, unlike other mHz sources with moderate eccentricity, the detection of stellar-mass bursting systems is mostly limited in the Milky Way and nearby galaxies (see, e.g., Figure 3.5). However, these sources' bursting nature also results in a long lifetime and a potentially large number in the entire mHz population. Therefore, it is very likely that we can find many bursting sources at a close distance (e.g., a few dozen bursting BBHs in the Milky Way), with hundreds to thousands of GW bursts detected in the LISA observation. By studying the properties of these sources, we can better understand the early stages of dynamical formation and map the compact objects' formation history in our galaxy.

3.5 Acknowledgments

The authors thank Cheyanne Shariat, Sanaea Rose, Brenna Mockler, Xian Chen, and Xiao Fang for their valuable discussions and the anonymous referee for their useful comments. ZX acknowledges partial support from the Bhaumik Institute for Theoretical Physics summer fellowship. ZX, SN, and EM acknowledge the partial support from NASA ATP 80NSSC20K0505 and from NSF-AST 2206428 grant and thank Howard and Astrid Preston for their generous support. This work was supported by the Science and Technology Facilities Council Grant Number ST/W000903/1 (to BK).

3.6 Appendix

3.6.1 Details of Numerical Simulations

3.6.1.1 BBHs in the Field

For the BBHs in the galactic field, flyby gravitational interactions with other neighbors may excite their high eccentricity, driving the binary into a merger (e.g., Michaely and Perets, 2019; Michaely and Naoz, 2022). In this work, we adopt the model in Michaely and Naoz (2022) to calculate the properties of bursting BBHs born from this channel.

In particular, we choose the configuration of a Milky-Way type galaxy, with the stellar density profile and wide BBHs fraction following Eq. (23)$\sim$(26) in Michaely and Perets (2019). For simplicity, we further assume that all the BBHs have the mass of $10 - 10$ $M_\odot$, with the log-uniform distribution in the semi-major axis (from 100 to 50000 au). Second, we run a Monte-Carlo simulation, randomly choose the position and semi-major axis of BBHs following the distribution mentioned above, and calculate the fly-by merger rate as a function

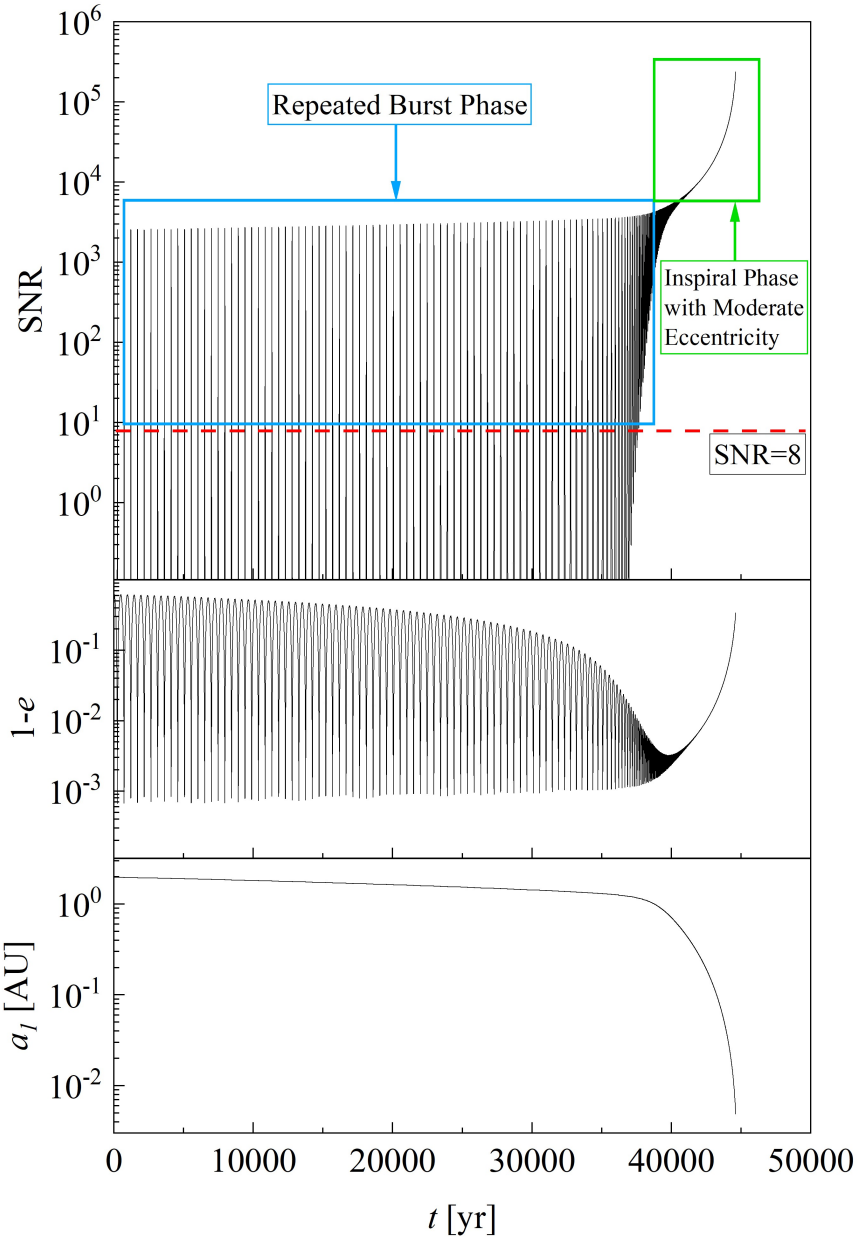


Figure 3.8: **An example of the repeated burst phase and inspiral phase during the evolution of an EKL merger.** We show a BBH system with $m_1 = 57.7\ \mathrm{M}_\odot$, $\mathrm{m}_2 = 51.9\ \mathrm{M}_\odot$, $a_1 = 1.97$ au, $e_1 = 0.38$, placed near a SMBH with $\mathrm{M} = 4 \times 10^6\ \mathrm{M}_\odot$, $a_2 = 4706$ au, $e_2 = 0.97$, $i = 88°$, $D_l = 8$ kpc . *Upper Panel* shows the signal-to-noise ratio of this source, for the observational time 4 yr. *Middle Panel* and *Bottom Panel* show its eccentricity and semi-major axis evolution as functions of time. As is shown in the figure, this example system undergoes strong EKL oscillation because of the SMBH. It spends a significant fraction of time in the repeated burst phase, bursting detectable GW signal via highly eccentric orbit, before finally reaching the inspiral phase with moderate eccentricity.

of semi-major axis (see Eq. (16)∼(23) in Michaely and Naoz, 2022).

After undergoing a fly-by interaction, the BBHs with a given semi-major axis need to have the eccentricity exceed a threshold, $e_{\rm crit}$, to make themselves merge before the next fly-by (see Eq. (2) in Michaely and Naoz, 2022). Therefore, we randomly generate the eccentricity of fly-by induced merger in the range of $e_{\rm crit}$ to 1, following the thermal distribution $F(e) = 2e$.

Using the methodology mentioned above, we can specify each merger system's semi-major axis and eccentricity in the simulation. This information allows us to calculate how many bursts they emit, and how long they stay detectable. For example, we can evolve a system following Eq. (3.16) and trace its signal-to-noise ratio using Eq. (3.17). Once the system becomes detectable, the merger timescale and number of bursts can be calculated via integration (see the example track in Figure. 3.4 for demonstration). The number of bursting systems in the fly-by channel is calculated using the steady-state approximation. In other words, we multiply the corresponding merger rate with the average detectable time for each semi-major axis, then do the summation over different semi-major axis to get the expectation of sources' number (see Eq. (8.15)).

Assuming a 10 yr LISA observation with the signal-to-noise ratio threshold 5, we got the expectation of fly-by induced, bursting field BBHs number is $N_{\rm field} \sim 3.3$ in the mHz band, with the number of detectable bursts $N_{\rm burst,field} \sim 61$ per year and merger rate $\Gamma_{\rm field} \sim 5 \times 10^{-7}{\rm yr}^{-1}$ in the Milky Way (or ~ 10 Gpc^{-3}yr^{-1} in the universe). Among these sources, we identified ~ 1.8 repeated burst source and ~ 1.5 non-repeated burst source (i.e., $T_{\rm orb} >$ 10 yr).

According to Michaely and Perets (2019), the BBH merger rate from the field channel can be within the range of $5^{+5}_{-3}{\rm Gpc}^{-3}{\rm yr}^{-1}$ in the local universe. Moreover, the number of bursts and bursting sources is proportional to the merger rate of BBHs. Therefore, to get a realistic estimation of the bursting sources' properties, the numbers we got from the simulation should

be multiplied by a factor of $0.5^{+0.5}_{-0.2}$, which is reflected in the results in Section 4.3.2.2.

3.6.1.2 BBHs in Globular Clusters

As is shown in Section 4.3.2.1, we use the eccentricity distribution of BBHs at a given frequency (see Fig. 4 in Martinez et al., 2020) and the spatial distribution of globular clusters in the Milky Way (Arakelyan et al., 2018) to generate the initial condition of bursting BBHs after undergoing dynamical interaction in GCs. For conservation purposes, we exclude the single-single capture and few body capture channels since the GW sources from these two channels are mostly formed above the mHz band, thus may not be suitable targets for LISA (Kocsis, 2020).

Adopting the same method as is shown in Section 3.6.1.1, we carried out Monte-Carlo Simulations and generated the parameters of bursting BBHs following the distribution mentioned above (Samsing and D'Orazio, 2019a; D'Orazio and Samsing, 2018; Martinez et al., 2020), then evolved them to the merger. The number of bursting sources and bursts is calculated under the steady-state approximation, taking into account the burst sources' properties from different channels of merger in GCs. Particularly, for a given sub-channel in GCs, we get the averaged bursting lifetime and the total number of bursts from the simulation, then multiply it with the merger rate (see Eq. (8.15)).

Assuming a 10 yr LISA observation with the signal-to-noise ratio threshold 5 and GCs merger rate $\Gamma_{\rm GC} \sim 1 \times 10^{-6}$ yr^{-1} in the Milky Way (~ 20 Gpc^{-3}yr^{-1} in the universe), we find the number of detectable bursting BBHs in the GCs of Milky Way to be $N_{\rm GC} \sim 14$, with the number of detectable bursts $N_{\rm burst,GC} \sim 176$ per year. Among these sources, we identified ~ 4 repeated burst source and ~ 10 non-repeated burst source. Similar to the case of field binaries in Section 4.3.2.2, the number of bursting sources is proportional to the merger rate ($\mathcal{R}_0 = 7.2^{+21.5}_{-5.5}$Gpc^{-3}yr^{-1} (Rodriguez et al., 2016; Kremer et al., 2020; Antonini and Gieles,

2020)). Therefore, the result in the simulation should be multiplied by a factor of $0.36^{+1.12}_{-0.26}$, which is reflected in the results of Section 4.3.2.1.

3.6.1.3 BBHs in the Galactic Nucleus

Stellar-mass BBHs surrounding the supermassive black hole in the galactic nucleus will naturally be in the configuration of a hierarchical triple system, thus undergoing eccentricity oscillation via the EKL mechanism. Based on the observational results, we carried out Monte-Carlo simulations of these BBHs' evolution. The simulations of hierarchical triple systems include the secular equations up to the octupole level of approximation (Naoz et al., 2013a), general relativity precession (Naoz et al., 2013b), and GW emission (Peters, 1964). In particular, we take into account three different populations of BBHs in the galactic nucleus:

1. **BBHs from the Main Population of Stars in the Galactic Nucleus.** This population is expected to have a distance to SMBH within 5 pc, age $\sim 2-8$ Gyr, total mass $\sim 1.8 \times 10^7$ $M_\odot$ (see, e.g., Pfuhl et al., 2011; Launhardt et al., 2002). In particular, we randomly generate BBHs with log uniform distribution in mass and semi-major axis, ranging from 6 to 100 $M_\odot$ and 0.1 to 50 au, respectively. For the spatial distribution of these BBHs, we adopt the isotropic distribution, with the radial density profile in the galactic center following Hoang et al. (2018). The number of systems is calibrated using the $m-\sigma$ relation. For conservation purposes, we rule out the systems that are too close to the SMBH to be classified as hierarchical triple systems (Naoz, 2016).

   After generating the initial condition for BBHs, we evolve these systems numerically, counting their bursting time and number of emitted bursts. The integration is stopped once the system becomes a GW merger or reaches the evaporation timescale (see Eq.(3) in Hoang et al., 2018). Because of the old age of the main population, we use the

steady-state approximation to work out the expectation of bursting sources' number, i.e.:

$$N_{\rm RB} = \Gamma_{\rm rep,all} f_{\rm RB} \tau_{\rm RB}, \tag{3.21}$$

in which $\Gamma_{\rm rep,all}$ is the replenishing rate of BBHs in the GN, $f_{\rm RB}$ is the fraction of BBHs in the GN that become a repeated burst source, and $\tau_{\rm RB}$ is the average lifetime time of bursting sources when they are detectable. Under the steady-state approximation, the total replenishing rate, $\Gamma_{\rm rep,all}$, equals the total empty rate at which BBHs merge or evaporate. Therefore, in the simulation, we determine the $\Gamma_{\rm rep,all}$ by multiplying the inverse of all the BBHs' average lifetime with their total number (~ 1500) in the inner 0.5 pc.

From the result of the simulation, $\Gamma_{\rm rep,all} \sim 3 \times 10^{-6}$ yr^{-1}. We note that this quantity equals the combined rate of GW merger plus evaporation, thus is higher than the GW merger rate constrained by LIGO. Moreover, the fraction of BBHs that turns into a bursting source is $f_{\rm RB} \sim 3\%$, and the average bursting time is $\tau_{\rm RB} \sim 1.4 \times 10^7$ yr. Therefore, we estimate the number of main population bursting sources as ~ 1 in the inner 0.5 pc of the Milky Way. A similar approach can be applied to calculate the number of bursts, and the result from the simulation is ~ 100 yr^{-1}.

2. **BBHs in the Young Nuclear Star Cluster** According to the observation (Paumard et al., 2006; Lu et al., 2008; Lu et al., 2013), the YNC has a distance to SMBH within ~ 0.5 pc, age $\sim 2 - 8$ Myr, and total mass $\sim 1.4 - 3.7 \times 10^4 M_\odot$, with top-heavy mass distribution. Because of their small mass and young age, we need to go beyond the steady-state approximation and simulate the time evolution of bursting GW sources as a function of time.

   For simplicity, we assume that this YNC is born in a starburst at $t = 0$, and all the massive stars are in the binary system. After evolving for a few Myr, the massive stars have all died and become black holes, and we get the corresponding black hole mass

following the results in Woosley et al. (2002); Belczynski (2020). According to the simulation result, there will be $\sim 100 - 400$ BBHs newly formed in the YNC. Because of the existence of mass gap (see, e.g., Bond et al., 1984; Fryer et al., 2001), most of these black holes have mass $\sim 10\ M_\odot$. We distribute the BBHs isotropically around the SMBH, with the same density profile as the main population, and trace their evolution as hierarchical triple systems.

As is discussed in Section 3.3.5, although the YNC has a relatively small total mass, its bursting BBHs number can be as much as 4, which is much higher than the main population with old age and a slow replenishing rate. We show the simulation results in Figure. 3.7. For completeness, we also show the expected number of bursts detected during the LISA mission as a function of the YNC's age (see Figure 3.9).

3. **BBHs in the Inner** 1000 **au of the Galactic Nucleus** The observation of stellar dynamics in the galactic center suggests that there can be up to $\sim 3000\ M_\odot$ unknown mass within the inner 1000 au of the SMBH (see, e.g., Ghez et al., 2008; GRAVITY Collaboration et al., 2020; Will et al., 2023). Therefore, we explored the possibility that these unknown objects are made up of stellar-mass BBHs (i.e., $\sim$ 150 BBHs). Since we are only aiming at a heuristic estimation, the simulation assumes that all these BBHs have the mass of $10 - 10\ M_\odot$, with the spatial density profile the same as for bursting BBHs in the YNC, and was born at $t = 0$.

   Adopting the same approach as modeling the time evolution of bursting sources in the YNC, we get the properties of this inner 1000 au population (see the hollow grey triangle in Figure 8.3). In particular, the existence of BBHs within the inner 1000 au, if any, will give a significantly higher fraction of bursting sources. When the cluster is a few Myr old, up to $\sim 13\%$ of all the BBHs can emit GW bursts, contributing to ~ 20 bursting sources and 200 bursts per year. On the other hand, if there is no such bursting source in future observation, we can put stringent constraints on the existence

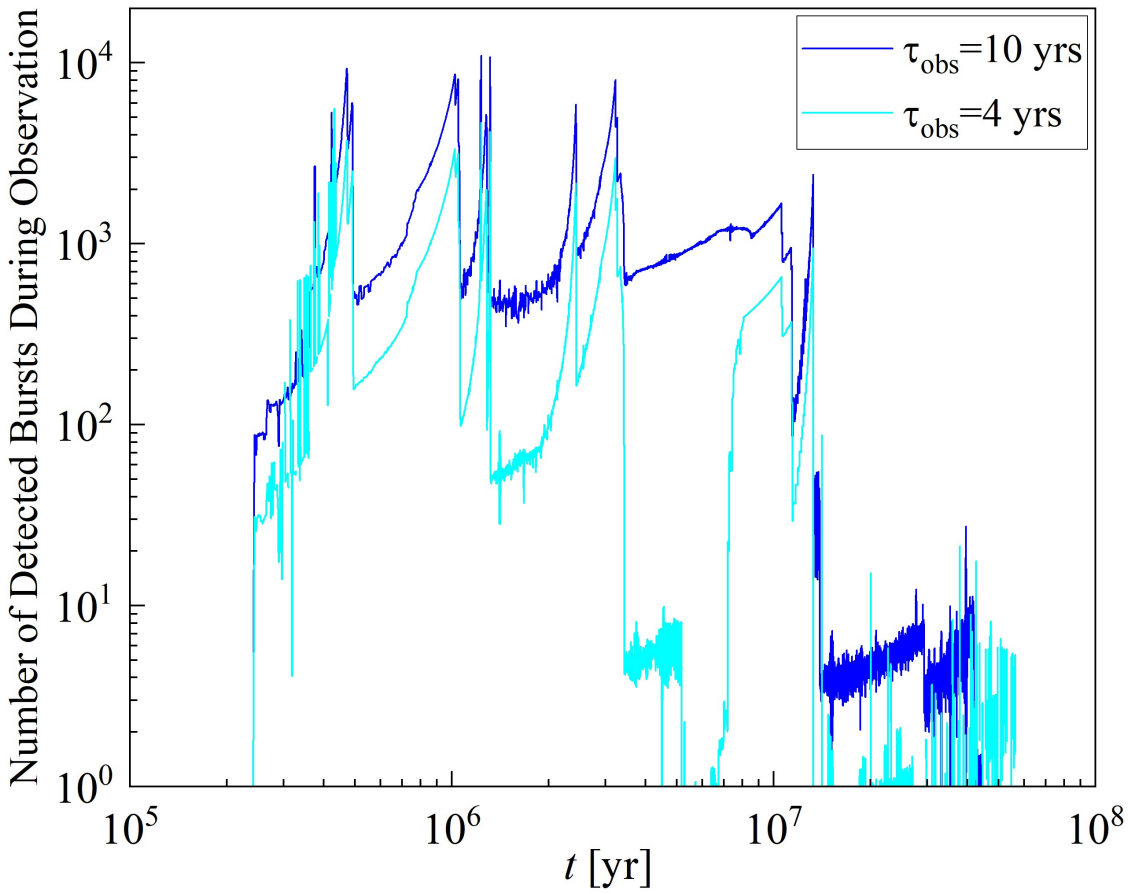


Figure 3.9: **Number of detectable bursts during LISA mission, as a function of the YNC's age.** Here we show the simulation result of observable bursts in the Milky Way center young nuclear cluster, as a function of the cluster's age. The deep blue line assumes the LISA observational period $\tau_{\rm obs} = 10$ yr while the light blue line represents $\tau_{\rm obs} = 4$ yr. The large fluctuation of the light blue line is caused by the limited number of systems in the simulation.

of BBHs in the center of our galaxy.

3.6.2 Numerical Approach to Calculate the SNR of Highly Eccentric Binaries

The time domain waveform of eccentric binaries, $h(a, e, t)$, can be decomposed into different harmonics, with the frequency $f_n = n f_{\rm orb}$ (Peters and Mathews, 1963; Kocsis and Levin, 2012):

$$h(a, e, t) = \sum_{n=1}^{\infty} h_n\left(a, e, f_n\right) \exp\left(2\pi i f_n t\right), \tag{3.22}$$

where

$$h_n\left(a, e, f_n\right) = \frac{2}{n}\sqrt{g(n, e)} h_0(a), \tag{3.23}$$

and:

$$h_0(a) = \sqrt{\frac{32}{5}} \frac{m_1 m_2}{D_l a} \tag{3.24}$$

$$g(n, e) = \frac{n^4}{32}\Big[\left(J_{n-2} - 2eJ_{n-1} + \frac{2}{n}J_n + 2eJ_{n+1} - J_{n+2}\right)^2 \tag{3.25}$$

$$+ \left(1 - e^2\right)\left(J_{n-2} - 2J_n + J_{n+2}\right)^2 + \frac{4}{3n^2}J_n^2\Big], \tag{3.26}$$

in which J_i is the i-th Bessel function evaluated at ne.

The integral of signal-to-noise ratio, in the frequency domain, is defined as (see, e.g., Robson et al., 2019a; Chen et al., 2019b):

$$\mathrm{SNR}^2(a, e) = \int \frac{h_c^2(a, e, f)}{f^2 S_n(f)} df, \tag{3.27}$$

in which h_c is the characteristic strain:

$$h_c^2(a, e, f) = 4f^2|\tilde{h}(a, e, f)|^2, \tag{3.28}$$

and $\tilde{h}(a, e, f)$ is the Fourier transform of the GW signal (Moore et al., 2014):

$$|\tilde{h}(a, e, f)|^2 = \sum_n \frac{h_n^2(a, e, f_n)}{2n\dot{f}_{\rm orb}}. \tag{3.29}$$

For highly eccentric binaries, the transient nature makes its frequency domain waveform split into millions of harmonics (peaks, see Figure 3.3). They are separated by an interval of $f_{\rm orb}$, and each peak has the width of $\Delta f \sim n\dot{f}_{\rm orb}T_{\rm obs}$ (caused by the orbital frequency shift of GW sources). Therefore, we can transform the expression of SNR into the summation of harmonics:

$$\mathrm{SNR}^2 = 8h_0^2(a) \sum_n \frac{g(n, e)}{S_n(nf_{\rm orb})n^2} T_{\rm obs} \ . \tag{3.30}$$

As is shown in Equation (7.33), the huge number (millions) of harmonics adds up to the numerical difficulty of calculating the SNR. However, we can further simplify this expression using the knowledge of the envelope of the frequency spectrum. In other words, instead of directly summing over millions of peaks, we can calculate the averaged amplitude in a wider frequency bin, and work out the density of peaks below that envelope (area enclosed by the power spectrum), then get a useful approximation of the SNR.

In particular, let's consider the integration in the frequency domain, take a value of f and the integration interval df around it. For each integration interval, the number of peaks contained in this frequency bin is $\Delta n \sim df/f_{\rm orb}$, while the amplitude of these peaks can be represented by the average value $g(n_{\rm avg}, e)$, with $n_{\rm avg} = f/f_{\rm orb}$.

Thus, the summation in Equation (7.33) can be turned into the integration of a smoothed

function:

$$\mathrm{SNR}^2 = 8h_0^2(a)\int \frac{g(n_{\mathrm{avg}},e)}{S_n(f)(\frac{f}{f_{\mathrm{orb}}})^2}T_{\mathrm{obs}}\frac{df}{f_{\mathrm{orb}}} = 8h_0^2(a)f_{\mathrm{orb}}T_{\mathrm{obs}}\int \frac{g(n_{\mathrm{avg}},e)}{S_n(f)f^2}df \tag{3.31}$$

Equation (7.34) serves as a fast numerical estimation of highly eccentric binaries' SNR. The accuracy of integration can be changed by adjusting df. In the limit of $df = f_{\mathrm{orb}}$, we recover the strict expression of Equation (7.33).

Chapter 4

Stochastic Gravitational Wave Background from Highly-Eccentric Stellar-Mass Binaries in the Milli-hertz Band

A version of this chapter was previously published in *Physical Review D* (Xuan et al., 2024b, Phys. Rev. D 110, 023020).

Abstract

Many gravitational wave (GW) sources are expected to have non-negligible eccentricity in the millihertz band. These highly eccentric compact object binaries may commonly serve as a progenitor stage of GW mergers, particularly in dynamical channels where environmental perturbations bring a binary with large initial orbital separation into a close pericenter

passage, leading to efficient GW emission and a final merger. This work examines the stochastic GW background from highly eccentric ($e \gtrsim 0.9$), stellar-mass sources in the mHz band. Our findings suggest that these binaries can contribute a substantial GW power spectrum, potentially exceeding the LISA instrumental noise at $\sim 3 - 7$ mHz. This stochastic background is likely to be dominated by eccentric sources within the Milky Way, thus introducing anisotropy and time dependence in LISA's detection. However, given efficient search strategies to identify GW transients from highly eccentric binaries, the unresolvable noise level can be substantially lower, approaching ~ 2 orders of magnitude below the LISA noise curve. Therefore, we highlight the importance of characterizing stellar-mass GW sources with extreme eccentricity, especially their transient GW signals in the millihertz band.

4.1 Introduction

The study of GW signals from eccentric compact object binaries plays an important role in GW astronomy. For example, extensive efforts have been made to measure the residual eccentricity of GW mergers in the data analysis of LIGO, Virgo, KARAGA (LVK) collaboration, which could shed light on the formation mechanisms of compact binaries (East et al., 2013; Samsing et al., 2014; Coughlin et al., 2015; Gondán et al., 2018b,a; Moore et al., 2019; Abbott et al., 2021; The LIGO Scientific Collaboration et al., 2021; Zevin et al., 2021; Lower et al., 2018; Romero-Shaw et al., 2019). However, so far, no confident evidence of residual eccentricity has been detected (see, e.g., Abbott et al., 2019; Lenon et al., 2020; Romero-Shaw et al., 2020; Gayathri et al., 2022; Samsing et al., 2022), primarily because GW radiation tends to circularize the orbit, rendering eccentricity negligible within the LVK frequency band (Peters, 1964; Hinder et al., 2008). In the future, the Laser Interferometer Space Antenna (LISA) (Amaro-Seoane et al., 2017b) is expected to observe sources in a lower frequency band ($10^{-4} - 10^{-1}$ Hz). Consequently, numerous eccentric GW sources, poten-

tially in their earlier evolutionary stages, may be present in the LISA data stream, providing valuable insights into their surrounding environments (see, e.g., Barack and Cutler, 2004b; Mikóczi et al., 2012b; Robson et al., 2018b; Chen et al., 2019b; Hoang et al., 2019; Fang et al., 2019b; Tamanini et al., 2020b; Torres-Orjuela et al., 2021; Amaro-Seoane et al., 2022; Xuan et al., 2021, 2024a).

Many eccentric GW sources formed through dynamical channels undergo a progenitor stage before the final merger. In this phase, the compact object binary, initially characterized by a large semi-major axis (e.g., $a \gtrsim 0.1\,\mathrm{au}$), attains extreme eccentricity (e.g., $e \gtrsim 0.9$) due to environmental perturbations. Although these sources have an orbital frequency well below the millihertz band, the binary's pericenter distance, $r_p = a(1-e)$, can become sufficiently close to induce strong millihertz GW emission (see, e.g., Loutrel and Yunes, 2017; Loutrel, 2020; Xuan et al., 2024a). This process leads to orbital energy loss, causing the orbit to shrink and circularize, resulting in a GW merger.

The GW signal emitted by wide, highly eccentric compact binaries exhibits distinctive characteristics compared to quasi-circular ones. In particular, when the binary's eccentricity is small, the GW signal can be effectively approximated by a near-monochromatic, sinusoidal wave, where the dominant GW frequency is twice the orbital frequency (see, e.g., Cutler and Flanagan, 1994). However, with an increase in the source's eccentricity, the GW emission becomes stronger upon each pericenter passage, turning the signal into a burst-like waveform (e.g., see Fig.1 in reference Xuan et al., 2024a). For example, a compact object binary with eccentricity $e = 0.9, 0.95, 0.99$ will emit more than $88.6\%, 99.5\%, 99.9996\%$ of its GW energy in less than 1% of the orbital period during the pericenter passage, regardless of its components' masses m_1, m_2, and semi-major axis a (Xuan et al., 2024a).

Various dynamic environments can give rise to stellar-mass bursting GW sources. For example, in dense star clusters, compact object binaries may attain non-negligible eccentricity due to external perturbations like GW capture, binary-single, and binary-binary scattering

(e.g., O'Leary et al., 2009a; Thompson, 2011; Aarseth, 2012; Kocsis and Levin, 2012; Breivik et al., 2016; Gondán et al., 2018b; D'Orazio and Samsing, 2018; Zevin et al., 2019; Samsing et al., 2019; Martinez et al., 2020; Antonini and Gieles, 2020; Kremer et al., 2020; Winter-Granić et al., 2023; Gondán and Kocsis, 2021; Purohit et al., 2024). Highly eccentric mergers can also arise in stellar disks or active galactic nucleus accretion disks (Tagawa et al., 2021; Samsing et al., 2022; Muñoz et al., 2022; Gautham Bhaskar et al., 2023). Additionally, fly-by interactions and galactic tides may excite the eccentricity of wide compact object binaries in the galactic field (e.g., Michaely and Perets, 2019, 2020; Michaely and Naoz, 2022), potentially leading to observable mergers. Moreover, in a hierarchical triple system (a tight binary orbiting a third body on a much wider "outer orbit"), the inner binary can undergo eccentricity oscillations via the eccentric Kozai-Lidov (EKL) mechanism (Kozai, 1962; Lidov, 1962; Naoz, 2016), becoming a GW source with high eccentricity in the LISA band. These channels can significantly contribute to the overall merger rate of stellar-mass compact objects (e.g., Wen, 2003; Hoang et al., 2018; Hamers, 2018; Stephan et al., 2019; Zevin et al., 2019; Bub and Petrovich, 2020; Deme et al., 2020; Wang et al., 2021; Zevin et al., 2021).

In this paper, our focus is on the stochastic GW background (GWB) originating from these bursting sources. In particular, as a collective GW signal of unresolved sources, the astrophysical stochastic GWB will compete with other expected LISA science sources, potentially producing a confusion noise that affects LISA sensitivity. Previous efforts have aimed to characterize various stochastic backgrounds, such as the collective GW signal from the galactic population of double white dwarf (DWD) binaries (see, e.g., Nelemans et al., 2004; Nissanke et al., 2012b; Klein et al., 2016b; Lamberts et al., 2018), extragalactic sources (Barack and Cutler, 2004b; Bonetti and Sesana, 2020; Chen et al., 2017), and cosmological stochastic backgrounds (Barack and Cutler, 2004a; Adams and Cornish, 2014; D'Orazio and Samsing, 2018; Boileau et al., 2021). Additionally, it was recently suggested that extreme mass ratio inspirals (EMRIs) might have orders of magnitude higher formation rate (Naoz et al., 2022) that may yield an order of magnitude noise level above LISA's sensitivity level (Naoz and

Haiman, 2023). By understanding these backgrounds, we not only address the potential impact of confusion noise on the parameter estimation of other resolved sources but also extract information about the stochastic background itself, thus constraining the population of GW sources (see, e.g., Agazie et al., 2023; Naoz and Haiman, 2023).

As a natural consequence of dynamical formation, the highly eccentric, stellar mass binaries may create a significant GW background in the LISA band. For example, in our previous studies (Xuan et al., 2024a), we anticipate the presence of approximately 3 to 45 detectable bursting binary black holes (BBHs) within the Milky Way, each with a signal-to-noise ratio (SNR) exceeding 5 for the upcoming LISA mission (Xuan et al., 2024a). Beyond these detectable cases, there could be a considerably larger number of bursting sources with SNR values falling below the detection threshold, yet their collective contribution remains significant.

Furthermore, the transient nature of these sources poses challenges in extracting their signals from the detector's output (Tai et al., 2014; Loutrel and Yunes, 2017; Loutrel, 2020), which potentially leads to a higher noise background level. In particular, the burst detection methods for stellar mass binaries, especially when multiple sources' bursts are present in the data stream simultaneously, remain relatively underdeveloped. Thus, there is uncertainty regarding our ability to identify all bursting sources in the detector's output, even if the sources' SNR is above the detection threshold. Moreover, the astrophysical burst signals may be intertwined with instrumental noise, such as glitches (see, e.g., Spadaro et al., 2023; Armano et al., 2016a, 2018a), and contribute to the unresolved GW background.

We note that there have been previous works examining the GWB from circular stellar mass BBHs (see, e.g., Sesana, 2016a) and eccentric stellar mass BBHs at a cosmological distance (see, e.g., Chen and Amaro-Seoane, 2017; D'Orazio and Samsing, 2018). These studies suggested that stellar-mass BBHs can make a non-negligible contribution to future observations, with eccentricity potentially affecting the overall shape of the millihertz GW background.

In this work, however, we extend this analysis beyond the cosmological population of BBHs to explore the GWB contribution of highly eccentric sources at close distances, specifically bursting sources in the Milky Way and nearby galaxies. As discussed before, even considering only the Milky Way population, the number of these sources may be substantial (Xuan et al., 2024a), and their close distance can potentially yield a significant overall GWB level. Furthermore, the transient nature of their GW emission can affect the pattern of the GWB, with a single bursting source capable of emitting GWs in a wide range of frequencies, which may cause confusion in future observations. In our analysis, we consider the realistic spatial distribution and non-equilibrium formation history of highly eccentric sources.

We organize this paper as follows. In Section 4.2.1, we first demonstrate the properties of bursting GW sources, then discuss their detectability (Section 4.2.2.1) and GW background calculation (Section 4.2.3). In Section 8.2, we introduce the population model of bursting sources, then carry out numerical simulations to predict the GW background level from highly-eccentric, stellar-mass BBHs in the Universe (Section 8.3.1). We show the results separately, for the globular clusters (Section 4.3.2.1), galactic field (Section 4.3.2.2), and the galactic nucleus (Section 4.3.2.3). In Section 7.6, we summarize and discuss the overall effect of stochastic GW background from stellar-mass bursting sources.

Unless otherwise specified, we set $G = c = 1$.

4.2 Theoretical Consideration

4.2.1 The Properties of GW Bursts from Highly Eccentric Binaries

In this section, for completion, we briefly summarize our previous results (Xuan et al., 2024a) on the detection of GW signals from individual bursting sources. The GW emission from a

highly eccentric binary is largely suppressed for most of the orbital period, $T_{\rm orb}$. However, it becomes significant during the pericenter passage time, T_p, resulting in a GW burst [1](O'Leary et al., 2009a; Xuan et al., 2024a),

$$T_p \sim \frac{r_p}{v_p} \sim (1-e)^{3/2} T_{\rm orb} \ , \tag{4.1}$$

where v_p is the orbital velocity at pericenter, and $T_{\rm orb} = 2\pi a^{3/2} m_{\rm bin}^{-1/2}$ is the period of a binary with a mass $m_{\rm bin}$.

The strain amplitude, $h_{\rm burst}$, and peak frequency, $f_{\rm burst}$ of a single GW pulse in the waveform of a highly eccentric compact object binary, can be estimated analytically [2] (for a detailed explanation, see (Xuan et al., 2024a)):

$$\begin{aligned} f_{\rm burst} &\sim 2 f_{\rm orb} (1-e)^{-\frac{3}{2}} \\ &\sim 3.16{\rm mHz} \left(\frac{m_{\rm bin}}{20{\rm M}_\odot}\right)^{\frac{1}{2}} \left(\frac{a}{1{\rm au}}\right)^{-\frac{3}{2}} \left(\frac{1-e}{0.002}\right)^{-\frac{3}{2}} \ , \end{aligned} \tag{4.2}$$

and

$$\begin{aligned} h_{\rm burst} &\sim \sqrt{\frac{32}{5}} \frac{m_1 m_2}{r_d a (1-e)} \\ &\sim 7.65 \times 10^{-21} \eta_s \left(\frac{m_{\rm bin}}{20{\rm M}_\odot}\right)^{\frac{5}{3}} \left(\frac{f_{\rm burst}}{3.16{\rm mHz}}\right)^{\frac{2}{3}} \left(\frac{r_d}{8{\rm kpc}}\right)^{-1} \ , \end{aligned} \tag{4.3}$$

in which $f_{\rm orb} = 1/T_{\rm orb}$ is the orbital frequency of the bursting source, r_d is the comoving distance of the binary, and $\eta_s = 4m_1 m_2/(m_1+m_2)^2$ is unity for equal mass sources.

Providing the analytical expression of $h_{\rm burst}$ and $f_{\rm burst}$, We can also estimate the signal-to-

[1]Note that we omit an order unity factor of $(1+e)^{-1/2}$, following our previous work, (Xuan et al., 2024a).

[2]The peak GW frequency of eccentric sources is often estimated as $f_{\rm peak} = f_{\rm orb}(1+e)^{1/2}(1-e)^{-3/2}$ (O'Leary et al., 2009a). A more detailed expression of the peak frequency can also be found in Refs. (Wen, 2003; Randall et al., 2022). For consistency with other definitions in our previous treatment (Xuan et al., 2024a), we adopt $f_{\rm burst} \sim 2 f_{\rm orb}(1-e)^{-3/2}$, which differs by an order of unity.

noise ratio of the bursting source (Xuan et al., 2024a):

$$\mathrm{SNR} \sim \begin{cases} \dfrac{h_{\mathrm{burst}}}{\sqrt{S_n\left(f_{\mathrm{burst}}\right)}} \sqrt{T_{\mathrm{obs}}\left(1-e\right)^{3/2}} & \left(T_{\mathrm{obs}} \geq T_{\mathrm{orb}}\right) \\ \dfrac{h_{\mathrm{burst}}}{\sqrt{f_{\mathrm{burst}} S_n(f_{\mathrm{burst}})}} & \left(T_{\mathrm{obs}} \leq T_{\mathrm{orb}}\right) \end{cases} \tag{4.4}$$

here T_{obs} is the observational time of the GW detector, and $S_{\mathrm{n}}(f)$ is the spectral noise density of LISA evaluated at GW frequency f (see e.g., Klein et al., 2016a; Robson et al., 2019a)

In the case of $T_{\mathrm{obs}} > T_{\mathrm{orb}}$, more than one GW bursts will be detected, and Equation (5.4) can also be expressed as:

$$\begin{aligned} \mathrm{SNR} \sim & 58\eta_s \left(\frac{m_{\mathrm{bin}}}{20\mathrm{M}_\odot}\right)^2 \left(\frac{a}{1\mathrm{au}}\right)^{-1} \left(\frac{1-e}{0.002}\right)^{-\frac{1}{4}} \\ & \left(\frac{r_d}{8\mathrm{kpc}}\right)^{-1} \left(\frac{T_{\mathrm{obs}}}{4\mathrm{yr}}\right)^{\frac{1}{2}} \left(\frac{S_n(f_{\mathrm{burst}})}{S_n(3.16\mathrm{mHz})}\right)^{-\frac{1}{2}}. \end{aligned} \tag{4.5}$$

A binary needs to emit GWs in the millihertz band to be potentially detectable with LISA. This condition constrains the orbital parameters of the observed GW sources. For example, a circular binary has its GW frequency equal twice the orbital frequency, and thus, the orbital radius must shrink to $r_{\mathrm{circ}} \sim 10^{-3}$au (for stellar-mass sources) to yield a GW signal detectable within the millihertz band. However, for a highly eccentric source, the peak frequency of GW bursts, $f_{\mathrm{burst}} \propto f_{\mathrm{orb}}(1-e)^{-\frac{3}{2}}$, can reach the millihertz band even when the binary is considerably wide and the orbital frequency is very low (Xuan et al., 2024a). During each orbit, the bursting source only emits GWs for a short period near the pericenter passage, resulting in a much slower orbital energy loss compared to circular binaries with the same GW frequency.

Due to the slower loss of orbital energy, highly eccentric sources could have a significantly longer detectable time within the LISA band. In particular, we can estimate the lifetime

of a bursting source, $\tau_{\rm burst}$, by considering the merger timescale of binaries with extreme eccentricity(Peters, 1964; Xuan et al., 2024a):

$$\begin{aligned}\tau_{\rm burst} &\sim \frac{3}{85\mu m_{\rm bin}^2} a^4 \left(1-e^2\right)^{7/2} \\ &\sim 1.17\times10^6{\rm yr}\,\frac{2}{q(1+q)}\left(\frac{m_{\rm bin}}{20{\rm M}_\odot}\right)^{-3}\left(\frac{a}{1{\rm au}}\right)^4\left(\frac{1-e}{0.002}\right)^{\frac{7}{2}},\end{aligned} \tag{4.6}$$

where $\mu = m_1 m_2/(m_1+m_2)$, and $q = m_1/m_2$. Note that this timescale is still much shorter than the Hubble time.

As shown above, the lifetime of millihertz bursting sources is promising, and this timescale is much longer than a millihertz circular binary's merger timescale, providing that circular binary has the same orbital radius, $r_{\rm circ}$, as the bursting sources' pericenter distance $a(1-e)$ (Peters, 1964):

$$\begin{aligned}\tau_{\rm circ,inspiral} &\sim \frac{5}{256\mu m_{\rm bin}^2} r_{\rm circ}^4 \\ &\sim 2.5\times10^3{\rm yr}\,\eta_s\left(\frac{m_{\rm bin}}{20{\rm M}_\odot}\right)^{-5/3}\left(\frac{f_{\rm circ,GW}}{3.16{\rm mHz}}\right)^{-\frac{8}{3}},\end{aligned} \tag{4.7}$$

here $f_{\rm circ,GW}$ is the GW frequency of the circular binary, which equals the eccentric source's burst frequency, $f_{\rm burst}$, in our comparison.

We note that Equation (7.3) can also be used to estimate the bursting binary's remaining inspiral timescale, when its orbit shrinks and circularizes after the bursting stage, if we replace $r_{\rm circ}$ in the equation with $a(1-e)$, and $f_{\rm circ,GW}$ with $f_{\rm burst}$ (note that the pericenter distance almost keeps constant during the evolution of a highly eccentric GW merger, see Peters, 1964; Xuan et al., 2024a). Therefore, combining Equation (7.1) and (7.3), we can estimate the ratio between the lifetime of a bursting source and its corresponding moderately-eccentric

inspiral stage within the same GW frequency band:

$$\tau_{\rm burst} \sim 20(1-e)^{-\frac{1}{2}}\tau_{\rm circ,inspiral} \ . \tag{4.8}$$

As mentioned above, dynamically formed GW sources are more likely to have wide eccentric configurations. This stage lasts much longer than the subsequent inspiral with moderate eccentricity, as indicated by Eq. (4.8). Consequently, along the evolution track of a dynamically formed eccentric source, the system will spend a considerably longer time in the first stage (millihertz bursting sources) compared to the second stage (millihertz near-circular inspiral). Therefore, if the dynamical formation channel significantly contributes to the GW merger rate, the potential number of millihertz bursting sources can be much greater than that of circular ones.

We note that Equation (4.8) is based on the comparison in the same GW frequency band and does not take into account the sources' detectability. However, since circular inspirals have a larger SNR than the highly eccentric configuration, they may exceed the LISA detection threshold below the millihertz band, extending their detectable time and enlarging the detected population. For example, in our previous work (Xuan et al., 2024a), we estimated the detectability of a $10-10{\rm M}_\odot$ BBH system with $e\sim 0, a\sim 0.03$ au in the Milky Way ($\sim$ 10kpc). It turns out that such a system will be detectable for 10^7 yr, with an orbital period of $T_{\rm orb}\sim 10^4$ s and GW frequency $f_{\rm circ,GW}\sim 10^{-4}$ Hz. Because we expect a large population of circular DWDs in the sub-millihertz band (see, e.g., Nissanke et al., 2012a; Lamberts et al., 2018), the identification of the near-circular, low-frequency systems is beyond the scope of this study. Thus, in this paper, we focus on the dynamically formed, highly-eccentric bursting sources and limit our aforementioned argument of the population in the same frequency band (e.g., $f_{\rm GW}\gtrsim$ 1mHz).

4.2.2 Stochastic GW Background from Bursting Sources

4.2.2.1 Identification of Bursting Signals and Residual Noise

Bursting sources have the potential to form a non-negligible GW background in the millihertz band, given their significant GW radiation (Equations (5.2)-(4.5)) and extended lifetime (Equation (7.1)). Particularly, frequent bursts from multiple sources with low SNR can accumulate to yield a stochastic background noise (see Eqs. (5.4) and (4.5)). For example, in Figure 5.8, we show the simulation result of the collective GW signal from bursting BBHs in the Milky Way globular clusters. We randomly generate BBH systems and estimate their ages based on a constant formation rate $\gamma_{\rm GC} = 10^{-6}\,{\rm yr}^{-1}$ in the Milky Way (for details of the population model, see Section 8.2). At the time of observation, we numerically compute the GW signal of each individual system (excluding merged ones) using the x-model (Hinder et al., 2010), then combine them to obtain the collective GW background in the time domain. Additionally, we also include the LISA detector's response to the bursting GW background, which yields a long-term modulation due to the orbit of LISA around the Sun (see *Upper Panel* of Figure 5.8). As shown in this example, the collective bursting signal is a superposition of GW transients, i.e., individual bursts, from various sources, each localized in time and frequency.

The transient nature of bursting signals (see *Lower Panel* of Figure 5.8) poses several challenges for existing data analysis strategies, such as the matched filtering method (Finn and Chernoff, 1993; Cutler and Flanagan, 1994), which relies on accurate templates of GW signals and may not perform optimally in fitting bursts (see, e.g., Tai et al., 2014; Loutrel and Yunes, 2017; Loutrel, 2020). In particular, GW templates for highly eccentric sources are underdeveloped, which adds to the difficulty of constructing a template bank for the extraction of the signal. Moreover, multiple bursting sources can be present in the detector's output, which may lead to the misidentification of sources and degeneracy of the fitted parameters.

We note that many efforts have been made to analyze transient events in LIGO data analysis (e.g., power stacking (East et al., 2013), wavelet decomposition (Klimenko and Mitselmakher, 2004), and the Q-transform (Bassetti et al., 2005; Tai et al., 2014)). Furthermore, several studies focused on the transients from highly eccentric EMRIs, which can be possibly seen by LISA (Barack and Cutler, 2004b; Cornish and Larson, 2003; Porter and Sesana, 2010; Mikóczi et al., 2012b; Fan et al., 2022). However, the burst detection methods for stellar mass binaries, particularly when multiple sources' bursts are present in the datastream simultaneously, remain relatively underdeveloped. In other words, there is uncertainty regarding our ability to identify all bursting sources, even when their signal-to-noise ratio is sufficiently high.

Therefore, we divide the following discussions into two parts, with different criteria for bursting source identification, to demonstrate the potential noise level in future data analysis:

1. **Total GW background** This criterion includes all the bursting sources regardless of their SNR, assuming that we do not include burst transient templates in the future LISA data analysis. It yields an upper limit for the potential stochastic background level from these sources.

2. **Unresolvable noise background** This criterion only includes the bursting sources with overall SNR < 8 for a 4 yr LISA mission, assuming that we successfully identify all the bursting sources with overall SNR > 8 and distinguish them from other signals. It gives a conservative estimation of the noise level from bursting sources.

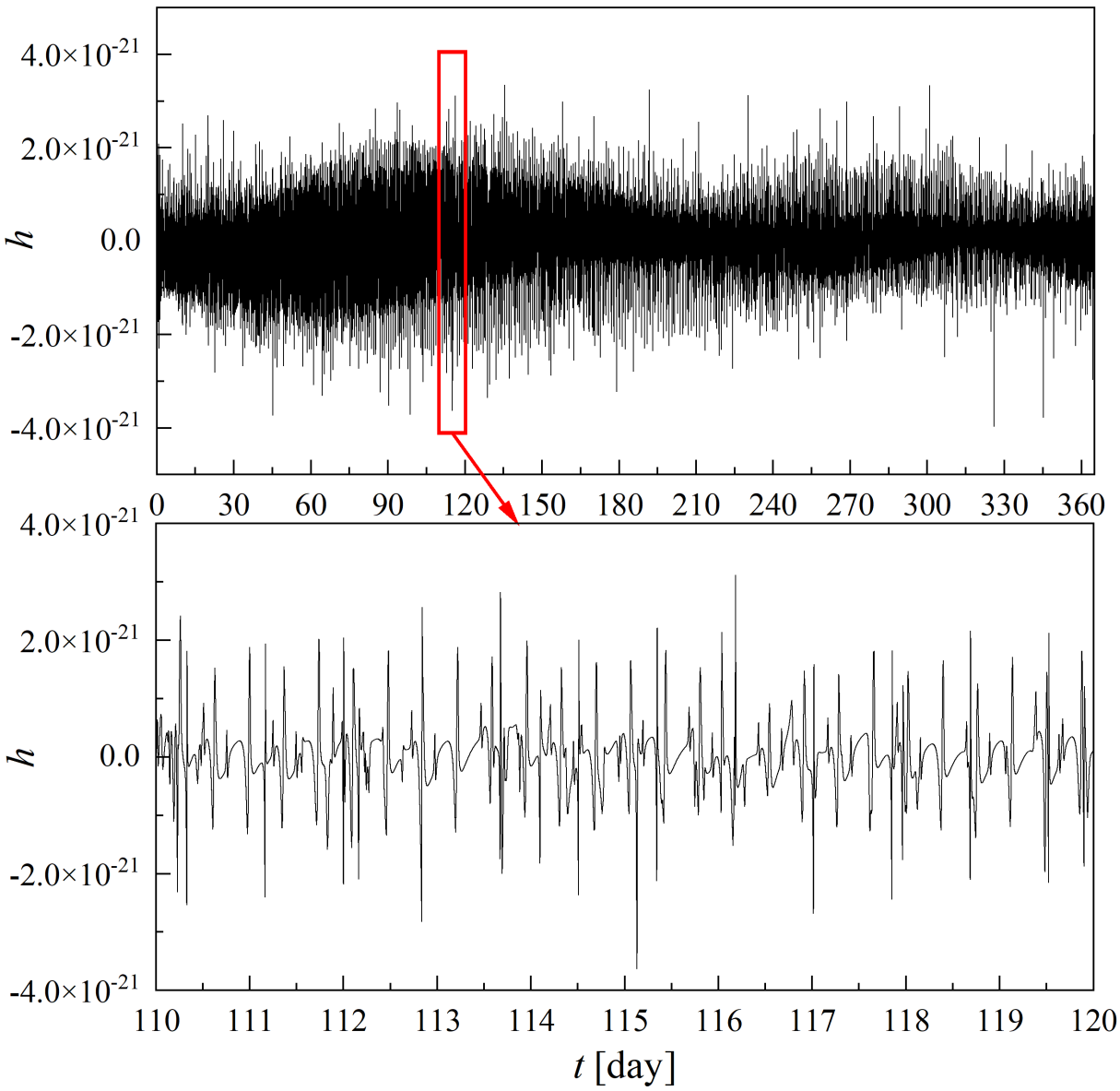


Figure 4.1: **GW background from bursting BBHs within the Milky Way globular clusters.** Here we generate the bursting BBHs population using the methodology described in Section 8.2, and calculate their collective GW signals observed by LISA. *Upper panel* shows the detector's Michelson response (Cutler, 1998; Cornish and Rubbo, 2003), $s_1(t)$, over a 1-yr period. *Lower panel* shows a zoom-in of the signal. In the *upper panel*, the modulation of the GW background is a result of the detector's annual motion around the sun.

4.2.3 Stochastic Background Calculation

4.2.3.1 Stochastic Background from GW Sources with Fixed Orbital Parameters

We follow Barack and Cutler (2004a) to calculate the stochastic GW background caused by stellar-mass bursting binaries in the LISA band, in which the one-sided noise spectral density is estimated as:

$$S_n(f) = \frac{4}{\pi f^2}\frac{d\rho}{df}, \tag{4.9}$$

here f is the observed frequency, and $d\rho/df$ is the total GW energy density in the corresponding frequency band.

For a single eccentric binary, its time domain waveform, $h(a, e, t)$, can be decomposed into different harmonics, each with the frequency of f_n (for simplicity, here we rms averaged over the binary inclination, see e.g., Peters and Mathews, 1963; O'Leary et al., 2009b; Kocsis and Levin, 2012; Kocsis et al., 2012):

$$h(a, e, t) = \sum_{n=1}^{\infty} h_{c,n}(a, e) \exp(2\pi i f_n t), \tag{4.10}$$

where

$$f_n = n f_{\rm orb}, \quad h_{c,n} = \frac{2}{n}\sqrt{g(n, e)}h_0(a) \tag{4.11}$$

and

$$h_0(a) = \sqrt{\frac{32}{5}}\frac{m_1 m_2}{r_d a}, \tag{4.12}$$

$$\begin{aligned} g(n, e) =& \frac{n^4}{32}\left[\left(J_{n-2} - 2eJ_{n-1} + \frac{2}{n}J_n + 2eJ_{n+1} - J_{n+1}\right)^2\right. \\ &\left. + \left(1 - e^2\right)\left(J_{n-2} - 2J_n + J_{n+2}\right)^2 + \frac{4}{3n^2}J_n^2\right], \end{aligned} \tag{4.13}$$

in which J_i is the i-th Bessel function evaluated at ne. Note that r_d is the comoving radial distance to the binary.

The energy density of a monochromatic GW signal with frequency f can be expressed as (see, e.g., Maggiore, 2000):

$$\rho_{\rm GW} = \frac{\pi}{8} f^2 \left\langle h_+^2 + h_\times^2 \right\rangle \sim \frac{\pi}{4} f^2 h_0^2, \tag{4.14}$$

where $h_+, h_\times$ are the amplitude of GW's two polarizations, and h_0 stands for the sky-averaged stain amplitude in Equation (4.12).

Since the gravitational wave signal from an eccentric source consists of multiple harmonics with different frequencies, the energy density is a superposition of each harmonic's contribution. In other words, by combining Equations (4.10)-(4.14), we can sum the contributions of all harmonics to determine the total gravitational wave energy density of an eccentric binary system:

$$\rho_{\rm ecc} = \sum_{n=1}^{\infty} \frac{\pi}{4} f_n^2 h_{{\rm c},n}^2 \ . \tag{4.15}$$

Here, we assume the GW source evolves slowly. Thus, the signal does not undergo a significant frequency shift during the observation, and each harmonic is a monochromatic signal where the power concentrates on $f = n f_{\rm orb}$ (see Equation (4.14)). We expect that most sources will be consistent with this assumption for the harmonics that contribute most to the detection signal-to-noise ratio (e.g., O'Leary et al., 2009a; Wang et al., 2021; Xuan et al., 2024a); however, in some cases, the signal may shift in a short timescale, (Hoang et al., 2019; Deme et al., 2020), which is beyond the scope of this study.

A key term in the noise spectral density, Eq. (4.9), is $d\rho/df$. To get this term from Equation (4.15), we need to calculate the distribution of energy density as the function of the GW signal's frequency. In other words, we sum the energy density contributions from the

harmonics within a given frequency bin (f_i, f_f):

$$\Delta\rho_{\rm ecc}\Big|_{f=f_i}^{f=f_f} = \sum_{n=n_i}^{n_f} \frac{\pi}{4} f_n^2 h_{{\rm c},n}^2 \approx \int_{n_i}^{n_f} \frac{\pi}{4} f_n^2 h_{{\rm c},n}^2 dn \ . \tag{4.16}$$

Here, $n = n_i, n_i + 1, ... n_f$ represents all the harmonic numbers between the initial and final frequencies, $f_i/f_{\rm orb}$ and $f_f/f_{\rm orb}$. Furthermore, as can be seen from Equation (4.10)-(4.16), the number of harmonics making a substantial contribution to the signal rises rapidly as eccentricity reaches extreme values. For example, we may have to consider millions to billions of harmonics when calculating the spectral density of GW signal from a binary with $e \gtrsim 0.95$. Consequently, using the sum in Equation (4.16) might not always be practical in noise spectral density calculations. Thus, for the highly eccentric systems in this paper, we average Equation (4.16) over the frequency bin to get a smoothed expression of $\rho(f)$. In particular, consider a frequency bin with the width of df at frequency f. Each GW harmonic in this bin contributes an energy density of approximately $\sim \frac{\pi}{4} f^2 h_{{\rm c},n(f)}^2$, where $n = f/f_{\rm orb}$, and the number of harmonics included in this bin equals $dn = df/f_{\rm orb} = ndf/f$. Therefore, the energy density in this bin for a single source, $d\rho_{\rm ecc,single}$, is obtained by multiplying the energy density of a single harmonic by the number of harmonics:

$$d\rho_{\rm ecc,single}(f) = \frac{\pi}{4} f^2 h_{{\rm c},n(f)}^2 \times \frac{n(f) df}{f}, \tag{4.17}$$

and thus,

$$\frac{d\rho_{\rm ecc,single}}{df} = \frac{\pi}{4} f h_{{\rm c},n(f)}^2 n(f). \tag{4.18}$$

Note that n in Equation (4.17) and (4.18) is a function of f.

Below, we substitute Equation (4.18) into (4.9) to calculate the energy spectrum of a single bursting source, then sum all the bursting sources' contributions to get the total GW power

spectrum:

$$S_{n,\mathrm{loc}}(f) = \frac{4}{\pi f^2}\frac{d\rho}{df} = \sum_{i\in\mathrm{sources}} \frac{n_i(f) h^2_{\mathrm{c},n_i(f)}}{f} \ , \tag{4.19}$$

where $n_i(f) = f/f_{\mathrm{orb},i}$ for the i^{th} source. Equation (4.19) is useful when calculating the bursting GW background from a group of local sources with determined orbital parameters (e.g., bursting BBHs in the Milky Way galactic center, at a given time in the numerical simulation).

4.2.3.2 Time-Averaged Stochastic Background Under the Steady State Approximation

For some bursting BBH populations, we assume a continuous birth and death of compact object binaries while keeping the total number of GW sources unchanged (i.e., adopt the steady-state approximation). Therefore, to obtain the expectation value of total GW power spectral density, we further average Equation (4.19) over the evolution of highly eccentric systems.

In particular, first, consider the contribution of the i^{th} bursting source in Equation (4.19). The average of this contribution over the single system's time evolution is:

$$\langle S_{n,\mathrm{loc}}(f)\rangle_{\mathrm{single,i^{th}}} = \int_{t_0}^{t_0+\tau_{\mathrm{merger}}} \frac{h^2_{\mathrm{c},n_i(f)}(f,t)}{f_{\mathrm{orb},i}(t)} \frac{dt}{\tau_{\mathrm{merger}}} \ , \tag{4.20}$$

in which $h_{\mathrm{c},n}(f,t) = \frac{2}{n(f,t)}\sqrt{g(n(f,t),e(t))}h_0(a(t))$ (see Equation (7.30)), and $n(f,t) = f/f_{\mathrm{orb}}(t)$.

In Equation (4.20), t_0 is the formation time of the BBH system in the simulations, and τ_{merger} represents the merger time of the BBH system with initial orbital parameters $a(t_0), e(t_0)$. When considering the long-term evolution of the source, parameters such as orbital frequency (f_{orb}), semi-major axis (a), and eccentricity (e) become functions of time. For bursting

systems undergoing isolated evolution, these parameters can be determined using Eqs. 5.6 - 5.14 in Peters (1964). However, for bursting systems affected by dynamical effects, such as the eccentric Kozai-Lidov mechanism, numerical simulations are required to determine the merger time and the evolution of other orbital parameters.

When integrating Equation (4.20) over the lifetime of a GW source, we determine its time-averaged GW power spectral density. Under the steady-state approximation, where the ensemble average equals the time average, Equation (4.20) provides the expectation value of spectrum contribution from the $i^{\rm th}$ GW source in observation.

Furthermore, we average Equation (4.20) over different BBH systems' initial conditions in the population synthesis. This average is computed by summing the GW power spectral density of all the simulated systems, $\langle S_{n,\rm loc}(f)\rangle_{\rm single,i^{th}}$ (see Equation (4.20)), and dividing by the number of systems generated in the simulation, N_s:

$$\langle S_{n,\rm loc}(f)\rangle\Big|_{\rm single,avg} = \frac{1}{N_s}\sum_{\rm i=1}^{N_s}\langle S_{n,\rm loc}(f)\rangle_{\rm single,i^{th}} \ . \tag{4.21}$$

We note that N_s is artificially introduced to enlarge the sample size and ensure numerical accuracy. It differs from the actual number of systems observed.

Finally, we multiply Equation (4.21) with the expected number of bursting BBHs in observation, $\langle N_{\rm tot}\rangle$, and get the collective GW power spectrum:

$$\langle S_{n,\rm loc}(f)\rangle\Big|_{\rm tot} = \frac{\langle N_{\rm tot}\rangle}{N_s}\sum_{\rm i=1}^{N_s}\langle S_n(f)\rangle_{\rm single,i} \ . \tag{4.22}$$

Here, $\langle N_{\rm tot}\rangle = \langle \tau_{\rm merger}\rangle \gamma_{\rm merger}$, where $\langle \tau_{\rm merger}\rangle$ represents the average lifetime of merger systems in the simulation, and $\gamma_{\rm merger} = dN/dt$ denotes the BBH merger rate per unit time in the considered region (see Section 4.3.1). Equation (4.22) is useful when calculating the ex-

pectation of bursting GW background from local sources in the Monte Carlo simulation (e.g., bursting BBHs in the Milky Way globular clusters, assuming they have reached equilibrium distribution with a fixed merger rate.).

4.2.3.3 Average Stochastic Background from Extragalactic Sources

For bursting sources at a cosmological distance, we further take into account the redshift z (e.g., see Naoz and Haiman, 2023; Barack and Cutler, 2004a):

$$S_{n,\cos}(f) = \frac{4}{\pi f^2} \int_0^z \frac{dt}{dz} \dot{\varepsilon}(f(1+z), z) dz, \tag{4.23}$$

here $\dot{\varepsilon}(f_{\rm em}, z)\Delta f_{\rm em}$ represents the rate (per unit proper time, per unit co-moving volume) at which GW energy between frequencies $f_{\rm em}$ and $f_{\rm em} + \Delta f_{\rm em}$ is emitted into the universe, at red-shift z. $f_{\rm em} = f(1+z)$ denotes the emitted GW frequency (i.e., the frequency measured by a contemporaneous observer, not the redshifted frequency f we measure today). We note that Equation (4.23) has taken into account the decrease in the waves' energy due to the redshift. For a detailed explanation, see Eqs. 34 - 35 in Barack and Cutler (2004a).

Furthermore, we calculate $\dot{\varepsilon}(f_{\rm em}, z)$ using the following relation:

$$\dot{\varepsilon}(f_{\rm em}, z) = \Gamma(z) \left\langle \frac{dE_{\rm GW}\left(f_{\rm em}\right)}{df_{\rm em}} \right\rangle. \tag{4.24}$$

In Equation (4.24), $\Gamma(z) = dN/(dtdV)$ represents the comoving merger rate of bursting BBHs per unit proper time, per unit co-moving volume; $\langle dE_{\rm GW}\left(f_{\rm em}\right)/df_{\rm em}\rangle$ is the emitted GW energy per unit frequency from a bursting BBH system, averaged over different BBH systems' initial conditions from the population synthesis.

We note that, the meaning of $dE_{\rm GW}/df_{\rm em}$ in Equation (4.24) is different from $d\rho_{\rm single}/df_{\rm em}$ in

Equation (4.18). In particular, $E_{\rm GW}$ accounts for the total gravitational wave energy emitted throughout the evolution of a source, while $\rho_{\rm single}$ represents the source's gravitational wave energy density at a given location in space (or equivalently, the energy flux $F_{\rm single} = c\rho_{\rm single}$, where $c = 1$ is the speed of light). These two quantities can be related by integrating the energy flux F on a spherical surface Ω_s, with a fixed radius of d_l from the BBH system, throughout the sources' time evolution. (see, e.g., Eq. 25 in Phinney (2001))

$$\int_{t_0}^{t_0+\tau_{\rm merger}} \langle F_{\rm single}(f_{\rm em}, t)\rangle_{\Omega_s} dt = \frac{1}{4\pi d_l^2} \int_0^{\infty} \frac{dE_{\rm GW}}{df_{\rm em}} df_{\rm em}, \tag{4.25}$$

and thus:

$$\begin{aligned} \frac{dE_{\rm GW}}{df_{\rm em}} &= 4\pi d_l^2 \frac{d}{df_{\rm em}} \int_{t_0}^{t_0+\tau_{\rm merger}} \langle F_{\rm single}(f_{\rm em}, t)\rangle_{\Omega_s} dt \\ &= 4\pi d_l^2 \int_{t_0}^{t_0+\tau_{\rm merger}} \left\langle \frac{d\rho_{\rm single}(f_{\rm em}, t)}{df_{\rm em}} \right\rangle_{\Omega_s} dt, \end{aligned} \tag{4.26}$$

In Equation (4.26), $F_{\rm single} = c\rho_{\rm single}$ can be expressed as a function of $f_{\rm em}$ and t. This is because, at any given time during the system's evolution, $\rho_{\rm single}$ is a function of the emitted GW frequency (see Equation (4.18)). However, over the long-term evolution, other orbital parameters also become functions of time (see the explanation below Equation (4.20)). Therefore, when integrating over the time evolution of a GW source, Equation (4.26) yields the cumulative energy emitted within a fixed frequency bin.

We note that, Eq. 25 in Phinney (2001) includes the effect of redshift at arbitrarily large luminosity distance, while here we drop the term of $1+z$ in Equation (4.25). This is because our purpose is to get the total energy measured as a function of the emitted frequency in the comoving frame of the source (the cosmological effects have been taken into account via Equation (4.23)). In other words, we choose the spherical surface Ω_s with a short distance d_l from the BBH system, such that the effect of redshift is negligible when we sum over the

energy flux. In fact, the factor d_l^2 will cancel out with the amplitude term in $\rho_{\rm single}$ on the right side of Equation (4.26), thus its value will not affect the calculation of $dE_{\rm GW}/df_{\rm em}$, since the energy density $\rho_{\rm single}$ is proportional to the square of the strain amplitude (see Equation (4.18)), while the strain amplitude is inversely proportional to the distance (see Equations (7.30) - (4.12)).

We emphasize that, in general, there exists a straightforward relationship between the spectrum of the gravitational wave background produced by a cosmological distribution of discrete gravitational wave sources and the present-day comoving number density of remnants, as described by Eq. 5 in Ref. (Phinney, 2001). Realistic examples and further discussions on this relationship can be found in studies such as Refs. (Kocsis and Sesana, 2011; Kocsis et al., 2012). For our cases, however, since the local population can have a non-negligible contribution to the overall GW background level, we include the inhomogeneous spatial distribution and non-equilibrium star formation history in the Monte Carlo simulations detailed below (see Section 4.3.1). Therefore, for consistency, we adopt Equations (4.19), (4.22) and (4.23) as a robust approach to estimate the GW background level across all channels, including cosmological background calculations.

4.3 Simulations of Different Bursting Galactic Sources

4.3.1 Configuration of the Simulations

As a proof of concept, we adopt the population model in Xuan et al. (2024a) to generate the parameters of highly eccentric, stellar-mass BBHs in the millihertz band [3]. We consider

[3]Note that for other kinds of bursting compact object binary, such as Double White Dwarfs (DWDs), there exists considerable uncertainty in their orbital evolution due to tidal interaction and mass transfer (see, e.g., Kremer et al., 2018a; Lau et al., 2022), particularly for cases involving extreme eccentricity. Therefore, our discussion is limited to BBHs, and we leave the discussion of other populations for future work. Nevertheless, it's worth noting that the tidal interaction of DWDs tends to circularize the orbit, preventing eccentricity

three regimes that are expected to host eccentric BBHs: Globular Clusters (GCs), Galactic Field, and Galactic Nuclei (GNs). Within each of these regimes, we split the discussion into several specific cases specified below.

In the simulation of BBHs in Globular Clusters and the Galactic Field, we adopt the steady-state approximation, assuming a continuous birth and death of compact object binaries in the universe while keeping the total number of GW sources unchanged. We calibrate our GW power spectrum based on the BBHs merger rate in the universe: $\Gamma_{\rm GC} = 7.2^{+21.5}_{-5.5}\,{\rm Gpc^{-3}\,yr^{-1}}$ (e.g., Rodriguez et al., 2016; Kremer et al., 2020; Antonini and Gieles, 2020), $\Gamma_{\rm Field,Fly-by} = 5^{+5}_{-2}\,{\rm Gpc^{-3}\,yr^{-1}}$ (Michaely and Perets, 2019). Moreover, adopting the galaxy number density of 0.02 $\rm Mpc^{-3}$ (Conselice et al., 2005), we can use the BBH merger rate in the universe to estimate the merger rate in an averaged galaxy: $\gamma_{\rm GC} = 3.6^{+10.8}_{-2.7} \times 10^{-7}\,{\rm yr^{-1}}$, $\gamma_{\rm Field,Fly-by} = 2.5^{+2.5}_{-1} \times 10^{-7}\,{\rm yr^{-1}}$.

For the Galactic Nuclei, we consider not only the old population of stars (calibrated using the steady-state approximation and the $m-\sigma$ relation (Merritt, 1999; Kormendy and Ho, 2013)), but also incorporate the non-equilibrium star formation history in the case of the Milky Way center, based on observational results (see, e.g., Paumard et al., 2006; Lu et al., 2008; Do et al., 2013; Chen et al., 2023).

We note that the merger rate of BBHs can depend on the star formation history and exceed the estimation in the local universe at high redshift. This phenomenon is especially significant for the globular cluster channel (see, e.g., Zwart and McMillan, 1999; Gnedin et al., 2014; Rodriguez et al., 2015, 2016; Fragione and Kocsis, 2018; Fragione et al., 2018). Therefore, when calculating the cosmological background of bursting GW sources from GCs, we additionally take into account the change of BBH merger rate as a function of redshift

from reaching extreme values (see, e.g., Shara and Hurley, 2002; Willems et al., 2007). Additionally, the close approach of bursting DWDs at their pericenter may induce mass transfer and spin interaction, further restricting the lifetime of highly eccentric sources (see, e.g., Fig.4 in Xuan et al., 2024a). Thus, we suspect a limited population of highly eccentric DWDs and a negligible noise background from bursting DWDs in the millihertz band, even in the presence of external dynamical perturbations.

and integrate Equation (4.23) up to redshift $z = 3$ (i.e., 11.5Gyr from present), following the merger rate evolution in figure 1 of Ref. (Fragione and Kocsis, 2018). The adopted redshift cutoff is partly justified because $z = 3$ represents the epoch of the peak of globular cluster formation rate (Gnedin et al., 2014).

For a more detailed description of the population model, see Sections 3.2-3.6 and Appendix A of Ref. (Xuan et al., 2024a).

4.3.2 Stochastic Background from the Simulations' Results

4.3.2.1 Dynamically Formed BBHs in Globular Clusters

Globular clusters are proposed to be a primary channel for the formation of GW mergers. In particular, the dense stellar environment within globular clusters results in various dynamical interactions, including scattering, few-body captures, the Eccentric Kozai-Lidov Mechanism, and non-secular triple interactions (see, e.g., Banerjee et al., 2010; D'Orazio and Samsing, 2018; Samsing, 2018; Antonini and Gieles, 2020; Fragione et al., 2019; Martinez et al., 2020; Kremer et al., 2020). Due to these frequent dynamical interactions, BBHs in globular clusters are anticipated to have non-negligible eccentricity, even within the frequency band of LIGO (see, e.g., D'Orazio and Samsing, 2018; Antonini and Gieles, 2020; Zevin et al., 2019; Samsing et al., 2019; Martinez et al., 2020; Kremer et al., 2020). Moreover, since globular clusters widely exist in the universe (e.g., approximately 150 in the Milky Way (Harris, 1996; Baumgardt and Hilker, 2018)), we expect a significant number of bursting sources originating from GCs.

For the GW background calculation, we adopt the BBH eccentricity and semi-major axis distribution from previous studies (see, e.g., figure 4 in Martinez et al., 2020, for a summary), and assume that all the BBHs have the mass of $10 - 10$ $M_\odot$ for simplicity. Since we are

interested in the bursting stage where BBHs are in a wide configuration, we evolve the systems shown in Martinez et al. (2020), which is in a higher frequency band, back to the former bursting stage. With the aforementioned parameter distribution, we carry out Monte Carlo simulations, randomly generate BBH systems, and evolve them until the merger happens. The stochastic background is calculated under the steady-state approximation, using Equation (4.22).

We adopt the spatial distribution of GCs in the Milky Way from Ref. (Arakelyan et al., 2018). For simplicity, we assume that the detector's distance to all GCs in M31 (M33) is 777 (835) kpc, respectively. The cosmological background of bursting BBHs in GCs is determined using Equation (4.23), with the assumption that the number density of Milky-Way like galaxies is 0.02 Mpc^{-3} (Conselice et al., 2005).

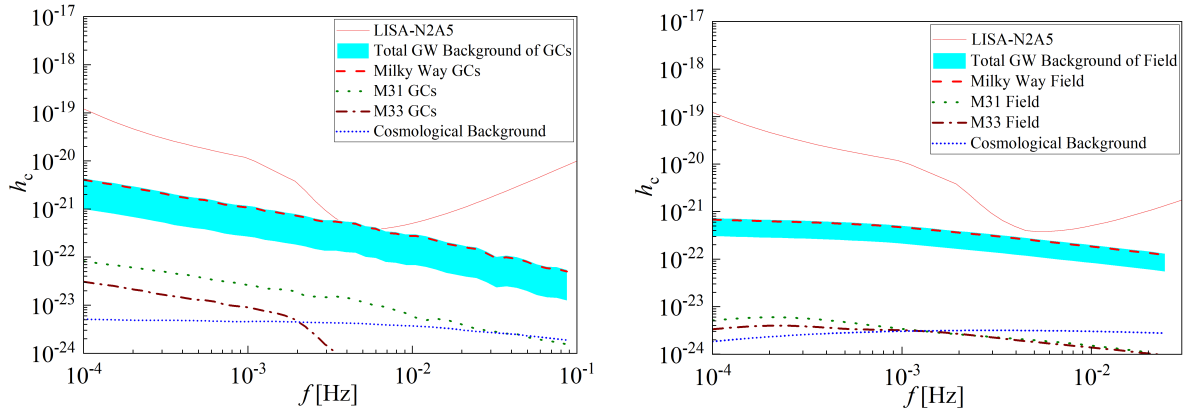


Figure 4.2: **Total GW background from bursting BBHs in Globular Clusters and Galactic Field.** Here we show (in dashed lines) the maximum collective GW power spectrum, $\sqrt{fS_n(f)}$, corresponding to bursting BBHs in the GCs (*Left Panel*) and Galactic Field (*Right Panel*) of Milky Way, M31, M33, and cosmological sources. The blue-colored region shows the total GW background from all four channels mentioned above, with its boundary representing the upper and lower limits. For comparison purposes, we also plot the LISA noise curve (N2A5 configuration (Klein et al., 2016a; Robson et al., 2019a), in the solid red line).

Figure 4.2, *Left Panel*, shows the maximum stochastic background from bursting BBHs in the Milky Way GCs (red dashed line), M31 GCs (green dotted line), M33 GCs (brown dashed-dot line), and GCs at a cosmological distance (blue dotted line). The overall GW

power spectrum (depicted by the blue-shaded band) is obtained by summing the contributions of all the sources mentioned above, where the maximum (minimum) value corresponds to the maximum (minimum) aforementioned merger rate. As can be seen in *Left Panel* of Figure 4.2, bursting BBHs within Milky Way GCs dominate the overall GW power spectrum. Meanwhile, the contributions from the other three channels have comparable levels, approximately two orders of magnitude weaker than Milky Way GCs. Moreover, the total GW background reaches the LISA noise curve at around 5 mHz, which suggests that neglecting these sources in future data analysis could significantly compromise LISA's sensitivity.

We note that previous studies (see, e.g., Sesana, 2016b; Nishizawa et al., 2016; D'Orazio and Samsing, 2018) have shown the overall cosmological GW background from stellar-mass BBHs, accounting for all the eccentricity values, is either comparable to or smaller than the millihertz LISA noise level. For our cases, as the highly eccentric binaries represent a subset of the entire BBH population, we anticipate their cosmological GW spectrum level to be lower than the overall background from BBHs and, thus, fall below the LISA noise curve. This prediction serves as an upper bound for the cosmological background of bursting sources in the simulation and turns out to be consistent with the simulation result (depicted by the blue dotted line in Figure 4.2).

Additionally, the noise background from the unresolvable sources (i.e., the GW spectrum of sources with SNR below 8 for a 4-year LISA mission), is over two orders of magnitude weaker than the LISA sensitivity. Thus, it is omitted here to avoid clutter, and we present this below, see Figure 4.4.

4.3.2.2 Fly-by Induced, Highly Eccentric BBHs in the Galactic Field

Recent studies show that external perturbations, such as flybys or galactic tides, can exert a significant influence on the orbital evolution of wide compact object binaries in the galactic

field (see, e.g., Kaib and Raymond, 2014; Michaely and Perets, 2019, 2020; Michaely and Naoz, 2022). Although the isolated wide binaries are not likely to merge due to their large GW merger timescale (sometimes exceeding the Hubble time, as indicated by Equation (7.3)), the dynamical perturbations from the environment can drive their eccentricity to extreme values, making the BBH system emit GW bursts during pericenter passage, and resulting in a GW merger. Given the substantial number of stars in the galactic field, the fly-by-induced bursting BBHs can significantly contribute to the overall GW background, even if their fraction within the entire stellar population is small.

We follow a similar approach for the GW background calculation as shown in Section 4.3.2.1. In particular, we generate the spacial distribution of wide BBHs according to the density profile of a Milky-Way type galaxy (see Eqs. 23 - 26 in Ref. (Michaely and Perets, 2019)). We randomly generate the semi-major axis of BBHs with the log-uniform distribution (from 100 to 50000 au), then calculate the fly-by merger rate as a function of semi-major axis (see Eqs. 16 - 23 in Michaely and Naoz, 2022). With a given semi-major axis, there is a critical eccentricity, $e_{\rm crit}$, for a BBH system to merge before the next fly-by (see Eq. 2 in Michaely and Naoz, 2022). Therefore, we randomly generate the initial eccentricity of fly-by induced merger in the range of $e_{\rm crit}$ to 1, following the thermal distribution $F(e) = 2e$.

Following the abovementioned approach, we compute the parameter distribution of fly-by-induced bursting BBHs, then adopt Equation (4.22) to estimate the overall GW background of Milky Way, M31, and M33, under the steady state approximation. For the cosmological background, we fix the BBHs merger rate $\Gamma_{\rm Field,Fly-by} = 5^{+5}_{-2}\,{\rm Gpc}^{-3}\,{\rm yr}^{-1}$ for simplicity, and integrate Equation (4.23) up to $z = 3$ to keep consistent with the case of GCs (see Section 4.3.1). As shown in the *Right Panel* of Figure 4.2, although the total GW background from bursting BBHs in the galactic field does not reach the LISA noise curve level, it still significantly contributes to the overall GW background.

4.3.2.3 BBHs in the Galactic Nuclei

The galactic nucleus, particularly if hosting an SMBH, can be a promising environment for the formation of stellar-mass bursting BBHs (see, e.g., Kocsis and Levin, 2012; Rodriguez et al., 2016; Hoang et al., 2018; Hoang et al., 2019; Trani et al., 2019; Stephan et al., 2019; Wang et al., 2021; Arca Sedda et al., 2023; Zhang and Chen, 2024a). For example, consider a stellar-mass BBH system orbiting the SMBH in the galactic nucleus. The EKL mechanism can induce eccentricity excitation in the inner binary's orbit, potentially driving the eccentricity to extreme values and triggering GW bursts (Wen, 2003; Naoz, 2016; Hoang et al., 2018; Hamers, 2018; Stephan et al., 2019; Bub and Petrovich, 2020; Deme et al., 2020; Wang et al., 2021). Consequently, we anticipate a high fraction of bursting BBHs in the galactic center, especially within the Nuclear Star Cluster, where the influence of the SMBH dominates the dynamical environment.

The number of bursting BBHs in the Galactic Nucleus can strongly depend on their formation history. For example, the main population of stars in the Milky Way Galactic Nuclei formed approximately $2 \sim 8$ Gyr ago (Lu et al., 2008; Chen et al., 2023). Consequently, this old population of stars may have reached an equilibrium state, resulting in a low rate of compact object binary formation. Therefore, we can use the steady-state approximation and adopt the same approach outlined in Section 4.3.2.1 and 4.3.2.2 to calculate their GW power spectrum.

However, observation shows there is a young nuclear star cluster (YNC) at the Milky Way center, which is formed approximately $2 \sim 8$ Myr ago (see, e.g., Paumard et al., 2006; Lu et al., 2006; Do et al., 2013; Chen et al., 2023). Moreover, there might be a hidden mass of ~ 3000 $M_\odot$ within the inner 1000 au of the Milky Way center (e.g., Do et al., 2019; GRAVITY Collaboration et al., 2020), supported by the observation of stellar motion and the theoretical arguments of the stability of S0-2, (e.g., Chu et al., 2018, 2023; Naoz et al.,

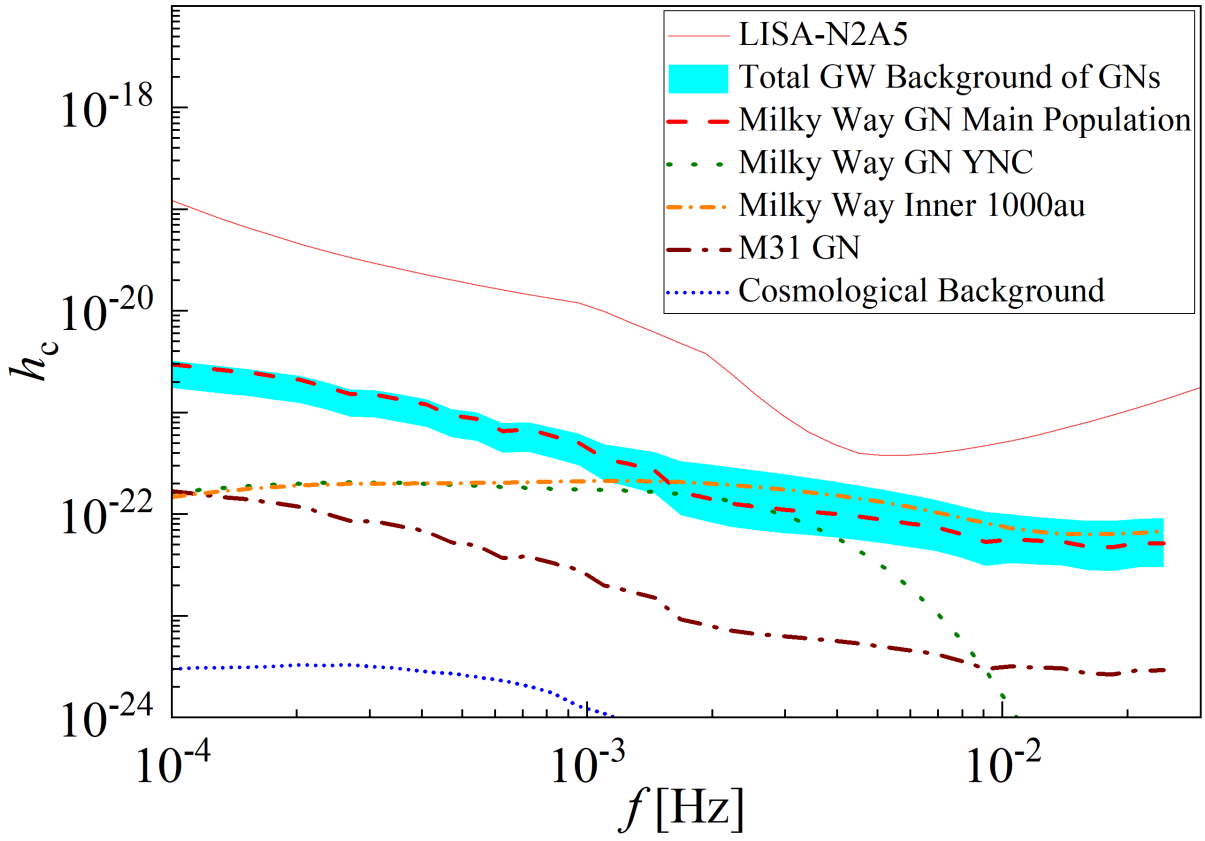


Figure 4.3: **Total GW background from bursting BBHs in the Galactic Nuclei.** Here we show the same GW background results as in Figure 4.2, but for the case of bursting BBHs in the galactic nuclei. We exclude the case of M33 in this figure since it does not have a SMBH in the galactic center. For a detailed explanation of the populations shown in the figure, see Section 4.3.2.3.

2020; Zhang et al., 2023b; Will et al., 2023). In our previous work (Xuan et al., 2024a), we carried out Monte-Carlo simulations of these BBHs' evolution, taking into account the EKL effect up to the octupole level of approximation (Naoz et al., 2013a), general relativity precession (e.g., Naoz et al., 2013b), and GW emission (Peters, 1964). The results indicated that the young population of stars potentially has a much higher fraction of bursting BBHs, especially when the YNC's age is below the detectable lifetime of bursting sources (see, e.g., Fig.7 in Xuan et al., 2024a).

The summary of the simulation results is presented in Figure 4.3. For the main population of stars in the Milky Way center, the galactic nuclei of nearby galaxies (M31), and the cosmological background, we follow a similar approach as mentioned in Sections 4.3.2.1 and 4.3.2.2, adopt the steady-state approximation, and use the simulation results in Xuan et al. (2024a) to calculate their GW background.

However, the steady-state assumption is no longer suitable for the bursting BBHs in the YNC and inner 1000 au of the Milky Way center. Thus, we track the time evolution of these populations as a function of the time, assuming that they were born in a starburst. The total GW power spectrum is calculated using Equation (4.19) and then averaged over the possible age range of the system. The blue-colored region in Figure 4.3 represents the collective GW power spectrum from all these channels' contributions. When computing its upper boundary, we sum over the maximum possible GW background level of all these channels. For its lower boundary, we exclude the contribution from bursting BBHs in the inner 1000 au, as the existence of this population is highly uncertain.

4.4 Discussion

Highly eccentric compact object binaries with wide orbits can naturally arise from the dynamical formation of gravitational wave sources. During each pericenter passage, these systems emit significant gravitational waves, potentially resulting in burst signals within the millihertz band. We adopted the analysis from our previous paper (Xuan et al., 2024a) and characterized the gravitational wave burst using Equations (5.2) - (4.5), detailed in Section 4.2.1, for completeness.

While the population of bursting sources may be large in the Universe, primarily due to their extended lifetime (see Equation (7.1)-(4.8)), their GW signals exhibit a transient nature, which poses challenges in the data analysis. In other words, current data analysis approaches may not properly identify bursting gravitational wave sources, even when the overall power of a signal (i.e., SNR) exceeds the conventional detection threshold for circular binaries (see the discussion in Section 4.2.2.1). Therefore, highly eccentric binaries can contribute to a non-negligible stochastic GW background in future millihertz detections (as depicted by the example in Figure 5.8).

In Section 4.2.3, we developed an analytical framework for computing the stochastic GW background from bursting sources. Subsequently, we carried out numerical simulations to determine the GW background from bursting BBHs in different formation channels, utilizing the population model of highly eccentric binaries outlined in Section 4.3.1. Specifically, Figure 4.2 depicts the example of the GW stochastic background from GCs and the Galactic Fields (left and right panels, respectively), adopting a steady-state approach for the sources' formation rate. In Figure 4.3, we also include the fact that a young population of stars has been observed in the center of the Milky Way (Lu et al., 2006; Do et al., 2009; Lu et al., 2013; Do et al., 2013, 2019; Chen et al., 2023). This young population implies that the center of our galaxy may deviate from the steady state restriction. Thus, we explore the impact of a young

population in the nuclear star cluster on the stochastic background. It produces a comparable contribution to the GW background (see Figure 4.2, dotted green line). Additionally, there have been observational and theoretical several studies that suggested the existence of about a few thousand of solar mass inwards to S0-2's orbit (GRAVITY Collaboration et al., 2020; Naoz et al., 2020; Zhang et al., 2023b; Will et al., 2023; Jurado et al., 2023). We thus add a population of compact objects inwards to S0-2's orbit ($\sim$ 1000 au). That may also have a significant contribution to the GW stochastic background.

As depicted in Figures 4.2-4.3, highly eccentric BBHs within the Milky Way dominate the stochastic background of GW bursts across all three channels (Globular Cluster, Galactic Field, and Galactic Nuclei), surpassing the contributions from other galaxies and the cosmological background. This pattern indicates that highly eccentric binaries are localized GW sources, like the galactic DWDs.

The dominance of the Milky Way's contribution, or in other words, the reason for the low level of cosmological background, can be understood by comparing the GW energy of bursting and non-bursting sources at the same frequency band (i.e., with the same pericenter distance $r_p = a(1-e)$, see Equation (5.2)). According to steady-state approximation, the number of GW sources is proportional to their lifetime, making the total number of bursting sources approximately $\sim 20(1-e)^{-1/2}$ times the number of circular inspirals formed via dynamical channels (see Equation (4.8)). However, since highly eccentric sources have lower GW emission power, the energy density contribution of a single bursting source is suppressed by a factor of $\sim (1-e)^{3/4}$ in the same frequency band (see Equation (5.4)). Consequently, the overall power spectrum of bursting sources is suppressed by a factor of $(1-e)^{1/4}$ compared to the contribution from all near-circular sources, implying that their signals are generally weaker, and detection is primarily limited to a short distance.

In Figure 4.4, we summarize the stochastic GW background from bursting BBHs. In particular, *Upper Panel* shows the maximum level of total GW background from bursting BBHs

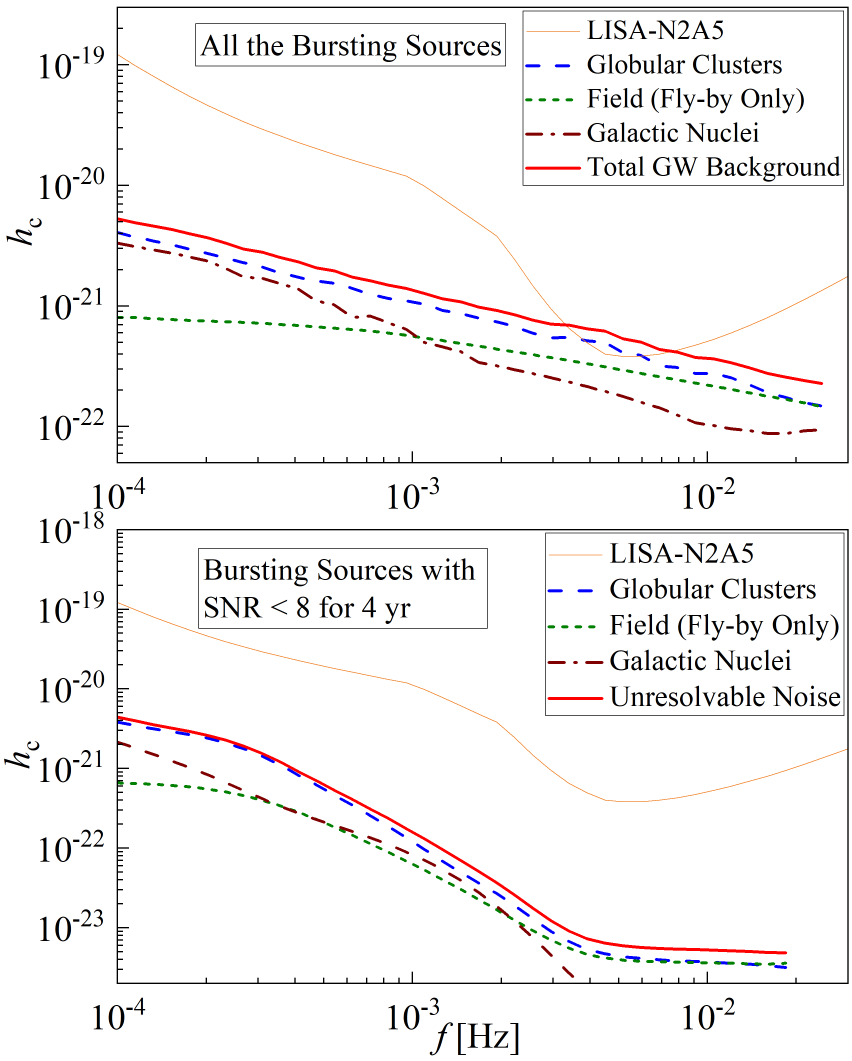


Figure 4.4: **Summary of the stochastic GW backgrounds from bursting BBHs.** Here, we show the upper limit of the GW background, $\sqrt{fS_n(f)}$, corresponding to highly eccentric BBHs from the Globular Clusters (blue dashed lines), Galactic Field (green dashed lines), and Galactic Nuclei (brown dash-dotted lines) in the universe. *Upper Panel* shows the maximum level of total GW background from bursting BBHs. *Bottom Panel* represents the unresolvable GW noise background from bursting sources with SNR $<$ 8 for a 4 yr LISA mission. For demonstration purposes, we sum the contribution of the three channels mentioned above and show the collective background in the solid red lines, and plot the LISA noise curve (N2A5 configuration (Klein et al., 2016a; Robson et al., 2019a), in orange).

in Globular Clusters, the Galactic Field, and the Galactic Nuclei, corresponding to the upper boundary of the blue-colored region in Figures 4.2 and 4.3. We depict the cumulative contribution of the three channels mentioned above with the solid red line. *Bottom Panel* represents the unresolvable GW noise background from bursting sources with SNR < 8 for a 4 yr LISA mission, which serves as a conservative estimation of the noise level under the assumption that we can identify all the bursting signals with proper templates in the data analysis.

As can be seen in the figure, highly eccentric, stellar mass BBHs can have a non-negligible GW background contribution in the LISA detection, potentially exceeding the LISA instrumental noise at $\sim 3-7$ mHz (see *Upper Panel*, in Figure 4.4). This phenomenon is especially significant if we do not have an effective search strategy for these sources' GW signals. In the LISA data analysis, if we only use the near-circular GW templates, the GW bursts from these sources will not be identified and will only be considered as a noise background in the detector's output. Therefore, even with promising SNR, the bursting GW sources will become part of the unresolvable noise background, thus affecting the LISA sensitivity (see Section 4.2.2.1).

However, providing that all the stellar mass bursting sources are properly identified in the future, the residual noise level is around two orders of magnitude lower than the LISA sensitivity curve, thus having a limited effect on the data analysis (see the *Bottom Panel*). Considering the abovementioned points, we highlight the importance of searching and identifying bursting GW sources in LISA detection. Particularly, we may need to develop portable GW templates for these sources in the matched filtering or adopt other time-frequency approaches, such as power stacking (East et al., 2013) and the Q-transform (Bassetti et al., 2005; Tai et al., 2014), to characterize the GW bursts from astrophysical sources in LISA data analysis.

Additionally, in realistic detection, the antenna pattern of LISA undergoes rotation across the

sky, causing its response to gravitational waves to change with time. As the bursting BBHs in the Milky Way predominantly contribute to the stochastic background and may have an anisotropic distribution, the amplitude of the GW burst background can vary considerably throughout the year. This observation is consistent with the pattern illustrated in Figure 5.8 (see, e.g., Digman and Cornish, 2022, for a similar case).

We note that the population model used in this study is subject to large uncertainties related to star formation and detailed dynamical evolution. It is intended as a heuristic estimate of the GW background from bursting sources. However, as demonstrated in this paper, the anticipated stochastic background of GW bursts can be significant, even when considering only Milky Way binary black holes. Furthermore, the noise level of GW bursts highly depends on the adopted data analysis strategy in LISA detection. Hence, we emphasize the significance of characterizing stellar-mass GW sources with extreme eccentricity, especially their transient GW signals in the millihertz band.

4.5 Acknowledgments

We thank the anonymous referee for useful comments. ZX acknowledges partial support from the Bhaumik Institute for Theoretical Physics summer fellowship. ZX, SN, and EM acknowledge the partial support from NASA ATP 80NSSC20K0505 and from NSF-AST 2206428 grant and thank Howard and Astrid Preston for their generous support. This work was supported by the Science and Technology Facilities Council Grant Number ST/W000903/1 (to BK).

Chapter 5

Extracting Astrophysical Information of Highly-Eccentric Binaries in the Millihertz Gravitational Wave Band

A version of this chapter was previously published in *Physical Review D* (Xuan et al., 2025a, Phys. Rev. D 111, 043018).

Abstract

Wide, highly eccentric ($e > 0.9$) compact binaries can naturally arise as progenitors of gravitational wave (GW) mergers. These systems are expected to have a significant population in the mHz band (e.g., $\sim 3 - 45$ detectable stellar-mass binary black holes with $e > 0.9$ in the Milky Way), with their GW signals characterized by "repeated bursts" emitted upon each pericenter passage. In this study, we show that the detection of mHz GW signals from highly eccentric stellar mass binaries in the local universe can strongly constrain their orbital

parameters. Specifically, it can achieve a relative measurement error of $\sim 10^{-6}$ for orbital frequency and $\sim 1\%$ for eccentricity (as $1-e$) in most of the detectable cases. On the other hand, the binary's mass ratio, distance, and intrinsic orbital orientation may be less precisely determined due to degeneracies in the GW waveform. We also perform mock LISA data analysis to evaluate the realistic detectability of highly eccentric compact binaries. Our results show that highly eccentric systems could be efficiently identified when multiple GW sources and stationary Gaussian instrumental noise are present in the detector output. This work highlights the potential of extracting the signal of "bursting" LISA sources to provide valuable insights into their orbital evolution, surrounding environment, and formation channels.

5.1 Introduction

Many compact object binaries are expected to have non-negligible eccentricity in the millihertz gravitational wave (GW) band. In particular, GW sources formed via dynamical channels can naturally undergo a progenitor stage before the final merger, during which the environment perturbs the binary and excites the orbital eccentricity (e.g., $e \gtrsim 0.9$); therefore, even if the GW source is initially characterized by a large semi-major axis (e.g., $a \gtrsim 0.1\,\mathrm{au}$), its pericenter distance, $r_p = a(1-e)$, can become sufficiently small to induce strong millihertz GW emission (Loutrel and Yunes, 2017; Loutrel, 2020; Xuan et al., 2024a), leading to orbital energy loss and eventually resulting in a GW merger. For example, in dense star clusters, external perturbations like GW capture, binary-single, and binary-binary scattering (e.g., O'Leary et al., 2009a; Thompson, 2011; Aarseth, 2012; Kocsis and Levin, 2012; Breivik et al., 2016; Gondán et al., 2018b; D'Orazio and Samsing, 2018; Zevin et al., 2019; Samsing et al., 2019; Stephan et al., 2016a; Hoang et al., 2020; Martinez et al., 2020; Antonini and Gieles, 2020; Kremer et al., 2020; Winter-Granić et al., 2023; Gondán and Kocsis, 2021;

Zhang et al., 2021; Fragione et al., 2022; Samsing et al., 2022; Rowan et al., 2023; Purohit et al., 2024) can drive a significant fraction of wide compact object binaries into highly eccentric orbits. In a hierarchical triple system, where a tight binary orbits a third body on a much wider “outer orbit", the inner binary can undergo eccentricity oscillations due to the eccentric Kozai-Lidov (EKL) mechanism (Kozai, 1962; Lidov, 1962; Li et al., 2015; Naoz, 2016; Hoang et al., 2018), potentially leading to an eccentric GW merger. Furthermore, eccentric compact binaries could form in stellar disks or active galactic nucleus accretion disks (Tagawa et al., 2020, 2021; Samsing et al., 2022; Muñoz et al., 2022; Gautham Bhaskar et al., 2023; Arca Sedda et al., 2023; Yan et al., 2023; Peng and Chen, 2023; Whitehead et al., 2024; Zhu and Chen, 2024). In the galactic field, fly-by interactions and galactic tides may also produce eccentric GW sources (e.g., Michaely and Perets, 2019, 2020; Michaely and Naoz, 2022; Stegmann et al., 2024). These eccentric binaries can significantly contribute to the number of sources in mHz GW detection (e.g., $\sim 3-45$ detectable stellar-mass binary black holes with $e > 0.9$ in the Milky Way (Xuan et al., 2024a)), and yield non-negligible merger rate of compact objects in the Local Group (Wen, 2003; Hoang et al., 2018; Hamers, 2018; Stephan et al., 2019; Zevin et al., 2019; Bub and Petrovich, 2020; Deme et al., 2020; Wang et al., 2021; Zevin et al., 2021) over the expected observation time of the future Laser Interferometer Space Antenna (LISA) mission (Amaro-Seoane et al., 2017b).

So far, many studies have focused on measuring the residual eccentricity of GW mergers detected by LIGO, Virgo, and KAGRA (LVK), which could significantly enhance our understanding of the formation mechanisms of compact binaries (East et al., 2013; Samsing et al., 2014; Coughlin et al., 2015; Gondán et al., 2018b,a; Moore et al., 2019; Abbott et al., 2021; The LIGO Scientific Collaboration et al., 2021; Zevin et al., 2021; Lower et al., 2018; Romero-Shaw et al., 2019; Knee et al., 2022). However, there is still a lack of clear observational evidence for the eccentricity of GW sources (see, e.g., Abbott et al., 2019; Lenon et al., 2020; Romero-Shaw et al., 2020; Gayathri et al., 2022; Samsing et al., 2022), mostly because GW radiation tends to circularize the orbit, rendering eccentricity negligible within

the sensitive frequency band of current detectors (Peters, 1964; Hinder et al., 2008). On the other hand, LISA (Amaro-Seoane et al., 2017b) will observe sources in a lower frequency band ($10^{-4} - 10^{-1}$ Hz), allowing us to probe the earlier evolutionary stages of these eccentric GW mergers (see, e.g., Barack and Cutler, 2004b; Mikóczi et al., 2012a; Robson et al., 2018b; Chen et al., 2019b; Hoang et al., 2019; Fang et al., 2019b; Tamanini et al., 2020b; Torres-Orjuela et al., 2021; Amaro-Seoane et al., 2022; Xuan et al., 2021, 2023). Therefore, it is crucial to evaluate the detectability and parameter measurement accuracy of eccentric GW sources, particularly for mHz detections by LISA.

This work focuses on the astrophysical inference of highly eccentric, stellar-mass compact object binaries. Specifically, the GW signal emitted by wide, highly eccentric compact binaries has a unique signature in the mHz band. For example, when a binary's eccentricity is small, its GW signal can be approximated by a near-monochromatic, sinusoidal wave (see, e.g., Cutler and Flanagan, 1994). However, as the eccentricity increases, the GW emission becomes stronger upon each pericenter passage, transforming the signal into a burst-like waveform (e.g., Kocsis and Levin, 2012; Xuan et al., 2024a,b). These bursting GW signals, characterized by transient pulses in the time domain, generate a frequency power spectrum with numerous harmonics (on the order of $\sim 10^3 - 10^6$) that contribute significantly to the total signal-to-noise ratio (see, e.g., Kocsis and Levin, 2012; Xuan et al., 2024a). As a result, the energy of the GW signal is spread across a wide frequency range, making it necessary to employ methods that can resolve broadband transient signals, such as wavelet decomposition (Klimenko and Mitselmakher, 2004; Chatterji et al., 2004, 2006; Bassetti et al., 2005; Tai et al., 2014). Furthermore, multiple bursting sources may simultaneously contribute to the signal (Xuan et al., 2024a), highlighting the need to identify and disentangle individual sources, as demonstrated below. The collective GW signal from multiple highly eccentric binaries could also form a stochastic GW background, where numerous GW harmonics from different sources overlap (Xuan et al., 2024b), and interfere with our understanding of other LISA sources.

It has been suggested that eccentric GW signals can be detected in the LISA band, leading to extracting information about the astrophysical sources (see, e.g., Seto, 2001; Glampedakis, 2005; Hopman and Alexander, 2006; Rubbo et al., 2006; Amaro-Seoane et al., 2007; Barack, 2009; Thompson, 2011; Mikóczi et al., 2012a; Berry and Gair, 2013; Chen and Han, 2018; Fang et al., 2019; Hoang et al., 2019; Wang et al., 2021; Randall et al., 2022; Fan et al., 2022; Oliver et al., 2023; Naoz et al., 2022; Naoz and Haiman, 2023; Zhang et al., 2021; Xuan et al., 2023; Shariat et al., 2023a; Nishizawa et al., 2016, 2017). Furthermore, many efforts have been made to analyze the mHz bursting GW signals using various waveform templates (Loutrel and Yunes, 2017; Moore et al., 2018; Han et al., 2020; Loutrel, 2020; Romero-Shaw et al., 2023; Knee et al., 2024; Zhang and Chen, 2024b). However, it remains unclear whether we can successfully distinguish highly eccentric ($e > 0.9$) sources in mHz data analysis and what level of parameter estimation accuracy can be realistically achieved for such systems. Below, we quantify the parameter measurement accuracy using a Fisher matrix analysis and, for the first time, demonstrate the application of matched filtering for identifying highly eccentric stellar-mass binaries in the LISA band, in the presence of multiple GW sources and instrumental detector noise. In this work, we analyze the bursting compact binaries in the Milky Way as a representative example. However, the results of Fisher matrix analysis and matched filtering can be generalized, with a rescaling of distance and signal-to-noise ratio, to bursting sources in the local universe with negligible redshift.

Note that the Fisher matrix analysis (Coe, 2009; Cutler and Flanagan, 1994) has been widely used in the literature to evaluate the parameter measurement accuracy for LISA, because of its simplicity and computational efficiency. However, this method can sometimes provide inaccurate results, particularly for waveforms with low expected signal-to-noise ratios (SNR) or for signals that depend weakly on certain parameters (see, e.g., Vallisneri, 2008; Toubiana et al., 2020). Therefore, the parameter measurement accuracy presented in our work should be interpreted as an initial estimation for this new class of sources (i.e., wide, highly eccentric binaries with slow orbital evolution). A Bayesian analysis is beyond the scope of this paper.

The paper is organized as follows: In Section 5.2.1, for completeness, we reviewed the astrophysical properties of highly eccentric GW sources (Xuan et al., 2024a,b). Next, we discussed the waveform model used in this work and described the parameterization of the waveform template (see Section 5.2.2). In Section 5.3.1, we estimated LISA's parameter measurement accuracy for highly eccentric GW sources using the Fisher matrix analysis. Furthermore, we carried out mock LISA data analysis to discuss the identification of bursting sources under realistic assumptions. In particular, we introduce the matched filtering method in Section 5.3.2, which is commonly adopted to analyze GW data, then highlight the difference between the data analysis of bursting and other quasi-circular GW sources (see Section 5.4.1). The simulation of mock LISA data is discussed in Section 5.4.2, and the mock analysis results are shown in Section 5.4.3. In Section 7.6, we summarized the paper and discussed the astrophysical implications. Throughout the paper, unless otherwise specified, we set $G = c = 1$.

5.2 Astrophysical Properties and Waveform Modeling

5.2.1 Astrophysical Properties

As discussed in Section 5.1, wide, highly eccentric compact binaries often serve as progenitors of GW mergers, particularly in dynamical channels where environmental perturbations cause close encounters between two compact objects. Furthermore, as shown in our previous works (Xuan et al., 2024a,b), these highly eccentric binaries could have promising prospects for detectability, extended lifetime, and a significant population in the local universe. Therefore, for completeness, we briefly summarize the relevant findings and discuss the signatures of highly eccentric waveforms in the mHz band in this section.

The GW emission from a highly eccentric binary is largely suppressed for most of the orbital

period. However, during each pericenter passage, the distance between the two components of the binary will decrease significantly, producing a sudden burst of GW radiation. Thus, the GW signal from wide, highly eccentric sources is characterized by “repeated bursts" (Kocsis et al., 2006c; Kocsis and Levin, 2012; Tai et al., 2014; Loutrel and Yunes, 2017; Gondán et al., 2018a; Fang et al., 2019a; Knee et al., 2024), where the separation between two bursts is the orbital period. Furthermore, the duration of each GW burst is approximately the pericenter passage time, T_p (O'Leary et al., 2009a; Xuan et al., 2024a), which can be estimated using the pericenter distance divided by the orbital velocity at pericenter:

$$T_p \sim \frac{r_p}{v_p} \sim (1-e)^{3/2} T_{\rm orb} \ , \tag{5.1}$$

where v_p is the orbital velocity at pericenter, and $T_{\rm orb} = 2\pi a^{3/2} M^{-1/2}$ is the period of a binary with a total mass M. Note that we omit an order unity factor of $(1+e)^{-1/2}$, following our previous work (Xuan et al., 2024a).

Furthermore, we can estimate the strain amplitude, $h_{\rm burst}$, and peak frequency, $f_{\rm burst}$, of a single GW pulse in the waveform of a highly eccentric compact binary using the following relations (Xuan et al., 2024a):

$$\begin{aligned} f_{\rm burst} &\sim 2 f_{\rm orb} (1-e)^{-\frac{3}{2}} \\ &\sim 3.16{\rm mHz} \left(\frac{M}{20{\rm M}_\odot}\right)^{\frac{1}{2}} \left(\frac{a}{1{\rm au}}\right)^{-\frac{3}{2}} \left(\frac{1-e}{0.002}\right)^{-\frac{3}{2}} \ , \end{aligned} \tag{5.2}$$

and

$$\begin{aligned} h_{\rm burst} &\sim \sqrt{\frac{32}{5}} \frac{m_1 m_2}{R a (1-e)} \\ &\sim 7.65 \times 10^{-21} \eta_s \left(\frac{M}{20{\rm M}_\odot}\right)^{\frac{5}{3}} \left(\frac{f_{\rm burst}}{3.16{\rm mHz}}\right)^{\frac{2}{3}} \left(\frac{R}{8{\rm kpc}}\right)^{-1} \ , \end{aligned} \tag{5.3}$$

in which $f_{\rm orb} = 1/T_{\rm orb}$ is the orbital frequency of the bursting source, R is the distance

of the binary from the observer, m_1, m_2 are the mass of the binary's components, and $\eta_s = 4m_1m_2/(m_1+m_2)^2$ is unity for equal mass sources. We note that the peak GW frequency of eccentric sources is often estimated as $f_{\rm peak} = f_{\rm orb}(1+e)^{1/2}(1-e)^{-3/2}$ (O'Leary et al., 2009a). A more detailed expression of the peak frequency can also be found in Refs. (Wen, 2003; Randall et al., 2022). For consistency with other definitions in our previous treatment (Xuan et al., 2024a), here we adopt $f_{\rm burst} \sim 2f_{\rm orb}(1-e)^{-3/2}$, which differs by an order of unity.

As shown in Equations (5.2) and (5.3), even when the binary is considerably wide and the orbital frequency is well below the LISA band (e.g., $a \sim$ 1au), an increase in the orbital eccentricity can result in mHz GW burst emission, with the strain amplitude strong enough to be detected by LISA. In particular, we can estimate the signal-to-noise ratio of these bursting sources using the following analytical equation (Xuan et al., 2024a)[1]:

$$\mathrm{SNR} \sim \begin{cases} \dfrac{h_{\rm burst}}{\sqrt{S_n\left(f_{\rm burst}\right)}}\sqrt{T_{\rm obs}\left(1-e\right)^{3/2}} & \left(T_{\rm obs} \geq T_{\rm orb}\right) \\ \dfrac{h_{\rm burst}}{\sqrt{f_{\rm burst}S_n(f_{\rm burst})/2}} & \left(T_{\rm obs} \leq T_{\rm orb}\right) \end{cases} \tag{5.4}$$

here $T_{\rm obs}$ is the observational time, and $S_{\rm n}(f)$ is the spectral noise density of LISA evaluated at GW frequency f (see e.g., Thorne, 1987; Klein et al., 2016b,a; Robson et al., 2019b) (Note that Equation (5.4) is an approximation. For a more precise expression of the SNR, see, for example, Appendix B of Ref. (Xuan et al., 2024a).).

We highlight that, for a bursting source, the strong GW emission only happens for a short amount of time near the pericenter passage, while the binary will remain quiescent for the rest of the orbital period. Therefore, the overall energy emission and SNR will be suppressed by a factor of $\sim (1-e)^{3/2}$ compared to circular binaries with the same GW frequency (see,

[1]Note that the second line of Equation (5.4) differs from Eq.11 in Ref. (Xuan et al., 2024a) by a factor of $\sqrt{2}$, which has been introduced to ensure consistency between the first and second lines.

e.g., Equation (5.4)). However, such suppression in energy emission also results in a much slower orbital shrinkage and a significantly longer detectable time within the LISA band. In particular, we can estimate the lifetime of a bursting source, $\tau_{\rm burst}$, by considering the merger timescale of binaries with extreme eccentricity (Peters, 1964; Xuan et al., 2024a):

$$\tau_{\rm burst} \sim \frac{3}{85\mu M^2} a^4 \left(1-e^2\right)^{7/2} \sim 1.17\times10^6 {\rm yr} \times \\ \frac{2}{q(1+q)} \left(\frac{M}{20{\rm M}_\odot}\right)^{-\frac{5}{3}} \left(\frac{f_{\rm burst}}{3.16{\rm mHz}}\right)^{-\frac{8}{3}} \left(\frac{1-e}{0.002}\right)^{-\frac{1}{2}}, \tag{5.5}$$

where $\mu = m_1 m_2/(m_1+m_2)$, and $q = m_1/m_2$.

As shown in Equation (7.1), with the parameters of $a \sim 1$ au, $e \sim 0.998$, $m_1 = m_2 = 10{\rm M}_\odot$, $R = 8$ kpc, a stellar-mass bursting sources can remain detectable in the mHz band for $\sim 10^6$ years (note that this system has a signal-to-noise ratio SNR ~ 50 for a 3 yr LISA observation; see Equation (5.4)). Such a lifetime is much longer than a stellar-mass circular binary's merger timescale, which is typically $\sim 10^3 - 10^4$ years in the mHz band (Peters, 1964). Therefore, as a progenitor stage of GW mergers, the extended lifetime of highly eccentric binary indicates their large population in the local universe. For future observation, we expect LISA to detect many slowly evolving bursting sources as a natural consequence of compact binaries' dynamical formation.

In Figure 5.1, we illustrate a representative example of bursting GW signals from highly eccentric, stellar-mass binary black hole (BBH) systems. Specifically, we choose the parameters of $m_1 = 15$ M$_\odot$, $m_2 = 10$ M$_\odot$, $a = 0.100148$au, $e = 0.99, \Theta = \Phi = \pi/4$ (note that Θ, Φ is the spherical polar angles of the observer's direction as viewed in the source's comoving frame, see Figure 5.2 and Section 5.2.2 for more details). This system is placed at $R = 8$ kpc and observed for 3 years, which stand for representative parameters of the bursting sources in the Milky Way (see, e.g., the population analysis in Kremer et al., 2018a; Xuan et al., 2024a,b). Furthermore, for this system, the SNR of a single GW burst is ~ 62 and the total

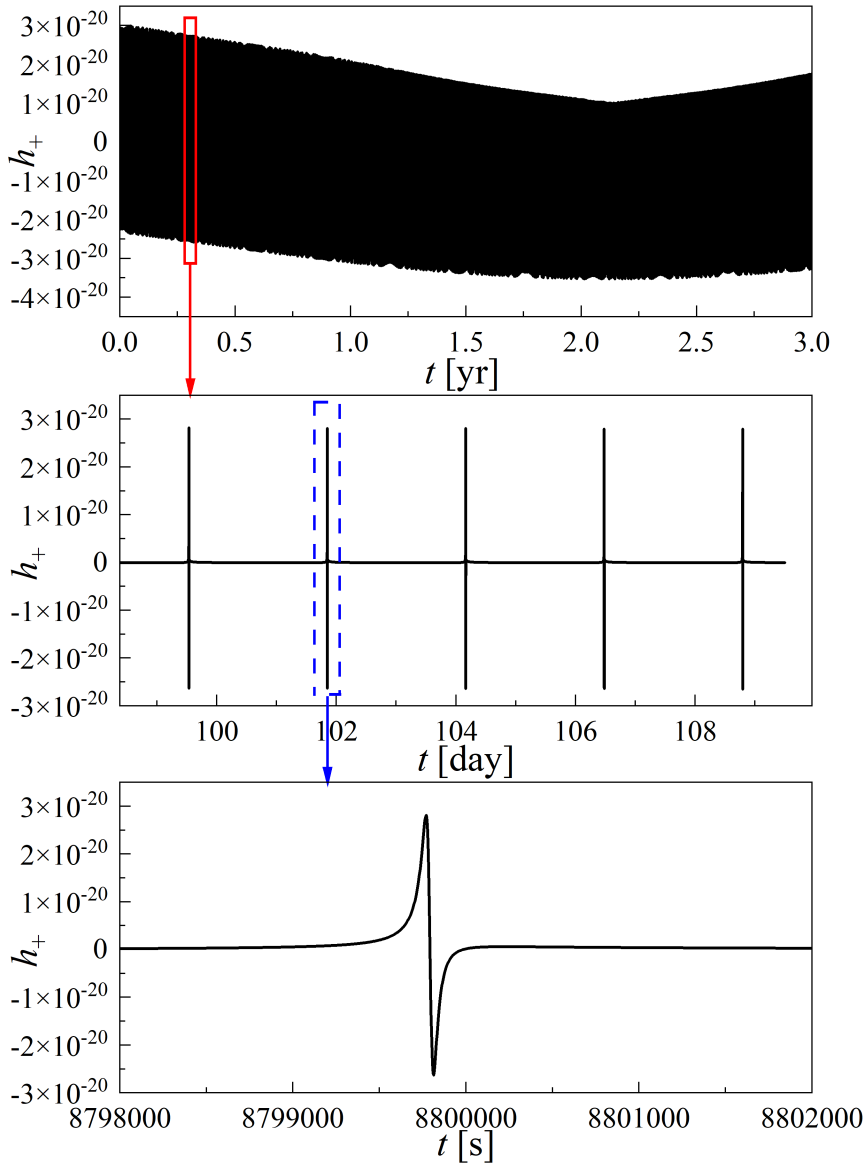


Figure 5.1: **Bursting GW waveform from a wide, highly eccentric BBH system.** Here we show the strain amplitude (h_+) of a BBH system with $m_1 = 15\,\mathrm{M}_\odot$, $m_2 = 10\,\mathrm{M}_\odot$, $a = 0.100148\mathrm{au}$, $e = 0.99, \Theta = \Phi = \pi/4$, placed at $R = 8$ kpc and observed for 3 years (see Section 5.2.2 for detailed definitions of Θ, Φ). The time domain waveform is generated using the x-model as described in Section 5.2.2. *Upper Panel* shows the entire 3-year-long signal, which is made up of ~ 473 GW bursts (clustering in the black-colored region). Furthermore, the amplitude modulation in the *Upper Panel* is caused by general relativistic precession of the binary's orbit (precession period ~ 11.8 yr). *Middle Panel* is a zoom-in of the signal for a ~ 10 days period, and *Bottom Panel* illustrates the details of waveform near a single GW burst. Note that in this example, we do not include the detector's response, otherwise, the LISA's annual motion around the sun will induce another long-term modulation on the amplitude and phase of the bursting signal.

SNR is $\sim$ 1353 (see Equation (5.4)). However, in realistic observations, some detectable bursting sources may have the SNR of a single GW burst below the detection threshold (see, e.g., Ref. (Xuan et al., 2024a)). The time domain waveform is generated using the x-model as described in Section 5.2.2, and we choose to show the plus polarization, h_+, for demonstration purposes.

We note that, the black-colored region in the *Upper Panel* of Figure 5.1 represents a clustering of $\sim$ 473 GW bursts, with the long-term amplitude modulation of their envelope caused by the general relativistic precession. Furthermore, due to the slow orbital evolution (see Equation (7.1)), the orbital frequency, $f_{\rm orb}$, of the binary is approximately constant during the observation period. Therefore, the waveform is characterized by repeated bursts with almost uniform separation (see *Middle Panel*). Additionally, as shown in *Bottom Panel*, a single GW burst roughly lasts hundreds of seconds, which indicates that the burst frequency lies in the mHz band. As shown in Figure 5.1, the "bursting" waveform of highly eccentric binaries has a unique signature compared with other quasi-circular waveforms. Thus, it can provide us with valuable insight into the binary's dynamical evolution, as well as test the theory of gravity. In the following sections, we will discuss how to practically extract the astrophysical information of these sources from simulated LISA data.

5.2.2 Waveform Model

In this paper, we adopt the x-model (Hinder et al., 2010) to generate the gravitational wave signal from eccentric binaries (assuming that the binaries are not perturbed during observation, and thus can be treated as isolated two-body systems). The x-model is a time-domain, post-Newtonian (pN)-based waveform family that captures all the critical features introduced by eccentricity in non-spinning binaries (Huerta et al., 2014). The binary orbit is parameterized using Keplerian parameterization to 3pN order, with the conservative evolution also

given to 3pN order. In the x-model, the loss of energy and angular momentum is mapped to changes in the orbital eccentricity e and the pN expansion parameter $x \equiv (\omega M)^{2/3}$, where ω is the mean Keplerian orbital frequency. These two parameters are evolved according to 2 pN equations. The x-model has been validated against numerical relativity for the case of equal mass BBHs with $e = 0.1$, 21 cycles before the merger. It also agrees with well-studied template families in GW data analysis for the zero-eccentricity case (Brown and Zimmerman, 2010).

In particular, we use Eqs. 9 - 10 in Hinder et al. (2010) to generate the time evolution of x and e (note that in the PN formalism, there are three different definitions of eccentricity parameters (e_r, e_ϕ, e_t), and the eccentricity here stands for e_t, see Refs. (Damour and Deruelle, 1985, 1986; Blanchet, 2002; Hinder et al., 2010; Knee et al., 2022)), then evolve the orbital phase φ and orbital radius r using their Eqs. 5 - 7. The strain amplitude of two polarizations, h_+ and $h_\times$, are given (to leading Newtonian order) by:

$$\begin{aligned} h_+ = &-\frac{M\eta}{R}\left\{(\cos^2\Theta+1)\left[\cos 2\varphi'\left(-\dot{r}^2+r^2\dot{\varphi}^2+\frac{M}{r}\right)\right.\right. \\ &\left.\left.+2r\dot{r}\dot{\varphi}\sin 2\varphi'\right]+\left(-\dot{r}^2-r^2\dot{\varphi}^2+\frac{M}{r}\right)\sin^2\Theta\right\}\ , \\ h_\times = &-\frac{2M\eta}{R}\cos\Theta\left\{\left(-\dot{r}^2+r^2\dot{\varphi}^2+\frac{M}{r}\right)\sin 2\varphi'\right. \\ &\left.-2r\cos 2\varphi'\dot{r}\dot{\varphi}\right\}\ , \end{aligned} \tag{5.6}$$

where $\eta = m_1 m_2/(m_1+m_2)^2$, $\varphi' = \varphi(t) - \Phi$, Θ and Φ are the spherical polar angles of the observer (i.e., the line of sight direction viewed in the source's frame), and a dot denotes the time derivative (i.e., $\dot{r} = dr/dt$, $\dot{\varphi} = d\varphi/dt$).

Hereafter, for simplicity, we set $\varphi(t=0) = 0$, $e(t=0) = e_0$, and start the waveform at the time when the binary is undergoing the pericenter passage ($\dot{r} = 0$, this choice fixes the initial pericenter direction in the binary's comoving frame). Note that the semi-major axis a is not well defined in the pN waveform. However, to better convey the astrophysical interpretation,

we define $r(t=0) = a_0(1-e_0)$ and parameterize the initial condition using the approximated "initial semi-major axis", a_0, in the Newtonian limit.

To better understand eccentric GW signals, we can also decompose the time-domain waveform of an eccentric binary into different harmonics (see, e.g., (Peters and Mathews, 1963; O'Leary et al., 2009b; Kocsis and Levin, 2012; Kocsis et al., 2012) for a detailed explanation),

$$h(t) \sim \sum_{n=1}^{\infty} h_n \exp\left(2\pi i f_n t\right). \tag{5.7}$$

where each harmonic is a sinusoidal signal with amplitude h_n and a frequency of $f_n = n f_{\rm orb}\,(n = 1, 2, 3\,...)$. This property is useful when deriving the detector's response to eccentric signals, which we will discuss subsequently. Furthermore, when GW sources evolve slowly (merger timescale $\tau \sim f_{\rm orb}/\dot{f}_{\rm orb} \gg T_{\rm obs}$), the orbital frequency $f_{\rm orb}$ almost keeps constant during observation. In this case, the harmonics in Equation (5.7) can be approximated as nearly monochromatic.

We note that there have been many works studying the analytic waveform models for eccentric binaries (see, e.g., Moore et al., 2018; Moore and Yunes, 2019a; Loutrel, 2020; Knee et al., 2022, for a review). However, we still lack sufficient validation of the pN waveform against numerical relativity for the extreme eccentricity case (e.g., $e > 0.999$). Despite this, the x-model can still give an accurate description of the highly eccentric waveform in the parameter space we consider in this paper. This argument is partly justified because we are focusing on the inspiral stage of stellar-mass binaries (i.e., the millihertz band for LISA detection) instead of the merger and ringdown stages in the LIGO band. For the systems that dominate the stellar-mass bursting source population in the local universe (Xuan et al., 2024a,b), their pericenter distance is typically larger than $a(1-e) \gtrsim 10^{-3}$au (or in other words $\sim 10^4$ Schwarzschild radii). Therefore, even if the eccentricity is extreme, the gravitational field at the closest approach is still much weaker than the strength of the field

for which the x-model has been validated against numerical relativity (21 cycles before the merger (Hinder et al., 2010)), and the expansion serves as a plausible description of the GW signal for the systems we discuss hereafter.

Furthermore, due to the orbit of LISA around the Sun, GW signals in the detector's output can have an annual modulation (see, e.g., Fig. 1 in Ref. (Xuan et al., 2024a)). Thus, we further include this effect by computing the LISA response function (Cornish and Rubbo, 2003) (Note that, in general, LISA's annual motion is expected to enhance the angular resolution of sources' sky location measurement (see, e.g., Cutler, 1998; Kocsis et al., 2007)):

$$\begin{aligned} s_1(t) = & F^{+}(t) A_{+} \cos\left(2\pi f\left[t + \hat{n}\cdot\mathbf{x}_1(t)\right]\right) \\ & + F^{\times}(t) A_{\times} \sin\left(2\pi f\left[t + \hat{n}\cdot\mathbf{x}_1(t)\right]\right) \ , \end{aligned} \tag{5.8}$$

where $s_1(t)$ represents one independent channel in the detector's output (Michelson response), $\hat{n}$ is the basis vector representing the sky location of the source, $\mathbf{x}_1(t)$ is the location of detector, $A_{+,\times}$ represents the strain amplitude for a monochromatic GW signal with frequency f, and $F^{+,\times}$ is the beam pattern factors:

$$\begin{aligned} F^{+}(t) &= \frac{1}{2}\left(\cos 2\psi D^{+}(t) - \sin 2\psi D^{\times}(t)\right) \\ F^{\times}(t) &= \frac{1}{2}\left(\sin 2\psi D^{+}(t) + \cos 2\psi D^{\times}(t)\right), \end{aligned} \tag{5.9}$$

in which ψ is the polarization angle of the GW signal (see Eq. 32 in (Cornish and Rubbo, 2003)), and $D_{+,\times}(t;\theta,\phi)$ depends on the spherical polar angles of the GW source in the sky, (θ, ϕ), as well as the detector's motion as a function of time (see Eqs. 54 -55 in Ref. (Cornish and Rubbo, 2003)). Note that the sky location angles (θ, ϕ) are different from the intrinsic propagation direction of GW radiation viewed in the GW source's frame (Θ, Φ), which we defined earlier in Equation (5.6).

We note that the output of LISA can be considered like a pair of two-arm detectors, with

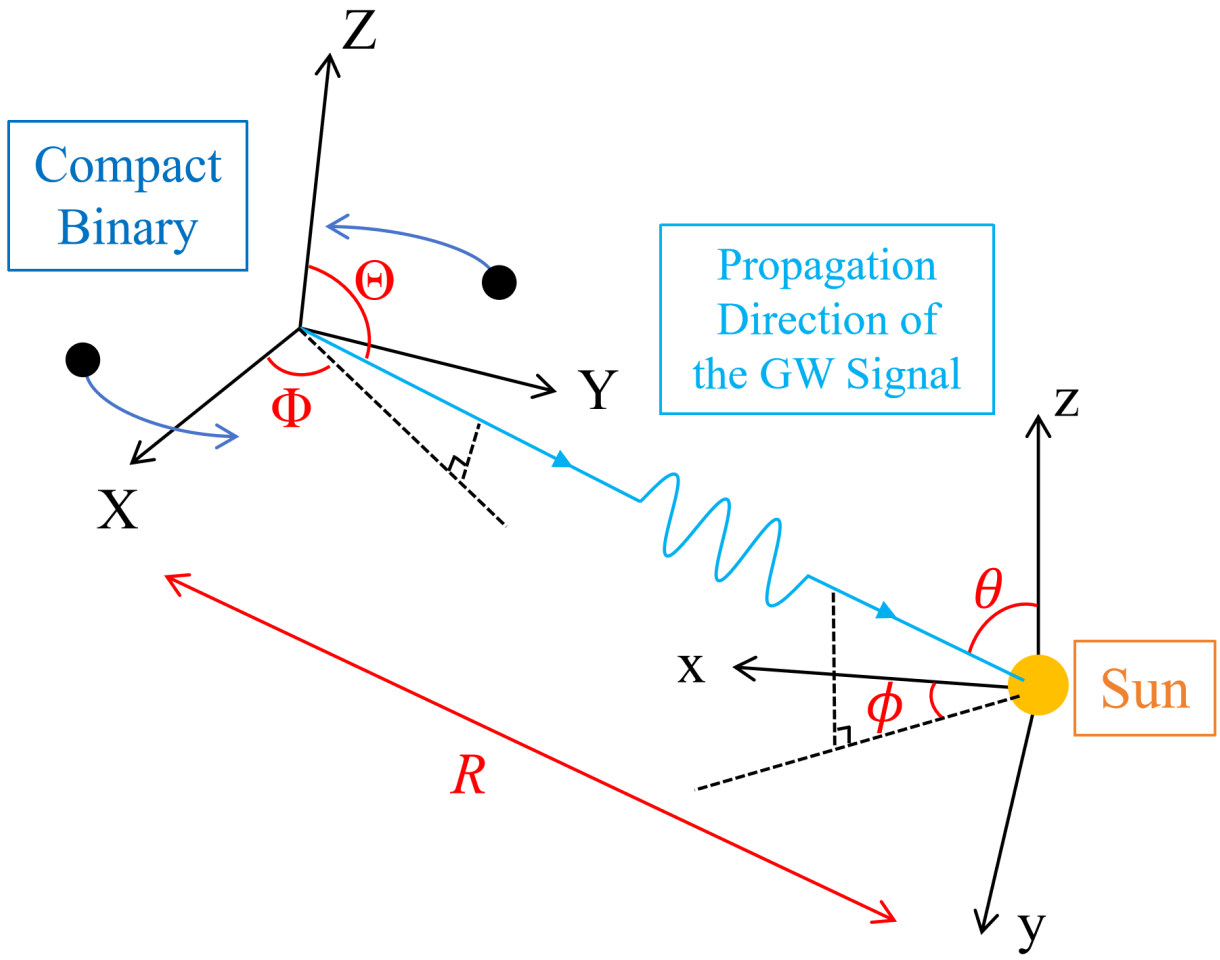


Figure 5.2: **The definition of $\Theta, \Phi, \theta, \phi$ and R (not to scale).** Here we show an example compact object binary, which is emitting GW signal and being detected by LISA, to illustrate the definition of angular parameters in Section 5.2.2. The coordinate system (X, Y, Z) is the non-rotating, comoving frame of the compact object binary, with the Z axis parallel to the orbital angular momentum vector and the X axis pointing in the direction of the (initial) pericenter. Θ, Φ represent the spherical polar angles of the source's orientation relative to the observer (i.e., the propagation direction of the GW signal viewed in the source's non-rotating, comoving frame). The coordinate system (x, y, z) is the comoving frame of the Sun, with θ, ϕ representing the sky location of the GW source. R is the distance between the compact binary system and the Sun.

two linearly independent signals (see, e.g., Sec.IIB2 in Ref. (Cutler, 1998) for more details). However, in this work, we only adopt the output of one channel, $s_1(t)$, for simplicity (see, e.g., Eq.46 in Ref. (Cornish and Rubbo, 2003)). This is due to the uncertainty of the realistic noise correlation between two channels and the complexity when considering multiple signals in data analysis. As a result, the detectability estimates presented here should be regarded as conservative, with the potential for improvement if the contributions from both channels are included in future studies.

In Figure 5.2, we present an illustration of $\Theta, \Phi, \theta, \phi$ and R definitions. In particular, Θ and Φ represent the propagation direction of the GW signal as viewed in the comoving frame of the compact object binary, with the binary's orbit lying in the $X-Y$ plane; θ and ϕ are the sky location of the GW source viewed in the comoving frame of the solar system, where the LISA detector undergoes annual motion around the sun. We note that the GW signal's polarization angle, ψ, is not explicitly shown in Figure 5.2, which contributes to one more degree of freedom. In the calculation, ψ can be worked out using $\psi = -\arctan(\hat{v}\cdot\mathbf{p}/\hat{u}\cdot\mathbf{p})$, where $\mathbf{p}$ is one of the principle polarization axes of GW beam, and $\hat{u}, \hat{v}$ represent two basis vectors in the (x, y, z) coordinate system (see Eq.3, 31, 32 in Ref. (Cornish and Rubbo, 2003)).

Additionally, since the annual motion of detectors around the Sun has a frequency of $f_{\rm detector} = 1\,yr^{-1}$, which is much lower than the frequency of GW signal in the millihertz band, we can take the adiabatic approximation. Under this approximation, the beam pattern factors, $F^{+,\times}$, remain nearly constant throughout each gravitational wave burst. Therefore, we can generalize Equation (5.8) to the eccentric case by summing over contributions from each near-monochromatic harmonic (note that, for harmonic frequencies f_n that predominantly contribute to the detection signal-to-noise ratio in the millihertz band, $F^{+,\times}$ can be treated as approximately constant and taken out of the summation (see e.g., O'Leary et al.,

2009a; Wang et al., 2021; Xuan et al., 2024a)):

$$\begin{aligned} s_1(t) &= F^{+}(t) \sum_{n=1}^{\infty} h_{n,+} \cos\left(2\pi f_n \left[t + \hat{n} \cdot \mathbf{x}_1(t)\right]\right) \\ &+ F^{\times}(t) \sum_{n=1}^{\infty} h_{n,\times} \sin\left(2\pi f_n \left[t + \hat{n} \cdot \mathbf{x}_1(t)\right]\right) \\ &= F^{+}(t) h_{+}(t') + F^{\times}(t) h_{\times}(t'), \end{aligned} \tag{5.10}$$

where $h_{n,+}, h_{n,\times}$ represent the amplitude of the n-th harmonic in the eccentric GW signal (see Equation (5.7)), $t' = t + \hat{n} \cdot \mathbf{x}_1(t)$ is the delayed arrival time of GW signals caused by the motion of the detector.

As can be seen from Equation (5.6) - (5.10), for a given antenna pattern of GW detector, the eccentric GW waveform in the detector's output can be parameterized using 10 parameters: the initial orbital parameters of the binary (a_0, e_0) (which enter the waveform via the initial condition), the total mass M, the symmetric mass ratio η (or equivalently, the mass ratio $q = m_1/m_2$), the line of sight (propagation) direction of GW radiation in the source's frame (Θ, Φ), the location of GW source on the sky (θ, ϕ), the distance of GW source R, and the polarization angle ψ.

Note that we set $\varphi(t = 0) = 0$ when introducing Equation (5.6); otherwise, there will be 11 parameters that affect the waveform, with the last one representing the initial orbital phase of the binary. Since this work focuses on the repeated burst sources, we assume that there is a significant number of bursts during observation. Thus, the initial phase of the first GW burst has little effect on the astrophysical interpretation, and we fix it for simplicity.

In the following sections, we will parameterize the GW templates using $\{f_{\rm orb,0}, 1 - e_0, M, q, \cos\Theta, \Phi, \cos\theta, \phi, R, \psi\}$. Note that hereafter we use $f_{\rm orb}$ as an abbreviation for the initial orbital frequency $f_{\rm orb,0}$, which is related to a_0 via $f_{\rm orb,0} = (2\pi)^{-1} M^{1/2} a_0^{-3/2}$.

5.3 Source Identification and Parameter Extraction

5.3.1 Fisher Matrix Analysis

To evaluate the astrophysical information that can be extracted from highly eccentric GW sources, we adopt the Fisher matrix analysis (Coe, 2009; Cutler and Flanagan, 1994). This method is commonly used as a linearized estimation for the parameter measurement error in the high SNR limit.

We start by defining the noise-weighted inner product between two gravitational waveforms, $h_1(t)$ and $h_2(t)$:

$$\langle h_1 \mid h_2 \rangle = 2 \int_0^\infty \frac{\tilde{h}_1(f)\tilde{h}_2^*(f) + \tilde{h}_1^*(f)\tilde{h}_2(f)}{S_{\rm n}(f)} {\rm d}f \ , \tag{5.11}$$

in which $\tilde{h}_l$ (with $l = 1, 2$) means a Fourier transform of the waveform, and the star indicates the complex conjugate.

Representing the parameters of a GW source as a vector $\boldsymbol{\lambda}$, the GW waveform h can be expressed as $h(t; \boldsymbol{\lambda})$. The Fisher matrix is defined as:

$$F_{ij} = \left\langle \frac{\partial h(\boldsymbol{\lambda})}{\partial \lambda_i} \middle| \frac{\partial h(\boldsymbol{\lambda})}{\partial \lambda_j} \right\rangle . \tag{5.12}$$

in which λ_i denotes the i-th parameter of the waveform.

We define C as the inverse of the Fisher matrix, $C = F^{-1}$. It approximates the sample covariance matrix of the Bayesian posterior distribution for the GW source's parameters. In other words, we can use the following equation to estimate the error of parameter measurement:

$$\Delta\lambda_i = \sqrt{\left\langle (\delta\lambda_i)^2 \right\rangle} = \sqrt{C_{ii}} \ . \tag{5.13}$$

As shown in Equations (7.20)–(6.8), the Fisher matrix is computed using the first-order derivatives of the waveform, without including higher-order corrections or Bayesian parameter estimation (see, e.g., Christensen and Meyer, 1998; Christensen et al., 2004). This makes the Fisher matrix a fast and accessible tool in GW data analysis. However, as mentioned earlier in the Introduction, recent studies have shown that the Fisher matrix can give inaccurate results in certain regions of the parameter space when compared with full Bayesian parameter estimation (see, e.g., the comparison in Ref. (Toubiana et al., 2020), for testing General Relativity using stellar mass BBHs). Thus, we remind the reader that the results presented in this work are a preliminary estimate of the parameter measurement accuracy for bursting stellar mass BBHs. These estimates highlight the astrophysical potential of detecting bursting GW sources from LISA's data stream. A full Bayesian analysis is left for future work.

5.3.1.1 Numerical Verification

After getting Equations (7.20) - (6.8), we further combine them with the waveform model introduced in Section 5.2.2 and estimate the parameter measurement error via numerical calculation.

In particular, first, we generate the waveform template using the x-model (see Section 5.2.2) and parameterize the waveform as $h(t) = h(t; \boldsymbol{\lambda} = \{f_{\rm orb}, 1-e_0, M, q, \cos\Theta, \Phi, \cos\theta, \phi, R, \psi\})$ (note that the detector's response function has been included in this step).

Second, we compute the partial derivative of the waveform relative to each parameter (see Equation (6.7)). For example, to get $\partial h/\partial M$, we vary the parameter $M \to M' = M + dM$, then generate a new waveform $h'(t) = h'(t; \boldsymbol{\lambda}' = \{f_{\rm orb}, 1-e_0, M+dM, q, \cos\Theta, \Phi, \cos\theta, \phi, R, \psi\})$. The partial derivative is obtained by computing the difference between h' and h, then divided by dM.

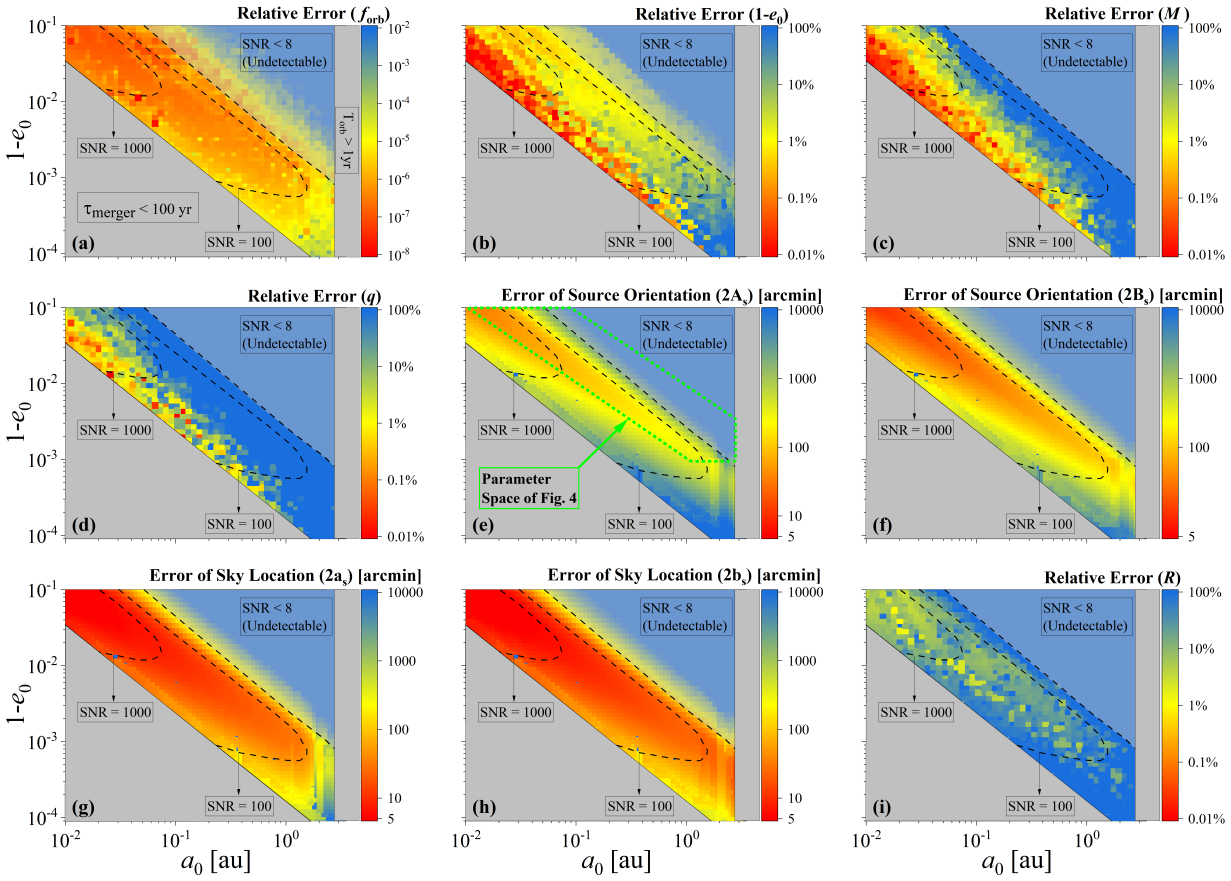


Figure 5.3: **The dependence of a compact binary's parameter measurement error on its semi-major axis and eccentricity, computed using the Fisher matrix analysis (for 1-yr observation).** Here we show a BBH system with $m_1 = 15\ \mathrm{M}_\odot$, $m_2 = 10\ \mathrm{M}_\odot$, (i.e., $M = 25\ \mathrm{M}_\odot$, $q = 3/2$), placed at $R = 8$ kpc and observed for 1 yr with LISA. In this example, we set $\Phi = \Theta = \theta = \phi = \pi/4$ for simplicity and map the compact binary's relative parameter measurement error as a function of its initial semi-major axis a_0 and eccentricity $1 - e_0$ (see different colors in the figure). In each panel, the dashed lines represent equal signal-to-noise ratio contours (analytically calculated using Eq. 17 in Ref. (Xuan et al., 2024a)), with SNR = 8, 100, 1000 from right to left. We exclude the parameter space where the binary has an orbital period $T_{\rm orb} > 1\,$yr (since their GW signal is not repeated bursts during the observation), or has a short merger timescale $\tau_{\rm merger} < 100\,$yr (since these short-living systems may have negligible number expectation in future detection). We note that the Fisher matrix analysis is computed for ten parameters $(f_{\rm orb}, 1-e_0, M, q, \cos\Theta, \Phi, \cos\theta, \phi, R, \psi)$, while here we only show nine of them. This is because the last parameter ψ, which represents the polarization angle of the GW beam relative to the observer, is less relevant to the astrophysical inference, and we put its estimation in the appendix to avoid clutter. Also, we convert the measurement accuracy of the source orientation, $\{\cos\Theta, \Phi\}$, and sky location, $\{\cos\theta, \phi\}$, into the major and minor axes of the sky error ellipsoids, $\{2A_s, 2B_s\}$, $\{2a_s, 2b_s\}$, respectively. See Appendix 5.7.3 for more details. Additionally, the green dotted lines in panel (e) of Figure 5.3 mark the parameter space that is later presented in Figure 5.4, for comparison.

We note that each partial derivative is a time series which represents the difference in the waveform caused by varying one of the parameters slightly around the central value. Thus, after getting all the partial derivative waveforms, we can adopt Equations (7.20) and (6.7) to compute their inner products, get the Fisher matrix, then take the inverse of the matrix to estimate the parameter measurement error (see Equation (6.8)).

In this work, the parameter set, $\{f_{\rm orb}, 1-e_0, M, q, \cos\Theta, \Phi, \cos\theta, \phi, R, \psi\}$, are intentionally chosen to avoid intrinsic degeneracies in the waveform model. However, since the aforementioned steps involve first-order-finite-difference derivatives and the numerical inversion of the Fisher matrix, they can still result in ill-conditioned outputs if not handled carefully (see, e.g., Sections IV and V in Ref. (Vallisneri, 2008)). To ensure numerical stability, we choose the parameter variation $d\lambda_i$ such that $\langle dh|\ dh\rangle \sim 10^{-3}\langle h|\ h\rangle$. This choice keeps the change in the waveform small when computing the numerical derivative, maintaining the accuracy of the Fisher matrix analysis. Furthermore, we rescale the unit of source parameters to improve the condition number and reduce the magnitude gap between the largest- and smallest-modulus eigenvalues. When computing the Fisher matrix for a given point, we design the code to automatically try and adjust the aforementioned properties (i.e., the finite variation in numerical derivative and the rescaling of parameters), to keep the resultant Fisher matrix non-singular.

In Figure 5.3, we show the Fisher matrix analysis results for the GW signal from a BBH system with $m_1 = 15\,{\rm M}_\odot$, $m_2 = 10\,{\rm M}_\odot$, placed at $R = 8$kpc, with the position of $\Phi = \Theta = \theta = \phi = \pi/4$, and observed for $T_{\rm obs} = 1\,{\rm yr}$. In particular, we generate different initial conditions of the system by changing a_0 and e_0. For each configuration, we compute the partial derivative of the waveform relative to the aforementioned 10 parameters $(f_{\rm orb}, 1-e_0, M, q, \cos\Theta, \Phi, \cos\theta, \phi, R, \psi)$, estimate their Fisher matrix, and get the measurement error. We plot the relative error of each parameter in different colors and map the result as a function of $(a_0, 1-e_0)$. To better compare with observation, we convert the measurement

accuracy of the source orientation, $\{\cos\Theta, \Phi\}$, and sky location, $\{\cos\theta, \phi\}$, into the major and minor axes of the sky error ellipsoids, $\{2A_s, 2B_s\}$, $\{2a_s, 2b_s\}$, respectively. See Appendix 5.7.3 for more details.

Note that this system serves as a representative example of the parameter measurement accuracy (see, e.g., the characteristic parameters of bursting BBHs in the population analysis of Ref. (Xuan et al., 2024a)). In realistic observations, however, the GW sources can have different orientations and sky locations, which can potentially affect the parameter measurement error (note that it is also straightforward to analyze other systems with different values of $(\Phi, \Theta, \theta, \phi)$). We emphasize that there have been previous works estimating the change in parameter measurement errors as a function of different initial conditions of the system (see, e.g., studies on supermassive black hole binaries (Kocsis et al., 2007; Kocsis et al., 2008; Mikóczi et al., 2012a)). In our case, the width of the distribution of parameter estimation errors could be significantly narrower, as the bursting BBHs are observed well before their merger, with slower orbital evolution. This provides a more stable signal, which allows for more precise parameter extraction. Furthermore, this work focuses on the stellar mass bursting BBHs in the local universe, but a similar approach may be applied to other cases, such as the parameter estimation of highly eccentric extreme mass-ratio inspirals (EMRIs) at a cosmological distance (see, e.g., Barack and Cutler, 2004b; Rubbo et al., 2006; Yunes et al., 2008; Berry and Gair, 2013; Han et al., 2020; Oliver et al., 2023; Fan et al., 2022; Naoz and Haiman, 2023).

Furthermore, Figure 5.3 covers the parameter space where bursting stellar-mass BBHs are most likely to be detected in the Milky Way with future millihertz GW detectors (Xuan et al., 2024a,b). In particular, as discussed in Section 5.1, many dynamical channels can generate wide, highly eccentric BBH systems. During the evolution, if these systems enter the parameter space with an orbital period smaller than the observation time (i.e., to the left of the grey-colored region with $T_{\rm orb} > 1\,{\rm yr}$), and a signal-to-noise ratio larger than the

detection threshold (i.e., below the dashed line of SNR = 8), their GW signal will be identified as “repeated bursts", and can be used for parameter extraction. Additionally, we calculate the Fisher matrix only for systems with $\tau_{\rm merger} > 100\,{\rm yr}$ (to the top right of the grey-colored triangle). This is because the sources to the top right of each panel will have a longer merger timescale compared with those on the bottom left (see, e.g., Fig.4 in Ref. (Xuan et al., 2024a)), thus are more likely to be detected due to their extended detectable time in mHz band (note that this also indicates the relative error estimation of sources with moderate SNR is more representative of the accuracy we will get in future observation of stellar-mass bursting sources, since they have the longest lifetime and largest number expectation among all the detectable systems). On the other hand, the expected number of short-living systems with $\tau_{\rm merger} < 100\,{\rm yr}$ is negligible (see, e.g., Section 3.2 in Ref. (Xuan et al., 2024a)), and the computational expense of their Fisher matrix is large, so we decide not to include them in this example.

Additionally, to provide an optimistic estimation of the measurement accuracy, we extend the observation time to 5 years and repeat the analysis from Section 5.3.1.1. For our analysis, we focus on the parameter space highlighted by the green dotted line in panel (e) in Figure 5.3. The results are summarized in Figure 5.4, where we consider the same systems as in Figure 5.3, but parameterized the x-axis using the pericenter distance of the binary system, $r_p = a_0(1 - e_0)$. As shown in Figure 5.4, this choice of x-axis (r_p), along with a zoomed-in view of the parameter space, highlights the region where a bursting BBH system has a signal-to-noise ratio of SNR $\sim 8 - 1000$, and provides more detailed estimation results.

We emphasize that, Figures 5.3 and 5.4 show the parameter measurement accuracy for bursting sources in the Milky Way (at a representative distance of 8 kpc). However, these results can be generalized to bursting sources in the local universe, provided the redshift is negligible. In particular, if a compact binary is located at a distance R different from 8 kpc, the overall amplitude of its GW signal will scale inversely with the distance ($h \sim R^{-1}$,

see Equation (5.6)). Furthermore, because the Fisher matrix elements are proportional to the square of the waveform amplitude ($F_{ij} \sim h^2 \sim R^{-2}$, see Equation (6.7)), the parameter measurement error, $\Delta\lambda_i$, after inverting the Fisher matrix and taking the square root, should scale proportionally to the distance ($\Delta\lambda_i \sim C_{ii}^{\frac{1}{2}} \sim R$, see Equation (6.8)). In other words, the results of Figures 5.3 and 5.4 can be rescaled using the following relation:

$$\Delta\lambda_i'(R) \sim \Delta\lambda_i(8\,\mathrm{kpc}) \left(\frac{R}{8\,\mathrm{kpc}}\right) , \tag{5.14}$$

where $\Delta\lambda_i'(R)$ represents the parameter measurement error for highly eccentric systems at a distance R, and $\Delta\lambda_i(8\ \mathrm{kpc})$ refers to the Fisher matrix analysis result (absolute error) for systems at 8 kpc, which can be estimated using Figures 5.3 and 5.4.

5.3.1.2 Astrophysical Interpretation

In this section, we will discuss the astrophysical interpretation of each panel (system's parameter) in Figures 5.3 and 5.4. First, as shown in panel (a) of these two figures, the relative error ($\Delta f_{\mathrm{orb}}/f_{\mathrm{orb}}$) of orbital frequency, f_{orb}, is smaller than $\sim 10^{-6}$ for most of the detectable cases. In other words, considering the value of f_{orb} for a $10-15\mathrm{M}_\odot$ BBH system with semi-major axis $a \sim 10^{-2} - 1\mathrm{au}$, the absolute error of orbital frequency measurement is roughly $\Delta f_{\mathrm{orb}} \sim 10^{-12} - 10^{-10}\,\mathrm{Hz}$ in the parameter space we consider.

Such high accuracy can be understood analytically. For example, the measurement accuracy depends on the waveform's sensitivity to changes in f_{orb}. Therefore, we can vary f_{orb} by df_{orb}, then identify the value of df_{orb} at which the new waveform significantly differs from the original one. Thus, this critical value is used to estimate the measurement accuracy, $df_{\mathrm{orb}} \sim \Delta f_{\mathrm{orb}}$. The concept here is similar to the Fisher matrix analysis (see Equations (6.7) and (6.8). Note that F_{ij} in the Fisher matrix analysis is, in general, estimating the waveform's sensitivity to the changes of parameters.).

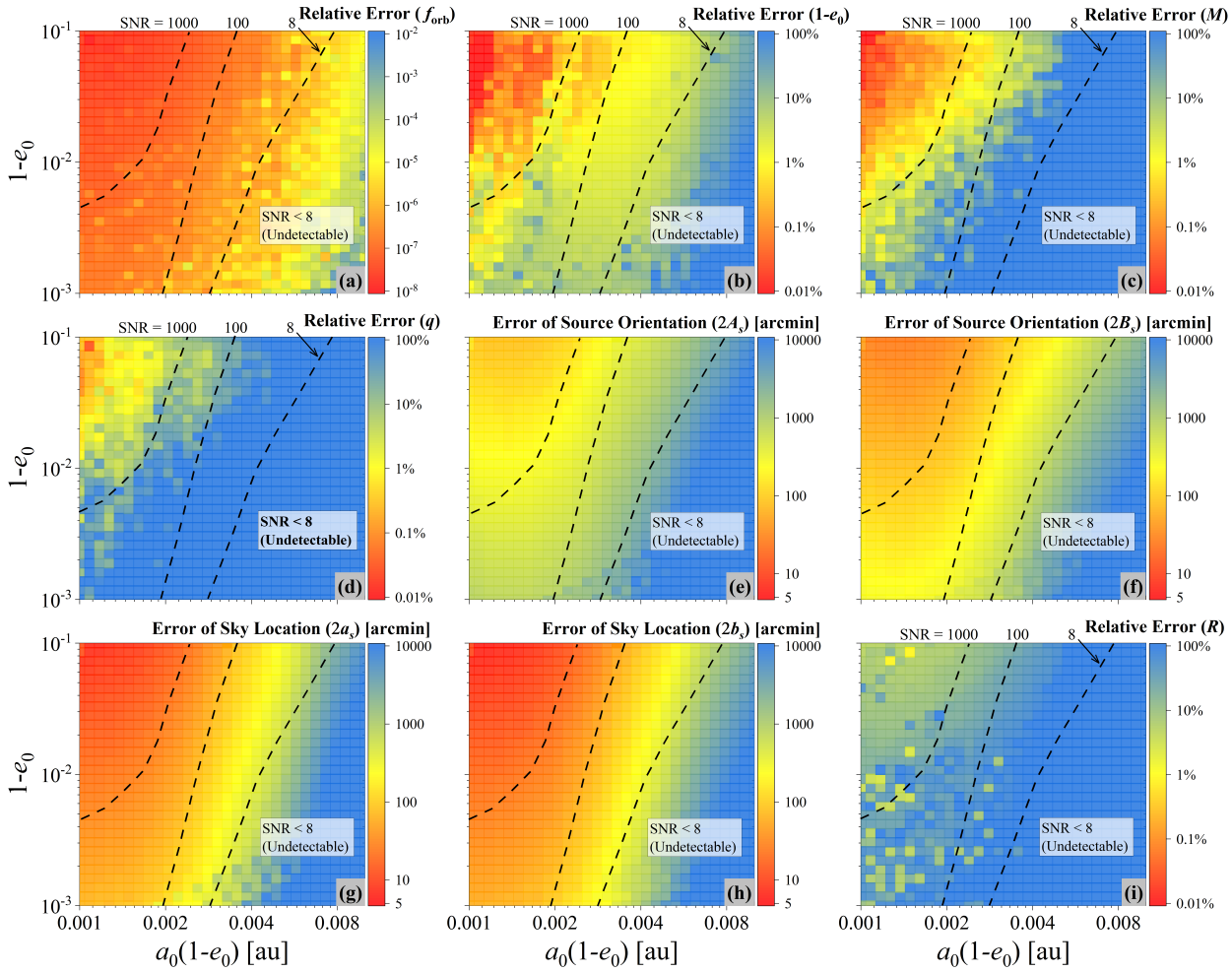


Figure 5.4: **The dependence of a compact binary's parameter measurement error on its initial pericenter distance, $r_p = a_0(1-e_0)$, and eccentricity e_0 (for 5-yr observation).** Here, we consider the same systems as in Figure 5.3, but re-parameterize the x-axis using $r_p = a_0(1-e_0)$ and zoom in to highlight the parameter space where we expect to detect most of the stellar mass bursting BBHs (Xuan et al., 2024a,b), i.e., SNR $\sim 8-1000$. Additionally, we changed the observation time from 1 year to 5 years to show an optimistic estimation of measurement accuracy (for the 1-year case, see Figure 5.7 in Appendix), and mark the parameter space of this figure with green dotted lines in panel (e) of Figure 5.3 for comparison purposes.

Following the aforementioned method, we consider two GW waveforms with slightly different orbital frequencies, i.e., $h_1(t; f_{\rm orb})$ and $h_2(t; f'_{\rm orb} = f_{\rm orb} + df_{\rm orb})$. Specifically, for a highly eccentric binary, the GW waveform can be approximated by a series of bursts, separated by $T_{\rm orb}$ in time. Because of the difference in orbital frequency, h_2 will have a different period of GW burst compared to h_1, which can be described using $dT_{\rm orb} = d(1/f_{\rm orb}) \sim df_{\rm orb}/f^2_{\rm orb}$ (note that we assume $f_{\rm orb}$ and $f'_{\rm orb}$ are constants during the observation, i.e., the sources chirp slowly). Therefore, the position of each GW burst in h_2 will shift in time relative to the bursts in h_1. During an observation time of $T_{\rm obs}$, the accumulated difference (i.e., position shift of the arrival time for the last GW burst of h_2, compared with h_1) can be estimated by:

$$dt_{\rm last\,burst} \sim N \cdot dT_{\rm orb} = T_{\rm obs} f_{\rm orb} \cdot \frac{df_{\rm orb}}{f^2_{\rm orb}}, \tag{5.15}$$

where N represents the number of bursts detected during the observation.

In realistic observation, two different GW waveforms can be distinguished when their match is below a given threshold (see, e.g., Eq. 28 in Ref. (Xuan et al., 2021)). For our cases, however, we simplify the condition and assume that h_1 is distinguishable from h_2 when the position shift of the last GW burst, $dt_{\rm lastburst}$, is greater than the width of that GW burst, $T_{\rm burst}$.

$$dt_{\rm lastburst} > T_{\rm burst}. \tag{5.16}$$

This estimation is partly justified because the time domain overlap between two waveforms, $\int h_1(t)h_2(t)dt$, will drop to $\lesssim 1/2$ of the fully matched value when Equation (5.16) is satisfied, which significantly reduces the match between h_1, h_2 and potentially makes them distinguishable in data analysis.

In Equation (5.16), the width of a GW burst, $T_{\rm burst}$, can be estimated using the binary's

pericenter passage time, T_p, (see, e.g., O'Leary et al., 2009a):

$$T_{\rm burst} \sim T_{\rm p} \sim (1-e)^{3/2} T_{\rm orb} \ . \tag{5.17}$$

Thus, we can plug in Equations (5.15) and (5.17) into Equation (5.16), and get a heuristic estimation of the measurement accuracy in orbital frequency, $\Delta f_{\rm orb}$:

$$\Delta f_{\rm orb} \sim df_{\rm orb} = \frac{f_{\rm orb}}{T_{\rm obs}} dt_{\rm lastburst} > \frac{f_{\rm orb}}{T_{\rm obs}} T_{\rm burst} \sim \frac{(1-e)^{\frac{3}{2}}}{T_{\rm obs}} \ . \tag{5.18}$$

In other words, our waveform analysis will be sensitive to any change in $f_{\rm orb}$ greater than $\sim (1-e)^{\frac{3}{2}}/T_{\rm obs}$. For a 1-yr observation of a BBH system with $(1-e) \sim 10^{-3} - 10^{-1}$, Equation (5.18) yields $\Delta f_{\rm orb} \sim 10^{-12} - 10^{-9}$Hz, which is consistent with the numerical result we discussed at the beginning of this section (see, e.g., Figure 5.9 in Appendix for more details).

We note that Equation (5.18) only serves as a heuristic estimation of $\Delta f_{\rm orb}$. It neglects the GW source's orbital frequency shift during observation, which limits the application of this formula in the high SNR region, where the binary quickly loses energy and shrinks. However, for the majority of stellar-mass binaries we consider in this work, especially those close to the dashed line of SNR = 8 in Figure 5.3, the GW merger timescale is typically much longer than the observation time (see, e.g., Fig.4 in Ref. (Xuan et al., 2024a)). In this cases, Equation (5.18) yields a quick analytical estimation of $f_{\rm orb}$ measurement error, and can help with determining the grid size of matched filtering, which we will introduce soon in the next section.

Second, the eccentricity measurement accuracy reaches $\Delta(1-e_0)/(1-e_0) \sim 1\%$ for most detectable cases (see panel (b) of Figure 5.3), allowing for precise constraints on the binary's dynamical origin (note that different dynamical channels may yield different characteristic eccentricities in the same frequency band, see, e.g., Fig.4 of Ref. (Martinez et al., 2020)).

Moreover, for 5-year integration, the accuracy may reach below 0.1% for a significant part of the parameter space, as depicted in Figure 5.4. This accuracy highlights the dominant role of eccentricity in shaping the overall form of the bursting GW waveform, as the term $1-e$ is directly related to the width of each GW burst we observe (see Equation (5.17)), and the waveform fitting is thus very sensitive to eccentricity.

Third, as illustrated in panels (c) and (d) of Figure 5.3, mHz GW detection may be less sensitive to the total mass M and mass ratio q of a bursting binary system. For example, during a 1-year observation, we can only constrain the total mass of bursting stellar mass BBHs ($\Delta M/M < 10\%$) when their SNR exceeds ~ 100. Moreover, for determining mass ratio q, the bursting sources need to have SNR greater than ~ 1000. This result is consistent with our analysis in Section 5.2.1. In particular, bursting sources have small radiation power compared to moderately eccentric sources in the same frequency band. Therefore, their orbital evolution is slow, and frequency shift rate $df_{\rm orb}/dt$ is hard to measure, which limits the accuracy of mass measurement (see, e.g., Cutler and Flanagan, 1994).

However, the measurement accuracy for M and q can significantly improve with extended observation time. For example, as shown in panel (c) of Figures 5.4 and 5.7 (in appendix), when increasing observation time from 1 year to 5 years, the total mass measurement accuracy is enhanced by a factor of ~ 10, which allows us to measure the mass of bursting binary system in many of the detectable cases (with moderate SNR). In other words, for the first ~ 1 year of LISA observation, we may not get a good constraint on the mass of stellar-mass bursting sources with SNR $\lesssim 100$, but most of them will have a mass measurement by the end of 5-year LISA mission (except for some marginal detectable cases with SNR ~ 8 for 5 years), which enables us to distinguish between different bursting sources, such as highly eccentric BBHs, binary neutron stars (BNSs), and double white dwarfs (DWDs).

Furthermore, as shown in panels (e) - (h) of Figures 5.3 and 5.4, the orientation (as the axes of error ellipsoid, $\{2A_s, 2B_s\}$, (Lang and Hughes, 2006; Kocsis et al., 2008; Kocsis et al., 2007;

Mikóczi et al., 2012a)) of bursting binary systems can only be constrained to an accuracy of $\sim 100 - 1000$ arc minutes when SNR exceeds ~ 100 (similar for 1-year or longer integration times). However, our analysis suggests that the detection will be more sensitive to the sky location of the sources. In particular, for a 5-year observation, the resulting sky error ellipsoids exhibit comparable angular sizes for a_s and b_s, typically ranging from $\sim 5 - 500$ arc minutes, depending on the SNR. This sky localization can enable the identification of specific host environments of GW sources in the Milky Way, such as globular clusters, the Galactic center, and the Galactic field, which potentially helps us to disentangle different formation channels of BBHs.

As shown in panel (i) of Figures 5.3 and 5.4, the distance of a bursting binary system is only marginally constrained in many detectable cases. For example, during a 1-year observation, $\Delta R/R$ reaches $\sim 10\%$ only when SNR exceeds ~ 100. This accuracy improves when we extend the observation time to 5 years, but the relative error of R still remains $\gtrsim 10\%$ for most of the systems with $8 < \mathrm{SNR} < 100$. Such low accuracy of distance measurement is also caused by the slow orbital evolution of the bursting binary system (see e.g., a similar discussion in the explanation of panels (c) and (d)). In particular, for bursting sources at low redshift, R only affects the overall amplitude of the GW signal (see the term $M\eta/R$ in Equation (5.6)). Therefore, if the GW source undergoes slow orbital evolution, the effect of R will degenerate with other mass parameters (such as the total mass M), thus adding to the difficulty of parameter extraction. However, we may still get a heuristic estimation of the binary's formation environment using the distance measurement, since an accuracy of $\sim 10\%$ is good enough to infer the binary's location in the local universe. Furthermore, with the potential for electromagnetic counterparts (e.g., if the source resides in a known stellar population like a globular cluster or contains a directly observable white dwarf), we may be able to disentangle the distance from other orbital parameters, thereby improving constraints on the location of the bursting sources.

We note that, in Figures 5.3 and 5.4, there are some data points with a relative error estimation inconsistent with the general distribution in the surrounding region (see, e.g., some of the bright-yellow points, to the bottom-left in panel (e) of Figure 5.4). Such fluctuation is caused by numerical error and degeneracy in the waveform model. In particular, for some bursting binary systems, only a few to a few dozen GW bursts will be detected during an observation time of $\sim 1-5$ years, which limits the numerical accuracy in the frequency domain inner product of waveforms. Furthermore, among all the 10 parameters we discuss (see Section 5.2.2), many of them will have a similar effect on the overall shape of the GW signal (e.g., the aforementioned degeneracy between distance R and total mass M). Therefore, with a certain combination of parameter values, the Fisher matrix may become singular in the numerical analysis, which leads to inconsistent relative error estimation.

Additionally, we emphasize that, it is possible to analytically estimate the parameter measurement error, especially in the cases when the GW waveform model is simple (see, e.g., Eqs. 27 - 29 in Ref. (Seto, 2002a)). In our cases, however, the complexity of the bursting system's parameters makes it hard to simplify the cross-terms in the Fisher matrix via an analytical approach. Therefore, although we tried to develop an analytical estimation, the outcome did not yield a well-performed constraint on the measurement accuracy, as shown in the Appendix 5.7.2. However, for the parameters that play a dominant role in the overall shape of bursting GW signal, such as the orbital frequency $f_{\rm orb}$, the analytical method can still be accurate even if we make many approximations (see Equation (5.18)). Therefore, it can yield an efficient estimation with no need to compute the numerical GW waveform.

5.3.2 Matched Filtering

In Section 5.3.1, we discussed the parameter measurement accuracy of highly eccentric GW sources. However, to get such astrophysical information in realistic observation, we need

to identify the bursting GW signals and extract them from the data stream. Therefore, in this section, we will briefly introduce the technique of matched filtering, which is commonly adopted in GW data analysis to detect signals from astrophysical sources (see, e.g., Cutler and Flanagan, 1994; Allen et al., 2012; Petigura et al., 2013; Abbott, 2021, 2023, for more details).

In particular, the measured strain amplitude in the detector's output can be described using $s(t) = h(t) + n(t)$, with the (possibly present) signal $h(t)$, and the detector noise $n(t)$. To extract the targeted GW signal, we first generate the GW waveform template based on our understanding of astrophysical sources, $h_{\rm template}(t)$, then convolve $s(t)$ with $h_{\rm template}(t)$ in the frequency domain (see, e.g., Eq.4.1 in Allen et al., 2012):

$$x\left(t_0\right) = 2\int_{-\infty}^{\infty} \frac{\tilde{s}(f)\tilde{h}^{*}_{\rm template}\left(f\right)}{S_n(f)} df, \tag{5.19}$$

in which $\tilde{s}(f)$ and $\tilde{h}_{\rm template}(f)$ are the Fourier transform of $s(t)$ and $h_{\rm template}(t)$, and the star stands for the complex conjugate. We note that, for GW mergers, the parameter t_0 represents the termination time (the time at the detector at which the coalescence occurs). Furthermore, we can change the termination time of the template $h_{\rm template}(t)$ and find the value of t_0 when the norm of $x(t_0)$ is maximized, i.e., $|x(t_0)|_{\rm max} = |x_m|$. Thus, this t_0 represents the correct (or the most likely) location of the GW signal in the detector's output. In our cases, the bursting binary may not merge for the entire observation. However, we can still use t_0 (with a modified definition) to describe the position shift of $h_{\rm template}(t)$ in the time domain. Hereafter, we define t_0 as the time at which the first GW burst of $h_{\rm template}(t)$ occurs.

As shown in Equation (5.19), for a given template $h_{\rm template}$, we can find the maximum norm of the convolution result, $|x_m|$. This quantity, with a proper normalization constant σ_m (see, e.g., Eq. 4.3 in Ref. (Allen et al., 2012)), represents the optimized signal-to-noise ratio for

the template we use in the search,

$$\mathrm{SNR_m} = \frac{|\mathrm{x_m}|}{\sigma_\mathrm{m}} \,, \tag{5.20}$$

note that the amplitude of $h_{\mathrm{template}}(t)$ will cancel in the computation of $\mathrm{SNR_m} = |\mathrm{x_m}|/\sigma_\mathrm{m}$, thus we can place the GW source at an arbitrary distance R when constructing the template. In realistic detection, if this signal-to-noise ratio $\mathrm{SNR_m}$ exceeds a certain threshold, we will identify the corresponding template $h_{\mathrm{template}}(t)$ as existing in the detector's output $s(t)$. In other words, we successfully identify the GW source and measure its parameters using the parameters of h_{template}.

In Section 5.4, we use the aforementioned method to conduct matched filtering and test the detectability of bursting sources in an example mock LISA observation. Additionally, in this work, we use the software package PyCBC for the numerical realization (Nitz et al., 2024), and acknowledge the supporting materials provided by the Gravitational Wave Open Science Center of the LIGO Scientific Collaboration, the Virgo Collaboration, and KAGRA (Li et al., 2023; Abbott, 2021, 2023).

5.4 An Example of Mock Data Analysis

5.4.1 The Difference Between a Bursting and Non-Bursting Data Analysis

As shown in Section 5.3, highly eccentric compact binaries can provide us with valuable information about their orbital parameters and formation environment. However, since their GW signals are made up of transient bursts in the time domain, the frequency power spectrum of bursting GW waveform will thus have many ($\sim 10^3 - 10^6$) harmonics that

contribute significantly to the total signal-to-noise ratio (see, e.g., Kocsis and Levin, 2012; Xuan et al., 2024a). Such a large number of harmonics distributes the energy of the GW signal in a wide range of frequencies, thus potentially adding to the difficulty of realistic data analysis. In particular, many existing data analysis methods, such as matched filtering, rely on accurate template fitting in the frequency domain; however, the bursting waveform could have many of the harmonics out of the sensitive frequency band of LISA. Furthermore, since there could be a large population of bursting sources, their collective GW signal may form a confusion background, with many GW harmonics from various sources overlapping with each other (Xuan et al., 2024a).

Therefore, in this section, we will explore whether these bursting binaries could be efficiently distinguished when multiple sources and instrumental noises are present simultaneously in the detector's output. Specifically, we carry out mock LISA observation, generating a population of wide, highly eccentric BBHs based on our previous studies of the Galactic center (Xuan et al., 2024a). We then compute the collective GW signal from these bursting BBHs, combine the signal with the detector's instrumental noise and astrophysical foreground caused by unresolved Galactic binaries (Cornish and Robson, 2017; Robson et al., 2019b), and apply the matched filtering as described in Section 5.3.2 to extract the information of the bursting BBHs.

5.4.2 Population Model and Waveform Generation

As a proof of concept, we consider the bursting BBHs formed in the Galactic Center as a representative example for the mock observation. In particular, the Milky Way's Galactic nucleus offers a promising environment for the formation of wide, highly eccentric BBHs (see, e.g., Kocsis and Levin, 2012; Hoang et al., 2018, 2019; Stephan et al., 2019; Wang et al., 2021; Rose et al., 2023; Arca Sedda et al., 2023; Zhang and Chen, 2024a). For example, the orbital

eccentricity of BBHs can be excited by the supermassive black hole in the galactic nucleus because of the Eccentric Kozai-Lidov mechanism (Kozai, 1962; Lidov, 1962; Naoz, 2016), resulting in the bursting signatures on their GW signal. In our previous works (Hoang et al., 2018; Xuan et al., 2024a,b), we have carried out detailed simulations of the aforementioned systems, including the secular equations (for the hierarchical triple system) up to the octupole level of approximation (Naoz et al., 2013a), general relativity precession (e.g., Naoz et al., 2013b), and GW emission (Peters, 1964; Zwick et al., 2020). Thus, here, we adopt the result of the simulation presented in Ref. (Xuan et al., 2024a) for the bursting BBH population in the mock LISA data.

Figure 8.3 illustrates the intrinsic parameters of BBHs we get from the simulation mentioned above, with each black dot representing the orbital parameter $(a, 1-e)$ of a binary system. As shown in the Figure, there could be ~ 50 highly eccentric BBHs simultaneously in the nuclear star cluster at the Milky Way Galactic center (note that there are many BBHs with moderate eccentricity as well, which are not shown in Figure 8.3). Furthermore, in this sample, we find 4 BBHs with the expected signal-to-noise ratio exceeding the detection threshold (i.e., analytical SNR > 8 for a 4-year observation, estimated using Equation (5.4)). These systems, if properly identified, will become detectable GW sources. The mass of these BBH systems is determined using the stellar evolution model in Appendix A.3 of Ref (Xuan et al., 2024a), with most of the black holes having a mass ~ 10 $M_\odot$. Additionally, the BBHs' orientation is generated randomly following an isotropic distribution, and we set their distance to the detector as $R = 8$ kpc.

Based on the aforementioned population model, we generate the time domain GW signal for each BBH system and compute the detector's response correspondingly (see Equations (5.6) - (5.10)). We then calculate the mock LISA data by combining all the BBHs' signals and adding the detector noise. For simplicity, we assume stationary Gaussian noise, and adopt the LISA noise spectrum from Ref. (Robson et al., 2019b), which includes the instrumental

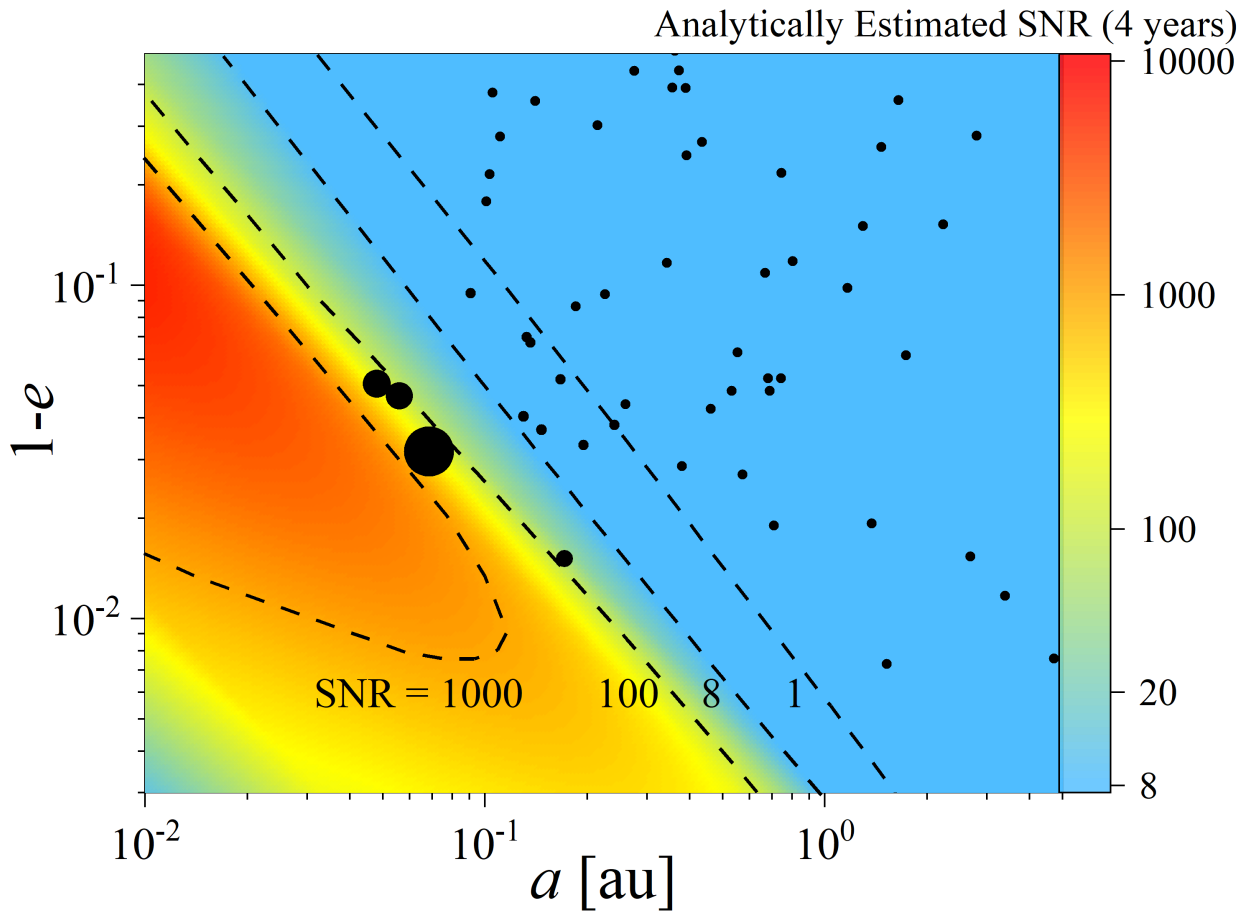


Figure 5.5: **An example of the intrinsic parameters of highly eccentric BBHs used in our mock LISA observation.** Here, we adopt the simulation result of the compact binary population in the Milky Way's nuclear star cluster (see Section 3.5 in Ref. (Xuan et al., 2024a)) and show the parameters of highly eccentric BBHs in black dots. The x-axis represents the binary's semi-major axis a, and the y-axis represents one minus the binary's eccentricity $(1-e)$. We estimate the overall signal-to-noise ratio of the BBH system during a 4-yr LISA observation, depicted in different colors. The dashed lines represent equal signal-to-noise ratio contours for SNR = 1000, 100, 8, and 1, from left to right. Here, the SNR is analytically calculated using Equation (5.4), assuming $m_1 = m_2 = 10$ $M_\odot$ and $R = 8$ kpc for simplicity. However, we note that the mass of BBHs in the mock data analysis is generated from the stellar evolution model and may slightly differ from ~ 10 $M_\odot$. Therefore, the numerical SNR is expected to vary slightly from the analytical calculation. For demonstration purposes, we enlarge the size of dots for the detectable BBH systems based on the SNR.

noise as well as the foreground from unresolved galactic binaries (see, e.g., Cornish and Robson, 2017).

5.4.3 Matched Filtering and Mock Observation Results

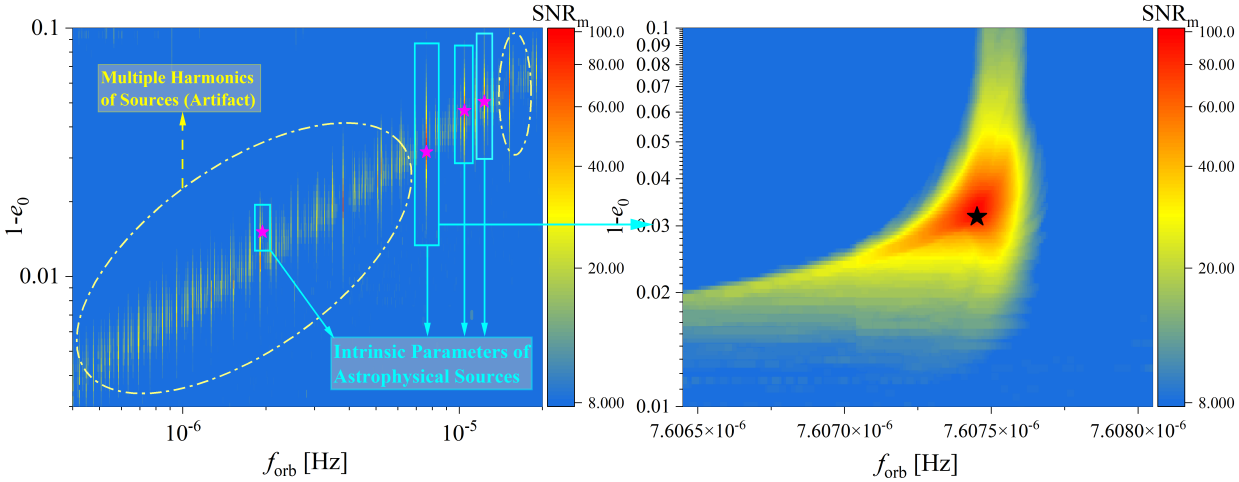


Figure 5.6: **The matched filtering output in the mock LISA data analysis of highly eccentric BBHs.** Here we fit the mock LISA data with different bursting GW templates and plot the optimal signal-to-noise ratio, $\mathrm{SNR_m}$, in different colors, as a function of $f_{\rm orb}$ and $1-e_0$ of the template (see Sections 5.2.2 and 5.4 for more details). Specifically, the optimal SNR is calculated numerically, using matched filtering as described in Section 5.4 (note that $\mathrm{SNR_m}$ represents the realistic fitting result, and is different from the analytical estimation of SNR in Equation (5.4) and Figures 5.3 - 8.3). *Left Panel* shows the fitting results for all the potential GW sources with an orbital frequency of $f_{\rm orb} \sim 4\times10^{-7} - 2\times10^{-5}$ Hz and eccentricity $e \sim 0.9 - 0.997$, while the *Right Panel* shows a zoom-in of the region near the parameters of a "real" GW source that appears in the mock data (i.e., the detection case). For demonstration purposes, we mark, in stars, the intrinsic parameters of the GW sources and highlight the region where we successfully fit these signals with high $\mathrm{SNR_m}$ (see the rectangular boxes in light blue). We note that, in some regions of *Left Panel*, numerical artifacts cause the fitted $\mathrm{SNR_m}$ to exceed the detection threshold of 8, while there are no astrophysical sources (see Section 5.4 for a more detailed discussion).

In the mock data analysis, we adopt the matched filtering method described in Section 5.3.2. Specifically, we first generate a waveform template bank using Equations (5.6) - (5.10), which include the effect of the detector's response and annual motion around the Sun. For simplicity, we fix the mass of the template binaries as $10-10\ \mathrm{M}_\odot$, with $\theta=\phi=\Theta=\Phi=\psi=\pi/4$, and change the initial orbital frequency $f_{\rm orb}$ and eccentricity e_0. We then convolve

each template signal with the mock LISA data and compute the optimal signal-to-noise ratio, $\mathrm{SNR_m}$ (see Section 5.3.2, and Eq. (5.20)). We remind the reader that the PyCBC software package is adopted for the numerical realization (Nitz et al., 2024). The results of the Match filtering output are shown in Figure 5.6.

We emphasize that, as discussed above, some parameters of the waveform template are fixed to avoid high computational costs in the mock data analysis. Specifically, we only scan the 2-dimensional parameter space of $(f_{\rm orb}, 1-e_0)$, while the template signals may not match the exact values of $(M, q, \cos\Theta, \Phi, \cos\theta, \phi, \psi)$ of the GW sources. (Note that matched filtering is independent of the overall amplitude of the waveform, so the distance R of the template binary will not affect the fitting result, assuming redshift is negligible.) Consequently, the $\mathrm{SNR_m}$ we show in Figure 5.6 does not represent a global optimum for the entire 10-dimensional parameter space (see Section 5.2.2). However, we expect such a loss of signal-to-noise ratio will not significantly impact the overall fitting result, as the bursting waveform is less sensitive to $(M, q, \cos\Theta, \Phi, \cos\theta, \phi, \psi)$ compared to $(f_{\rm orb}, 1-e_0)$ (see, e.g., the Fisher matrix analysis result in Section 5.3.1.1; note that the parameters with larger measurement error will have a weaker influence on the waveform). For example, the GW source with $a \sim 0.068$ au, $(1-e) \sim 0.032$ has an analytical estimation of SNR ~ 200 in Figure 8.3 (see the biggest black dot). On the other hand, this source is successfully identified in the mock data analysis, numerically fitted with $\mathrm{SNR_m} = 96$ and almost no bias in the measured values of $(f_{\rm orb}, 1-e_0)$ (see the black star in the *Right Panel* of Figure 5.6). Therefore, even without fitting the global optimum across the 10-dimensional parameter space, we can effectively apply the matched filtering to search for $(f_{\rm orb}, 1-e_0)$, which are the dominant parameters that affect the shape of bursting waveform, and still detect most of the bursting sources with high SNR in future LISA observation.

In Figure 5.6, we plot the fitted $\mathrm{SNR_m}$ in different colors as a function of the template's $f_{\rm orb}$ and $1-e_0$. As shown in the *Left Panel*, we successfully identify multiple bursting sources

in the mock data. In particular, the stars represent the intrinsic parameters of four GW sources that have a high analytical SNR in the mock data (note that these sources, as well as other low SNR sources in Figure 8.3, are present simultaneously in the mock LISA signal). After applying the matched filtering, we get the $\mathrm{SNR_m}$ distribution as highlighted by the rectangular boxes in light blue, which has a clear high $\mathrm{SNR_m}$ peak that centers around the intrinsic parameters of the binary (with the peak $\mathrm{SNR_m} = 15, 96, 54, 47$, from left to right, exceeding the detection threshold of 8). This result verifies that matched filtering can perform well in extracting the "bursting" GW signal from LISA data, even when multiple sources are contributing to a wide range of harmonics in the frequency domain (see Section 5.4.1) and when there are instrumental noises plus the Galactic foreground.[2]

Furthermore, *Right Panel* illustrates a zoom-in of the region near the intrinsic parameters of a detected source. We emphasize that the matched filtering of bursting GW signal is highly sensitive to the choice of the initial orbital frequency, f_{orb}. For example, the high $\mathrm{SNR_m}$ peak in *Left Panel* only spans a frequency range of $\sim 10^{-10}$ Hz. This sensitivity implies that, for LISA data analysis, we need to choose a grid size smaller than this value (or, more precisely, as estimated in Equation (5.18)) to avoid missing any bursting sources in the search. Given the parameter space scale of $f_{\mathrm{orb}} \sim 10^{-7} - 10^{-4}$ Hz, this grid size requires computing $\sim 10^6$ grids in the dimension of f_{orb}, which greatly increases the computational expense. However, once the sources are identified, we can take advantage of this high sensitivity to f_{orb} and accurately determine the orbital parameters of bursting binaries. Moreover, because of the small error in orbital frequency measurement, two bursting sources with similar orbital frequencies are less likely to be confused in the data analysis, which could help suppress any

[2]We applied a high-pass filter in the data analysis before the matched filtering to suppress the loud instrumental noise and astrophysical foreground at frequencies below 10^{-4} Hz. Additionally, to reduce computational costs, we generated mock LISA data with a sample rate of 0.1 Hz. Note that the matched filtering produces a SNR time series for each template (see, e.g., Equation (5.19)). To overcome numerical artifacts caused by the finite length of the GW signal, we implemented a cutoff in the SNR time series at $t_0 < 5/f_{\mathrm{orb}}$ and $t_{\mathrm{end}} - t_0 < 5/f_{\mathrm{orb}}$ (in which $t_{\mathrm{end}} = 1$ yr is the ending time of the GW signal), before finding the $\mathrm{SNR_m}$ and outputting the result. A similar approach can be found in LIGO data analysis, see, e.g., Sec.VII in Ref. (Allen et al., 2012).

potential confusion background.

We note that there are numerical artifacts in the *Left Panel* of Figure 5.6, which cause the fitted SNR to exceed the detection threshold of 8 even when there are no astrophysical sources. Specifically, in the region surrounded by yellow dash-dotted lines, most of the high $\mathrm{SNR_m}$ peaks do not represent real parameters of astrophysical sources (except for the four $\mathrm{SNR_m}$ peaks highlighted by rectangular boxes in light blue). Instead, these peaks are caused by the higher-order harmonics of astrophysical bursting signals. Specifically, for a given astrophysical signal with burst period $1/f_{\mathrm{orb}}$, all the templates $h_{\mathrm{template}}(t)$ with the following orbital frequencies could have high $\mathrm{SNR_m}$ in the template fitting:

$$f'_{\mathrm{orb}} = \frac{m}{n} f_{\mathrm{orb}},\ (m, n = 1, 2, 3...) \tag{5.21}$$

Equation (5.21) can be explained using the property of bursting signals. In particular, most of the observed stellar mass bursting systems are expected to have slow orbital evolution (see Section 5.2.1), and their GW emission can be characterized by repeated bursts, with a separation of $\delta\tau = 1/f_{\mathrm{orb}}$ in the time domain. For example, when using a template with a burst separation of $2\delta\tau$, $3\delta\tau$, $4\delta\tau$... or $\frac{1}{2}\delta\tau$, $\frac{1}{3}\delta\tau$, $\frac{1}{4}\delta\tau$... to fit the signal, the GW bursts of the template will also match (some of) the bursts from astrophysical sources, thus yielding a high $\mathrm{SNR_m}$ in the matched filtering result (note that, in the frequency domain, this effect can be described as the overlapping of harmonics between two signals with different fundamental frequencies, with one fundamental frequency being multiple integer times the other one; Also, a similar effect has been found in the literature of EMRI data analysis, see, e.g., Chua and Cutler (2022)).

Additionally, to excite the highest $\mathrm{SNR_m}$ peak at a given harmonic frequency f'_{orb}, the templates need to have most of the GW energy distributed in the same frequency band as the astrophysical source. In other words, the template should have a burst frequency that

closely matches the astrophysical GW signal (see Equation (5.2)):

$$f'_{\rm orb}(1-e')^{-\frac{3}{2}} \sim f_{\rm orb}(1-e_0)^{-\frac{3}{2}}\,, \tag{5.22}$$

in which e' is the eccentricity of the harmonic template. Notably, Equation (5.22) also suggests that the width of a GW burst in the template coincides with the width of the burst in the actual astrophysical signal.

Equations (5.21) and (5.22) provide a prediction for the orbital frequency and eccentricity of the harmonic template (see, e.g., the harmonic peak locations in Figure 5.6), which can significantly enhance source identification in future data analysis. For example, the system with $f_{\rm orb} = 7.60745 \times 10^{-6}$ Hz will excite multiply harmonics at the frequencies such as $3.80372, 2.53581, 1.90186 \times 10^{-6}$ Hz and $1.52149, 2.28223, 3.04298 \times 10^{-5}$ Hz (which represent the 2nd, 3rd, and 4th harmonics, see the peaks in the *Left Panel* of Figure 5.6). Once finding these high $\rm SNR_m$ peaks, we can try to fit their locations using Equations (5.21) and (5.22), thus extracting the intrinsic parameters of the source. We note that, the fitted $\rm SNR_m$ will be suppressed as the harmonic numbers m, n increase, resulting in a finite number of detectable harmonics. These harmonics can be efficiently distinguished due to the high accuracy of $f_{\rm orb}$ measurement. Furthermore, Figure 5.6 shows the matched filtering result for simultaneously fitting all bursting sources. However, in practical data analysis, we can identify the loudest bursting sources, remove them from the dataset, and thereby prevent their harmonics from interfering with the fitting of other astrophysical signals.

Here, we aim at a proof-of-concept example of a bursting source search in LISA data analysis. Thus, this mock observation does not include all the potential bursting source populations. Furthermore, we assume a stationary Gaussian instrumental noise in the mock LISA data, which may not capture all the influence of noise on the fitting results of the bursting signals. For example, there have been many studies highlighting the importance of instrumental

glitches (see, e.g., Robson and Cornish, 2019; Baghi et al., 2022; Armano et al., 2022). We expect this phenomenon to appear in future detection, as shown recently by the LISA Pathfinder (see, e.g., Refs. (Armano et al., 2016b, 2018b)). Therefore, it is important to characterize whether these noise transients will affect LISA's performance in detecting highly eccentric compact binaries, which we leave for future works.

Additionally, as discussed above, the matched filtering of bursting GW signals is very sensitive to the orbital frequency, with $\sim 10^6$ grids required for a complete search of $f_{\rm orb}$ in the parameter space that we focus on. Moreover, there are 9 more dimensions ($1-e_0, M, q, \cos\Theta, \Phi, \cos\theta, \phi, R, \psi$) that contribute to the total number of grids we need to compute. However, computing bursting waveforms in the time domain is time-consuming, which leads to a high computational cost for the search of these sources. Thus, we highlight the importance of constructing accurate frequency-domain waveforms for highly eccentric binaries, as they could greatly accelerate realistic data analysis. Also, we may need to incorporate other sub-optimal time-frequency approaches to search for the signal, such as power stacking (East et al., 2013), the TFCLUSTER algorithm (Sylvestre, 2002), wavelet decomposition (Klimenko and Mitselmakher, 2004), and the Q-transform (Chatterji et al., 2004, 2006; Bassetti et al., 2005; Tai et al., 2014), which are more robust to different kinds of transients and have lower computational costs.

5.5 Discussion

Wide, highly eccentric compact binaries can naturally arise as a progenitor stage of GW mergers, particularly in dynamical channels where environmental perturbations bring two compact objects into close encounters (see, e.g., O'Leary et al., 2009a; Thompson, 2011; Aarseth, 2012; Kocsis and Levin, 2012; Breivik et al., 2016; Gondán et al., 2018b; D'Orazio and Samsing, 2018; Zevin et al., 2019; Samsing et al., 2019; Martinez et al., 2020; Antonini

and Gieles, 2020; Kremer et al., 2020; Winter-Granić et al., 2023; Gondán and Kocsis, 2021; Michaely and Perets, 2019, 2020; Michaely and Naoz, 2022; Wen, 2003; Hoang et al., 2018; Hamers, 2018; Stephan et al., 2019; Zevin et al., 2019; Bub and Petrovich, 2020; Deme et al., 2020; Wang et al., 2021; Zevin et al., 2021; Xuan et al., 2021, 2024a; Mockler et al., 2023; Melchor et al., 2024; Xuan et al., 2024b). These systems will undergo effective GW emission upon each pericenter passage, which potentially creates a burst-like pattern in the mHz GW detection, as demonstrated in Figure 5.1 (note that there could be $\sim 3-45$ detectable bursting BBHs in the Milky Way, which contribute to $\sim 10^2 - 10^4$ GW bursts during the LISA mission (Xuan et al., 2024a)). This work focuses on the source identification and parameter extraction of stellar mass bursting binaries. Particularly, we explored the astrophysical inference of these highly eccentric systems, quantified their parameter measurement error, and carried out mock LISA observation to test whether these bursting binaries could be efficiently distinguished when multiple sources and instrumental noises are present simultaneously in the detector's output.

Throughout this paper, we have adopted the x-model to generate GW signals for all of the bursting binaries (see Section 5.2.1). This model includes the dynamics of eccentric compact binaries to 3 pN order, and we further account for the detector's annual motion around the Sun (see Equations (5.6) - (5.10)). The definition of coordinates is illustrated in Figure 5.2.

To assess the detectability and parameter measurement accuracy of bursting GW sources in the LISA band, we utilize the Fisher matrix analysis (see Section 5.3.1) and the matched filtering method (see Section 5.3.2). In particular, using the Fisher matrix analysis, we compute the relative measurement error of $\{f_{\rm orb}, 1-e_0, M, q, \cos\Theta, \Phi, \cos\theta, \phi, R, \psi\}$, for the bursting GW signals from a $10-15\,{\rm M}_\odot$ BBH system at a distance of 8 kpc, in a representative parameter space of semi-major axis $a_0 \sim 0.01 - 3$ au, eccentricity $e_0 \sim 0.9 - 0.9999$. The results are shown in Figures 5.3 and 5.4, with Figure 5.3 representing 1-year LISA observation and Figure 5.4 representing 5 years (which yields a higher accuracy).

As illustrated in Figures 5.3 and 5.4, for a highly eccentric binary system, its orbital frequency, eccentricity (as $1 - e_0$), and the sky location can be retrieved with relatively high accuracy. Notably, LISA could determine these bursting sources' orbital frequency to an accuracy of $\Delta f_{\rm orb} \sim 10^{-12} - 10^{-10}$ Hz, with the relative error of $1 - e_0$ measurement smaller than $\sim 1\%$ in the detected cases, which could greatly help with the understanding of these binaries' formation channels. Furthermore, the sky location of bursting sources could be measured to an accuracy of $\sim 0.1 - 10$ degrees (depending on the signal-to-noise ratio), while the bursting waveform detection may be less sensitive to other parameters, including the binary's intrinsic orientation $\{\Theta, \Phi\}$, the distance R, and the polarization angle ψ of GW signal. Additionally, the mass ratio q is poorly constrained, but we could estimate the total mass M with an accuracy of $\Delta M \lesssim 10\%$ in a 5 yr observation, when the SNR exceeds ~ 100. We discussed the astrophysical interpretation of the aforementioned results in Section 5.3.1.2, and give an analytical estimation of $f_{\rm orb}$ measurement error in Equation (5.18).

We note that, due to the limitation of the Fisher matrix analysis, the aforementioned parameter measurement accuracy only serves as a heuristic estimation for this new source class. In particular, the resultant measurement error of our work can become unreliable when compared with full Bayesian analyses (see, e.g., the discussion in Ref. (Vallisneri, 2008)), especially for those parameters with weak influence on the waveform (i.e., mass ratio q, intrinsic orientation Θ, Φ, and distance R). Thus, we emphasize the need for full Bayesian analyses in future work. While computationally expensive, these methods can consistently include sophisticated priors, and explore the secondary maxima of the posterior. Nonetheless, our results provide compelling evidence that bursting GW sources are promising candidates for inferring astrophysical properties.

Moreover, to measure the source parameters in realistic observation, the bursting GW signals need to be properly identified and extracted from the data stream. Thus, we further test the detectability of the highly eccentric compact binaries via the mock LISA data analysis.

Specifically, we construct an example of mock LISA data (see Section 5.4.2), which includes a representative population of bursting BBHs in the Milky Way Galactic center nuclear star cluster (see Figure 8.3), the instrumental noise of detector, and the astrophysical GW noise foreground caused by unresolved Galactic binaries. We then adopt the matched filtering method as described in Section 5.3.2, to compute the optimal signal-to-noise ratio in the search of bursting GW sources.

The mock data analysis results are summarized in Figure 5.6. Interestingly, even without fitting the global optimum in the 10-dimensional parameter space, the matched filtering search of bursting GW templates in the plane of $(f_{\rm orb}, 1-e_0)$ still identifies most of the bursting sources with high SNR in the mock observation (which is mostly because $(f_{\rm orb}, 1-e_0)$ are the dominant parameters that characterize the bursting GW signals). Furthermore, the matched filtering results show a high sensitivity to orbital frequency (see the *Left Panel*), which indicates a small grid size requirement, $\Delta f_{\rm orb} \sim 10^{-10}$ Hz, for future data analysis. On the other hand, this phenomenon also means there could be less confusion between bursting binaries with different values of $f_{\rm orb}$. Thus, multiple sources can be distinguished simultaneously in the detector's output. We also explore the potential artifacts in burst data analysis, such as the non-astrophysical signals caused by the higher-order harmonics of highly eccentric GW sources, as described in Equation (5.21).

We emphasize that the mock data analysis in this work does not include all the potential GW source populations and the non-Gaussian instrumental noise (such as glitches). However, it serves as a proof-of-concept example of bursting source search in LISA data analysis, which verifies the detectability of highly eccentric compact binaries with the current LISA design and data analysis methods. Also, our analysis provides a guideline for the future bursting GW signal search, including an estimation of parameter space, computational expense, and potential artifacts.

To conclude, wide, highly eccentric compact binaries can provide us with valuable informa-

tion about their formation channels and the surrounding environment. In particular, we show that these sources could be properly identified and extracted from the LISA detector's output, with high accuracy in the measurement of orbital frequency, eccentricity, and sky location. However, the computational expense may be large for the search of bursting signals. Therefore, it is important to develop ready-to-use frequency domain templates for bursting GW sources or incorporate other efficient time-frequency approaches in future detection.

5.6 Acknowledgments

The authors thank Aditya Vijaykumar for the valuable discussions and the anonymous referee for their useful comments. ZX acknowledges partial support from the Bhaumik Institute for Theoretical Physics summer fellowship. ZX and SN acknowledge the partial support from NASA ATP 80NSSC20K0505 and from NSF-AST 2206428 grant and thank Howard and Astrid Preston for their generous support. Further, ZX and SN thank LISA Sprint 2024 for organizing an interactive and productive meeting. JM acknowledges support from the Canada Research Chairs program. AMK acknowledges funding support from a Killam Doctoral Scholarship. This work was supported by the Science and Technology Facilities Council Grant Number ST/W000903/1 (to BK).

5.7 Appendix

5.7.1 Time Domain Estimation of the Inner Product

For quasi-periodic gravitational waves h_1, h_2 with frequency close to f_0, the GW signal is a nearly monochromatic, sinusoidal waveform. In this case, the frequency-domain expression of inner product (see Equation (7.20)) can be simplified. In particular, the noise curve $S_n(f)$

can be taken out of the integration because of the small variation of f:

$$\langle h_1 \mid h_2 \rangle \approx \frac{2}{S_n(f_0)} \int_0^\infty \left[\tilde{h}_1^*(f)\tilde{h}_2(f) + \tilde{h}_1(f)\tilde{h}_2^*(f) \right] df. \tag{5.23}$$

Furthermore, using Parseval's theorem, we can compute the integral in Equation (6.11) using time domain waveforms:

$$\langle h_1 \mid h_2 \rangle \approx \frac{4}{S_n(f_0)} \int_0^\infty h_1(t)h_2(t)dt. \tag{5.24}$$

Equation (5.24) is commonly adopted when analyzing the gravitational waves from circular binaries when the evolutionary timescale is much longer than the observational period of LISA (see, e.g., (Chen et al., 2019b; Seto, 2002b)[3]).

5.7.2 Analytical Estimation of the Fisher Matrix

In this section, we develop an analytical method to estimate the Fisher matrix for eccentric GW sources in the LISA band. In particular, we first adopt a simplified waveform model for eccentric sources from Ref. (Moreno-Garrido et al., 1995) (see also (Seto, 2001; Mikóczi et al., 2012a; Gondán et al., 2018b)), in which $h_\times$, h_+ denote two polarizations of the gravitational wave and $n = 1, 2, 3...$ denotes the number of harmonics:

[3]Note that Eq. 22 in Seto (2002b) differs from the value of frequency inner product in Eq. 2.3 of Cutler and Flanagan (1994) by a factor of 2, to recover the value of signal-to-noise ratio the consistent coefficient in the time domain inner product should be 4 instead of 2.

$$h_{\times}(t) = -h\cos\Theta\sum_{n}\left[B_{n-}\sin\Phi^{t}_{n+} + B_{n+}\sin\Phi^{t}_{n-}\right], \tag{5.25}$$

$$h_{+}(t) = -\frac{h}{2}\sum_{n}\left[\sin^{2}\Theta A_{n}\cos\Phi^{t}_{n} + \left(1+\cos^{2}\Theta\right)\right.$$
$$\left.\times\left(B_{n+}\cos\Phi^{t}_{n-} - B_{n-}\cos\Phi^{t}_{n+}\right)\right]. \tag{5.26}$$

here $h = 4m_1m_2/(aR)$ is the strain amplitude of gravitational wave. For a detailed description of orbital parameters, see Fig.1 in Ref. (Mikóczi et al., 2012a).

In Equation (5.26), $B_{n\pm} = (S_n \pm C_n)/2$ and A_n are linear combinations of the Bessel functions of the first kind, $J_n(ne)$, and their derivatives:

$$S_n = -\frac{2\left(1-e^2\right)^{1/2}}{e}n^{-1}J'_n(ne) + \frac{2\left(1-e^2\right)^{3/2}}{e^2}nJ_n(ne), \tag{5.27}$$
$$C_n = -\frac{2-e^2}{e^2}J_n(ne) + \frac{2\left(1-e^2\right)}{e}J'_n(ne),$$
$$A_n = J_n(ne),$$

where a prime denotes the derivative, i.e., $J'_n(ne) \equiv dJ_n(ne)/de = n\left[J_{n-1}(ne) - J_{n+1}(ne)\right]/2$.

The frequency component of an eccentric GW waveform is made up of a series of harmonics, with the power of each harmonic concentrate near $f_n = nf_{\rm orb}$ (see, e.g., Peters, 1964; Seto, 2001; Xuan et al., 2023, 2024a,b). Furthermore, the pericenter precession makes the orbital phase of each harmonic split into a triplet, Φ_n, $\Phi_{n\pm}$. Therefore, in Equation (5.26), the time evolution of orbital phases can be expressed as (Seto, 2001):

$$\Phi^{t}_{n} = 2\pi n f_{\rm orb}\left(t-t_0\right), \Phi^{t}_{n\pm} = 2\pi n f_{\rm orb}\left(t-t_0\right) \pm 2\pi\delta f t \pm 2\gamma_0, \tag{5.28}$$

in which $f_{\rm orb} = T^{-1}_{\rm orb}$ is the Keplerian orbital frequency (here $T_{\rm orb} = 2\pi M^{-1/2}a^{3/2}$ is the Newtonian radial orbital period), t_0 is the time of pericenter passage (hereafter, we set

$t_0 = 0$), γ_0 is the initial angle of the pericenter, and here we define δf as twice of the (general relativistic) pericenter precession frequency Seto (2001):

$$\delta f = 2 \times \frac{1}{2\pi}\frac{d\gamma}{dt} = \frac{3M^{\frac{3}{2}}}{\pi a^{\frac{5}{2}}(1-e^2)} = \frac{6(2\pi)^{\frac{2}{3}}M^{\frac{2}{3}}f_{\rm orb}^{\frac{5}{3}}}{(1-e^2)}. \tag{5.29}$$

After setting up the waveform, we can take its derivative of different orbital parameters and get an analytical estimation of the Fisher matrix using Equation (6.7). In the most general case, all the six parameters could affect the waveform in Equation (5.26), i.e., $(h, \Theta, f_{\rm orb}, \delta f, e, \gamma_0)$. However, for simplicity, here we will only focus on three parameters, i.e., $(f_{\rm orb}, \delta f, e)$. This simplification is partly justified because $(f_{\rm orb}, \delta f, e)$ dominates the long-term phase evolution of the GW waveform, thus mostly affecting the overlap in the computation of Fisher matrix (see Equation (6.7)). Also, we are interested in these three parameters because they represent the accuracy of measurement for the (redshifted) intrinsic parameters of the binary system.

$$\frac{\partial h_\times}{\partial f_{\rm orb}} = -h\cos\Theta\sum_n \Big[B_{n-}\cos\Phi^t_{n+}\cdot(2\pi nt) + B_{n+}\cos\Phi^t_{n-}\cdot(2\pi nt)\Big] \tag{5.30}$$

$$\frac{\partial h_\times}{\partial \delta f} = -h\cos\Theta\sum_n \Big[B_{n-}\cos\Phi^t_{n+}\cdot(2\pi t) + B_{n+}\cos\Phi^t_{n-}\cdot(-2\pi t)\Big] \tag{5.31}$$

$$\frac{\partial h_\times}{\partial e} = -h\cos\Theta\sum_n \Big[B'_{n-}\sin\Phi^t_{nt} + B'_{n+}\sin\Phi^t_{n-}\Big] \tag{5.32}$$

in which $B'_{n\pm}(n,e) = dB_{n\pm}/de$ is the derivative as a function of the binary's eccentricity. Note that, in Equations (5.30) and (5.31), the factor of $2\pi nt$ ($2\pi t$) is because of taking the derivative of $\Phi^t_{n\pm}$ over $f_{\rm orb}$ (δf) (see Equation (5.28)).

We note that, on the other hand, h represents the overall amplitude of the waveform, while Θ and γ_0 describe the inclination and orientation of the binary relative to the observer. Since there are degeneracies between some of these parameters (e.g., h and $\cos\Theta$ in Equation (5.25)), and the highly eccentric GW waveform is less sensitive to these parameters (see e.g., they are weakly constrained in Figure 5.3), we neglect their contribution for simplicity. However, in realistic observation, these parameters may still interfere with the measurement of $(f_{\rm orb}, \delta f, e)$. In other words, our result in the following discussion only considers the submatrix of $(f_{\rm orb}, \delta f, e)$, and the corresponding estimation serves as a lower bound of parameter measurement error.

Here, we assume the GW source evolves slowly. Thus, the signal does not undergo a significant frequency shift during the observation, and each harmonic is a near-monochromatic signal with the power concentrates near $f_n = nf_{\rm orb}$. We expect that most sources will be consistent with this assumption for the harmonics that contribute most to the detection signal-to-noise ratio (e.g., O'Leary et al., 2009a; Wang et al., 2021; Xuan et al., 2024a); however, in some cases, the signal may shift in a short timescale, or the precession of orbit is fast (Hoang et al., 2019; Deme et al., 2020), which is beyond the scope of this study.

In particular, we make the following assumptions:

$$\begin{cases} \frac{f_{\rm orb}}{\dot{f}_{\rm orb}} \gg T_{\rm obs} \\ T_{\rm obs} \gg \frac{1}{f_{\rm orb}} \\ f_{\rm orb} \gg \delta f \end{cases} \tag{5.33}$$

here $\dot{f}_{\rm orb}$ represents the time derivative of orbital frequency, which can be estimated using (Peters, 1964; Xuan et al., 2021):

$$\dot{f}_{\rm orb} = \frac{1}{2} \times \frac{96\pi^{8/3}}{5} \mathcal{M}_c^{5/3} \left(2 f_{\rm orb}\right)^{11/3} F(e) \ , \tag{5.34}$$

in which $\mathcal{M}_c$ is the chirp mass of the binary, $\mathcal{M}_c \equiv (m_1 m_2)^{3/5}/(m_1+m_2)^{1/5}$, $F(e)$ is a function of the compact binary's eccentricity (the enhancement function)(Peters and Mathews, 1963):

$$F(e) \equiv \frac{1 + \frac{73}{24} e^2 + \frac{37}{96} e^4}{(1-e^2)^{7/2}} \ . \tag{5.35}$$

In Equation (5.33), the first assumption ensures that the source evolves slowly (merger timescale $\tau \sim f_{\rm orb}/\dot{f}_{\rm orb} \gg T_{\rm obs}$), the second assumption ensures that there is a significant number of bursts detected during the observation, and the third assumption ensures that pericenter precession is small during each orbit (i.e., every single harmonic and its corresponding triplet frequencies will only overlap with itself in the frequency domain, see Equation (5.28)).

Therefore, under the assumption that $f_{\rm orb}$ evolves slowly and δf is much smaller than $f_{\rm orb}$, each single harmonic (and its corresponding triplet frequencies) can be taken as a near-monochromatic signal, which does not overlap with other harmonics. This property allows us to compute the inner product of each individual harmonic using Equation (5.24), then sum over all the harmonics' contributions to get the total inner product.

For example, combining Equations (5.24) and (5.30), we have:

$$\left\langle \frac{\partial h_\times}{\partial f_{\rm orb}} \middle| \frac{\partial h_\times}{\partial f_{\rm orb}} \right\rangle = h^2 \cos^2\Theta \cdot \sum_n \frac{4}{S_n(n f_{\rm orb})} \cdot (2\pi n)^2 \times \int_0^{T_{\rm obs}} \left[B_{n-}^2 \cos^2 \Phi_{n+}^t + B_{n+}^2 \cos \Phi_{n-}^2 + 2 B_{n+} B_{n-} \cos \Phi_{n+}^t \cos \Phi_{n-}^t \right] t^2 dt \ , \tag{5.36}$$

in which:

$$\begin{aligned} &\int_0^{T_{\rm obs}} \cos^2 \Phi_{n\pm}^t t^2 dt = \frac{1}{2} \int_0^{T_{\rm obs}} (1 + \cos 2\Phi_{n\pm}^t) t^2 dt \\ &= \frac{1}{6} T_{\rm obs}^3 + \frac{1}{2} \int_0^{t_{\rm obs}} \cos\left[4\pi \left(n f_{\rm orb} \pm \delta f\right) t \pm 4\gamma_0\right] t^2 dt \\ &\simeq \frac{1}{6} T_{\rm obs}^3 (1 + \mathcal{O}(1)) \ , \end{aligned} \tag{5.37}$$

and:

$$\begin{aligned} &\int_0^{t_{\rm obs}} \cos \Phi_{n+}^t \cos \Phi_{n-}^t t^2 dt \\ &= \frac{1}{2} \int_0^{T_{\rm obs}} \left[\cos\left(4\pi n f_{\rm orb} t\right) + \cos\left(4\pi \delta f t + 4\gamma_0\right)\right] t^2 dt \ . \end{aligned} \tag{5.38}$$

We note that, the integration of $\cos\left(4\pi\delta f t + 4\gamma_0\right) t^2 dt$ in Equation (5.38) may yield a significant contribution to the inner product. This is because many highly eccentric systems have their precession timescale $1/\delta f$ comparable to or longer than the observation time, $T_{\rm obs}$. Therefore, Equation (5.38) can be on the same order of $\sim T_{\rm obs}^3$. (Note that we didn't assume $T_{\rm obs} \gg 1/\delta f$ in Equation (5.33), otherwise, all the terms in Equation (5.38) can be neglected compared with $T_{\rm obs}^3$.)

In other words, the initial angle of the pericenter, γ_0, can affect the parameter extraction, providing that the eccentric GW source has slow precession during the observation. However,

since here we are focusing on a heuristic estimation of the parameter extraction accuracy, we further average over different orientations of the source, i.e., the angle of γ_0, to get the general order of magnitude for the matrix element. The average over γ_0 makes the term of $\cos\left(4\pi\delta f t + 4\gamma_0\right) t^2 dt$ vanish. Therefore, after taking this average, the terms in Equation (5.38) can be neglected because they are much smaller than $T_{\rm obs}^3$ (the leading order contribution, see e.g., Equation (5.37)).

Plug the result of Equations (5.37) and (5.38) into Equation (5.36), we can get:

$$\begin{aligned}\left\langle \Gamma^{\times}_{f_{\rm orb}f_{\rm orb}} \right\rangle_{\gamma_0} &= \left\langle \frac{\partial h_\times}{\partial f_{\rm orb}} \middle| \frac{\partial h_\times}{\partial f_{\rm orb}} \right\rangle_{\gamma_0} \\ &\sim \frac{8\pi^2}{3} h^2 \cos^2\Theta T_{\rm obs}^3 \sum_n \frac{n^2}{S_n(nf_{\rm orb})} (B_{n+}^2 + B_{n-}^2)\end{aligned} \tag{5.39}$$

in which $\langle\cdot\rangle_{\gamma_0}$ represents taking the average over γ_0.

Similarly, we can adopt this method for the other two parameters, δf and e, and get:

$$\begin{aligned}\left\langle \Gamma^{\times}_{\delta f \delta f} \right\rangle_{\gamma_0} &= \left\langle \frac{\partial h_\times}{\partial \delta f} \middle| \frac{\partial h_\times}{\partial \delta f} \right\rangle_{\gamma_0} \\ &\sim \frac{8\pi^2}{3} h^2 \cos^2\Theta T_{\rm obs}^3 \sum_n \frac{1}{S_n(nf_{\rm orb})} (B_{n+}^2 + B_{n-}^2)\end{aligned} \tag{5.40}$$

$$\begin{aligned}\left\langle \Gamma^{\times}_{ee} \right\rangle_{\gamma_0} &= \left\langle \frac{\partial h_\times}{\partial e} \middle| \frac{\partial h_\times}{\partial e} \right\rangle_{\gamma_0} \\ &\sim 2h^2 \cos^2\Theta T_{\rm obs} \sum_n \frac{1}{S_n(nf_{\rm orb})} (B_{n+}'^2 + B_{n-}'^2)\end{aligned} \tag{5.41}$$

where a prime denotes the derivative, i.e., $B'_{n\pm} \equiv dB_{n\pm}/de$.

We apply the same analysis to the plus polarization (see Equation (5.26)), and get:

$$\begin{aligned}\left\langle \Gamma^{+}_{f_{\rm orb}f_{\rm orb}} \right\rangle_{\gamma_0} &= \left\langle \frac{\partial h_+}{\partial f_{\rm orb}} \middle| \frac{\partial h_+}{\partial f_{\rm orb}} \right\rangle_{\gamma_0} \\ \sim \frac{2\pi^2}{3} h^2 T^3_{\rm obs} \sum_n & \frac{n^2}{S_n(n f_{\rm orb})} \\ & \times \left[\sin^4\Theta A_n^2 + (1+\cos^2\Theta)^2 (B_{n+}^2 + B_{n-}^2)\right] \ ,\end{aligned} \tag{5.42}$$

$$\begin{aligned}\left\langle \Gamma^{+}_{\delta f \delta f} \right\rangle_{\gamma_0} &= \left\langle \frac{\partial h_+}{\partial \delta f} \middle| \frac{\partial h_+}{\partial \delta f} \right\rangle_{\gamma_0} \\ &\sim \frac{2\pi^2}{3} h^2 T^3_{\rm obs} \sum_n \frac{(1+\cos^2\Theta)^2}{S_n(n f_{\rm orb})} (B_{n+}^2 + B_{n-}^2) \ .\end{aligned} \tag{5.43}$$

$$\begin{aligned}\left\langle \Gamma^{+}_{ee} \right\rangle_{\gamma_0} &= \left\langle \frac{\partial h_+}{\partial e} \middle| \frac{\partial h_+}{\partial e} \right\rangle_{\gamma_0} \\ &\sim \frac{1}{2} h^2 T_{\rm obs} \sum_n \frac{1}{S_n(n f_{\rm orb})} \\ &\times \left[\sin^4\Theta A_n'^2 + (1+\cos^2\Theta)^2 (B_{n+}'^2 + B_{n-}'^2)\right]\end{aligned} \tag{5.44}$$

In realistic observation, the detector's output is a linear combination of two polarizations of the gravitational wave, and the coefficients depend on the sources' sky location and detector's orientation (see the discussions in Section 5.3.1.1. Here, for simplicity, we combine the matrix elements for $h_\times$, h_+ using:

$$\Gamma = \Gamma^{\times} + \Gamma^{+} \tag{5.45}$$

We note that, after taking the approximations in Equation (5.33) and averaging the matrix elements over γ_0, the cross-terms between different parameters will vanish because of the

same reason as discussed below Equations (5.37) and (5.38), i.e.,

$$\left\langle \Gamma^{\times+}_{f_{\rm orb}\delta f} \right\rangle_{\gamma_0} \sim 0, \left\langle \Gamma^{\times+}_{f_{\rm orb}e} \right\rangle_{\gamma_0} \sim 0, \left\langle \Gamma^{\times+}_{\delta f e} \right\rangle_{\gamma_0} \sim 0 \ , \tag{5.46}$$

therefore, the diagonal terms in the inverse of the Fisher matrix, C_{ii}, can be simplified as $C_{ii} \sim \langle \Gamma_{ii} \rangle^{-1}_{\gamma_0}$, which gives the following relation (see Equation (6.8)):

$$\Delta\lambda_i = C_{ii}^{\frac{1}{2}} \sim \langle \Gamma_{ii} \rangle_{\gamma_0}^{-\frac{1}{2}} \ . \tag{5.47}$$

We can plug Equations (5.39) - (5.44) into Equation (5.45), then use Equation (5.47) to calculate the parameter measurement error:

$$\begin{aligned} \Delta f_{\rm orb} &\sim \left(\left\langle \Gamma^{\times}_{f_{\rm orb} f_{\rm orb}} \right\rangle_{\gamma_0} + \left\langle \Gamma^{+}_{f_{\rm orb} f_{\rm orb}} \right\rangle_{\gamma_0} \right)^{-\frac{1}{2}} \\ &= h^{-1} T_{\rm obs}^{-\frac{3}{2}} \left\{ \frac{2\pi^2}{3} \sum_n \frac{n^2}{S_n(n f_{\rm orb})} \right. \\ &\left. \times \left[\sin^4\Theta A_n^2 + (1 + 6\cos^2\Theta + \cos^4\Theta)(B_{n+}^2 + B_{n-}^2) \right] \right\}^{-\frac{1}{2}} \ , \end{aligned} \tag{5.48}$$

$$\begin{aligned} \Delta(\delta f) &\sim \left(\left\langle \Gamma^{\times}_{\delta f \delta f} \right\rangle_{\gamma_0} + \left\langle \Gamma^{+}_{\delta f \delta f} \right\rangle_{\gamma_0} \right)^{-\frac{1}{2}} \\ &= h^{-1} T_{\rm obs}^{-\frac{3}{2}} \left\{ \frac{2\pi^2}{3} \sum_n \frac{(1 + 6\cos^2\Theta + \cos^4\Theta)}{S_n(n f_{\rm orb})} (B_{n+}^2 + B_{n-}^2) \right\}^{-\frac{1}{2}} \ , \end{aligned} \tag{5.49}$$

$$\begin{aligned} \Delta e &\sim \left(\left\langle \Gamma^{\times}_{ee} \right\rangle_{\gamma_0} + \left\langle \Gamma^{+}_{ee} \right\rangle_{\gamma_0} \right)^{-\frac{1}{2}} \\ &= h^{-1} T_{\rm obs}^{-\frac{1}{2}} \left\{ \frac{1}{2} \sum_n \frac{1}{S_n(n f_{\rm orb})} \right. \\ &\left. \times \left[\sin^4\Theta A_n'^2 + (1 + 6\cos^2\Theta + \cos^4\Theta)(B_{n+}'^2 + B_{n-}'^2) \right] \right\}^{-\frac{1}{2}} \ . \end{aligned} \tag{5.50}$$

We emphasize that, Equations (5.48) - (5.50) serve as a lower bound of the measurement error since we exclude (h, Θ, γ_0) when analyzing the elements of the Fisher matrix. In fact, it turns out that this estimation may differ from the numerical results by orders of magnitude (see, e.g., Figure 5.3). However, we expect it to show the correct dependence of $\Delta f_{\rm orb}$, $\Delta(\delta f)$, and Δe on the observational time, as well as the orbital parameters of the binary.

5.7.3 Computing the Major and Minor Axes of Sky Error Ellipsoids

To estimate the parameter measurement errors for GW sources, we computed their Fisher matrix using the partial derivatives of the waveform with respect to 10 parameters: $f_{\rm orb}, 1-e_0, M, q, \cos\Theta, \Phi, \cos\theta, \phi, R, \psi$ (see Section 5.3.1.1). On the other hand, instead of directly estimating the errors in the spherical polar angles $\{\cos\Theta, \Phi, \cos\theta, \phi\}$, the source orientation and sky location measurement accuracy can be better described using sky error ellipsoids (see, e.g., Lang and Hughes, 2006; Kocsis et al., 2008; Kocsis et al., 2007; Mikóczi et al., 2012a). Therefore, this section will briefly summarize how to convert the Fisher matrix analysis results of $\{\cos\Theta, \Phi, \cos\theta, \phi\}$ into the major and minor axes of the corresponding sky error ellipsoids, $\{2A_s, 2B_s\}$,$\{2a_s, 2b_s\}$.

In particular, we follow the method described in Sec. VI C of Ref. (Lang and Hughes, 2006). For example, to estimate the error ellipsoid of sky location, $\{2a_s, 2b_s\}$, we first consider the relevant terms in the covariance matrix, $C = F^{-1}$, (see Equations (6.7) and (6.8)):

$$\begin{cases} \Sigma_{\cos\theta,\cos\theta} = C_{77}, \\ \Sigma_{\cos\theta,\phi} = \Sigma_{\phi,\cos\theta} = C_{78}, \\ \Sigma_{\phi,\phi} = C_{88}, \end{cases} \tag{5.51}$$

where indices 7 and 8 correspond to the parameters $\cos\theta, \phi$ in the Fisher matrix F_{ij} and covariance matrix C_{ij}.

Defining the error ellipse such that the probability of the source lying outside the ellipse is e^{-1} (Cutler, 1998), the major axis $2a_s$ and minor axis $2b_s$ of the ellipse are given by

$$2\left[\csc^2\theta\Sigma_{\cos\theta,\cos\theta}+\sin^2\theta\Sigma_{\phi,\phi}\pm\sqrt{\left(\csc^2\theta\Sigma_{\cos\theta,\cos\theta}-\sin^2\theta\Sigma_{\phi,\phi}\right)^2+4\left(\Sigma_{\cos\theta,\phi}\right)^2}\right]^{1/2} \tag{5.52}$$

Similarly, this method can be applied to the parameters $\{\cos\Theta,\Phi\}$, by substituting $\cos\theta\rightarrow\cos\Theta$, $\phi\rightarrow\Phi$ in Equations (5.51) and (5.52), yielding the major and minor axes of error ellipse for source orientation, $\{2A_s,2B_s\}$.

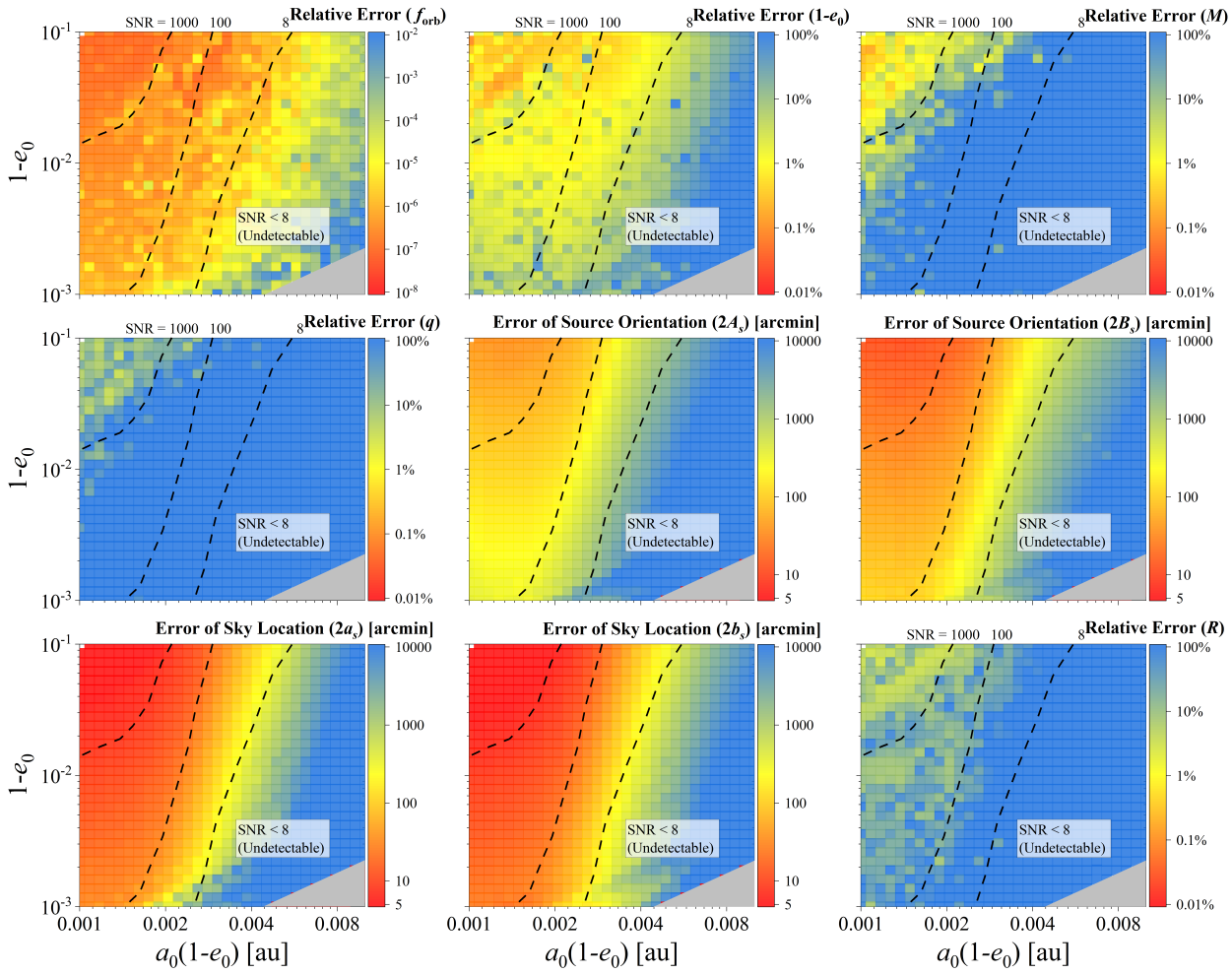


Figure 5.7: **The dependence of a compact binary's parameter measurement error on its initial pericenter distance, $r_p = a_0(1-e_0)$, and eccentricity e_0. (1-yr observation)** Here we consider the same systems as in Figure 5.3, but re-parameterize the x-axis using $r_p = a_0(1-e_0)$. We exclude the grey-colored region at the bottom of each panel since here the binary's orbital period is longer than the observation time (1 year).

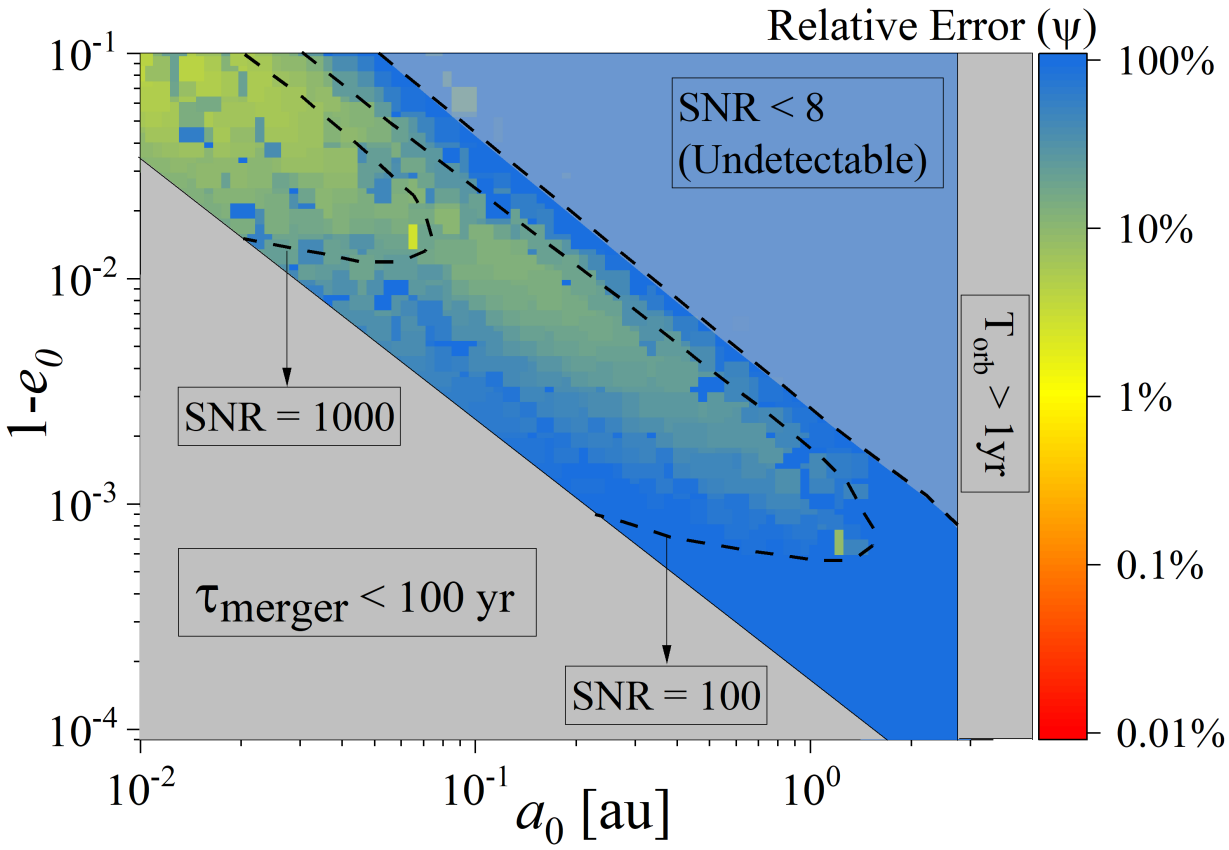


Figure 5.8: **The dependence of a compact binary's polarization angle measurement error on its semi-major axis and eccentricity, computed using the Fisher matrix analysis. (1-yr observation)** Here we consider the same systems as in Figure 5.3, but show the result according to parameter ψ for completeness.

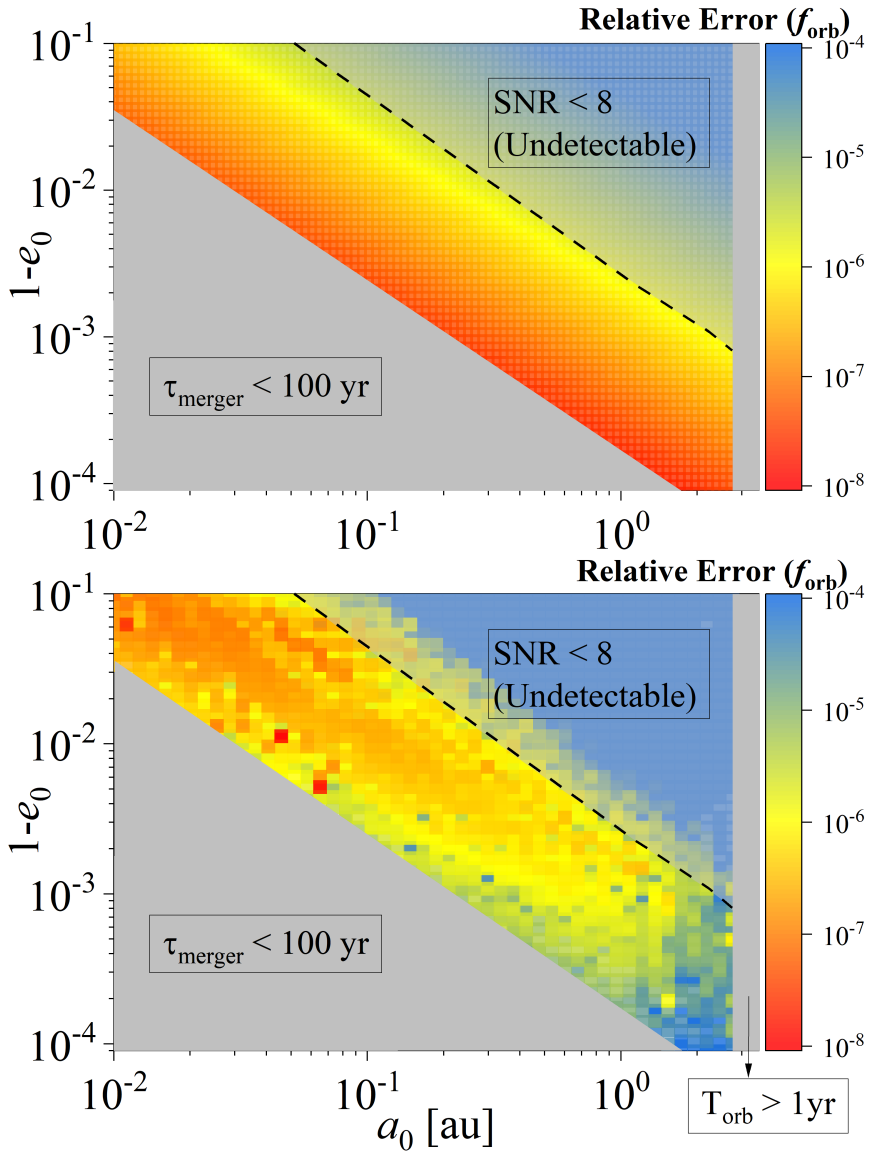


Figure 5.9: **Comparison between the analytical and numerical estimation of $f_{\rm orb}$ measurement error.** Here we consider the same systems as shown in Figure 5.3, but calculate the relative $f_{\rm orb}$ measurement error using Equation (5.18) (*Upper Panel*), and compare it with the numerical results from Fisher matrix analysis (*Bottom Panel*). As shown in the figure, the analytical approach provides an accurate estimation of $f_{\rm orb}$ measurement error in the moderate SNR region (i.e., close to the dashed line of SNR = 8). However, its performance is limited when the binary has a short merger timescale (to the bottom left of each panel) and becomes inconsistent with the Fisher matrix analysis.

Chapter 6

Localizing Dynamically-Formed Black Hole Binaries in Milky Way Globular Clusters with LISA

A version of this chapter was previously published in *The Astrophysical Journal Letters* (Xuan et al., 2025b, ApJL 985 L42).

Abstract

The dynamical formation of binary black holes (BBHs) in globular clusters (GCs) may contribute significantly to the observed gravitational wave (GW) merger rate. Furthermore, LISA may detect many BBH sources from GCs at mHz frequencies, enabling the characterization of such systems within the Milky Way and nearby Universe. In this work, we use Monte Carlo N-body simulations to construct a realistic sample of Galactic clusters, thus estimating the population, detectability, and parameter measurement accuracy of BBHs

hosted within them. In particular, we show that the GW signal from 0.7 ± 0.7, 2.0 ± 1.7, 3.6 ± 2.3, 13.4 ± 4.7 BBHs in Milky Way GCs can exceed the signal-to-noise ratio threshold of SNR = 30, 5, 3, and 1 for a 10-year LISA observation, with $\sim 50\%$ of detectable sources exhibiting high eccentricities ($e \gtrsim 0.9$). Moreover, the Fisher matrix and Bayesian analyses of the GW signals indicate these systems typically feature highly-resolved orbital frequencies ($\delta f_{\rm orb}/f_{\rm orb} \sim 10^{-7} - 10^{-5}$) and eccentricities ($\delta e/e \sim 10^{-3} - 0.1$), as well as a measurable total mass when SNR exceeds ~ 20. Notably, we show that high-SNR BBHs can be confidently localized to specific Milky Way GCs, with a sky localization accuracy of $\delta\Omega \sim 1$ deg^2, and address the large uncertainties in their distance measurement ($\delta R \sim 0.3 - 20$ kpc). The detection and localization of even a single BBH in a Galactic GC would allow accurate tracking of its long-term orbital evolution, enable a direct test of the role of GCs in BBH formation, and provide a unique probe into the evolutionary history of Galactic clusters.

6.1 Introduction

The LIGO/Virgo/KAGRA (LVK) collaboration (e.g., The LIGO Scientific Collaboration et al., 2021) has detected approximately 100 extragalactic binary black holes (BBH) mergers (e.g., Abbott et al., 2023a). However, the formation channels for these mergers remain unclear, with various proposed mechanisms potentially contributing, including isolated binary evolution (e.g., Belczynski et al., 2016; Stevenson et al., 2017; Eldridge et al., 2019); dynamical formation in galactic centers (Kocsis and Levin, 2012; Hoang et al., 2019; Stephan et al., 2019; Arca Sedda et al., 2023; Zhang and Chen, 2024a), galactic fields (Michaely and Perets, 2019, 2020; Michaely and Naoz, 2022; Stegmann et al., 2024), globular clusters (GCs) (e.g., Rodriguez et al., 2016; Fragione and Bromberg, 2019; Kremer et al., 2020), active galactic nuclei disks (Tagawa et al., 2021; Peng and Chen, 2021; Samsing et al., 2022; Muñoz et al., 2022; Gautham Bhaskar et al., 2023), hierarchical triple systems (Wen, 2003; Naoz, 2016;

Hoang et al., 2018; Antonini and Gieles, 2020), and primordial black hole scenarios (Bird et al., 2016; Sasaki et al., 2016). A key challenge in distinguishing these channels arises from the large distances and limited sky localization accuracy of extragalactic BBH mergers (e.g., Vitale and Whittle, 2018), which prevent confident identification of specific host environments. On the other hand, the future Laser Interferometer Space Antenna (LISA) (Amaro-Seoane et al., 2017b) will observe BBHs in a lower frequency band ($10^{-4} - 10^{-1}$ Hz), which potentially allows us to probe their earlier evolutionary stages in the local Universe and distinguish between different hosting environments (see, e.g., Barack and Cutler, 2004b; Mikóczi et al., 2012a; Robson et al., 2018b; Chen et al., 2019b; Hoang et al., 2019; Fang et al., 2019b; Tamanini et al., 2020b; Breivik et al., 2020; Torres-Orjuela et al., 2021; Wang et al., 2021; Xuan et al., 2021; Zhang et al., 2021; Naoz et al., 2022; Amaro-Seoane et al., 2022; Naoz and Haiman, 2023).

In particular, GCs are considered ideal places for the dynamical formation of mHz BBHs (Benacquista et al., 2001; Miller and Hamilton, 2002; Portegies Zwart and McMillan, 2002; Morscher et al., 2015; Rodriguez et al., 2015, 2016; Samsing and D'Orazio, 2019b; Samsing, 2018; D'Orazio and Samsing, 2018; Zevin et al., 2019; Kremer et al., 2019a; Gerosa et al., 2019; Vitale, 2021). For example, a large number of black holes (BHs) can form through stellar evolution in clusters (see, e.g., Kroupa, 2001; Morscher et al., 2015). Due to mass segregation, these BHs gradually sink to the cluster core on sub-gigayear timescales, leading to the formation of a BH-dominated central region (Spitzer, 1969; Kulkarni et al., 1993; Sigurdsson and Hernquist, 1993). In the BH-dominated core, dynamically hard BH binaries promptly form through three-body interactions and further harden through gravitational wave (GW) capture, binary-single, and binary-binary scattering events (Heggie, 2001; Merritt et al., 2004; Mackey et al., 2007; Breen and Heggie, 2013; Peuten et al., 2016; Wang et al., 2016; Arca Sedda et al., 2018; Kremer et al., 2018a; Zocchi et al., 2019; Zevin et al., 2019; Kremer et al., 2020; Antonini and Gieles, 2020). Collectively, these dynamical processes result in BBH merger events at an estimated rate of $\mathcal{R}_0 \approx 7.2^{+21.5}_{-5.5}\mathrm{Gpc}^{-3}\mathrm{yr}^{-1}$ in the

local universe (e.g., Rodriguez et al., 2016; Kremer et al., 2020; Antonini and Gieles, 2020), potentially making a significant contribution to the total GW merger rate detected by the LVK.

Moreover, dynamically-formed BBHs in GCs can provide valuable information about their astrophysical environment. For example, BBH mergers in a dense stellar environment typically have non-negligible eccentricity (e.g., O'Leary et al., 2009a; Thompson, 2011; Aarseth, 2012; Kocsis and Levin, 2012; Breivik et al., 2016; D'Orazio and Samsing, 2018; Zevin et al., 2019; Samsing et al., 2019; Martinez et al., 2020; Antonini and Gieles, 2020; Kremer et al., 2020; Winter-Granić et al., 2023; Rom et al., 2024), which could greatly enhance our understanding of their formation mechanisms (see, e.g., East et al., 2013; Samsing et al., 2014; Coughlin et al., 2015; Breivik et al., 2016; Vitale, 2016; Nishizawa et al., 2017; Zevin et al., 2017; Gondán et al., 2018b,a; Lower et al., 2018; Romero-Shaw et al., 2019; Moore et al., 2019; Abbott et al., 2021; The LIGO Scientific Collaboration et al., 2021; Zevin et al., 2021), improve parameter estimation accuracy (Xuan et al., 2023), or help with detecting the presence of tertiary companions through eccentricity oscillations (Thompson, 2011; Antognini et al., 2014; Hoang et al., 2018; Stephan et al., 2019; Martinez et al., 2020; Hoang et al., 2020; Naoz et al., 2020; Stephan et al., 2019; Wang et al., 2021; Knee et al., 2022). Further, as shown by recent studies, many BBHs undergo a wide (semi-major axis $a \gtrsim 0.1\,\mathrm{au}$), highly eccentric (eccentricity $e \gtrsim 0.9$) progenitor stage before the final merger (see, e.g., Kocsis and Levin, 2012; Hoang et al., 2019; Xuan et al., 2024a; Knee et al., 2024), which can also have unique imprints on mHz GW detections (Xuan et al., 2024b, 2025b).

In this work, we will explore the properties of dynamically-formed BBHs in Milky Way GCs, with a focus on their detectability and parameter measurement accuracy in the mHz GW detection of LISA. Particularly, previous studies have shown that LISA can detect a handful of BBHs formed through *isolated* binary channels in the Milky Way (see, e.g., Lamberts et al., 2018; Sesana et al., 2020; Wagg et al., 2022; Tang et al., 2024). On the other hand, with

approximately 150 GCs in the Milky Way (e.g., Harris, 1996; Baumgardt and Hilker, 2018), we expect a significant number of *dynamically*-formed BBH sources from these clusters (see, e.g., Kremer et al., 2018a), for which more specific predictions of their population are still needed.

We highlight that the detection of even a single BH in Milky Way GCs would provide a *direct test* of the role of GCs in BBH formation, offering valuable insights into the relative contributions of different formation channels to the observed BBH population. Therefore, it is essential to create a realistic sample of globular clusters that harbor binary black holes in the Milky Way, which will enable us to constrain the underlying populations of black holes and BBHs in GCs and assess which specific Galactic globular clusters are most likely to host resolvable BBHs within the LISA frequency band.

This paper is organized as follows. In Section 8.2, we introduce the simulation of globular clusters (the `CMC Cluster Catalog` cluster model) used in this work. Next, we fit the simulated clusters to Galactic globular clusters, thus estimating the population of Galactic BBHs in GCs today. Based on the simulations, we estimate the number of BBHs detectable by LISA, their eccentricity and mass distributions (see Section 8.3.2), and which specific Galactic GCs are most likely to host these sources (see Section 6.3.2). Furthermore, we adopt the Fisher matrix and Bayesian analyses in Section 6.3.3, and assess the parameter measurement accuracy of BBHs in the Milky Way GCs. In Section 7.6, we summarize the results and discuss the astrophysical implications. Throughout the paper, unless otherwise specified, we set $G = c = 1$.

6.2 Creating a Mock Galactic Sample

To assemble a realistic sample of globular cluster BBHs, we use the `CMC Cluster Catalog` cluster models of Kremer et al. (2020). This suite of models is computed using the Monte Carlo N-body dynamics code `CMC`, which includes the most up-to-date physics for studying the formation and evolution of BHs in dense clusters (for review, see Rodriguez et al., 2022). Each of the 148 independent simulations of this catalog models the gravitational dynamics and stellar evolution for each of the N stars in the system, keeping track of various properties (e.g., masses, semi-major axis, eccentricity) of all BBHs present in the cluster from formation to present day. The `CMC Cluster Catalog` has been tested rigorously against observations of Galactic globular clusters and successfully reproduces global features like surface brightness profiles, velocity dispersion profiles, and color-magnitude diagrams (Rui et al., 2021) as well as specific compact object populations including millisecond pulsars (Ye et al., 2019), X-ray binaries (Kremer et al., 2019a), cataclysmic variables (Kremer et al., 2021), and connections to BBHs observed by LIGO/Virgo (Kremer et al., 2020).

For this study, we aim to predict which specific Galactic GCs are most likely to host resolvable LISA sources at present. In this case, we must identify a single "best-fit" model from the `CMC Cluster Catalog` for each observed Milky Way GC. The `CMC Catalog` models can be sorted into a three-dimensional grid in $M_{\rm cl} - Z - R_{\rm gc}$ space, where $M_{\rm cl}$ is the total cluster mass at present (set by our choice of initial $N = [2, 4, 8, 16, 32] \times 10^5$ stars and evolved to the current value), $Z = [0.01, 0.1, 1] \times Z_\odot$ is the current cluster metallicity, and $R_{\rm gc} = [2, 8, 20]\,{\rm kpc}$ is the current Galactocentric position. For a given observed GC, we identify the appropriate $M_{\rm cl} - Z - R_{\rm gc}$ model bin based on that GC's observed mass and metallicity values (taken from Harris, 2010). Each distinct $M_{\rm cl} - Z - R_{\rm gc}$ bin contains 4 models of varying initial virial radius, which determines the clusters' final core and half-light radius. To find the single best-fit model, we identify the model in the appropriate $M_{\rm cl} - Z - R_{\rm gc}$ bin which has

core radius at $t = 12\,\mathrm{Gyr}$ closest to the observed core radius value (Harris, 2010).[1] Once the best fit model is identified, we select a cluster age by randomly sampling from that model's available time snapshot outputs in the range $8 - 13.7\,\mathrm{Gyr}$ (typically this consists of a sample of 10-50 snapshots per model). This range is intended to reflect the uncertainty in cluster ages at present. Once a cluster snapshot is selected, we then identify the number and properties of all BBHs present in the best-fit model at that time. By repeating these steps for each observed GC, we build a sample of the full population of BBHs present in each of the Milky Way's GCs at present. We then repeat this full procedure ten times to assemble ten separate Galactic realizations (the random time snapshot draw enables us to create distinct ten distinct samples).

Once this population is assembled, we compute the gravitational wave strain for each of the individual BBHs predicted within each Galactic cluster at present. Component masses, semi-major axes, and eccentricities are obtained directly from our best-fit `CMC` snapshot and the source distance and position is simply the heliocentric distance of the GC of interest (Harris, 2010).

Figure 8.3 shows an example of the simulated BBH population in Milky Way GCs. In particular, we choose one representative Galactic realization from the best-fit result of the `CMC Catalog`, and plot the orbital frequency ($f_{\rm orb}$) and the peak GW frequency ($f_{\rm peak}$) of each BBH system (e.g., O'Leary et al., 2009a):

$$f_{\rm peak} = f_{\rm orb}(1+e)^{1/2}(1-e)^{-3/2}\,. \tag{6.1}$$

We note that most of the dynamically-formed systems have non-negligible eccentricity. In this case, $f_{\rm peak}$ of the eccentric GW signal indicates the frequency of the peak GW power, which typically needs to be within the mHz band for LISA to detect the source. Furthermore,

[1] We also tried fitting using half-light radius in place of core radius, and found no major differences in our results.

in Figure 8.3, we can estimate the eccentricity of each system by comparing $f_{\rm peak}$ and $f_{\rm orb}$ (see the dashed lines with $e = 0.99, 0.97, 0.9, 0.7, 0.2, 0$, from left to right). For example, a system with $f_{\rm peak} \sim f_{\rm orb}$ should have moderate eccentricity, and a system with $f_{\rm peak} \gg f_{\rm orb}$ is highly eccentric.

In Figure 8.3, we use different colors to represent the signal-to-noise ratio (SNR) of BBHs, which is estimated analytically by summing the contributions from all the harmonics of their GW signal (see, e.g., Peters and Mathews, 1963; Kocsis and Levin, 2012; Xuan et al., 2024a):

$$\mathrm{SNR}^2 = 8h_0^2(a) \sum_n \frac{g(n,e)}{S_n(nf_{\rm orb})n^2} T_{\rm obs} \ , \tag{6.2}$$

in which $n = 1, 2, 3...$ represents the number of harmonics, $T_{\rm obs}$ is the observation time, and $h_0(a) = \sqrt{32/5}\, m_1 m_2/(Ra)$ depends on the binary's component mass m_1, m_2, semi-major axis a, and distance R. Additionally, $S_{\rm n}(f)$ is the spectral noise density of LISA evaluated at GW frequency f (we adopt the LISA-N2A5 noise model, see, e.g., Klein et al., 2016a; Robson et al., 2019a), and $g(n,e)$ can be evaluated using:

$$\begin{aligned} g(n,e) \ &= \tfrac{n^4}{32} \Big[\big(J_{n-2} - 2eJ_{n-1} + \tfrac{2}{n} J_n + 2eJ_{n+1} - J_{n+2} \big)^2 \\ &\quad + (1-e^2) \left(J_{n-2} - 2J_n + J_{n+2} \right)^2 + \tfrac{4}{3n^2} J_n^2 \Big] \ , \end{aligned} \tag{6.3}$$

in which J_i is the i-th Bessel function evaluated at ne.

We note that the estimation of SNR in Equation (7.33) is based on the sky-average power of GW emission. In reality, the inclination and sky location of the GW source will also affect the detected SNR, making it different from the average value. Therefore, the value of SNR shown in Figure 8.3 should be understood as a heuristic estimation (in most cases, the variation in SNR caused by different inclinations is within an order of magnitude of the average value). For a detailed discussion, see the appendix of Xuan et al. (2024a).

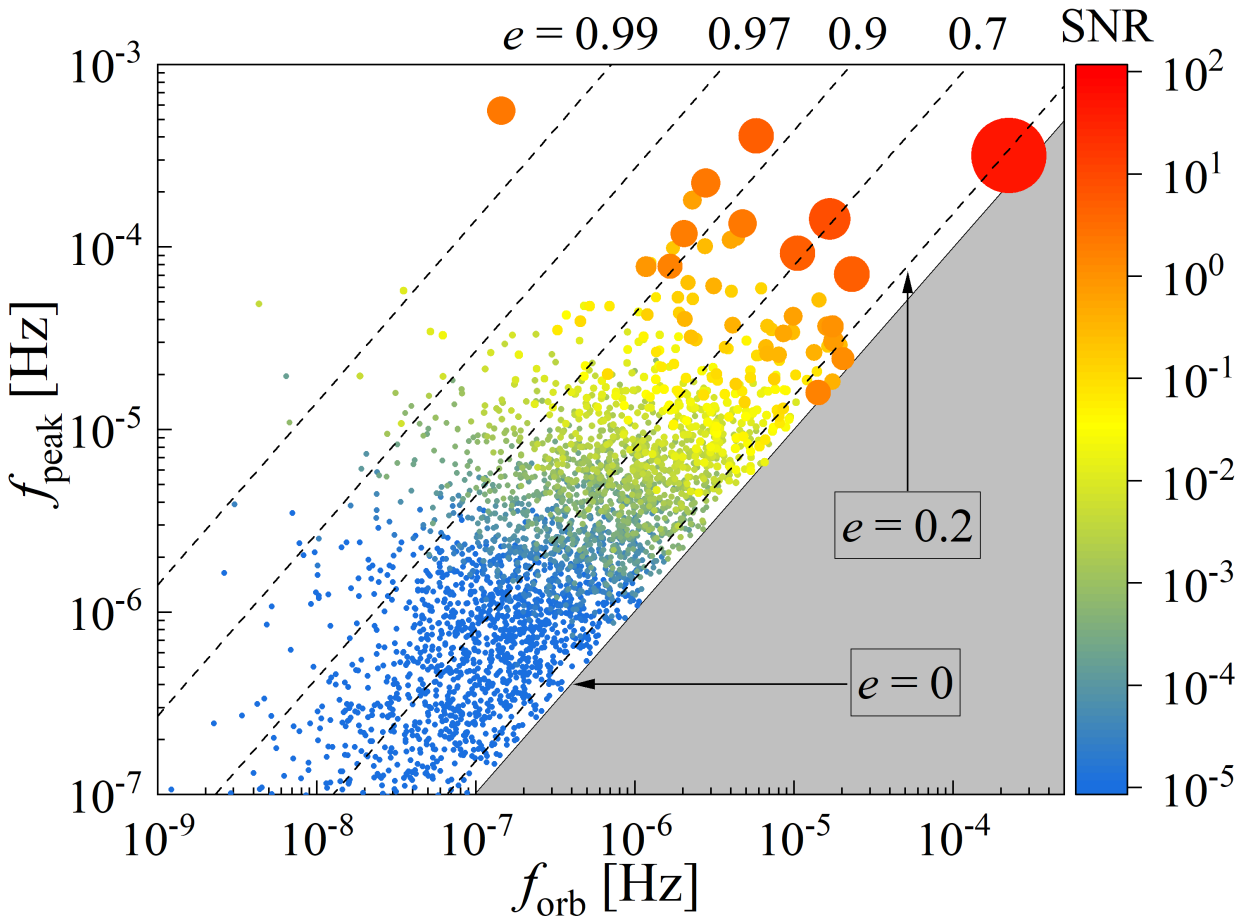


Figure 6.1: **An example of simulated BBHs population in Milky Way GCs.** Here, we plot the orbital frequency and peak GW frequency of BBH systems from a single realization of our simulated Milky Way GCs (see Equation (7.2)). The SNR of each BBH, estimated analytically using Equation (7.33) for a 5-year LISA observation, is represented by different colors. Detectable BBHs, based on their SNR, are highlighted with enlarged dots. Dashed lines indicate the eccentricity of BBHs in different regions, with $e = 0.99, 0.97, 0.9, 0.7, 0.2, 0$, from left to right. The simulated BBHs have an average component mass of $m_1 = 15.56\ \mathrm{M}_\odot$, $m_2 = 15.21\ \mathrm{M}_\odot$ for in-cluster BBHs and $m_1 = 20.73\ \mathrm{M}_\odot$, $m_2 = 20.46\ \mathrm{M}_\odot$ for ejected BBHs, but the mass of individual systems may vary.

As can be seen in Figure 8.3, the simulated orbital frequency and eccentricity of BBHs in Milky Way GCs distribute in a wide range of parameter space, with the majority of the binaries lying below the threshold of SNR = 5 for a 5-year LISA observation. However, there can be a handful of detectable sources with both moderate and high eccentricities. For example, we identified 3 detectable sources in this realization, which have the orbital parameters of $f_{\rm orb} = 2.24 \times 10^{-4}, 1.67 \times 10^{-5}, 5.79 \times 10^{-6}$ Hz ($a = 0.0075, 0.048, 0.079$ au) and $e = 0.17, 0.71, 0.93$, respectively. Furthermore, there is a larger number (~ 20) of highly eccentric BBHs in the region of SNR $\sim 1-5$ (see the orange and yellow dots), which could be detected by LISA given a longer observation time, or contribute to a stochastic background of GW bursts (see, e.g., Xuan et al., 2024b).

6.3 Source Localization and Astrophysical Implications

6.3.1 Detectability and Eccentricity Distribution

Based on the simulation in Section 8.2, we computed the expected number of detectable BBHs formed in Milky Way GCs. In total, we expect the GW signal from 0.7 ± 0.7, 2.0 ± 1.7, 3.6 ± 2.3, 13.4 ± 4.7 BBHs to exceed the threshold of SNR = 30, 5, 3, and 1, respectively, for a 10-year observation of LISA [2]. Furthermore, the simulation yields significant eccentricity for all the detectable BBH systems, with the eccentricity ranges from 0.167 - 0.994 for systems with SNR > 3, which is consistent with the expected eccentricity distribution of dynamically-formed binaries in GCs (see, e.g., Kremer et al., 2018a, for a LISA source expectations from Newtonian modeling of GCs).

We highlight that $\sim 50\%$ of the BBHs with SNR > 5 have high eccentricity in the detection

[2]Here the error bar reflects the standard derivative of BBH number in each SNR bin, accounting for 10 realizations in the simulation (see Section 8.2).

($e \gtrsim 0.9$); the fraction becomes even larger ($\sim 70\%$) for the population with SNR $\sim 1-5$. This phenomenon reflects the highly eccentric nature of compact binary formation in a dense stellar environment. It also indicates that most of the GW signals from BBHs in Galactic GCs will be characterized by "repeated bursts" (Xuan et al., 2024a), for which the detectability and parameter extraction accuracy have been recently investigated (Xuan et al., 2025b).

The large fraction of highly eccentric BBHs can be understood analytically. In particular, the GW signal from eccentric binaries is made up of multiple harmonics, some of which have frequencies much higher than the binary's orbital frequency (see, e.g., Equation (7.2)). Therefore, compared with circular BBHs, eccentric sources in GCs could enter the sensitive band of LISA with a much wider orbital separation a, when their $f_{\rm orb}$ is well below the mHz band. In other words, these eccentric binaries will be detected at the earlier evolution stages, with more extended lifetimes and larger number expectations than circular sources in the same frequency band. For example, highly eccentric, stellar mass BBHs can stay in the mHz GW band with a lifetime of (Peters and Mathews, 1963; Xuan et al., 2024b):

$$\begin{aligned}\tau_{\rm ecc} &\sim \frac{3}{85\mu M^2} a^4 \left(1-e^2\right)^{7/2} \\ &\sim 1.17\times 10^6 {\rm yr}\, \frac{2}{q(1+q)} \left(\frac{M}{20{\rm M}_\odot}\right)^{-3} \left(\frac{a}{1{\rm au}}\right)^4 \left(\frac{1-e}{0.002}\right)^{\frac{7}{2}},\end{aligned} \tag{6.4}$$

where $M = m_1 + m_2$, $\mu = m_1 m_2/(m_1+m_2)$, and $q = m_1/m_2$. Note that this timescale is much longer than the merger timescale of a circular BBH system in mHz band (which typically lasts for $\sim 10^3 - 10^5$ years). Thus, these highly eccentric BBHs may dominate the population of BBHs in the local Universe, where their GW signals are strong enough to be identified. [3]

Additionally, binary mergers originating from GCs can be categorized into different types,

[3] However, stellar mass BBHs at larger distances are unlikely to be detected with high eccentricity (e.g., at a few hundred Mpc, detectable BBHs in GCs have eccentricities of at most 0.01, as shown in Kremer et al. (2019b)). This is because highly eccentric sources, in general, have a smaller power of GW emission, but LISA can only detect high-SNR GW sources at cosmological distances.

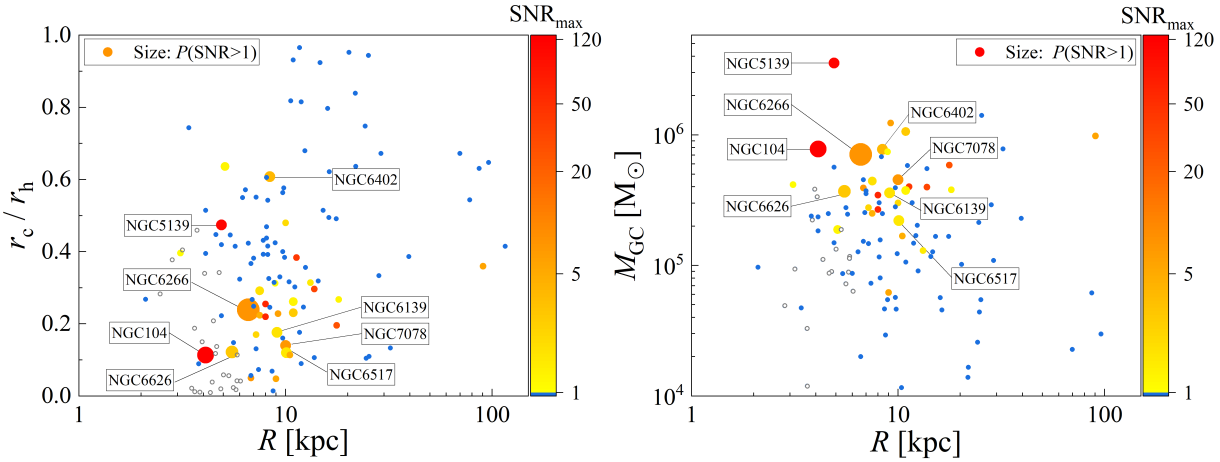


Figure 6.2: **Properties of Milky Way globular clusters likely to host detectable BBHs in the mHz GW band.** Here we adopt the simulation results of the BBH population in the Milky Way GCs, based on 10 realizations of in-cluster sources. The size of solid dots represents the expected probability for a cluster to host a BBH system with SNR > 1, $P(\mathrm{SNR} > 1)$, and the color represents the maximum SNR of detectable BBHs, assuming a 10-year observation. *Left Panel* plots the distance R (x-axis) against the ratio of the core radius to the half-light radius, r_c/r_h (y-axis); *Right Panel* plots the distance R (x-axis) against the estimated total mass $M_{\rm GC}$ of each globular cluster. The largest dot corresponds to the GC hosting 9 BBHs with SNR > 1 across the 10 realizations (i.e., an expected probability of $\sim 90\%$), while the smallest dots represent GCs hosting 1 BBH system with SNR > 1 (expected probability $\sim 10\%$). Solid blue dots represent GCs with no detectable BBHs (maximum SNR < 1), and hollow gray dots represent GCs without any BBHs in the simulation. We highlight the names of the top 8 GCs most likely to host detectable BBHs.

based on their evolution history. On top of the binaries merging within the GC after dynamical interactions (in-cluster mergers), a significant fraction of BBHs can undergo multiple hardening encounters before being ejected from the cluster, eventually merging in the galactic field (ejected mergers; see, e.g., Downing et al., 2010; Rodriguez et al., 2016, 2018; Kremer et al., 2019b). In our simulations, we find that in-cluster BBHs contribute approximately 0.7, 1.5, 2.2, and 5.8 GW sources, while the ejected population contributes around 0, 0.5, 1.4, and 7.6 GW sources above the thresholds of SNR = 30, 5, 3, and 1, respectively, for a 10-year LISA observation.

6.3.2 The Location of Gravitational Wave Sources

Next, we analyze which specific Galactic globular clusters are most likely to host resolvable BBHs, using the `CMC Catalog` from Kremer et al. (2020). In particular, we take the observational properties of Milky Way GCs following Harris (2010) (see dots in Figure 6.2), and choose the best-fit model in the `CMC Catalog` that matches the mass, metallicity, Galactic position, and core radius of each cluster (see Section 8.2). For each fitted cluster, we then compute the population properties of BHs and estimate their expectation of hosting a detectable BBH system.

The results are summarized in Figure 6.2. Specifically, *Left Panel* depicts the ratio of the clusters' core radius to the half-light radius, r_c/r_h (y-axis), versus their distance, R, from the detector (x-axis); *Right Panel* shows the estimated total mass of each cluster, $M_{\rm GC}$, against their distance R (x-axis) (see Harris (2010)). In Figure 6.2, the size of solid dots represents the expected probability for a cluster to host a BBH system with SNR > 1:

$$P(\mathrm{SNR} > 1) = \frac{N_{\mathrm{SNR}>1}}{N_{\mathrm{realization}}} \ , \tag{6.5}$$

where $N_{\mathrm{realization}} = 10$ represents the total number of realizations for Milky Way GCs (see

Section 8.2), and $N_{\rm SNR>1}$ represents the total number of BBHs with SNR > 1 in a GC, summed across all the realizations.

The color of dots in Figure 6.2 represents the detectability of their largest SNR GW source in the simulation, with colors ranging from yellow to red. Furthermore, we use solid blue dots to represent GCs with no detectable BBHs (maximum SNR < 1) and hollow gray dots to represent GCs without any BBHs in the simulation at all. In the Figure, we highlight the names of the eight fitted GCs that we predict are most likely to host detectable BBHs.

As illustrated in Figure 6.2, GCs with a high probability of hosting detectable BBHs tend to cluster within specific regions of the parameter space. Notably, we predict detectable BBHs are most likely to be resolved in GCs that are close in distance ($R \lesssim 10$ kpc), exhibit a small r_c/r_h ($\sim 0.1 - 0.3$, indicative of denser, more dynamically-active GCs, see *Left Panel*), and have a large total mass (see *Right Panel*).

6.3.3 Astrophysical Implication

In this section, we first adopt the Fisher matrix analysis to explore the astrophysical information that can be extracted from dynamically-formed BBHs in Milky Way GCs. This method is commonly used as a linearized estimation of the parameter measurement error in the high SNR limit (see, e.g., Coe, 2009; Cutler and Flanagan, 1994). For completeness, we briefly summarize the relevant equations and waveform model used in this work (see our previous works Xuan et al., 2023, 2025b, for similar applications).

We begin by defining the noise-weighted inner product between two gravitational waveforms, $h_1(t)$ and $h_2(t)$, as follows:

$$\langle h_1 \mid h_2 \rangle = 2 \int_0^\infty \frac{\tilde{h}_1(f)\tilde{h}_2^*(f) + \tilde{h}_1^*(f)\tilde{h}_2(f)}{S_{\rm n}(f)} {\rm d}f \ , \tag{6.6}$$

where $\tilde{h}_l$ (with $l = 1, 2$) denotes the Fourier transform of the waveform, and the star represents the complex conjugate.

Representing the parameters of a GW source as a vector $\boldsymbol{\lambda}$, the GW waveform h can be expressed as $h(t; \boldsymbol{\lambda})$. The Fisher matrix is then defined as:

$$F_{ij} = \left\langle \frac{\partial h(\boldsymbol{\lambda})}{\partial \lambda_i} \middle| \frac{\partial h(\boldsymbol{\lambda})}{\partial \lambda_j} \right\rangle . \tag{6.7}$$

where λ_i denotes the i-th parameter of the waveform.

Let C denote the inverse of the Fisher matrix, $C = F^{-1}$. This matrix approximates the sample covariance matrix of the Bayesian posterior distribution for the parameters of the GW source. Using this, we estimate the error in parameter measurement as follows:

$$\delta\lambda_i = \sqrt{\left\langle (\Delta\lambda_i)^2 \right\rangle} = \sqrt{C_{ii}} \ . \tag{6.8}$$

To evaluate Equations (7.20) - (6.8) numerically, we further compute the GW signal, $h(t)$, from eccentric BBHs. Specifically, we adopt the x-model (Hinder et al., 2010) for the waveform generation, assuming that the binaries undergo isolated evolution during observation. The x-model is a time-domain, post-Newtonian (pN)-based waveform family, designed to capture all key features introduced by eccentricity in non-spinning binaries (Huerta et al., 2014). It has been validated against numerical relativity for equal mass BBHs with $e = 0.1$, covering 21 cycles before the merger, and also aligns with well-established waveform template families used in GW data analysis for the zero-eccentricity case (Brown and Zimmerman, 2010). In this model, the binary orbit is described using the Keplerian parameterization at 3pN order, with the conservative evolution also given to 3pN order. The energy and angular momentum losses are mapped to changes in the orbital eccentricity e and the pN expansion parameter $x \equiv (\omega M)^{2/3}$, where ω is the mean Keplerian orbital frequency. These two pa-

rameters evolve according to 2 pN equations. We note that, stellar-mass BBHs in the local universe typically have a pericenter distance larger than $\sim 10^{-3}$au in the mHz GW band (including the highly eccentric BBHs, see, e.g., Xuan et al. (2024a,b)). Thus, their gravitational field is much weaker than the strength of the field for which the x-model has been validated against numerical relativity, and the x-model represents a plausible description of their GW signal[4].

Furthermore, we include the detector's annual motion around the Sun to analyze the realistic detection of Milky Way BBHs (the detector response function, see, e.g., Cutler (1998); Cornish and Rubbo (2003); Kocsis et al. (2007) for more details). Consequently, the GW signal from an eccentric binary can be parameterized using:

$$h(t) = h(t; \boldsymbol{\lambda} = \{f_{\rm orb,0}, 1-e_0, M, q, \cos\Theta, \Phi, \cos\theta, \phi, R, \psi\}), \tag{6.9}$$

in which $f_{\rm orb,0}, e_0$ are the initial orbital frequency and eccentricity of the binary [5], Θ and Φ represent the spherical polar angles of the observer as viewed in the non-rotating, comoving frame of the compact object binary (i.e., the propagation direction of the GW signal viewed in the source's frame); θ and ϕ are the spherical polar angles describing the sky location of the GW source viewed in the comoving frame of the solar system, where the LISA detector undergoes annual motion around the sun; R is the binary's distance from the detector (which is set as the distance of the GC hosting this binary), and ψ is the polarization angle of the GW signal. For more details on the parameterization, see Sec. B in Xuan et al. (2025b).

After generating the GW signal as described by Equation (6.9), we compute the partial

[4]Also, there have been recent studies focusing on fast and accurate waveform generation, such as for the case of eccentric extreme mass ratio inspirals (EMRIs) (Chua et al., 2021; Hughes et al., 2021; Katz et al., 2021). However, the mass ($\sim 10\,{\rm M}_\odot$) and eccentricity range ($\sim 0.1-0.999$) of BBHs we discuss here are different. Therefore, we adopt the x-model for simplicity.

[5]Hereafter, we use $f_{\rm orb}$ as an abbreviation for the initial orbital frequency $f_{\rm orb,0}$, which is related to the initial semi-major axis a_0 via $f_{\rm orb,0} = (2\pi)^{-1} M^{1/2} a_0^{-3/2}$; and use e as an abbreviation for the initial eccentricity e_0.

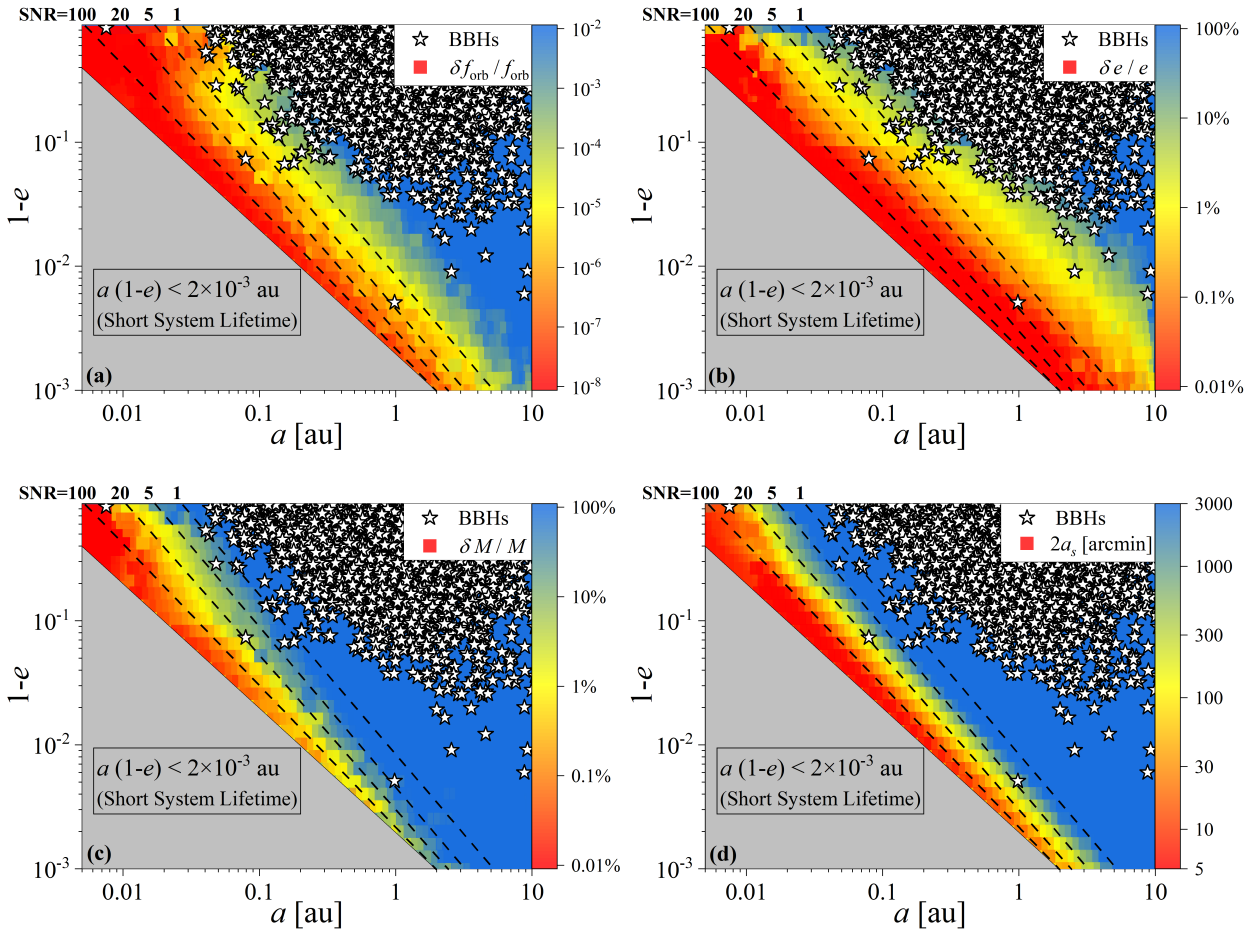


Figure 6.3: **The population of BBHs from simulated Milky Way GCs, and their estimated parameter measurement error as a function of semi-major axis and eccentricity (for 5-yr observation).** Here, we adopt the simulation result of the compact binary population in the Milky Way globular clusters (see Section 8.2, note that here we show a single realization of the in-cluster and ejected BBHs from Milky Way GCs), and plot the semi-major axis and eccentricity (as $1-e$) of each BBH system (see the white stars). The background color maps the compact binary's parameter measurement error, for the orbital frequency ($\delta f_{\rm orb}/f_{\rm orb}$, *Panel a*), eccentricity ($\delta e/e$, *Panel b*), total mass ($\delta M/M$, *Panel c*), and sky location (major axis of sky error ellipsoid, $2a_s$, *Panel d*). We note that, in reality, the BBHs can have different mass, inclination, and sky locations, which affects their parameter measurement. However, for simplicity, here we assume a fixed intrinsic parameter of $m_1 = 10\ {\rm M}_\odot$, $m_2 = 15\ {\rm M}_\odot$, $R = 8$ kpc and $\Phi = \Theta = \theta = \phi = \psi = \pi/4$ when estimating the Fisher matrix and mapping the parameter measurement accuracy. In each panel, the dashed lines represent equal signal-to-noise ratio contours (analytically calculated using Equation (7.33)), with SNR = 1, 5, 20, 100 from right to left. We exclude the parameter space where the binary has a pericenter distance smaller than $a(1-e) < 2\times10^{-3}$ au, since they have a short merger timescale and negligible number expectation in our simulation.

derivatives of the waveform with respect to each parameter (see Equation (6.7)). For example, to calculate $\partial h/\partial M$, we vary the total mass $M \to M' = M + \Delta M$, and generate a new waveform $h'(t) = h'(t; \boldsymbol{\lambda}')$, where $\boldsymbol{\lambda}' = \{f_{\rm orb}, 1-e, M+\Delta M, q, \cos\Theta, \Phi, \cos\theta, \phi, R, \psi\}$. The partial derivative is then approximated as $\partial h/\partial M \approx [h'(t) - h(t)]/\Delta M$. Note that each partial derivative is a time series representing the difference in the waveform caused by slightly varying one of the parameters around the central value. Also, in the numerical computation, we choose the parameter variation $d\lambda_i$ such that $\langle dh|\ dh\rangle \sim 10^{-3}\,\langle h|\ h\rangle$, ensuring the change in the waveform is small when computing the numerical derivative.

Finally, we compute the inner products between derivative waveforms using Equation (7.20), then substitute the results into Equation (6.7) to calculate F_{ij}. The parameter measurement errors are then estimated by inverting F_{ij}, as described in Equation (6.8)). We summarize the results in Figures 6.3 - 6.4 (note that Fisher matrix analysis yields the measurement error for all the parameters, $\{f_{\rm orb,0}, 1-e_0, M, q, \cos\Theta, \Phi, \cos\theta, \phi, R, \psi\}$, but here we only show some of them to avoid clustering).

In Figure 6.3, we present a realistic example of the parameter measurement error for BBHs in Milky Way GCs. The white stars in the figure represent all the in-cluster and ejected BBHs from one realization of our simulated Milky Way GCs. In the background, we use different colors to show the parameter measurement errors, $\delta\lambda_i$, as a function of the BBHs' orbital parameters, $(a, 1-e)$. Particularly, *Panel a* shows the relative error in orbital frequency measurement, $\delta f_{\rm orb}/f_{\rm orb}$; *Panel b* shows the relative error in eccentricity measurement, $\delta e/e$; *Panel c* shows the relative error in total mass, $\delta M/M$; and *Panel d* shows the absolute error in sky location ($2a_s$, as the major axis of the sky error ellipsoids, see e.g., Lang and Hughes (2006); Kocsis et al. (2008); Kocsis et al. (2007); Mikóczi et al. (2012a)). To ensure consistency in mapping the parameter measurement errors, we fix specific BBH parameters when computing the Fisher matrix results shown in Figure 6.3 ($m_1 = 10$ M$_\odot$, $m_2 = 15$ M$_\odot$, $R = 8$ kpc and $\Phi = \Theta = \theta = \phi = \pi/4$, assuming a 5-year observation). However, BBHs in

Milky Way GCs can have different mass, inclination, and sky locations, which potentially affects their parameter measurement [6]. Therefore, the value shown by background colors in Figure 6.3 should be interpreted as heuristic estimates of the realistic accuracy.

We highlight that the estimation shown in Figure 6.3 is agnostic to different BBH formation channels. In other words, for any potential BBH population in the galaxy, not necessarily from the GCs, their orbital parameter $(a, 1-e)$ can be over-plotted on the figure to estimate the parameter measurement errors in a similar way. Moreover, Figure 6.3 indicates that our analysis of the parameter measurement accuracy is robust to variations in simulation results. For example, in *Panels a and b*, regions with SNR > 1 (to the left of the dashed line at SNR $= 1$) show $\delta f_{\rm orb}/f_{\rm orb} \lesssim 10^{-5}$ and $\delta e/e \lesssim 10\%$. This suggests that, in realistic observations, BBH systems detected in the Milky Way GCs can typically achieve high accuracy measurements of $f_{\rm orb}$ and e. Furthermore, as shown by *Panel c*, BBHs with SNR > 20 can have a mass measurement accuracy of $\delta M/M \lesssim 10\%$. However, marginally detectable sources may have poorly constrained total mass (blue regions near the dashed line of SNR $= 5$). Similarly, *Panel d* shows that BBHs with SNR > 20 can have a sky localization accuracy of $2a_s \lesssim$ 300 arcmins (yellow regions), which indicates that high-SNR BBHs can generally be localized with an angular resolution of a few degrees in the Milky Way.

In Figure 6.4, we summarize all BBHs with SNR > 3 (assuming a 5-year observation) from the simulation and compute their exact parameter measurement errors. These BBHs are drawn from 10 realizations in total, excluding the ejected population due to the poor constraints on their location within the Milky Way. In particular, *Upper Panel* shows the relative errors in orbital frequency and eccentricity measurements; *Middle Panel* shows the relative error in total mass and mass ratio measurements; and *Bottom Panel* shows the absolute error in the distance (x-axis) and sky localization (y-axis) measurements. In each panel, we use different colors to show the SNR of BBHs and the shape of dots to show

[6] We note that, the parameter measurement accuracy in Figure 6.3 can be rescaled for BBHs with different distances, see Eq.14 in Xuan et al. (2025b) for more details.

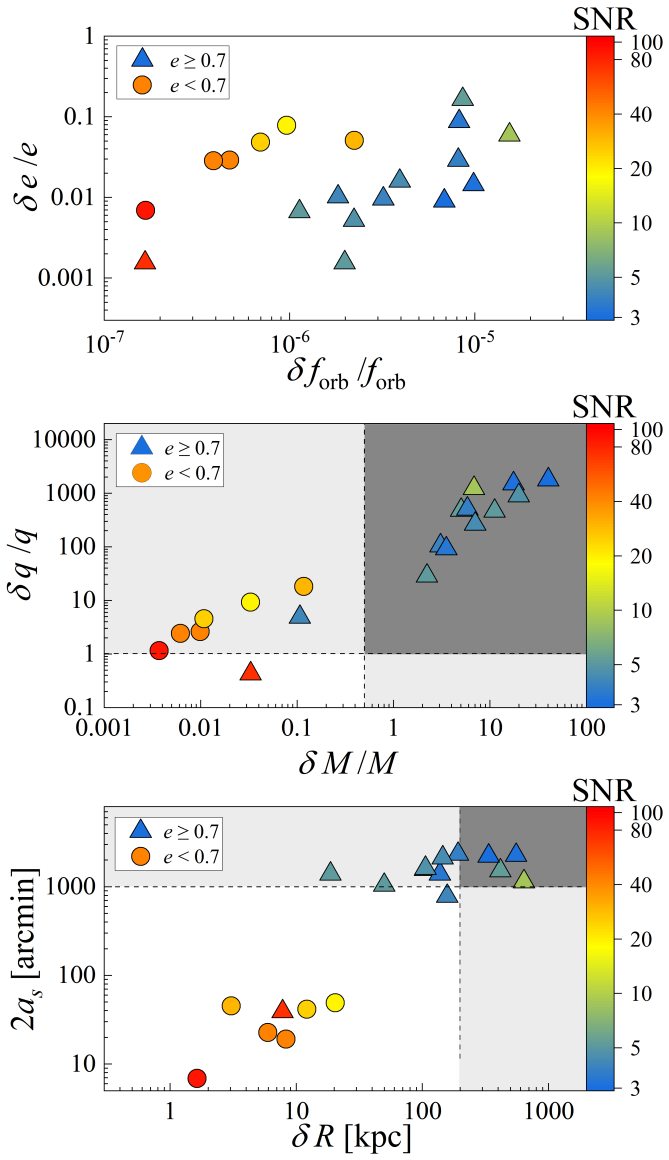


Figure 6.4: **Parameter Measurement error of the detectable BBHs in simulated Milky Way GCs, estimated using Fisher matrix analysis.** Here we adopt the simulation results of BBHs population in Milky Way GCs, with a total of 10 realizations. Each point in the figure represents a BBH system in the simulation, with the color showing the SNR of its GW signal (assuming a 5-year observation) and the shape showing the eccentricity of the orbit ($e > 0.7$, plotted in triangles; $e < 0.7$, plotted in circles). *Upper Panel* shows the relative error of orbital frequency and eccentricity measurement. *Middle Panel* shows the relative error of total mass and mass ratio measurement. In *Bottom Panel*, we show the absolute error of the BBHs' distance measurement (x-axis), and their sky localization accuracy (as the major axis of the sky error ellipsoids, $2a_s$, on the y-axis). We exclude the parameter space where measurement accuracy is insufficient to help with the astrophysical interpretation, as marked using grey-shaded regions.

the eccentricity ($e > 0.7$, plotted in triangles; $e < 0.7$, plotted in circles). Additionally, we exclude the parameter space where measurement accuracy is insufficient for astrophysical interpretation, as marked using grey-shaded regions. Specifically, in the *Middle Panel*, regions with $\delta M/M > 50\%$ and $\delta q/q > 100\%$ are excluded, as the BBHs in these regions are indistinguishable from other compact binary sources, such as binary neutron stars (BNSs) or double white dwarfs (DWDs). Similarly, in the *Bottom Panel*, BBHs with $2a_s > 1000$ arcmins ($\sim 5-10$ times the typical tidal radius of the Milky Way GCs) and $\delta R > 200$ kpc (halo radius of the Milky Way) cannot be confidently localized within a Milky Way globular cluster.

As shown in the *Upper Panel*, most detectable BBHs in Milky Way GCs have well-constrained orbital frequency and eccentricity. In particular, the fractional error in orbital frequency, $\delta f_{\rm orb}/f_{\rm orb}$, reaches an accuracy of $\sim 10^{-7} - 10^{-5}$ for BBHs with SNR > 3, which indicates a frequency resolution of $\delta f_{\rm orb} \lesssim 10^{-10}$ Hz in LISA data analysis (see, e.g., Eq.18 in Xuan et al., 2025b, for an analytical explanation). Furthermore, all sources in Figure 6.4 have eccentricity measurement errors below $\delta e/e < 1$, which allows us to confidently detect non-zero eccentricities and distinguish dynamically-formed BBHs from circular binaries created via isolated evolutionary channels. Additionally, highly eccentric sources typically exhibit higher accuracy in eccentricity measurement, with $\delta e/e$ reaching $\sim 0.1\% - 10\%$ for BBHs with $e > 0.7$. This trend is consistent with the results of our previous works (Xuan et al., 2023), which shows that eccentricity can break the degeneracy of waveform and significantly enhance the parameter measurement. In general, accurate measurements of orbital frequency and eccentricity can provide valuable insights into the long-term evolution of BBHs, enable the detection of potential environmental effects, and help infer different formation channels.

On the other hand, mHz GW detection may be less sensitive to the mass of BBHs in the Milky Way, primarily due to degeneracies in the waveform [7]. For example, most BBHs

[7]Note that we expect most detectable BBHs in the Milky Way to be long-living systems, thus their orbital evolution is slow and their chirp rate is hard to measure (see, e.g. Section 3.2 in Xuan et al., 2024a).

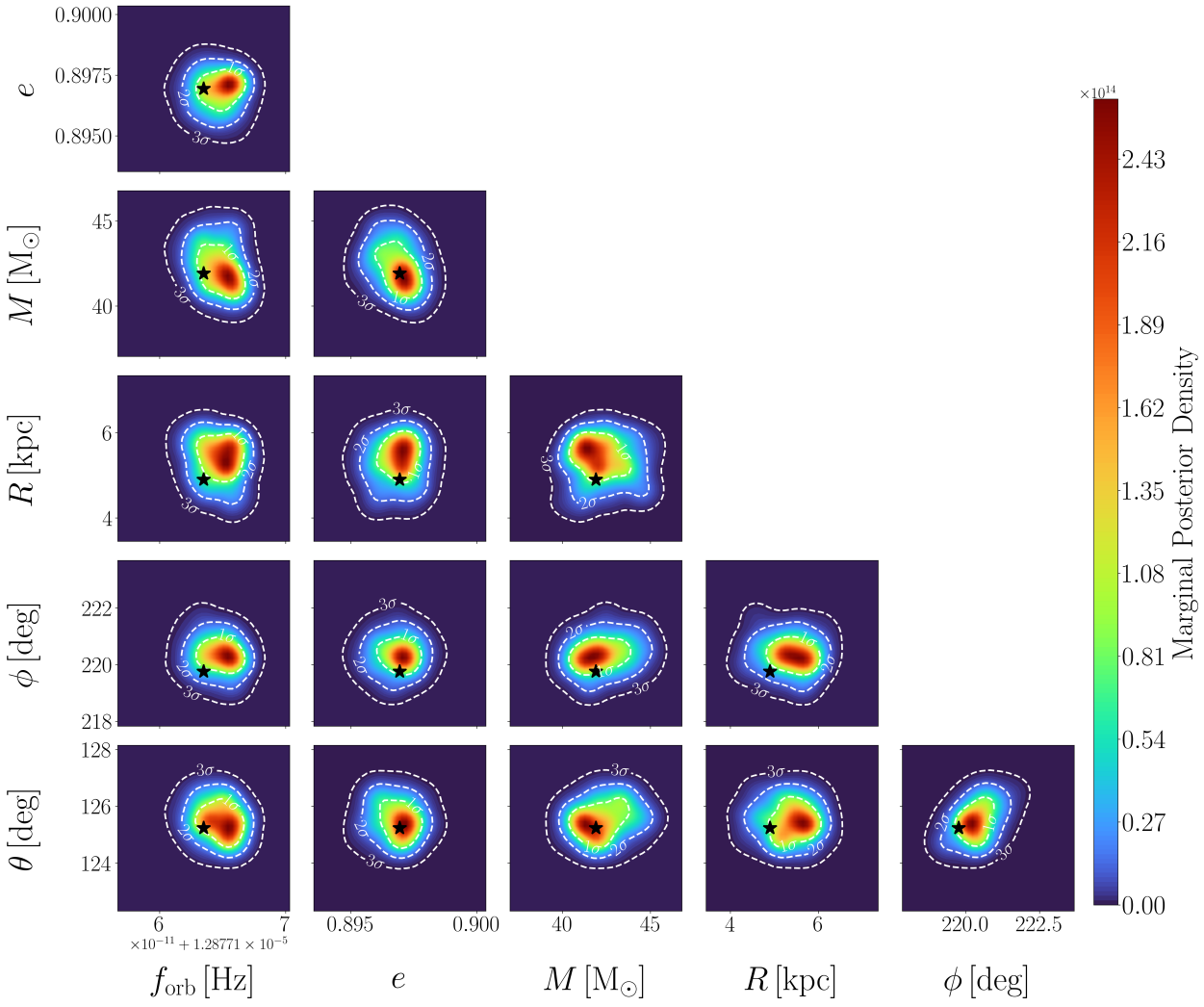


Figure 6.5: **Parameter Measurement error of an example BBH system in Milky Way Globular Clusters, estimated using Bayesian analysis (for 5-yr observation).** Here we consider a BBH system with $m_1 = 23.3$ M$_\odot$, $m_2 = 18.6$ M$_\odot$, $f_{\rm orb} = 1.2877164 \times 10^{-5}$ Hz, $e = 0.897$, $R = 4.9$ kpc, $\Phi = 158.7°$, $\Theta = 141.4°$, $\phi = 219.9°$, $\theta = 125.2°$, $\psi = 153.9°$. (Note that this system has SNR ~ 77, and we keep 8 significant digits of $f_{\rm orb}$ to highlight its realistic measurement accuracy.) The color maps show the marginal posterior density of the binary's observed parameters, assuming a flat, 10-dimensional hyperrectangular prior and stationary Gaussian LISA noise. We use the star in each panel to indicate the system's intrinsic parameters, and plot 68%, 95%, and 99.7% credible regions for the marginal posterior densities (i.e, $1 - 3\,\sigma$ level sets defined analogously to a bivariate Gaussian density). To avoid clutter, we plot the results for the binary's intrinsic parameters $f_{\rm orb}$, e, M; distance R; and sky location ϕ, θ, which are mostly relevant to its astrophysical inference. Additionally, the peak of posterior density exhibits a small offset from some parameters' intrinsic value (typically within 1σ level), which is caused by the random fluctuation of time-domain LISA noise and the limit of numerical accuracy for highly eccentric binary waveforms.

in the *Middle Panel* do not have a well-constrained mass ratio, with the relative error of measurement exceeding $\delta q/q \gtrsim 100\%$ (except for one highly eccentric BBH system with SNR ~ 75, indicated by the red triangle in the bottom-left corner of *Middle Panel*). However, the total mass measurement is sufficiently accurate for a significant fraction of detectable BBHs, reaching $\delta M/M \sim 1\% - 10\%$ for sources with SNR $\gtrsim 20$ (see the red and orange dots to the left of the dashed line). Therefore, we expect LISA to accurately measure the mass of these high-SNR BBHs in the Milky Way GCs, making them distinguishable from BNSs and DWDs.

Furthermore, we highlight that, LISA can accurately localize most BBHs with SNR > 20 in Milky Way GCs (see the red and orange dots in *Bottom Panel*). In particular, these GW sources have a sky localization accuracy of $\sim 10 - 100$ arcmins (i.e., less than a few degrees), which is comparable to the typical diameter of Milky Way GCs ($\sim 10 - 120$ arcmins [8]). Additionally, while the distance of BBHs is less precisely constrained compared to their sky location, most systems with SNR > 20 have a distance measurement error of $\delta R \sim 1 - 100$ kpc in the Milky Way. Given the significant distance to the nearby galaxies (e.g., the Andromeda Galaxy is located at ~ 780 kpc), we expect these BBHs to be distinguishable from extragalactic GW sources.

6.3.4 Further Validation of BBH Localization Using Bayesian Analysis

As shown by Section 6.3.3, LISA has the potential to confidently localize a BBH system in specific Milky Way GCs, which could provide unique information about the Milky Way's compact binary formation and the dynamical environment of GCs. In this section, we further

[8] Note that detectable BBHs are more likely to be hosted by nearby, massive GCs (see Section 6.3.2); as a result, their host clusters tend to have larger angular sizes than the general Milky Way GC population. For BBHs with SNR > 1, the average host GC diameter is ~ 38 arcmins (see Figure 6.6 in the Appendix).

verify this point using a Bayesian analysis and address the uncertainty introduced by the BBHs' distance measurement.

First, we note that, although the Fisher matrix analysis adopted in Section 6.3.3 has been widely used to estimate the parameter measurement error for LISA sources, this method can sometimes yield inaccurate results, particularly for degenerate parameters or parameters with weak influences on the shape of GW signal (see, e.g., Vallisneri, 2008; Toubiana et al., 2020). Consequently, the parameter measurement accuracy presented in Figures 6.3 and 6.4 should be interpreted as a heuristic estimation. Nevertheless, these estimates provide compelling evidence that BBHs in Milky Way GCs are promising targets for inferring their astrophysical properties.

To further validate the Fisher matrix results, we performed a full 10-dimensional Bayesian analysis for individual systems (see, e.g., Finn, 1992; Cutler and Flanagan, 1994; Christensen and Meyer, 1998; Christensen and Meyer, 2001), as shown in Figure 6.5 and Table 6.1. Particularly, in Figure 6.5, we choose an example BBH system from the simulation results ($m_1 = 23.3$ M$_\odot$, $m_2 = 18.6$ M$_\odot$, $a = 0.06332$ au, $e = 0.897$, $R = 4.9$ kpc), and inject its GW signal $s_0(t; \boldsymbol{\lambda})$[9] into a simulated stationary Gaussian LISA noise $n(t)$, which yields the mock LISA signal:

$$z(t) = s_0(t; \boldsymbol{\lambda}) + n(t) \ . \tag{6.10}$$

We then adopted Monte-Carlo sampling, generating GW templates $s(t; \boldsymbol{\lambda}')$ with parameters slightly different from their intrinsic values of $\boldsymbol{\lambda}$, and computing their inner product with the mock signal (see Equation (7.20)):

$$\langle z \mid s \rangle = 2 \int_0^\infty \frac{\tilde{z}(f)\tilde{s}^*(f) + \tilde{z}^*(f)\tilde{s}(f)}{S_\mathrm{n}(f)} \mathrm{d}f \ . \tag{6.11}$$

[9]Note that this system has SNR ~ 77 for 5-yr observation, and the detector response function is included in $s_0(t)$, see Section 6.3.3.

Assuming a uniform hyperrectangular prior, the posterior probability density of the observed parameters can be computed using the aforementioned inner products (see, e.g., Eqs 1-6 in Christensen and Meyer (2001)):

$$p(\boldsymbol{\lambda}' \mid z) \propto p(z \mid \boldsymbol{\lambda}') = K \exp[2\langle z \mid s(\boldsymbol{\lambda}')\rangle - \langle s(\boldsymbol{\lambda}') \mid s(\boldsymbol{\lambda}')\rangle] \ , \tag{6.12}$$

where K is a constant.

As shown in Figure 6.5, the marginal posterior density of the binary's observed parameters, as indicated by the color maps, yields a parameter measurement error comparable with the Fisher matrix estimation. Particularly, the Fisher matrix estimation of this example BBH system is represented by the red triangle to the bottom-left of each panel in Figure 6.4, with its parameter measurement error $\delta f_{\rm orb} \sim 2.1 \times 10^{-12}$ Hz, $\delta e \sim 1.4 \times 10^{-3}$, $\delta M \sim 1.4$ $M_\odot$, $\delta R \sim 7.8$ kpc, and sky localization accuracy $2a_s \sim 39$ arcmin~ 0.65 degrees. These values are generally consistent with the 1σ levels in Bayesian analysis, which yields $\delta f_{\rm orb} \sim 2.8 \times 10^{-12}$ Hz, $\delta e \sim 1.2 \times 10^{-3}$, $\delta M \sim 3.1$ $M_\odot$, $\delta R \sim 1.1$ kpc, and sky localization accuracy ~ 1.3 degrees (see Figure 6.5). Therefore, the Bayesian study of this specific case partly justifies the Fisher matrix results of Figures 6.3 and 6.4. We also show the Bayesian analysis results of a BBH with SNR ~ 9 (see Figure 6.7 in the appendix), which validates the parameter measurement accuracy for sources in the marginal detection case.

Using the aforementioned method, we showcase three representative systems from the mock Milky Way GC catalog, with $e = 0.1671 - 0.8969$ (see Table 6.1 in the appendix). To better describe the sources' localization accuracy, we convert the posterior of their sky location angles, (ϕ, θ), into the solid angle of the corresponding sky area $\delta\Omega_{\rm Bayesian}$ (68% credible region). We then compare $\delta\Omega_{\rm Bayesian}$ with the area of sky error ellipsoid from Fisher matrix analysis, $\delta\Omega_{\rm Fisher}$, and the size of their host GCs. As shown in Table 6.1, the Fisher matrix and Bayesian analysis generally yield consistent results in the sources' sky localization accuracy,

although the Fisher results are systematically smaller by a factor of ~ 2 in angular size estimation (or ~ 5 in sky area). Furthermore, for high-SNR BBHs (see, e.g., the three systems with SNR $= 35 - 94$ in Table 6.1), their sky area accuracy from both Fisher matrix and Bayesian analysis, $\sim 0.40, 1.00, 1.85$ deg^2, are comparable with (or even smaller than) the size of their host clusters, $\sim 2.84, 2.13, 0.52$ deg^2.[10] These results further confirm that BBHs in the Milky Way can be localized to the sky area of specific host GCs, especially for significant detection cases.

Notably, Figures 6.4-6.5 and Table 6.1 indicate a distance measurement error of $\delta R \sim 1 - 100$ kpc for the Milky Way BBH sources, which is much larger than the tidal diameter of globular clusters (typically on the order of a few tens of pc). Therefore, LISA is unlikely to directly associate the spatial position of a BBH system with its host GC because of the large uncertainty in the radial distance measurement. However, when determining the host environment of BBH sources, this uncertainty can be resolved, mostly because stellar density in the Milky Way halo is much lower than that of GCs. In other words, the total number of stars in a BBH-hosting GC ($\sim 10^5 - 10^6$, see Figure 6.2) is much larger than the total number of halo stars in other parts of the error volume[11], which makes it highly possible that a detected source is hosted in the cluster instead of other regions of the local universe.

For example, assuming a halo stellar mass density of $\rho_{\rm halo} \sim 10^{-4} {\rm M}_\odot/{\rm pc}^3$ (Deason et al., 2019), the total halo stellar mass in the error volume $V_{\rm err}$ of GW detection can be estimated as:

$$M_{\rm halostars} = \rho_{\rm halo} \times V_{\rm err} \sim \rho_{\rm halo} R^2 \delta R \delta \Omega_{\rm Bayesian} \ , \tag{6.13}$$

which yields $M_{\rm halostars} \sim 51 {\rm M}_\odot, 1.5 \times 10^3 {\rm M}_\odot, 6.5 \times 10^4 {\rm M}_\odot$ for the first three confidently-localized systems in Table 6.1. These values are much smaller than the total stellar mass

[10] However, marginally detectable BBHs (SNR ~ 8) can have poor sky localization. For example, the system in Figure 6.7 has a sky localization error of ~ 233 deg^2 in Bayesian analysis, far exceeding the angular size of its host cluster NGC7078 (~ 0.39 deg^2).

[11] Note that most GCs reside in the Galactic halo (see,e.g., Harris, 2010).

of their host GCs, which is estimated as $M_{\rm GC} \sim 7 \times 10^5 {\rm M}_\odot, 1.5 \times 10^6 {\rm M}_\odot, 2 \times 10^5 {\rm M}_\odot$ for NGC104, NGC5139, and NGC6341, respectively (see, e.g., Marks and Kroupa, 2010).

We note that the relative contributions of GCs and the Galactic field to the total BBH merger rate remain uncertain (see Mandel and Broekgaarden, 2022, for a review). However, recent studies suggest both are likely contributing at a comparable rate (see, e.g., Zevin et al., 2021; Fishbach and Fragione, 2023). Furthermore, even if the galactic field has a larger contribution to the *total* merger rate, considering the significant difference in total stellar mass between the field ($\sim 10^{10} {\rm M}_\odot$ for the Milky Way; Cautun et al., 2020) and GCs ($\sim 10^7 {\rm M}_\odot$ for the Milky Way; Harris, 2010), the BBH merger rate *per unit stellar mass* in GCs is likely comparable to, or higher than in the field. Thus, we assume that all stellar mass (in the Galactic halo and in globular clusters) has an equal probability of hosting a BBH source. Under this assumption, the probability that a given BBH resides in a GC can be estimated as:

$$P_{\rm incluster} \sim \frac{M_{\rm GC}}{M_{\rm GC} + M_{\rm halostars}} \ . \tag{6.14}$$

Therefore, once a source is accurately located in the sky area of a GC, the probability for the system to be a GC BBH source can be significantly boosted, especially because a globular cluster contributes to the majority of stellar mass in the error volume. Additionally, the highly eccentric formation nature of BBHs in GC (see, e.g., Section 8.3.2) can also help with distinguishing them from other BBHs from isolated evolution channels in the galactic field, which are expected to have negligible eccentricities (e.g., Belczynski et al., 2016; Stevenson et al., 2017; Eldridge et al., 2019). [12]

[12] However, the localization method discussed earlier in this section is agnostic to the expected eccentricity distributions of different BBH formation channels. For example, if a population of eccentric BBHs is accurately localized toward the Galactic field rather than any GCs, this method can also distinguish it from the in-cluster BBH population.

6.4 Discussion

In this work, we explore the realistic detectability and parameter measurement accuracy of BBHs in Galactic GCs for observations with LISA. Particularly, since GCs are considered ideal environments for the dynamical formation of BBHs (see, e.g., Miller and Hamilton, 2002; Rodriguez et al., 2015; Samsing, 2018), constraining their detectability potential is of prime importance for the community. Notably, Kremer et al. (2018a) predicted that LISA might detect a significant number of BBH sources from ~ 150 GCs in the Milky Way, with various orbital parameters. Furthermore, many dynamically-formed BBHs can undergo a wide ($a \gtrsim 0.1\,\mathrm{au}$), highly eccentric ($e \gtrsim 0.9$) progenitor phase before merger (Kocsis and Levin, 2012; Hoang et al., 2019; Xuan et al., 2024a,b, 2025b; Knee et al., 2024), which has been recently proposed to have unique imprints on the mHz GW detection. By detecting these eccentric sources, we can distinguish between different formation mechanisms (East et al., 2013; Samsing et al., 2014; Coughlin et al., 2015; Breivik et al., 2016; Vitale, 2016; Nishizawa et al., 2017; Zevin et al., 2017; Gondán et al., 2018b,a; Lower et al., 2018; Romero-Shaw et al., 2019; Moore et al., 2019; Abbott et al., 2021; The LIGO Scientific Collaboration et al., 2021; Zevin et al., 2021), enhance the parameter measurement accuracy (such as the orbital frequency evolution and source location, see Xuan et al., 2023, 2025b), and probe the potential presence of tertiary companions through eccentricity oscillations (Thompson, 2011; Antognini et al., 2014; Hoang et al., 2018; Stephan et al., 2019; Martinez et al., 2020; Hoang et al., 2020; Naoz et al., 2020; Stephan et al., 2019; Wang et al., 2021; Knee et al., 2022).

Using `CMC Cluster Catalog` of Kremer et al. (2020) we generate a best-fit model for each Milky Way globular cluster [13], and estimate the BBH population within these clusters (illustrated in Figure 8.3). We then generate the BBHs' GW signals using the x-model (Hinder et al., 2010), which incorporates the dynamics of eccentric compact binaries up to 3PN order.

[13] Which is computed using the Monte Carlo N-body dynamics code `CMC`.

Additionally, the waveform analysis includes the detector's annual motion around the Sun so that our results can represent the realistic detection of GW signals. More details of the waveform model and analysis method can be found in Xuan et al. (2025b).

Based on the simulation, we compute the number of detectable BBHs formed in Galactic GCs (see Section 8.3.2). In total, we expect the GW signal from 0.7 ± 0.7, 2.0 ± 1.7, 3.6 ± 2.3, 13.4 ± 4.7 BBHs to exceed the threshold of SNR = 30, 5, 3, and 1, respectively, for a 10-year observation of LISA. Among all these sources, in-cluster BBHs contribute to 0.7, 1.5, 2.2, and 5.8 GW sources, and the ejected population contributes to $\sim$ 0, 0.5, 1.4, and 7.6 GW sources above the threshold of SNR = 30, 5, 3, 1. We highlight that $\sim$ 50% of the BBHs with SNR $>$ 5 has high eccentricity in the detection ($e \gtrsim 0.9$), which reflects the dominant population of eccentric BBHs in GCs (as they are long-living sources, see, e,g., Equation (7.1)), and indicates that most of the GW signals from BBHs in Milky Way GCs are characterized by highly eccentric "GW bursts" in future LISA detection (see, e.g., Xuan et al., 2024a).

Furthermore, we analyze the properties of Galactic GCs that are most likely to host resolvable LISA sources (see Figure 6.2). Specifically, we calculate the expected probability for a cluster to host a BBH system with SNR $>$ 1 during a 10-year LISA observation. As shown in Figure 6.2, these BBH-hosting GCs tend to cluster within specific regions of the parameter space, where the GCs have a close distance to the detector ($R \lesssim 10$ kpc), exhibit a small r_c/r_h ($\sim 0.1 - 0.3$), and have a large total mass.

To evaluate the measurement accuracy achievable with LISA, we performed a Fisher matrix analysis on the simulated BBH population, as illustrated in Figures 6.3 and 6.4. Particularly, Figure 6.3 maps the intrinsic parameters, $(a, 1-e)$, of the simulated Milky Way GC BBH population and uses the background color to show their different parameter measurement errors (5-year observation); Figure 6.4 depicts the measurement error of $\{f_{\rm orb}, e, M, q, R, 2a_s\}$ for all the simulated BBHs with SNR $>$ 3, across all the 10 realizations, for 5-year observa-

tion. As illustrated in both figures, most of the BBHs with SNR > 3 have well-constrained orbital frequency and eccentricity, reaching $\delta f_{\rm orb}/f_{\rm orb} \sim 10^{-7} - 10^{-5}$ and $\delta e/e < 1$. Furthermore, eccentricity can, in general, enhance the measurement accuracy, with $\delta e/e$ reaching $\sim 10^{-3} - 0.1$ for detectable BBHs with $e > 0.7$. On the other hand, BBHs with SNR > 20 can have a total mass measurement accuracy of $\delta M/M \lesssim 10\%$, but most of the marginally detectable sources may not have a well-constrained total mass and mass ratio. Also, we expect BBHs with SNR > 20 to be confidently localized with an angular resolution of $\sim 10 - 100$ arcmins, which enables us to localize these sources in specific Milky Way GCs.

In Section 6.3.4, we adopt Bayesian analysis to verify the localization accuracy of BBH sources. As shown in Figure 6.5 and Table 6.1, the full 10-dimensional Bayesian analysis for individual BBH sources yields parameter measurement error (at the 1σ levels of the marginal posterior distributions) that are consistent with those from Fisher matrix analysis, within one order of magnitude. Notably, Table 6.1 presents localization results for representative systems from the mock Milky Way GC catalog. For BBHs with SNR $= 35$, 77, and 94, the typical sky localization errors exhibit similar values ($\sim 1\text{deg}^2$) compared to their host cluster size. This result further confirms LISA's potential to confidently localize BBHs within individual Galactic GCs. Additionally, Milky Way BBH sources typically have large uncertainty in their radial distance measurement ($\sim$ 1–100 kpc). However, as shown in Equations (6.13)-(6.14), once a BBH is localized within the sky area of a GC, the probability of its cluster origin is significantly enhanced due to the large number of stars in GCs ($\sim 10^5$–10^6 stars) compared to the stars within the rest of the error volume (i.e., the low-density Galactic halo).

Although our collective sample of GC simulations effectively spans the full parameter space of Galactic GCs (Kremer et al., 2020), this simulation suite is a grid, which inevitably means some specific observed GCs do not necessarily have a strong "one-to-one" model match. For example, Ref. Rui et al. (2021), demonstrated how the `CMC Catalog` may be augmented with

additional models to match particular GCs with observed properties lying in between grid points. In another recent study, Ye et al. (2022) showed that especially massive GCs like 47 Tuc (NGC 104) may require additional adjustments (in particular variations to the initial density profile and initial stellar mass function) to produce a precise model match. The ideal solution is to produce a separate model for every single Galactic cluster (for some examples, see Kremer et al., 2018b, 2019a; Ye et al., 2022, 2024); however, this is computationally expensive, and outside the scope of the current study. We tested the LISA predictions from our best-fit model for NGC 104 with the predictions from the more precise model in Ye et al. (2022), and found that the number of LISA sources is consistent within a factor of 3 for SNR$>$ 1. Furthermore, the multimodality of the posterior, particularly in angular parameters, can pose additional challenges for accurate sky localization (see, e.g., Marsat et al., 2021). However, a comprehensive analysis of this effect is beyond the scope of the present work.

Additionally, this work simulates the BBH population in observed GCs of the Milky Way, which does not include other potential GW sources in the local galaxy, such as BBHs formed in the Galactic nucleus, Galactic Field, and evaporated GCs. Thus, the number expectation presented here only serves as a lower bound for the LISA detection. Notably, the high computational cost of $N-$body simulation limits the sample size presented in this paper (in total 10 realizations), which may result in uncertainty of the predicted BBH population. However, the prediction of source number and parameter measurement accuracy in this work is expected to be a realistic estimation, based on one of the most up-to-date simulations of GCs (Kremer et al., 2020). Also, the population properties presented here agree with previous works with different GC models (see, e.g., Kremer et al., 2018a), which indicates the robustness of the result that LISA can detect a handful of BBHs formed in the Milky Way GCs.

To conclude, mHz-frequency BBHs in Milky Way GCs have the potential to enable direct

test of the role of GCs in the formation of GW sources. Given a 5-10 year LISA observation, these systems typically have highly-resolved orbital frequency ($\delta f_{\rm orb}/f_{\rm orb} \sim 10^{-7} - 10^{-5}$) and eccentricity ($\delta e/e \sim 10^{-3} - 0.1$), as well as a measurable total mass when the signal-to-noise ratio exceeds ~ 20. Furthermore, these high SNR BBHs can be confidently localized in a specific GC of the Milky Way, with an angular resolution of $\sim 10 - 100$ arcmins in the sky. Therefore, we highlight the potential of detecting BBHs in Milky Way GCs, which allows for accurate tracking of their long-term orbital evolution, distinguishing the compact binary formation mechanisms, and understanding the properties of GCs in the local galaxy.

6.5 Acknowledgments

The authors thank the anonymous referee for their valuable feedback and helpful suggestions. ZX acknowledges partial support from the Bhaumik Institute for Theoretical Physics summer fellowship. ZX and SN acknowledge the partial support from NASA ATP Grant No. 80NSSC20K0505 and from NSF-AST Grant No. 2206428 and thank Howard and Astrid Preston for their generous support. Further, ZX, KK and SN thank LISA Sprint 2024 for organizing an interactive and productive meeting.

6.6 Appendix

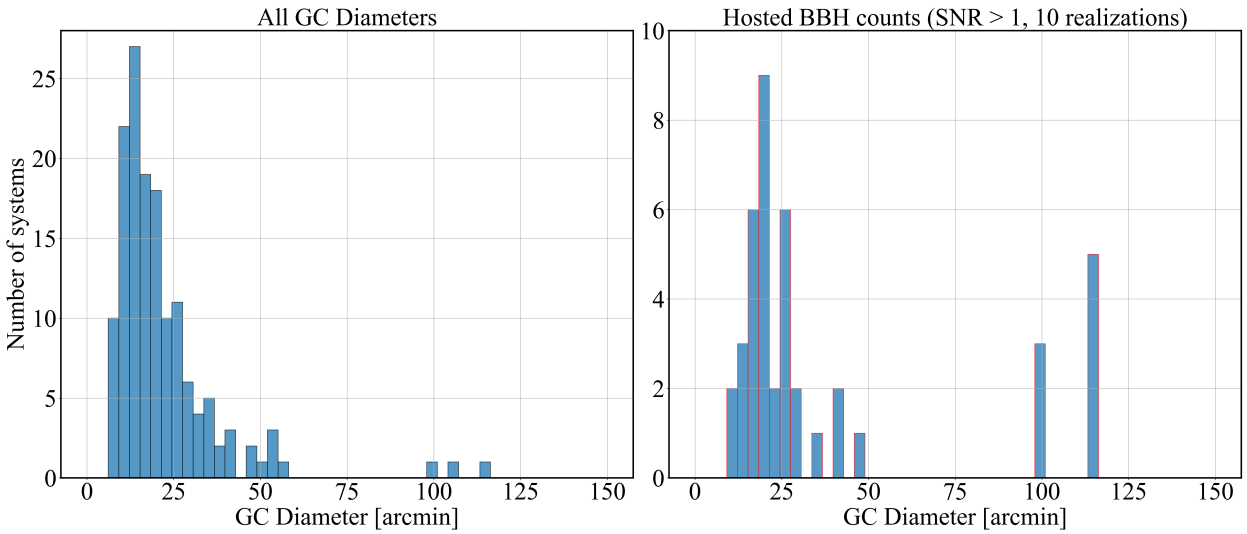


Figure 6.6: **Histogram of Milky Way GC angular diameters and their hosted BBH counts.** Here we show the distribution of GC angular diameters (left), taken from the Milky Way Star Clusters Catalog (Kharchenko et al., 2012, 2013; Schmeja et al., 2014; Scholz et al., 2015), and the number of hosted BBH systems with SNR > 1 in each GC diameter bin (right), based on 10 realizations from the `CMC Cluster Catalog`. The difference between the left and right panels arises because detectable BBH systems tend to be hosted by more massive and nearby GCs, which also have a larger angular size.

Table 6.1: Sky location and distance measurement accuracy of representative systems in the mock Milky Way GC catalog, compared with their host cluster size (5-yr observation)

Host Cluster	Cluster Size [deg^2]	$\delta\Omega_{\rm Bayesian}$ [deg^2]	$\delta\Omega_{\rm Fisher}$ [deg^2]	δR [kpc]	M [M$_\odot$]	a [au]	e	SNR (5-yrs)
NGC104	2.84	0.40	0.073	0.25	29.5	0.01102	0.2803	94
NGC5139	2.13	1.00	0.17	2.16	41.9	0.06332	0.8969	77
NGC6341	0.52	1.85	0.38	18.0	21.2	0.00750	0.1671	35

Note: Here $\delta\Omega_{\rm Bayesian}$ represents the sky area of 68% credible regions of the marginal posterior densities (see, e.g., the bottom right panel of Figure 6.5); $\delta\Omega_{\rm Fisher} = \pi a_s b_s$ represents the area of sky error ellipsoid, as estimated by Fisher matrix analysis; δR shows the distance measurement accuracy, as of 3σ level from Bayesian analysis; M, a, e represent the total mass, semi-major axis, and eccentricity of the binary system, respectively. For comparison purposes, we show the name and sky area of each binary's host cluster (inferred from their angular radius in the Milky Way Star Clusters Catalog, Kharchenko et al., 2012, 2013; Schmeja et al., 2014; Scholz et al., 2015).

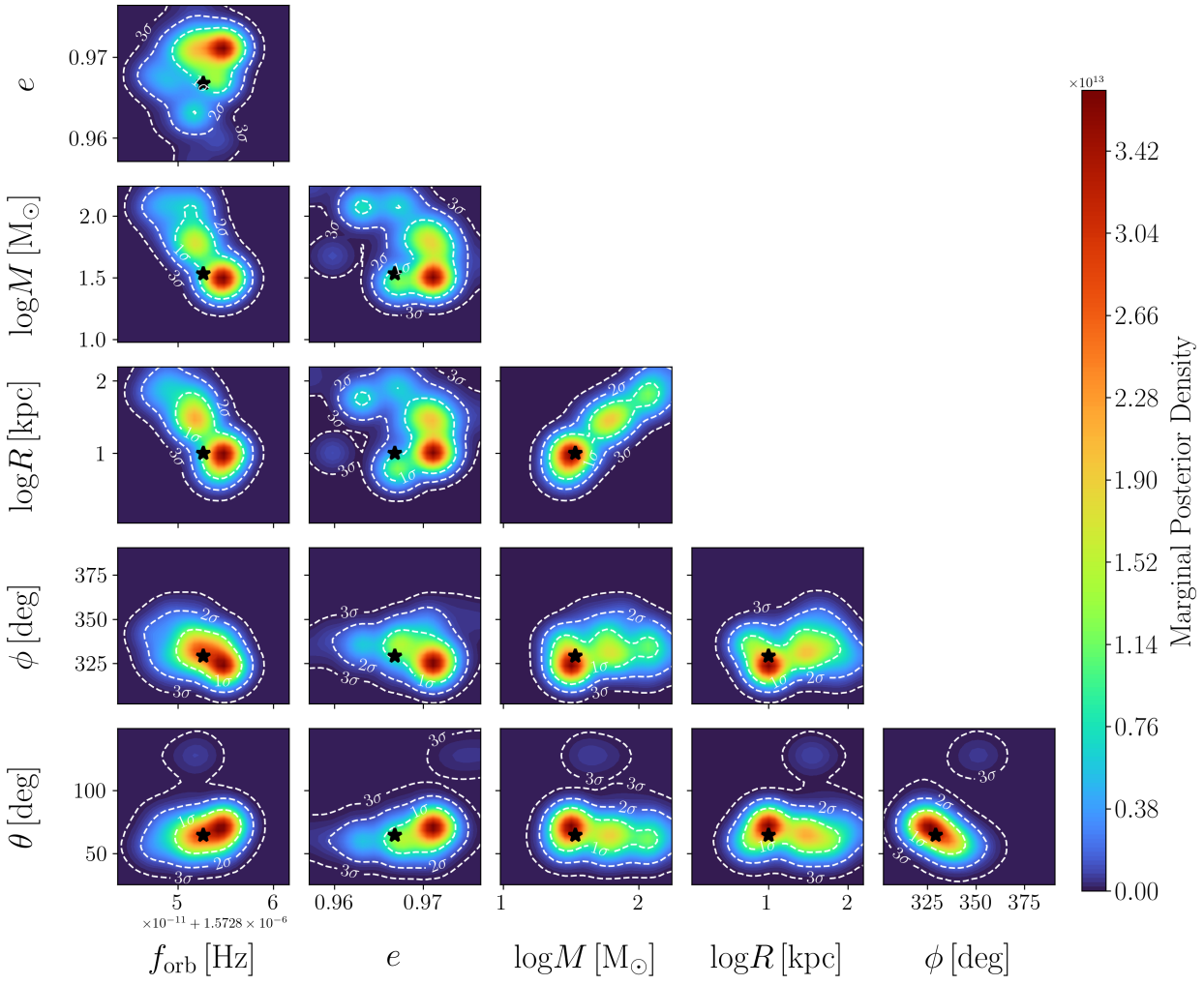


Figure 6.7: **Parameter Measurement error of an example BBH system in Milky Way Globular Clusters.** Here we adopt the same method as Figure 6.5, but consider a different BBH system with $m_1 = 17.6\ \mathrm{M}_\odot$, $m_2 = 16.5\ \mathrm{M}_\odot$, $f_{\mathrm{orb}} = 1.572852 \times 10^{-6}$ Hz, $e = 0.9668$, $R = 10$ kpc, $\Phi = 329.2°$, $\Theta = 64.5°$, $\phi = 341.4°$, $\theta = 149.8°$, $\psi = 14.8°$ (SNR ~ 9).

Chapter 7

Eccentric Stellar-mass Binary Black Holes: Population, Detectability, and Waveform Analysis in the LISA and LIGO Era

A version of this chapter has been submitted for publication in *Physical Review D* (Xuan et al., 2026, arXiv:2605.15265).

Abstract

Eccentric binary black holes (BBHs) formed through dynamical interactions can significantly contribute to gravitational wave (GW) detections. In this work, we present a simulated catalog of dynamically-formed, stellar-mass BBHs in the local universe, incorporating contributions from the Galactic field (flyby interactions), Galactic nucleus (eccentric Kozai–Lidov

evolution), and globular clusters (N-body interactions). Our results predict a wide, highly eccentric BBH population in the Milky Way (MW), with source counts of $\sim 25, 9, 3, 1$, and < 1 for a 4-year LISA mission ($\sim 36, 13, 5, 2$, and 1 for a 10-year extended mission), for SNR $> 1, 3, 8, 20$, and 50, respectively. Extending this model to cosmological populations, we show that different dynamical channels can produce distinct eccentricity distributions in the LVK band and can contribute hundreds of additional low-SNR mHz sources. Specifically, our model yields a merger rate of $\Gamma \sim 9\ \mathrm{Gpc}^{-3}\mathrm{yr}^{-1}$ and ~ 150 extragalactic mHz BBHs with SNR > 1. However, due to the lower mass and weaker GW signals of stellar-mass BBHs, this number declines sharply at higher detection thresholds (e.g., ~ 1 for SNR > 8). We further highlight the impact of eccentric BBH signals on the LISA global fit, showing that their individual harmonics can be independently detected in the Milky Way, and may mimic circular binaries with systematically biased chirp masses. Lastly, we show that post-Newtonian waveforms converge reliably for eccentric BBHs with masses of $\lesssim 10^3\, M_\odot$ in the mHz band. Overall, eccentric BBHs represent a prevalent and promising target for future space-based GW observatories. The simulated catalog and the *LISA Eccentricity Astrophysics Package* (`LEAP`) developed in this work are publicly available at https://github.com/zeyuanxuan/lisa-leap/.

7.1 Introduction

The detection of gravitational waves (GWs) by the LIGO/Virgo/KAGRA (LVK) collaboration has opened a new window beyond traditional electromagnetic observations (see, e.g., Abbott et al., 2016; The LIGO Scientific Collaboration et al., 2021; Abbott et al., 2023a). Building on this success, space-borne detectors such as LISA, TianQin, and Taiji will probe the mHz GW band in the 2030s, vastly expanding the observable source population (see, e.g., Amaro-Seoane et al., 2023; Luo et al., 2016; Ruan et al., 2020). A key distinction be-

tween ground-based and space-borne detectors lies in the evolutionary stages they probe: the LVK network observes compact object binaries during their final merger phase, when gravitational radiation has largely circularized their orbits (Peters, 1964). In contrast, LISA will observe binaries at much earlier stages (see, e.g., Barack and Cutler, 2004b; Mikóczi et al., 2012a; Robson et al., 2018b; Chen et al., 2020a; Amaro-Seoane et al., 2022), where orbital eccentricity leaves distinct imprints on the waveform and encodes valuable information about their dynamical environments (e.g., Hoang et al., 2019; Fang et al., 2019b; Tamanini et al., 2020b; Torres-Orjuela et al., 2021; Xuan et al., 2021, 2023, 2025b,c).

In particular, eccentric stellar-mass binary black holes (BBHs) can have a significant population in the mHz GW band (e.g., Sesana, 2016a; Fang et al., 2019). The existence of such systems is well motivated, as the LVK network has already detected over two hundred stellar-mass BBH mergers, with the latest GWTC-4.0 catalog hinting at their complex dynamical origins (Collaboration et al., 2025b). Notably, current ground-based observations have not yet provided definitive evidence for residual eccentricities in BBH mergers, primarily because gravitational radiation efficiently circularizes orbits by the time binaries enter the high-frequency LIGO band (see, e.g., Abbott et al., 2019; Lenon et al., 2020; Romero-Shaw et al., 2020; Zevin et al., 2021; Gayathri et al., 2022). Nevertheless, simulations strongly suggest that a substantial fraction of these observed BBHs might originate from dynamical formation channels. For example, BBHs assembled dynamically in star clusters can undergo frequent external perturbations, including scatterings and GW captures (O'Leary et al., 2009a; Kocsis and Levin, 2012; Breivik et al., 2016; Rodriguez et al., 2016; D'Orazio and Samsing, 2018), which efficiently excite their orbital eccentricities and lead to eccentric mergers (Kremer et al., 2019b; Zevin et al., 2019; Samsing et al., 2019; Martinez et al., 2020; Antonini and Gieles, 2020; Winter-Granić et al., 2023; Xuan et al., 2025a). BBHs in hierarchical triple systems, particularly those near supermassive black holes (SMBH) in galactic nuclei, can undergo significant eccentricity oscillations driven by the eccentric Kozai-Lidov (EKL) mechanism (Kozai, 1962; Lidov, 1962; Naoz, 2016), potentially leading to observable

mergers (Hoang et al., 2018; Stephan et al., 2019; Randall and Xianyu, 2019c; Bub and Petrovich, 2020; Deme et al., 2020; Wang et al., 2021; Xuan et al., 2024a; Knee et al., 2024; Grishin et al., 2026). In addition, fly-by interactions and galactic tides in the field (e.g., Kocsis et al., 2006c; Michaely and Perets, 2019, 2020; Michaely and Naoz, 2022; Stegmann et al., 2024), as well as interactions within active galactic nucleus (AGN) accretion disks (Tagawa et al., 2021; Peng and Chen, 2021; Samsing et al., 2022; Muñoz et al., 2022; Gautham Bhaskar et al., 2023), can also provide significant contributions to the population of eccentric mHz GW sources. These dynamically-formed systems can retain significant, or even extreme, eccentricities at earlier evolutionary stages, resulting in a large underlying mHz GW source population (e.g., Stephan et al., 2019; Hoang et al., 2019; Wang et al., 2021; Xuan et al., 2024a).

Traditionally, the detectable population of stellar-mass BBHs at cosmological distances was expected to be small, primarily because their signals in the mHz band are relatively weak and often overshadowed by louder, more massive sources such as extreme mass-ratio inspirals (EMRIs) and supermassive black hole binaries (see, e.g., Amaro-Seoane et al., 2022; Robson et al., 2018b). However, recent studies have shown that many dynamically-formed, stellar-mass binaries naturally undergo a wide (semi-major axis $a \gtrsim 0.1\,\mathrm{au}$) and highly eccentric (eccentricity $e \gtrsim 0.9$) progenitor stage before merger (see, e.g., Xuan et al., 2024a; Knee et al., 2024). Although these highly eccentric progenitors are detectable only within short distances ($\sim 10\,\mathrm{Mpc}$), they can remain in the mHz GW band for very long timescales ($\sim 10^5$–10^7 years). Such a long observable lifetime leads to a large number of wide, highly eccentric BBHs, which is especially important for the detection of mHz GWs in the very local universe (such as the Milky Way), where proximity naturally compensates for weaker signal strains. As a result, these systems can significantly enlarge the total catalog of stellar-mass GW sources detected in the mHz regime.

However, a self-consistent treatment of astrophysical populations and data analysis strategies

for highly eccentric GW sources remains largely unexplored, which creates an urgent need for precise models to unlock LISA's full scientific potential. In particular, the dominant GW emission from highly eccentric BBHs occurs near pericenter, where the pericenter distance $r_p = a(1-e)$ becomes small (Peters, 1964). As a result, their emission takes the form of repeated, short-duration bursts (see, e.g., Kocsis and Levin, 2012; Tai et al., 2014; Loutrel and Yunes, 2017; Loutrel, 2020; Romero-Shaw et al., 2023; Xuan et al., 2024a, 2025b). These burst-like features differ qualitatively from the continuous, quasi-circular inspirals targeted by standard GW data analysis methods. Consequently, quasi-circular inspiral templates are both computationally inefficient and morphologically inaccurate for these signals. This mismatch may hinder future detections. For example, the combined unresolved signal from a population of highly eccentric stellar-mass BBHs could form a stochastic gravitational wave background that contaminates the detection of other mHz sources (Xuan et al., 2024b; Chen et al., 2026). On the other hand, previous works have conceptually proven that extracting highly eccentric GW signals in mock mHz data analysis is feasible (Xuan et al., 2025b). Accurately identifying these signals is critical not only for uncovering their dynamical origins, but also for probing their surrounding environments (e.g., Thompson, 2011; Hoang et al., 2018; Stephan et al., 2019; Hoang et al., 2020; Naoz et al., 2020; Xuan et al., 2023) and improving overall parameter estimation accuracy (Xuan et al., 2025b).

In this paper, we construct a ready-to-use mock source catalog for eccentric, stellar-mass BBHs, with a particular focus on their orbital parameter distributions and the detectability of their signals in the mHz GW band. The simulated population focuses primarily on the local universe population, where more observational data and simulation results are available, while we also probe the generalization for BBHs at cosmological distances to provide a comprehensive picture. Furthermore, we discuss the validity of post-Newtonian (PN) waveform models for analyzing these eccentric GW sources. Addressing these theoretical and computational challenges is especially important for the development of the LISA global fit pipeline, which requires highly accurate and computationally efficient templates to identify

and subtract individual sources from the data stream.

This paper is organized as follows. Section 7.2 outlines the physical properties, orbital timescales, and mHz GW signatures of eccentric BBHs. In Section 7.3, we detail the construction of our mock BBH catalog and explore its astrophysical implications for local and cosmological populations. Section 7.4 examines the challenges these multi-harmonic sources pose to the LISA global fit, including potential signal confusion and parameter biases. Section 7.5 evaluates the convergence and validity limits of post-Newtonian waveform models for analyzing these eccentric systems. Finally, we summarize our results in Section 7.6, and provide a guide to the analytical and numerical conventions for eccentric GW signal analysis in Appendix 7.8.1. The simulated catalog in this work is publicly available via an open-source Python package, the *LISA Eccentricity Astrophysics Package* (`LEAP`). This package is also designed for eccentric GW signal analysis, supporting binary orbital evolution, time-domain waveform generation, and SNR estimations in the mHz band.

Unless otherwise specified, we set $G = c = 1$.

7.2 Key Aspects of Eccentric GW Sources in the Millihertz Band

7.2.1 Basic Properties

Due to their proximity, many BBH sources in the local universe can be observed during early evolutionary stages, where they exhibit wide and highly eccentric orbits. Such systems naturally arise as progenitors in a variety of dynamical formation channels. In these scenarios, transient interactions (e.g., fly-bys) or secular processes (e.g., hierarchical triple evolution) can efficiently excite the eccentricity of compact object binaries, leading to strong, "burst-

like" GW emission during pericenter passages. The intense excitation of GW radiation further decouples the binary system from its surrounding dynamical environment, effectively shrinking and circularizing the orbit until it transitions into a standard, quasi-circular merger. Previous works (Xuan et al., 2024a,b, 2025a) have shown that highly eccentric binaries could significantly contribute to the population of stellar-mass GW sources in the mHz band. For completeness, below we briefly summarize the relevant findings.

The lifetime of wide, eccentric compact object binaries is generally longer than that of circular binaries with the same peak GW radiation frequency. This longevity occurs because effective energy emission for a highly eccentric orbit only happens during the pericenter passage, which suppresses the time-averaged energy loss. In particular, for a highly eccentric GW source with component masses m_1, m_2, its merger timescale can be estimated as (Peters and Mathews, 1963; Xuan et al., 2024a):

$$t_{\rm merger} \sim \frac{3}{85 m_1 m_2 M} a^4 \left(1-e^2\right)^{7/2} \sim 1.12\times10^7 {\rm yr} \times \eta_s^{-1} \left(\frac{M}{20{\rm M}_\odot}\right)^{-\frac{5}{3}} \left(\frac{f_{\rm GW}}{1{\rm mHz}}\right)^{-\frac{8}{3}} \left(\frac{1-e}{0.01}\right)^{-\frac{1}{2}}, \tag{7.1}$$

where $M = m_1 + m_2$, $\eta_s = 4m_1m_2/(m_1+m_2)^2 = 4q/(1+q)^2$ is unity for equal-mass sources, with $q = m_1/m_2$ denoting the mass ratio, and $f_{\rm GW}$ denotes the characteristic peak GW frequency associated with the binary's pericenter passage:

$$f_{\rm GW} \sim 2 f_{\rm orb} (1-e)^{-3/2}, \tag{7.2}$$

where $f_{\rm orb}$ is the orbital frequency. We adopt this convention because it smoothly reduces to the circular-orbit GW frequency in the limit $e \to 0$. An alternative definition commonly adopted in the literature is $f_{\rm peak} = f_{\rm orb}(1+e)^{1/2}(1-e)^{-3/2}$ (O'Leary et al., 2009a) (see also

Hamers, 2021, for more details); for highly eccentric systems, the two definitions differ by a factor of $\sqrt{2}$.

Note that the merger timescale in Equation (7.1) is much longer than that of a circular inspiral with the same $f_{\rm GW}$ (Xuan et al., 2024a):

$$t_{\rm inspiral} \sim 5.5 \times 10^4 {\rm yr}\, \eta_s^{-1} \left(\frac{M}{20\,{\rm M}_\odot}\right)^{-\frac{5}{3}} \left(\frac{f_{\rm GW}}{1\,{\rm mHz}}\right)^{-\frac{8}{3}} , \tag{7.3}$$

The longer lifetime of eccentric progenitor systems indicates a larger population expectation in the universe, which yields an advantage for detecting these systems.

On the other hand, highly eccentric GW signals have unique time and frequency patterns. For example, Figure 7.1 shows a comparison between GWs from circular and highly eccentric BBHs. As shown, the GW signal from eccentric systems (blue lines) is radiated primarily during their periapsis passages, rather than continuously throughout the orbit. Therefore, eccentric signals in GW data analysis can appear as a sequence of *repeated bursts*, with the time interval between each burst equal $1/f_{\rm orb}$ (see the *Upper Panel*) and radiated power distributed over a wide range of harmonic frequencies (see the *Bottom Panel*).

The unique waveform patterns of eccentric binaries present challenges for realistic data analysis. Nevertheless, a robust estimate of their detectability can be obtained by computing the total signal-to-noise ratio through summing the energy contributions from all individual frequency harmonics (e.g., O'Leary et al., 2009a; Kocsis and Levin, 2012; Hoang et al., 2019; Xuan et al., 2024a). Furthermore, for sources with slow orbital evolution (i.e., $t_{\rm merger}$ much longer than the observation time $T_{\rm obs}$), their SNR can be analytically approximated as:

$${\rm SNR} \sim \frac{h_{\rm burst}}{\sqrt{S_n\left(f_{\rm GW}\right)}} \sqrt{T_{\rm obs}\left(1-e\right)^{3/2}} , \tag{7.4}$$

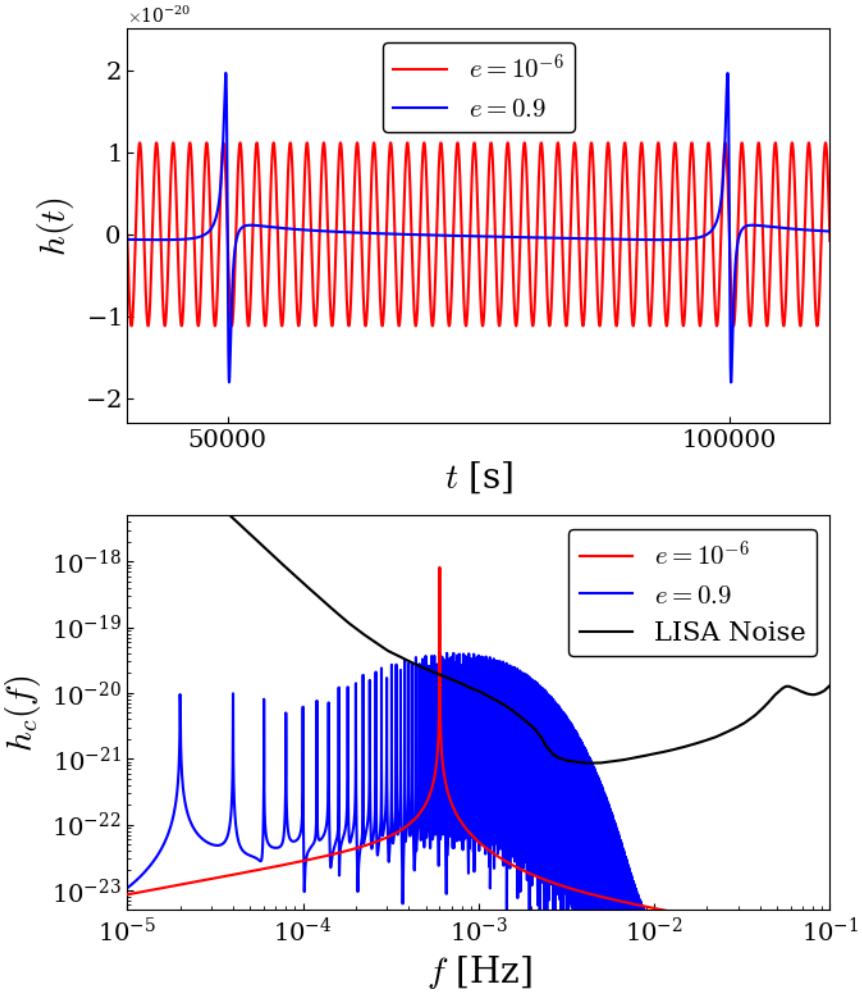


Figure 7.1: **GW waveforms and corresponding characteristic strains for BBHs with different eccentricities.** We show the GW signals (plus polarization) from BBH systems with $m_1 = 25\ \mathrm{M}_\odot$, $m_2 = 20\ \mathrm{M}_\odot$, placed at 8 kpc and observed for 0.5 yrs. Blue curves represent a highly eccentric BBH with $f_{\rm orb} = 2 \times 10^{-5}$ Hz, $e = 0.9$, Red curves represent a quasi-circular BBH with $f_{\rm orb} = 3 \times 10^{-4}$ Hz, $e = 10^{-6}$. These parameters are chosen such that both BBHs will have SNR ~ 120 for a 0.5-year observation. *Upper Panel* shows a zoom-in view of their time-domain waveforms, $h(t)$; *Bottom Panel* shows their characteristic strains (*numerical spectrum*, $h_{\rm c,num}$, see Appendix 7.8.1.3 for details), compared with the LISA noise curve ($\sqrt{fS_n(f)}$, black line). The signals are numerically generated using a post-Newtonian waveform model (see Section 7.5).

in which $S_{\rm n}(f)$ is the spectral noise density of LISA evaluated at GW frequency f (Klein et al., 2016b; Robson et al., 2019a). The subscript "n" in $S_n(f)$ stands for "noise", which is different from the harmonic index n used throughout this paper. $h_{\rm burst}$ is the strain amplitude of a GW burst during the binary's pericenter passage (Peters and Mathews, 1963; Kocsis and Levin, 2012):

$$\begin{aligned} h_{\rm burst} &\sim \sqrt{\frac{32}{5}} \frac{m_1 m_2}{D_l a(1-e)} \\ &\sim 3.49 \times 10^{-21} \eta_s \left(\frac{M}{20\,{\rm M}_\odot}\right)^{\frac{5}{3}} \left(\frac{f_{\rm GW}}{1\,{\rm mHz}}\right)^{\frac{2}{3}} \left(\frac{D_l}{8\,{\rm kpc}}\right)^{-1} , \end{aligned} \tag{7.5}$$

where D_l is the luminosity distance of the source, and the constant coefficient $\sqrt{32/5}$ is due to the average of the GW strain amplitude over the binary's orientation and sky location.

Additionally, if a wide eccentric binary has an orbital period longer than the observation time, its GW emission may not occur within the entire observation window. In this case, the SNR estimate in Equation (8.19) can be written as the product of the probability of detecting a burst during the observation window, $P_{\rm burst} = f_{\rm orb} T_{\rm obs}$, and the SNR of a single GW burst:

$$\mathrm{SNR}_{\rm singleburst} \sim \frac{h_{\rm burst}}{\sqrt{f_{\rm GW} S_n(f_{\rm GW})}} . \tag{7.6}$$

We note that Equations (8.19)–(7.6) provide quick analytical estimates of the SNR. However, for a more rigorous treatment, we adopt the full summation over GW harmonic power to compute the SNR throughout this work (see Equation (7.35) in Appendix 7.8.1). These two approaches generally agree within a factor of ~ 2, as shown in Figure 7.14.

In addition, the detection and parameter estimation of eccentric binaries differ substantially from those of quasi-circular systems. In particular, source confusion and parameter

degeneracies in the LISA global fit may complicate their identification, especially at low signal-to-noise ratios. Nevertheless, previous works have shown that these systems can be effectively recovered with appropriate eccentric waveform templates in mock data analyses (Xuan et al., 2025b). Furthermore, their multiple harmonic signatures and orbital precession patterns can provide additional observables that help break degeneracies and improve source identification and parameter estimation (Xuan et al., 2025a, 2023). Therefore, throughout this paper, detectable source populations are reported using a threshold of SNR > 8 for the nominal 4-year LISA mission (Amaro-Seoane et al., 2023), while corresponding results for a 10-year extended mission are also included for comparison.

In Table 7.1, we summarize the typical orbital properties, lifetimes, and detectable distances of stellar-mass black hole binaries at different evolutionary stages. As shown in the table, highly eccentric progenitors of BBH mergers are typically detectable out to $\sim 10 - 10^4$ kpc, enabling LISA to detect such systems across the local universe. This detection range, combined with their long lifetimes and potentially large population, makes highly eccentric BBHs promising targets for mHz GW observations in the local universe, and motivates studying their population in the local universe (see Section 7.3.1).

7.2.2 Characteristic Strain Representations

As discussed above, the waveform and spectral structure of highly eccentric GW sources differ qualitatively from those of quasi-circular binaries. As a result, there are different ways in the literature to plot their characteristic strain spectrum (e.g., O'Leary et al., 2009a; Kocsis and Levin, 2012; D'Orazio and Samsing, 2018; Hoang et al., 2019; Kremer et al., 2019b; Emami and Loeb, 2020; Deme et al., 2020; Xuan et al., 2024a; Naoz and Haiman, 2023). For completeness, we summarize these approaches here; see Appendix 7.8.1 for further details.

We begin by recalling the standard definition of the characteristic strain for a quasi-circular

source (see, e.g., Finn and Thorne, 2000; Moore et al., 2014; Kupfer et al., 2018; Tauris, 2018; Robson et al., 2019a):

$$h_c = \sqrt{2} h_0 \sqrt{\min\left\{\frac{f^2}{\dot{f}},\, f T_{\rm obs}\right\}}\,, \tag{7.7}$$

in which $h_0 = \sqrt{32/5}\, m_1 m_2/(D_l a)$ is the root-mean-square (rms) time-domain GW amplitude, $f \sim 2 f_{\rm orb}$ is the GW frequency for a quasi-circular binary (corresponding to the dominant second harmonic), and $\dot{f}$ is the frequency shift rate driven by GW emission (chirp rate).

The two regimes in the minimum function of Equation (7.7) differ fundamentally in their physical meaning, in the $f^2/\dot{f}$ regime, the frequency of the source evolves rapidly during $T_{\rm obs}$, and the *integrated area* between $h_c = \sqrt{2} h_0 \sqrt{f^2/\dot{f}}$ contour and detector noise curve in the characteristic strain plot represents the SNR of the corresponding GW harmonic (Finn and Thorne, 2000; Moore et al., 2014); in the $f T_{\rm obs}$ regime, the source evolves slowly, and the *height* of $h_c = \sqrt{2} h_0 \sqrt{f T_{\rm obs}}$ in the characteristic strain plot directly reflects the SNR of signal (Kupfer et al., 2018; Tauris, 2018; Robson et al., 2019a).

For an eccentric binary, the GW signal is made up of multiple harmonics (see, e.g., Figure 7.1), therefore, a natural way to plot its h_c is to treat each harmonic component as an individual "quasi-circular" source, and plot their h_c following Equation (7.7) (see, e.g., O'Leary et al., 2009a; Kocsis and Levin, 2012; D'Orazio and Samsing, 2018; Kremer et al., 2019b; Emami and Loeb, 2020):

$$h_{c,n} = \sqrt{2} h_n \sqrt{\min\left\{\frac{f_n^2}{\dot{f}_n},\, f_n T_{\rm obs}\right\}}\,, \tag{7.8}$$

in which h_n is the rms time domain amplitude of the n-th harmonic (Equation 7.26), $f_n = n f_{\rm orb}$, and $\dot{f}_n = n \dot{f}_{\rm orb}$ can be directly related to the eccentric binary's orbital evolution. This approach, which we refer to as the *individual harmonic representation*, plots each harmonic

independently. The height of each harmonic reflects its *individual* detectability (see, e.g., orange points in Figure 7.2).

However, for highly eccentric sources, the number of harmonics is large, and their number density varies depending on binary orbital frequency. As a result, plotting individual harmonics can become overwhelmingly cluttered, and their height does not directly reflect the *overall* detectability of an eccentric source. This motivates the second approach in the literature to plot the h_c envelope for an eccentric GW source, which we refer to as the *smoothed spectrum representation* (see, e.g., Hoang et al., 2019; Deme et al., 2020; Xuan et al., 2024a; Naoz and Haiman, 2023):

$$h_{c,\mathrm{env}}(f) = \sqrt{2}\, h_n(f) \sqrt{\frac{f^2 T_{\mathrm{obs}}}{f_{\mathrm{orb}}}} \,, \tag{7.9}$$

where $h_n(f)$ represents the interpolated rms time-domain strain amplitude as a continuous function of frequency, constructed from the discrete harmonic values h_n, and satisfies $h_n(f_n) = h_n$ at each harmonic frequency f_n (see Equation (7.44) for details).

Note that Equation (7.9) assumes the source has negligible orbital evolution during T_{obs}. For the general evolving cases, the contour of Equation (7.9) can shift in the characteristic strain plot (see, e.g., fig.1 in Hoang et al., 2019), and the overall spectrum can be computed via an integral of $h^2_{c,\mathrm{env}}(f)$ over dT_{obs}. For more details, see Appendix 7.8.1.3.

The definition in Equation (7.9) is constructed to capture the correct spectral contribution of a single eccentric binary across frequencies, such that the standard characteristic strain integral yields the correct accumulated SNR (see Equation 7.29). In this representation, the area between the envelope and the detector noise curve provides a visually intuitive estimate of the total SNR contribution (see, e.g., the cyan line in Figure 7.2).

We note that $h_{c,\mathrm{env}}$ does not correspond to the geometric upper envelope of individual harmonics $h_{c,n}$. For example, Figure 7.2 compares the *individual harmonic representation*, $h_{c,n}$; the *smoothed spectrum representation*, $h_{c,\mathrm{env}}$; and the *numerical spectrum*, $h_{c,\mathrm{num}}$, for a slowly

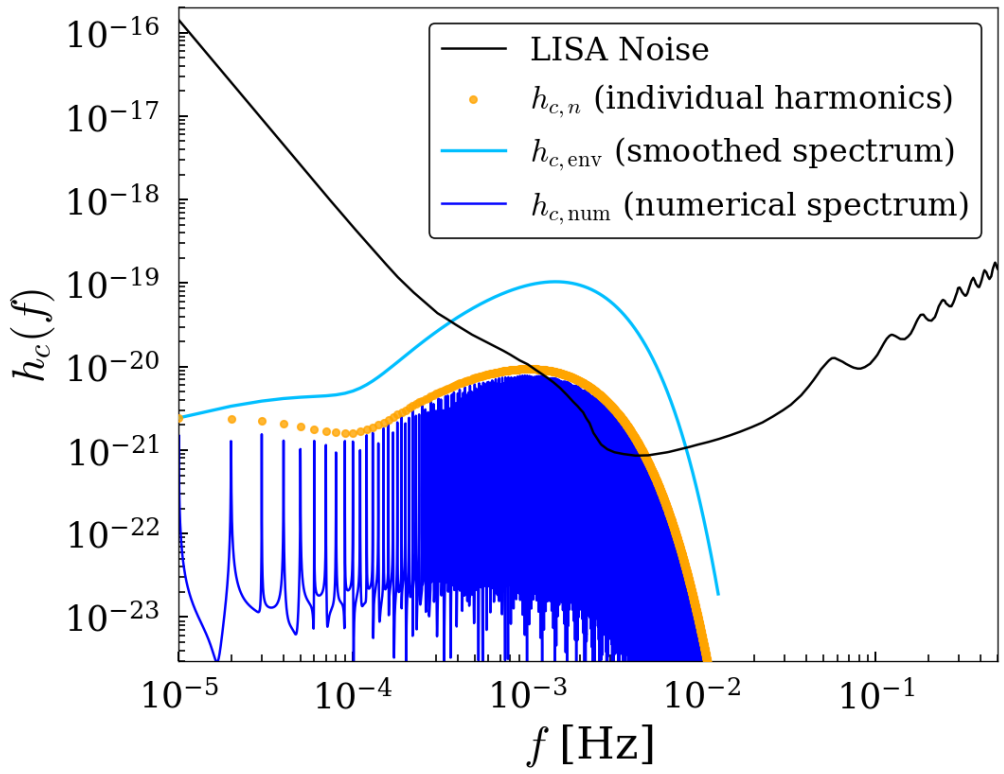


Figure 7.2: **Comparison of three different characteristic strain representations for the same eccentric BBH source.** The plot displays the individual harmonic representation ($h_{c,n}$, scatter points), the smoothed spectrum representation ($h_{c,\mathrm{env}}$, solid envelope), and the numerical spectrum representation ($h_{c,\mathrm{num}}$, oscillatory curve) for the characteristic strain of a BBH system with $m_1 = 15M_\odot$, $m_2 = 10M_\odot$, $f_{\mathrm{orb}} = 10^{-5}$ Hz, $e = 0.95$, $T_{\mathrm{obs}} = 0.5$ yr, and $D_l = 8$ kpc. In the non-evolving limit ($\dot{f} \to 0$), the peak heights of the numerical spectrum coincide with the individual harmonics, and differ from the smoothed spectrum envelope by a factor of $\sqrt{f_{\mathrm{orb}}/\dot{f}}$. This system has an overall SNR of ~ 60.

evolving BBH system with $m_1 = 15\,M_\odot$, $m_2 = 10\,M_\odot$, $e = 0.95$, $f_{\rm orb} = 10^{-5}\,$Hz, $D_l = 8\,$kpc, and $T_{\rm obs} = 0.5\,$yr. The numerical spectrum $h_{c,\rm num}$ is obtained by numerically generating the binary's time-domain waveform, computing its Fast Fourier Transform, and normalizing the result (see Appendix 7.8.1.5 for details).

As shown in the figure, the discrete amplitudes of individual harmonics ($h_{c,n}$; Equation 7.8) closely match the peak heights in the numerical spectrum ($h_{c,\rm num}$; Equation 7.50). Small differences arise because $h_{c,n}$ represents the sky-averaged GW amplitude, whereas $h_{c,\rm num}$ in this example is computed using only the plus polarization and with fixed observation angles. In addition, when the harmonic frequencies $nf_{\rm orb}$ do not coincide exactly with the discrete FFT frequency grid (spaced by $1/T_{\rm obs}$), the finite-window effect causes the sampled peak in $h_{c,\rm num}$ to fall slightly below the true harmonic amplitude, with the "leaked" power redistributed into adjacent bins; this redistribution preserves the total SNR by Parseval's theorem, but can lower individual peak heights by up to a factor of $2/\pi$ in the worst case of bin misalignment.

Furthermore, both $h_{c,n}$ and $h_{c,\rm num}$ lie below the smoothed spectral envelope ($h_{c,\rm env}$; Equation 7.9). This offset reflects the fact that $h_{c,\rm env}$ renormalizes the power of discrete harmonics to preserve the integrated SNR, whereas the harmonic number density in the $h_{c,n}$ representation is not uniform in logarithmic frequency space and depends on the binary parameters. As a result, for eccentric sources satisfying $\dot{f}_{\rm orb} < f_{\rm orb}/T_{\rm obs}$, the individual harmonic amplitude at the n-th harmonic is lower than the smoothed envelope by a factor of $\sqrt{f_{\rm orb}/f}$ (see Equations 7.8 and 7.9):

$$h_{c,n} = \sqrt{2} h_n \sqrt{f_n T_{\rm obs}} = h_{c,\rm env}(f_n) \sqrt{\frac{f_{\rm orb}}{f_n}} \,. \tag{7.10}$$

Table 7.1: Typical Orbital Parameters and Lifetimes of Dynamically-Formed, Stellar-mass BBHs at Different Evolutionary Stages

Evolutionary Stage	a	e	$t_{\rm merger}$	$D_{l,\rm max}$	GW Band
Highly Eccentric Progenitor	$\sim 10^{-1} - 10^{2}\,\rm au$	$\gtrsim 0.9$	$\sim 10^{5} - 10^{8}\,\rm yr$	$10\,\rm kpc - 10\,Mpc$	mHz
Quasi-circular Inspiral	$\sim 10^{-3}\,\rm au$	Moderate	$\sim 10^{2} - 10^{5}\,\rm yr$	$\sim 500\,\rm Mpc$	mHz
Merger	$\sim 10^{-6}\,\rm au$	~ 0	$\lesssim 1\,\rm s$	$\sim 1 - 10\,\rm Gpc$	$\sim 100\,\rm Hz$

Note: Summary of typical orbital parameters, remaining lifetimes ($t_{\rm merger}$), maximum detectable luminosity distances ($D_{l,\rm max}$), and primary gravitational wave observational bands for dynamically formed stellar-mass BBHs. The table illustrates the evolution from wide, highly eccentric progenitor binaries down to the final merger phase (Sesana, 2016a; Collaboration and Collaboration, 2020). Note that exact merger timescales and maximum detectable distances are highly dependent on the total system mass; the bounds presented here are estimated using a fiducial mass range of $10 - 100\,M_{\odot}$. The mHz GW band detectability is estimated for LISA, whereas the $\sim 100\,\rm Hz$ band represents the current ground-based detector networks like LIGO-Virgo-KAGRA.

7.3 Simulated Eccentric BBH Population

7.3.1 Creating a mock BBH Catalog

We first assemble a realistic sample of dynamically-formed BBHs in the Milky Way. In particular, we adopt the models developed by Xuan et al. (2024a) (see their Appendix A) and Xuan et al. (2025a) (see their Section 2). This suite of models combines multiple dynamical formation channels that are theoretically expected to produce a significant number of GW sources in different regions of the galaxy, and involves the recent simulation results and observational constraints on the corresponding compact object populations. Specifically:

Galactic Field We model the population of fly-by-induced highly eccentric GW sources in the Galactic field, following the approach in Michaely and Perets (2019); Michaely and Naoz (2022); Michaely and Perets (2020). These sources originate from wide binary black holes ($a \sim 10^{2} - 10^{4}\,\rm au$) residing in the Milky Way disk, with their initial spatial distribution assumed to follow the Galactic stellar density profile (see eqs. 23 – 26 of Michaely and Perets (2019)). For simplicity, we set a fixed fly-by perturber mass of $0.6\,M_{\odot}$ and adopt a stellar velocity dispersion of $50\,\rm km\,s^{-1}$ for the Galactic disk. The initial BBH mass follows the

standard LIGO-inferred distribution (Abbott et al., 2023b), and is set to form in a starburst 10 Gyr ago, with a wide BBH fraction $f_{\rm BBH} = 7 \times 10^{-4}$ relative to the total stellar population (Michaely and Perets, 2019). We then evolve this initial sample to the present day, including the effect of depletion due to binary evaporation and fly-by induced mergers. The resulting present-day merger rate is $\sim 3 \times 10^{-7}\,{\rm yr}^{-1}$ in the Milky Way, and translates to a volumetric rate of $\sim 3\ {\rm Gpc}^{-3}\,{\rm yr}^{-1}$ in the Universe, assuming a galaxy number density of 0.01 ${\rm Mpc}^{-3}$ (Conselice et al., 2005; van Dokkum et al., 2013).

Galactic Nucleus (GN) We model BBH mergers in Galactic nucleus following Hoang et al. (2018, 2019); Xuan et al. (2024a). Specifically, the Galactic center SMBH can secularly perturb its surrounding stellar-mass binaries through hierarchical triple evolution (eccentric Kozai–Lidov mechanism; see, e.g., Kozai, 1962; Lidov, 1962; Naoz, 2016), resulting in eccentricity excitation and subsequent GW mergers. We model this hierarchical triple evolution using secular equations up to the octupole level of approximation (Naoz et al., 2013a), including general relativistic precession (Naoz et al., 2013b) and GW emission (Peters, 1964). The initial orientations of stellar-mass black hole binaries are set to be isotropic, and systems that do not satisfy the hierarchical stability criteria at formation are excluded (Naoz et al., 2013a; Naoz, 2016).

Within this framework, the BBH population is further divided into two sub-components (see Appendix A of Xuan et al. (2024a) for details):

- *Main Population:* The main stellar population of the Galactic center nuclear star cluster is expected to lie within ~ 5 pc from the SMBH, with ages of $\sim$ 2–8 Gyr and a total stellar mass of $\sim 1.8 \times 10^7\ {\rm M}_\odot$ (e.g., Pfuhl et al., 2011; Launhardt et al., 2002). We assume BBHs form in this population with a continuous steady-state distribution, with an effective replenishment rate of $\Gamma_{\rm rep} \sim 3 \times 10^{-6}\ {\rm yr}^{-1}$, and with masses following the LIGO-inferred distribution. The spatial distribution of systems follows a radial density profile scaling as $\rho \propto r^{-2}$ toward the Galactic center. We note that under the steady-

state approximation, the total replenishment rate $\Gamma_{\rm rep}$ equals the total depletion rate due to BBH mergers or evaporation, and is therefore larger than the actual GW merger rate. This configuration results in a simulated BBH merger rate of $2 \times 10^{-7}\,{\rm yr}^{-1}$ in the Milky Way, or $\sim 2\ {\rm Gpc}^{-3}\,{\rm yr}^{-1}$ in the Universe, assuming a galaxy number density of $0.01\ {\rm Mpc}^{-3}$.

- *Young Nuclear Cluster (YNC) Population:* Observations have shown the presence of a young nuclear star cluster in the Milky Way center (Paumard et al., 2006; Lu et al., 2013), located within ~ 0.5 pc from the SMBH, with ages of ~ 2 – 8 Myr and a total mass of ~ 1.4 – $3.7 \times 10^4\ M_\odot$. To simulate the corresponding BBH population, we assume that this YNC was formed in a starburst ~ 2 – 8 Myr ago, with a top-heavy mass distribution and all massive stars residing in binary systems (Pfuhl et al., 2014b). The massive main-sequence binaries are then evolved into their compact object stage, with remnant black hole masses following Woosley et al. (2002); Belczynski (2020). According to the simulation results, $\sim$ 100–400 BBHs are formed in the YNC (assuming no natal kicks), with most of these black holes having masses of $\sim 10\ M_\odot$ (see, e.g., Bond et al., 1984; Fryer et al., 2001). For conservative purposes, we adopt a number of 100 newly formed BBHs and evolve them using the same hierarchical triple simulations. Since this model is time-evolving, it does not correspond to a fixed LIGO merger rate; however, it is expected to contribute ~ 1 – 4 BBHs detectable by LISA (see fig. 7 of Xuan et al. (2024a)).

Globular Clusters (GCs) The GC population is drawn from the `CMC` (Cluster Monte Carlo) Catalog of Kremer et al. (2020), which is based on Monte Carlo N-body simulations, and later calibrated to reproduce the observed properties of Milky Way globular clusters (Xuan et al., 2025a). These simulations self-consistently follow the dynamical evolution and stellar evolution of dense star clusters, and track the formation and evolution of BBHs within them, including their masses, semi-major axes, and eccentricities across cosmic time.

Table 7.2: Expected Number of Dynamically-formed BBHs in the MW, for Different SNR Thresholds.

SNR	$T_{\rm obs}$	Total	Field	GN	GCs
> 50	4 yr	0.39 (0.65)	0.10 (0.30)	0.15 (0.36)	0.14 (0.42)
	10 yr	1.04 (0.97)	0.17 (0.43)	0.44 (0.64)	0.43 (0.62)
> 20	4 yr	1.45 (1.31)	0.31 (0.58)	0.57 (0.76)	0.57 (0.83)
	10 yr	2.26 (1.34)	0.36 (0.57)	1.02 (0.88)	0.88 (0.87)
> 8	4 yr	3.04 (1.77)	0.61 (0.76)	1.37 (1.23)	1.06 (1.12)
	10 yr	4.74 (1.98)	0.93 (0.80)	2.20 (1.27)	1.61 (1.30)
> 3	4 yr	8.52 (2.96)	1.39 (1.14)	3.46 (1.84)	3.67 (1.86)
	10 yr	12.95 (3.47)	2.23 (1.22)	5.46 (2.38)	5.26 (2.30)
> 1	4 yr	24.65 (5.17)	3.45 (1.76)	10.00 (3.50)	11.20 (3.32)
	10 yr	36.38 (5.13)	4.51 (1.98)	15.99 (3.37)	15.88 (4.06)

Note: Number of simulated eccentric BBHs within the Milky Way that are above different SNR thresholds, for the nominal 4-year and the extended 10-year LISA mission durations. The primary value in each cell represents the expected number of observable systems, while the value in parentheses indicates the 1σ standard deviation derived from the simulated population. The total expected counts are subdivided by their local environment: the Galactic field (Field), the Galactic nucleus (GN), and globular clusters (GCs).

To construct a Galactic GC population, each observed Milky Way GC is associated with a best-fit `CMC` model based on its present-day global properties (e.g., cluster mass, metallicity, and Galactocentric distance). From the corresponding model, we sample cluster snapshots at late evolutionary times ($\sim$ 8–13.7 Gyr) to account for uncertainties in cluster ages, and extract the full BBH population present at that epoch. This procedure is repeated to generate multiple realizations of the Galactic GC system. For each BBH identified in these clusters, we compute its GW properties using the orbital parameters directly provided by the `CMC` simulations. The source distance adopted for SNR calculations is taken to be the present-day heliocentric distance of its host GC. For BBHs that have been dynamically ejected from their parent clusters, we also approximate their distances using the current location of the original host GC. Our model results in a simulated BBH merger rate of $4 \times 10^{-7}\,\mathrm{yr}^{-1}$ in the Milky Way, or $\sim 4\ \mathrm{Gpc}^{-3}\,\mathrm{yr}^{-1}$ in the Universe, assuming a galaxy number density of $0.01\ \mathrm{Mpc}^{-3}$.

Table 7.2 shows the expected number of detectable systems originating from the aforementioned dynamical channels. The projected SNR of the systems is estimated based on their simulated orbital parameters and spatial distances within the mock catalog using Equation (7.37), assuming a 4-year (10-year) LISA observation period, respectively. The numbers enclosed in brackets indicate the statistical uncertainty (standard deviation) inherent to the model, arising primarily from the finite sampling size of the numerical simulations. As shown by the table, dynamical channels alone can contribute a highly significant number of detectable systems, even when restricting our analysis to the Milky Way's population. Specifically, for a 4-year (10-year) LISA observation, approximately $25, 8.5, 3.0, 1.5, 0.4$ $(36, 13, 4.7, 2.3, 1.0)$ dynamically-formed MW BBHs can exceed SNR thresholds of $1, 3, 8, 20, 50$, respectively. This result is consistent with our previous theoretical frameworks (Xuan et al., 2024a, 2025a), and demonstrates that these bursting systems represent promising targets for future data analysis pipelines.

We note that this catalog is not complete, and the BBH source numbers presented here should be regarded as conservative estimates. In particular, this catalog includes the full BBH populations from the three major dynamical formation channels: fly-by mergers in the Galactic field, EKL-driven mergers in the Galactic Center, and dynamically assembled mergers from GC N-body simulations; however, the overall BBH population in the Milky Way likely includes contributions from other pathways not modeled here, notably the isolated binary evolution channel (e.g., Mandel and de Mink, 2016; Breivik et al., 2016) and alternative dynamical mechanisms such as hierarchical field triples. Including these additional populations would likely increase the number of detectable stellar-mass BBHs in LISA. Furthermore, the assumptions of each model have inherent uncertainties; for example, the exact density profiles and spatial orientation distributions of BBHs in the Galactic nucleus remain highly uncertain, and the fraction of wide BBHs in the Galactic Field is poorly constrained due to the lack of observation. However, this model captures the major dynamical formation channels as proposed by current theoretical studies, and involves the most up-to-date sim-

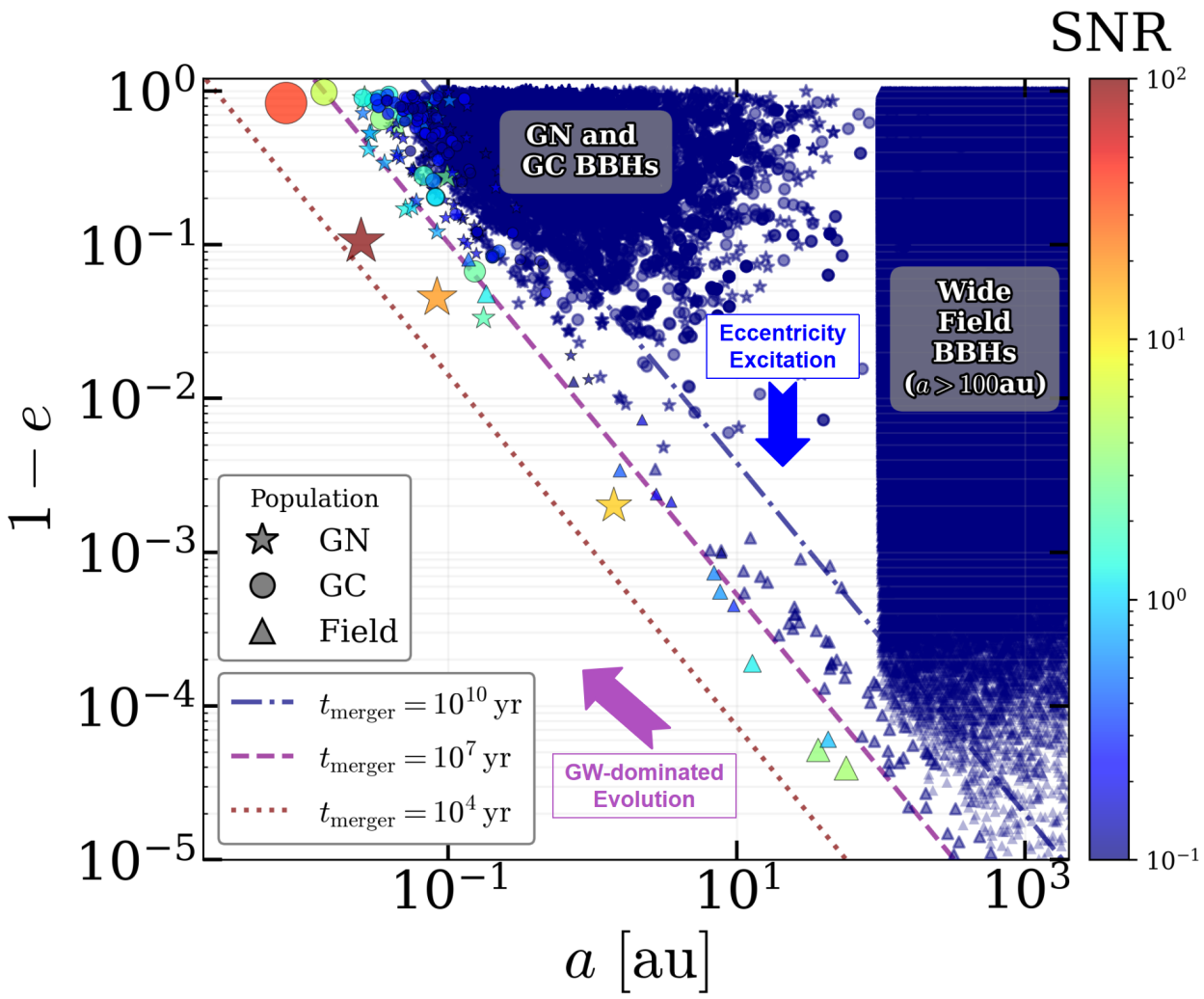


Figure 7.3: **Dynamically-formed BBHs in a mock realization of the Milky Way.** We plot the orbital parameter distribution $(a, 1-e)$ of simulated BBHs in a mock realization of the Milky Way. Different formation channels are indicated by marker shapes: Galactic nucleus (GN; stars), globular clusters (GC; circles), and the Galactic field (triangles). Marker colors and sizes represent the expected GW signal-to-noise ratio, assuming a 4-year LISA observation. Diagonal dashed and dotted lines show contours of constant merger timescale ($t_{\rm merger} = 10^{10}, 10^{7}$, and 10^{4} yr) for an example BBH mass of $10\,M_\odot + 10\,M_\odot$. We further illustrate the evolutionary pathways using arrows. In particular, dynamical perturbations excite eccentricity (blue arrow) until GW emission becomes strong enough to decouple the system from the environment ($t_{\rm merger} \sim 10^4 - 10^{10}$ yr), which further shrinks and circularizes the orbit (purple arrow). We note that a cutoff at $a = 100$ au is artificially imposed on the wide field population for conservative purposes. In addition, most of the detectable BBH systems cluster near the $t_{\rm merger} \sim 10^7$ yr contour, which is because contours of constant signal-to-noise ratio (e.g., SNR = 8) are approximately parallel to those of constant $t_{\rm merger}$ in this regime, see Sections 7.3.1 and 7.3.2 for details.

ulation results and observational constraints on compact object populations. Furthermore, each individual channel yields merger rates that are consistent with the LIGO-inferred rate (14–26 Gpc^{-3} yr^{-1}; Collaboration et al., 2025a). In future LISA observations, targeted searches for these specific sources can, in turn, constrain the underlying model assumptions and population properties.

Figure 7.3 shows a mock realization of the Milky Way BBH population from our simulation. We plot the semimajor axis a and eccentricity (as $1 - e$) for each BBH system in the mock catalog. Galactic nucleus BBHs are shown as stars, globular cluster BBHs as circles, and Galactic field BBHs as triangles. The expected GW SNR is mapped to the color of each point, assuming a 4-year LISA observation. For visual clarity, we also enlarge the size of the systems with higher SNR, and overplot contours of equal merger timescale, corresponding to $t_{\mathrm{merger}} = 10^4$, 10^7, and 10^{10} years for a representative BBH mass of $10\,M_\odot + 10\,M_\odot$. We note that the wide field BBH population exhibits a sharp boundary at $a = 100\,\mathrm{au}$, which is caused by our conservative modeling assumptions. The existence of BBHs with tighter initial separations remains highly uncertain due to the common-envelope evolution; therefore, systems with $a < 100\,\mathrm{au}$ are excluded.

As shown by the figure, detectable BBH systems span a variety of orbital parameters, with a substantial fraction having significant or even extreme eccentricities upon entering the mHz band. This phenomenon is a direct physical consequence of their dynamical formation nature. As discussed in the Introduction, dynamically-formed BBHs are more likely to be born from a wide orbital configuration (see the top-middle and top-right corners of Figure 7.3). Environmental perturbations excite their eccentricity (driving the population downwards in Figure 7.3), until the gravitational wave radiation becomes sufficiently dominant to decouple the binary system from further eccentricity increase (see, e.g., the parameter region where $t_{\mathrm{merger}} \lesssim 10^7$ yrs). Once decoupled, the systems can further shrink and circularize until becoming a standard merger event (migrating towards the top-left corner, as indicated by

the purple arrow).

In addition, Figure 7.3 shows that the observable mHz BBH population in the Milky Way is dominated by long-living systems, with a significant fraction being wide and highly eccentric. This is a natural consequence of the fact that the expected number of systems in a specific evolutionary stage is proportional to the lifetime of that stage. Interestingly, BBHs located in the Milky Way typically cross the detection threshold of LISA when their remaining merger timescale reaches $\sim 10^7$ years (thus, we expect the majority of the population to cluster here). This coincidence arises because the analytical contours defining constant $t_{\rm merger}$ ($\log_{10}a + 0.88\log_{10}(1-e) \sim$ constant) is nearly parallel to the lines defining constant observational SNR ($\log_{10}a + 0.83\log_{10}(1-e) \sim$ constant). This parallel alignment indicates that reaching a specific SNR level roughly corresponds to reaching a specific remaining merger timescale across the parameter space (for a detailed derivation, see Xuan et al. (2024a)).

The mock catalog used in this work is publicly available at https://github.com/zeyuanxuan/lisa-leap/.

7.3.2 Astrophysical Implication

In this section, we examine the detailed population properties of the simulated BBH catalog. In particular, Figure 7.4 presents the orbital parameter distributions of BBHs formed through different channels, assuming a snapshot of the Milky Way is taken. The upper panels show the distribution of BBHs with SNR > 0.1, in the a – $(1-e)$ plane, with the color scale indicating the system number density. We also include the corresponding one-dimensional probability density projections along each axis (e.g., $\mathrm{d}P/\mathrm{d}\log a$ shown as histograms along the top axis), with the 1%, 10%, and 50% percentiles marked by green dash-dotted, blue dashed, and red solid lines, respectively. The lower panels provide zoomed-in views of the parameter space for each population, with the remaining background population shown as

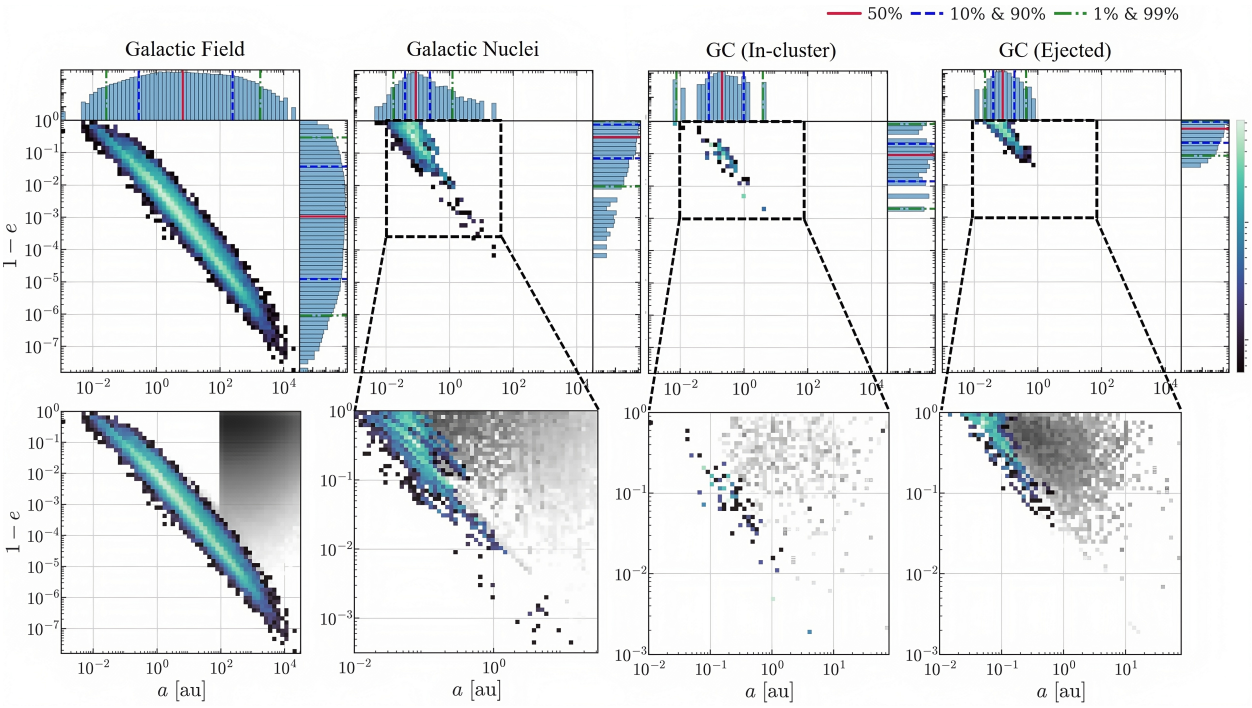


Figure 7.4: **Orbital parameter distributions of simulated Milky Way BBHs across different dynamical formation channels.** The four columns correspond to the Galactic Field, Galactic Nuclei, GC In-cluster, and GC Ejected BBH population, respectively. *Top panels* show the 2D probability density distributions in the a and $1-e$ plane, for systems with SNR > 0.1 for a 4-yr LISA observation. The top and right sub-panels show the marginalized 1D probability density projections ($\mathrm{d}P/\mathrm{d}\log a$ and $\mathrm{d}P/\mathrm{d}\log(1-e)$). Vertical and horizontal lines indicate the 50% (red solid), 10% and 90% (blue dashed), and 1% and 99% (green dash-dotted) percentiles of the distributions. *Bottom panels* show zoomed-in views of the regions containing the SNR > 0.1 populations, with the semi-transparent grey squares representing the underlying background population. Note that this figure assumes a local Milky Way snapshot. For populations at larger cosmological distances, the observable distribution would shift toward the upper-left region of the parameter space.

semi-transparent grey points. Note that we show the distribution of BBHs with SNR > 0.1 to better illustrate their overall population properties. This should not be interpreted as the parameter distribution of detectable mHz BBHs, for which a typical detection threshold of SNR > 8 is adopted.

As shown in Figure 7.4, different formation channels produce distinct orbital parameter distributions in the mHz GW source population. The Field (fly-by induced) channel is characterized by wider separations and more extreme eccentricities, with a median semi-major axis $a_{\rm mid} \sim 7\,{\rm au}$ and median eccentricity $e_{\rm mid} \sim 0.999$ (when they enter the mHz band with SNR > 0.1). In contrast, the Galactic Nucleus and globular cluster in-cluster populations are less extreme, with $a_{\rm mid} \sim 0.1$ and $0.2\,{\rm au}$, and $e_{\rm mid} \sim 0.7$ and 0.9, respectively. The GC ejected population exhibits the smallest characteristic separations ($a_{\rm mid} \sim 0.09\,{\rm au}$) and the lowest median eccentricity ($e_{\rm mid} \sim 0.6$). As shown, the overall trends in the BBH orbital parameter distribution are consistent with the dynamical characteristics of their formation environments. Specifically, Field binaries are typically wider, such that only those driven to the extreme high-eccentricity tail can experience efficient GW energy loss and evolve towards the merger stage. In contrast, GN and GC in-cluster populations originate from intrinsically more compact progenitors (see the grey regions in Figure 7.4), and frequent dynamical interactions in these dense environments (e.g., scattering and three-body encounters) drive a larger fraction of systems into the GW-dominated regime. In addition, the ejected GC population tends to retain lower eccentricities, while the high-eccentricity cluster binaries have shorter inspiral times and therefore tend to merge inside their host cluster before they can be dynamically ejected (see, e.g., Kremer, 2025). Overall, these features provide guidance for targeted searches in LISA data and may help disentangle the contributions of different BBH formation channels in future observations.

We note that despite differences in orbital separations and eccentricities, mHz BBHs from different dynamical formation channels tend to occupy a narrow band in the a – $(1-e)$

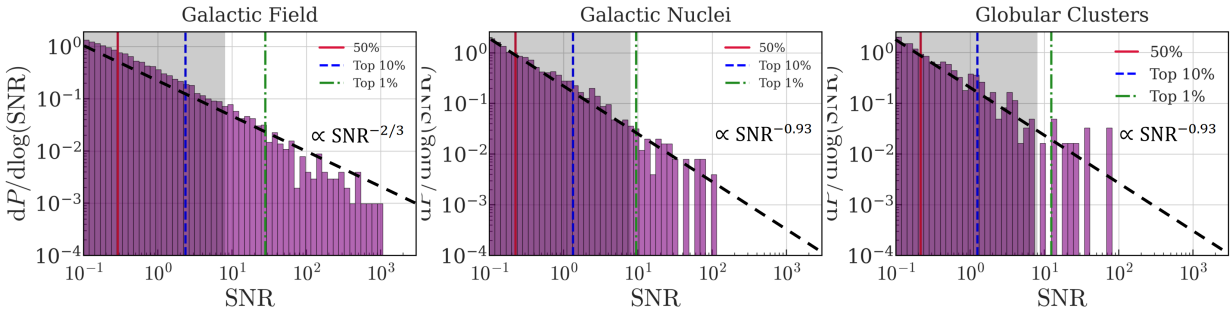


Figure 7.5: **Expected number of dynamically-formed Milky Way BBHs in each SNR bin.** The histograms display the differential probability distribution $\mathrm{d}P/\mathrm{d}\log(\mathrm{SNR})$ for all the simulated systems with an expected SNR > 0.1 in a 4-yr LISA observation. Vertical lines denote the 50% (red solid), top 10% (blue dashed), and top 1% (green dash-dotted) percentiles of the population in SNR distribution. The shaded region marks systems below the nominal detectability threshold, SNR < 8, while the unshaded region corresponds to detectable sources. The black dashed lines illustrate the analytically derived power-law scaling, for comparison. Notably, the highly eccentric Field population follows a shallower slope ($\sim$ SNR$^{-2/3}$), whereas the GN and GC populations exhibit a steeper slope ($\sim$ SNR$^{-0.93}$). For a detailed analysis of these power-law dependencies, see Section 7.3.2.

plane, corresponding to merger timescales $t_{\mathrm{merger}} \sim 10^4$–$10^{10}$ yr (see, e.g., Figure 7.3 and 7.4). This behavior arises from a selection effect similar to that discussed in Section 7.3.1. In particular, systems are most likely to be detected by mHz GW detectors when they have a long lifetime (t_{merger}), while a given remaining merger timescale approximately corresponds to a characteristic SNR level across the a–$(1-e)$ parameter space. As a result, the observed snapshot population in the Milky Way is dominated by sources near the detection threshold (SNR ~ 5 – 100), which occupies an elongated band in parameter space.

We emphasize that these quantitative results apply specifically to the Milky Way population. For sources at larger cosmological distances, only binaries in later evolutionary stages can reach sufficiently high signal-to-noise ratios. Consequently, the observed population is biased toward smaller semi-major axes and lower eccentricities, corresponding to a shift toward the upper-left region of parameter space and toward shorter merger timescales. We further discuss extragalactic sources in Section 7.3.3.

Figure 7.5 shows the SNR distribution of dynamically formed BBHs in the Milky Way. We

compute the probability density in log SNR for all sources with SNR > 0.1 in the mHz band. The distributions for the Field, GN, and GC populations are shown separately, with the 1%, 10%, and 50% percentiles indicated by vertical lines. As shown in the figure, the SNR distributions for different formation channels approximately follow power-law behavior. In particular, the GC and GN populations are consistent with a slope of ~ -1, while the Field population exhibits a slightly shallower slope ($\sim -2/3$).

This power-law behavior can be understood analytically. In particular, randomly choosing an observation window $T_{\rm obs}$ during the long-term inspiral of a BBH system, the differential probability of the binary being observed emitting GW at a given SNR, $\mathrm{d}P/\mathrm{dSNR}$, is proportional to the differential evolution time spent at that SNR, (i.e., $\mathrm{d}t_{\rm merger}/\mathrm{dSNR}$, note that here we assume the binary evolves slowly, $T_{\rm obs} \ll t_{\rm merger}$). For BBHs with fixed masses, the merger timescale scales as $t_{\rm merger} \propto f_{\rm GW}^{-8/3}(1-e)^{-1/2}$ (Equation 7.1). Meanwhile, at a fixed source distance, the signal-to-noise ratio scales as $\mathrm{SNR} \propto S_n(f_{\rm GW})^{-1/2} f_{\rm GW}^{2/3}(1-e)^{3/4}$ (Equations 8.19 and 7.5). In the $\sim$1–3 mHz frequency range, the detector noise is dominated by the Galactic foreground, which approximately follows $S_n(f) \propto f^{-4.4}$ (see, e.g., Klein et al., 2016b).

Combining these scalings, we get:

$$\begin{aligned} t_{\rm merger} &\propto f_{\rm GW}^{-8/3}(1-e)^{-1/2} \ , \\ \mathrm{SNR} &\propto f_{\rm GW}^{8.6/3}(1-e)^{3/4} \ . \end{aligned} \tag{7.11}$$

Furthermore, when $e \to 1$, the change of binary's pericenter distance is negligible during the GW-dominated orbital evolution, $dr_p = d[a(1-e)] \sim 0$ (see eq. 5.8 in Peters, 1964), which results in highly eccentric BBHs emitting GW with almost the same $f_{\rm GW}$ until e drops to moderate values. In other words, the eccentricity evolution dominates the change in remaining merger time $t_{\rm merger}$ and observed SNR, and $f_{\rm GW}$ can be taken as approximately

constant. In this case, Equation (7.11) yields $t_{\rm merger} \propto (1-e)^{-1/2} \propto {\rm SNR}^{-2/3}$. On the other hand, when $e \to 0$, the $(1-e)$ term in Equation (7.11) has negligible influence on the system's evolution, and we approximately have $t_{\rm merger} \propto f_{\rm GW}^{-8/3} \propto {\rm SNR}^{-0.93}$.

Finally, since the expected number of observed systems within a given logarithmic SNR bin is proportional to the fraction of the binary's lifetime spent in that state, we can analytically derive the functional forms shown in Figure 7.5. Specifically, using the relation of $\mathrm{d}P/\mathrm{d}\log({\rm SNR}) = {\rm SNR} \cdot dP/{\rm dSNR} \propto {\rm SNR} \cdot \mathrm{d}t_{\rm merger}/{\rm dSNR}$, and plug in the aforementioned power law relation between $t_{\rm merger}$ and SNR (i.e., Equation (7.11), in the high e and low e limit):

$$\begin{aligned} \frac{dP}{d\log({\rm SNR})} &\propto {\rm SNR}^{-2/3}\,(\text{when}\, e \to 1)\,, \\ \frac{dP}{d\log({\rm SNR})} &\propto {\rm SNR}^{-0.93}\,(\text{when}\, e \to 0)\,. \end{aligned} \tag{7.12}$$

We note that, Equation (7.12) estimates the SNR distribution for a BBH population with fixed mass and distance to the observer, assuming its GW radiation is dominated by highly eccentric ($e \to 1$) or quasi-circular sources ($e \to 0$), respectively; In reality, the BBHs in the Milky Way have different distances and mass, and consist of both circular and eccentric systems. Therefore, the realistic slope in the SNR distribution may vary in the range of $\sim [-0.93, -0.67]$. Additionally, the power law relation we adopt here applies specifically for low-frequency source populations ($f_{\rm GW} \sim 1 - 3\,{\rm mHz}$), while the GW emission of BBHs population at cosmological distances may be dominated by high frequency components, thus having a different power law relation. However, Equation (7.12) still matches well and further verifies the simulation results in Figure 7.5. In particular, the eccentric Field BBH population exhibits a shallower slope ~ -0.67, while the GN and GC populations, characterized by less extreme eccentricities, show steeper slopes closer to ~ -0.93.

7.3.3 BBHs at Cosmological Distances

We further explore the population of eccentric BBHs at cosmological distances, for both the LIGO and LISA detection. Specifically, we adopt the same population model as in Section 7.3.1, evolve the Field and GN populations forward, and compute their eccentricities when entering the LIGO band at $f_{\rm GW} = 10\,{\rm Hz}$. The resulting distributions are shown in Figure 7.6. For comparison, we also include the eccentricity distributions of in-cluster and ejected GC populations from fig. 4 of Martinez et al. (2020). Here the in-cluster GC curve combines contributions from the triple, capture, and in-cluster binary channels in their results. For consistency, we adapt our peak GW frequency definition, $f_{\rm GW} = 2f_{\rm orb}(1-e)^{-1.5}$, to their eq. 16, $f_{\rm GW} = 2f_{\rm orb}(1-e)^{-1.5}(1+e)^{-0.3046}$ in Figure 7.6. These two definitions differ by a factor of order unity in the high-e regime, and both reduce to $f_{\rm GW} = 2f_{\rm orb}$ in the low-e limit.

As shown in Figure 7.6, the merger eccentricities from different formation channels span a wide range, with an overall trend similar to that in the mHz band. In particular, globular cluster in-cluster mergers and field fly-by induced mergers tend to retain higher eccentricities, which are potentially detectable by LIGO when entering the 10 Hz band. In contrast, although GN and GC ejected populations may have high eccentricities at formation (see Figure 7.4), their residual eccentricities in the LIGO band are typically very small ($\lesssim 10^{-2}$), making them nearly indistinguishable from mergers formed via isolated binary evolution.

This channel dependence has important implications for interpreting BBH mergers in the LVK data. For example, recent studies have explored using eccentric detections, or their null detection, to constrain the contribution of dynamically-formed BBHs in the observed merger population (e.g., Zevin et al., 2021). Our results suggest that such constraints should be interpreted on a channel-by-channel basis. In particular, many dynamically-formed binaries are born with high eccentricity, but their eccentricities are efficiently damped through

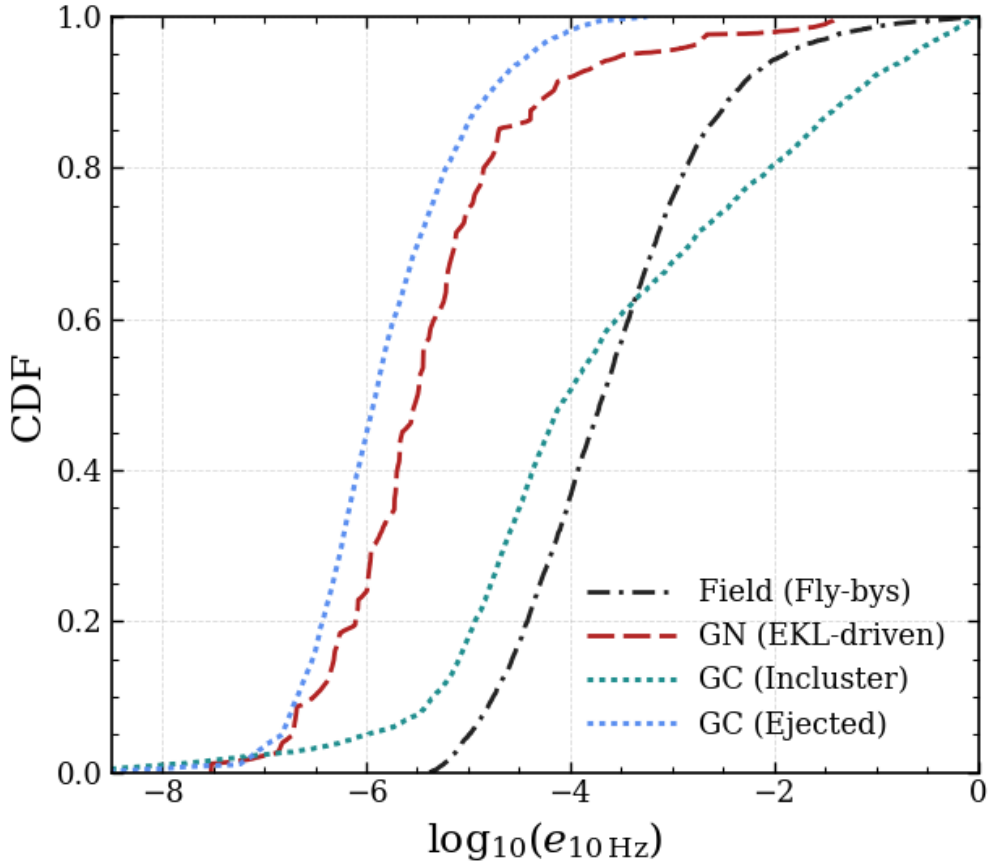


Figure 7.6: **Eccentricity distribution of dynamically-formed BBHs in the LIGO band.** The plot compares the cumulative distribution functions (CDFs) of eccentricities at $f_{\rm GW} = 10\,{\rm Hz}$, for BBH mergers formed via Galactic Field fly-bys (black dot-dashed line), Galactic Nucleus EKL-driven mergers (red dashed line), and two Globular Cluster populations (in-cluster mergers as the teal dotted line, and ejected mergers as the blue dotted line). The GC distributions are adapted from Martinez et al. (2020). The in-cluster GC curve shown here combines contributions from the KL and non-KL triple channels, few-body and single-single capture channels, and the in-cluster binary channel, following their fig. 4. This figure provides a unified comparison of the eccentricity distributions of dynamically formed BBHs at the final merger stage, combining previously published GC results with new predictions for the eccentricity distribution of Galactic Field fly-by and Galactic Nucleus EKL-induced merger channels.

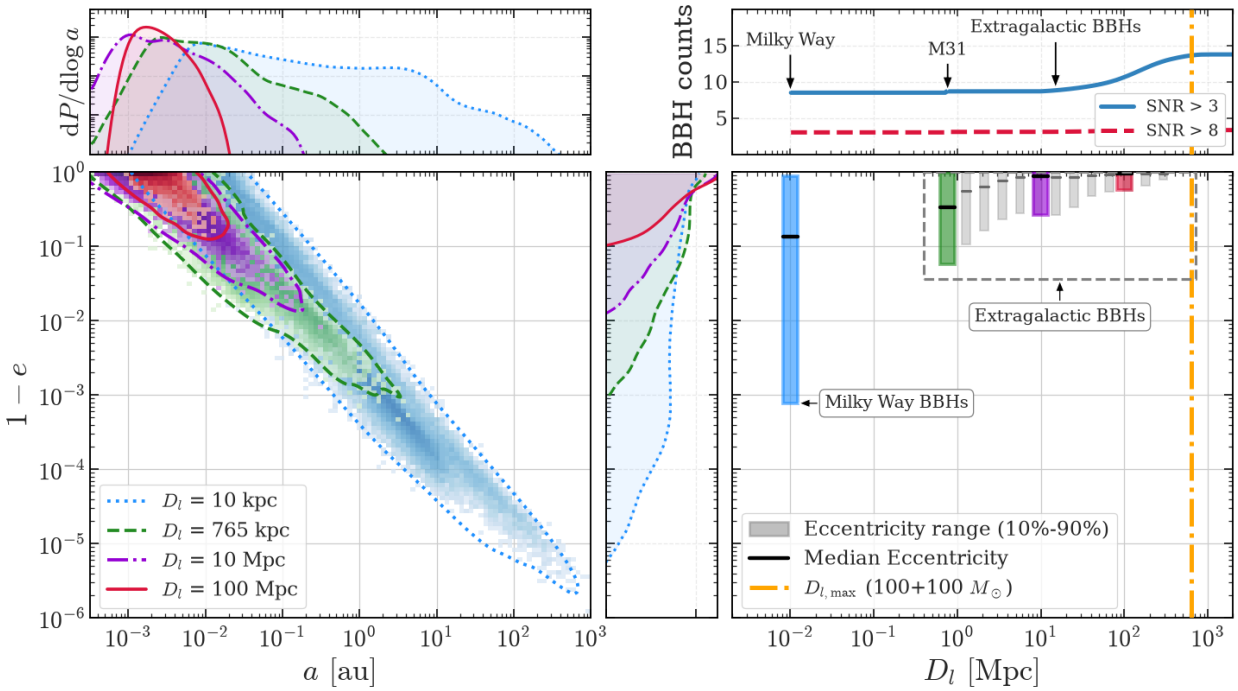


Figure 7.7: **Orbital properties and number of mHz eccentric BBHs at different luminosity distances.** All panels assume a 4-year LISA observation and a SNR threshold of 8. The *bottom-left panel* shows the 2D probability density distribution of the detectable dynamically-formed BBH population in the a – $(1-e)$ parameter space. Overlaid contours indicate the 99% percentiles for populations placed at different luminosity distances: 10 kpc (blue dotted), 765 kpc (green dashed), 10 Mpc (purple dot-dashed), and 100 Mpc (red solid). The *top-left* and *center vertical* panels display the corresponding 1D marginal distributions for the semi-major axis ($\mathrm{d}P/\mathrm{d}\log a$) and eccentricity ($\mathrm{d}P/\mathrm{d}\log(1-e)$), respectively. The *top-right panel* illustrates the cumulative number of expected BBHs as a function of distance, starting from the Milky Way local contribution to the extragalactic population. The *bottom-right panel* presents the 1-D eccentricity distribution (10% to 90% percentiles, with black median ticks) at different D_l, with highlighted color bars directly matching the populations in the left panels. The vertical orange dot-dashed line across the right panels marks the maximum detectable distance ($D_{l,\mathrm{max}} \sim 1\,\mathrm{Gpc}$) for a fiducial binary mass of $100 + 100\,M_\odot$. As distance increases, the observable BBH population systematically shifts toward tighter and more circular orbits due to the selection effect.

GW emission long before entering the LVK band. As a result, the absence of eccentric detections primarily constrains those channels that retain measurable eccentricities, while many other dynamical channels, such as GN EKL-driven mergers and GC-ejected binaries, may still contribute substantially to the LVK merger rate despite appearing nearly circular in detection.

On the other hand, as discussed in Section 7.3.2, the detectability of wide, highly eccentric sources in the mHz band is limited to the local Universe. Nevertheless, the general population of dynamically-formed BBHs can still be observed at cosmological distances, provided that they are approaching the final evolution stages. For example, a $100 + 100\,M_\odot$ BBH can be detected up to $\sim 1\,\mathrm{Gpc}$ for a 4-year LISA observation (see the right panel of Figure 7.7). As the distance increases, the detectable population gradually shifts toward less eccentric, more compact, and shorter-lived systems, as they have a larger signal-to-noise ratio.

This trend is reflected in Figure 7.7. In particular, we adopt the same population model as in Section 7.3.1, place sources at different distances, and compute their orbital parameter distributions for systems with signal-to-noise ratio SNR > 8 over a 4-year LISA observation. The *bottom-left panel* of Figure 7.7 shows the population in the a – $(1 - e)$ parameter space at distances of 10 kpc, 765 kpc, 10 Mpc, and 100 Mpc (blue, green, purple, and red contours, respectively), along with their corresponding 1D marginal distributions on the top and right axes. The *bottom-right panel* further shows the distribution of eccentricity (10%–90% percentiles and median) as a function of distance. As illustrated, in the local Universe (e.g., the Milky Way at 10 kpc, or M31 at 765 kpc), a large number of wide, highly eccentric systems are detectable, with median eccentricities around $e \sim 0.9$ and a significant fraction of BBHs reaching extreme eccentricity values ($e \gtrsim 0.999$). As the distance increases, the detectable parameter space shrinks toward the upper-left region, and only less eccentric and more compact systems remain observable. For example, at distances of ~ 10 Mpc, the median eccentricity drops to $e \lesssim 0.1$, and the semi-major axis is typically below 10^{-2} AU,

indicating a transition to typical mHz quasi-circular inspirals.

In addition to the orbital properties, the *top-right panel* of Figure 7.7 demonstrates the estimated cumulative number of detectable BBHs as a function of distance. Specifically, we adopt the Milky Way simulation's result (~ 9 sources with SNR > 3 at $D_l \sim 10^{-2}$ Mpc), and consider the contribution from nearby galaxies, such as M31. Assuming M31 hosts a BBH population similar to the Milky Way but scaled by its stellar mass (approximately twice as large), we find the expected detectable source number is ~ 0.2 (due to the larger distance and weaker signal strength), which indicates the nearby galaxies have a limited contribution to the eccentric BBHs detection.

We then incorporate the cosmological contribution by assuming that extragalactic BBHs follow similar orbital parameter distributions and population properties as in our Milky Way model. The corresponding merger rates are taken directly from our simulation, yielding ~ 3, 2, and $4 \times 10^{-7}\,\mathrm{yr}^{-1}$ per Milky-Way-like galaxy for the Field, GN, and GC channels, respectively. These rates translate to volumetric merger rates of ~ 3, 2, and 4 $\mathrm{Gpc}^{-3}\,\mathrm{yr}^{-1}$, assuming a galaxy number density of 0.01 Mpc^{-3} (Conselice et al., 2005; van Dokkum et al., 2013). For each distance, we compute the average detectable lifetime of BBHs (for a 4-yr LISA observation) and multiply it by the merger rate within the corresponding comoving volume shell to estimate the expected number of observable sources.

As shown in the cumulative curve in the *top-right panel*, BBHs at cosmological distances (e.g., 10–1000 Mpc) provide a significant background population, yielding $\sim 6(150)$ sources with SNR $> 3(1)$. However, the number of detectable sources decreases rapidly with an increasing SNR threshold. For example, at SNR $= 8$, the expected number of extragalactic sources drops to $\lesssim 1$. This indicates that extragalactic sources are typically faint and contribute primarily at low SNR, with a steeper decline toward higher SNR compared to nearby highly eccentric sources (see Table 7.2).

We note that our calculation assumes that BBHs at cosmological distances follow the same parameter distributions as those in our local dynamical simulations, which may introduce biases. In addition, our model does not account for all the potential dynamically-formed BBH populations. Nevertheless, our results illustrate a robust picture for the detection of eccentric BBHs in the mHz band. Specifically, the observed population is dominated by two regimes: very local sources in the Milky Way, which are wide and highly eccentric and are detectable due to their proximity and long lifetimes; and extragalactic populations at $\sim$ 100–1000 Mpc, which are more compact and nearly circular and are detectable due to the large detection volume, but typically have lower signal-to-noise ratios.

7.4 Eccentric BBHs in the LISA Global Fit

As previously discussed, dynamically-formed BBHs can constitute a significant population in the mHz GW band. Their signals are characterized by multiple-harmonic structures that span a broad frequency range. This distinct feature presents both opportunities and challenges for practical signal processing. In this section, we will focus on the confusion that their multiple harmonic structures may cause in the LISA global fit, as well as the corresponding stochastic background. (Xuan et al., 2021; Chen et al., 2020b)

Specifically, the current global fit often relies on quasi-circular templates to search for Galactic binaries. However, highly eccentric sources possess multiple harmonics, and these harmonics often appear as slowly-evolving, near-monochromatic components. Without introducing specific search methods to separate them, the signal of a single eccentric BBH could be misidentified as multiple circular signals at different harmonics. For example, Figure 7.8 shows a mock realization of dynamically formed BBHs in the Milky Way (which is the same mock population as shown in Figure 7.3). We plot the characteristic strain for all the harmonics from MW BBHs with $e > 0.1$ (assuming a 4-yr LISA observation, see Equation 7.40),

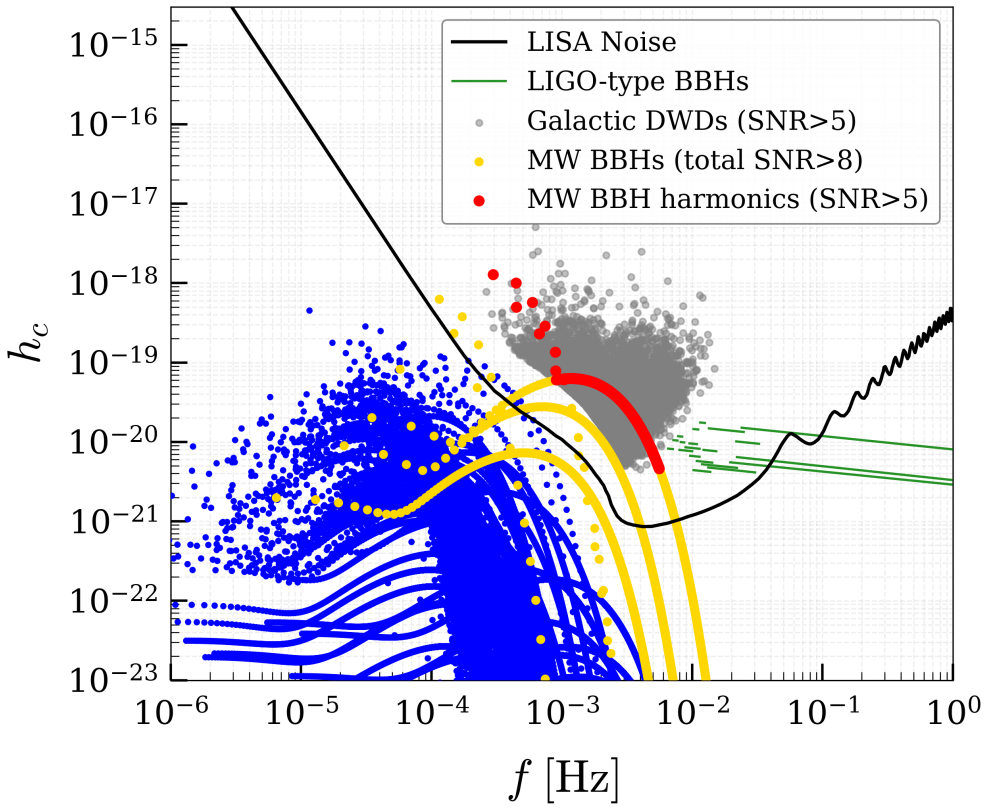


Figure 7.8: **Individual GW harmonics of dynamically-formed BBHs in one realization of the Milky Way.** The plot shows the characteristic strain for dynamically-formed BBHs in a single realization of the Milky Way (*individual harmonic representation* $h_{c,n}$, see Equation 7.8). The red markers highlight GW harmonics that have an individual SNR > 5. The blue points represent the background harmonics from all GW sources with a total SNR ≥ 0.1 for a 4-yr LISA observation, and the yellow points represent BBHs with total SNR (summing over all harmonics) greater than 8, but individual harmonic SNR smaller than 5. For comparison, we also plotted the Galactic double white dwarf population (grey point, see, e.g., Lamberts et al., 2018) and extragalactic circular BBHs (green curves, see, e.g., Amaro-Seoane et al., 2022).

as shown by the blue points. In addition, we highlight the harmonics with an individual SNR greater than 5 in red, and harmonics with an individual SNR < 5 but correspond to a BBH source with a combined SNR > 8 in yellow. For comparison, we also plotted the Galactic double white dwarf population (grey points) and extragalactic, LIGO-type BBHs (green curves, see, e.g., Robson et al., 2018b).

As shown by Figure 7.8, while the majority of eccentric MW BBHs are not detectable, a subset of systems can exhibit multiple harmonics that exceed the detection threshold. Due to their extreme eccentricities, once a system crosses the detection threshold, it typically produces a dense sequence of resolvable harmonics, which inevitably introduces the risk of signal overlap and confusion, particularly if they are inadvertently analyzed using standard quasi-circular templates. In addition, some BBHs (in yellow) do not have harmonics lying beyond the noise curve, while they still have a total SNR > 8. This is because here we are plotting the energy of individual harmonics. For highly eccentric systems, the density of harmonics is extremely large, which, when summed together, yield a significant SNR. Therefore, if we adopt the *smooth spectrum representation* as explained in Appendix 7.8.1.3, these systems will have a spectrum curve beyond the noise curve.

Figure 7.9 further quantifies the expected number of individual detectable GW harmonics from bursting BBHs across different SNR bins, averaged over 100 mock realizations of the Milky Way. As demonstrated, dynamically formed BBHs can contribute an average of $\sim$ 216, 60, 10, and 3 individual harmonics with SNR > 1, 3, 8, and 20, respectively, to the LISA data stream, which can significantly complicate source extraction. Notably, our results show that these counts are characterized by large standard deviations, typically comparable to or even exceeding the aforementioned average numbers. This massive variance arises from the highly non-Gaussian nature of the harmonic distribution. In a typical realization, the entire population of detectable harmonics originates from only $1 - 3$ high-SNR sources. However, once such a source is present with high eccentricity, it simultaneously produces a

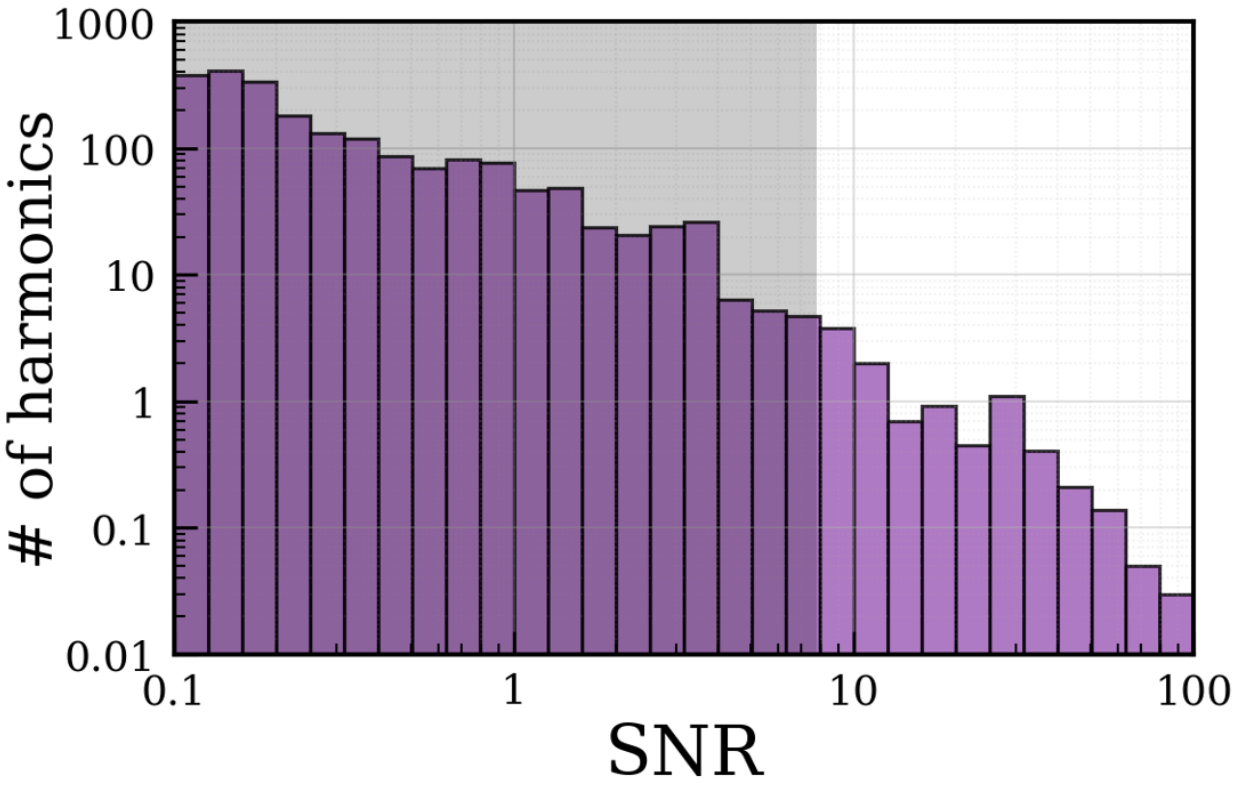


Figure 7.9: **Distribution of individual GW harmonics in each SNR bin, for BBHs in the Milky Way.** The histogram displays the average number of individual GW harmonics per Milky Way realization as a function of their single-harmonic SNR. The purple bars represent the expected count of harmonics within each log-uniform SNR bin, derived by averaging over 100 realizations of the Galactic population. The shaded region marks harmonics below the nominal detectability threshold, SNR < 8, while the unshaded region corresponds to detectable harmonics. The distribution highlights the relative abundance of sub-threshold harmonics versus individually resolvable harmonics for a 4-yr LISA observation.

substantial cluster of harmonics with intrinsically correlated frequencies and SNRs.

To further understand the extent of this overlap and confusion, we derive the parameter bias introduced when an individual harmonic of an eccentric BBH is mistakenly identified as the dominant $2f_{\rm orb}$ mode of a circular binary. In particular, for an eccentric system with a true chirp mass $\mathcal{M}_{c,0}$ and orbital eccentricity e, the orbital frequency $f_{\rm orb}$ evolution can be estimated using (Peters, 1964):

$$\dot{f}_{\rm orb} = \frac{96}{5}\pi^{8/3}\mathcal{M}_{c,0}^{5/3} f_{\rm orb}^{11/3} F(e) 2^{8/3}\,, \tag{7.13}$$

where $F(e) = (1+\frac{73}{24}e^2+\frac{37}{96}e^4)/(1-e^2)^{7/2}$ is the eccentricity enhancement factor. The factor of $2^{8/3}$ arises because here we use the orbital frequency $f_{\rm orb}$ instead of the gravitational wave frequency.

Since the frequency of the n-th harmonic is $f_n = nf_{\rm orb}$, its time derivative is $\dot{f}_n = n\dot{f}_{\rm orb}$. Rearranging the terms to isolate f_n, we obtain:

$$\dot{f}_n = \frac{96}{5}\pi^{8/3}\mathcal{M}_{c,0}^{5/3}\left[F(e)2^{8/3}n^{-8/3}\right] f_n^{11/3}\,. \tag{7.14}$$

If a data analysis pipeline fits this individual spectral track using the standard circular chirp formula, $\dot{f} = \frac{96}{5}\pi^{8/3}(\mathcal{M}_c')^{5/3}f^{11/3}$, the inferred apparent chirp mass $\mathcal{M}_c'$ will be biased compared with the true chirp mass of the eccentric source:

$$\mathcal{M}_c' = \mathcal{M}_{c,0}F(e)^{3/5}\left(\frac{2}{n}\right)^{8/5}\,. \tag{7.15}$$

In addition, the gravitational wave radiation of highly eccentric systems is strongly localized at periapsis, which produces a broadband signal peaked at the harmonic $n_{\rm peak} \sim 2(1-e)^{-3/2}$ (see Equation 7.2). Substituting this peak harmonic estimate into Equation (7.15) yields the

analytic mass bias near the peak radiation frequency:

$$\left.\frac{\mathcal{M}_c'}{\mathcal{M}_{c,0}}\right|_{n=n_{\rm peak}} = \frac{(1-e)^{3/10}}{(1+e)^{21/10}}\left(1+\frac{73}{24}e^2+\frac{37}{96}e^4\right)^{3/5} . \tag{7.16}$$

This analytic mapping is visualized in Figure 7.10. Because of the strong $(1-e)^{0.3}$ dependence in the numerator, as $e \to 1$, this ratio approaches zero. Consequently, a highly eccentric stellar-mass BBH radiating near its peak frequency would mimic a circular binary with a much smaller chirp mass. This degeneracy highlights the danger of mischaracterizing individual harmonics if they are not jointly analyzed using a fully eccentric template framework.

We note that the bias derived here is only a rough estimate based on matching the first frequency derivative, $\dot{f}$, rather than a full waveform fit. In principle, this degeneracy could be broken by considering higher-order frequency evolution. For circular binaries, the second derivative $\ddot{f}$ is uniquely determined by $\dot{f}$, whereas for eccentric harmonics the additional dependence on harmonic number n and eccentricity e breaks this relation. A measurement of $\ddot{f}$ could therefore, in principle, distinguish between the two cases. In practice, however, the local BBH population consists of long-lived systems with merger timescales typically exceeding $\sim 10^6$ yr (see Equation 7.1), making them effectively non-chirping over a 4-10 yr observation window. For such sources, the observational sensitivity to $\ddot{f}$ is orders of magnitude below the intrinsic $\ddot{f}$ of the dominant harmonics, so the signals are effectively characterized by $\dot{f}$ alone, or are nearly monochromatic. In this regime, $\ddot{f}$ cannot realistically break the degeneracy, and the apparent chirp-mass bias derived above therefore remains relevant (see also Xuan et al., 2021; Chen et al., 2020b).

Additionally, the collective GW background of highly eccentric BBHs can also impact the LISA global fit. For example, Figure 7.11 displays the characteristic strain envelope and the stochastic GW background from the simulated highly eccentric BBHs ($e > 0.9$) in the

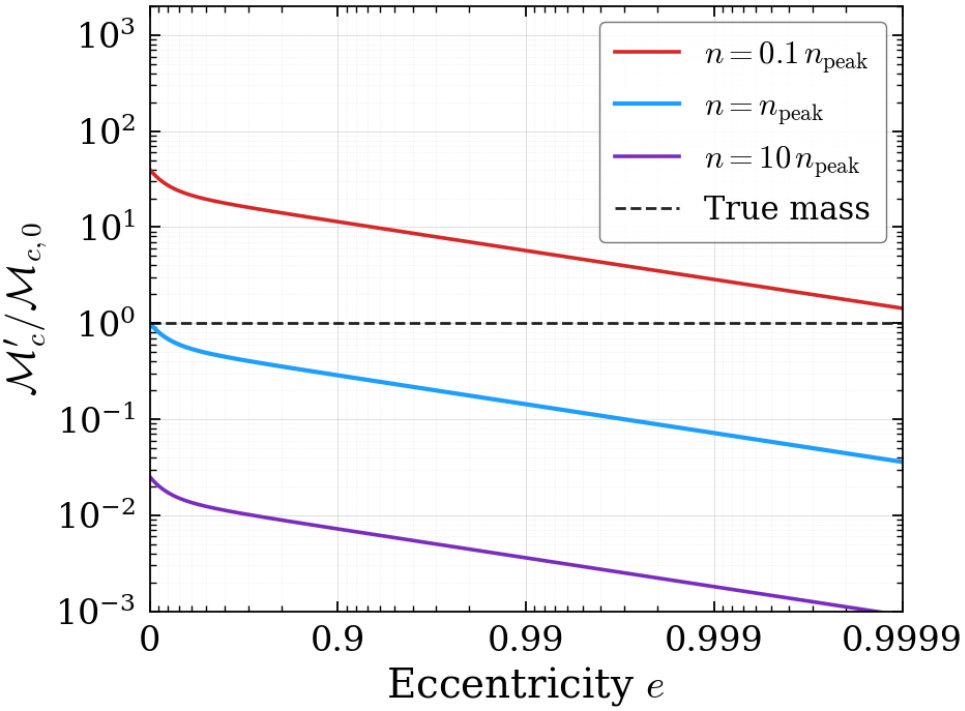


Figure 7.10: **Apparent chirp mass bias for highly eccentric sources.** The curve demonstrates the ratio of the inferred apparent chirp mass $\mathcal{M}_c'$ to the true chirp mass $\mathcal{M}_{c,0}$ when the peak radiating harmonic of an eccentric binary is mistakenly fitted with a quasi-circular waveform template. As the eccentricity approaches unity, the apparent mass significantly underestimates the true system mass.

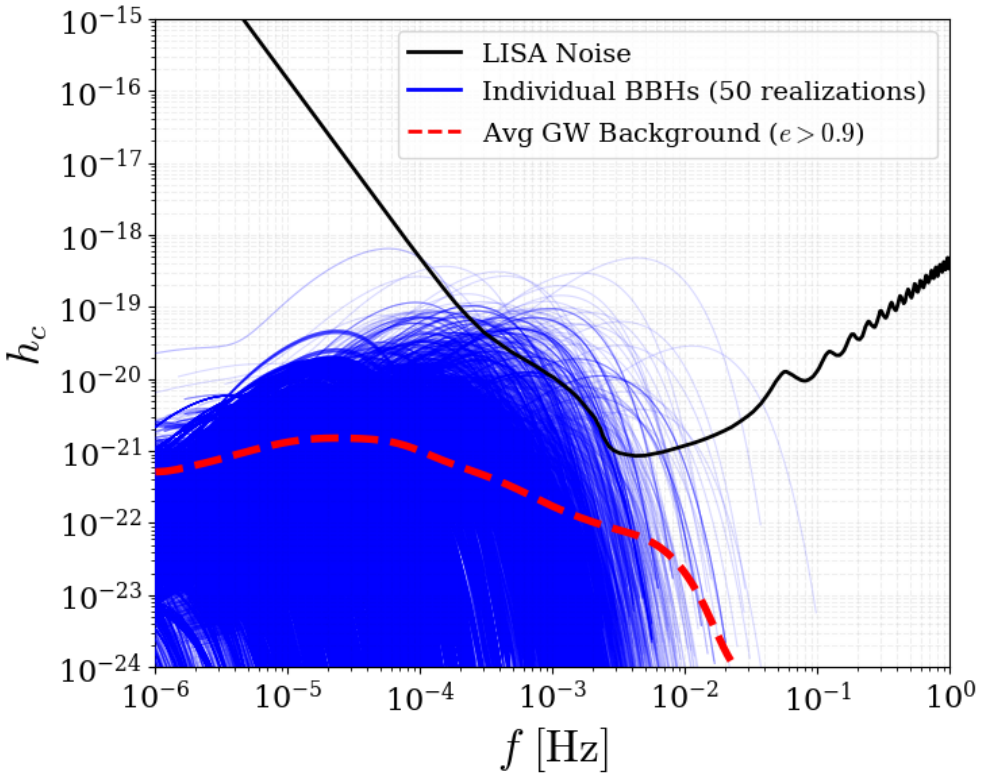


Figure 7.11: **Characteristic strain spectrum and collective GW background of highly eccentric BBHs in the Milky Way.** The plot shows the characteristic strain for BBH sources with $e > 0.9$ in the Milky Way (*smoothed spectrum representation* $h_{c,\mathrm{env}}$, see Equation 7.9). The thin blue curves represent the characteristic strains of dynamically formed BBHs, compiled from 50 realizations of our mock Galactic catalog, assuming a 4-year LISA observation. The thick red dashed curve illustrates the average stochastic GW background produced by this highly eccentric subpopulation in a single MW realization, calculated following eq.19 in Xuan et al. (2024b). For reference, the solid black curve denotes the nominal LISA instrumental noise.

Milky Way. As shown, the collective background from the Milky Way BBH population alone approaches the nominal LISA noise curve. In fact, if we additionally account for extragalactic high-eccentricity sources, this stochastic background will exceed the LISA instrumental noise within its most sensitive mHz band (see Xuan et al., 2024b, for more details). This implies that if high-eccentricity GW bursts are not appropriately modeled and subtracted, they can become a substantial astrophysical foreground, which could interfere with the detection and parameter estimation of other mHz GW sources. The specific implementation of these eccentric sources within the comprehensive LISA global fit pipeline is left for future work.

7.5 Waveform Generation and Validation

Accurate waveform modeling is essential for the detection and characterization of eccentric BBHs in GW data analysis. However, the validity of existing GW waveform models for highly eccentric systems remains poorly understood. In particular, some analytical models used in GW data analysis rely on small-eccentricity expansions (e.g., Buonanno et al., 2009; Moore and Yunes, 2019b; Wette, 2020), which may break down in the high-eccentricity regime. Furthermore, as the eccentricity increases, changes between the pericenter and apocenter introduce significant dynamical scale differences, posing challenges for constructing surrogate models calibrated to numerical relativity simulations.

Nevertheless, for eccentric, stellar-mass mHz sources, post-Newtonian waveforms based on the quasi-Keplerian parametrization can still be effective. This is because, first, the conservative orbital dynamics in quasi-Keplerian parametrization are expressed in closed form, which does not require a Taylor expansion in eccentricity and can mathematically treat arbitrarily large e. Second, for these systems, the pericenter distance can remain sufficiently large for the post-Newtonian expansion to be valid; in particular, it can be related to the peak gravitational-wave frequency as:

$$r_p = \left(\frac{M}{\pi^2 f_{\rm GW}^2}\right)^{1/3}, \tag{7.17}$$

which implies

$$\begin{aligned} \frac{r_p}{r_s} &= \frac{1}{2(\pi M f_{\rm GW})^{2/3}} \\ &\sim 1.1\times 10^4 \left(\frac{M}{20\,{\rm M}_\odot}\right)^{-2/3} \left(\frac{f_{\rm GW}}{1\,{\rm mHz}}\right)^{-2/3}, \end{aligned} \tag{7.18}$$

where $r_s = 2M$ is the Schwarzschild radius corresponding to the total mass of the binary. Equation (7.18) can also be related to the binary's pericenter velocity via $(v_p/c)^2 \simeq \frac{1}{2}(r_p/r_s)^{-1}(1+e)$.

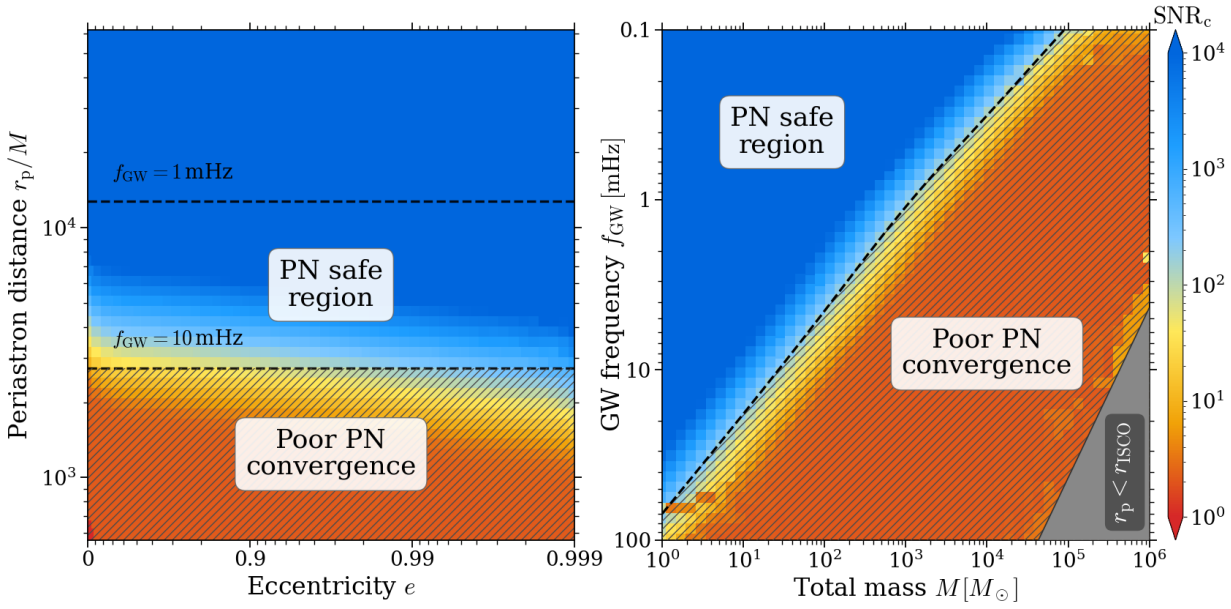


Figure 7.12: **Parameter spaces for post-Newtonian waveforms to converge well in eccentric GW data analysis.** The colormaps show the critical signal-to-noise ratio (SNR$_c$) required to distinguish between waveforms generated using 2PN and 3PN expansions over a 1-year observation, computed numerically using waveform fitting methods (Equation 7.24). The red hatched regions ("Poor PN convergence") indicate parameter spaces where the PN expansion may break down (SNR$_c \lesssim 100$), making it inadequate for data analysis (see also Khalil et al., 2022, note that their fig.1 compares PN with PM expansion, whereas we focus on the *intrinsic* convergence of PN expansion.). *Left Panel:* SNR$_c$ as a function of periastron distance r_p and eccentricity e for a fixed binary mass of $20 + 25\,M_\odot$. The horizontal dashed lines mark constant GW peak frequencies of 1 mHz and 10 mHz. As shown, PN waveforms are highly accurate for stellar-mass systems with high eccentricities, provided $f_{GW} \lesssim 10$ mHz. *Right Panel:* SNR$_c$ as a function of f_{GW} and total mass M, assuming an equal-mass binary with $e = 0.9$. The solid gray region is excluded because the periastron distance falls below the innermost stable circular orbit ($r_p < r_{ISCO}$, in which $r_{ISCO} = 6M$ for a Schwarzschild BH). It demonstrates that as total mass increases, PN waveforms can only converge at lower frequencies for mHz GW data analysis.

Therefore, even for extremely eccentric BBHs, the dynamics near pericenter remain well within the weak-field and low-velocity regime (i.e., $r_p/r_s \sim 10^4$ and $v_p/c \sim 10^{-2}$), provided the system lies in the stellar-mass range and emits gravitational waves in the mHz band. This suggests that the PN expansion converges well and can be appropriate for modeling eccentric inspiral signals in the LISA band.

We can further quantify the convergence of the PN expansion by computing the overlap between waveforms of different PN orders. For example, setting h_1 as the 2PN waveform model with GW source parameters $\boldsymbol{\lambda}_1$, and h_2 as the 3PN waveform model with GW source parameters $\boldsymbol{\lambda}_2$, the normalized overlap between $h_1(\boldsymbol{\lambda}_1)$ and $h_2(\boldsymbol{\lambda}_2)$ is defined as (see, e.g., section IV of Afle et al., 2018):

$$\mathcal{O}(h_1(\boldsymbol{\lambda}_1), h_2(\boldsymbol{\lambda}_2)) = \frac{\langle h_1(\boldsymbol{\lambda}_1)|h_2(\boldsymbol{\lambda}_2)\rangle}{\sqrt{\langle h_1(\boldsymbol{\lambda}_1)|h_1(\boldsymbol{\lambda}_1)\rangle\langle h_2(\boldsymbol{\lambda}_2)|h_2(\boldsymbol{\lambda}_2)\rangle}} \ , \tag{7.19}$$

in which $\langle h_1|h_2\rangle$ represents the noise-weighted inner product between h_1 and h_2:

$$\langle h_1 \mid h_2\rangle = 2\int_0^\infty \frac{\tilde{h}_1(f)\tilde{h}_2^*(f) + \tilde{h}_1^*(f)\tilde{h}_2(f)}{S_{\rm n}(f)}{\rm d}f \ , \tag{7.20}$$

where $\tilde{h}_j$ (with $j = 1, 2$) stands for the Fourier transformation of the waveform, and the star stands for the complex conjugate.

The overlap in Equation (7.19) reflects the similarity between waveforms $h_1(\boldsymbol{\lambda}_1)$ and $h_2(\boldsymbol{\lambda}_2)$. For example, the absolute value of $\mathcal{O}(h_1, h_2)$ varies from 0 to 1, and a perfect match between two waveforms would give $\mathcal{O}(h_1, h_2) = 1$.

Furthermore, the fitting factor (FF) between these two waveform families, h_1 and h_2, is defined as the maximized overlap over the signal's arrival time t_0, phase Φ_0, and all the template parameters $\boldsymbol{\lambda}$:

$$\mathrm{FF} = \max_{\boldsymbol{\lambda}_2, \mathrm{t}_0, \Phi_0} \{\mathcal{O}(\mathrm{h}_1(\boldsymbol{\lambda}_1), \mathrm{h}_2(\boldsymbol{\lambda}_2))\} \ . \tag{7.21}$$

In reality, FF exceeding a given threshold, as set by the signal-to-noise ratio, means the waveform models h_1 and h_2 are indistinguishable (i.e., equally good) for data analysis (Lindblom et al., 2008; Chatziioannou et al., 2017; Takahashi and Seto, 2002b; Cutler and Vallisneri, 2007):

$$\mathrm{FF} > 1 - (D-1)/(2\ \mathrm{SNR}^2)\ , \tag{7.22}$$

in which D represents the dimension of parameter space where the data analysis is carried out (~ 10 for LISA-band sources, depending on the template).

However, since our focus is on the *intrinsic* convergence of PN expansion, we will fix the template parameters ($\boldsymbol{\lambda}_1 = \boldsymbol{\lambda}_2 = \boldsymbol{\lambda}$) in the following comparison, computing the overlap using Equation (7.19), and directly assessing it against the right side of Equation (7.22):

$$\mathcal{O}(h_1(\boldsymbol{\lambda}), h_2(\boldsymbol{\lambda})) = \left.\frac{\langle h_1|h_2\rangle}{\sqrt{\langle h_1|h_1\rangle\langle h_2|h_2\rangle}}\right|_{\boldsymbol{\lambda}} > 1 - \frac{D-1}{2\ \mathrm{SNR}^2}\ . \tag{7.23}$$

Because the fixed-parameter overlap is always a lower bound on the fitting factor, $\mathrm{FF} \geq \mathcal{O}(h_1(\boldsymbol{\lambda}), h_2(\boldsymbol{\lambda}))$, satisfying Equation (7.23) is a *sufficient* condition for the standard indistinguishability criterion of Equation (7.21) to hold in realistic, D-dimensional data analysis. Equation (7.23) therefore imposes a more stringent (conservative) constraint on waveform validity.

We use the x-model to generate PN waveforms in this work (see, e.g., Hinder et al., 2010). The x-model is a time-domain, PN-based waveform family that incorporates features introduced by eccentricity in non-spinning binaries (Huerta et al., 2014). In this approach, the binary dynamics are described through a Keplerian parameterization up to 3PN order, with the conservative evolution also given to 3PN. The gravitational wave energy and angular momentum losses are mapped to the evolution of the orbital eccentricity e and the PN expansion parameter $x \equiv (\omega M)^{2/3}$, where ω denotes the mean Keplerian orbital frequency. These quantities are evolved using equations up to 2PN. This model has been verified against

numerical relativity simulations for equal-mass BBHs with moderate eccentricity ($e = 0.1$), showing good agreement over the final ∼21 inspiral cycles before merger. In the circular limit, it is also consistent with standard waveform templates commonly used in gravitational wave data analysis (e.g., Brown and Zimmerman, 2010).

To match the realistic observation, we set $T_{\rm obs} = 1\,{\rm yr}$ and compute the overlaps between time-domain PN signals generated with the x-model. Specifically, for a given set of source parameters, we generate two waveforms: waveform 1, denoted as $h_{\rm 2PN}$, constructed using 2PN conservative orbital dynamics and 1PN radiation reaction; and waveform 2, denoted as $h_{\rm 3PN}$, constructed using 3PN conservative dynamics and 2PN radiation reaction (see Appendix of Hinder et al. (2010) for details). We then compute the overlap $\mathcal{O}(h_{\rm 2PN}, h_{\rm 3PN})$ in frequency domain (Equation 7.19), and estimate the critical signal-to-noise ratio, ${\rm SNR_c}$, for $h_{\rm 2PN}, h_{\rm 3PN}$ to be indistinguishable in data analysis (see Equation (7.23):

$$ {\rm SNR_c} = \sqrt{\frac{D-1}{2[1-\mathcal{O}(h_{\rm 2PN}, h_{\rm 3PN})]}}\ , \tag{7.24} $$

where D equals 10 for eccentric, non-spinning BBHs (Xuan et al., 2025b).

In general, ${\rm SNR_c}$ represents the SNR threshold below which PN expansion converges well (thus may be safe to use). For example, ${\rm SNR_c} = 100$ implies that the difference between 2PN and 3PN waveforms is indistinguishable for the GW sources' parameter inference, provided that the detected signals have SNR below 100.

Figure 7.12 shows the resulting ${\rm SNR}_c$, as estimated via numerical waveform generation and overlap computation. In particular, the *Left Panel* displays the color map of ${\rm SNR}_c$ as a function of the periastron distance $r_{\rm p}$ and eccentricity e, assuming a fixed BBH mass of $20 + 25\,M_\odot$. For reference, we plot the contours of constant peak GW frequencies $f_{\rm GW} = 1\,{\rm mHz}$ and $10\,{\rm mHz}$ (dashed lines), and use red hatches to shade the region where ${\rm SNR}_c \lesssim 100$, indicating that the 2PN and 3PN waveforms fail to converge. The primary takeaway from

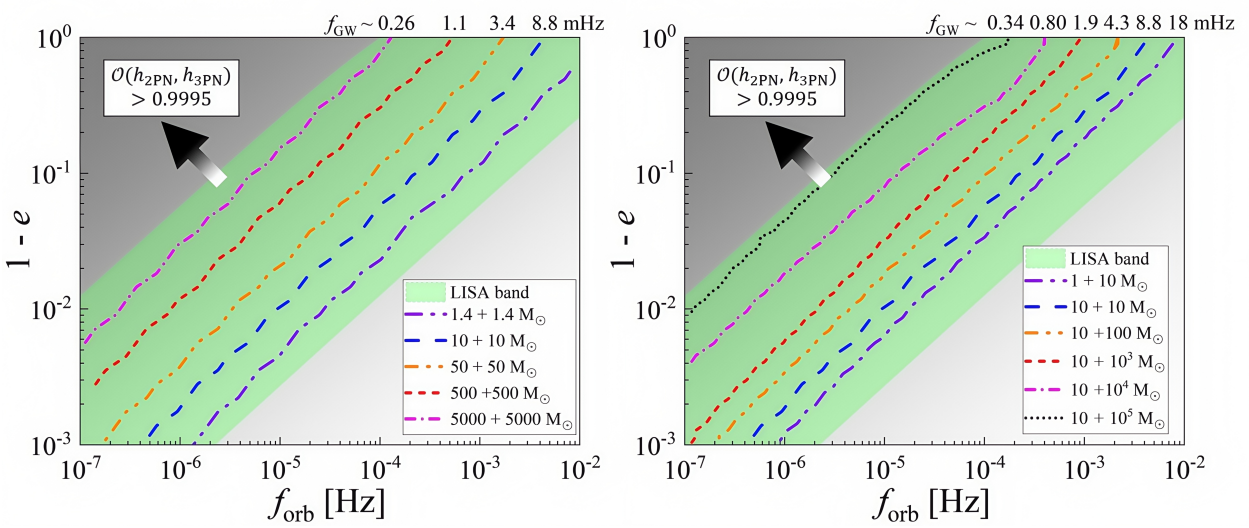


Figure 7.13: **Regime of validity for PN waveforms with different binary orbital frequencies, eccentricities, and masses.** We plot the boundary of parameter space where 2PN and 3PN waveforms converge well in data analysis ($\mathcal{O}(h_{2\mathrm{PN}}, h_{3\mathrm{PN}}) > 0.9995$, corresponding to $\mathrm{SNR}_c > 100$) over a 1-year LISA observation. *Left Panel* shows the boundaries for equal-mass binaries ranging from $1.4 + 1.4\,M_\odot$ to $5000 + 5000\,M_\odot$. *Right Panel* shows unequal-mass systems ranging from $1 + 10\,M_\odot$ to $10 + 10^5\,M_\odot$. For a given mass, the region to the upper-left of the dashed contour, as indicated by the dark grey arrow, represents the high-accuracy regime where the PN waveforms are safe to use. The green shaded area represents the LISA sensitive band (0.1 mHz – 0.1 Hz). We note that the minor "wiggles" along the contours are computational artifacts caused by numerical fluctuations and the discrete parameter grid sampling in the overlap integrals (see Equation 7.19).

the *Left Panel* is that for stellar-mass binaries, the validity of the PN approximation is mostly determined by the peak GW frequency at pericenter, with little dependency on the orbital eccentricity. As long as the GW signal remains below $f_{\rm GW} \sim 10\,{\rm mHz}$, ${\rm SNR}_c$ can safely exceed 100. This indicates that PN waveforms can be reliable for analyzing eccentric, including highly eccentric, stellar-mass BBH signals in the mHz band.

The *Right Panel* shows ${\rm SNR}_c$ as a function of the total binary mass M and peak frequency $f_{\rm GW}$, assuming an equal-mass binary with a fixed eccentricity of $e = 0.9$. The solid gray region in the bottom-right corner is excluded from the analysis because the periastron distance in this regime is smaller than the radius of the innermost stable circular orbit ($r_{\rm p} < r_{\rm ISCO}$). As demonstrated, the convergence of the PN expansion exhibits a strong dependence on the total mass. While stellar-mass binaries converge well in the typical mHz band, the ${\rm SNR}_c \gtrsim 100$ threshold shifts to lower frequencies as the mass grows. Therefore, for massive and supermassive black hole binaries, PN waveforms are only reliable for low-frequency GW data analysis (e.g., $f_{\rm GW} \sim 0.1 - 1$ mHz). Additionally, we test the convergence of PN expansion for different mass ratios by fixing the secondary mass at $m_2 = 10\,M_\odot$ and increasing the primary mass m_1. It turns out that the $f_{\rm GW}$ threshold for PN convergence behaves similarly to the equal mass binary cases (Figure 7.12, *Right Panel*), generally agreeing within a factor of two.

Figure 7.13 shows a generalized view of the PN waveform convergence test, across the parameter space of orbital frequency, eccentricity, and mass. In particular, we select a set of representative compact object masses (see the legend in Figure 7.13). For each mass, the ${\rm SNR}_{\rm c}$ distribution is computed and mapped following a procedure similar to Figure 7.12. Here, however, the distribution is mapped as a function of $f_{\rm orb}$ and $1 - e$, instead of e and r_p. We then extract the equal-${\rm SNR}_{\rm c}$ contour corresponding to ${\rm SNR}_{\rm c} = 100$ in the map, which defines the boundary of the region where PN waveforms converge sufficiently well (i.e., $\mathcal{O}(h_{\rm 2PN}, h_{\rm 3PN}) > 0.9995$, see Equation 7.24). By varying the total mass of the binary,

we track how this high-accuracy boundary shifts across the $f_{\rm orb}$–$(1-e)$ parameter space, as shown by the dashed lines in Figure 7.13.

Left Panel of Figure 7.13 represents the cases of equal-mass binaries, while *Right Panel* shows unequal-mass systems. For comparison, we highlight the region corresponding to the LISA band ($0.1\,{\rm mHz} < f_{\rm GW} < 0.1\,{\rm Hz}$, green shaded band), and mark on the top axis the GW frequency corresponding to each dashed line in the circular limit. As shown, the high accuracy region of PN waveforms spans a broad range of parameter space (toward the upper-left side of each contour). As the mass of binaries increases, this highly PN accuracy region gradually shrinks and shifts toward lower frequencies, eventually moving below the LISA band.

This behavior effectively sets an upper limit of GW frequency for each binary mass, above which PN waveforms are no longer reliable in data analysis. However, as suggested by Figure 7.13, PN methods can safely cover most of mHz sources with stellar mass. Specifically, the high accuracy region extends up to $f_{\rm GW} \sim 9\,{\rm mHz}$ for a $10+10\,M_\odot$ BBH, even at extreme eccentricity values (provided that $f_{\rm GW} \sim 2f_{\rm orb}(1-e)^{-3/2} \lesssim 9\,{\rm mHz}$). Additionally, PN methods may still be useful for analyzing massive systems at lower GW frequencies, such as $\sim 1\,{\rm mHz}$ signals from intermediate-mass black hole binaries ($M \sim 1000\,M_\odot$), and $\sim 0.3\,{\rm mHz}$ signals from extreme mass ratio inspirals ($M \sim 10^5\,M_\odot$).

7.6 Discussion

Eccentric stellar-mass BBHs arise naturally in dynamical formation environments and can contribute significantly to mHz gravitational wave observations (see, e.g., Fang et al., 2019b; Xuan et al., 2024a, 2025a). Their signals exhibit distinctive waveform features, characterized by "repeated bursts" near periapsis (Kocsis and Levin, 2012; Loutrel, 2020; Xuan et al., 2024a;

Romero-Shaw et al., 2023; Knee et al., 2024). In this work, we present a simulated catalog of BBHs formed via dynamical channels, characterizing their population properties in both the Milky Way and at cosmological distances. We further evaluate the impact of these eccentric sources on the LISA global fit, assess the validity of corresponding PN waveform templates, and provide a ready-to-use software package for their population and waveform analysis.

Specifically, we introduce the GW radiation and evolutionary properties of eccentric binaries in Section 7.2.1 (see Figure 7.1 and Table 7.1), then discuss different conventions in the literature to plot their characteristic strain spectrum (Section 7.2.2, Figure 7.2). Based on recent dynamical simulations, we constructed a mock catalog in Section 7.3.1, which incorporates contributions from the Galactic field (fly-by induced mergers, Michaely and Perets, 2019; Michaely and Naoz, 2022), Galactic nuclei (EKL induced mergers, Hoang et al., 2018; Xuan et al., 2024a), and globular clusters (Monte-Carlo N-body results, Kremer et al., 2020; Xuan et al., 2025a). Our study shows that a significant number of eccentric BBHs will be detectable in the Milky Way. For a 4-year (10-year) LISA observation, approximately $25, 8.5, 3.0, 1.5, 0.4$ $(36, 13, 4.7, 2.3, 1.0)$ dynamically-formed MW BBHs can exceed SNR thresholds of $1, 3, 8, 20, 50$, respectively (see Table 7.2).

Because of their dynamical origins, these BBHs exhibit distinct yet universally scaled parameter and SNR distributions. In particular, their evolutionary tracks trace a characteristic pathway in the a–$(1-e)$ plane: systems begin on wide orbits and undergo eccentricity excitation to very high e (with negligible change in a), until gravitational wave emission decouples them from their dynamical environments. This transition appears as a sharp feature in the a–$(1-e)$ plane, followed by GW-dominated orbital shrinkage and circularization (see Figure 7.3).

Meanwhile, different formation channels can exhibit distinct distributions in semi-major axis and eccentricity. For example, the Galactic field channel typically produces wider BBHs ($a \sim$ 1–10 au) with more extreme eccentricities ($e \sim 0.999$) upon entering the LISA band, whereas

globular cluster and Galactic nucleus channels yield more compact systems ($a \sim 0.1$ au) with moderately high eccentricities ($e \sim 0.7$–0.9). Interestingly, our simulations suggest a similar number of detectable sources for different channels (Field, GC, and GN) in high SNR thresholds (up to a factor of a few). However, these channels do exhibit a different power-law SNR distribution (Figure 7.5), which results in different low-SNR BBH populations. Furthermore, despite their specific population distribution, detectable mHz BBHs in the MW all reside along a narrow, elongated region in the $a - (1 - e)$ parameter space (see, e.g., Figures 7.3, 7.4, and 7.7), which roughly corresponds to a GW merger timescale of $t_{\rm merger} \sim 10^7$ yrs and marks the region where GW radiation decouples the system from the dynamical environment.

We further expanded this analysis to extragalactic sources in Section 7.3.3, evaluating both their merger eccentricities in the LVK band (Figure 7.6) and their orbital parameters in the LISA band (Figure 7.7). Our results show that the observable BBHs are dominated by two major populations: wide, highly eccentric BBHs in the local universe ($D_l \sim 10\,$kpc, median $e \sim 0.9$) that produce mHz repeated GW bursts; and quasi-circular, LIGO-type inspirals at cosmological distances ($D_l \sim 100 - 1000\,$Mpc; median $e \sim 0.1 - 0.2$ in mHz band; with varying LVK merger eccentricities, see Figure 7.6). While the extragalactic population contributes significantly at low-SNR regime (~ 150 sources with SNR > 1), this number drops drastically at higher thresholds in mHz GW detection (~ 6 for SNR > 3, and $\lesssim 1$ for SNR > 8), making them a largely faint background compared to the loud local GW bursts.

Notably, eccentric BBHs will significantly affect the LISA global fit. In Section 7.4, we demonstrated that individual harmonics from the local eccentric BBH population can be independently detected. Specifically, we expect an average of ~ 216, 60, 10, and 3 individual harmonics with SNR $> 1, 3, 8, 20$, respectively (Figure 7.9). These harmonics can be misidentified as circular signals from binaries with biased, systematically smaller chirp masses (Figures 7.8 and 7.10). Furthermore, our estimation of the stochastic background

indicates that the collective background from Milky Way highly eccentric BBHs sits roughly one order of magnitude below the nominal LISA noise curve (Figure 7.11). However, combining it with the extragalactic cosmological background could produce a confusion noise that may interfere with the detection of other mHz sources (see Xuan et al., 2024b, for details).

We further test the accuracy of PN waveforms for the data analysis of eccentric stellar-mass BBHs in LISA. Specifically, we used numerical waveform generation and inner product overlaps to map the convergence regions of PN-based templates (Figures 7.12 and 7.13). We found that the PN expansion generally converges well for eccentric stellar-mass BBH detection, provided that the system has a peak GW frequency $f_{\rm GW} \lesssim 10\,{\rm mHz}$. Furthermore, the PN method could be leveraged for lower-frequency searches of heavier sources, and remains accurate for binary masses up to $\sim 10^3\,M_\odot$ (with $f_{\rm GW} \lesssim 1\,{\rm mHz}$). However, in both low and high eccentricity cases, the PN method has strict limitations; the upper boundary of its valid frequency range is typically insufficient to support signal processing near the LISA high-frequency limit ($\sim 0.1\,{\rm Hz}$), or for sources with SMBH components (e.g., eccentric extreme mass ratio inspirals). This highlights the need for waveform modeling techniques, such as post-Minkowskian expansion (e.g., Bern et al., 2019; Khalil et al., 2022), self-force approach (e.g., Barack and Pound, 2018), and numerical relativity (e.g., Pretorius, 2005; Baker et al., 2006).

The mock catalog presented here should be viewed as a conservative baseline rather than a complete representation of the Galactic BBH population. In particular, it does not include binaries formed through isolated binary evolution, nor other potentially important dynamical channels such as mergers in AGN accretion disks or isolated hierarchical triples in the field. Nevertheless, our results, based on recent simulations and observational evidence (Hoang et al., 2019; Kremer et al., 2020; Michaely and Perets, 2020; Xuan et al., 2024a, 2025a), provide a ready-to-use population model for LISA data challenges and global fit studies. Moreover, since eccentricity is a generic outcome of dynamical formation, there

exist other potential eccentric GW populations, such as dynamically-formed BH-WD or BH-NS binaries (e.g., Xuan et al., 2025c), as well as eccentric extreme mass ratio inspirals (e.g., Amaro-Seoane, 2019). While these sources may exhibit different orbital features, they are expected to share the characteristic burst-like GW signatures and highly eccentric evolutionary behavior highlighted in this work.

The catalog generation and waveform modeling developed in this work are implemented in an open-source Python package, the *LISA Eccentricity Astrophysics Package* (`LEAP`). This package provides mock catalogs, along with PN-based time-domain waveform generation and data analysis tools tailored for eccentric systems, enabling these bursting sources to be accurately modeled and fully leveraged in the upcoming era of space-based GW astronomy.

7.7 Acknowledgments

The authors thank the anonymous referee for their useful comments, and thank Pau Amaro Seoane, Yonadav Barry Ginat, and Mor Rozner for their valuable discussions. ZX acknowledges partial support from the Bhaumik Institute for Theoretical Physics summer fellowship. ZX and SN acknowledge partial support from NASA ATP Grant No. 80NSSC24K0773, and thank Howard and Astrid Preston for their generous support. MLK's research was carried out at the Jet Propulsion Laboratory, California Institute of Technology, under a contract with the National Aeronautics and Space Administration (80NM0018D0004).

7.8 Appendix

7.8.1 Eccentric GW signal analysis

7.8.1.1 Analytical SNR Calculation

For completeness, here we summarize and refine the derivations from previous works (see, e.g., Appendix B of Xuan et al., 2024a) regarding the signal-to-noise ratio calculation of eccentric GW sources.

We first present the analytical calculation of the sky-averaged SNR. The time-domain waveform of an eccentric binary, $h(a, e, t)$, can be decomposed into different harmonics, with the frequency of the n-th harmonic given by $f_n = n f_{\rm orb}$ (Peters and Mathews, 1963; Kocsis et al., 2012):

$$h(a, e, t) = \sum_{n=1}^{\infty} h_n(a, e, f_n) \exp(2\pi i f_n t), \tag{7.25}$$

where $h(a, e, t)$ represents the complex waveform combining both polarizations. The corresponding effective real waveform can be written as $h(t)_{\rm real} = \sum_{n=1}^{\infty} \sqrt{2}\, h_n(a, e, f_n) \cos(2\pi f_n t + \phi_n)$, where ϕ_n is the initial phase of the n-th harmonic. Furthermore, the harmonic amplitude is given by:

$$h_n(a, e, f_n) = \frac{2}{n} \sqrt{g(n, e)} h_0(a) \tag{7.26}$$

which represents the inclination-averaged, time-domain root-mean-square (rms) strain amplitude of the n-th harmonic. This quantity incorporates the combined contributions from both GW polarizations. In addition, the overall amplitude $h_0(a)$ is defined as:

$$h_0(a) = \sqrt{\frac{32}{5}} \frac{m_1 m_2}{D_l a}\,, \tag{7.27}$$

and $g(n, e)$ is given by:

$$g(n,e) = \frac{n^4}{32}\Bigg[\left(J_{n-2} - 2eJ_{n-1} + \frac{2}{n}J_n + 2eJ_{n+1} - J_{n+2}\right)^2 + (1-e^2)\left(J_{n-2} - 2J_n + J_{n+2}\right)^2 + \frac{4}{3n^2}J_n^2\Bigg], \tag{7.28}$$

where J_i is the i-th Bessel function of the first kind evaluated at ne.

The SNR of a given GW waveform can be computed via an integral in the frequency domain (see, e.g., Robson et al., 2019a; Chen et al., 2019b):

$$\mathrm{SNR}^2(a,e) = \int \frac{h_c^2(a,e,f)}{f^2 S_n(f)} df, \tag{7.29}$$

where h_c is the characteristic strain and $S_n(f)$ is the effective noise power spectral density of the detector, weighted by the sky and polarization-averaged signal response function of the instrument. We note that the subscript "n" in $S_n(f)$ stands for "noise", which is different from the harmonic index n used throughout this section.

For an eccentric GW source, its characteristic strain $h_c(f)$ peaks at each harmonic's frequency, and its amplitude at the n-th harmonic, $h_{c,n}$, can be estimated as (Finn and Thorne, 2000):

$$h_{c,n}^2 = h_n^2 \cdot \frac{2f_n^2}{\dot{f}_n}, \tag{7.30}$$

where $\dot{f}_n = n \cdot \dot{f}_{\mathrm{orb}}$ is the time derivative of the n-th harmonic frequency, driven by the intrinsic orbital decay of the binary. A more detailed discussion of characteristic strain will be presented in Appendix 7.8.1.2. Also, note that here we take the pre-integral (fundamental) definition of $h_{c,n}$, see Equation (7.40) for details.

As Equation (7.30) shows, the value of h_c is inversely proportional to the binary's orbital frequency shift. In the limit of a non-evolving source (i.e., $\dot{f}_n \to 0$), the value of $h_{c,n}^2$ in

Equation (7.30) diverges mathematically. This divergence reflects the fact that a perfectly monochromatic signal would deposit its energy into an infinitesimally narrow frequency bin Δf_n over an infinite observation time; however, it is an artifact of the stationary phase approximation (SPA) underlying Equation (7.30), and does *not* imply a divergent SNR. As we show next, evaluating the frequency integral in Equation (7.29) yields a per-harmonic contribution that is independent of $\dot{f}_n$ (Equation 7.33). Moreover, for genuinely non-evolving sources ($\dot{f}_n = 0$), the finiteness of the SNR is guaranteed independently by the post-integral characteristic strain (Equation 7.39) together with Parseval's theorem, rather than by the formal cancellation shown below; the two routes nonetheless yield consistent final results.

Specifically, assuming the binary has an orbital chirping rate $\dot{f}_{\rm orb}$ over an observation time $\Delta T_{\rm obs}$, the frequency shift of its n-th GW harmonic can be estimated as:

$$\Delta f_n = \dot{f}_n \Delta T_{\rm obs} = n \dot{f}_{\rm orb} \Delta T_{\rm obs} \,, \tag{7.31}$$

which effectively represents the frequency width of the n-th harmonic peak. Assuming $S_n(f)$ is roughly constant across this narrow bin, we can sum the contributions of each harmonic peak to the integral in Equation (7.29):

$$\begin{aligned} {\rm SNR}^2(a,e) &\approx \sum_n \int_{f_n}^{f_n+\Delta f_n} \frac{h_c^2(a,e,f)}{f^2 S_n(f)} df \\ &\approx \sum_n \frac{h_{c,n}^2}{f_n^2 S_n(f_n)} \Delta f_n . \end{aligned} \tag{7.32}$$

Plugging in Equations (7.30) and (7.31), we get:

$$\begin{aligned}\mathrm{SNR}^2(a,e) &\approx \sum_n \frac{h_{c,n}^2}{f_n^2 S_n(f_n)} \Delta f_n \\ &= \sum_n \frac{h_n^2 \cdot \left(2f_n^2/\dot{f}_n\right)}{f_n^2 S_n(f_n)} \cdot \dot{f}_n \Delta T_{\mathrm{obs}} \\ &= \sum_n \frac{2h_n^2}{S_n(f_n)} \Delta T_{\mathrm{obs}} \,.\end{aligned} \tag{7.33}$$

Equation (7.33) essentially demonstrates that the total squared SNR (power) of an eccentric GW signal is the sum of the squared SNRs of its individual harmonics, where each harmonic is mathematically treated as an independent circular GW source (see, e.g., eq. 35 in Moore et al., 2014). A visual representation of this discrete harmonic structure is shown in Figure 7.1.

We note that the cancellation of $\dot{f}_n$ between Equations (7.30) and (7.31) is carried out in the evolving regime, where $\Delta f_n \gg 1/T_{\mathrm{obs}}$ and the SPA underlying Equation (7.30) holds. The resulting per-harmonic contribution, $2h_n^2 \Delta T_{\mathrm{obs}}/S_n$, is itself independent of $\dot{f}_n$, and therefore extends smoothly to the non-evolving (long-lived) sources discussed below. In that limit, the same result follows directly from the post-integral characteristic strain (Equations 7.39 and 7.41) and is independently guaranteed by Parseval's theorem (Appendix 7.8.1.4), without invoking the SPA. This agreement between the two routes is what justifies applying Equation (7.34) to long-lived sources, as we do next.

Specifically, substitute h_n from Equation (7.27) into Equation (7.33), and get:

$$\mathrm{SNR}^2 = 8h_0^2(a) \sum_n \frac{g(n,e)}{S_n(nf_{\mathrm{orb}})n^2} \Delta T_{\mathrm{obs}} \,. \tag{7.34}$$

Equation (7.34) can be directly applied to the SNR estimation of long-lived GW sources, assuming that the evolution of the orbital parameters is negligible during ΔT_{obs}. In a more

general case, however, the system's parameters $(a, e, f_{\rm orb})$ evolve as functions of time during the observation window. Therefore, the result in Equation (7.34) should be treated as the differential SNR contribution ($\mathrm{SNR}^2 \to d\mathrm{SNR}^2$) over an infinitesimal observation window ($\Delta T_{\rm obs} \to dt$). The total SNR over a finite observation time, $\mathrm{SNR}_{\rm tot}$, is then obtained by integration:

$$\begin{aligned}\mathrm{SNR}^2_{\rm tot} &= \int_0^{T_{\rm obs}} d\mathrm{SNR}^2(t) \\ &= \int_0^{T_{\rm obs}} 8h_0^2(a(t)) \sum_n \frac{g(n, e(t))}{S_n(n f_{\rm orb}(t))\, n^2} dt\,. \end{aligned} \tag{7.35}$$

Equation (7.35) provides the most general SNR formulation for evolving eccentric GW sources.

Additionally, when the binary's orbit is highly eccentric, calculating the sum over millions of harmonics in Equations (7.34) and (7.35) becomes computationally expensive. However, we can accelerate this mode summation by utilizing the continuous envelope of the frequency spectrum. In other words, instead of summing over millions of discrete harmonics, we can estimate their average amplitude within a wider frequency bin and multiply by the density of peaks below that envelope, thereby approximating the SNR via a smoothed frequency integration.

Consider a fixed frequency f and a narrow integration interval df around it. The number of harmonic peaks contained within this interval is proportional to the bin width, $dn = df/f_{\rm orb}$ (note that the separation between harmonics is $f_{\rm orb}$), and the average amplitude of these peaks can be estimated using a local average of $g(n_{\rm avg}, e)$ in Equation (7.35), where $n_{\rm avg} = f/f_{\rm orb}$.

Thus, the discrete mode summation in Equation (7.34) transforms into a continuous fre-

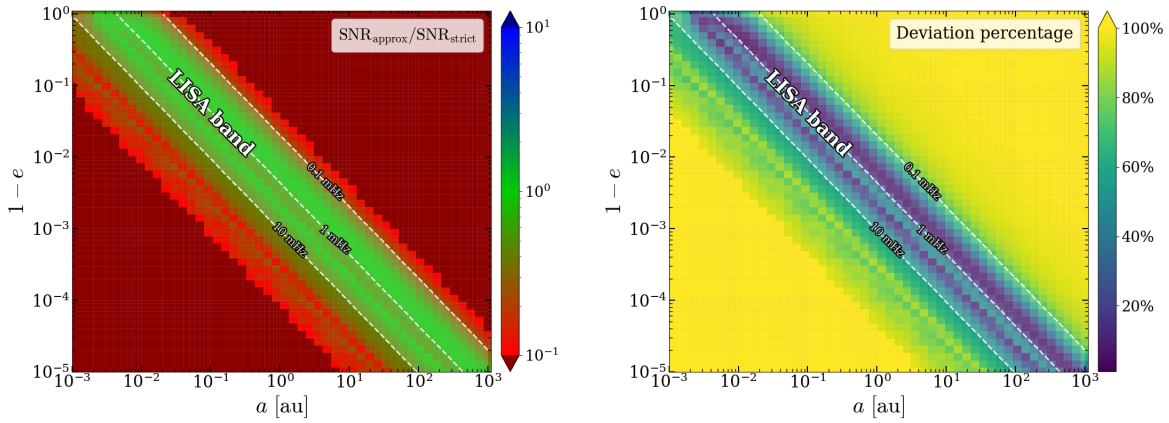


Figure 7.14: **Comparison between different SNR calculation methods.** Here we compute the analytical SNR approximation, $\mathrm{SNR}_{\rm approx}$, Equation (8.19), and the strictly computed SNR, $\mathrm{SNR}_{\rm strict}$, Equation (7.35) for a $10+10\ M_\odot$ binary with different orbital parameters. *Left panel:* The numerical ratio of $\mathrm{SNR}_{\rm approx}$ to $\mathrm{SNR}_{\rm strict}$. The green region highlights where the ratio is close to unity. *Right panel:* The relative deviation percentage between the two calculations. The region bounded by the white dashed lines represents the LISA sensitivity band (0.1 mHz to 10 mHz). Within this band, the analytical approximation is consistent with the strict calculation, with the relative deviation generally below 60%.

quency integral:

$$\begin{aligned}\mathrm{SNR}^2 &\approx 8h_0^2(a)\Delta T_{\rm obs}\int \frac{g(n_{\rm avg},e)}{S_n(f)n_{\rm avg}^2}dn \\ &= 8h_0^2(a)\Delta T_{\rm obs}\int \frac{g(n_{\rm avg},e)}{S_n(f)\left(\frac{f}{f_{\rm orb}}\right)^2}\frac{df}{f_{\rm orb}} \\ &= 8h_0^2(a)f_{\rm orb}\Delta T_{\rm obs}\int \frac{g(n_{\rm avg},e)}{S_n(f)f^2}df\ ,\end{aligned} \tag{7.36}$$

and similarly for Equation (7.35):

$$\mathrm{SNR}^2_{\rm tot} \approx \int_0^{T_{\rm obs}} 8h_0^2(a(t))f_{\rm orb}(t)\left[\int \frac{g(n_{\rm avg},e(t))}{S_n(f)f^2}df\right]dt\ . \tag{7.37}$$

Equations (7.36) and (7.37) serve as fast numerical estimators for the SNR of highly eccentric binaries. The accuracy of the integral can be controlled by adjusting the step size df. In the limit of $df = f_{\rm orb}$, the strict discrete summation of Equations (7.34) and (7.35) is recovered.

In addition, to validate the analytical approximation discussed in Section 7.2, we compare the strictly calculated SNR from Equation (7.35) with the approximate analytical estimation

given by Equation (8.19). The comparison across the parameter space is illustrated in Figure 7.14. As shown in the figure, both methods yield generally consistent results within the LISA band. The ratio of the approximated SNR to the strict SNR ($\mathrm{SNR}_{\mathrm{approx}}/\mathrm{SNR}_{\mathrm{strict}}$) is distributed closely around unity, and the relative deviation percentage is below 60% for the majority of the parameter space. This consistency confirms that Equation (8.19) is a reliable SNR estimation for general BBH population studies within the LISA band.

7.8.1.2 Analytical Characteristic Strain Calculation

In the gravitational wave literature, the definition and computation of the characteristic strain, h_c, often depend on the observational context and the evolutionary stage of the source. These varying conventions can introduce ambiguities when comparing sensitivity curves with source amplitudes. In this section, we clarify the conventions adopted in this work and relate them to the literature.

For an inspiraling source with GW frequency derivative $\dot{f}$ and time-domain rms strain amplitude h_0, the characteristic strain is defined as (Finn and Thorne, 2000; Moore et al., 2014)

$$h_{c,\mathrm{insp}} = h_0 \sqrt{\frac{2f^2}{\dot{f}}} \,. \tag{7.38}$$

This definition has a clear physical interpretation: as the signal evolves, the area enclosed by the h_c evolution track and the noise curve in a log-log plot is directly proportional to the square of the signal-to-noise ratio (see eq. 19 in Moore et al., 2014).

However, for non-evolving or slowly evolving sources such as Galactic binaries, their GW frequency shift is negligible during observation ($\dot{f} \to 0$). Applying the previous definition would cause h_c to diverge, resulting in an infinitely high and narrow track in the characteristic strain plot (since an infinite time to evolve across a frequency bin implies an infinite SNR accumulation). In reality, the observation time T_{obs} is finite, which always yields a finite SNR.

Therefore, it is conventional to plot the h_c of slowly evolving systems using an alternative definition (see, e.g., Kupfer et al., 2018; Tauris, 2018; Robson et al., 2019a):

$$h_{c,\mathrm{non-evolve}} = \sqrt{2}h_0\sqrt{N} = \sqrt{2}h_0\sqrt{fT_{\mathrm{obs}}}\ , \tag{7.39}$$

meaning the characteristic strain of a monochromatic signal is proportional to the square root of the number of cycles, $N = fT_{\mathrm{obs}}$, that the signal undergoes during the observation. The additional factor of $\sqrt{2}$ accounts for the fact that our h_0 is defined as the time-averaged rms amplitude rather than the peak amplitude. This alternative definition plots the signals as discrete points in the characteristic strain plot, with the height of each point representing their post-integration SNR.

In the literature, the definitions in Equations (7.38) and (7.39) are frequently mixed or combined into a unified formula. Adapted for our rms amplitude convention, this becomes:

$$h_c = \sqrt{2}h_0\sqrt{\min\left\{\frac{f^2}{\dot{f}},\ fT_{\mathrm{obs}}\right\}}\ . \tag{7.40}$$

However, the physical meanings of the two regimes in Equation (7.40) are fundamentally different: The $\dot{f}$-dependent characteristic strain (Equation 7.38) is a *pre-integral* quantity, which is related to the SNR via the standard frequency integral (Equation 7.29); In contrast, the T_{obs}-dependent expression (Equation 7.39) is a *post-integral* quantity, for which the SNR is evaluated directly without performing the frequency integral:

$$\mathrm{SNR}^2 = \frac{h^2_{c,\mathrm{non-evolve}}}{fS_n(f)}\ . \tag{7.41}$$

This distinction is reflected in the characteristic strain plot: for evolving sources with $f^2/\dot{f} < fT_{\mathrm{obs}}$, the height of their characteristic strain curve is independent of T_{obs}, while T_{obs} determines the evolution time for $h_{c,\mathrm{insp}}$, thus affecting the enclosed area and accumu-

lated SNR. Conversely, for non-evolving sources, the height of the point depends on $T_{\rm obs}$, and its ratio to the detector noise directly represents the accumulated SNR over $T_{\rm obs}$.

7.8.1.3 Plotting Characteristic Strain of (Highly) Eccentric Systems

There are different approaches to visualizing the characteristic strain of (highly) eccentric sources, each serving a different analytical purpose.

The first approach, which we refer to as the *individual harmonic representation*, plots each harmonic independently using the h_c definitions in Equation (7.8). However, for highly eccentric sources, the number of harmonics is large, and their frequency evolution is often slow in the mHz band ($\dot{f} \to 0$). As a result, plotting individual harmonics can become overwhelmingly cluttered, and hard to reflect the overall detectability of an eccentric source (see, e.g., the scatter points in Figure 7.8).

The second approach, which we refer to as the *smoothed spectrum representation*, introduces a smoothed characteristic strain envelope, $h_{c,\rm env}(f)$, for a highly eccentric GW source. This approach is designed to capture the cumulative spectral contribution of a single eccentric binary across different GW frequencies (see Equation 7.9).

Specifically, consider a fixed frequency f and a narrow interval df around it. The number of harmonics contained within this interval is $dn = df/f_{\rm orb}$. Treating each harmonic as a monochromatic, slowly evolving source, its contribution to the SNR can be estimated using Equations (7.39) and (7.41):

$$\Delta{\rm SNR}^2_{\rm single} \sim \frac{h^2_{c,n}(f)}{f S_n(f)} = \frac{(\sqrt{2}h_n(f)\sqrt{fT_{\rm obs}})^2}{f S_n(f)} = \frac{2h^2_n(f)T_{\rm obs}}{S_n(f)} \ , \tag{7.42}$$

where $h_{c,n}(f) = \sqrt{2}h_n(f)\sqrt{fT_{\rm obs}}$ is the averaged characteristic strain for harmonics near frequency f, $h_n(f) = 2/n_{\rm avg} \cdot \sqrt{g(n_{\rm avg}, e)}h_0(a)$ and $n_{\rm avg} = f/f_{\rm orb}$, see Equations (7.26) -

(7.28). See also Equations (7.36) - (7.37) for a similar derivation.

Therefore, the total contribution to the signal-to-noise ratio from all harmonics within a frequency interval df around f is

$$d\mathrm{SNR}^2 = dn \times \Delta\mathrm{SNR}^2_{\mathrm{single}} = \frac{df}{f_{\mathrm{orb}}} \frac{2h_n^2(f)T_{\mathrm{obs}}}{S_n(f)} \ . \tag{7.43}$$

where dn denotes the number of harmonics within df.

We then define the continuous characteristic strain envelope as:

$$h_{c,\mathrm{env}}(f) = \sqrt{2}\, h_n(f) \sqrt{\frac{f^2 T_{\mathrm{obs}}}{f_{\mathrm{orb}}}} \ , \tag{7.44}$$

This definition ensures that the standard characteristic strain integral of $h_{c,\mathrm{env}}$ (Equation 7.29) over a frequency bin df reproduces the correct accumulated SNR from all harmonic peaks within the same bin, as computed previously in Equation (7.43):

$$\int d\mathrm{SNR}^2 = \int \frac{df}{f_{\mathrm{orb}}} \frac{2h_n^2(f)T_{\mathrm{obs}}}{S_n(f)} = \int \frac{h^2_{c,\mathrm{env}}(f)}{f^2 S_n(f)}\, df \ . \tag{7.45}$$

We note that $h_{c,\mathrm{env}}$ does not correspond to the geometric upper envelope of individual harmonic tracks in Equation (7.40). Instead, its physical interpretation is that, on a log–log characteristic strain plot, the area between $h_{c,\mathrm{env}}(f)$ and $\sqrt{fS_n(f)}$ is directly related to the SNR. This allows one to visually estimate the detectability of the source (Moore et al., 2014), as well as the GW energy contribution from different frequency ranges (see, e.g., the blue curves in Figure 7.11).

Finally, the third approach, which we refer to as the *numerical spectrum representation*, is used in numerical waveform analysis, where the time-domain waveform with finite length is transformed to a spectrum via a Fast Fourier Transform (FFT). This yields $h_{c,\mathrm{num}}[k]$, as

described below in Appendix 7.8.1.5.

While the individual harmonic ($h_{c,n}$), smoothed spectrum ($h_{c,\mathrm{env}}(f)$), and numerical spectrum ($h_{c,\mathrm{num}}[k]$) representations describe the same underlying physical signal, they differ fundamentally in their construction and in how the total SNR is computed. In the *individual harmonic representation*, each harmonic in the eccentric signal is treated as a quasi-circular source. Their SNR^2 is computed using Equation (7.29) when $f^2/\dot{f} < fT_{\mathrm{obs}}$, and Equation (7.41) when $f^2/\dot{f} > fT_{\mathrm{obs}}$, then summed together to yield the total SNR^2 of the eccentric source; In the *smoothed spectrum representation*, $h_{c,\mathrm{env}}$ renormalize discrete harmonic power over frequency, and the total SNR is obtained via a continuous integral (Equation 7.45); In contrast, *the numerical spectrum* $h_{c,\mathrm{num}}$ can apply to arbitrary time-domain waveforms, and its SNR is computed via a direct, discrete summation (Equation 7.51). Although all three approaches converge to the same total SNR for highly eccentric systems, their visual representations on the h_c plot can differ significantly. See Figure 7.2 for a comparison.

7.8.1.4 Numerical SNR Calculation

Consider a discrete time-domain signal $h_t[i] = h(i \cdot t_s)$, where $i = 0, 1, \ldots, N-1$, t_s is the sample interval, and the total observation time is $T_{\mathrm{obs}} = Nt_s$. We assume the total number of samples N is an even integer for simplicity.

Applying a one-sided Fast Fourier Transform to $h_t[i]$ yields the complex frequency-domain array $H[k]$ (for the positive frequency components). To extract the physical time-domain amplitude, we apply the normalization:

$$\sqrt{2}h_{\mathrm{FFT}}[k] = |H[k]|\frac{2}{N}\,, \tag{7.46}$$

where $h_{\mathrm{FFT}}[k]$ is the rms time-domain amplitude of the k-th discrete Fourier component at

frequency $f[k]$ (which equals $1/\sqrt{2}$ times of the maximum time-domain amplitude); $|H[k]|$ is the norm of the complex array $H[k]$; the factor of $2/N$ arises because of the numerical property of FFT and the fact that we only take the positive frequency components. While the full one-sided spectrum spans $k = 0, 1, \ldots, N/2$ (yielding $N/2 + 1$ discrete bins with $\Delta f = 1/T_{\rm obs}$), in practical numerical implementations, both the DC component ($k = 0$) and the Nyquist component ($k = N/2$) are dropped. This prevents singular noise power at zero frequency and potential high-frequency artifacts.

With the corresponding phase $\phi[k]$ of $H[k]$, the time-domain signal can be reconstructed as a sum of monochromatic components at frequencies $f[k]$:

$$h_t[i] \sim \sum_k \sqrt{2} h_{\rm FFT}[k] \cos(2\pi f[k] i t_s + \phi[k]) \,. \tag{7.47}$$

This decomposition holds for an arbitrary signal: $h_{\rm FFT}[k]$ is simply the amplitude of the k-th component on the FFT frequency grid required to reconstruct $h_t[i]$, without any assumption about the underlying signal form.

Note that any realistic signal has a finite duration, which introduces non-trivial effects in the numerical results of $h_{\rm FFT}[k]$. In particular, a finite observation window of duration $T_{\rm obs}$ is equivalent to multiplying the underlying signal by a rectangular window in the time domain, which corresponds to convolving the true spectrum with a sinc-shaped kernel of width $\sim 1/T_{\rm obs}$ in the frequency domain. For the multi-harmonic signals considered in this work, $h_{\rm FFT}[k]$ recovers the true harmonic amplitude h_n at $f[k] = n f_{\rm orb}$ only when every harmonic frequency $n f_{\rm orb}$ coincides exactly with an FFT grid point (i.e., when $n f_{\rm orb} T_{\rm obs}$ is an integer for all relevant n); in that case, the sinc kernel's zeros happen to fall on all neighboring grid points, leaving $h_{\rm FFT}[k]$ non-zero only at the harmonic bins. In the more general case, where the harmonic frequencies do not align with the FFT grid, each harmonic's power can leak into neighboring bins, so that $h_{\rm FFT}[k]$ stays non-zero even when $f[k]$ does not equal the

harmonic frequencies $nf_{\rm orb}$; and the sampled peak at $f[k] \approx nf_{\rm orb}$ falls slightly below h_n. Nevertheless, Parseval's theorem guarantees that the total signal power is preserved across all bins, so that summing $|h_{\rm FFT}[k]|^2$ over the bins into which a given harmonic leaks recovers the true power $|h_n|^2$ of that harmonic. Consequently, the bin-wise SNR sum constructed below correctly accounts for the leaked power and remains insensitive to the alignment between $nf_{\rm orb}$ and the FFT grid.

Specifically, treating $h_{\rm FFT}[k]$ at each frequency $f[k]$ as an independent, monochromatic signal within finite duration $T_{\rm obs}$, its squared SNR contribution is (see Equation 7.41):

$$\mathrm{snr}_k^2 = \frac{(\sqrt{2}h_{\rm FFT}[k] \cdot \sqrt{f[k]T_{\rm obs}})^2}{f[k] \cdot S_n(f[k])} = \frac{2h_{\rm FFT}[k]^2 T_{\rm obs}}{S_n(f[k])}\,, \tag{7.48}$$

where $S_n(f[k])$ is the one-sided noise Power Spectral Density, and the term $\sqrt{f[k]T_{\rm obs}}$ accounts for the number of cycles this frequency component contributes during $T_{\rm obs}$. The total SNR^2 for $h_t[i]$ waveform is simply the sum over the valid AC frequency bins:

$$\mathrm{SNR}^2 = \sum_{k=1}^{N/2-1} \mathrm{snr}_k^2\,. \tag{7.49}$$

7.8.1.5 Numerical Characteristic Strain Calculation

For an arbitrary numerical waveform (such as those generated from highly eccentric binaries with complex harmonic structures), there is generally no *a priori* analytical expression for the frequency derivative $\dot{f}$ at a given global frequency f. Consequently, the conventional analytical definition of the characteristic strain derived from the Stationary Phase Approximation, $h_c \propto \sqrt{f^2/\dot{f}}$, cannot be directly applied.

Instead, we adopt the discrete time-domain representation $h_t[i]$. As established in the previous section, the FFT directly provides the discrete monochromatic physical amplitude

$h_{\mathrm{FFT}}[k]$ at each frequency $f[k]$. For an individual frequency component observed over the total duration T_{obs}, the effective number of accumulated cycles is given by $N_{\mathrm{eff}} = f[k]T_{\mathrm{obs}}$.

The numerical characteristic strain $h_{c,\mathrm{num}}[k]$ at frequency $f[k]$ is then defined by scaling the discrete time-domain amplitude by the square root of the effective cycles:

$$h_{c,\mathrm{num}}[k] = \sqrt{2}h_{\mathrm{FFT}}[k]\sqrt{N_{\mathrm{eff}}} = \sqrt{2}h_{\mathrm{FFT}}[k]\sqrt{f[k]T_{\mathrm{obs}}}\,. \tag{7.50}$$

Note that this numerical formulation avoids the ambiguous $\dot{f}$ interpretation. The blue curves in Figure 7.1 are calculated following this method.

This definition guarantees mathematical consistency with the SNR calculation. By substituting $h_{c,\mathrm{num}}[k]$ back into Equation (7.41), we naturally recover the numerical SNR per bin:

$$\begin{aligned}\mathrm{snr}_k^2 &= \frac{h_{c,\mathrm{num}}[k]^2}{f[k]S_n(f[k])} \\ &= \frac{\left(\sqrt{2}h_{\mathrm{FFT}}[k]\sqrt{f[k]T_{\mathrm{obs}}}\right)^2}{f[k]S_n(f[k])} = \frac{2h_{\mathrm{FFT}}[k]^2 T_{\mathrm{obs}}}{S_n(f[k])}\,.\end{aligned} \tag{7.51}$$

Equation (7.51) demonstrates that defining $h_{c,\mathrm{num}}[k] = \sqrt{2}h_{\mathrm{FFT}}[k]\sqrt{f[k]T_{\mathrm{obs}}}$ correctly maps the raw FFT output to the physical sensitivity curve without requiring any assumptions about the orbital evolution rate.

Chapter 8

From Wide Triples to UCXBs: Multimessenger Signatures of Dynamically-formed Black Hole-White Dwarf Systems in the LISA Band

A version of this chapter was previously published in *The Astrophysical Journal* (Xuan et al., 2025c, ApJ 995 27).

Abstract

Ultracompact X-ray binaries (UCXBs) are a subclass of low-mass X-ray binaries characterized by tight orbits and degenerate donors, which pose significant challenges to our understanding of their formation. Recent discoveries of black hole (BH) candidates with main-sequence (MS) or red giant (RG) companions suggest that BH–white dwarf (BH-WD)

binaries are common in the Galactic field. Motivated by these observations and the fact that most massive stars are born in triples, we show that wide BH-WD systems can naturally form UCXBs through the eccentric Kozai-Lidov (EKL) mechanism. Notably, EKL-driven eccentricity excitations combined with gravitational wave (GW) emission and WD dynamical tides can effectively shrink and circularize the orbit, leading to mass-transferring BH-WD binaries. These systems represent promising multimessenger sources in both X-ray and GW observations. Specifically, we predict that the wide triple channel can produce $\sim 3-27$ ($\sim 1-5$) detectable UCXBs in the Milky Way (Andromeda galaxy), including ~ 1 system observable by the mHz GW detection of LISA. If the final WD mass can reach sufficiently small values, this channel could contribute up to $\sim 10^3$ UCXBs in the Galaxy. Furthermore, the identification of tertiary companions in observed UCXBs would provide direct evidence for this formation pathway and yield unique insights into their dynamical origins.

8.1 Introduction

Ultracompact X-ray binaries (UCXBs) are a subclass of low-mass X-ray binaries (LMXBs) with orbital periods shorter than ~ 1 hr (Savonije et al., 1986). These systems host a neutron star or black hole accreting material from a compact, degenerate companion (e.g., a white dwarf; see Nelson et al., 1986; in 't Zand et al., 2007; Armas Padilla et al., 2023). Due to the short orbital period and high mass-transfer rate, UCXBs are luminous X-ray emitters (luminosity $L_X \sim 10^{39}$ erg s^{-1}; e.g., Maccarone et al., 2007) and strong candidates for mHz gravitational wave (GW) observation (e.g., Qin et al., 2023; Chen and Liu, 2025). Studying their observable properties can place robust constraints on compact-object formation and the physics of mass transfer. Furthermore, understanding their population demographics is especially important for joint X-ray and GW studies in a multi-messenger framework, while also enabling the development and validation of data analysis pipelines for future space-based

GW detectors, such as LISA, TianQin, and Taiji (e.g., Amaro-Seoane et al., 2017a, 2022; Luo et al., 2016; Ruan et al., 2020).

Recent observations have confirmed $\sim$ 20 UCXBs in the Milky Way, with the majority hosting a neutron star accretor (see, e.g., Armas Padilla et al., 2023). Additionally, some systems exhibit evidence for a black hole accretor (BH-UCXB). For example, 47 Tuc X9, a bright X-ray source in the globular cluster (GC) 47 Tucanae with a 28-minute orbital period, is among the most promising BH-UCXB candidates (Miller-Jones et al., 2015; Bahramian et al., 2017; Church et al., 2017; Tudor et al., 2018). More recently, a BH-UCXB candidate in the Andromeda galaxy has been reported, with an exceptionally short orbital period of only 7.7 minutes (e.g., Zhang et al., 2024; Yang et al., 2025).

Despite these discoveries, the formation channels of UCXBs, especially those with black hole accretors, remain poorly understood. A common explanation of UCXB formation is the isolated evolution of main-sequence binaries (e.g., Podsiadlowski et al., 2002; van Haaften et al., 2012), in which two main-sequence stars undergo one or two common-envelope (CE) phases, and possibly a supernova, to form a compact-object binary in a tight orbit. However, BH progenitors (main sequence stars with mass $M \gtrsim 20$ $M_\odot$) can expand to $\sim 1000 - 3000$ $R_\odot$ during their stellar evolution (e.g., Levesque et al., 2005; Romagnolo et al., 2023). Consequently, any companion star within $\lesssim 10$ au will undergo mass transfer with the BH progenitor. If the secondary star is significantly less massive, as is the case for BH-UCXB progenitors, unstable mass transfer will be initiated, whereby the secondary spirals through the primary's envelope in a CE event. Given the extreme mass ratio at this stage ($q \lesssim 0.1$), the most probable outcome of CE is a merger, as the available orbital energy is often insufficient to completely eject the primary's envelope. To overcome this difficulty, alternative energy sources for CE ejection have been proposed, see, e.g., Podsiadlowski et al. (2010); Ivanova (2011); Ivanova et al. (2015). These studies further suggest that additional contributions, such as thermonuclear or recombination energy, may assist envelope ejection,

implying that the isolated binary channel, while highly challenging, cannot be entirely ruled out in the formation of BH-UCXBs.

On the other hand, a natural resolution for BH-UCXB formation arises by considering dynamical formation channels. For example, studies have shown that globular clusters can efficiently produce BH-UCXBs through direct collisions, tidal captures, and exchange interactions (e.g., Rasio et al., 2000; Ivanov et al., 2005; Lombardi et al., 2006; Ivanova et al., 2010). Moreover, since most ($\approx 70\%$) BH progenitors are born in triple systems (Moe and Di Stefano, 2017; Sana et al., 2012, 2014; Offner et al., 2023), three-body dynamics are an inescapable consideration for the evolution of BHs in the galaxy. In particular, effectively all triple star systems in the field initially reside in hierarchical configurations (e.g., Tokovinin et al., 2008; Tokovinin, 2022; Shariat et al., 2025a), where a close inner binary is orbited by a distant tertiary companion. In such hierarchical triples, the inner binary can initially be wide enough for the BH to form without ever transferring mass to its companion. Furthermore, over long-term evolution, the tertiary can induce secular eccentric Kozai–Lidov (EKL) oscillations (Lidov, 1962; Kozai, 1962; Naoz, 2016), driving the inner binary to extreme eccentricities. Such high eccentricities drastically reduce the pericenter distance, allowing short-range forces, such as gravitational waves, tides, and magnetic braking, to shrink the orbit. For double-compact-object inner binaries, this triple-induced channel is efficient at producing highly eccentric GW sources (Wen, 2003; Hoang et al., 2018; Hamers, 2018; Stephan et al., 2019; Bub and Petrovich, 2020; Deme et al., 2020; Wang et al., 2021; Xuan et al., 2023, 2024a,b, 2025b,a; Stegmann and Klencki, 2025), while for BH–MS inner binaries it can efficiently form BH–LMXBs (Naoz et al., 2016; Shariat et al., 2025b).

In fact, V404 Cygni, a prototypical BH–LMXB and one of the nearest known, was recently confirmed to host a tertiary companion (Burdge et al., 2024). Its properties are consistent with formation via the triple-induced high-eccentricity channel (Shariat et al., 2025b), demonstrating that field BHs can reside in long-lived hierarchical triples and some are born

with negligible natal kicks ($v_{\rm k} \lesssim 5$ km s^{-1} Burdge et al., 2024; Shariat et al., 2025b). Moreover, V404 Cygni likely evolved from an initially wide BH–MS binary (Shariat et al., 2025b), and such a stellar population yields an even larger population of wide BH–WD inner binaries (separation $a_1 \gtrsim 10 - 100$ au) in triples. The long-lived, wide BH-WD inner binaries could later experience strong secular EKL oscillations and form UCXBs.

In this study, we investigate the dynamical evolution of detached BH–WD binaries in hierarchical triple systems. In particular, we model their evolution by incorporating eccentric Kozai–Lidov oscillations, general relativistic precession, gravitational wave emission, WD dynamical tides, and WD mass transfer. We then estimate the fraction of systems that evolve into BH–UCXBs, evaluate their expected observational signatures in both X-ray and GW bands, and predict the contribution of the triple channel to the UCXB population in the Milky Way and the Andromeda galaxy.

This letter is organized as follows. Section 8.2.1 introduces the formation mechanism and initial population of detached BH–WDs with tertiaries. Section 8.2.2 describes their general behavior in triple evolution and the treatment of WD dynamical tides. Section 8.2.3 focuses on the subsequent mass-transfer evolution of BH–WD systems that undergo strong orbital shrinkage and form UCXBs after the triple stage. We present the simulation results in Section 8.3.1, evaluate the X-ray and GW detectabilities of BH–UCXBs in Section 8.3.2, and outline the assumptions and limitations of our work in Section 8.3.3. Finally, Section 8.4 discusses the results and their astrophysical implications.

8.2 Simulation Setup

8.2.1 Generating the Initial BH-WD Population

In this work, we take the initial wide BH-WD population from the simulation results of Shariat et al. (2025b) (see their fig.4), and further evolve the hierarchical triple systems up to a Hubble time, or until mass transfer starts. For completeness, we briefly summarize their population synthesis setup below, and discuss the resultant BH-WD population.

At t=0, the triples were initialized with all three stars on the zero-age main sequence (ZAMS): a primary of $m_1 = 22$ M$_\odot$ (expected to produce a ~ 10 M$_\odot$ black hole; Sukhbold et al., 2016), a secondary drawn from a uniform mass distribution between $m_2 \sim 1.2-2$ M$_\odot$, and a tertiary of $m_3 = 1.2$ M$_\odot$, chosen to match the observed properties of V404 Cygni, the only known black hole in a triple (Burdge et al., 2024).

Inner and outer orbital periods were drawn from a log-uniform distribution between 0.1 and 10^4 yr (e.g., Sana et al., 2012). Eccentricities were sampled from a uniform distribution for the inner and outer orbits. Mutual inclinations were drawn from an isotropic distribution (uniform in $\cos i$), and spin–orbit angles chosen uniformly. This choice is consistent with observations indicating that wide triples have mutual inclinations consistent with an isotropic distribution (e.g., Tokovinin, 2022; Shariat et al., 2025a).

Each set of initial conditions is required to satisfy both hierarchical and long-term dynamical stability criteria. For hierarchy, we use the octupole-level parameter ϵ (e.g., Naoz et al., 2013a),

$$\epsilon = \frac{a_1}{a_2}\frac{e_2}{1-e_2^2} < 0.1 \ , \tag{8.1}$$

where a_1 and a_2 are the inner and outer semi-major axes, and e_2 is the outer eccentricity.

For long-term stability, we adopt the Mardling and Aarseth (2001) criterion:

$$\frac{a_2}{a_1} > 2.8 \left(1 + \frac{m_3}{m_1 + m_2}\right)^{2/5} \frac{(1+e_2)^{2/5}}{(1-e_2)^{6/5}} \left(1 - \frac{0.3i}{180^\circ}\right) , \tag{8.2}$$

where m_1 and m_2 are the inner binary masses, m_3 is the tertiary mass, and i is the mutual inclination. Hereafter, we use a to represent a_1.

Deviation from strict hierarchy does not necessarily lead to the immediate disruption of the system or the onset of dynamical instability (Grishin et al., 2017; Mushkin and Katz, 2020; Bhaskar et al., 2021; Toonen et al., 2022; Zhang et al., 2023a). Nevertheless, recent observations indicate that virtually all field triples are hierarchical and stable according to the above criteria, reinforcing our choice to focus on hierarchically stable configurations (Shariat et al., 2025a).

Using the above numerical setup, Shariat et al. (2025b) evolves a large population of 50,000 triples using detailed dynamical simulations, which includes the secular equations up to the octupole level of approximation (Naoz et al., 2013a; Naoz, 2016), and general relativity precession (e.g., Naoz et al., 2013b). Prior to BH-WD formation, the simulations also included main-sequence stellar evolution using `MESA` (Paxton et al., 2011) grids from the `POSYDON` (Fragos et al., 2023) framework. For main-sequence stars, they assumed equilibrium tides that change from convective to radiative depending on the stellar type.

Beyond producing a few hundred BH-LMXBs through the triple channel, this population produces an even larger number of detached BH+WD inner binaries (a sample of 1242 systems), which are the focus of this study. These BH-WD inner binaries in triples are all detached and have never transferred mass. Therefore, most of them are wide ($a_1 \sim 10 - 4000$ au), with wide tertiaries companions ($a_2 \sim 200 - 15000$ au), see e.g., Figure 8.4 in Appendix 8.6.1. Notably, the inner binaries of these systems have presumably lost at least half of their initial mass, making their orbits at least twice as large as the initial ones.

8.2.2 Evolution of BH-WDs in Triples and the Inclusion of Dynamical Tides

To evaluate the subsequent evolution of BH-WD systems, we further include the GW emission (e.g., Peters, 1964; Zwick et al., 2020; Xuan et al., 2024a) and dynamical tides, in addition to the previous features of the triple simulation code. Notably, when compact binaries have a pericenter passage time ranging from minutes to hours, dynamical tides excited in the WD component can play a crucial role in shaping the system's physical properties, including the orbital separation, eccentricity, and WD spin. In this work, we adopt the models developed by Fuller and Lai (2012a); Vick et al. (2017); Su and Lai (2022) and incorporate the dynamical tides into the long-term orbital evolution of hierarchical triple systems[1]. We assume a representative mass of $m_1 = 10\ \mathrm{M}_\odot$, $m_2 = 0.6\ \mathrm{M}_\odot$ for BH-WD binaries during this evolution stage (e.g., Corral-Santana et al., 2016; Bahramian and Degenaar, 2023; Pelisoli and Williams, 2025).

In particular, we follow eqs. 34-35 in Vick et al. (2017) to compute the angular momentum and energy transfer rate of dynamical tides in the inertial frame:

$$\dot{J}_{\rm tide} = T_0 \sum_{-\infty}^{\infty} F_{N2}^2 \,\mathrm{sgn}\left(N\Omega - 2\Omega_{\rm s}\right) \hat{F}\left(\omega = |N\Omega - 2\Omega_{\rm s}|\right), \tag{8.3}$$

$$\begin{aligned} \dot{E}_{\rm tide,\ in} &= T_0 \left[\left(\frac{W_{20}}{W_{22}}\right)^2 \sum_{N=1}^{\infty} N\Omega F_{N0}^2 \hat{F}(\omega = |N\Omega|) \right. \\ &\left. + \frac{1}{2} \sum_{-\infty}^{\infty} N\Omega F_{N2}^2 \,\mathrm{sgn}\left(N\Omega - 2\Omega_{\rm s}\right) \hat{F}\left(\omega = |N\Omega - 2\Omega_{\rm s}|\right) \right], \end{aligned} \tag{8.4}$$

where $T_0 \equiv G m_1^2 R_2^5 / a^6$ is a function of WD radius[2] R_2,$W_{20} = \sqrt{\pi/5}$, $W_{22} = \sqrt{3\pi/10}$; Ω is the orbital frequency of the binary, Ω_s is the WD spin angular frequency, and $\hat{F}(\omega)$ is

[1]Note that here tidal dissipation in white dwarfs is assumed to be 100% efficient.

[2]The WD mass stays unchanged during the triple evolution, thus, for simplicity, we assume a fixed $R_2 \sim 5.3 \times 10^{-5}$ au when computing the dynamical tides.

the dimensionless tidal torque of the WD[3]. Hereafter, we use $\dot{E}_{\rm tide}$ to represent $\dot{E}_{\rm tide,in}$ for simplicity.

In Equations (8.3) and (8.4), the summing of integer number N reflects the multiple harmonics of dynamical tides for a general eccentric orbit, and F_{Nm} is the Hansen coefficient (Murray and Dermott, 1999; Storch and Lai, 2013):

$$F_{Nm} = \frac{1}{\pi}\int_0^\pi \frac{\cos[N(E - e\sin E) - mf(E)]}{(1 - e\cos E)^2}\,{\rm d}E\ , \tag{8.5}$$

in which e is the eccentricity of the BH-WD binary; $f(E)$ is the true anomaly, as a function of eccentric anomaly E.

We note that, the Hansen coefficients F_{N2} and F_{N0} can be evaluated using analytical approximations (Su and Lai, 2022):

$$F_{N2} \approx \begin{cases} C_2 N^p e^{-N/\eta_2} & N \geq 0 \\ 0 & N < 0 \end{cases} \tag{8.6}$$

and

$$F_{N0} = C_0 e^{-|N|/\eta_0}\ , \tag{8.7}$$

in which C_0, C_2, p, and η_0, η_2 are fitting coefficients that can be expressed as a function of binary eccentricity (see eqs. (20) - (31) in Su and Lai (2022)). To accelerate the numerical simulation, we further employ empirical relations to analytically fit the results of Equations (8.3)–(8.7); see Appendix 8.6.2 for details.

Furthermore, the orbital evolution of the binary can be related to the energy and angular

[3] $\hat{F}(\omega) \sim 150\omega^5$ for a $T_2 \sim 5000$ K WD, as a function of tidal frequency, ω in $G = M = R = 1$ unit, see e.g., fig.6 in Vick et al. (2017).

momentum transfer rate (Su and Lai, 2022):

$$\frac{\dot{a}_{\rm tide}}{a} = -\frac{2a\dot{E}_{\rm tide}}{Gm_1m_2}, \tag{8.8}$$

$$\frac{e\dot{e}_{\rm tide}}{1-e^2} = -\frac{a\dot{E}_{\rm tide}}{Gm_1m_2} + \frac{T}{J_{\rm orb}}, \tag{8.9}$$

where $J_{\rm orb} = m_1m_2\left[Ga\left(1-e^2\right)/\left(m_1+m_2\right)\right]^{1/2}$ is the orbital angular momentum and T is tidal torque, which equals the angular momentum transfer rate $\dot{J}_{\rm tide}$. Note that here we only show the time derivative of orbital separation and eccentricity ($\dot{a}_{\rm tide}$ and $\dot{e}_{\rm tide}$) contributed by dynamical tides. In a realistic simulation, there will be additional terms from GW radiation (Peters, 1964) and triple interaction (Naoz, 2016) that contribute to the final result of orbit evolution.

Additionally, as can be seen from Equations (8.3) and (8.4), Ω_s can significantly affect the tidal torque. Therefore, it is necessary to include the spin evolution in the simulation. Specifically, we compute its time derivative, $\dot{\Omega}_s$, assuming that the WD rotates rigidly:

$$\dot{\Omega}_{\rm s} = \frac{T}{km_2R_2^2} \tag{8.10}$$

where $km_2R_2^2$ is the moment of inertia of the WD. For simplicity, we assume that $k = 0.2$, and initialize the spin of the WD to zero, i.e., $\Omega_s = 0$. We further assume that the spin aligns with the orbital angular momentum. This is because the spin of WD is only excited after dynamical tides become strong, which have shrunk the orbit, suppressed the EKL oscillation, and frozen the orientation of the system.

During the long-term orbital evolution, the WD spin tends to pseudo-synchronize with the orbital pericenter frequency, $\Omega_p \sim \Omega(1-e)^{-3/2}$ (Vick et al., 2017). In this case, the angular momentum transfer rate will vanish, yielding zero net torque on the WD (see Equation (8.3)). However, if the orbital eccentricity is non-zero, it can always excite multiple harmonics of

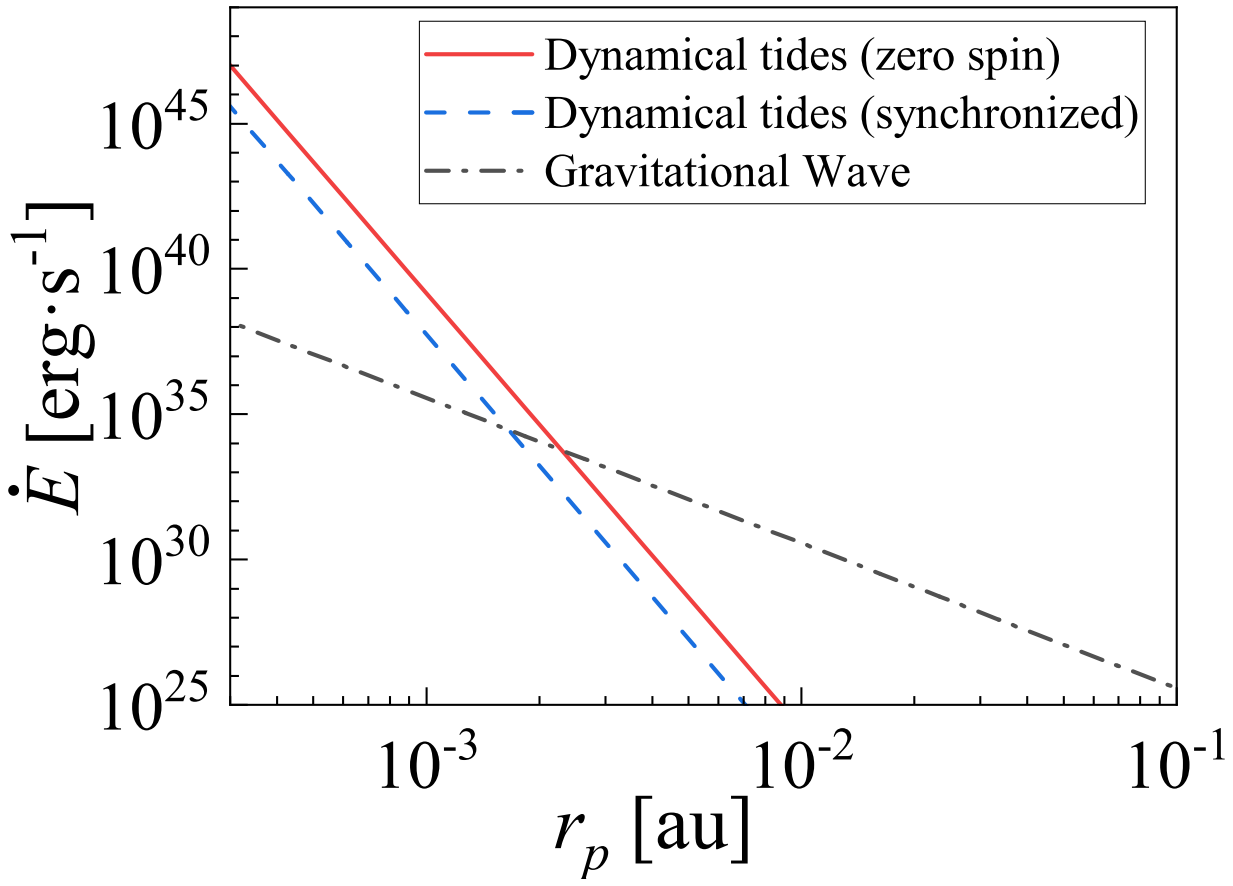


Figure 8.1: **Comparison between the energy transfer rate of dynamical tides and GW radiation, for a highly eccentric BH–WD system.** Here we consider a 10–0.6 $M_\odot$ BH–WD binary with $e = 0.95$, WD radius $R_2 = 5.3 \times 10^{-5}$ au, and WD dimensionless tidal torque $\hat{F}(\omega) \sim 150\omega^5$. The energy transfer rates from WD dynamical tides and from GW radiation are plotted as functions of the binary's pericenter distance r_p. We show two cases for dynamical tides: the zero-spin case (red solid line, fixing $\Omega_s = 0$) and the synchronized-spin case (blue dashed line, when Ω_s synchronizes with pericenter frequency and satisfies $\dot{J}_{\rm tide} = 0$). The energy loss due to GW radiation is shown as the grey dash-dotted line. We note that when eccentricity is nonzero, there will be a residual tidal heating rate (blue dashed line) even when there is no net torque on the WD. This rate will vanish in the circular limit.

dynamical tides in the WD, which creates a residual tidal heating rate. In other words, even if $\dot{J}_{\rm tide} = 0$, $\dot{E}_{\rm tide}$ in Equation (8.4) keeps non-zero. For systems in our simulation, Equation (8.4) will only vanish when both the spin is fully synchronized and the orbit gets fully circularized.

Figure 8.1 shows the energy transfer rate of dynamical tide (red solid line, Equation (8.4)), compared with the power of GW radiation (grey dash-dotted line, Peters, 1964), for a highly eccentric BH-WD binary. As can be seen in the figure, the effect of dynamical tides strongly depends on the pericenter distance. Notably, it can well-exceed the GW radiation power when $r_p \lesssim 10^{-3}$ au. This means WD tides can effectively shrink the orbit during the highly eccentric pericenter passage and help with the formation of UCXBs. Furthermore, even when the WD spin is synchronized with the orbit (blue dashed line, $\Omega_s \sim \Omega_p$), the residual tidal heating is still significant, because of the eccentricity. This means the dynamical tide can keep dissipating energy efficiently, until the binary circularizes and $\dot{E}_{\rm tide}$ vanishes.

We further illustrate the time evolution of a representative BH–WD system in Figure 8.2, with the left column showing its dynamical formation stage. Initially, the inner binary undergoes significant EKL effect because of the distant tertiary companion, which is reflected in the top-left panel in the form of eccentricity oscillation. At the time $t_c - t \sim 0.3$ Myr, the inner binary reaches extreme eccentricity ($1 - e \sim 10^{-5}$), driving the pericenter distance down to $\sim 10^{-3}$ au and triggering strong dynamical tides. In particular, the dynamical tide is excited under conditions of high eccentricity and negligible WD spin, which results in a sharp peak in the ratio of tidal dissipation to GW radiation power (see third row, left panel). As the system evolves, the WD spin synchronizes with the orbital pericenter motion over a short timescale ($\sim 10^5$ yr, see the blue dash-dotted line). This synchronization occurs along with the significant orbital decay and circularization, which eventually suppresses the dynamical tides and leads to the decoupling of the inner binary from the influence of the tertiary companion. By the time the orbital separation a shrinks to $\sim 10^{-3}$ au, systems typically

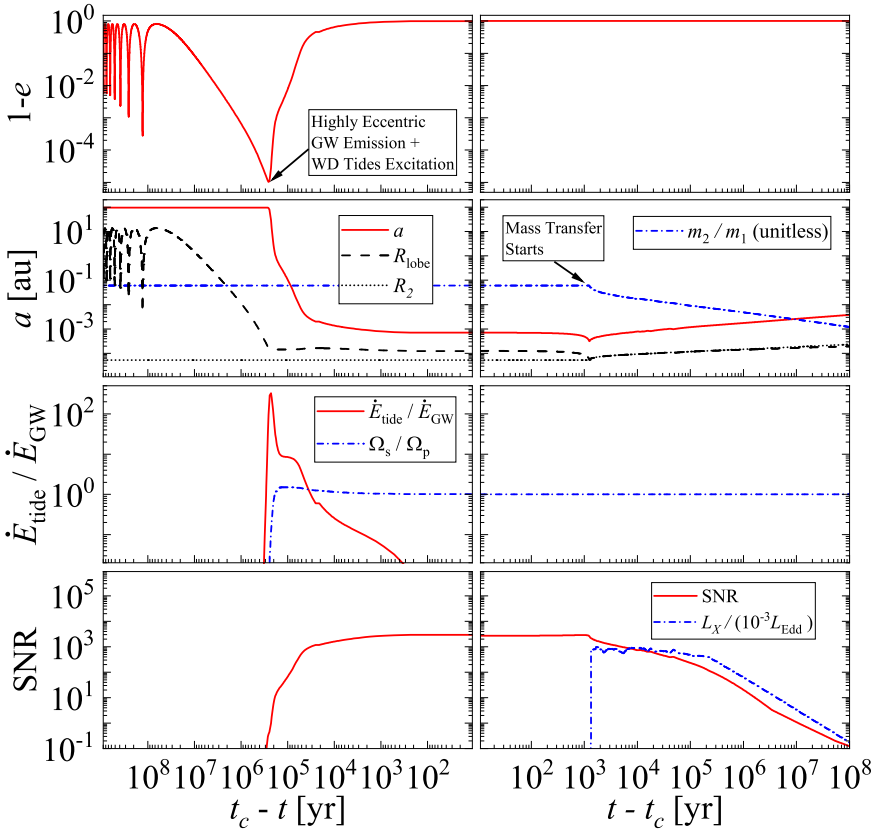


Figure 8.2: **Time evolution of an example BH-WD system that undergoes strong EKL oscillations during the dynamical formation stage (left column) and transitions into a mass-transferring UCXB (right column).** Here we show the time evolution of a representative BH-WD system from our simulation, with initial mass $m_1 = 10$ M$_\odot$, $m_2 = 0.6$ M$_\odot$, orbit separation $a_0 = 95.3$ au, eccentricity $e_0 = 0.199$. This binary is orbited by a tertiary companion with mass $m_3 = 0.836$ M$_\odot$, outer orbit separation $a_2 = 4997$ au, eccentricity $e_2 = 0.602$, and mutual inclination $i = 91.8°$ to the inner binary. We define t_c as the time when the BH–WD binary becomes fully circularized ($e < 0.01$). The system's evolution during the dynamical formation stage is shown in the left column as a function of $t_c - t$ (log-scale), while its post-circularization evolution is shown in the right column as a function of $t - t_c$. The first row shows the inner binary's orbital eccentricity, as $1 - e$. The second row shows the inner orbital separation (red solid line, a), the WD–BH mass ratio (blue dash-dotted line, m_2/m_1), the Roche lobe radius (black dashed line, $R_{\rm lobe}$, see, e.g., eq.28 in Ye et al. (2023)), and the WD radius (black dotted line, R_2). The third row plots two ratios: the tidal energy dissipation rate (red solid line, see Equation (8.4)) to the GW radiation power (see, e.g., eq. 5.4 in Peters (1964)), and the WD spin angular frequency Ω_s to the binary's pericenter frequency $\Omega_p = \Omega(1-e)^{-3/2}$ (blue dash-dotted line). The bottom row shows the expected gravitational wave SNR at distance $D_l = 8$ kpc (red solid line) for a 4-year LISA observation, and the binary's X-ray luminosity L_X (blue dash-dotted line), normalized by 0.1% of the BH Eddington luminosity, $L_0 = 10^{-3} L_{\rm Edd} \sim 1.26 \times 10^{36}$erg s^{-1}.

exhibit nearly circular orbits and synchronized WD spins (see, e.g., when $t_c - t \lesssim 10^2$ yr).

8.2.3 Evolution of Mass-transfer BH-WDs

Following the highly eccentric dynamical evolution (see Section 8.2.2), the BH-WD system's orbit can further shrink and circularize under the influence of GW emission and tidal dissipation, until the Roche lobe of the white dwarf component is smaller than its volume. At this stage, the white dwarf starts to lose surface matter, transferring mass to its BH companion. This process has been studied in depth and is expected to cause X-ray emission, making the system observable as a UCXB. (e.g., Deloye and Bildsten, 2003; van Haaften et al., 2012; Heinke et al., 2013; Sengar et al., 2017; Bobrick et al., 2017; Church et al., 2017; Chen et al., 2020; Suvorov, 2021; Qin et al., 2023; Chen and liu, 2025)

To estimate the orbital evolution of a UCXB system, we assume the binary has decoupled from the tertiary and evolves in isolation, with the orbit fully circularized and the WD spin synchronized[4] (see the discussion in Section 8.2.2). For simplicity, we also assume that the accretion is stable, with mass lost by the donor either accreted or leaving the system as unbound material. Therefore, the change of total orbital angular momentum is given by (see, e.g., eq.2 in van Haaften et al., 2012)[5]:

$$\dot{J}_{\rm orb} = \dot{J}_{\rm GW} + \dot{J}_{\rm eject}. \tag{8.11}$$

where $\dot{J}_{\rm GW}$ is the angular momentum loss caused by the binary's gravitational wave radiation (eq 5.5 in Peters, 1964), and $\dot{J}_{\rm eject}$ is the angular momentum loss caused by the ejected matter

[4]When synchronized with the orbit, the WD's spin angular momentum is usually much smaller than the orbital angular momentum (e.g., $J_{\rm spin}/J_{\rm orb} \lesssim 10^{-4}$ for orbital frequency lower than 10mHz). Therefore, we neglect the term caused by spin angular momentum transfer.

[5]As a proof of concept, we adopt this simplified model which ignores the feedback from the disk. For a more detailed analysis, see, e.g., Deloye and Bildsten (2003); van Haaften et al. (2012); Sengar et al. (2017).

(see, e.g., eq.18 in van Haaften et al., 2012):

$$\frac{\dot{J}_{\rm eject}}{J_{\rm orb}} = q\frac{\dot{M}_{\rm tot}}{M_{\rm tot}}. \tag{8.12}$$

where $q = m_2/m_1$ is the mass ratio of the binary, $M_{\rm tot} = m_1 + m_2$, and $\dot{M}_{\rm tot}$ is the mass loss rate of the system.

On the other hand, from the functional form of the orbital angular momentum $J_{\rm orb}$, we have (see, e.g., eq.23 in van Haaften et al., 2012):

$$\frac{\dot{J}_{\rm orb}}{J_{\rm orb}} = \frac{\dot{m}_1}{m_1} + \frac{\dot{m}_2}{m_2} - \frac{1}{2}\frac{\dot{M}_{\rm tot}}{M_{\rm tot}} + \frac{1}{2}\frac{\dot{a}}{a}. \tag{8.13}$$

where $\dot{m}_1$, $\dot{m}_2$ are the mass transfer rate of BH (positive) and WD (negative), respectively. Define η as the accretion efficiency, we have $\dot{m}_1 = -\eta\dot{m}_2$, and $\dot{M}_{\rm tot} = \dot{m}_1 + \dot{m}_2 = (1-\eta)\dot{m}_2$.

The change of orbital separation can be estimated by combining Equations (8.11) and (8.13), then inserting Equation (8.12):

$$\frac{1}{2}\frac{\dot{a}}{a} = \frac{\dot{J}_{\rm GW}}{J_{\rm orb}} - \frac{\dot{m}_2}{m_2}\left[1 - q + (1-\eta)\frac{q}{2(q+1)}\right]. \tag{8.14}$$

Notably, the coefficient of $\dot{m}_2/m_2$ in the right side of Equation (8.14) is always negative, provided that $q < 1$ and $\eta < 1$. In other words, stable mass transfer from WD to BH ($\dot{m}_2 < 0$) tends to widen the orbit ($\dot{a} > 0$), stopping the binary from orbit shrinkage by GW radiation, and making them long-living UCXB sources.

Furthermore, we adopt the result of van Haaften et al. (2012), taking $\dot{m}_2$, and η as functions of the UCXB orbital parameters from their figs. 1 and 4. Consequently, all the quantities in Equation (8.14) can be expressed in terms of m_1, m_2, and a, and the system's evolution can be determined by integrating the differential equations of dm_1/dt, dm_2/dt, and da/dt.

We evolve the BH-WD systems until the WD mass is too light (specifically $m_2 \sim 0.01$–$0.02\ \mathrm{M}_\odot$, which may result in disrupting the WD), and the orbit is too wide to maintain a stable mass transfer. Notably, the final WD mass puts a constraint on the lifetime of a UCXB system, yet this value remains highly uncertain. In particular, previous studies suggest that the accretion disk in a BH–WD UCXB becomes thermally unstable when the donor mass decreases to $m_2 \sim 0.02\ \mathrm{M}_\odot$ at an orbital period of $P_{\rm orb} \sim 28$ minutes (orbital frequency $f_{\rm orb} \sim 0.6$ mHz, see van Haaften et al., 2012). This WD mass value is supported by recent observations that have detected BH-WD UCXBs with donor masses $m_2 \sim 0.01 - 0.016\ \mathrm{M}_\odot$ (see, e.g., Tudor et al., 2018). However, van Haaften et al. (2012) also estimates that BH–WD systems may evolve to orbital periods as long as 110 minutes with a final donor mass $m_2 \sim 0.0026\ \mathrm{M}_\odot$, provided the system is not disrupted.

Here, we assume that the UCXB phase terminates when the WD mass decreases to $m_2 \sim$ 0.01–0.02 $\mathrm{M}_\odot$ (representing an estimated range of final WD mass, based on discussions in van Haaften et al. (2012) and observed UCXB donor masses). Substituting this range into Equation (8.14) gives a UCXB lifetime of $\tau \sim$ 20–180 Myr for a 10–0.6 $\mathrm{M}_\odot$ system. We note, however, that if the final donor mass can indeed extend to extremely low values ($\sim 0.0026\ \mathrm{M}_\odot$), the UCXB lifetime could extend up to ~ 10 Gyr.

In the right column of Figure 8.2, we show the mass-transfer evolution of a representative BH–WD system, following its earlier dynamical evolution shown in the left column (see Section 8.2.2). As illustrated in the second-row panels, the mass transfer starts at $t - t_c \sim 6 \times 10^3$ yr, when the orbital separation drops to $\sim 3 \times 10^{-4}$ au (red solid line) and the WD radius (black dotted line) fills its Roche lobe (black dashed line). Following the onset of mass transfer, the WD begins to lose mass, which increases the orbital separation a (see Equation (8.14)) and causes the expansion of the WD radius R_2. Consequently, the Roche lobe radius increases along with the WD radius, leading to a wider orbit, a decreasing mass ratio m_2/m_1 (see the blue dash-dotted line), and a gradual decrease in gravitational wave

emission (see the red line in the last row).

Furthermore, we compute the binary's X-ray luminosity using the accretion rate of the BH, assuming that $L_X \sim 0.1\dot{m}_1 c^2$ (see the blue dash-dotted line of the last row). Notably, the X-ray luminosity of simulated UCXBs typically lies between $10^{35} - 10^{38}$ erg s^{-1}. Assuming a luminosity distance of $D_l \sim 20$ kpc, these systems can be observed with an X-ray flux of $F_X = L_X/(4\pi D_l^2) \gtrsim 10^{-12}$ erg cm^{-2} s^{-1}, which is exceeding the detection sensitivity of most present-day X-ray telescopes ($\sim 10^{-14}$ erg cm^{-2} s^{-1}, see, e.g., Kim et al. (2007)). In other words, once a mass-transferring BH-WD system is formed, its X-ray signal is well detectable in the Milky Way throughout the stable mass-transfer lifetime[6]. Furthermore, the detection of BH-UCXBs can be well extended to other galaxies, up to a luminosity distance of $\sim 10 - 100$ Mpc, see, e.g., Figure 8.6 in Appendix 8.6.3.

8.3 Results and Discussion

8.3.1 Triple Path of UCXB Formation

Following the method described in Section 8.2, we adopt a sample of 1242 detached BH-WD systems with stellar-mass tertiary companions (see, e.g., the initial condition in Appendix 8.6.1, Figure 8.4). These triples have survived the main sequence evolution in the previous study (Shariat et al., 2025b), and meet the criteria of hierarchy and long-term stability. These systems' initial configurations are depicted in the $(1 - e)$ - a parameter space in Figure 8.3, left panel. After evolving them, we identify 78 out of 1242 that end up as ultracompact X-ray binaries, corresponding to a formation efficiency of $f_{\rm UCXB} = 6.3\%$. The evolution trajectories of these systems are shown as pink points in the right panel of

[6]Assuming the WD final mass is as low as ~ 0.0026 M$_\odot$ and the system evolves up to 10 Gyr, its X-ray flux is still beyond $F_X \gtrsim 10^{-14}$ erg cm^{-2} s^{-1} at 20 kpc.

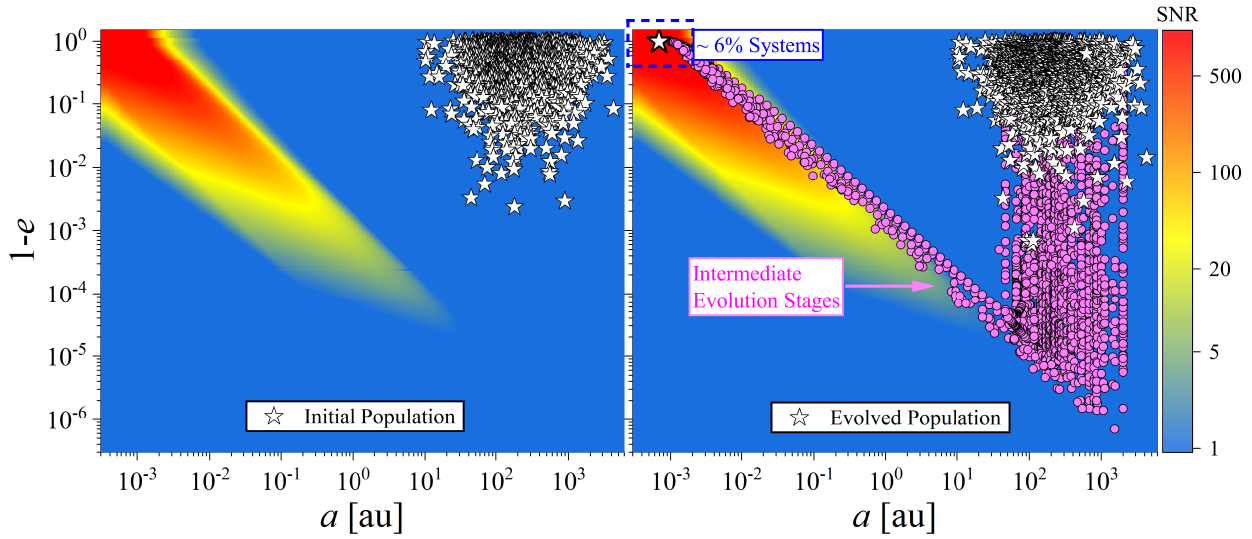


Figure 8.3: **The population of BH-WD systems from simulated Milky Way Galactic field, and their estimated GW SNR as a function of semi-major axis and eccentricity (for a 4-yr LISA observation).** Here, we plot the semi-major axis, a, and eccentricity, as $1-e$, of each simulated BH-WD system (see the white stars). The *Left Panel* shows the initial conditions, while the *Right Panel* represents the final state of each system, either when its dynamical evolution ends at the Hubble time or when the orbit separation shrinks to $\lesssim 10^{-3}$ au and triggers the mass transfer. The background color maps the binary's expected gravitational wave SNR, assuming a fixed distance $D_l = 8$ kpc and a 4-yr LISA observation. In the *Right Panel*, we also plot intermediate evolutionary stages (pink dots) for binaries that eventually evolve into UCXBs. These dots represent the evolution track of UCXBs formed via the wide triple channel, and highlight the region of parameter space where they may become detectable.

Figure 8.3.

As shown by the figure, during the dynamical formation stages, these systems are perturbed by the EKL effect and excited to extreme eccentricities, $(1-e) \sim 10^{-7} - 10^{-5}$. However, the rapid circularization due to dynamical tides typically causes the binary to first evolve into circular configurations, rather than becoming even more eccentric and being tidally disrupted. Furthermore, the combination of high eccentricity and small pericenter distance leads to rapid orbital decay driven by GW emission and WD dynamical tides, with an average GW detectable lifetime $\tau_{\rm GW,\,dyn} \sim 0.25$ Myr of this stage (assuming random distance in MW, 4 yr LISA detection, see Section 8.3.2 for details). By the end of this stage, the orbit of these BH-WDs typically shrinks to $\sim 10^{-3}$ au with residual eccentricity $\lesssim 0.01$, and the WD spin frequencies are mostly synchronized with their orbit frequency.

Following the orbital shrinkage and the decoupling from EKL oscillations, the BH-WD systems start mass transfer and X-ray emission (at $a \sim 3 \times 10^{-4}$ au). During this stage, the binary undergoes long-term evolution due to the combined effect of GW radiation and mass transfer, resulting in a gradual widening of the orbit (see, e.g., Equation (8.14) and the right column of Figure 8.2). From our simulations, we infer an averaged GW detectable lifetime of UCXB stage $\tau_{\rm GW,\,UCXB} \sim 3.6$ Myr, and X-ray detectable time $\tau_{\rm UCXB} \sim 20 - 180$ Myr in the MW, depending on the assumed final WD mass ($0.02 - 0.01$ $M_\odot$) when the mass transfer becomes unstable (see Section 8.2.3).

8.3.2 UCXB Detectability and Expected Population

To estimate the number of detectable BH-WD systems in GW and X-ray observations, we need to take into account both their formation rate and detectable time. Particularly, here we assume a constant star formation rate (SFR), i.e., a continuous birth and death of compact object binaries in the Milky Way, keeping the total number of systems unchanged. Thus,

the expected number of systems in a given stage is simply achieved by taking the UCXB rate, $\Gamma_{\rm UCXB}$, and multiplying by the average detectable lifetime, τ. Namely:

$$N = \Gamma_{\rm UCXB}\,\tau\ . \tag{8.15}$$

To estimate the formation rate of UCXBs in the Milky Way, we adopt the following relation:

$$\begin{aligned}\Gamma_{\rm UCXB} =& {\rm SFR} \times f_{\rm triple} \times f_{m_1,m_2,m_3} \\ & \times f_{\text{no kick}} \times f_{\text{BH-WD triple}} \times f_{\rm UCXB},\end{aligned} \tag{8.16}$$

where SFR $\sim$ 2 yr^{-1}, which roughly corresponds to a constant star formation rate of 1 M$_\odot$ yr^{-1} with a Kroupa IMF (Kroupa, 2001). $f_{\rm triple} = 0.11$ is the fraction *of all stars formed* that reside in triples (Shariat et al., 2025a) and f_{m_1,m_2,m_3} is the fraction of triples with $20 < m_1/{\rm M}_\odot < 40$, $0.8 < m_2/{\rm M}_\odot < 8$, and $0.5 < m_3/{\rm M}_\odot < 8$, chosen such that the primary becomes a black hole, the secondary becomes a white dwarf within a Hubble time, and the tertiary does not become a neutron star/BH. We derive these values by generating a mock stellar population with singles, binaries, and triples following Shariat et al. (2025a). Their publicly available prescription[7] samples inner binary parameters following the multi-dimensional distributions of Moe and Di Stefano (2017) and tertiary masses from a $q^{-1.4}$ power law distribution. Shariat et al. (2025a) calibrate this procedure to maintain empirically constrained multiplicity statistics (e.g., Moe and Di Stefano, 2017; Tokovinin, 2014; Winters et al., 2019; Moe and Kratter, 2021) and to reproduce observations of the *Gaia* resolved triple population. This provides $f_{m_1,m_2,m_3} = 2 \times 10^{-3}$ and $f_{\rm triple} = 0.11$. Additionally, $f_{\text{BH-WD triple}} \sim 5.49\%$ is the fraction of triples that survive the main sequence evolution and the inner binary evolves into a detached BH-WD system (see table 2 in Shariat et al., 2025b). $f_{\rm UCXB} \sim 6.3\%$ is the fraction of detached BH-WDs with a tertiary companion that undergo strong EKL oscillation and end up being a UCXB source[8].

[7] https://github.com/cheyanneshariat/gaia_triples

[8] Note that $f_{\rm UCXB}$ is inferred from the dynamical simulation results of this paper, see Section 8.3

$f_{\rm no,kick}$ denotes the fraction of triples that experience negligible BH natal kicks. We introduce this factor because the estimate of $f_{\rm BH\text{–}WD\ triple}$ in Shariat et al. (2025b) assumes no natal kicks, whereas in reality some triples can receive strong kicks, become unbound, and need to be excluded from the rate estimate (see Section 8.3.3 for details). The strength and prevalence of BH natal kicks remain highly uncertain. Observations of BH–LMXBs indicate that some systems form with little to no kick while others experience strong ones (e.g., Nagarajan and El-Badry, 2025, though selection biases favor weak kicks). Notably, the only confirmed BH–LMXB in a triple, V404 Cygni, also appears to have formed with a negligible kick ($v_{\rm k} \lesssim 5$ km s^{-1}; Burdge et al., 2024; Shariat et al., 2025b). For conservative purposes, we therefore adopt $f_{\rm no,kick} \sim 10\%$. Incorporating this fraction into Equation (8.16) gives a total BH–UCXB formation rate of $\Gamma_{\rm UCXB} \sim 1.5 \times 10^{-7}$ yr^{-1} in the Milky Way.

Thus, combining Equations (8.15) and (8.16), we have:

$$\begin{aligned} N_{\rm UCXB} &= \Gamma_{\rm UCXB} \times \tau_{\rm UCXB} \\ &\sim 1.5 \times 10^{-7}{\rm yr}^{-1} \times \tau_{\rm UCXB}, \\ &\sim 3 - 27\ , \end{aligned} \tag{8.17}$$

in which $\tau_{\rm UCXB}$ is the average X-ray detectable time for a UCXB in the Milky Way.

In the last transition of Equation (8.17), we adopt a lifetime of $\tau_{\rm UCXB} \sim 20 - 180$ Myr. This value is motivated by the fact that the X-ray luminosity of a UCXB system typically exceeds $\sim 10^{34}$erg s^{-1} throughout its evolution (see discussion in Section 8.2.3). Consequently, such systems are well detectable within the Milky Way, with X-ray fluxes $\gtrsim 10^{-12}$erg cm^{-2} s^{-1} above the sensitivity thresholds of most present-day X-ray observatories. Therefore, the average detectable time of a UCXB in the Galaxy can be approximated by its mass-transfer lifetime ($\sim 10^7$–10^8 yr; it may be as long as 10 Gyr in the most optimistic case, see Section 8.2.3). Such a timescale is primarily determined by the orbital separation and initial mass at the onset of mass transfer, thus is nearly identical across the BH–WD systems

considered in this paper.

On the other hand, however, the gravitational wave signals from UCXBs are not always detectable in the Milky Way, as can be seen from the signal-to-noise ratio (SNR) in the last row of Figure 8.2. Therefore, we further take into account the distance and SNR evolution of UCXBs to estimate their average GW detectable time.

Specifically, we randomly generate BH-WD systems in the disk of MW, following the density profile of:

$$\rho(R,z) = \rho_0 \exp\left(-\frac{R}{R_d}\right) \exp\left(-\frac{|z|}{z_d}\right) \tag{8.18}$$

where ρ_0 is a constant, R is the galactocentric cylindrical radius, z is the vertical height above the galactic plane, $R_d \approx 2.6$kpc is the radial scale length, and $z_d \approx 0.3$kpc is the vertical scale height (Jurić et al., 2008).

For each generated system, we look into its time evolution, computing the GW SNR at all evolution stages (Xuan et al., 2024a):

$$\mathrm{SNR} \sim \frac{h_{\rm burst}}{\sqrt{S_n\left(f_{\rm burst}\right)}} \sqrt{T_{\rm obs}\left(1-e\right)^{3/2}}, \tag{8.19}$$

where $h_{\rm burst} \sim \sqrt{\frac{32}{5}} \frac{m_1 m_2}{D_l a(1-e)}$ is the peak GW strain amplitude, $f_{\rm burst} = f_{\rm orb}(1+e)^{1/2}(1-e)^{-3/2}$ is the peak GW frequency, $S_{\rm n}(f)$ is the spectral noise density of LISA evaluated at GW frequency f (Klein et al., 2016a; Robson et al., 2019a), and $T_{\rm obs} = 4$ yr is the LISA observation time. We then count the total amount of time each system spent observable in the LISA band (SNR larger than 8 for 4-yr observation), and estimate the average GW detectable time of BH-UCXB systems in the Milky Way. Our estimation yields $\tau_{\rm GW,\,dyn} \sim 0.25$ Myr for the eccentric dynamical formation stage, and $\tau_{\rm GW,\,UCXB} \sim 3.6$ Myr for the circular mass transfer stage (see appendix A1 of Xuan et al. (2024a), for a similar method).

Therefore, our analysis yields the following number of GW-detectable sources[9]:

$$\begin{aligned} N_{\mathrm{GW,\,UCXB}} &= \Gamma_{\mathrm{UCXB}} \times (\tau_{\mathrm{GW,\,dyn}} + \tau_{\mathrm{GW,\,UCXB}}) \\ &\sim 1.5 \times 10^{-7} \mathrm{yr}^{-1} \times 4\,\mathrm{Myr}, \\ &\sim 1\ , \end{aligned} \tag{8.20}$$

where we adopted a similar approach to the calculation presented in Equation (8.17), only here we consider the overall GW detectable lifetime. Notably, since the average GW-detectable lifetime during the mass transfer (3.6 Myr) exceeds the dynamical formation (0.25 Myr), we expect the BH-WD GW sources to most likely appear as circular, mass-transferring systems.

We further estimate the number of extragalactic sources contributed by this triple channel (see, e.g., their average detectable time as a function of distance in Appendix 8.6.3). Using the Andromeda galaxy as an example, assuming a star formation rate of 0.4 $\mathrm{M}_\odot\ \mathrm{yr}^{-1}$ (Rahmani et al., 2016), we find that Andromeda could host ∼1–5 UCXBs formed through this channel. However, due to the large distance, only a negligible fraction of them ($\sim 1\%$) are expected to be detectable GW sources. These systems exhibit observational features consistent with some recently detected periodic X-ray sources (e.g., Zhang et al., 2024), and may offer a potential explanation for the short-period low-mass X-ray binaries observed in M31.

8.3.3 Discussion

In this study, we specifically focus on the UCXB formation channel through isolated field triples. However, we note that other potential pathways, such as the mass transfer evolution of BH–MS binaries (e.g., Qin et al., 2023), or dynamical formation through frequent interac-

[9]The expected GW source number can increase (to ~ 2) if LISA mission is extended to 10 years.

tions in globular clusters (e.g., Ivanova et al., 2010, 2017), may also contribute substantially to the Galactic UCXB population.

While BH–UCXBs formed through different channels may appear observationally similar, as circular, mass-transferring BH–WD binaries, those formed through the wide triple channel could potentially be differentiated by identifying a distant tertiary companion ($a_2 \sim 500 - 15000$ au) using photometric and/or astrometric observations. Additionally, LISA may be able to detect highly eccentric BH–WD progenitors in the Milky Way before they begin mass transfer, presenting a promising opportunity to distinguish between these formation channels. We note that EKL is not the only mechanism that can drive eccentricity in BH–WD systems. For example, mass-loss-induced kicks (Hills, 1983; Kalogera, 2000; Lu and Naoz, 2019; Shariat et al., 2023b), fly-by interactions (Michaely and Perets, 2020; Michaely and Naoz, 2022), and collisions (Ivanova et al., 2008) may also contribute. These alternative channels may produce different eccentricity distributions and, if a tertiary companion is observed, the inclination between inner and outer orbits may help to distinguish EKL-induced systems from those formed through other mechanisms.

Notably, the inclusion of dynamical tides plays a crucial role in the formation of UCXBs. For example, when WD tides are neglected, a comparable fraction of BH–WD systems ($\sim 4.7\%$) can still undergo strong EKL oscillation and lose orbital energy in the simulation. However, instead of gradually shrinking their orbits and forming nearly-circular UCXBs, the majority ($> 90\%$) of these systems reach the Roche limit at pericenter ($r_p \lesssim 10^{-4}$ au) while retaining very high eccentricities ($e > 0.9999$, see, e.g., Fragione et al. (2020) for a similar result). In other words, omitting WD tides can lead to unphysical outcomes, in which many systems behave as "direct plunge-in" mergers or highly eccentric tidal disruption events (TDEs), rather than stable mass transfer UCXBs.

Furthermore, previous studies have shown that compact binaries containing a WD can undergo significant tidal heating prior to merger. This process can brighten the WD, potentially

trigger runaway fusion in its hydrogen envelope, and lead to a tidal nova (Fuller and Lai, 2012b, 2013; Vick et al., 2017). In our simulations, we have a similar effect in UCXB progenitor systems: when the orbital eccentricity is significant and the WD has not yet synchronized its spin, the tidal heating rate can reach up to $\sim 10^{34}$–10^{36}erg s^{-1}. In other words, during the dynamical evolution of triple BH–WD systems, tidal dissipation may heat the hydrogen layer of the WD and ignite it before the orbit evolves into the UCXB phase, which could yield observable signatures. For simplicity, we neglect the effect of tidal heating on the internal structure of the WD and adopt a fixed-temperature WD model when computing the tidal torque. However, we note that heating the WD may reduce the dimensionless tidal torque, thereby further suppressing the overall tidal dissipation after the highly-eccentric formation stage (see, e.g., Fuller and Lai, 2012b, 2013). Conversely, highly eccentric WD binaries may also undergo chaotic tides, where repeated pericenter passages stochastically excite large-amplitude stellar oscillations before significant damping, enhancing tidal heating and orbital decay (e.g., Vick et al., 2017; Lau and Yu, 2025). Future work may improve this model by incorporating thermal feedback and chaotic tides into the WD evolution.

Additionally, our simulations adopt a representative configuration for all BH-WD systems (10 $M_\odot$ for the BH and 0.6 $M_\odot$ for the WD, with dimensionless tidal torque $\hat{F}(\omega) \sim 150\omega^5$), following Shariat et al. (2025b). However, in reality, BH–WD binaries span a range of component masses and WD temperatures, which inevitably influences their orbital evolution and the detectability in GW and X-rays. Nonetheless, our results for the triple formation channel remain robust. In particular, the point mass EKL dynamics are largely insensitive to the details of the mass ratio q as long as it is small, such as in the case of BH and WD progenitors (Naoz et al., 2013b; Naoz, 2016; Stephan et al., 2016b). Also, white dwarf masses in compact binaries are strongly clustered around $0.5 - 0.7$ $M_\odot$(see, e.g., Toonen et al., 2018; Xuan et al., 2021), and recent Gaia observations confirm that stellar-mass BH in wide binaries typically lie within the few- to tens-of-solar-mass regime (e.g., *Gaia* BH1 and BH2 have masses of $9.62 \pm 0.18 M_\odot$ and $8.94 \pm 0.34 M_\odot$ respectively, see Chakrabarti et al.

(2023); El-Badry et al. (2023)). In addition, we also test a wide range of WD temperatures (i.e., dimensionless tidal torque prescriptions, from $\hat{F}(\omega) \sim 10\omega^5$ to $\sim 1000\omega^5$), and find that our simulation results are not significantly affected, with the resultant UCXB formation rate and lifetime varying by less than a factor of two.

Notably, adopting a realistic mass distribution yields a comparable UCXB fraction. For example, we resample the component masses of BH–WD systems from progenitor distributions of $20 < m_1/\mathrm{M}_\odot < 40$, $0.8 < m_2/\mathrm{M}_\odot < 8$, and $0.5 < m_3/\mathrm{M}_\odot < 8$, motivated by the observed Gaia triple population (see the discussion below Equation (8.16)). This sample results in a UCXB fraction of $f_{\rm UCXB} \sim 9\%$, close to the fraction obtained from our fiducial model ($f_{\rm UCXB} \sim 6.3\%$). We also tested extreme cases by fixing $m_1 = 30$ $\mathrm{M}_\odot$ or $m_3 = 0.1$ $\mathrm{M}_\odot$ in all simulated systems, which gives $f_{\rm UCXB} \sim 4.8\%$ and 1.5%, respectively. These tests confirm that the EKL+tides channel can robustly form BH–WD UCXBs, despite uncertainties in the initial mass distribution of Galactic triples, and predict source numbers consistent in order of magnitude with the observed UCXB population in the Milky Way.

We note that, the magnitude and prevalence of BH natal kicks remain extremely uncertain. Some theoretical models predict negligible kicks from direct collapse (e.g., Woosley and Weaver, 1995; Sukhbold et al., 2016; Mirabel, 2017), while observational studies of BH–LMXBs indicate a mixed picture, with some systems receiving little to no kick and others experiencing large ones (e.g., Fragos et al., 2009; Reid et al., 2014; Mirabel, 2017; Shenar et al., 2022; Andrews and Kalogera, 2022; Kimball et al., 2023; Dashwood Brown et al., 2024; Burdge et al., 2024; Shariat et al., 2025b; Nagarajan and El-Badry, 2025, see the latter for a recent overview). However, the only confirmed BH-LMXB in a triple, V404 Cygni, formed with a negligible kick ($v_{\rm k} \lesssim 5$ km s^{-1} Burdge et al., 2024; Shariat et al., 2025b), providing justification for our baseline assumption.

For the initial population used here, Shariat et al. (2025b) also modeled triples with natal kick magnitudes ($v_{\rm k}$) drawn from a Maxwellian distribution with $\sigma = 265$ kms^{-1} (as for neutron

stars) scaled by the BH gravitational mass (Hansen and Phinney, 1997; Arzoumanian et al., 2002; Hobbs et al., 2004). Their results, with this assumed $v_{\rm k}$ model, show that kicks primarily unbind wide triples but keep the orbital properties of those that survive largely unchanged from the no-kick population. In this framework, the main effect of including kicks is to scale the predicted rates in Equation (8.16) by the survival fraction $f_{\rm survive}$. For example, in the extreme high-kick case above, $f_{\rm survive} \approx 2\%$ (Shariat et al., 2025b), whereas a more realistic scenario in which some BHs receive large kicks and others receive almost none (Nagarajan and El-Badry, 2025) would yield a fraction closer to $f_{\rm survive} \approx 50\%$.

Given that the only known BH in a triple formed without a natal kick (V404 Cygni; Burdge et al., 2024; Shariat et al., 2025b), there is strong empirical support for at least a subset of BHs forming with low or negligible kicks, implying that a substantial population of detached BH–WD inner binaries in triples should exist in the Galactic stellar population.

8.4 Conclusions

Ultracompact X-ray binaries are important multi-messenger sources emitting both X-rays and gravitational wave signals. Observational evidence has confirmed their existence, making them valuable targets for probing compact binary evolution. In this work, we focus on the evolution of detached BH–WD binaries in the Galactic field, and show that they can naturally form UCXBs through the dynamical perturbation of distant tertiary companions.

In particular, based on the previous study of massive main-sequence triples, we generate an observationally motivated BH-WD population with tertiary companions (see Section 8.2.1 and Figure 8.4 in Appendix 8.6.1). We then simulated their evolution (see Sections 8.2.2 and 8.2.3), including the eccentric Kozai–Lidov mechanism, general relativistic precession, gravitational wave emission, WD dynamical tides, and WD mass transfer. We find that

a significant fraction ($\sim 6.3\%$) of BH-WDs are perturbed by the EKL effect and excited to extreme eccentricities. Such highly eccentric orbits produce strong dynamical tides and gravitational wave radiation at pericenter (Figure 8.1). Therefore, the BH-WD binary can undergo rapid orbital decay and circularization (Figure 8.2), which in turn initiates mass transfer and transforms the system into a UCXB. We further explore the evolution track of these triple-induced UCXBs (see Figure 8.3), and couple the time evolution of their GW signatures with the EM counterpart. Our simulation shows these BH-UCXBs have a formation rate of $\sim 1.5 \times 10^{-7}$ yr^{-1} in the Milky Way, with an average GW detectable time of ~ 4 Myr and X-ray detectable time $\sim 20 - 180$ Myr.

To conclude, the triple formation channel can yield a promising number of BH-WD sources detectable via both GW (~ 1 source in the MW) and X-rays ($\sim 3 - 27$ sources in the MW, $\sim 1 - 5$ sources in M31), which offers a unique opportunity for multimessenger studies. We further suggest that electromagnetic observations searching for distant tertiary companions ($a_2 \sim 500 - 15000$ au) in known UCXBs could serve as a direct test of their triple origin. The detection of UCXBs formed via this channel would not only shed light on the dynamical evolution of field triples but also help constrain the physics of WD dynamical tides and contribute a valuable population of LISA verification binaries for future gravitational wave observation.

8.5 Acknowledgments

The authors thank the anonymous referee for their valuable feedback and helpful suggestions. We also thank Jim Fuller and Linhao Ma for the valuable discussions, and thank the 56th Annual Meeting of the Division on Dynamical Astronomy (DDA) for sparking early conversations about these topics. ZX acknowledges partial support from the Bhaumik Institute for Theoretical Physics summer fellowship. ZX and SN acknowledge the partial support from

NSF-AST Grant No. 2206428, and thank Howard and Astrid Preston for their generous support. C.S. acknowledges support from the Joshua and Beth Friedman Foundation Fund and the Department of Energy Computational Science Graduate Fellowship supported by the U.S. Department of Energy, Office of Science, Office of Advanced Scientific Computing Research, under Award Number DE-SC0026073. This research was supported by the Munich Institute for Astro-, Particle and BioPhysics (MIAPbP), which is funded by the Deutsche Forschungsgemeinschaft (DFG, German Research Foundation) under Germany´s Excellence Strategy – EXC-2094 – 390783311.

8.6 Appendix

8.6.1 Initial Conditions

Here, we show the initial separation of detached BH-WDs versus the outer orbit semi-major axis of their tertiary companions. These systems have survived the main sequence evolution in Shariat et al. (2025b). Notably, because the inner binaries of these systems have lost mass when becoming a BH-WD system, their inner orbits are, in general, wider than the separation during main-sequence evolution (see Figure 8.4). Such a wider separation enhances the EKL effect, making the BH-WD more likely to be excited to high eccentricity during the subsequent evolution.

8.6.2 An Analytical Approximation of WD Dynamical Tides

As discussed in Section 8.2.2, the tidal energy and angular momentum transfer rate of a BH-WD system can be computed using Equations (8.3) and (8.4). However, for highly eccentric stages during dynamical evolution, the summation in these two equations may

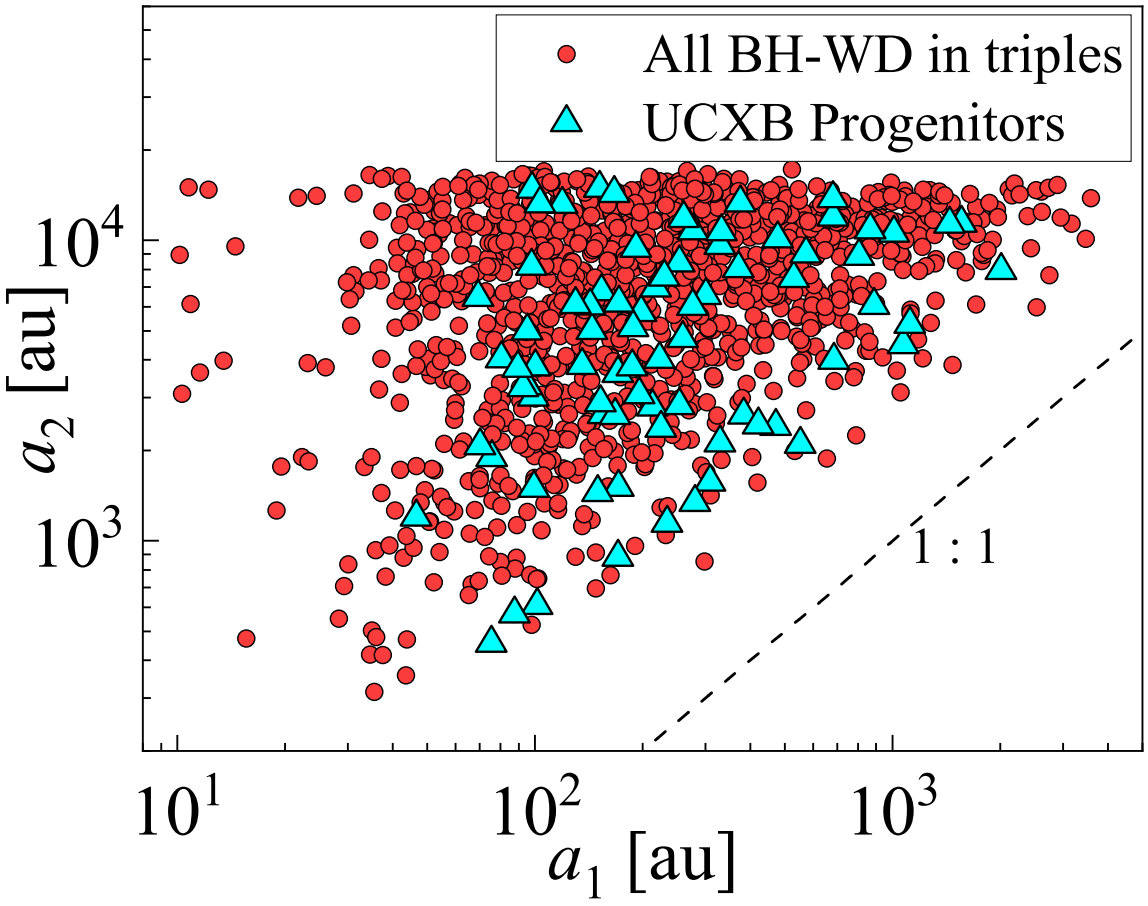


Figure 8.4: **Parameters of detached BH-WD systems in triples after main sequence evolution.** Here we plot the semimajor axis of inner (a_1) and outer orbits (a_2) for the BH–WD binaries and their tertiary companions, immediately after the inner binary has evolved into a BH–WD configuration. Red circles represent all systems, while blue triangles indicate those that later form UCXBs in our simulations. The dashed line indicates $a_2/a_1 = 1$.

include thousands to millions of harmonics, which is computationally expensive. Thus, here we further fit the results of Equations (8.3) and (8.4) using empirical formulas.

In particular, when fixing the system mass, $\dot{E}_{\rm tide}$ and $\dot{J}_{\rm tide}$ can be expressed as functions of the orbital eccentricity e, pericenter distance r_p, and WD spin frequency Ω_s. For simplicity, we start by fitting the zero-spin case. Notably, $\dot{E}_{\rm tide}(\Omega_s = 0)$ and $\dot{J}_{\rm tide}(\Omega_s = 0)$ have a straightforward power law relation to the pericenter distance r_p (see, e.g., Equations (8.3) - (8.4) and Figure 8.1):

$$\begin{cases} \dot{E}_{\rm tide}\ (\Omega_s = 0) \propto T_0 \cdot \Omega \cdot \hat{F}(\Omega) \propto a^{-15} \sim r_p^{-15} \\ \dot{J}_{\rm tide}\ (\Omega_s = 0) \propto T_0 \cdot \hat{F}(\Omega) \propto a^{-13.5} \sim r_p^{-13.5} \end{cases} . \tag{8.21}$$

This relation is understood because the WD's dimensionless tidal torque has an approximated power law relation to the orbital frequency ($\hat{F}(\omega) \sim 150\omega^5$ for a 5000K WD in $G = M = R = 1$ unit, see, e.g., Vick et al., 2017). Furthermore, changing r_p (or effectively the orbital separation a) simultaneously changes the terms of $\omega \sim N\Omega$ in Equations (8.3) and (8.4).

Equation (8.21) highlights the strong dependence of dynamical tides on the pericenter distance, which also indicates that r_p most strongly determines the order-of-magnitude of tidal effects. Furthermore, given the same r_p, orbits with different eccentricities can have different tidal torque magnitudes, which is reflected in the Hansen coefficients and sum of harmonics in Equations (8.3) and (8.4). To estimate this effect, we numerically computed the magnitude of $\dot{E}_{\rm tide}$, $\dot{J}_{\rm tide}$, and fit them as functions of eccentricity e. Empirically, we find that, instead of fitting the exact values of $\dot{E}_{\rm tide}$ and $\dot{J}_{\rm tide}$, the results are better approximated when fitting the ratio between tidal and GW energy (angular momentum) transfer rates (see, e.g.,

equations 5.4 and 5.5 in Peters, 1964):[10]

$$\frac{\dot{E}_{\rm tide}(\Omega_s=0)}{\dot{E}_{\rm GW}} \sim (92.7+1204e+3124e^2)\times\left(\frac{r_p}{10^{-3}\ {\rm au}}\right)^{-10} \tag{8.22}$$

$$\frac{\dot{J}_{\rm tide}(\Omega_s=0)}{\dot{J}_{\rm GW}} \sim (105+691e+708e^2)\times\left(\frac{r_p}{10^{-3}\ {\rm au}}\right)^{-10} \tag{8.23}$$

Next, we consider the general case by releasing the assumption of $\Omega_s = 0$. Notably, the evolution of Ω_s significantly affects $\dot{E}_{\rm tide}$ and $\dot{J}_{\rm tide}$. For example, Figure 8.5 plots $\dot{J}_{\rm tide}$ and $\dot{E}_{\rm tide}$ as functions of the ratio between the WD spin angular frequency Ω_s and orbital pericenter frequency Ω_p (computed strictly using Equations (8.3) and (8.4) for a $e = 0.9$ system). As shown in the figure, starting from the zero-spin case, the magnitude of dynamical tides is suppressed as a WD spins up. Consequently, the WD can spin up to the position of $\Omega_{\rm crit,J}$, where the tidal torque stops transferring angular momentum ($\dot{J} = 0$) and the spin pseudo-synchronizes with the orbit. This phenomenon also applies to the energy transfer rate, with $\Omega_{\rm crit,E}$ representing the critical spin when there is no net tidal energy loss from the orbit. However, we note that $\Omega_{\rm crit,J}$ is smaller than $\Omega_{\rm crit,E}$ when $e > 0$. In other words, once an eccentric system get tidally locked at $\Omega_s = \Omega_{\rm crit,J}$, it still has a residual energy transfer rate (at $\Omega_s < \Omega_{\rm crit,E}$, see, e.g., the position of $\Omega_s = 1.46\Omega_p$ in the figure). This is because eccentricity always excites multiple harmonics of dynamical tides and causes tidal heating, see the discussion in Section 8.2.2.

We characterize the effect of Ω_s on $\dot{E}_{\rm tide}$ and $\dot{J}_{\rm tide}$ using an extra suppression factor K (K_E for the energy, K_J for the angular momentum, respectively). In particular, when $\Omega_s < \Omega_{\rm s,\,crit}$,

[10]Note that here we only fit the empirical equations for $0.2 < e < 1$, as the nearly circular system has few number of harmonics and the analytical approximation breaks. Furthermore, here we specifically fit the coefficient for the $10 - 0.6$ $M_\odot$ BH-WD system, with $R_2 = 5.3\times10^{-5}$ au and dimensionless tidal torque $\hat{F}(\omega) = 150\omega^5$. However, it is straightforward to rescale the result for other configurations. For example, when fixing a and e and changing m_1, $\dot{E}$ scales as $m_1^2(m_1+m_2)^3$ and $\dot{J}$ scales as $m_1^2(m_1+m_2)^{5/2}$, since m_1 affects both T_0 and orbital frequency.

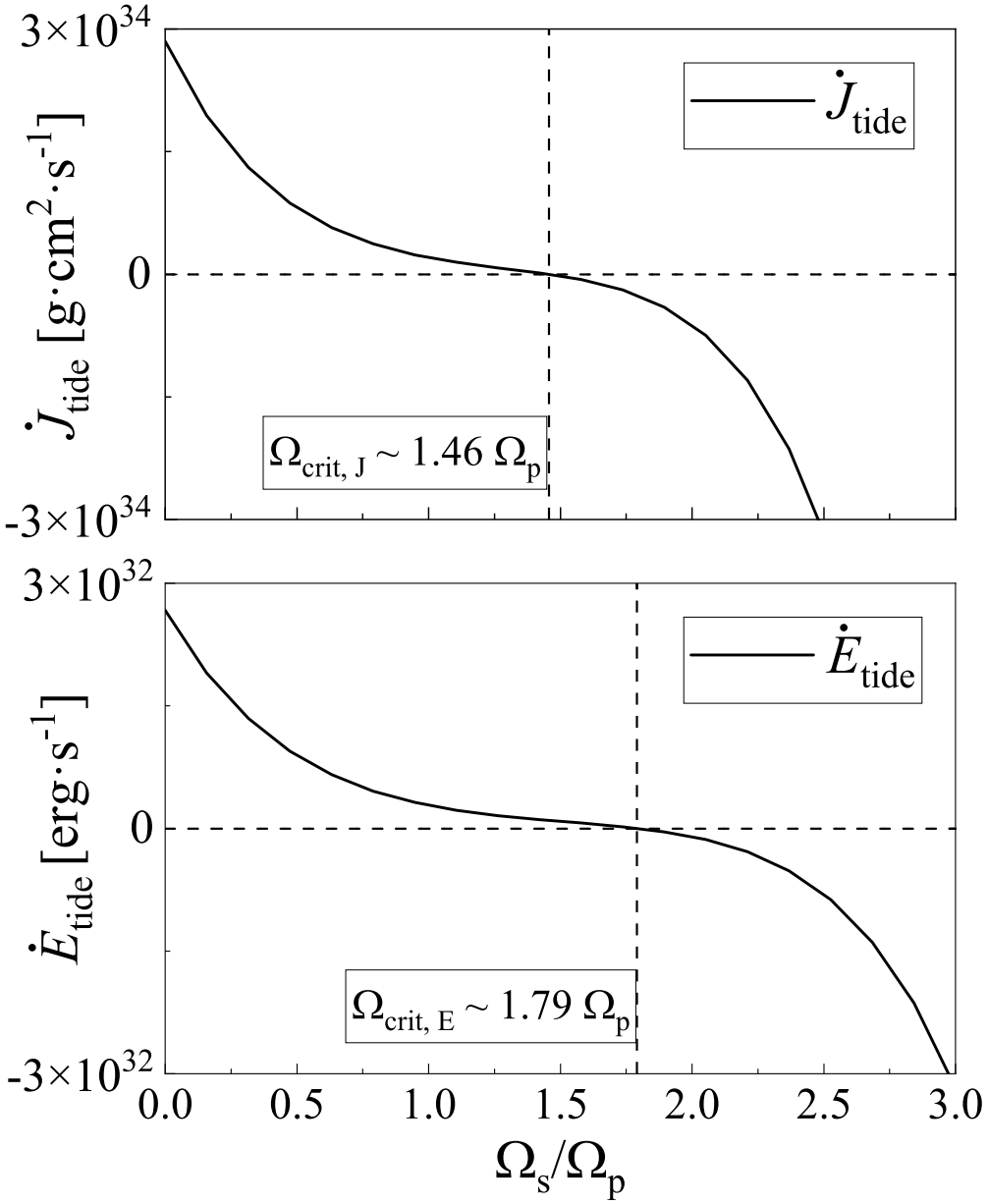


Figure 8.5: **Comparison between tidal angular momentum and energy transfer rate, $\dot{J}_{\rm tide}$ and $\dot{E}_{\rm tide}$, as functions of the WD spin.** Here we consider a $10 - 0.6$ $M_\odot$ BH-WD system with $e = 0.9$, $r_p = 3 \times 10^{-3}$ au, $\hat{F}(\omega) = 150\omega^5$, and plot $\dot{J}_{\rm tide}$ and $\dot{E}_{\rm tide}$ as functions of the ratio between the WD spin angular frequency, Ω_s, and orbital pericenter frequency, Ω_p.

we have:

$$\begin{cases} \dot{E}_{\rm tide}\left(\Omega_s\right) = \dot{E}_{\rm tide}\left(\Omega_s = 0\right) \cdot \left[K_E(\Omega_s, e) - K_E(\Omega_{\rm s,\,Ecrit}, e)\right] / \left[K_E(0, e) - K_E(\Omega_{\rm s,\,Ecrit}, e)\right] \\ \dot{J}_{\rm tide}\left(\Omega_s\right) = \dot{J}_{\rm tide}\left(\Omega_s = 0\right) \cdot \left[K_J(\Omega_s, e) - K_J(\Omega_{\rm s,\,Jcrit}, e)\right] / \left[K_J(0, e) - K_J(\Omega_{\rm s,\,Jcrit}, e)\right] \end{cases} \tag{8.24}$$

where K_E, K_J are the suppression factors. They can be approximated using the following relations (fitted for $0.2 < e < 1$):

$$\begin{cases} K_E\left(\Omega_s, e\right) \sim \exp\{[-5.23 + 9.06e - 10.1e^2 + 4.34e^3] \cdot (\Omega_{\rm s}/\Omega_p)\} \\ K_J\left(\Omega_s, e\right) \sim \exp\{[-5.70 + 9.82e - 11.0e^2 + 4.79e^3] \cdot (\Omega_{\rm s}/\Omega_p)\} \end{cases} \tag{8.25}$$

and $\Omega_{\rm s,\,Ecrit}$, $\Omega_{\rm s,\,Jcrit}$ represent the critical WD spin rate at which the energy flux and the angular momentum flux equal zero, respectively, which can be estimated using:

$$\begin{cases} \Omega_{\rm s,\,Ecrit}/\Omega_p \sim 1 + 1.10e - 1.75e^2 + 5.28e^3 - 6.23e^4 + 2.47e^5 \\ \Omega_{\rm s,\,Jcrit}/\Omega_p \sim 1 + 0.886e - 3.95e^2 + 10.9e^3 - 11.6e^4 + 4.3e^5 \end{cases} \tag{8.26}$$

We note that Equations (8.24) - (8.26) is only valid for $\Omega_s < \Omega_{\rm crit}$. On the other hand, the WD spin in principle can exceed $\Omega_{\rm s,\,Jcrit}$ ($\Omega_{\rm s,\,Ecrit}$), thus transferring angular momentum (energy) back to the orbit. For completeness, we also fit the value of $\dot{E}$ and $\dot{J}$ at $\Omega_s > \Omega_{\rm s,\,crit}$.

$$\begin{cases} \dot{E}_{\rm tide}\left(\Omega_s\right) = \dot{E}_{\rm tide}\left(\Omega_s = 0\right) \cdot \left[K'_E(\Omega_s, e) - K'_E(\Omega_{\rm s,\,Ecrit}, e)\right] \\ \dot{J}_{\rm tide}\left(\Omega_s\right) = \dot{J}_{\rm tide}\left(\Omega_s = 0\right) \cdot \left[K'_J(\Omega_s, e) - K'_J(\Omega_{\rm s,\,Jcrit}, e)\right] \end{cases} \tag{8.27}$$

where K'_E, K'_J are the factor controlling the growth of tidal effect when $\Omega_s > \Omega_{\rm s,\,Ecrit}$, $\Omega_s >$

$\Omega_{\rm s,\,Ecrit}$, respectively:

$$\begin{cases} K'_E\left(\Omega_s, e\right) \sim -(0.652 - 2.10e + 2.46e^2 - 1.00e^3) \\ \qquad\qquad \times \left[(\Omega_s/\Omega_p) - (0.620 + 0.889e - 1.27e^2 + 0.627e^3)\right]^5 \\ K'_J\left(\Omega_s, e\right) \sim -(1.48 - 5.38e + 7.22e^2 - 3.33e^3) \\ \qquad\qquad \times \left[(\Omega_s/\Omega_p) - (1.07 - 2.44e + 6.02e^2 - 6.37e^3 + 2.55e^4 - 0.112e^5)\right]^5 \end{cases} \tag{8.28}$$

8.6.3 X-ray Detectable Time of UCXBs

Here, we adopt the simulated X-ray luminosity evolution of BH-UCXB systems (see, e.g., Figure 8.2), and evaluate their detectable lifetime. In particular, we show the maximum detectable time of a $10 - 0.6$ $M_\odot$ UCXB as a function of its distance to the observer, assuming the X-ray detector has a limiting flux of $F_{\rm X,crit} = 10^{-15}$, 10^{-14}, 10^{-13} erg cm^{-2} s^{-1}, respectively. This range of limiting fluxes is representative of modern present-day X-ray observatories, such as Chandra, XMM-Newton, or eROSITA.The grey-shaded region in Figure 8.6 represents where the WD donor has a mass lower than 0.01 $M_\odot$. Such a light mass may cause instability and stop the mass transfer evolution (see Section 8.2.3), thus we exclude those systems in our work, for conservative purposes. The figure demonstrates that even out to $D_{\rm l} \gtrsim 10 - 100$ Mpc, these UCXBs can be observed as transient X-ray sources among all-sky surveys.

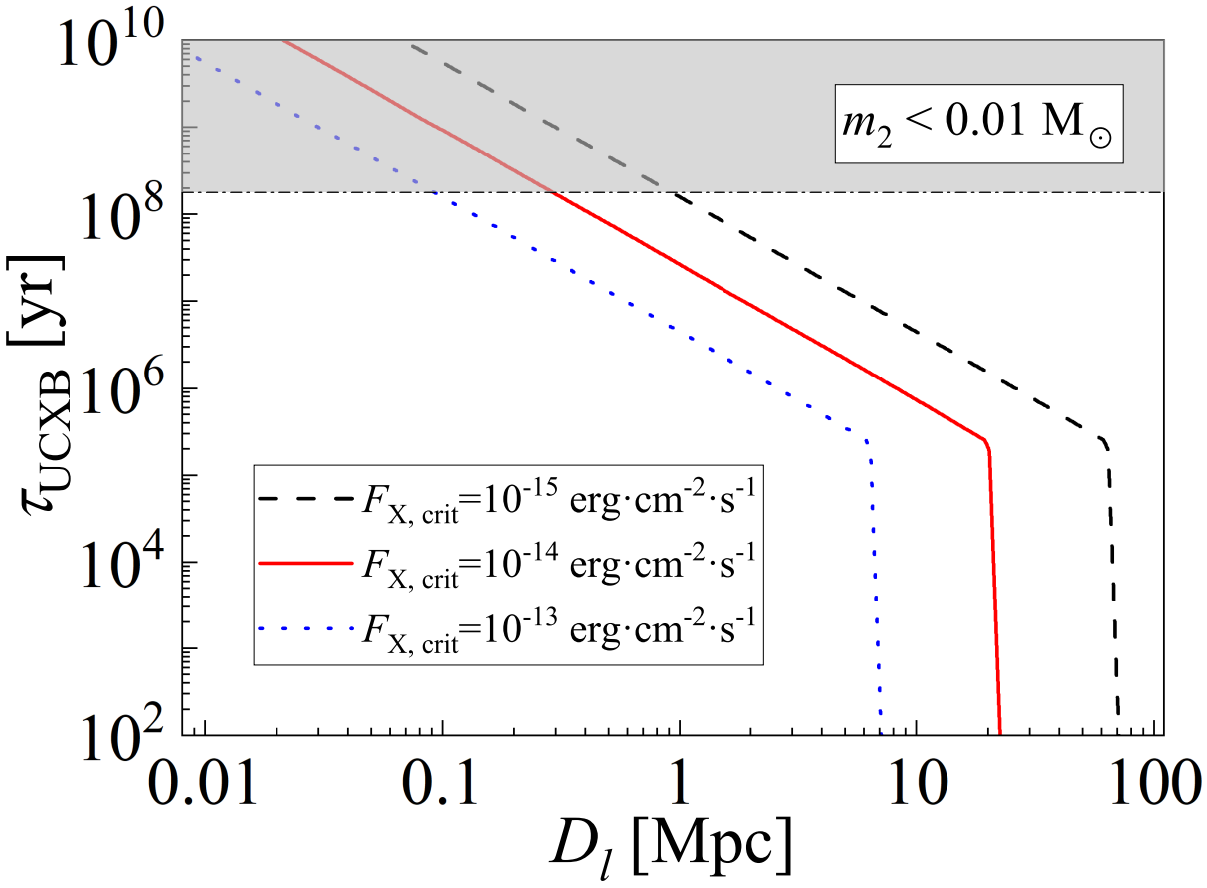


Figure 8.6: **The X-ray detectable time of a representative UCXB source, as a function of its distance.** Here we consider a mass-transferring BH-WD system with initial mass $m_1 = 10$ M$_\odot$, $m_2 = 0.6$ M$_\odot$, and computed its total detectable lifetime in X-ray, assuming a detector sensitivity of $F_{\rm X,crit} = 10^{-15}$, 10^{-14}, 10^{-13} erg cm^{-2} s^{-1}, respectively (from left to right).

Bibliography

Aarseth, S. J. (2012). Mergers and ejections of black holes in globular clusters. *MNRAS*, 422(1):841–848.

Abbott, B., Abbott, R., Abbott, T., Abernathy, M., Acernese, F., Ackley, K., Adams, C., Adams, T., Addesso, P., Adhikari, R., Adya, V., Affeldt, C., Agathos, M., Agatsuma, K., Aggarwal, N., Aguiar, O., Aiello, L., Ain, A., Ajith, P., Allen, B., Allocca, A., Altin, P., Anderson, S., Anderson, W., Arai, K., Arain, M., Araya, M., Arceneaux, C., Areeda, J., Arnaud, N., Arun, K., Ascenzi, S., Ashton, G., Ast, M., Aston, S., Astone, P., Aufmuth, P., Aulbert, C., Babak, S., Bacon, P., Bader, M., Baker, P., Baldaccini, F., Ballardin, G., Ballmer, S., Barayoga, J., Barclay, S., Barish, B., Barker, D., Barone, F., Barr, B., Barsotti, L., Barsuglia, M., Barta, D., Bartlett, J., Barton, M., Bartos, I., Bassiri, R., Basti, A., Batch, J., Baune, C., Bavigadda, V., Bazzan, M., Behnke, B., Bejger, M., Belczynski, C., Bell, A., Bell, C., Berger, B., Bergman, J., Bergmann, G., Berry, C., Bersanetti, D., Bertolini, A., Betzwieser, J., Bhagwat, S., Bhandare, R., Bilenko, I., Billingsley, G., Birch, J., Birney, I. A., Birnholtz, O., Biscans, S., Bisht, A., Bitossi, M., Biwer, C., Bizouard, M., Blackburn, J., Blair, C., Blair, D., Blair, R., Bloemen, S., Bock, O., Bodiya, T., Boer, M., Bogaert, G., Bogan, C., Bohe, A., Bojtos, P., Bond, C., Bondu, F., Bonnand, R., Boom, B., Bork, R., Boschi, V., Bose, S., Bouffanais, Y., Bozzi, A., Bradaschia, C., Brady, P., Braginsky, V., Branchesi, M., Brau, J., Briant, T., Brillet, A., Brinkmann, M., Brisson, V., Brockill, P., Brooks, A., Brown, D., Brown, D., Brown, N.,

Buchanan, C., Buikema, A., Bulik, T., Bulten, H., Buonanno, A., Buskulic, D., Buy, C., Byer, R., Cabero, M., Cadonati, L., Cagnoli, G., Cahillane, C., Bustillo, J. C., Callister, T., Calloni, E., Camp, J., Cannon, K., Cao, J., Capano, C., Capocasa, E., Carbognani, F., Caride, S., Diaz, J. C., Casentini, C., Caudill, S., Cavaglià, M., Cavalier, F., Cavalieri, R., Cella, G., Cepeda, C., Baiardi, L. C., Cerretani, G., Cesarini, E., Chakraborty, R., Chalermsongsak, T., Chamberlin, S., Chan, M., Chao, S., Charlton, P., Chassande-Mottin, E., Chen, H., Chen, Y., Cheng, C., Chincarini, A., Chiummo, A., Cho, H., Cho, M., Chow, J., Christensen, N., Chu, Q., Chua, S., Chung, S., Ciani, G., Clara, F., Clark, J., Cleva, F., Coccia, E., Cohadon, P.-F., Colla, A., Collette, C., Cominsky, L., Constancio, M., Conte, A., Conti, L., Cook, D., Corbitt, T., Cornish, N., Corsi, A., Cortese, S., Costa, C., Coughlin, M., Coughlin, S., Coulon, J.-P., Countryman, S., Couvares, P., Cowan, E., Coward, D., Cowart, M., Coyne, D., Coyne, R., Craig, K., Creighton, J., Creighton, T., Cripe, J., Crowder, S., Cruise, A., Cumming, A., Cunningham, L., Cuoco, E., Canton, T. D., Danilishin, S., D'Antonio, S., Danzmann, K., Darman, N., Da Silva Costa, C., Dattilo, V., Dave, I., Daveloza, H., Davier, M., Davies, G., Daw, E., Day, R., De, S., DeBra, D., Debreczeni, G., Degallaix, J., De Laurentis, M., Deléglise, S., Del Pozzo, W., Denker, T., Dent, T., Dereli, H., Dergachev, V., DeRosa, R., De Rosa, R., DeSalvo, R., Dhurandhar, S., Díaz, M., Di Fiore, L., Di Giovanni, M., Di Lieto, A., Di Pace, S., Di Palma, I., Di Virgilio, A., Dojcinoski, G., Dolique, V., Donovan, F., Dooley, K., Doravari, S., Douglas, R., Downes, T., Drago, M., Drever, R., Driggers, J., Du, Z., Ducrot, M., Dwyer, S., Edo, T., Edwards, M., Effler, A., Eggenstein, H.-B., Ehrens, P., Eichholz, J., Eikenberry, S., Engels, W., Essick, R., Etzel, T., Evans, M., Evans, T., Everett, R., Factourovich, M., Fafone, V., Fair, H., Fairhurst, S., Fan, X., Fang, Q., Farinon, S., Farr, B., Farr, W., Favata, M., Fays, M., Fehrmann, H., Fejer, M., Feldbaum, D., Ferrante, I., Ferreira, E., Ferrini, F., Fidecaro, F., Finn, L., Fiori, I., Fiorucci, D., Fisher, R., Flaminio, R., Fletcher, M., Fong, H., Fournier, J.-D., Franco, S., Frasca, S., Frasconi, F., Frede, M., Frei, Z., Freise, A., Frey, R., Frey, V., Fricke, T., Fritschel, P., Frolov, V.,

Fulda, P., Fyffe, M., Gabbard, H., Gair, J., Gammaitoni, L., Gaonkar, S., Garufi, F., Gatto, A., Gaur, G., Gehrels, N., Gemme, G., Gendre, B., Genin, E., Gennai, A., George, J., Gergely, L., Germain, V., Ghosh, A., Ghosh, A., Ghosh, S., Giaime, J., Giardina, K., Giazotto, A., Gill, K., Glaefke, A., Gleason, J., Goetz, E., Goetz, R., Gondan, L., González, G., Castro, J. G., Gopakumar, A., Gordon, N., Gorodetsky, M., Gossan, S., Gosselin, M., Gouaty, R., Graef, C., Graff, P., Granata, M., Grant, A., Gras, S., Gray, C., Greco, G., Green, A., Greenhalgh, R., Groot, P., Grote, H., Grunewald, S., Guidi, G., Guo, X., Gupta, A., Gupta, M., Gushwa, K., Gustafson, E., Gustafson, R., Hacker, J., Hall, B., Hall, E., Hammond, G., Haney, M., Hanke, M., Hanks, J., Hanna, C., Hannam, M., Hanson, J., Hardwick, T., Harms, J., Harry, G., Harry, I., Hart, M., Hartman, M., Haster, C.-J., Haughian, K., Healy, J., Heefner, J., Heidmann, A., Heintze, M., Heinzel, G., Heitmann, H., Hello, P., Hemming, G., Hendry, M., Heng, I., Hennig, J., Heptonstall, A., Heurs, M., Hild, S., Hoak, D., Hodge, K., Hofman, D., Hollitt, S., Holt, K., Holz, D., Hopkins, P., Hosken, D., Hough, J., Houston, E., Howell, E., Hu, Y., Huang, S., Huerta, E., Huet, D., Hughey, B., Husa, S., Huttner, S., Huynh-Dinh, T., Idrisy, A., Indik, N., Ingram, D., Inta, R., Isa, H., Isac, J.-M., Isi, M., Islas, G., Isogai, T., Iyer, B., Izumi, K., Jacobson, M., Jacqmin, T., Jang, H., Jani, K., Jaranowski, P., Jawahar, S., Jiménez-Forteza, F., Johnson, W., Johnson-McDaniel, N., Jones, D., Jones, R., Jonker, R., Ju, L., Haris, K., Kalaghatgi, C., Kalogera, V., Kandhasamy, S., Kang, G., Kanner, J., Karki, S., Kasprzack, M., Katsavounidis, E., Katzman, W., Kaufer, S., Kaur, T., Kawabe, K., Kawazoe, F., Kéfélian, F., Kehl, M., Keitel, D., Kelley, D., Kells, W., Kennedy, R., Keppel, D., Key, J., Khalaidovski, A., Khalili, F., Khan, I., Khan, S., Khan, Z., Khazanov, E., Kijbunchoo, N., Kim, C., Kim, J., Kim, K., Kim, N.-G., Kim, N., Kim, Y.-M., King, E., King, P., Kinzel, D., Kissel, J., Kleybolte, L., Klimenko, S., Koehlenbeck, S., Kokeyama, K., Koley, S., Kondrashov, V., Kontos, A., Koranda, S., Korobko, M., Korth, W., Kowalska, I., Kozak, D., Kringel, V., Krishnan, B., Królak, A., Krueger, C., Kuehn, G., Kumar, P., Kumar, R., Kuo, L., Kutynia, A., Kwee, P., Lackey, B., Landry,

M., Lange, J., Lantz, B., Lasky, P., Lazzarini, A., Lazzaro, C., Leaci, P., Leavey, S., Lebigot, E., Lee, C., Lee, H., Lee, H., Lee, K., Lenon, A., Leonardi, M., Leong, J., Leroy, N., Letendre, N., Levin, Y., Levine, B., Li, T., Libson, A., Littenberg, T., Lockerbie, N., Logue, J., Lombardi, A., London, L., Lord, J., Lorenzini, M., Loriette, V., Lormand, M., Losurdo, G., Lough, J., Lousto, C., Lovelace, G., Lück, H., Lundgren, A., Luo, J., Lynch, R., Ma, Y., MacDonald, T., Machenschalk, B., MacInnis, M., Macleod, D., Magaña-Sandoval, F., Magee, R., Mageswaran, M., Majorana, E., Maksimovic, I., Malvezzi, V., Man, N., Mandel, I., Mandic, V., Mangano, V., Mansell, G., Manske, M., Mantovani, M., Marchesoni, F., Marion, F., Márka, S., Márka, Z., Markosyan, A., Maros, E., Martelli, F., Martellini, L., Martin, I., Martin, R., Martynov, D., Marx, J., Mason, K., Masserot, A., Massinger, T., Masso-Reid, M., Matichard, F., Matone, L., Mavalvala, N., Mazumder, N., Mazzolo, G., McCarthy, R., McClelland, D., McCormick, S., McGuire, S., McIntyre, G., McIver, J., McManus, D., McWilliams, S., Meacher, D., Meadors, G., Meidam, J., Melatos, A., Mendell, G., Mendoza-Gandara, D., Mercer, R., Merilh, E., Merzougui, M., Meshkov, S., Messenger, C., Messick, C., Meyers, P., Mezzani, F., Miao, H., Michel, C., Middleton, H., Mikhailov, E., Milano, L., Miller, J., Millhouse, M., Minenkov, Y., Ming, J., Mirshekari, S., Mishra, C., Mitra, S., Mitrofanov, V., Mitselmakher, G., Mittleman, R., Moggi, A., Mohan, M., Mohapatra, S., Montani, M., Moore, B., Moore, C., Moraru, D., Moreno, G., Morriss, S., Mossavi, K., Mours, B., Mow-Lowry, C., Mueller, C., Mueller, G., Muir, A., Mukherjee, A., Mukherjee, D., Mukherjee, S., Mukund, N., Mullavey, A., Munch, J., Murphy, D., Murray, P., Mytidis, A., Nardecchia, I., Naticchioni, L., Nayak, R., Necula, V., Nedkova, K., Nelemans, G., Neri, M., Neunzert, A., Newton, G., Nguyen, T., Nielsen, A., Nissanke, S., Nitz, A., Nocera, F., Nolting, D., Normandin, M., Nuttall, L., Oberling, J., Ochsner, E., O'Dell, J., Oelker, E., Ogin, G., Oh, J., Oh, S., Ohme, F., Oliver, M., Oppermann, P., Oram, R. J., O'Reilly, B., O'Shaughnessy, R., Ott, C., Ottaway, D., Ottens, R., Overmier, H., Owen, B., Pai, A., Pai, S., Palamos, J., Palashov, O., Palomba, C., Pal-Singh, A., Pan, H., Pan, Y., Pankow, C., Pannarale, F., Pant,

B., Paoletti, F., Paoli, A., Papa, M., Paris, H., Parker, W., Pascucci, D., Pasqualetti, A., Passaquieti, R., Passuello, D., Patricelli, B., Patrick, Z., Pearlstone, B., Pedraza, M., Pedurand, R., Pekowsky, L., Pele, A., Penn, S., Perreca, A., Pfeiffer, H., Phelps, M., Piccinni, O., Pichot, M., Pickenpack, M., Piergiovanni, F., Pierro, V., Pillant, G., Pinard, L., Pinto, I., Pitkin, M., Poeld, J., Poggiani, R., Popolizio, P., Post, A., Powell, J., Prasad, J., Predoi, V., Premachandra, S., Prestegard, T., Price, L., Prijatelj, M., Principe, M., Privitera, S., Prix, R., Prodi, G., Prokhorov, L., Puncken, O., Punturo, M., Puppo, P., Pürrer, M., Qi, H., Qin, J., Quetschke, V., Quintero, E., Quitzow-James, R., Raab, F., Rabeling, D., Radkins, H., Raffai, P., Raja, S., Rakhmanov, M., Ramet, C., Rapagnani, P., Raymond, V., Razzano, M., Re, V., Read, J., Reed, C., Regimbau, T., Rei, L., Reid, S., Reitze, D., Rew, H., Reyes, S., Ricci, F., Riles, K., Robertson, N., Robie, R., Robinet, F., Rocchi, A., Rolland, L., Rollins, J., Roma, V., Romano, J., Romano, R., Romanov, G., Romie, J., Rosińska, D., Rowan, S., Rüdiger, A., Ruggi, P., Ryan, K., Sachdev, S., Sadecki, T., Sadeghian, L., Salconi, L., Saleem, M., Salemi, F., Samajdar, A., Sammut, L., Sampson, L., Sanchez, E., Sandberg, V., Sandeen, B., Sanders, G., Sanders, J., Sassolas, B., Sathyaprakash, B., Saulson, P., Sauter, O., Savage, R., Sawadsky, A., Schale, P., Schilling, R., Schmidt, J., Schmidt, P., Schnabel, R., Schofield, R., Schönbeck, A., Schreiber, E., Schuette, D., Schutz, B., Scott, J., Scott, S., Sellers, D., Sengupta, A., Sentenac, D., Sequino, V., Sergeev, A., Serna, G., Setyawati, Y., Sevigny, A., Shaddock, D., Shaffer, T., Shah, S., Shahriar, M., Shaltev, M., Shao, Z., Shapiro, B., Shawhan, P., Sheperd, A., Shoemaker, D., Shoemaker, D., Siellez, K., Siemens, X., Sigg, D., Silva, A., Simakov, D., Singer, A., Singer, L., Singh, A., Singh, R., Singhal, A., Sintes, A., Slagmolen, B., Smith, J., Smith, M., Smith, N., Smith, R., Son, E., Sorazu, B., Sorrentino, F., Souradeep, T., Srivastava, A., Staley, A., Steinke, M., Steinlechner, J., Steinlechner, S., Steinmeyer, D., Stephens, B., Stevenson, S., Stone, R., Strain, K., Straniero, N., Stratta, G., Strauss, N., Strigin, S., Sturani, R., Stuver, A., Summerscales, T., Sun, L., Sutton, P., Swinkels, B., Szczepańczyk, M., Tacca, M., Talukder, D., Tanner, D., Tápai, M.,

Tarabrin, S., Taracchini, A., Taylor, R., Theeg, T., Thirugnanasambandam, M., Thomas, E., Thomas, M., Thomas, P., Thorne, K., Thorne, K., Thrane, E., Tiwari, S., Tiwari, V., Tokmakov, K., Tomlinson, C., Tonelli, M., Torres, C., Torrie, C., Töyrä, D., Travasso, F., Traylor, G., Trifirò, D., Tringali, M., Trozzo, L., Tse, M., Turconi, M., Tuyenbayev, D., Ugolini, D., Unnikrishnan, C., Urban, A., Usman, S., Vahlbruch, H., Vajente, G., Valdes, G., Vallisneri, M., van Bakel, N., van Beuzekom, M., van den Brand, J., Van Den Broeck, C., Vander-Hyde, D., van der Schaaf, L., van Heijningen, J., van Veggel, A., Vardaro, M., Vass, S., Vasúth, M., Vaulin, R., Vecchio, A., Vedovato, G., Veitch, J., Veitch, P., Venkateswara, K., Verkindt, D., Vetrano, F., Viceré, A., Vinciguerra, S., Vine, D., Vinet, J.-Y., Vitale, S., Vo, T., Vocca, H., Vorvick, C., Voss, D., Vousden, W., Vyatchanin, S., Wade, A., Wade, L., Wade, M., Waldman, S., Walker, M., Wallace, L., Walsh, S., Wang, G., Wang, H., Wang, M., Wang, X., Wang, Y., Ward, H., Ward, R., Warner, J., Was, M., Weaver, B., Wei, L.-W., Weinert, M., Weinstein, A., Weiss, R., Welborn, T., Wen, L., Weßels, P., Westphal, T., Wette, K., Whelan, J., Whitcomb, S., White, D., Whiting, B., Wiesner, K., Wilkinson, C., Willems, P., Williams, L., Williams, R., Williamson, A., Willis, J., Willke, B., Wimmer, M., Winkelmann, L., Winkler, W., Wipf, C., Wiseman, A., Wittel, H., Woan, G., Worden, J., Wright, J., Wu, G., Yablon, J., Yakushin, I., Yam, W., Yamamoto, H., Yancey, C., Yap, M., Yu, H., Yvert, M., Zadrożny, A., Zangrando, L., Zanolin, M., Zendri, J.-P., Zevin, M., Zhang, F., Zhang, L., Zhang, M., Zhang, Y., Zhao, C., Zhou, M., Zhou, Z., Zhu, X., Zucker, M., Zuraw, S., and Zweizig, J. a. (2016). Observation of gravitational waves from a binary black hole merger. *Physical Review Letters*, 116(6).

Abbott, B. P., Abbott, R., Abbott, T. D., Abraham, S., Acernese, F., Ackley, K., Adams, C., Adhikari, R. X., Adya, V. B., Affeldt, C., Agathos, M., Agatsuma, K., Aggarwal, N., Aguiar, O. D., Aiello, L., Ain, A., Ajith, P., Allen, G., Allocca, A., Aloy, M. A., Altin, P. A., Amato, A., Anand, S., Ananyeva, A., Anderson, S. B., Anderson, W. G., Angelova, S. V., Antier, S., Appert, S., Arai, K., Araya, M. C., Areeda, J. S., Arène, M.,

Arnaud, N., Aronson, S. M., Arun, K. G., Ascenzi, S., Ashton, G., Aston, S. M., Astone, P., Aubin, F., Aufmuth, P., AultONeal, K., Austin, C., Avendano, V., Avila-Alvarez, A., Babak, S., Bacon, P., Badaracco, F., Bader, M. K. M., Bae, S., Baird, J., Baker, P. T., Baldaccini, F., Ballardin, G., Ballmer, S. W., Bals, A., Banagiri, S., Barayoga, J. C., Barbieri, C., Barclay, S. E., Barish, B. C., Barker, D., Barkett, K., Barnum, S., Barone, F., Barr, B., Barsotti, L., Barsuglia, M., Barta, D., Bartlett, J., Bartos, I., Bassiri, R., Basti, A., Bawaj, M., Bayley, J. C., Bazzan, M., Bécsy, B., Bejger, M., Belahcene, I., Bell, A. S., Beniwal, D., Benjamin, M. G., Bergmann, G., Bernuzzi, S., Berry, C. P. L., Bersanetti, D., Bertolini, A., Betzwieser, J., Bhandare, R., Bidler, J., Biggs, E., Bilenko, I. A., Bilgili, S. A., Billingsley, G., Birney, R., Birnholtz, O., Biscans, S., Bischi, M., Biscoveanu, S., Bisht, A., Bitossi, M., Bizouard, M. A., Blackburn, J. K., Blackman, J., Blair, C. D., Blair, D. G., Blair, R. M., Bloemen, S., Bobba, F., Bode, N., Boer, M., Boetzel, Y., Bogaert, G., Bondu, F., Bonnand, R., Booker, P., Boom, B. A., Bork, R., Boschi, V., Bose, S., Bossilkov, V., Bosveld, J., Bouffanais, Y., Bozzi, A., Bradaschia, C., Brady, P. R., Bramley, A., Branchesi, M., Brau, J. E., Breschi, M., Briant, T., Briggs, J. H., Brighenti, F., Brillet, A., Brinkmann, M., Brockill, P., Brooks, A. F., Brooks, J., Brown, D. D., Brunett, S., Buikema, A., Bulik, T., Bulten, H. J., Buonanno, A., Buskulic, D., Buy, C., Byer, R. L., Cabero, M., Cadonati, L., Cagnoli, G., Cahillane, C., Calderón Bustillo, J., Callister, T. A., Calloni, E., Camp, J. B., Campbell, W. A., Canepa, M., Cannon, K. C., Cao, H., Cao, J., Carapella, G., Carbognani, F., Caride, S., Carney, M. F., Carullo, G., Casanueva Diaz, J., Casentini, C., Caudill, S., Cavaglià, M., Cavalier, F., Cavalieri, R., Cella, G., Cerdá-Durán, P., Cesarini, E., Chaibi, O., Chakravarti, K., Chamberlin, S. J., Chan, M., Chao, S., Charlton, P., Chase, E. A., Chassande-Mottin, E., Chatterjee, D., Chaturvedi, M., Cheeseboro, B. D., Chen, H. Y., Chen, X., Chen, Y., Cheng, H.-P., Cheong, C. K., Chia, H. Y., Chiadini, F., Chincarini, A., Chiummo, A., Cho, G., Cho, H. S., Cho, M., Christensen, N., and Chu, Q. (2019). Search for Eccentric Binary Black Hole Mergers with Advanced LIGO and Advanced Virgo during Their First

and Second Observing Runs. *ApJ*, 883(2):149.

Abbott, R., Abbott, T. D., Abraham, S., Acernese, F., Ackley, K., Adams, A., Adams, C., Adhikari, R. X., Adya, V. B., Affeldt, C., Agathos, M., Agatsuma, K., Aggarwal, N., Aguiar, O. D., Aiello, L., Ain, A., Ajith, P., Allen, G., Allocca, A., Altin, P. A., Amato, A., Anand, S., Ananyeva, A., Anderson, S. B., Anderson, W. G., Angelova, S. V., Ansoldi, S., Antelis, J. M., Antier, S., Appert, S., Arai, K., Araya, M. C., Areeda, J. S., Arè ne, M., Arnaud, N., Aronson, S. M., Arun, K. G., Asali, Y., Ascenzi, S., Ashton, G., Aston, S. M., Astone, P., Aubin, F., Aufmuth, P., AultONeal, K., Austin, C., Avendano, V., Babak, S., Badaracco, F., Bader, M. K. M., Bae, S., Baer, A. M., Bagnasco, S., Baird, J., Ball, M., Ballardin, G., Ballmer, S. W., Bals, A., Balsamo, A., Baltus, G., Banagiri, S., Bankar, D., Bankar, R. S., Barayoga, J. C., Barbieri, C., Barish, B. C., Barker, D., Barneo, P., Barnum, S., Barone, F., Barr, B., Barsotti, L., Barsuglia, M., Barta, D., Bartlett, J., Bartos, I., Bassiri, R., Basti, A., Bawaj, M., Bayley, J. C., Bazzan, M., Becher, B. R., Bécsy, B., Bedakihale, V. M., Bejger, M., Belahcene, I., Beniwal, D., Benjamin, M. G., Bennett, T. F., Bentley, J. D., Bergamin, F., Berger, B. K., Bergmann, G., Bernuzzi, S., Berry, C. P. L., Bersanetti, D., Bertolini, A., Betzwieser, J., Bhandare, R., Bhandari, A. V., Bhattacharjee, D., Bidler, J., Bilenko, I. A., Billingsley, G., Birney, R., Birnholtz, O., Biscans, S., Bischi, M., Biscoveanu, S., Bisht, A., Bitossi, M., Bizouard, M.-A., Blackburn, J. K., Blackman, J., Blair, C. D., Blair, D. G., Blair, R. M., Blanch, O., Bobba, F., Bode, N., Boer, M., Boetzel, Y., Bogaert, G., Boldrini, M., Bondu, F., Bonilla, E., Bonnand, R., Booker, P., Boom, B. A., Bork, R., Boschi, V., Bose, S., Bossilkov, V., Boudart, V., Bouffanais, Y., Bozzi, A., Bradaschia, C., Brady, P. R., Bramley, A., Branchesi, M., Brau, J. E., Breschi, M., Briant, T., Briggs, J. H., Brighenti, F., Brillet, A., Brinkmann, M., Brockill, P., Brooks, A. F., Brooks, J., Brown, D. D., Brunett, S., Bruno, G., Bruntz, R., Buikema, A., Bulik, T., Bulten, H. J., Buonanno, A., Buscicchio, R., Buskulic, D., Byer, R. L., Cabero, M., Cadonati, L., Caesar, M., Cagnoli, G., Cahillane, C., Bustillo, J. C., Callaghan, J. D., Callister, T. A., Calloni, E., Camp, J. B., Canepa,

M., Cannon, K. C., Cao, H., Cao, J., Carapella, G., Carbognani, F., Carney, M. F., Carpinelli, M., Carullo, G., Carver, T. L., Diaz, J. C., Casentini, C., Caudill, S., Cavaglià, M., Cavalier, F., Cavalieri, R., Cella, G., Cerdá-Durán, P., Cesarini, E., Chaibi, W., Chakravarti, K., Chan, C.-L., Chan, C., Chandra, K., Chanial, P., Chao, S., Charlton, P., Chase, E. A., Chassande-Mottin, E., Chatterjee, D., Chattopadhyay, D., Chaturvedi, M., Chatziioannou, K., Chen, A., Chen, H. Y., Chen, X., Chen, Y., Cheng, H.-P., Cheong, C. K., Chia, H. Y., Chiadini, F., Chierici, R., Chincarini, A., Chiummo, A., Cho, G., Cho, H. S., Cho, M., Choate, S., Christensen, N., Chu, Q., Chua, S., Chung, K. W., Chung, S., Ciani, G., Ciecielag, P., Cieślar, M., Cifaldi, M., Ciobanu, A. A., Ciolfi, R., Cipriano, F., Cirone, A., Clara, F., Clark, E. N., Clark, J. A., Clarke, L., Clearwater, P., Clesse, S., Cleva, F., Coccia, E., Cohadon, P.-F., Cohen, D. E., Colleoni, M., Collette, C. G., Collins, C., Colpi, M., Constancio, M., Conti, L., Cooper, S. J., Corban, P., Corbitt, T. R., Cordero-Carrión, I., Corezzi, S., Corley, K. R., Cornish, N., Corre, D., Corsi, A., Cortese, S., Costa, C. A., Cotesta, R., Coughlin, M. W., Coughlin, S. B., Coulon, J.-P., Countryman, S. T., Couvares, P., Covas, P. B., Coward, D. M., Cowart, M. J., Coyne, D. C., Coyne, R., Creighton, J. D. E., Creighton, T. D., Croquette, M., Crowder, S. G., Cudell, J. R., Cullen, T. J., Cumming, A., Cummings, R., Cunningham, L., Cuoco, E., Curylo, M., Canton, T. D., Dálya, G., Dana, A., DaneshgaranBajastani, L. M., D'Angelo, B., Danilishin, S. L., D'Antonio, S., Danzmann, K., Darsow-Fromm, C., Dasgupta, A., Datrier, L. E. H., Dattilo, V., Dave, I., Davier, M., Davies, G. S., Davis, D., Daw, E. J., Dean, R., DeBra, D., Deenadayalan, M., Degallaix, J., Laurentis, M. D., Deléglise, S., Favero, V. D., Lillo, F. D., Lillo, N. D., Pozzo, W. D., DeMarchi, L. M., Matteis, F. D., D'Emilio, V., Demos, N., Denker, T., Dent, T., Depasse, A., Pietri, R. D., Rosa, R. D., Rossi, C. D., DeSalvo, R., de Varona, O., Dhurandhar, S., Díaz, M. C., Diaz-Ortiz, M., Didio, N. A., Dietrich, T., Fiore, L. D., DiFronzo, C., Giorgio, C. D., Giovanni, F. D., Giovanni, M. D., Girolamo, T. D., Lieto, A. D., Ding, B., Pace, S. D., Palma, I. D., Renzo, F. D., Divakarla, A. K., Dmitriev, A., Doctor, Z., D'Onofrio, L., Donovan, F.,

Dooley, K. L., Doravari, S., Dorrington, I., Downes, T. P., Drago, M., Driggers, J. C., Du, Z., Ducoin, J.-G., Dupej, P., Durante, O., D'Urso, D., Duverne, P.-A., Dwyer, S. E., Easter, P. J., Eddolls, G., Edelman, B., Edo, T. B., Edy, O., Effler, A., Eichholz, J., Eikenberry, S. S., Eisenmann, M., Eisenstein, R. A., Ejlli, A., Errico, L., Essick, R. C., Estellés, H., Estevez, D., Etienne, Z. B., Etzel, T., Evans, M., Evans, T. M., Ewing, B. E., Fafone, V., Fair, H., Fairhurst, S., Fan, X., Farah, A. M., Farinon, S., Farr, B., Farr, W. M., Fauchon-Jones, E. J., Favata, M., Fays, M., Fazio, M., Feicht, J., Fejer, M. M., Feng, F., Fenyvesi, E., Ferguson, D. L., Fernandez-Galiana, A., Ferrante, I., Ferreira, T. A., Fidecaro, F., Figura, P., Fiori, I., Fiorucci, D., Fishbach, M., Fisher, R. P., Fishner, J. M., Fittipaldi, R., Fitz-Axen, M., Fiumara, V., Flaminio, R., Floden, E., Flynn, E., Fong, H., Font, J. A., Forsyth, P. W. F., Fournier, J.-D., Frasca, S., Frasconi, F., Frei, Z., Freise, A., Frey, R., Frey, V., Fritschel, P., Frolov, V. V., Fronzé, G. G., Fulda, P., Fyffe, M., Gabbard, H. A., Gadre, B. U., Gaebel, S. M., Gair, J. R., Gais, J., Galaudage, S., Gamba, R., Ganapathy, D., Ganguly, A., Gaonkar, S. G., Garaventa, B., García-Quirós, C., Garufi, F., Gateley, B., Gaudio, S., Gayathri, V., Gemme, G., Gennai, A., George, D., George, J., Gergely, L., Ghonge, S., Ghosh, A., Ghosh, A., Ghosh, S., Giacomazzo, B., Giacoppo, L., Giaime, J. A., Giardina, K. D., Gibson, D. R., Gier, C., Gill, K., Giri, P., Glanzer, J., Gleckl, A. E., Godwin, P., Goetz, E., Goetz, R., Gohlke, N., Goncharov, B., González, G., Gopakumar, A., Gossan, S. E., Gosselin, M., Gouaty, R., Grace, B., Grado, A., Granata, M., Granata, V., Grant, A., Gras, S., Grassia, P., Gray, C., Gray, R., Greco, G., Green, A. C., Green, R., Gretarsson, E. M., Griggs, H. L., Grignani, G., Grimaldi, A., Grimes, E., Grimm, S. J., Grote, H., Grunewald, S., Gruning, P., Guerrero, J. G., Guidi, G. M., Guimaraes, A. R., Guixé, G., Gulati, H. K., Guo, Y., Gupta, A., Gupta, A., Gupta, P., Gustafson, E. K., Gustafson, R., Guzman, F., Haegel, L., Halim, O., Hall, E. D., Hamilton, E. Z., Hammond, G., Haney, M., Hanke, M. M., Hanks, J., Hanna, C., Hannuksela, O. A., Hannuksela, O., Hansen, H., Hansen, T. J., Hanson, J., Harder, T., Hardwick, T., Haris, K., Harms, J., Harry, G. M., Harry, I. W., Hartwig,

D., Hasskew, R. K., Haster, C.-J., Haughian, K., Hayes, F. J., Healy, J., Heidmann, A., Heintze, M. C., Heinze, J., Heinzel, J., Heitmann, H., Hellman, F., Hello, P., Helmling-Cornell, A. F., Hemming, G., Hendry, M., Heng, I. S., Hennes, E., Hennig, J., Hennig, M. H., Vivanco, F. H., Heurs, M., Hild, S., Hill, P., Hines, A. S., Hochheim, S., Hofgard, E., Hofman, D., Hohmann, J. N., Holgado, A. M., Holland, N. A., Hollows, I. J., Holmes, Z. J., Holt, K., Holz, D. E., Hopkins, P., Horst, C., Hough, J., Howell, E. J., Hoy, C. G., Hoyland, D., Huang, Y., Hübner, M. T., Huddart, A. D., Huerta, E. A., Hughey, B., Hui, V., Husa, S., Huttner, S. H., Hutzler, B. M., Huxford, R., Huynh-Dinh, T., Idzkowski, B., Iess, A., Imperato, S., Inchauspe, H., Ingram, C., Intini, G., Isi, M., Iyer, B. R., JaberianHamedan, V., Jacqmin, T., Jadhav, S. J., Jadhav, S. P., James, A. L., Jani, K., Janssens, K., Janthalur, N. N., Jaranowski, P., Jariwala, D., Jaume, R., Jenkins, A. C., Jeunon, M., Jiang, J., Johns, G. R., Jones, A. W., Jones, D. I., Jones, J. D., Jones, P., Jones, R., Jonker, R. J. G., Ju, L., Junker, J., Kalaghatgi, C. V., Kalogera, V., Kamai, B., Kandhasamy, S., Kang, G., Kanner, J. B., Kapadia, S. J., Kapasi, D. P., Karathanasis, C., Karki, S., Kashyap, R., Kasprzack, M., Kastaun, W., Katsanevas, S., Katsavounidis, E., Katzman, W., Kawabe, K., Kéfélian, F., Keitel, D., Key, J. S., Khadka, S., Khalili, F. Y., Khan, I., Khan, S., Khazanov, E. A., Khetan, N., Khursheed, M., Kijbunchoo, N., Kim, C., Kim, G. J., Kim, J. C., Kim, K., Kim, W. S., Kim, Y.-M., Kimball, C., King, P. J., Kinley-Hanlon, M., Kirchhoff, R., Kissel, J. S., Kleybolte, L., Klimenko, S., Knowles, T. D., Knyazev, E., Koch, P., Koehlenbeck, S. M., Koekoek, G., Koley, S., Kolstein, M., Komori, K., Kondrashov, V., Kontos, A., Koper, N., Korobko, M., Korth, W. Z., Kovalam, M., Kozak, D. B., Krämer, C., Kringel, V., Krishnendu, N. V., Królak, A., Kuehn, G., Kumar, A., Kumar, P., Kumar, R., Kumar, R., Kuns, K., Kwang, S., Lackey, B. D., Laghi, D., Lalande, E., Lam, T. L., Lamberts, A., Landry, M., Lane, B. B., Lang, R. N., Lange, J., Lantz, B., Lanza, R. K., Rosa, I. L., Lartaux-Vollard, A., Lasky, P. D., Laxen, M., Lazzarini, A., Lazzaro, C., Leaci, P., Leavey, S., Lecoeuche, Y. K., Lee, H. M., Lee, H. W., Lee, J., Lee, K., Lehmann, J., Leon, E., Leroy, N., Letendre,

N., Levin, Y., Li, A., Li, J., Li, K. J. L., Li, T. G. F., Li, X., Linde, F., Linker, S. D., Linley, J. N., Littenberg, T. B., Liu, J., Liu, X., Llorens-Monteagudo, M., Lo, R. K. L., Lockwood, A., London, L. T., Longo, A., Lorenzini, M., Loriette, V., Lormand, M., Losurdo, G., Lough, J. D., Lousto, C. O., Lovelace, G., Lück, H., Lumaca, D., Lundgren, A. P., Ma, Y., Macas, R., MacInnis, M., Macleod, D. M., MacMillan, I. A. O., Macquet, A., Hernandez, I. M., Magaña-Sandoval, F., Magazzù, C., Magee, R. M., Majorana, E., Maksimovic, I., Maliakal, S., Malik, A., Man, N., Mandic, V., Mangano, V., Mansell, G. L., Manske, M., Mantovani, M., Mapelli, M., Marchesoni, F., Marion, F., Márka, S., Márka, Z., Markakis, C., Markosyan, A. S., Markowitz, A., Maros, E., Marquina, A., Marsat, S., Martelli, F., Martin, I. W., Martin, R. M., Martinez, M., Martinez, V., Martynov, D. V., Masalehdan, H., Mason, K., Massera, E., Masserot, A., Massinger, T. J., Masso-Reid, M., Mastrogiovanni, S., Matas, A., Mateu-Lucena, M., Matichard, F., Matiushechkina, M., Mavalvala, N., Maynard, E., McCann, J. J., McCarthy, R., McClelland, D. E., McCormick, S., McCuller, L., McGuire, S. C., McIsaac, C., McIver, J., McManus, D. J., McRae, T., McWilliams, S. T., Meacher, D., Meadors, G. D., Mehmet, M., Mehta, A. K., Melatos, A., Melchor, D. A., Mendell, G., Menendez-Vazquez, A., Mercer, R. A., Mereni, L., Merfeld, K., Merilh, E. L., Merritt, J. D., Merzougui, M., Meshkov, S., Messenger, C., Messick, C., Metzdorff, R., Meyers, P. M., Meylahn, F., Mhaske, A., Miani, A., Miao, H., Michaloliakos, I., Michel, C., Middleton, H., Milano, L., Miller, A. L., Miller, S., Millhouse, M., Mills, J. C., Milotti, E., Milovich-Goff, M. C., Minazzoli, O., Minenkov, Y., Mir, L. M., Mishkin, A., Mishra, C., Mistry, T., Mitra, S., Mitrofanov, V. P., Mitselmakher, G., Mittleman, R., Mo, G., Mogushi, K., Mohapatra, S. R. P., Mohite, S. R., Molina, I., Molina-Ruiz, M., Mondin, M., Montani, M., Moore, C. J., Moraru, D., Morawski, F., Moreno, G., Morisaki, S., Mours, B., Mow-Lowry, C. M., Mozzon, S., Muciaccia, F., Mukherjee, A., Mukherjee, D., Mukherjee, S., Mukherjee, S., Mukund, N., Mullavey, A., Munch, J., Muñiz, E. A., Murray, P. G., Nadji, S. L., Nagar, A., Nardecchia, I., Naticchioni, L., Nayak, R. K., Neil, B. F., Neilson, J., Nelemans, G., Nelson, T. J. N., Nery, M., Neunzert,

A., Ng, K. Y., Ng, S., Nguyen, C., Nguyen, P., Nguyen, T., Nichols, S. A., Nissanke, S., Nocera, F., Noh, M., North, C., Nothard, D., Nuttall, L. K., Oberling, J., O'Brien, B. D., O'Dell, J., Oganesyan, G., Ogin, G. H., Oh, J. J., Oh, S. H., Ohme, F., Ohta, H., Okada, M. A., Olivetto, C., Oppermann, P., Oram, R. J., O'Reilly, B., Ormiston, R. G., Ormsby, N., Ortega, L. F., O'Shaughnessy, R., Ossokine, S., Osthelder, C., Ottaway, D. J., Overmier, H., Owen, B. J., Pace, A. E., Pagano, G., Page, M. A., Pagliaroli, G., Pai, A., Pai, S. A., Palamos, J. R., Palashov, O., Palomba, C., Pan, H., Panda, P. K., Pang, T. H., Pankow, C., Pannarale, F., Pant, B. C., Paoletti, F., Paoli, A., Paolone, A., Parker, W., Pascucci, D., Pasqualetti, A., Passaquieti, R., Passuello, D., Patel, M., Patricelli, B., Payne, E., Pechsiri, T. C., Pedraza, M., Pegoraro, M., Pele, A., Penn, S., Perego, A., Perez, C. J., Périgois, C., Perreca, A., Perriès, S., Petermann, J., Petterson, D., Pfeiffer, H. P., Pham, K. A., Phukon, K. S., Piccinni, O. J., Pichot, M., Piendibene, M., Piergiovanni, F., Pierini, L., Pierro, V., Pillant, G., Pilo, F., Pinard, L., Pinto, I. M., Piotrzkowski, K., Pirello, M., Pitkin, M., Placidi, E., Plastino, W., Pluchar, C., Poggiani, R., Polini, E., Pong, D. Y. T., Ponrathnam, S., Popolizio, P., Porter, E. K., Poverman, A., Powell, J., Pracchia, M., Prajapati, A. K., Prasai, K., Prasanna, R., Pratten, G., Prestegard, T., Principe, M., Prodi, G. A., Prokhorov, L., Prosposito, P., Puecher, A., Punturo, M., Puosi, F., Puppo, P., Pürrer, M., Qi, H., Quetschke, V., Quinonez, P. J., Quitzow-James, R., Raab, F. J., Raaijmakers, G., Radkins, H., Radulesco, N., Raffai, P., Rafferty, H., Rail, S. X., Raja, S., Rajan, C., Rajbhandari, B., Rakhmanov, M., Ramirez, K. E., Ramirez, T. D., Ramos-Buades, A., Rana, J., Rao, K., Rapagnani, P., Rapol, U. D., Ratto, B., Raymond, V., Razzano, M., Read, J., Regimbau, T., Rei, L., Reid, S., Reitze, D. H., Rettegno, P., Ricci, F., Richardson, C. J., Richardson, J. W., Richardson, L., Ricker, P. M., Riemenschneider, G., Riles, K., Rizzo, M., Robertson, N. A., Robinet, F., Rocchi, A., Rocha, J. A., Rodriguez, S., Rodriguez-Soto, R. D., Rolland, L., Rollins, J. G., Roma, V. J., Romanelli, M., Romano, R., Romel, C. L., Romero, A., Romero-Shaw, I. M., Romie, J. H., Ronchini, S., Rose, C. A., Rose, D., Rose, K., Rosell, M.

J. B., Rosińska, D., Rosofsky, S. G., Ross, M. P., Rowan, S., Rowlinson, S. J., Roy, S., Roy, S., Ruggi, P., Ryan, K., Sachdev, S., Sadecki, T., Sakellariadou, M., Salafia, O. S., Salconi, L., Saleem, M., Samajdar, A., Sanchez, E. J., Sanchez, J. H., Sanchez, L. E., Sanchis-Gual, N., Sanders, J. R., Santiago, K. A., Santos, E., Saravanan, T. R., Sarin, N., Sassolas, B., Sathyaprakash, B. S., Sauter, O., Savage, R. L., Savant, V., Sawant, D., Sayah, S., Schaetzl, D., Schale, P., Scheel, M., Scheuer, J., Schindler-Tyka, A., Schmidt, P., Schnabel, R., Schofield, R. M. S., Schönbeck, A., Schreiber, E., Schulte, B. W., Schutz, B. F., Schwarm, O., Schwartz, E., Scott, J., Scott, S. M., Seglar-Arroyo, M., Seidel, E., Sellers, D., Sengupta, A. S., Sennett, N., Sentenac, D., Sequino, V., Sergeev, A., Setyawati, Y., Shaffer, T., Shahriar, M. S., Sharifi, S., Sharma, A., Sharma, P., Shawhan, P., Shen, H., Shikauchi, M., Shink, R., Shoemaker, D. H., Shoemaker, D. M., Shukla, K., ShyamSundar, S., Sieniawska, M., Sigg, D., Singer, L. P., Singh, D., Singh, N., Singha, A., Singhal, A., Sintes, A. M., Sipala, V., Skliris, V., Slagmolen, B. J. J., Slaven-Blair, T. J., Smetana, J., Smith, J. R., Smith, R. J. E., Somala, S. N., Son, E. J., Soni, S., Sorazu, B., Sordini, V., Sorrentino, F., Sorrentino, N., Soulard, R., Souradeep, T., Sowell, E., Spencer, A. P., Spera, M., Srivastava, A. K., Srivastava, V., Staats, K., Stachie, C., Steer, D. A., Steinke, M., Steinlechner, J., Steinlechner, S., Steinmeyer, D., Stevenson, S. P., Stolle-McAllister, G., Stops, D. J., Stover, M., Strain, K. A., Stratta, G., Strunk, A., Sturani, R., Stuver, A. L., Südbeck, J., Sudhagar, S., Sudhir, V., Suh, H. G., Summerscales, T. Z., Sun, H., Sun, L., Sunil, S., Sur, A., Suresh, J., Sutton, P. J., Swinkels, B. L., Szczepańczyk, M. J., Tacca, M., Tait, S. C., Talbot, C., Tanasijczuk, A. J., Tanner, D. B., Tao, D., Tapia, A., Martin, E. N. T. S., Tasson, J. D., Taylor, R., Tenorio, R., Terkowski, L., Thirugnanasambandam, M. P., Thomas, L., Thomas, M., Thomas, P., Thompson, J. E., Thondapu, S. R., Thorne, K. A., Thrane, E., Tiwari, S., Tiwari, S., Tiwari, V., Toland, K., Tolley, A. E., Tonelli, M., Tornasi, Z., Torres-Forné, A., Torrie, C. I., e Melo, I. T., Töyrä, D., Tran, A. T., Trapananti, A., Travasso, F., Traylor, G., Tringali, M. C., Tripathee, A., Trovato, A., Trudeau, R. J., Tsai, D. S., Tsang, K. W., Tse, M., Tso, R., Tsukada,

L., Tsuna, D., Tsutsui, T., Turconi, M., Ubhi, A. S., Udall, R. P., Ueno, K., Ugolini, D., Unnikrishnan, C. S., Urban, A. L., Usman, S. A., Utina, A. C., Vahlbruch, H., Vajente, G., Vajpeyi, A., Valdes, G., Valentini, M., Valsan, V., van Bakel, N., van Beuzekom, M., van den Brand, J. F. J., Broeck, C. V. D., Vander-Hyde, D. C., van der Schaaf, L., van Heijningen, J. V., Vardaro, M., Vargas, A. F., Varma, V., Vass, S., Vasúth, M., Vecchio, A., Vedovato, G., Veitch, J., Veitch, P. J., Venkateswara, K., Venneberg, J., Venugopalan, G., Verkindt, D., Verma, Y., Veske, D., Vetrano, F., Viceré, A., Viets, A. D., Villa-Ortega, V., Vinet, J.-Y., Vitale, S., Vo, T., Vocca, H., Vorvick, C., Vyatchanin, S. P., Wade, A. R., Wade, L. E., Wade, M., Walet, R. C., Walker, M., Wallace, G. S., Wallace, L., Walsh, S., Wang, J. Z., Wang, S., Wang, W. H., Wang, Y. F., Ward, R. L., Warner, J., Was, M., Washington, N. Y., Watchi, J., Weaver, B., Wei, L., Weinert, M., Weinstein, A. J., Weiss, R., Wellmann, F., Wen, L., Weßels, P., Westhouse, J. W., Wette, K., Whelan, J. T., White, D. D., White, L. V., Whiting, B. F., Whittle, C., Wilken, D. M., Williams, D., Williams, M. J., Williamson, A. R., Willis, J. L., Willke, B., Wilson, D. J., Wimmer, M. H., Winkler, W., Wipf, C. C., Woan, G., Woehler, J., Wofford, J. K., Wong, I. C. F., Wrangel, J., Wright, J. L., Wu, D. S., Wysocki, D. M., Xiao, L., Yamamoto, H., Yang, L., Yang, Y., Yang, Z., Yap, M. J., Yeeles, D. W., Yoon, A., Yu, H., Yu, H., Yuen, S. H. R., Zadrożny, A., Zanolin, M., Zelenova, T., Zendri, J.-P., Zevin, M., Zhang, J., Zhang, L., Zhang, R., Zhang, T., Zhao, C., Zhao, G., Zhou, M., Zhou, Z., Zhu, X. J., Zimmerman, A. B., Zucker, M. E., and Zweizig, J. (2021). Population properties of compact objects from the second LIGO–virgo gravitational-wave transient catalog. *The Astrophysical Journal Letters*, 913(1):L7.

Abbott, R., Abbott, T. D., Acernese, F., Ackley, K., Adams, C., Adhikari, N., Adhikari, R. X., Adya, V. B., Affeldt, C., Agarwal, D., Agathos, M., Agatsuma, K., Aggarwal, N., Aguiar, O. D., Aiello, L., Ain, A., Ajith, P., Akcay, S., Akutsu, T., Albanesi, S., Allocca, A., Altin, P. A., Amato, A., Anand, C., Anand, S., Ananyeva, A., Anderson, S. B., Anderson, W. G., Ando, M., Andrade, T., Andres, N., Andrić, T., Angelova, S. V., Ansoldi,

S., Antelis, J. M., Antier, S., Appert, S., Arai, K., Arai, K., Arai, Y., Araki, S., Araya, A., Araya, M. C., Areeda, J. S., Arène, M., Aritomi, N., Arnaud, N., Arogeti, M., Aronson, S. M., Arun, K. G., Asada, H., Asali, Y., Ashton, G., Aso, Y., Assiduo, M., Aston, S. M., Astone, P., Aubin, F., Austin, C., Babak, S., Badaracco, F., Bader, M. K. M., Badger, C., Bae, S., Bae, Y., Baer, A. M., Bagnasco, S., Bai, Y., Baiotti, L., Baird, J., Bajpai, R., Ball, M., Ballardin, G., Ballmer, S. W., Balsamo, A., Baltus, G., Banagiri, S., Bankar, D., Barayoga, J. C., Barbieri, C., Barish, B. C., Barker, D., Barneo, P., Barone, F., Barr, B., Barsotti, L., Barsuglia, M., Barta, D., Bartlett, J., Barton, M. A., Bartos, I., Bassiri, R., Basti, A., Bawaj, M., Bayley, J. C., Baylor, A. C., Bazzan, M., Bécsy, B., Bedakihale, V. M., Bejger, M., Belahcene, I., Benedetto, V., Beniwal, D., Bennett, T. F., Bentley, J. D., BenYaala, M., Bergamin, F., Berger, B. K., Bernuzzi, S., Berry, C. P. L., Bersanetti, D., Bertolini, A., Betzwieser, J., Beveridge, D., Bhandare, R., Bhardwaj, U., Bhattacharjee, D., Bhaumik, S., Bilenko, I. A., Billingsley, G., Bini, S., Birney, R., Birnholtz, O., Biscans, S., Bischi, M., Biscoveanu, S., Bisht, A., Biswas, B., Bitossi, M., Bizouard, M.-A., Blackburn, J. K., Blair, C. D., Blair, D. G., Blair, R. M., Bobba, F., Bode, N., Boer, M., Bogaert, G., Boldrini, M., Bonavena, L. D., Bondu, F., Bonilla, E., Bonnand, R., Booker, P., Boom, B. A., Bork, R., Boschi, V., Bose, N., Bose, S., Bossilkov, V., Boudart, V., Bouffanais, Y., Bozzi, A., Bradaschia, C., Brady, P. R., Bramley, A., Branch, A., Branchesi, M., Brandt, J., Brau, J. E., Breschi, M., Briant, T., Briggs, J. H., Brillet, A., Brinkmann, M., Brockill, P., Brooks, A. F., Brooks, J., Brown, D. D., Brunett, S., Bruno, G., Bruntz, R., Bryant, J., Bulik, T., Bulten, H. J., Buonanno, A., Buscicchio, R., Buskulic, D., Buy, C., Byer, R. L., Davies, G. S. C., Cadonati, L., Cagnoli, G., Cahillane, C., Bustillo, J. C., Callaghan, J. D., Callister, T. A., Calloni, E., Cameron, J., Camp, J. B., Canepa, M., Canevarolo, S., Cannavacciuolo, M., Cannon, K. C., Cao, H., Cao, Z., Capocasa, E., Capote, E., Carapella, G., Carbognani, F., Carlin, J. B., Carney, M. F., Carpinelli, M., Carrillo, G., Carullo, G., Carver, T. L., Diaz, J. C., Casentini, C., Castaldi, G., Caudill, S., Cavaglià, M., Cavalier, F., Cavalieri, R., Ceasar, M., Cella, G.,

Cerdá-Durán, P., Cesarini, E., Chaibi, W., Chakravarti, K., Subrahmanya, S. C., Champion, E., Chan, C.-H., Chan, C., Chan, C. L., Chan, K., Chan, M., Chandra, K., Chanial, P., Chao, S., Chapman-Bird, C. E. A., Charlton, P., Chase, E. A., Chassande-Mottin, E., Chatterjee, C., Chatterjee, D., Chatterjee, D., Chaturvedi, M., Chaty, S., Chatziioannou, K., Chen, C., Chen, H. Y., Chen, J., Chen, K., Chen, X., Chen, Y.-B., Chen, Y.-R., Chen, Z., Cheng, H., Cheong, C. K., Cheung, H. Y., Chia, H. Y., Chiadini, F., Chiang, C.-Y., Chiarini, G., Chierici, R., Chincarini, A., Chiofalo, M. L., Chiummo, A., Cho, G., Cho, H. S., Choudhary, R. K., Choudhary, S., Christensen, N., Chu, H., Chu, Q., Chu, Y.-K., Chua, S., Chung, K. W., Ciani, G., Ciecielag, P., Cieślar, M., Cifaldi, M., Ciobanu, A. A., Ciolfi, R., Cipriano, F., Cirone, A., Clara, F., Clark, E. N., Clark, J. A., Clarke, L., Clearwater, P., Clesse, S., Cleva, F., Coccia, E., Codazzo, E., Cohadon, P.-F., Cohen, D. E., Cohen, L., Colleoni, M., Collette, C. G., Colombo, A., Colpi, M., Compton, C. M., Constancio, M., Conti, L., Cooper, S. J., Corban, P., Corbitt, T. R., Cordero-Carrión, I., Corezzi, S., Corley, K. R., Cornish, N., Corre, D., Corsi, A., Cortese, S., Costa, C. A., Cotesta, R., Coughlin, M. W., Coulon, J.-P., Countryman, S. T., Cousins, B., Couvares, P., Coward, D. M., Cowart, M. J., Coyne, D. C., Coyne, R., Creighton, J. D. E., Creighton, T. D., Criswell, A. W., Croquette, M., Crowder, S. G., Cudell, J. R., Cullen, T. J., Cumming, A., Cummings, R., Cunningham, L., Cuoco, E., Curyło, M., Dabadie, P., Canton, T. D., Dall'Osso, S., Dálya, G., Dana, A., DaneshgaranBajastani, L. M., D'Angelo, B., Danila, B., Danilishin, S., D'Antonio, S., Danzmann, K., Darsow-Fromm, C., Dasgupta, A., Datrier, L. E. H., Dattilo, V., Dave, I., Davier, M., Davis, D., Davis, M. C., Daw, E. J., de Alarcón, P. F., Dean, R., DeBra, D., Deenadayalan, M., Degallaix, J., De Laurentis, M., Deléglise, S., Del Favero, V., De Lillo, F., De Lillo, N., Del Pozzo, W., DeMarchi, L. M., De Matteis, F., D'Emilio, V., Demos, N., Dent, T., Depasse, A., De Pietri, R., De Rosa, R., De Rossi, C., DeSalvo, R., De Simone, R., Dhurandhar, S., Díaz, M. C., Diaz-Ortiz, M., Didio, N. A., Dietrich, T., Di Fiore, L., Di Fronzo, C., Di Giorgio, C., Di Giovanni, F., Di Giovanni, M., Di Girolamo, T., Di Lieto, A., Ding, B., Di Pace,

S., Di Palma, I., Di Renzo, F., Divakarla, A. K., Dmitriev, A., Doctor, Z., D'Onofrio, L., Donovan, F., Dooley, K. L., Doravari, S., Dorrington, I., Drago, M., Driggers, J. C., Drori, Y., Ducoin, J.-G., Dupej, P., Durante, O., D'Urso, D., Duverne, P.-A., Dwyer, S. E., Eassa, C., Easter, P. J., Ebersold, M., Eckhardt, T., Eddolls, G., Edelman, B., Edo, T. B., Edy, O., Effler, A., Eguchi, S., Eichholz, J., Eikenberry, S. S., Eisenmann, M., Eisenstein, R. A., Ejlli, A., Engelby, E., Enomoto, Y., Errico, L., Essick, R. C., Estellés, H., Estevez, D., Etienne, Z., Etzel, T., Evans, M., Evans, T. M., Ewing, B. E., Fafone, V., Fair, H., Fairhurst, S., Farah, A. M., Farinon, S., Farr, B., Farr, W. M., Farrow, N. W., Fauchon-Jones, E. J., Favaro, G., Favata, M., Fays, M., Fazio, M., Feicht, J., Fejer, M. M., Fenyvesi, E., Ferguson, D. L., Fernandez-Galiana, A., Ferrante, I., Ferreira, T. A., Fidecaro, F., Figura, P., Fiori, I., Fishbach, M., Fisher, R. P., Fittipaldi, R., Fiumara, V., Flaminio, R., Floden, E., Fong, H., Font, J. A., Fornal, B., Forsyth, P. W. F., Franke, A., Frasca, S., Frasconi, F., Frederick, C., Freed, J. P., Frei, Z., Freise, A., Frey, R., Fritschel, P., Frolov, V. V., Fronzé, G. G., Fujii, Y., Fujikawa, Y., Fukunaga, M., Fukushima, M., Fulda, P., Fyffe, M., Gabbard, H. A., Gabella, W. E., Gadre, B. U., Gair, J. R., Gais, J., Galaudage, S., Gamba, R., Ganapathy, D., Ganguly, A., Gao, D., Gaonkar, S. G., Garaventa, B., García, F., García-Núñez, C., García-Quirós, C., Garufi, F., Gateley, B., Gaudio, S., Gayathri, V., Ge, G.-G., Gemme, G., Gennai, A., George, J., George, R. N., Gerberding, O., Gergely, L., Gewecke, P., Ghonge, S., Ghosh, A., Ghosh, A., Ghosh, S., Ghosh, S., Giacomazzo, B., Giacoppo, L., Giaime, J. A., Giardina, K. D., Gibson, D. R., Gier, C., Giesler, M., Giri, P., Gissi, F., Glanzer, J., Gleckl, A. E., Godwin, P., Goetz, E., Goetz, R., Gohlke, N., Golomb, J., Goncharov, B., González, G., Gopakumar, A., Gosselin, M., Gouaty, R., Gould, D. W., Grace, B., Grado, A., Granata, M., Granata, V., Grant, A., Gras, S., Grassia, P., Gray, C., Gray, R., Greco, G., Green, A. C., Green, R., Gretarsson, A. M., Gretarsson, E. M., Griffith, D., Griffiths, W., Griggs, H. L., Grignani, G., Grimaldi, A., Grimm, S. J., Grote, H., Grunewald, S., Gruning, P., Guerra, D., Guidi, G. M., Guimaraes, A. R., Guixé, G., Gulati, H. K., Guo, H.-K., Guo, Y., Gupta, A.,

Gupta, A., Gupta, P., Gustafson, E. K., Gustafson, R., Guzman, F., Ha, S., Haegel, L., Hagiwara, A., Haino, S., Halim, O., Hall, E. D., Hamilton, E. Z., Hammond, G., Han, W.-B., Haney, M., Hanks, J., Hanna, C., Hannam, M. D., Hannuksela, O., Hansen, H., Hansen, T. J., Hanson, J., Harder, T., Hardwick, T., Haris, K., Harms, J., Harry, G. M., Harry, I. W., Hartwig, D., Hasegawa, K., Haskell, B., Hasskew, R. K., Haster, C.-J., Hattori, K., Haughian, K., Hayakawa, H., Hayama, K., Hayes, F. J., Healy, J., Heidmann, A., Heidt, A., Heintze, M. C., Heinze, J., Heinzel, J., Heitmann, H., Hellman, F., Hello, P., Helmling-Cornell, A. F., Hemming, G., Hendry, M., Heng, I. S., Hennes, E., Hennig, J., Hennig, M. H., Hernandez, A. G., Hernandez Vivanco, F., Heurs, M., Hild, S., Hill, P., Himemoto, Y., Hines, A. S., Hiranuma, Y., Hirata, N., Hirose, E., Hochheim, S., Hofman, D., Hohmann, J. N., Holcomb, D. G., Holland, N. A., Holley-Bockelmann, K., Hollows, I. J., Holmes, Z. J., Holt, K., Holz, D. E., Hong, Z., Hopkins, P., Hough, J., Hourihane, S., Howell, E. J., Hoy, C. G., Hoyland, D., Hreibi, A., Hsieh, B.-H., Hsu, Y., Huang, G.-Z., Huang, H.-Y., Huang, P., Huang, Y.-C., Huang, Y.-J., Huang, Y., Hübner, M. T., Huddart, A. D., Hughey, B., Hui, D. C. Y., Hui, V., Husa, S., Huttner, S. H., Huxford, R., Huynh-Dinh, T., Ide, S., Idzkowski, B., Iess, A., Ikenoue, B., Imam, S., Inayoshi, K., Ingram, C., Inoue, Y., Ioka, K., Isi, M., Isleif, K., Ito, K., Itoh, Y., Iyer, B. R., Izumi, K., JaberianHamedan, V., Jacqmin, T., Jadhav, S. J., Jadhav, S. P., James, A. L., Jan, A. Z., Jani, K., Janquart, J., Janssens, K., Janthalur, N. N., Jaranowski, P., Jariwala, D., Jaume, R., Jenkins, A. C., Jenner, K., Jeon, C., Jeunon, M., Jia, W., Jin, H.-B., Johns, G. R., Johnson-McDaniel, N. K., Jones, A. W., Jones, D. I., Jones, J. D., Jones, P., Jones, R., Jonker, R. J. G., Ju, L., Jung, P., Jung, K., Junker, J., Juste, V., Kaihotsu, K., Kajita, T., Kakizaki, M., Kalaghatgi, C. V., Kalogera, V., Kamai, B., Kamiizumi, M., Kanda, N., Kandhasamy, S., Kang, G., Kanner, J. B., Kao, Y., Kapadia, S. J., Kapasi, D. P., Karat, S., Karathanasis, C., Karki, S., Kashyap, R., Kasprzack, M., Kastaun, W., Katsanevas, S., Katsavounidis, E., Katzman, W., Kaur, T., Kawabe, K., Kawaguchi, K., Kawai, N., Kawasaki, T., Kéfélian, F., Keitel, D., Key, J. S., Khadka, S., Khalili, F. Y.,

Khan, S., Khazanov, E. A., Khetan, N., Khursheed, M., Kijbunchoo, N., Kim, C., Kim, J. C., Kim, J., Kim, K., Kim, W. S., Kim, Y.-M., Kimball, C., Kimura, N., Kinley-Hanlon, M., Kirchhoff, R., Kissel, J. S., Kita, N., Kitazawa, H., Kleybolte, L., Klimenko, S., Knee, A. M., Knowles, T. D., Knyazev, E., Koch, P., Koekoek, G., Kojima, Y., Kokeyama, K., Koley, S., Kolitsidou, P., Kolstein, M., Komori, K., Kondrashov, V., Kong, A. K. H., Kontos, A., Koper, N., Korobko, M., Kotake, K., Kovalam, M., Kozak, D. B., Kozakai, C., Kozu, R., Kringel, V., Krishnendu, N. V., Królak, A., Kuehn, G., Kuei, F., Kuijer, P., Kulkarni, S., Kumar, A., Kumar, P., Kumar, R., Kumar, R., Kume, J., Kuns, K., Kuo, C., Kuo, H.-S., Kuromiya, Y., Kuroyanagi, S., Kusayanagi, K., Kuwahara, S., Kwak, K., Lagabbe, P., Laghi, D., Lalande, E., Lam, T. L., Lamberts, A., Landry, M., Lane, B. B., Lang, R. N., Lange, J., Lantz, B., La Rosa, I., Lartaux-Vollard, A., Lasky, P. D., Laxen, M., Lazzarini, A., Lazzaro, C., Leaci, P., Leavey, S., Lecoeuche, Y. K., Lee, H. K., Lee, H. M., Lee, H. W., Lee, J., Lee, K., Lee, R., Lehmann, J., Lemaître, A., Leonardi, M., Leroy, N., Letendre, N., Levesque, C., Levin, Y., Leviton, J. N., Leyde, K., Li, A. K. Y., Li, B., Li, J., Li, K. L., Li, T. G. F., Li, X., Lin, C.-Y., Lin, F.-K., Lin, F.-L., Lin, H. L., Lin, L. C.-C., Linde, F., Linker, S. D., Linley, J. N., Littenberg, T. B., Liu, G. C., Liu, J., Liu, K., Liu, X., Llamas, F., Llorens-Monteagudo, M., Lo, R. K. L., Lockwood, A., Loh, M., London, L. T., Longo, A., Lopez, D., Portilla, M. L., Lorenzini, M., Loriette, V., Lormand, M., Losurdo, G., Lott, T. P., Lough, J. D., Lousto, C. O., Lovelace, G., Lucaccioni, J. F., Lück, H., Lumaca, D., Lundgren, A. P., Luo, L.-W., Lynam, J. E., Macas, R., MacInnis, M., Macleod, D. M., MacMillan, I. A. O., Macquet, A., Hernandez, I. M. n., Magazzù, C., Magee, R. M., Maggiore, R., Magnozzi, M., Mahesh, S., Majorana, E., Makarem, C., Maksimovic, I., Maliakal, S., Malik, A., Man, N., Mandic, V., Mangano, V., Mango, J. L., Mansell, G. L., Manske, M., Mantovani, M., Mapelli, M., Marchesoni, F., Marchio, M., Marion, F., Mark, Z., Márka, S., Márka, Z., Markakis, C., Markosyan, A. S., Markowitz, A., Maros, E., Marquina, A., Marsat, S., Martelli, F., Martin, I. W., Martin, R. M., Martinez, M., Martinez, V. A., Martinez, V., Martinovic, K., Martynov,

D. V., Marx, E. J., Masalehdan, H., Mason, K., Massera, E., Masserot, A., Massinger, T. J., Masso-Reid, M., Mastrogiovanni, S., Matas, A., Mateu-Lucena, M., Matichard, F., Matiushechkina, M., Mavalvala, N., McCann, J. J., McCarthy, R., McClelland, D. E., McClincy, P. K., McCormick, S., McCuller, L., McGhee, G. I., McGuire, S. C., McIsaac, C., McIver, J., McRae, T., McWilliams, S. T., Meacher, D., Mehmet, M., Mehta, A. K., Meijer, Q., Melatos, A., Melchor, D. A., Mendell, G., Menendez-Vazquez, A., Menoni, C. S., Mercer, R. A., Mereni, L., Merfeld, K., Merilh, E. L., Merritt, J. D., Merzougui, M., Meshkov, S., Messenger, C., Messick, C., Meyers, P. M., Meylahn, F., Mhaske, A., Miani, A., Miao, H., Michaloliakos, I., Michel, C., Michimura, Y., Middleton, H., Milano, L., Miller, A. L., Miller, A., Miller, B., Millhouse, M., Mills, J. C., Milotti, E., Minazzoli, O., Minenkov, Y., Mio, N., Mir, L. M., Miravet-Tenés, M., Mishra, C., Mishra, T., Mistry, T., Mitra, S., Mitrofanov, V. P., Mitselmakher, G., Mittleman, R., Miyakawa, O., Miyamoto, A., Miyazaki, Y., Miyo, K., Miyoki, S., Mo, G., Modafferi, L. M., Moguel, E., Mogushi, K., Mohapatra, S. R. P., Mohite, S. R., Molina, I., Molina-Ruiz, M., Mondin, M., Montani, M., Moore, C. J., Moraru, D., Morawski, F., More, A., Moreno, C., Moreno, G., Mori, Y., Morisaki, S., Moriwaki, Y., Morrás, G., Mours, B., Mow-Lowry, C. M., Mozzon, S., Muciaccia, F., Mukherjee, A., Mukherjee, D., Mukherjee, S., Mukherjee, S., Mukherjee, S., Mukund, N., Mullavey, A., Munch, J., Muñiz, E. A., Murray, P. G., Musenich, R., Muusse, S., Nadji, S. L., Nagano, K., Nagano, S., Nagar, A., Nakamura, K., Nakano, H., Nakano, M., Nakashima, R., Nakayama, Y., Napolano, V., Nardecchia, I., Narikawa, T., Naticchioni, L., Nayak, B., Nayak, R. K., Negishi, R., Neil, B. F., Neilson, J., Nelemans, G., Nelson, T. J. N., Nery, M., Neubauer, P., Neunzert, A., Ng, K. Y., Ng, S. W. S., Nguyen, C., Nguyen, P., Nguyen, T., Quynh, L. N., Ni, W.-T., Nichols, S. A., Nishizawa, A., Nissanke, S., Nitoglia, E., Nocera, F., Norman, M., North, C., Nozaki, S., Siles, J. F. N. n., Nuttall, L. K., Oberling, J., O'Brien, B. D., Obuchi, Y., O'Dell, J., Oelker, E., Ogaki, W., Oganesyan, G., Oh, J. J., Oh, K., Oh, S. H., Ohashi, M., Ohishi, N., Ohkawa, M., Ohme, F., Ohta, H., Okada, M. A., Okutani, Y., Okutomi, K., Olivetto, C., Oohara, K., Ooi, C.,

Oram, R., O'Reilly, B., Ormiston, R. G., Ormsby, N. D., Ortega, L. F., O'Shaughnessy, R., O'Shea, E., Oshino, S., Ossokine, S., Osthelder, C., Otabe, S., Ottaway, D. J., Overmier, H., Pace, A. E., Pagano, G., Page, M. A., Pagliaroli, G., Pai, A., Pai, S. A., Palamos, J. R., Palashov, O., Palomba, C., Pan, H., Pan, K., Panda, P. K., Pang, H., Pang, P. T. H., Pankow, C., Pannarale, F., Pant, B. C., Panther, F. H., Paoletti, F., Paoli, A., Paolone, A., Parisi, A., Park, H., Park, J., Parker, W., Pascucci, D., Pasqualetti, A., Passaquieti, R., Passuello, D., Patel, M., Pathak, M., Patricelli, B., Patron, A. S., Paul, S., Payne, E., Pedraza, M., Pegoraro, M., Pele, A., Arellano, F. E. P. n., Penn, S., Perego, A., Pereira, A., Pereira, T., Perez, C. J., Périgois, C., Perkins, C. C., Perreca, A., Perriès, S., Petermann, J., Petterson, D., Pfeiffer, H. P., Pham, K. A., Phukon, K. S., Piccinni, O. J., Pichot, M., Piendibene, M., Piergiovanni, F., Pierini, L., Pierro, V., Pillant, G., Pillas, M., Pilo, F., Pinard, L., Pinto, I. M., Pinto, M., Piotrzkowski, B., Piotrzkowski, K., Pirello, M., Pitkin, M. D., Placidi, E., Planas, L., Plastino, W., Pluchar, C., Poggiani, R., Polini, E., Pong, D. Y. T., Ponrathnam, S., Popolizio, P., Porter, E. K., Poulton, R., Powell, J., Pracchia, M., Pradier, T., Prajapati, A. K., Prasai, K., Prasanna, R., Pratten, G., Principe, M., Prodi, G. A., Prokhorov, L., Prosposito, P., Prudenzi, L., Puecher, A., Punturo, M., Puosi, F., Puppo, P., Pürrer, M., Qi, H., Quetschke, V., Quitzow-James, R., Qutob, N., Raab, F. J., Raaijmakers, G., Radkins, H., Radulesco, N., Raffai, P., Rail, S. X., Raja, S., Rajan, C., Ramirez, K. E., Ramirez, T. D., Ramos-Buades, A., Rana, J., Rapagnani, P., Rapol, U. D., Ray, A., Raymond, V., Raza, N., Razzano, M., Read, J., Rees, L. A., Regimbau, T., Rei, L., Reid, S., Reid, S. W., Reitze, D. H., Relton, P., Renzini, A., Rettegno, P., Reza, A., Rezac, M., Ricci, F., Richards, D., Richardson, J. W., Richardson, L., Riemenschneider, G., Riles, K., Rinaldi, S., Rink, K., Rizzo, M., Robertson, N. A., Robie, R., Robinet, F., Rocchi, A., Rodriguez, S., Rolland, L., Rollins, J. G., Romanelli, M., Romano, R., Romel, C. L., Romero-Rodríguez, A., Romero-Shaw, I. M., Romie, J. H., Ronchini, S., Rosa, L., Rose, C. A., Rosińska, D., Ross, M. P., Rowan, S., Rowlinson, S. J., Roy, S., Roy, S., Roy, S., Rozza, D., Ruggi, P., Ruiz-Rocha, K., Ryan,

K., Sachdev, S., Sadecki, T., Sadiq, J., Sago, N., Saito, S., Saito, Y., Sakai, K., Sakai, Y., Sakellariadou, M., Sakuno, Y., Salafia, O. S., Salconi, L., Saleem, M., Salemi, F., Samajdar, A., Sanchez, E. J., Sanchez, J. H., Sanchez, L. E., Sanchis-Gual, N., Sanders, J. R., Sanuy, A., Saravanan, T. R., Sarin, N., Sassolas, B., Satari, H., Sathyaprakash, B. S., Sato, S., Sato, T., Sauter, O., Savage, R. L., Sawada, T., Sawant, D., Sawant, H. L., Sayah, S., Schaetzl, D., Scheel, M., Scheuer, J., Schiworski, M., Schmidt, P., Schmidt, S., Schnabel, R., Schneewind, M., Schofield, R. M. S., Schönbeck, A., Schulte, B. W., Schutz, B. F., Schwartz, E., Scott, J., Scott, S. M., Seglar-Arroyo, M., Sekiguchi, T., Sekiguchi, Y., Sellers, D., Sengupta, A. S., Sentenac, D., Seo, E. G., Sequino, V., Sergeev, A., Setyawati, Y., Shaffer, T., Shahriar, M. S., Shams, B., Shao, L., Sharma, A., Sharma, P., Shawhan, P., Shcheblanov, N. S., Shibagaki, S., Shikauchi, M., Shimizu, R., Shimoda, T., Shimode, K., Shinkai, H., Shishido, T., Shoda, A., Shoemaker, D. H., Shoemaker, D. M., ShyamSundar, S., Sieniawska, M., Sigg, D., Singer, L. P., Singh, D., Singh, N., Singha, A., Sintes, A. M., Sipala, V., Skliris, V., Slagmolen, B. J. J., Slaven-Blair, T. J., Smetana, J., Smith, J. R., Smith, R. J. E., Soldateschi, J., Somala, S. N., Somiya, K., Son, E. J., Soni, K., Soni, S., Sordini, V., Sorrentino, F., Sorrentino, N., Sotani, H., Soulard, R., Souradeep, T., Sowell, E., Spagnuolo, V., Spencer, A. P., Spera, M., Srinivasan, R., Srivastava, A. K., Srivastava, V., Staats, K., Stachie, C., Steer, D. A., Steinhoff, J., Steinlechner, J., Steinlechner, S., Stevenson, S. P., Stops, D. J., Stover, M., Strain, K. A., Strang, L. C., Stratta, G., Strunk, A., Sturani, R., Stuver, A. L., Sudhagar, S., Sudhir, V., Sugimoto, R., Suh, H. G., Sullivan, A. G., Sullivan, J. M., Summerscales, T. Z., Sun, H., Sun, L., Sunil, S., Sur, A., Suresh, J., Sutton, P. J., Suzuki, T., Suzuki, T., Swinkels, B. L., Szczepańczyk, M. J., Szewczyk, P., Tacca, M., Tagoshi, H., Tait, S. C., Takahashi, H., Takahashi, R., Takamori, A., Takano, S., Takeda, H., Takeda, M., Talbot, C. J., Talbot, C., Tanaka, H., Tanaka, K., Tanaka, K., Tanaka, T., Tanaka, T., Tanasijczuk, A. J., Tanioka, S., Tanner, D. B., Tao, D., Tao, L., Martín, E. N. T. S., Taranto, C., Tasson, J. D., Telada, S., Tenorio, R., Terhune, J. E., Terkowski, L., Thirugnanasambandam, M. P., Thomas, L., Thomas, M.,

Thomas, P., Thompson, J. E., Thondapu, S. R., Thorne, K. A., Thrane, E., Tiwari, S., Tiwari, S., Tiwari, V., Toivonen, A. M., Toland, K., Tolley, A. E., Tomaru, T., Tomigami, Y., Tomura, T., Tonelli, M., Torres-Forné, A., Torrie, C. I., e Melo, I. T., Töyrä, D., Trapananti, A., Travasso, F., Traylor, G., Trevor, M., Tringali, M. C., Tripathee, A., Troiano, L., Trovato, A., Trozzo, L., Trudeau, R. J., Tsai, D. S., Tsai, D., Tsang, K. W., Tsang, T., Tsao, J.-S., Tse, M., Tso, R., Tsubono, K., Tsuchida, S., Tsukada, L., Tsuna, D., Tsutsui, T., Tsuzuki, T., Turbang, K., Turconi, M., Tuyenbayev, D., Ubhi, A. S., Uchikata, N., Uchiyama, T., Udall, R. P., Ueda, A., Uehara, T., Ueno, K., Ueshima, G., Unnikrishnan, C. S., Uraguchi, F., Urban, A. L., Ushiba, T., Utina, A., Vahlbruch, H., Vajente, G., Vajpeyi, A., Valdes, G., Valentini, M., Valsan, V., van Bakel, N., van Beuzekom, M., van den Brand, J. F. J., Van Den Broeck, C., Vander-Hyde, D. C., van der Schaaf, L., van Heijningen, J. V., Vanosky, J., van Putten, M. H. P. M., van Remortel, N., Vardaro, M., Vargas, A. F., Varma, V., Vasúth, M., Vecchio, A., Vedovato, G., Veitch, J., Veitch, P. J., Venneberg, J., Venugopalan, G., Verkindt, D., Verma, P., Verma, Y., Veske, D., Vetrano, F., Viceré, A., Vidyant, S., Viets, A. D., Vijaykumar, A., Villa-Ortega, V., Vinet, J.-Y., Virtuoso, A., Vitale, S., Vo, T., Vocca, H., von Reis, E. R. G., von Wrangel, J. S. A., Vorvick, C., Vyatchanin, S. P., Wade, L. E., Wade, M., Wagner, K. J., Walet, R. C., Walker, M., Wallace, G. S., Wallace, L., Walsh, S., Wang, J., Wang, J. Z., Wang, W. H., Ward, R. L., Warner, J., Was, M., Washimi, T., Washington, N. Y., Watchi, J., Weaver, B., Webster, S. A., Weinert, M., Weinstein, A. J., Weiss, R., Weller, C. M., Weller, R. A., Wellmann, F., Wen, L., Weßels, P., Wette, K., Whelan, J. T., White, D. D., Whiting, B. F., Whittle, C., Wilken, D., Williams, D., Williams, M. J., Williams, N., Williamson, A. R., Willis, J. L., Willke, B., Wilson, D. J., Winkler, W., Wipf, C. C., Wlodarczyk, T., Woan, G., Woehler, J., Wofford, J. K., Wong, I. C. F., Wu, C., Wu, D. S., Wu, H., Wu, S., Wysocki, D. M., Xiao, L., Xu, W.-R., Yamada, T., Yamamoto, H., Yamamoto, K., Yamamoto, K., Yamamoto, T., Yamashita, K., Yamazaki, R., Yang, F. W., Yang, L., Yang, Y., Yang, Y., Yang, Z., Yap, M. J., Yeeles, D. W., Yelikar, A. B., Ying, M.,

Yokogawa, K., Yokoyama, J., Yokozawa, T., Yoo, J., Yoshioka, T., Yu, H., Yu, H., Yuzurihara, H., Zadrożny, A., Zanolin, M., Zeidler, S., Zelenova, T., Zendri, J.-P., Zevin, M., Zhan, M., Zhang, H., Zhang, J., Zhang, L., Zhang, T., Zhang, Y., Zhao, C., Zhao, G., Zhao, Y., Zhao, Y., Zheng, Y., Zhou, R., Zhou, Z., Zhu, X. J., Zhu, Z.-H., Zimmerman, A. B., Zlochower, Y., Zucker, M. E., and Zweizig, J. (2023a). Gwtc-3: Compact binary coalescences observed by ligo and virgo during the second part of the third observing run. *Phys. Rev. X*, 13:041039.

Abbott, R., Abbott, T. D., Acernese, F., Ackley, K., Adams, C., Adhikari, N., Adhikari, R. X., Adya, V. B., Affeldt, C., Agarwal, D., Agathos, M., Agatsuma, K., Aggarwal, N., Aguiar, O. D., Aiello, L., Ain, A., Ajith, P., Akutsu, T., de Alarcón, P. F., Akcay, S., Albanesi, S., Allocca, A., Altin, P. A., Amato, A., Anand, C., Anand, S., Ananyeva, A., Anderson, S. B., Anderson, W. G., Ando, M., Andrade, T., Andres, N., Andrić, T., Angelova, S. V., Ansoldi, S., Antelis, J. M., Antier, S., Antonini, F., Appert, S., Arai, K., Arai, K., Arai, Y., Araki, S., Araya, A., Araya, M. C., Areeda, J. S., Arène, M., Aritomi, N., Arnaud, N., Arogeti, M., Aronson, S. M., Arun, K. G., Asada, H., Asali, Y., Ashton, G., Aso, Y., Assiduo, M., Aston, S. M., Astone, P., Aubin, F., Austin, C., Babak, S., Badaracco, F., Bader, M. K. M., Badger, C., Bae, S., Bae, Y., Baer, A. M., Bagnasco, S., Bai, Y., Baiotti, L., Baird, J., Bajpai, R., Ball, M., Ballardin, G., Ballmer, S. W., Balsamo, A., Baltus, G., Banagiri, S., Bankar, D., Barayoga, J. C., Barbieri, C., Barish, B. C., Barker, D., Barneo, P., Barone, F., Barr, B., Barsotti, L., Barsuglia, M., Barta, D., Bartlett, J., Barton, M. A., Bartos, I., Bassiri, R., Basti, A., Bawaj, M., Bayley, J. C., Baylor, A. C., Bazzan, M., Bécsy, B., Bedakihale, V. M., Bejger, M., Belahcene, I., Benedetto, V., Beniwal, D., Bennett, T. F., Bentley, J. D., BenYaala, M., Bergamin, F., Berger, B. K., Bernuzzi, S., Berry, C. P. L., Bersanetti, D., Bertolini, A., Betzwieser, J., Beveridge, D., Bhandare, R., Bhardwaj, U., Bhattacharjee, D., Bhaumik, S., Bilenko, I. A., Billingsley, G., Bini, S., Birney, I. A., Birnholtz, O., Biscans, S., Bischi, M., Biscoveanu, S., Bisht, A., Biswas, B., Bitossi, M., Bizouard, M.-A., Blackburn, J. K.,

Blair, C. D., Blair, D. G., Blair, R. M., Bobba, F., Bode, N., Boer, M., Bogaert, G., Boldrini, M., Bonavena, L. D., Bondu, F., Bonilla, E., Bonnand, R., Booker, P., Boom, B. A., Bork, R., Boschi, V., Bose, N., Bose, S., Bossilkov, V., Boudart, V., Bouffanais, Y., Bozzi, A., Bradaschia, C., Brady, P. R., Bramley, A., Branch, A., Branchesi, M., Brandt, J., Brau, J. E., Breschi, M., Briant, T., Briggs, J. H., Brillet, A., Brinkmann, M., Brockill, P., Brooks, A. F., Brooks, J., Brown, D. D., Brunett, S., Bruno, G., Bruntz, R., Bryant, J., Bulik, T., Bulten, H. J., Buonanno, A., Buscicchio, R., Buskulic, D., Buy, C., Byer, R. L., Cadonati, L., Cagnoli, G., Cahillane, C., Bustillo, J. C., Callaghan, J. D., Callister, T. A., Calloni, E., Cameron, J., Camp, J. B., Canepa, M., Canevarolo, S., Cannavacciuolo, M., Cannon, K. C., Cao, H., Cao, Z., Capocasa, E., Capote, E., Carapella, G., Carbognani, F., Carlin, J. B., Carney, M. F., Carpinelli, M., Carrillo, G., Carullo, G., Carver, T. L., Diaz, J. C., Casentini, C., Castaldi, G., Caudill, S., Cavaglià, M., Cavalier, F., Cavalieri, R., Ceasar, M., Cella, G., Cerdá-Durán, P., Cesarini, E., Chaibi, W., Chakravarti, K., Subrahmanya, S. C., Champion, E., Chan, C.-H., Chan, C., Chan, C. L., Chan, K., Chan, M., Chandra, K., Chanial, P., Chao, S., Chapman-Bird, C. E. A., Charlton, P., Chase, E. A., Chassande-Mottin, E., Chatterjee, C., Chatterjee, D., Chatterjee, D., Chaturvedi, M., Chaty, S., Chatziioannou, K., Chen, C., Chen, H. Y., Chen, J., Chen, K., Chen, X., Chen, Y.-B., Chen, Y.-R., Chen, Z., Cheng, H., Cheong, C. K., Cheung, H. Y., Chia, H. Y., Chiadini, F., Chiang, C.-Y., Chiarini, G., Chierici, R., Chincarini, A., Chiofalo, M. L., Chiummo, A., Cho, G., Cho, H. S., Choudhary, R. K., Choudhary, S., Christensen, N., Chu, H., Chu, Q., Chu, Y.-K., Chua, S., Chung, K. W., Ciani, G., Ciecielag, P., Cieślar, M., Cifaldi, M., Ciobanu, A. A., Ciolfi, R., Cipriano, F., Cirone, A., Clara, F., Clark, E. N., Clark, J. A., Clarke, L., Clearwater, P., Clesse, S., Cleva, F., Coccia, E., Codazzo, E., Cohadon, P.-F., Cohen, D. E., Cohen, L., Colleoni, M., Collette, C. G., Colombo, A., Colpi, M., Compton, C. M., Constancio, M., Conti, L., Cooper, S. J., Corban, P., Corbitt, T. R., Cordero-Carrión, I., Corezzi, S., Corley, K. R., Cornish, N., Corre, D., Corsi, A., Cortese, S., Costa, C. A., Cotesta, R., Coughlin, M. W.,

Coulon, J.-P., Countryman, S. T., Cousins, B., Couvares, P., Coward, D. M., Cowart, M. J., Coyne, D. C., Coyne, R., Creighton, J. D. E., Creighton, T. D., Criswell, A. W., Croquette, M., Crowder, S. G., Cudell, J. R., Cullen, T. J., Cumming, A., Cummings, R., Cunningham, L., Cuoco, E., Curyło, M., Dabadie, P., Canton, T. D., Dall'Osso, S., Dálya, G., Dana, A., DaneshgaranBajastani, L. M., D'Angelo, B., Danila, B., Danilishin, S., D'Antonio, S., Danzmann, K., Darsow-Fromm, C., Dasgupta, A., Datrier, L. E. H., Datta, S., Dattilo, V., Dave, I., Davier, M., Davies, G. S., Davis, D., Davis, M. C., Daw, E. J., Dean, R., DeBra, D., Deenadayalan, M., Degallaix, J., De Laurentis, M., Deléglise, S., Del Favero, V., De Lillo, F., De Lillo, N., Del Pozzo, W., DeMarchi, L. M., De Matteis, F., D'Emilio, V., Demos, N., Dent, T., Depasse, A., De Pietri, R., De Rosa, R., De Rossi, C., DeSalvo, R., De Simone, R., Dhurandhar, S., Díaz, M. C., Diaz-Ortiz, M., Didio, N. A., Dietrich, T., Di Fiore, L., Di Fronzo, C., Di Giorgio, C., Di Giovanni, F., Di Giovanni, M., Di Girolamo, T., Di Lieto, A., Ding, B., Di Pace, S., Di Palma, I., Di Renzo, F., Divakarla, A. K., Dmitriev, A., Doctor, Z., D'Onofrio, L., Donovan, F., Dooley, K. L., Doravari, S., Dorrington, I., Drago, M., Driggers, J. C., Drori, Y., Ducoin, J.-G., Dupej, P., Durante, O., D'Urso, D., Duverne, P.-A., Dwyer, S. E., Eassa, C., Easter, P. J., Ebersold, M., Eckhardt, T., Eddolls, G., Edelman, B., Edo, T. B., Edy, O., Effler, A., Eguchi, S., Eichholz, J., Eikenberry, S. S., Eisenmann, M., Eisenstein, R. A., Ejlli, A., Engelby, E., Enomoto, Y., Errico, L., Essick, R. C., Estellés, H., Estevez, D., Etienne, Z., Etzel, T., Evans, M., Evans, T. M., Ewing, B. E., Fafone, V., Fair, H., Fairhurst, S., Farah, A. M., Farinon, S., Farr, B., Farr, W. M., Farrow, N. W., Fauchon-Jones, E. J., Favaro, G., Favata, M., Fays, M., Fazio, M., Feicht, J., Fejer, M. M., Fenyvesi, E., Ferguson, D. L., Fernandez-Galiana, A., Ferrante, I., Ferreira, T. A., Fidecaro, F., Figura, P., Fiori, I., Fishbach, M., Fisher, R. P., Fittipaldi, R., Fiumara, V., Flaminio, R., Floden, E., Fong, H., Font, J. A., Fornal, B., Forsyth, P. W. F., Franke, A., Frasca, S., Frasconi, F., Frederick, C., Freed, J. P., Frei, Z., Freise, A., Frey, R., Fritschel, P., Frolov, V. V., Fronzé, G. G., Fujii, Y., Fujikawa, Y., Fukunaga, M., Fukushima, M., Fulda, P.,

Fyffe, M., Gabbard, H. A., Gadre, B. U., Gair, J. R., Gais, J., Galaudage, S., Gamba, R., Ganapathy, D., Ganguly, A., Gao, D., Gaonkar, S. G., Garaventa, B., García, F., García-Núñez, C., García-Quirós, C., Garufi, F., Gateley, B., Gaudio, S., Gayathri, V., Ge, G.-G., Gemme, G., Gennai, A., George, J., George, R. N., Gerberding, O., Gergely, L., Gewecke, P., Ghonge, S., Ghosh, A., Ghosh, A., Ghosh, S., Ghosh, S., Giacomazzo, B., Giacoppo, L., Giaime, J. A., Giardina, K. D., Gibson, D. R., Gier, C., Giesler, M., Giri, P., Gissi, F., Glanzer, J., Gleckl, A. E., Godwin, P., Golomb, J., Goetz, E., Goetz, R., Gohlke, N., Goncharov, B., González, G., Gopakumar, A., Gosselin, M., Gouaty, R., Gould, D. W., Grace, B., Grado, A., Granata, M., Granata, V., Grant, A., Gras, S., Grassia, P., Gray, C., Gray, R., Greco, G., Green, A. C., Green, R., Gretarsson, A. M., Gretarsson, E. M., Griffith, D., Griffiths, W., Griggs, H. L., Grignani, G., Grimaldi, A., Grimm, S. J., Grote, H., Grunewald, S., Gruning, P., Guerra, D., Guidi, G. M., Guimaraes, A. R., Guixé, G., Gulati, H. K., Guo, H.-K., Guo, Y., Gupta, A., Gupta, A., Gupta, P., Gustafson, E. K., Gustafson, R., Guzman, F., Ha, S., Haegel, L., Hagiwara, A., Haino, S., Halim, O., Hall, E. D., Hamilton, E. Z., Hammond, G., Han, W.-B., Haney, M., Hanks, J., Hanna, C., Hannam, M. D., Hannuksela, O., Hansen, H., Hansen, T. J., Hanson, J., Harder, T., Hardwick, T., Haris, K., Harms, J., Harry, G. M., Harry, I. W., Hartwig, D., Hasegawa, K., Haskell, B., Hasskew, R. K., Haster, C.-J., Hattori, K., Haughian, K., Hayakawa, H., Hayama, K., Hayes, F. J., Healy, J., Heidmann, A., Heidt, A., Heintze, M. C., Heinze, J., Heinzel, J., Heitmann, H., Hellman, F., Hello, P., Helmling-Cornell, A. F., Hemming, G., Hendry, M., Heng, I. S., Hennes, E., Hennig, J., Hennig, M. H., Hernandez, A. G., Vivanco, F. H., Heurs, M., Hild, S., Hill, P., Himemoto, Y., Hines, A. S., Hiranuma, Y., Hirata, N., Hirose, E., Hochheim, S., Hofman, D., Hohmann, J. N., Holcomb, D. G., Holland, N. A., Hollows, I. J., Holmes, Z. J., Holt, K., Holz, D. E., Hong, Z., Hopkins, P., Hough, J., Hourihane, S., Howell, E. J., Hoy, C. G., Hoyland, D., Hreibi, A., Hsieh, B.-H., Hsu, Y., Huang, G.-Z., Huang, H.-Y., Huang, P., Huang, Y.-C., Huang, Y.-J., Huang, Y., Hübner, M. T., Huddart, A. D., Hughey, B., Hui, D. C. Y., Hui, V., Husa, S.,

Huttner, S. H., Huxford, R., Huynh-Dinh, T., Ide, S., Idzkowski, B., Iess, A., Ikenoue, B., Imam, S., Inayoshi, K., Ingram, C., Inoue, Y., Ioka, K., Isi, M., Isleif, K., Ito, K., Itoh, Y., Iyer, B. R., Izumi, K., JaberianHamedan, V., Jacqmin, T., Jadhav, S. J., Jadhav, S. P., James, A. L., Jan, A. Z., Jani, K., Janquart, J., Janssens, K., Janthalur, N. N., Jaranowski, P., Jariwala, D., Jaume, R., Jenkins, A. C., Jenner, K., Jeon, C., Jeunon, M., Jia, W., Jin, H.-B., Johns, G. R., Jones, A. W., Jones, D. I., Jones, J. D., Jones, P., Jones, R., Jonker, R. J. G., Ju, L., Jung, P., Jung, k., Junker, J., Juste, V., Kaihotsu, K., Kajita, T., Kakizaki, M., Kalaghatgi, C. V., Kalogera, V., Kamai, B., Kamiizumi, M., Kanda, N., Kandhasamy, S., Kang, G., Kanner, J. B., Kao, Y., Kapadia, S. J., Kapasi, D. P., Karat, S., Karathanasis, C., Karki, S., Kashyap, R., Kasprzack, M., Kastaun, W., Katsanevas, S., Katsavounidis, E., Katzman, W., Kaur, T., Kawabe, K., Kawaguchi, K., Kawai, N., Kawasaki, T., Kéfélian, F., Keitel, D., Key, J. S., Khadka, S., Khalili, F. Y., Khan, S., Khazanov, E. A., Khetan, N., Khursheed, M., Kijbunchoo, N., Kim, C., Kim, J. C., Kim, J., Kim, K., Kim, W. S., Kim, Y.-M., Kimball, C., Kimura, N., Kinley-Hanlon, M., Kirchhoff, R., Kissel, J. S., Kita, N., Kitazawa, H., Kleybolte, L., Klimenko, S., Knee, A. M., Knowles, T. D., Knyazev, E., Koch, P., Koekoek, G., Kojima, Y., Kokeyama, K., Koley, S., Kolitsidou, P., Kolstein, M., Komori, K., Kondrashov, V., Kong, A. K. H., Kontos, A., Koper, N., Korobko, M., Kotake, K., Kovalam, M., Kozak, D. B., Kozakai, C., Kozu, R., Kringel, V., Krishnendu, N. V., Królak, A., Kuehn, G., Kuei, F., Kuijer, P., Kulkarni, S., Kumar, A., Kumar, P., Kumar, R., Kumar, R., Kume, J., Kuns, K., Kuo, C., Kuo, H.-S., Kuromiya, Y., Kuroyanagi, S., Kusayanagi, K., Kuwahara, S., Kwak, K., Lagabbe, P., Laghi, D., Lalande, E., Lam, T. L., Lamberts, A., Landry, M., Landry, P., Lane, B. B., Lang, R. N., Lange, J., Lantz, B., La Rosa, I., Lartaux-Vollard, A., Lasky, P. D., Laxen, M., Lazzarini, A., Lazzaro, C., Leaci, P., Leavey, S., Lecoeuche, Y. K., Lee, H. K., Lee, H. M., Lee, H. W., Lee, J., Lee, K., Lee, R., Lehmann, J., Lemaître, A., Leonardi, M., Leroy, N., Letendre, N., Levesque, C., Levin, Y., Leviton, J. N., Leyde, K., Li, A. K. Y., Li, B., Li, J., Li, K. L., Li, T. G. F., Li, X., Lin, C.-Y., Lin, F.-K., Lin,

F.-L., Lin, H. L., Lin, L. C.-C., Linde, F., Linker, S. D., Linley, J. N., Littenberg, T. B., Liu, G. C., Liu, J., Liu, K., Liu, X., Llamas, F., Llorens-Monteagudo, M., Lo, R. K. L., Lockwood, A., Loh, M., London, L. T., Longo, A., Lopez, D., Portilla, M. L., Lorenzini, M., Loriette, V., Lormand, M., Losurdo, G., Lott, T. P., Lough, J. D., Lousto, C. O., Lovelace, G., Lucaccioni, J. F., Lück, H., Lumaca, D., Lundgren, A. P., Luo, L.-W., Lynam, J. E., Macas, R., MacInnis, M., Macleod, D. M., MacMillan, I. A. O., Macquet, A., Hernandez, I. M. n., Magazzù, C., Magee, R. M., Maggiore, R., Magnozzi, M., Mahesh, S., Majorana, E., Makarem, C., Maksimovic, I., Maliakal, S., Malik, A., Man, N., Mandic, V., Mangano, V., Mango, J. L., Mansell, G. L., Manske, M., Mantovani, M., Mapelli, M., Marchesoni, F., Marchio, M., Marion, F., Mark, Z., Márka, S., Márka, Z., Markakis, C., Markosyan, A. S., Markowitz, A., Maros, E., Marquina, A., Marsat, S., Martelli, F., Martin, I. W., Martin, R. M., Martinez, M., Martinez, V. A., Martinez, V., Martinovic, K., Martynov, D. V., Marx, E. J., Masalehdan, H., Mason, K., Massera, E., Masserot, A., Massinger, T. J., Masso-Reid, M., Mastrogiovanni, S., Matas, A., Mateu-Lucena, M., Matichard, F., Matiushechkina, M., Mavalvala, N., McCann, J. J., McCarthy, R., McClelland, D. E., McClincy, P. K., McCormick, S., McCuller, L., McGhee, G. I., McGuire, S. C., McIsaac, C., McIver, J., McRae, T., McWilliams, S. T., Meacher, D., Mehmet, M., Mehta, A. K., Meijer, Q., Melatos, A., Melchor, D. A., Mendell, G., Menendez-Vazquez, A., Menoni, C. S., Mercer, R. A., Mereni, L., Merfeld, K., Merilh, E. L., Merritt, J. D., Merzougui, M., Meshkov, S., Messenger, C., Messick, C., Meyers, P. M., Meylahn, F., Mhaske, A., Miani, A., Miao, H., Michaloliakos, I., Michel, C., Michimura, Y., Middleton, H., Milano, L., Miller, A. L., Miller, A., Miller, B., Miller, S., Millhouse, M., Mills, J. C., Milotti, E., Minazzoli, O., Minenkov, Y., Mio, N., Mir, L. M., Miravet-Tenés, M., Mishra, C., Mishra, T., Mistry, T., Mitra, S., Mitrofanov, V. P., Mitselmakher, G., Mittleman, R., Miyakawa, O., Miyamoto, A., Miyazaki, Y., Miyo, K., Miyoki, S., Mo, G., Modafferi, L. M., Moguel, E., Mogushi, K., Mohapatra, S. R. P., Mohite, S. R., Molina, I., Molina-Ruiz, M., Mondin, M., Montani, M., Moore, C. J., Moraru, D., Morawski, F., More, A.,

Moreno, C., Moreno, G., Mori, Y., Morisaki, S., Moriwaki, Y., Morrás, G., Mours, B., Mow-Lowry, C. M., Mozzon, S., Muciaccia, F., Mukherjee, A., Mukherjee, D., Mukherjee, S., Mukherjee, S., Mukherjee, S., Mukund, N., Mullavey, A., Munch, J., Muñiz, E. A., Murray, P. G., Musenich, R., Muusse, S., Nadji, S. L., Nagano, K., Nagano, S., Nagar, A., Nakamura, K., Nakano, H., Nakano, M., Nakashima, R., Nakayama, Y., Napolano, V., Nardecchia, I., Narikawa, T., Naticchioni, L., Nayak, B., Nayak, R. K., Negishi, R., Neil, B. F., Neilson, J., Nelemans, G., Nelson, T. J. N., Nery, M., Neubauer, P., Neunzert, A., Ng, K. Y., Ng, S. W. S., Nguyen, C., Nguyen, P., Nguyen, T., Quynh, L. N., Ni, W.-T., Nichols, S. A., Nishizawa, A., Nissanke, S., Nitoglia, E., Nocera, F., Norman, M., North, C., Nozaki, S., Siles, J. F. N. n., Nuttall, L. K., Oberling, J., O'Brien, B. D., Obuchi, Y., O'Dell, J., Oelker, E., Ogaki, W., Oganesyan, G., Oh, J. J., Oh, K., Oh, S. H., Ohashi, M., Ohishi, N., Ohkawa, M., Ohme, F., Ohta, H., Okada, M. A., Okutani, Y., Okutomi, K., Olivetto, C., Oohara, K., Ooi, C., Oram, R., O'Reilly, B., Ormiston, R. G., Ormsby, N. D., Ortega, L. F., O'Shaughnessy, R., O'Shea, E., Oshino, S., Ossokine, S., Osthelder, C., Otabe, S., Ottaway, D. J., Overmier, H., Pace, A. E., Pagano, G., Page, M. A., Pagliaroli, G., Pai, A., Pai, S. A., Palamos, J. R., Palashov, O., Palomba, C., Pan, H., Pan, K., Panda, P. K., Pang, H., Pang, P. T. H., Pankow, C., Pannarale, F., Pant, B. C., Panther, F. H., Paoletti, F., Paoli, A., Paolone, A., Parisi, A., Park, H., Park, J., Parker, W., Pascucci, D., Pasqualetti, A., Passaquieti, R., Passuello, D., Patel, M., Pathak, M., Patricelli, B., Patron, A. S., Paul, S., Payne, E., Pedraza, M., Pegoraro, M., Pele, A., Arellano, F. E. P. n., Penn, S., Perego, A., Pereira, A., Pereira, T., Perez, C. J., Périgois, C., Perkins, C. C., Perreca, A., Perriès, S., Petermann, J., Petterson, D., Pfeiffer, H. P., Pham, K. A., Phukon, K. S., Piccinni, O. J., Pichot, M., Piendibene, M., Piergiovanni, F., Pierini, L., Pierro, V., Pillant, G., Pillas, M., Pilo, F., Pinard, L., Pinto, I. M., Pinto, M., Piotrzkowski, B., Piotrzkowski, K., Pirello, M., Pitkin, M. D., Placidi, E., Planas, L., Plastino, W., Pluchar, C., Poggiani, R., Polini, E., Pong, D. Y. T., Ponrathnam, S., Popolizio, P., Porter, E. K., Poulton, R., Powell, J., Pracchia, M., Pradier, T., Prajapati,

A. K., Prasai, K., Prasanna, R., Pratten, G., Principe, M., Prodi, G. A., Prokhorov, L., Prosposito, P., Prudenzi, L., Puecher, A., Punturo, M., Puosi, F., Puppo, P., Pürrer, M., Qi, H., Quetschke, V., Quitzow-James, R., Raab, F. J., Raaijmakers, G., Radkins, H., Radulesco, N., Raffai, P., Rail, S. X., Raja, S., Rajan, C., Ramirez, K. E., Ramirez, T. D., Ramos-Buades, A., Rana, J., Rapagnani, P., Rapol, U. D., Ray, A., Raymond, V., Raza, N., Razzano, M., Read, J., Rees, L. A., Regimbau, T., Rei, L., Reid, S., Reid, S. W., Reitze, D. H., Relton, P., Renzini, A., Rettegno, P., Reza, A., Rezac, M., Ricci, F., Richards, D., Richardson, J. W., Richardson, L., Riemenschneider, G., Riles, K., Rinaldi, S., Rink, K., Rizzo, M., Robertson, N. A., Robie, R., Robinet, F., Rocchi, A., Rodriguez, S., Rolland, L., Rollins, J. G., Romanelli, M., Romano, R., Romel, C. L., Romero-Rodríguez, A., Romero-Shaw, I. M., Romie, J. H., Ronchini, S., Rosa, L., Rose, C. A., Rosińska, D., Ross, M. P., Rowan, S., Rowlinson, S. J., Roy, S., Roy, S., Roy, S., Rozza, D., Ruggi, P., Ryan, K., Sachdev, S., Sadecki, T., Sadiq, J., Sago, N., Saito, S., Saito, Y., Sakai, K., Sakai, Y., Sakellariadou, M., Sakuno, Y., Salafia, O. S., Salconi, L., Saleem, M., Salemi, F., Samajdar, A., Sanchez, E. J., Sanchez, J. H., Sanchez, L. E., Sanchis-Gual, N., Sanders, J. R., Sanuy, A., Saravanan, T. R., Sarin, N., Sassolas, B., Satari, H., Sathyaprakash, B. S., Sato, S., Sato, T., Sauter, O., Savage, R. L., Sawada, T., Sawant, D., Sawant, H. L., Sayah, S., Schaetzl, D., Scheel, M., Scheuer, J., Schiworski, M., Schmidt, P., Schmidt, S., Schnabel, R., Schneewind, M., Schofield, R. M. S., Schönbeck, A., Schulte, B. W., Schutz, B. F., Schwartz, E., Scott, J., Scott, S. M., Seglar-Arroyo, M., Sekiguchi, T., Sekiguchi, Y., Sellers, D., Sengupta, A. S., Sentenac, D., Seo, E. G., Sequino, V., Sergeev, A., Setyawati, Y., Shaffer, T., Shahriar, M. S., Shams, B., Shao, L., Sharma, A., Sharma, P., Shawhan, P., Shcheblanov, N. S., Shibagaki, S., Shikauchi, M., Shimizu, R., Shimoda, T., Shimode, K., Shinkai, H., Shishido, T., Shoda, A., Shoemaker, D. H., Shoemaker, D. M., ShyamSundar, S., Sieniawska, M., Sigg, D., Singer, L. P., Singh, D., Singh, N., Singha, A., Sintes, A. M., Sipala, V., Skliris, V., Slagmolen, B. J. J., Slaven-Blair, T. J., Smetana, J., Smith, J. R., Smith, R. J. E., Soldateschi, J., Somala, S. N.,

Somiya, K., Son, E. J., Soni, K., Soni, S., Sordini, V., Sorrentino, F., Sorrentino, N., Sotani, H., Soulard, R., Souradeep, T., Sowell, E., Spagnuolo, V., Spencer, A. P., Spera, M., Srinivasan, R., Srivastava, A. K., Srivastava, V., Staats, K., Stachie, C., Steer, D. A., Steinhoff, J., Steinlechner, J., Steinlechner, S., Stevenson, S. P., Stops, D. J., Stover, M., Strain, K. A., Strang, L. C., Stratta, G., Strunk, A., Sturani, R., Stuver, A. L., Sudhagar, S., Sudhir, V., Sugimoto, R., Suh, H. G., Sullivan, A. G., Summerscales, T. Z., Sun, H., Sun, L., Sunil, S., Sur, A., Suresh, J., Sutton, P. J., Suzuki, T., Suzuki, T., Swinkels, B. L., Szczepańczyk, M. J., Szewczyk, P., Tacca, M., Tagoshi, H., Tait, S. C., Takahashi, H., Takahashi, R., Takamori, A., Takano, S., Takeda, H., Takeda, M., Talbot, C. J., Talbot, C., Tanaka, H., Tanaka, K., Tanaka, K., Tanaka, T., Tanaka, T., Tanasijczuk, A. J., Tanioka, S., Tanner, D. B., Tao, D., Tao, L., Martín, E. N. T. S., Taranto, C., Tasson, J. D., Telada, S., Tenorio, R., Terhune, J. E., Terkowski, L., Thirugnanasambandam, M. P., Thomas, L., Thomas, M., Thomas, P., Thompson, J. E., Thondapu, S. R., Thorne, K. A., Thrane, E., Tiwari, S., Tiwari, S., Tiwari, V., Toivonen, A. M., Toland, K., Tolley, A. E., Tomaru, T., Tomigami, Y., Tomura, T., Tonelli, M., Torres-Forné, A., Torrie, C. I., e Melo, I. T., Töyrä, D., Trapananti, A., Travasso, F., Traylor, G., Trevor, M., Tringali, M. C., Tripathee, A., Troiano, L., Trovato, A., Trozzo, L., Trudeau, R. J., Tsai, D. S., Tsai, D., Tsang, K. W., Tsang, T., Tsao, J.-S., Tse, M., Tso, R., Tsubono, K., Tsuchida, S., Tsukada, L., Tsuna, D., Tsutsui, T., Tsuzuki, T., Turbang, K., Turconi, M., Tuyenbayev, D., Ubhi, A. S., Uchikata, N., Uchiyama, T., Udall, R. P., Ueda, A., Uehara, T., Ueno, K., Ueshima, G., Unnikrishnan, C. S., Uraguchi, F., Urban, A. L., Ushiba, T., Utina, A., Vahlbruch, H., Vajente, G., Vajpeyi, A., Valdes, G., Valentini, M., Valsan, V., van Bakel, N., van Beuzekom, M., van den Brand, J. F. J., Van Den Broeck, C., Vander-Hyde, D. C., van der Schaaf, L., van Heijningen, J. V., Vanosky, J., van Putten, M. H. P. M., van Remortel, N., Vardaro, M., Vargas, A. F., Varma, V., Vasúth, M., Vecchio, A., Vedovato, G., Veitch, J., Veitch, P. J., Venneberg, J., Venugopalan, G., Verkindt, D., Verma, P., Verma, Y., Veske, D., Vetrano, F., Viceré, A., Vidyant, S., Viets, A. D.,

Vijaykumar, A., Villa-Ortega, V., Vinet, J.-Y., Virtuoso, A., Vitale, S., Vo, T., Vocca, H., von Reis, E. R. G., von Wrangel, J. S. A., Vorvick, C., Vyatchanin, S. P., Wade, L. E., Wade, M., Wagner, K. J., Walet, R. C., Walker, M., Wallace, G. S., Wallace, L., Walsh, S., Wang, J., Wang, J. Z., Wang, W. H., Ward, R. L., Warner, J., Was, M., Washimi, T., Washington, N. Y., Watchi, J., Weaver, B., Webster, S. A., Weinert, M., Weinstein, A. J., Weiss, R., Weller, C. M., Wellmann, F., Wen, L., Weßels, P., Wette, K., Whelan, J. T., White, D. D., Whiting, B. F., Whittle, C., Wilken, D., Williams, D., Williams, M. J., Williamson, A. R., Willis, J. L., Willke, B., Wilson, D. J., Winkler, W., Wipf, C. C., Wlodarczyk, T., Woan, G., Woehler, J., Wofford, J. K., Wong, I. C. F., Wu, C., Wu, D. S., Wu, H., Wu, S., Wysocki, D. M., Xiao, L., Xu, W.-R., Yamada, T., Yamamoto, H., Yamamoto, K., Yamamoto, K., Yamamoto, T., Yamashita, K., Yamazaki, R., Yang, F. W., Yang, L., Yang, Y., Yang, Y., Yang, Z., Yap, M. J., Yeeles, D. W., Yelikar, A. B., Ying, M., Yokogawa, K., Yokoyama, J., Yokozawa, T., Yoo, J., Yoshioka, T., Yu, H., Yu, H., Yuzurihara, H., Zadrożny, A., Zanolin, M., Zeidler, S., Zelenova, T., Zendri, J.-P., Zevin, M., Zhan, M., Zhang, H., Zhang, J., Zhang, L., Zhang, T., Zhang, Y., Zhao, C., Zhao, G., Zhao, Y., Zhao, Y., Zheng, Y., Zhou, R., Zhou, Z., Zhu, X. J., Zhu, Z.-H., Zimmerman, A. B., Zlochower, Y., Zucker, M. E., and Zweizig, J. (2023b). Population of merging compact binaries inferred using gravitational waves through gwtc-3. *Phys. Rev. X*, 13:011048.

Abbott, R. et al. (2021). Population Properties of Compact Objects from the Second LIGO-Virgo Gravitational-Wave Transient Catalog. *ApJ Lett.*, 913(1):L7.

Abbott, R. e. (2021). Open data from the first and second observing runs of Advanced LIGO and Advanced Virgo. *SoftwareX*, 13:100658.

Abbott, R. e. (2023). Open Data from the Third Observing Run of LIGO, Virgo, KAGRA, and GEO. *ApJ*, 267(2):29.

Adams, M. R. and Cornish, N. J. (2014). Detecting a stochastic gravitational wave back-

ground in the presence of a galactic foreground and instrument noise. *Phys. Rev. D*, 89(2):022001.

Afle, C., Gupta, A., Gadre, B., Kumar, P., Demos, N., Lovelace, G., Choi, H. G., Lee, H. M., Mitra, S., Boyle, M., Hemberger, D. A., Kidder, L. E., Pfeiffer, H. P., Scheel, M. A., and Szilagyi, B. (2018). Detection and characterization of spin-orbit resonances in the advanced gravitational wave detectors era. *Phys. Rev. D*, 98(8):083014.

Agazie, G., Anumarlapudi, A., Archibald, A. M., Arzoumanian, Z., Baker, P. T., Bécsy, B., Blecha, L., Brazier, A., Brook, P. R., Burke-Spolaor, S., Burnette, R., Case, R., Charisi, M., Chatterjee, S., Chatziioannou, K., Cheeseboro, B. D., Chen, S., Cohen, T., Cordes, J. M., Cornish, N. J., Crawford, F., Cromartie, H. T., Crowter, K., Cutler, C. J., DeCesar, M. E., DeGan, D., Demorest, P. B., Deng, H., Dolch, T., Drachler, B., Ellis, J. A., Ferrara, E. C., Fiore, W., Fonseca, E., Freedman, G. E., Garver-Daniels, N., Gentile, P. A., Gersbach, K. A., Glaser, J., Good, D. C., Gültekin, K., Hazboun, J. S., Hourihane, S., Islo, K., Jennings, R. J., Johnson, A. D., Jones, M. L., Kaiser, A. R., Kaplan, D. L., Kelley, L. Z., Kerr, M., Key, J. S., Klein, T. C., Laal, N., Lam, M. T., Lamb, W. G., Lazio, T. J. W., Lewandowska, N., Littenberg, T. B., Liu, T., Lommen, A., Lorimer, D. R., Luo, J., Lynch, R. S., Ma, C.-P., Madison, D. R., Mattson, M. A., McEwen, A., McKee, J. W., McLaughlin, M. A., McMann, N., Meyers, B. W., Meyers, P. M., Mingarelli, C. M. F., Mitridate, A., Natarajan, P., Ng, C., Nice, D. J., Ocker, S. K., Olum, K. D., Pennucci, T. T., Perera, B. B. P., Petrov, P., Pol, N. S., Radovan, H. A., Ransom, S. M., Ray, P. S., Romano, J. D., Sardesai, S. C., Schmiedekamp, A., Schmiedekamp, C., Schmitz, K., Schult, L., Shapiro-Albert, B. J., Siemens, X., Simon, J., Siwek, M. S., Stairs, I. H., Stinebring, D. R., Stovall, K., Sun, J. P., Susobhanan, A., Swiggum, J. K., Taylor, J., Taylor, S. R., Turner, J. E., Unal, C., Vallisneri, M., van Haasteren, R., Vigeland, S. J., Wahl, H. M., Wang, Q., Witt, C. A., Young, O., and Collaboration, T. N. (2023). The nanograv 15 yr data set: Evidence for a gravitational-wave background. *The Astrophysical*

Journal Letters, 951(1):L8.

Alexander, T. and Hopman, C. (2009). Strong Mass Segregation Around a Massive Black Hole. *ApJ*, 697(2):1861–1869.

Alexander, T. and Pfuhl, O. (2014). Constraining the Dark Cusp in the Galactic Center by Long-period Binaries. *ApJ*, 780(2):148.

Allen, B., Anderson, W. G., Brady, P. R., Brown, D. A., and Creighton, J. D. E. (2012). FINDCHIRP: An algorithm for detection of gravitational waves from inspiraling compact binaries. *Phys. Rev. D*, 85(12):122006.

Amaro-Seoane, P. (2019). Extremely large mass-ratio inspirals. *Physical Review D*, 99(12).

Amaro-Seoane, P., Andrews, J., Arca Sedda, M., Askar, A., Baghi, Q., Balasov, R., Bartos, I., Bavera, S. S., Bellovary, J., Berry, C. P. L., Berti, E., Bianchi, S., Blecha, L., Blondin, S., Bogdanović, T., Boissier, S., Bonetti, M., Bonoli, S., Bortolas, E., Breivik, K., Capelo, P. R., Caramete, L., Cattorini, F., Charisi, M., Chaty, S., Chen, X., Chruślińska, M., Chua, A. J. K., Church, R., Colpi, M., D'Orazio, D., Danielski, C., Davies, M. B., Dayal, P., De Rosa, A., Derdzinski, A., Destounis, K., Dotti, M., Duţan, I., Dvorkin, I., Fabj, G., Foglizzo, T., Ford, S., Fouvry, J.-B., Franchini, A., Fragos, T., Fryer, C., Gaspari, M., Gerosa, D., Graziani, L., Groot, P., Habouzit, M., Haggard, D., Haiman, Z., Han, W.-B., Istrate, A., Johansson, P. H., Khan, F. M., Kimpson, T., Kokkotas, K., Kong, A., Korol, V., Kremer, K., Kupfer, T., Lamberts, A., Larson, S., Lau, M., Liu, D., Lloyd-Ronning, N., Lodato, G., Lupi, A., Ma, C.-P., Maccarone, T., Mandel, I., Mangiagli, A., Mapelli, M., Mathis, S., Mayer, L., McGee, S., McKernan, B., Miller, M. C., Mota, D. F., Mumpower, M., Nasim, S. S., Nelemans, G., Noble, S., Pacucci, F., Panessa, F., Paschalidis, V., Pfister, H., Porquet, D., Quenby, J., Ricarte, A., Röpke, F. K., Regan, J., Rosswog, S., Ruiter, A., Ruiz, M., Runnoe, J., Schneider, R., Schnittman, J., Secunda, A., Sesana, A., Seto, N., Shao, L., Shapiro, S., Sopuerta, C., Stone, N. C., Suvorov, A.,

Tamanini, N., Tamfal, T., Tauris, T., Temmink, K., Tomsick, J., Toonen, S., Torres-Orjuela, A., Toscani, M., Tsokaros, A., Unal, C., Vázquez-Aceves, V., Valiante, R., van Putten, M., van Roestel, J., Vignali, C., Volonteri, M., Wu, K., Younsi, Z., Yu, S., Zane, S., Zwick, L., Antonini, F., Baibhav, V., Barausse, E., Bonilla Rivera, A., Branchesi, M., Branduardi-Raymont, G., Burdge, K., Chakraborty, S., Cuadra, J., Dage, K., Davis, B., de Mink, S. E., Decarli, R., Doneva, D., Escoffier, S., Gandhi, P., Haardt, F., Lousto, C. O., Nissanke, S., Nordhaus, J., O'Shaughnessy, R., Portegies Zwart, S., Pound, A., Schussler, F., Sergijenko, O., Spallicci, A., Vernieri, D., and Vigna-Gómez, A. (2023). Astrophysics with the laser interferometer space antenna. *Living Reviews in Relativity*, 26(1).

Amaro-Seoane, P., Audley, H., Babak, S., Baker, J., Barausse, E., Bender, P., Berti, E., Binetruy, P., Born, M., and Bortoluzzi, D. e. a. (2017a). Laser Interferometer Space Antenna. *ArXiv e-prints*.

Amaro-Seoane, P. et al. (2017b). Laser Interferometer Space Antenna. *arXiv e-prints*, page arXiv:1702.00786.

Amaro-Seoane, P. et al. (2022). Astrophysics with the Laser Interferometer Space Antenna. *arXiv e-prints*, page arXiv:2203.06016.

Amaro-Seoane, P., Gair, J. R., Freitag, M., Miller, M. C., Mandel, I., Cutler, C. J., and Babak, S. (2007). Intermediate and extreme mass-ratio inspirals—astrophysics, science applications and detection using LISA. *Classical and Quantum Gravity*, 24(17):R113–R169.

Andrews, J. J. and Kalogera, V. (2022). Constraining Black Hole Natal Kicks with Astrometric Microlensing. *ApJ*, 930(2):159.

Antognini, J. M., Shappee, B. J., Thompson, T. A., and Amaro-Seoane, P. (2014). Rapid ec-

centricity oscillations and the mergers of compact objects in hierarchical triples. *MNRAS*, 439(1):1079–1091.

Antognini, J. M. O. and Thompson, T. A. (2016). Dynamical formation and scattering of hierarchical triples: cross-sections, Kozai-Lidov oscillations, and collisions. *MNRAS*, 456:4219–4246.

Antonini, F. and Gieles, M. (2020). Merger rate of black hole binaries from globular clusters: Theoretical error bars and comparison to gravitational wave data from GWTC-2. *Physical Review D*, 102(12).

Antonini, F. and Gieles, M. (2020). Population synthesis of black hole binary mergers from star clusters. *MNRAS*, 492(2):2936–2954.

Antonini, F., Murray, N., and Mikkola, S. (2014). Black Hole Triple Dynamics: A Breakdown of the Orbit Average Approximation and Implications for Gravitational Wave Detections. *ApJ*, 781(1):45.

Antonini, F. and Perets, H. B. (2012). Secular Evolution of Compact Binaries near Massive Black Holes: Gravitational Wave Sources and Other Exotica. *ApJ*, 757(1):27.

Arakelyan, N. R., Pilipenko, S. V., and Libeskind, N. I. (2018). Spatial distribution of globular clusters in the galaxy. *Monthly Notices of the Royal Astronomical Society*, 481(1):918–929.

Arca Sedda, M., Naoz, S., and Kocsis, B. (2023). Quiescent and Active Galactic Nuclei as Factories of Merging Compact Objects in the Era of Gravitational Wave Astronomy. *Universe*, 9(3):138.

Arca Sedda, M., Askar, A., and Giersz, M. (2018). MOCCA-Survey Database – I. Unravelling black hole subsystems in globular clusters. *Monthly Notices of the Royal Astronomical Society*, 479(4):4652–4664.

Armano, M., Audley, H., Auger, G., Baird, J. T., Bassan, M., Binetruy, P., Born, M., Bortoluzzi, D., Brandt, N., Caleno, M., Carbone, L., Cavalleri, A., Cesarini, A., Ciani, G., Congedo, G., Cruise, A. M., Danzmann, K., de Deus Silva, M., De Rosa, R., Diaz-Aguiló, M., Di Fiore, L., Diepholz, I., Dixon, G., Dolesi, R., Dunbar, N., Ferraioli, L., Ferroni, V., Fichter, W., Fitzsimons, E. D., Flatscher, R., Freschi, M., García Marín, A. F., García Marirrodriga, C., Gerndt, R., Gesa, L., Gibert, F., Giardini, D., Giusteri, R., Guzmán, F., Grado, A., Grimani, C., Grynagier, A., Grzymisch, J., Harrison, I., Heinzel, G., Hewitson, M., Hollington, D., Hoyland, D., Hueller, M., Inchauspé, H., Jennrich, O., Jetzer, P., Johann, U., Johlander, B., Karnesis, N., Kaune, B., Korsakova, N., Killow, C. J., Lobo, J. A., Lloro, I., Liu, L., López-Zaragoza, J. P., Maarschalkerweerd, R., Mance, D., Martín, V., Martin-Polo, L., Martino, J., Martin-Porqueras, F., Madden, S., Mateos, I., McNamara, P. W., Mendes, J., Mendes, L., Monsky, A., Nicolodi, D., Nofrarias, M., Paczkowski, S., Perreur-Lloyd, M., Petiteau, A., Pivato, P., Plagnol, E., Prat, P., Ragnit, U., Raïs, B., Ramos-Castro, J., Reiche, J., Robertson, D. I., Rozemeijer, H., Rivas, F., Russano, G., Sanjuán, J., Sarra, P., Schleicher, A., Shaul, D., Slutsky, J., Sopuerta, C. F., Stanga, R., Steier, F., Sumner, T., Texier, D., Thorpe, J. I., Trenkel, C., Tröbs, M., Tu, H. B., Vetrugno, D., Vitale, S., Wand, V., Wanner, G., Ward, H., Warren, C., Wass, P. J., Wealthy, D., Weber, W. J., Wissel, L., Wittchen, A., Zambotti, A., Zanoni, C., Ziegler, T., and Zweifel, P. (2016a). Sub-femto-g free fall for space-based gravitational wave observatories: Lisa pathfinder results. *Phys. Rev. Lett.*, 116:231101.

Armano, M., Audley, H., Auger, G., Baird, J. T., Bassan, M., Binetruy, P., Born, M., Bortoluzzi, D., Brandt, N., Caleno, M., Carbone, L., Cavalleri, A., Cesarini, A., Ciani, G., Congedo, G., Cruise, A. M., Danzmann, K., de Deus Silva, M., De Rosa, R., Diaz-Aguiló, M., Di Fiore, L., Diepholz, I., Dixon, G., Dolesi, R., Dunbar, N., Ferraioli, L., Ferroni, V., Fichter, W., Fitzsimons, E. D., Flatscher, R., Freschi, M., García Marín, A. F., García Marirrodriga, C., Gerndt, R., Gesa, L., Gibert, F., Giardini, D., Giusteri, R., Guzmán, F., Grado, A., Grimani, C., Grynagier, A., Grzymisch, J., Harrison, I., Heinzel,

G., Hewitson, M., Hollington, D., Hoyland, D., Hueller, M., Inchauspé, H., Jennrich, O., Jetzer, P., Johann, U., Johlander, B., Karnesis, N., Kaune, B., Korsakova, N., Killow, C. J., Lobo, J. A., Lloro, I., Liu, L., López-Zaragoza, J. P., Maarschalkerweerd, R., Mance, D., Martín, V., Martin-Polo, L., Martino, J., Martin-Porqueras, F., Madden, S., Mateos, I., McNamara, P. W., Mendes, J., Mendes, L., Monsky, A., Nicolodi, D., Nofrarias, M., Paczkowski, S., Perreur-Lloyd, M., Petiteau, A., Pivato, P., Plagnol, E., Prat, P., Ragnit, U., Raïs, B., Ramos-Castro, J., Reiche, J., Robertson, D. I., Rozemeijer, H., Rivas, F., Russano, G., Sanjuán, J., Sarra, P., Schleicher, A., Shaul, D., Slutsky, J., Sopuerta, C. F., Stanga, R., Steier, F., Sumner, T., Texier, D., Thorpe, J. I., Trenkel, C., Tröbs, M., Tu, H. B., Vetrugno, D., Vitale, S., Wand, V., Wanner, G., Ward, H., Warren, C., Wass, P. J., Wealthy, D., Weber, W. J., Wissel, L., Wittchen, A., Zambotti, A., Zanoni, C., Ziegler, T., and Zweifel, P. (2016b). Sub-femto-g free fall for space-based gravitational wave observatories: Lisa pathfinder results. *Phys. Rev. Lett.*, 116:231101.

Armano, M., Audley, H., Baird, J., Binetruy, P., Born, M., Bortoluzzi, D., Castelli, E., Cavalleri, A., Cesarini, A., Chiavegato, V., Cruise, A. M., Dal Bosco, D., Danzmann, K., De Deus Silva, M., Diepholz, I., Dixon, G., Dolesi, R., Ferraioli, L., Ferroni, V., Fitzsimons, E. D., Freschi, M., Gesa, L., Giardini, D., Gibert, F., Giusteri, R., Grimani, C., Grzymisch, J., Harrison, I., Hartig, M. S., Heinzel, G., Hewitson, M., Hollington, D., Hoyland, D., Hueller, M., Inchauspé, H., Jennrich, O., Jetzer, P., Johlander, B., Karnesis, N., Kaune, B., Korsakova, N., Killow, C. J., Lobo, J. A., López-Zaragoza, J. P., Maarschalkerweerd, R., Mance, D., Martín, V., Martin-Polo, L., Martin-Porqueras, F., Martino, J., McNamara, P. W., Mendes, J., Mendes, L., Meshksar, N., Nofrarias, M., Paczkowski, S., Perreur-Lloyd, M., Petiteau, A., Plagnol, E., Ramos-Castro, J., Reiche, J., Rivas, F., Robertson, D. I., Russano, G., Sala, L., Sarra, P., Slutsky, J., Sopuerta, C. F., Sumner, T., Texier, D., Thorpe, J. I., Vetrugno, D., Vitale, S., Wanner, G., Ward, H., Wass, P., Weber, W. J., Wissel, L., Wittchen, A., Zanoni, C., and Zweifel, P. (2022). Transient acceleration events in lisa pathfinder data: Properties and possible physical origin. *Phys. Rev. D*, 106:062001.

Armano, M., Audley, H., Baird, J., Binetruy, P., Born, M., Bortoluzzi, D., Castelli, E., Cavalleri, A., Cesarini, A., Cruise, A. M., Danzmann, K., de Deus Silva, M., Diepholz, I., Dixon, G., Dolesi, R., Ferraioli, L., Ferroni, V., Fitzsimons, E. D., Freschi, M., Gesa, L., Gibert, F., Giardini, D., Giusteri, R., Grimani, C., Grzymisch, J., Harrison, I., Heinzel, G., Hewitson, M., Hollington, D., Hoyland, D., Hueller, M., Inchauspé, H., Jennrich, O., Jetzer, P., Karnesis, N., Kaune, B., Korsakova, N., Killow, C. J., Lobo, J. A., Lloro, I., Liu, L., López-Zaragoza, J. P., Maarschalkerweerd, R., Mance, D., Meshksar, N., Martín, V., Martin-Polo, L., Martino, J., Martin-Porqueras, F., Mateos, I., McNamara, P. W., Mendes, J., Mendes, L., Nofrarias, M., Paczkowski, S., Perreur-Lloyd, M., Petiteau, A., Pivato, P., Plagnol, E., Ramos-Castro, J., Reiche, J., Robertson, D. I., Rivas, F., Russano, G., Slutsky, J., Sopuerta, C. F., Sumner, T., Texier, D., Thorpe, J. I., Vetrugno, D., Vitale, S., Wanner, G., Ward, H., Wass, P. J., Weber, W. J., Wissel, L., Wittchen, A., and Zweifel, P. (2018a). Beyond the required lisa free-fall performance: New lisa pathfinder results down to 20 μHz. *Phys. Rev. Lett.*, 120:061101.

Armano, M., Audley, H., Baird, J., Binetruy, P., Born, M., Bortoluzzi, D., Castelli, E., Cavalleri, A., Cesarini, A., Cruise, A. M., Danzmann, K., de Deus Silva, M., Diepholz, I., Dixon, G., Dolesi, R., Ferraioli, L., Ferroni, V., Fitzsimons, E. D., Freschi, M., Gesa, L., Gibert, F., Giardini, D., Giusteri, R., Grimani, C., Grzymisch, J., Harrison, I., Heinzel, G., Hewitson, M., Hollington, D., Hoyland, D., Hueller, M., Inchauspé, H., Jennrich, O., Jetzer, P., Karnesis, N., Kaune, B., Korsakova, N., Killow, C. J., Lobo, J. A., Lloro, I., Liu, L., López-Zaragoza, J. P., Maarschalkerweerd, R., Mance, D., Meshksar, N., Martín, V., Martin-Polo, L., Martino, J., Martin-Porqueras, F., Mateos, I., McNamara, P. W., Mendes, J., Mendes, L., Nofrarias, M., Paczkowski, S., Perreur-Lloyd, M., Petiteau, A., Pivato, P., Plagnol, E., Ramos-Castro, J., Reiche, J., Robertson, D. I., Rivas, F., Russano, G., Slutsky, J., Sopuerta, C. F., Sumner, T., Texier, D., Thorpe, J. I., Vetrugno, D., Vitale, S., Wanner, G., Ward, H., Wass, P. J., Weber, W. J., Wissel, L., Wittchen, A., and Zweifel, P. (2018b). Beyond the required lisa free-fall performance: New lisa pathfinder

results down to 20 μHz. *Phys. Rev. Lett.*, 120:061101.

Armas Padilla, M., Corral-Santana, J. M., Borghese, A., Cúneo, V. A., Muñoz-Darias, T., Casares, J., and Torres, M. A. P. (2023). Ultracompcat: A comprehensive catalogue of ultra-compact and short orbital period x-ray binaries. *Astronomy and amp; Astrophysics*, 677:A186.

Arzoumanian, Z., Chernoff, D. F., and Cordes, J. M. (2002). The Velocity Distribution of Isolated Radio Pulsars. *ApJ*, 568(1):289–301.

Baghi, Q., Korsakova, N., Slutsky, J., Castelli, E., Karnesis, N., and Bayle, J.-B. (2022). Detection and characterization of instrumental transients in lisa pathfinder and their projection to lisa. *Phys. Rev. D*, 105:042002.

Bahramian, A. and Degenaar, N. (2023). *Low-Mass X-ray Binaries*, page 1–62. Springer Nature Singapore.

Bahramian, A., Heinke, C. O., Tudor, V., Miller-Jones, J. C. A., Bogdanov, S., Maccarone, T. J., Knigge, C., Sivakoff, G. R., Chomiuk, L., Strader, J., Garcia, J. A., and Kallman, T. (2017). The ultracompact nature of the black hole candidate x-ray binary 47 tuc x9. *Monthly Notices of the Royal Astronomical Society*, 467(2):2199–2216.

Baker, J. G., Centrella, J., Choi, D.-I., Koppitz, M., and van Meter, J. (2006). Gravitational-wave extraction from an inspiraling configuration of merging black holes. *Physical Review Letters*, 96(11).

Banerjee, S., Baumgardt, H., and Kroupa, P. (2010). Stellar-mass black holes in star clusters: implications for gravitational wave radiation. *MNRAS*, 402:371–380.

Barack, L. (2009). Gravitational self-force in extreme mass-ratio inspirals. *Classical and Quantum Gravity*, 26(21):213001.

Barack, L. and Cutler, C. (2004a). Confusion noise from LISA capture sources. *Phys. Rev. D*, 70(12):122002.

Barack, L. and Cutler, C. (2004b). LISA capture sources: Approximate waveforms, signal-to-noise ratios, and parameter estimation accuracy. *Phys. Rev. D*, 69(8):082005.

Barack, L. and Pound, A. (2018). Self-force and radiation reaction in general relativity. *Reports on Progress in Physics*, 82(1):016904.

Bassetti, M. J., Chatterjee, A. N., Aluru, N., and Beebe, D. J. (2005). Development and modeling of electrically triggered hydrogels for microfluidic applications. *Journal of Microelectromechanical Systems*, 14(5):1198–1207.

Baumgardt, H. and Hilker, M. (2018). A catalogue of masses, structural parameters, and velocity dispersion profiles of 112 Milky Way globular clusters. *MNRAS*, 478(2):1520–1557.

Bécsy, B., Raffai, P., Gill, K., Littenberg, T. B., Millhouse, M., and Szczepańczyk, M. J. (2020). Interpreting gravitational-wave burst detections: constraining source properties without astrophysical models. *Classical and Quantum Gravity*, 37(10):105011.

Belczynski, K. (2020). The most ordinary formation of the most unusual double black hole merger. *The Astrophysical Journal Letters*, 905(2):L15.

Belczynski, K., Holz, D. E., Bulik, T., and O'Shaughnessy, R. (2016). The first gravitational-wave source from the isolated evolution of two stars in the 40-100 solar mass range. *Nature*, 534:512–515.

Benacquista, M. J., Portegies Zwart, S., and Rasio, F. A. (2001). LISA sources in globular clusters. *Classical and Quantum Gravity*, 18(19):4025–4031.

Bern, Z., Cheung, C., Roiban, R., Shen, C.-H., Solon, M. P., and Zeng, M. (2019). Scattering amplitudes and the conservative hamiltonian for binary systems at third post-minkowskian order. *Physical Review Letters*, 122(20).

Berry, C. P. L. and Gair, J. R. (2013). Expectations for extreme-mass-ratio bursts from the galactic centre. *Monthly Notices of the Royal Astronomical Society*, 435(4):3521–3540.

Bhaskar, H., Li, G., Hadden, S., Payne, M. J., and Holman, M. J. (2021). Mildly Hierarchical Triple Dynamics and Applications to the Outer Solar System. *AJ*, 161(1):48.

Binney, J. and Tremaine, S. (2008). *Galactic Dynamics: Second Edition*. Princeton University Press.

Bird, S., Cholis, I., Muñoz, J. B., Ali-Haïmoud, Y., Kamionkowski, M., Kovetz, E. D., Raccanelli, A., and Riess, A. G. (2016). Did ligo detect dark matter? *Physical Review Letters*, 116(20).

Blanchet, L. (2002). Gravitational radiation from post-newtonian sources and inspiralling compact binaries. *Living Reviews in Relativity*, 5(1).

Bobrick, A., Davies, M. B., and Church, R. P. (2017). Mass transfer in white dwarf-neutron star binaries. *MNRAS*, 467(3):3556–3575.

Boileau, G., Lamberts, A., Christensen, N., Cornish, N. J., and Meyer, R. (2021). Spectral separation of the stochastic gravitational-wave background for LISA in the context of a modulated Galactic foreground. *MNRAS*, 508(1):803–826.

Bond, J. R., Arnett, W. D., and Carr, B. J. (1984). The evolution and fate of Very Massive Objects. *ApJ*, 280:825–847.

Bonetti, M. and Sesana, A. (2020). Gravitational wave background from extreme mass ratio inspirals. *Phys. Rev. D*, 102(10):103023.

Bonvin, C., Caprini, C., Sturani, R., and Tamanini, N. (2017). Effect of matter structure on the gravitational waveform. *Phys. Rev. D*, 95(4):044029.

Breen, P. G. and Heggie, D. C. (2013). Dynamical evolution of black hole subsystems in idealized star clusters. *Monthly Notices of the Royal Astronomical Society*, 432(4):2779–2797.

Breivik, K., Mingarelli, C. M. F., and Larson, S. L. (2020). Constraining Galactic Structure with the LISA White Dwarf Foreground. *ApJ*, 901(1):4.

Breivik, K., Rodriguez, C. L., Larson, S. L., Kalogera, V., and Rasio, F. A. (2016). Distinguishing between Formation Channels for Binary Black Holes with LISA. *ApJ Lett.*, 830:L18.

Broadhurst, T., Diego, J. M., and Smoot, George, I. (2018). Reinterpreting Low Frequency LIGO/Virgo Events as Magnified Stellar-Mass Black Holes at Cosmological Distances. *arXiv e-prints*, page arXiv:1802.05273.

Broekgaarden, F. S. and Berger, E. (2021). Formation of the First Two Black Hole-Neutron Star Mergers (GW200115 and GW200105) from Isolated Binary Evolution. *ApJ Lett.*, 920(1):L13.

Brown, D. A. and Zimmerman, P. J. (2010). Effect of eccentricity on searches for gravitational waves from coalescing compact binaries in ground-based detectors. *Phys. Rev. D*, 81(2):024007.

Bub, M. W. and Petrovich, C. (2020). Compact-object Mergers in the Galactic Center: Evolution in Triaxial Clusters. *ApJ*, 894(1):15.

Buonanno, A., Iyer, B. R., Ochsner, E., Pan, Y., and Sathyaprakash, B. S. (2009). Comparison of post-newtonian templates for compact binary inspiral signals in gravitational-wave detectors. *Physical Review D*, 80(8).

Burdge, K. B., El-Badry, K., Kara, E., Canizares, C., Chakrabarty, D., Frebel, A., Millholland, S. C., Rappaport, S., Simcoe, R., and Vanderburg, A. (2024). The black hole low

mass x-ray binary v404 cygni is part of a wide hierarchical triple, and formed without a kick.

Burdge, K. B., El-Badry, K., Kara, E., Canizares, C., Chakrabarty, D., Frebel, A., Millholland, S. C., Rappaport, S., Simcoe, R., and Vanderburg, A. (2024). The black hole low-mass X-ray binary V404 Cygni is part of a wide triple. *Nature*, 635(8038):316–320.

Cautun, M., Benítez-Llambay, A., Deason, A. J., Frenk, C. S., Fattahi, A., Gómez, F. A., Grand, R. J. J., Oman, K. A., Navarro, J. F., and Simpson, C. M. (2020). The milky way total mass profile as inferred from gaia dr2. *Monthly Notices of the Royal Astronomical Society*, 494(3):4291–4313.

Chakrabarti, S., Simon, J. D., Craig, P. A., Reggiani, H., Brandt, T. D., Guhathakurta, P., Dalba, P. A., Kirby, E. N., Chang, P., Hey, D. R., Savino, A., Geha, M., and Thompson, I. B. (2023). A Noninteracting Galactic Black Hole Candidate in a Binary System with a Main-sequence Star. *AJ*, 166(1):6.

Chandramouli, R. S. and Yunes, N. (2022). Ready-to-use analytic model for gravitational waves from a hierarchical triple with kozai-lidov oscillations. *Phys. Rev. D*, 105:064009.

Chatterji, S., Blackburn, L., Martin, G., and Katsavounidis, E. (2004). Multiresolution techniques for the detection of gravitational-wave bursts. *Classical and Quantum Gravity*, 21(20):S1809–S1818.

Chatterji, S., Lazzarini, A., Stein, L., Sutton, P. J., Searle, A., and Tinto, M. (2006). Coherent network analysis technique for discriminating gravitational-wave bursts from instrumental noise. *Phys. Rev. D*, 74(8):082005.

Chatziioannou, K., Klein, A., Yunes, N., and Cornish, N. (2017). Constructing gravitational waves from generic spin-precessing compact binary inspirals. *Phys. Rev. D*, 95(10):104004.

Chen, M. and liu, J. (2025). New potential ultra-compact x-ray binaries for space-based gravitational wave detectors from low-mass main-sequence companion channel.

Chen, M. and Liu, J. (2025). New Potential Ultracompact X-Ray Binaries for Space-based Gravitational-wave Detectors from a Low-mass Main-sequence Companion Channel. *ApJ*, 981(2):175.

Chen, R., Chandramouli, R. S., Pozzoli, F., Buscicchio, R., and Barausse, E. (2026). Implications of the lisa stochastic signal from eccentric stellar mass black hole binaries in vacuum.

Chen, S., Sesana, A., and Del Pozzo, W. (2017). Efficient computation of the gravitational wave spectrum emitted by eccentric massive black hole binaries in stellar environments. *MNRAS*, 470(2):1738–1749.

Chen, W.-C., Liu, D.-D., and Wang, B. (2020). Detectability of ultra-compact x-ray binaries as lisa sources. *The Astrophysical Journal Letters*, 900(1):L8.

Chen, X. (2020). Distortion of Gravitational-wave Signals by Astrophysical Environments. *arXiv e-prints*, page arXiv:2009.07626.

Chen, X. and Amaro-Seoane, P. (2017). Revealing the Formation of Stellar-mass Black Hole Binaries: The Need for Deci-Hertz Gravitational-wave Observatories. *ApJ Lett.*, 842:L2.

Chen, X. and Han, W.-B. (2018). Extreme-mass-ratio inspirals produced by tidal capture of binary black holes. *Communications Physics*, 1(1).

Chen, X., Li, S., and Cao, Z. (2019a). Mass-redshift degeneracy for the gravitational-wave sources in the vicinity of supermassive black holes. *MNRAS*, 485(1):L141–L145.

Chen, X., Li, S., and Cao, Z. (2019b). Mass-redshift degeneracy for the gravitational-wave sources in the vicinity of supermassive black holes. *MNRAS*, 485(1):L141–L145.

Chen, X., Xuan, Z.-Y., and Peng, P. (2020a). Fake Massive Black Holes in the Milli-Hertz Gravitational-wave Band. *ApJ*, 896(2):171.

Chen, X., Xuan, Z.-Y., and Peng, P. (2020b). Fake Massive Black Holes in the Milli-Hertz Gravitational-wave Band. *ApJ*, 896(2):171.

Chen, Z., Do, T., Ghez, A. M., Hosek, M. W., Feldmeier-Krause, A., Chu, D. S., Bentley, R. O., Lu, J. R., and Morris, M. R. (2023). The Star Formation History of the Milky Way's Nuclear Star Cluster. *ApJ*, 944(1):79.

Christensen, N., Dupuis, R. J., Woan, G., and Meyer, R. (2004). Metropolis-hastings algorithm for extracting periodic gravitational wave signals from laser interferometric detector data. *Phys. Rev. D*, 70:022001.

Christensen, N. and Meyer, R. (1998). Markov chain monte carlo methods for bayesian gravitational radiation data analysis. *Phys. Rev. D*, 58:082001.

Christensen, N. and Meyer, R. (2001). Using Markov chain Monte Carlo methods for estimating parameters with gravitational radiation data. *Phys. Rev. D*, 64(2):022001.

Chu, D. S., Do, T., Ghez, A., Gautam, A. K., Ciurlo, A., O'neil, K. K., Hosek, M. W., Hees, A., Naoz, S., Sakai, S., Lu, J. R., Chen, Z., Bentley, R. O., Becklin, E. E., and Matthews, K. (2023). Evidence of a Decreased Binary Fraction for Massive Stars within 20 milliparsecs of the Supermassive Black Hole at the Galactic Center. *ApJ*, 948(2):94.

Chu, D. S., Do, T., Hees, A., Ghez, A., Naoz, S., Witzel, G., Sakai, S., Chappell, S., Gautam, A. K., Lu, J. R., and Matthews, K. (2018). Investigating the Binarity of S0-2: Implications for Its Origins and Robustness as a Probe of the Laws of Gravity around a Supermassive Black Hole. *ApJ*, 854(1):12.

Chua, A. J. and Cutler, C. J. (2022). Nonlocal parameter degeneracy in the intrinsic space of gravitational-wave signals from extreme-mass-ratio inspirals. *Physical Review D*, 106(12).

Chua, A. J. K., Katz, M. L., Warburton, N., and Hughes, S. A. (2021). Rapid Generation of Fully Relativistic Extreme-Mass-Ratio-Inspiral Waveform Templates for LISA Data Analysis. *Phys. Rev. Lett.*, 126(5):051102.

Church, R. P., Strader, J., Davies, M. B., and Bobrick, A. (2017). Formation constraints indicate a black hole accretor in 47 tuc x9. *The Astrophysical Journal Letters*, 851(1):L4.

Coe, D. (2009). Fisher Matrices and Confidence Ellipses: A Quick-Start Guide and Software. *arXiv e-prints*, page arXiv:0906.4123.

Collaboration, L. S. and Collaboration, V. (2020). Gw190521: A binary black hole merger with a total mass of 150 $M_{\odot}$. *Phys. Rev. Lett.*, 125:101102.

Collaboration, T. L. S., the Virgo Collaboration, the KAGRA Collaboration, Abac, A. G., Abouelfettouh, I., Acernese, F., Ackley, K., Adamcewicz, C., Adhicary, S., Adhikari, D., Adhikari, N., Adhikari, R. X., Adkins, V. K., Afroz, S., Agarwal, D., Agathos, M., Abchouyeh, M. A., Aguiar, O. D., Ahmadzadeh, S., Aiello, L., Ain, A., Ajith, P., Akutsu, T., Albanesi, S., Alfaidi, R. A., Al-Jodah, A., Alléné, C., Allocca, A., Al-Shammari, S., Altin, P. A., Alvarez-Lopez, S., Amarasinghe, O., Amato, A., Amra, C., Ananyeva, A., Anderson, S. B., Anderson, W. G., Andia, M., Ando, M., Andrade, T., Andrés-Carcasona, M., Andrić, T., Anglin, J., Ansoldi, S., Antelis, J. M., Antier, S., Aoumi, M., Appavuravther, E. Z., Appert, S., Apple, S. K., Arai, K., Araya, A., Araya, M. C., Sedda, M. A., Areeda, J. S., Argianas, L., Aritomi, N., Armato, F., Armstrong, S., Arnaud, N., Arogeti, M., Aronson, S. M., Arun, K. G., Ashton, G., Aso, Y., Assiduo, M., de Souza Melo, S. A., Aston, S. M., Astone, P., Attadio, F., Aubin, F., AultONeal, K., Avallone, G., Babak, S., Badaracco, F., Badger, C., Bae, S., Bagnasco, S., Bagui, E., Baiotti, L., Bajpai, R., Baka, T., Baker, T., Ball, M., Ballardin, G., Ballmer, S. W., Banagiri, S., Banerjee, B., Bankar, D., Baptiste, T. M., Baral, P., Barayoga, J. C., Barish, B. C., Barker, D., Barman, N., Barneo, P., Barone, F., Barr, B., Barsotti, L., Barsuglia, M., Barta, D., Bartoletti, A. M., Barton, M. A., Bartos, I., Basak, S., Basalaev, A., Bassiri, R., Basti,

A., Bates, D. E., Bawaj, M., Baxi, P., Bayley, J. C., Baylor, A. C., II, P. A. B., Bazzan, M., Bedakihale, V. M., Beirnaert, F., Bejger, M., Belardinelli, D., Bell, A. S., Bellie, D. S., Bellizzi, L., Beltran-Martinez, D., Benoit, W., Bentara, I., Bentley, J. D., Yaala, M. B., Bera, S., Bergamin, F., Berger, B. K., Bernuzzi, S., Beroiz, M., Berry, C. P. L., Bersanetti, D., Bertolini, A., Betzwieser, J., Beveridge, D., Bevilacqua, G., Bevins, N., Bhandare, R., Bhatt, R., Bhattacharjee, D., Bhaumik, S., Bhowmick, S., Biancalana, V., Bianchi, A., Bilenko, I. A., Billingsley, G., Binetti, A., Bini, S., Binu, C., Birnholtz, O., Biscoveanu, S., Bisht, A., Bitossi, M., Bizouard, M. A., Blaber, S., Blackburn, J. K., Blagg, L. A., Blair, C. D., Blair, D. G., Bobba, F., Bode, N., Boileau, G., Boldrini, M., Bolingbroke, G. N., Bolliand, A., Bonavena, L. D., Bondarescu, R., Bondu, F., Bonilla, E., Bonilla, M. S., Bonino, A., Bonnand, R., Booker, P., Borchers, A., Borhanian, S., Boschi, V., Bose, S., Bossilkov, V., Boudon, A., Bozzi, A., Bradaschia, C., Brady, P. R., Branch, A., Branchesi, M., Braun, I., Briant, T., Brillet, A., Brinkmann, M., Brockill, P., Brockmueller, E., Brooks, A. F., Brown, B. C., Brown, D. D., Brozzetti, M. L., Brunett, S., Bruno, G., Bruntz, R., Bryant, J., Bu, Y., Bucci, F., Buchanan, J., Bulashenko, O., Bulik, T., Bulten, H. J., Buonanno, A., Burtnyk, K., Buscicchio, R., Buskulic, D., Buy, C., Byer, R. L., Davies, G. S. C., Cabras, G., Cabrita, R., Cáceres-Barbosa, V., Cadonati, L., Cagnoli, G., Cahillane, C., Calafat, A., Bustillo, J. C., Callister, T. A., Calloni, E., Canepa, M., Santoro, G. C., Cannon, K. C., Cao, H., Capistran, L. A., Capocasa, E., Capote, E., Capurri, G., Carapella, G., Carbognani, F., Carlassara, M., Carlin, J. B., Carlson, T. K., Carney, M. F., Carpinelli, M., Carrillo, G., Carter, J. J., Carullo, G., Diaz, J. C., Casentini, C., Castro-Lucas, S. Y., Caudill, S., Cavaglià, M., Cavalieri, R., Cella, G., Cerdá-Durán, P., Cesarini, E., Chaibi, W., Chakraborty, P., Chakraborty, S., Subrahmanya, S. C., Chan, J. C. L., Chan, M., Chang, R. J., Chao, S., Charlton, E. L., Charlton, P., Chassande-Mottin, E., Chatterjee, C., Chatterjee, D., Chatterjee, D., Chattopadhyay, D., Chaturvedi, M., Chaty, S., Chatziioannou, K., Checchia, C., Chen, A., Chen, A. H. Y., Chen, D., Chen, H., Chen, H. Y., Chen, S., Chen, Y., Chen, Y., Chen, Y., Cheng, H. P.,

Chessa, P., Cheung, H. T., Cheung, S. Y., Chiadini, F., Chiarini, G., Chierici, R., Chincarini, A., Chiofalo, M. L., Chiummo, A., Chou, C., Choudhary, S., Christensen, N., Chua, S. S. Y., Chugh, P., Ciani, G., Ciecielag, P., Cieślar, M., Cifaldi, M., Ciolfi, R., Clara, F., Clark, J. A., Clarke, J., Clarke, T. A., Clearwater, P., Clesse, S., Clyne, S. M., Coccia, E., Codazzo, E., Cohadon, P. F., Colace, S., Colangeli, E., Colleoni, M., Collette, C. G., Collins, J., Colloms, S., Colombo, A., Compton, C. M., Connolly, G., Conti, L., Corbitt, T. R., Cordero-Carrión, I., Corezzi, S., Cornish, N. J., Corsi, A., Cortese, S., Cottingham, R., Coughlin, M. W., Couineaux, A., Coulon, J. P., Coupechoux, J. F., Couvares, P., Coward, D. M., Coyne, R., Craig, K., Creighton, J. D. E., Creighton, T. D., Cremonese, P., Criswell, A. W., Crook, S., Crouch, R., Csizmazia, J., Cudell, J. R., Cullen, T. J., Cumming, A., Cuoco, E., Cusinato, M., Dabadie, P., Conceição, L. V. D., Canton, T. D., Dall'Osso, S., Pra, S. D., Dálya, G., D'Angelo, B., Danilishin, S., D'Antonio, S., Danzmann, K., Darroch, K. E., Dartez, L. P., Dasgupta, A., Datta, S., Dattilo, V., Daumas, A., Davari, N., Dave, I., Davenport, A., Davier, M., Davies, T. F., Davis, D., Davis, L., Davis, M. C., Davis, P., Dax, M., Bolle, J. D., Deenadayalan, M., Degallaix, J., Laurentis, M. D., Deléglise, S., Lillo, F. D., Dell'Aquila, D., Valle, F. D., Pozzo, W. D., Marco, F. D., Demasi, G., Matteis, F. D., D'Emilio, V., Demos, N., Dent, T., Depasse, A., DePergola, N., Pietri, R. D., Rosa, R. D., Rossi, C. D., Desai, M., DeSalvo, R., DeSimone, A., Simone, R. D., Dhani, A., Diab, R., Díaz, M. C., Cesare, M. D., Dideron, G., Didio, N. A., Dietrich, T., Fiore, L. D., Fronzo, C. D., Giovanni, M. D., Girolamo, T. D., Diksha, D., Michele, A. D., Ding, J., Pace, S. D., Palma, I. D., Renzo, F. D., Divyajyoti, Dmitriev, A., Doctor, Z., Doerksen, N., Dohmen, E., Dominguez, D., D'Onofrio, L., Donovan, F., Dooley, K. L., Dooney, T., Doravari, S., Dorosh, O., Drago, M., Driggers, J. C., Ducoin, J. G., Dunn, L., Dupletsa, U., D'Urso, D., Duval, H., Dwyer, S. E., Eassa, C., Ebersold, M., Eckhardt, T., Eddolls, G., Edelman, B., Edo, T. B., Edy, O., Effler, A., Eichholz, J., Einsle, H., Eisenmann, M., Eisenstein, R. A., Ejlli, A., Emma, M., Endo, K., Enficiaud, R., Engl, A. J., Errico, L., Espinosa, R., Esposito, M., Essick, R. C., Estellés, H., Etzel, T.,

Evans, M., Evstafyeva, T., Ewing, B. E., Ezquiaga, J. M., Fabrizi, F., Faedi, F., Fafone, V., Fairhurst, S., Farah, A. M., Farr, B., Farr, W. M., Favaro, G., Favata, M., Fays, M., Fazio, M., Feicht, J., Fejer, M. M., Felicetti, R., Fenyvesi, E., Ferguson, D. L., Fernandes, T., Fernando, A., Fernando, D., Ferraiuolo, S., Ferrante, I., Ferreira, T. A., Fidecaro, F., Figura, P., Fiori, A., Fiori, I., Fishbach, M., Fisher, R. P., Fittipaldi, R., Fiumara, V., Flaminio, R., Fleischer, S. M., Fleming, L. S., Floden, E., Fong, H., Font, J. A., Foo, C., Fornal, B., Forsyth, P. W. F., Franceschetti, K., Franchini, N., Frasca, S., Frasconi, F., Mascioli, A. F., Frei, Z., Freise, A., Freitas, O., Frey, R., Frischhertz, W., Fritschel, P., Frolov, V. V., Fronzé, G. G., Fuentes-Garcia, M., Fujii, S., Fujimori, T., Fulda, P., Fyffe, M., Gadre, B., Gair, J. R., Galaudage, S., Galdi, V., Gallagher, H., Gallego, B., Gamba, R., Gamboa, A., Ganapathy, D., Ganguly, A., Garaventa, B., García-Bellido, J., Núñez, C. G., García-Quirós, C., Gardner, J. W., Gardner, K. A., Gargiulo, J., Garron, A., Garufi, F., Garver, P. A., Gasbarra, C., Gateley, B., Gautier, F., Gayathri, V., Gayer, T., Gemme, G., Gennai, A., Gennari, V., George, J., George, R., Gerberding, O., Gergely, L., Ghosh, A., Ghosh, S., Ghosh, S., Ghosh, S., Ghosh, S., Ghosh, T., Giaime, J. A., Giardina, K. D., Gibson, D. R., Gibson, D. T., Gier, C., Gkaitatzis, S., Glanzer, J., Glotin, F., Godfrey, J., Godwin, P., Goettel, A. S., Goetz, E., Golomb, J., Lopez, S. G., Goncharov, B., Gong, Y., González, G., Goodarzi, P., Goode, S., Goodwin-Jones, A. W., Gosselin, M., Gouaty, R., Gould, D. W., Govorkova, K., Goyal, S., Grace, B., Grado, A., Graham, V., Granados, A. E., Granata, M., Granata, V., Gras, S., Grassia, P., Gray, A., Gray, C., Gray, R., Greco, G., Green, A. C., Green, S. M., Green, S. R., Gretarsson, A. M., Gretarsson, E. M., Griffith, D., Griffiths, W. L., Griggs, H. L., Grignani, G., Grimaud, C., Grote, H., Grunewald, S., Guerra, D., Guetta, D., Guidi, G. M., Guimaraes, A. R., Gulati, H. K., Gulminelli, F., Gunny, A. M., Guo, H., Guo, W., Guo, Y., Gupta, A., Gupta, A., Gupta, I., Gupta, N. C., Gupta, P., Gupta, S. K., Gupta, T., Gupta, V., Gupte, N., Gurs, J., Gutierrez, N., Guzman, F., Haba, D., Haberland, M., Haino, S., Hall, E. D., Hamilton, E. Z., Hammond, G., Han, W. B., Haney, M., Hanks, J.,

Hanna, C., Hannam, M. D., Hannuksela, O. A., Hanselman, A. G., Hansen, H., Hanson, J., Harada, R., Hardison, A. R., Harikumar, S., Haris, K., Harmark, T., Harms, J., Harry, G. M., Harry, I. W., Hart, J., Haskell, B., Haster, C. J., Haughian, K., Hayakawa, H., Hayama, K., Hayes, R., Heffernan, A., Heintze, M. C., Heinze, J., Heinzel, J., Heitmann, H., Hellman, F., Helmling-Cornell, A. F., Hemming, G., Henderson-Sapir, O., Hendry, M., Heng, I. S., Hennig, M. H., Henshaw, C., Heurs, M., Hewitt, A. L., Heyns, J., Higginbotham, S., Hild, S., Hill, S., Himemoto, Y., Hirata, N., Hirose, C., Hochheim, S., Hofman, D., Holland, N. A., Holz, D. E., Honet, L., Hong, C., Hoshino, S., Hough, J., Hourihane, S., Howard, N. T., Howell, E. J., Hoy, C. G., Hrishikesh, C. A., Hsieh, H. F., Hsieh, H. Y., Hsiung, C., Hsu, W. F., Hu, Q., Huang, H. Y., Huang, Y., Huang, Y. T., Huddart, A. D., Hughey, B., Hui, D. C. Y., Hui, V., Husa, S., Huxford, R., Iampieri, L., Iandolo, G. A., Ianni, M., Ierardi, A., Iess, A., Imafuku, H., Inayoshi, K., Inoue, Y., Iorio, G., Iosif, P., Iqbal, M. H., Irwin, J., Ishikawa, R., Isi, M., Itoh, Y., Iwanaga, H., Iwaya, M., Iyer, B. R., Jacquet, C., Jacquet, P. E., Jadhav, S. J., Jadhav, S. P., Jain, T., James, A. L., James, P. A., Jamshidi, R., Jani, K., Janquart, J., Janssens, K., Janthalur, N. N., Jaraba, S., Jaranowski, P., Jaume, R., Javed, W., Jennings, A., Jia, W., Jiang, J., Johanson, C., Johns, G. R., Johnson, N. A., Johnston, M. C., Johnston, R., Johny, N., Jones, D. H., Jones, D. I., Jones, E. J., Jones, R., Jose, S., Joshi, P., Joshi, S. K., Ju, J., Ju, L., Jung, K., Junker, J., Juste, V., Kabagoz, H. B., Kajita, T., Kaku, I., Kalogera, V., Kalomenopoulos, M., Kamiizumi, M., Kanda, N., Kandhasamy, S., Kang, G., Kannachel, N. C., Kanner, J. B., Kapadia, S. J., Kapasi, D. P., Karat, S., Kashyap, R., Kasprzack, M., Kastaun, W., Kato, T., Katsavounidis, E., Katzman, W., Kaushik, R., Kawabe, K., Kawamoto, R., Kazemi, A., Kedia, A., Keitel, D., Kennington, J., Kesharwani, R., Key, J. S., Khadela, R., Khadka, S., Khalili, F. Y., Khan, F., Khan, I., Khanam, T., Khursheed, M., Khusid, N. M., Kiendrebeogo, W., Kijbunchoo, N., Kim, C., Kim, J. C., Kim, K., Kim, M. H., Kim, S., Kim, Y. M., Kimball, C., Kinley-Hanlon, M., Kinnear, M., Kissel, J. S., Klimenko, S., Knee, A. M., Knust, N., Kobayashi, K., Koch, P., Koehlenbeck, S. M.,

Koekoek, G., Kohri, K., Kokeyama, K., Koley, S., Kolitsidou, P., Komori, K., Kong, A. K. H., Kontos, A., Korobko, M., Kossak, R. V., Kou, X., Koushik, A., Kouvatsos, N., Kovalam, M., Kozak, D. B., Kranzhoff, S. L., Kringel, V., Krishnendu, N. V., Królak, A., Kruska, K., Kubisz, J., Kuehn, G., Kulkarni, S., Ramamohan, A. K., Kumar, A., Kumar, P., Kumar, P., Kumar, R., Kumar, R., Kume, J., Kuns, K., Kuntimaddi, N., Kuroyanagi, S., Kuwahara, S., Kwak, K., Kwan, K., Kwok, J., Lacaille, G., Lagabbe, P., Laghi, D., Lai, S., Lalande, E., Lalleman, M., Lalremruati, P. C., Landry, M., Landry, P., Lane, B. B., Lang, R. N., Lange, J., Langgin, R., Lantz, B., Rana, A. L., Rosa, I. L., Larsen, J., Lartaux-Vollard, A., Lasky, P. D., Lawrence, J., Lawrence, M. N., Laxen, M., Lazarte, C., Lazzarini, A., Lazzaro, C., Leaci, P., Leali, L., Lecoeuche, Y. K., Lee, H. M., Lee, H. W., Lee, J., Lee, K., Lee, R. K., Lee, R., Lee, S., Lee, S., Lee, Y., Legred, I. N., Lehmann, J., Lehner, L., Jean, M. L., Lemaître, A., Lenti, M., Leonardi, M., Lequime, M., Leroy, N., Lesovsky, M., Letendre, N., Lethuillier, M., Levin, Y., Leyde, K., Li, A. K. Y., Li, K. L., Li, T. G. F., Li, X., Li, Y., Li, Z., Lihos, A., Lin, C.-Y., Lin, E. T., Lin, L. C. C., Lin, Y. C., Lindsay, C., Linker, S. D., Littenberg, T. B., Liu, A., Liu, G. C., Liu, J., Villarreal, F. L., Llobera-Querol, J., Lo, R. K. L., Locquet, J. P., Loizou, M. R., London, L. T., Longo, A., Lopez, D., Portilla, M. L., Lorenzini, M., Lorenzo-Medina, A., Loriette, V., Lormand, M., Losurdo, G., Lotti, E., IV, T. P. L., Lough, J. D., Loughlin, H. A., Lousto, C. O., Low, N., Lowry, M. J., Lu, N., Lucchesi, L., Lück, H., Lumaca, D., Lundgren, A. P., Lussier, A. W., Ma, L. T., Ma, S., Macas, R., Macedo, A., MacInnis, M., Maciy, R. R., Macleod, D. M., MacMillan, I. A. O., Macquet, A., Macri, D., Maeda, K., Maenaut, S., Magare, S. S., Magee, R. M., Maggio, E., Maggiore, R., Magnozzi, M., Mahesh, M., Maini, M., Majhi, S., Majorana, E., Makarem, C. N., Malakar, D., Malaquias-Reis, J. A., Mali, U., Maliakal, S., Malik, A., Mallick, L., Malz, A., Man, N., Mandic, V., Mangano, V., Mannix, B., Mansell, G. L., Mansingh, G., Manske, M., Mantovani, M., Mapelli, M., Marchesoni, F., Marinelli, C., Pina, D. M., Marion, F., Márka, S., Márka, Z., Markosyan, A. S., Markowitz, A., Maros, E., Marsat, S., Martelli, F., Martin,

I. W., Martin, R. M., Martinez, B. B., Martinez, M., Martinez, V., Martini, A., Martins, J. C., Martynov, D. V., Marx, E. J., Massaro, L., Masserot, A., Masso-Reid, M., Mastrodicasa, M., Mastrogiovanni, S., Matcovich, T., Matiushechkina, M., Matsuyama, M., Mavalvala, N., Maxwell, N., McCarrol, G., McCarthy, R., McClelland, D. E., McCormick, S., McCuller, L., McEachin, S., McElhenny, C., McGhee, G. I., McGinn, J., McGowan, K. B. M., McIver, J., McLeod, A., McRae, T., Meacher, D., Meijer, Q., Melatos, A., Mellaerts, S., Menoni, C. S., Mera, F., Mercer, R. A., Mereni, L., Merfeld, K., Merilh, E. L., Mérou, J. R., Merritt, J. D., Merzougui, M., Messenger, C., Messick, C., Mestichelli, B., Meyer-Conde, M., Meylahn, F., Mhaske, A., Miani, A., Miao, H., Michaloliakos, I., Michel, C., Michimura, Y., Middleton, H., Miller, S. J., Millhouse, M., Milotti, E., Milotti, V., Minenkov, Y., Mio, N., Mir, L. M., Mirasola, L., Miravet-Tenés, M., Miritescu, C. A., Mishra, A. K., Mishra, A., Mishra, C., Mishra, T., Mitchell, A. L., Mitchell, J. G., Mitra, S., Mitrofanov, V. P., Mittleman, R., Miyakawa, O., Miyamoto, S., Miyoki, S., Mo, G., Mobilia, L., Mohapatra, S. R. P., Mohite, S. R., Molina-Ruiz, M., Mondal, C., Mondin, M., Montani, M., Moore, C. J., Moraru, D., More, A., More, S., Moreno, E. A., Moreno, G., Morisaki, S., Moriwaki, Y., Morras, G., Moscatello, A., Mould, M., Mourier, P., Mours, B., Mow-Lowry, C. M., Muciaccia, F., Mukherjee, D., Mukherjee, S., Mukherjee, S., Mukherjee, S., Mukherjee, S., Mukund, N., Mullavey, A., Mullock, H., Munch, J., Mundi, J., Mungioli, C. L., Murakami, Y., Murakoshi, M., Murray, P. G., Muusse, S., Nabari, D., Nadji, S. L., Nagar, A., Nagarajan, N., Nakagaki, K., Nakamura, K., Nakano, H., Nakano, M., Nanadoumgar-Lacroze, D., Nandi, D., Napolano, V., Narayan, P., Nardecchia, I., Narikawa, T., Narola, H., Naticchioni, L., Nayak, R. K., Nela, A., Nelson, A., Nelson, T. J. N., Nery, M., Neunzert, A., Ng, S., Quynh, L. N., Nichols, S. A., Nielsen, A. B., Nieradka, G., Nishino, Y., Nishizawa, A., Nissanke, S., Nitoglia, E., Niu, W., Nocera, F., Norman, M., North, C., Novak, J., Siles, J. F. N., Nuttall, L. K., Obayashi, K., Oberling, J., O'Dell, J., Oertel, M., Offermans, A., Oganesyan, G., Oh, J. J., Oh, K., O'Hanlon, T., Ohashi, M., Ohkawa, M., Ohme, F., Oliveri, R., Omer, R., O'Neal, B., Oohara, K.,

O'Reilly, B., Ormsby, N. D., Orselli, M., O'Shaughnessy, R., O'Shea, S., Oshima, Y., Oshino, S., Osthelder, C., Ota, I., Ottaway, D. J., Ouzriat, A., Overmier, H., Owen, B. J., Pace, A. E., Pagano, R., Page, M. A., Pai, A., Paiella, L., Pal, A., Pal, S., Palaia, M. A., Pálfi, M., Palma, P. P., Palomba, C., Palud, P., Pan, J., Pan, K. C., Panai, R., Panda, P. K., Pandey, S., Pandey, S., Pang, P. T. H., Pannarale, F., Pannone, K. A., Pant, B. C., Panther, F. H., Paoletti, F., Paolone, A., Papadopoulos, A., Papalexakis, E. E., Papalini, L., Papigkiotis, G., Paquis, A., Parisi, A., Park, B. J., Park, J., Parker, W., Pascale, G., Pascucci, D., Pasqualetti, A., Passaquieti, R., Passenger, L., Passuello, D., Patane, O., Pathak, D., Pathak, L., Patra, A., Patricelli, B., Patron, A. S., Patterson, B. G., Paul, K., Paul, S., Payne, E., Pearce, T., Pedraza, M., Pele, A., Arellano, F. E. P., Penn, S., Penuliar, M. D., Perego, A., Pereira, Z., Perez, J. J., Périgois, C., Perna, G., Perreca, A., Perret, J., Perriès, S., Perry, J. W., Pesios, D., Petracca, S., Petrillo, C., Pfeiffer, H. P., Pham, H., Pham, K. A., Phukon, K. S., Phurailatpam, H., Piarulli, M., Piccari, L., Piccinni, O. J., Pichot, M., Piendibene, M., Piergiovanni, F., Pierini, L., Pierra, G., Pierro, V., Pietrzak, M., Pillas, M., Pilo, F., Pinard, L., Pinto, I. M., Pinto, M., Piotrzkowski, B. J., Pirello, M., Pitkin, M. D., Placidi, A., Placidi, E., Planas, M. L., Plastino, W., Plunkett, C., Poggiani, R., Polini, E., Pompili, L., Poon, J., Porcelli, E., Porter, E. K., Posnansky, C., Poulton, R., Powell, J., Pracchia, M., Pradhan, B. K., Pradier, T., Prajapati, A. K., Prasai, K., Prasanna, R., Prasia, P., Pratten, G., Principe, G., Principe, M., Prodi, G. A., Prokhorov, L., Prosperi, P., Prosposito, P., Providence, A. C., Puecher, A., Pullin, J., Punturo, M., Puppo, P., Pürrer, M., Qi, H., Qin, J., Quéméner, G., Quetschke, V., Quinonez, P. J., Rainho, I., Raja, S., Rajan, C., Rajbhandari, B., Ramirez, K. E., Vidal, F. A. R., Ramos-Buades, A., Rana, D., Ranjan, S., Ransom, K., Rapagnani, P., Ratto, B., Ray, A., Raymond, V., Razzano, M., Read, J., Payo, M. R., Regimbau, T., Rei, L., Reid, S., Reitze, D. H., Relton, P., Renzini, A. I., Revenu, B., Reyes, R., Rezaei, A. S., Ricci, F., Ricci, M., Ricciardone, A., Richardson, J. W., Richardson, M., Rijal, A., Riles, K., Riley, H. K., Rinaldi, S., Rittmeyer, J., Robertson, C., Robinet, F., Robinson,

M., Rocchi, A., Rolland, L., Rollins, J. G., Romano, A. E., Romano, R., Romero, A., Romero-Shaw, I. M., Romie, J. H., Ronchini, S., Roocke, T. J., Rosa, L., Rosauer, T. J., Rose, C. A., Rosińska, D., Ross, M. P., Rossello-Sastre, M., Rowan, S., Roy, S., Roy, S. K., Rozza, D., Ruggi, P., Ruhama, N., Morales, E. R., Ruiz-Rocha, K., Sachdev, S., Sadecki, T., Sadiq, J., Saffarieh, P., Safi-Harb, S., Sah, M. R., Saha, S., Sainrat, T., Menon, S. S., Sakai, K., Sakellariadou, M., Sakon, S., Salafia, O. S., Salces-Carcoba, F., Salconi, L., Saleem, M., Salemi, F., Sallé, M., Salunkhe, S. U., Salvador, S., Samajdar, A., Sanchez, A., Sanchez, E. J., Sanchez, J. H., Sanchez, L. E., Sanchis-Gual, N., Sanders, J. R., Sänger, E. M., Santoliquido, F., Sarandrea, F., Saravanan, T. R., Sarin, N., Sarkar, P., Sasaoka, S., Sasli, A., Sassi, P., Sassolas, B., Sathyaprakash, B. S., Sato, R., Sato, Y., Sauter, O., Savage, R. L., Sawada, T., Sawant, H. L., Sayah, S., Scacco, V., Schaetzl, D., Scheel, M., Schiebelbein, A., Schiworski, M. G., Schmidt, P., Schmidt, S., Schnabel, R., Schneewind, M., Schofield, R. M. S., Schouteden, K., Schulte, B. W., Schutz, B. F., Schwartz, E., Scialpi, M., Scott, J., Scott, S. M., Sedas, R. M., Seetharamu, T. C., Seglar-Arroyo, M., Sekiguchi, Y., Sellers, D., Sengupta, A. S., Sentenac, D., Seo, E. G., Seo, J. W., Sequino, V., Serra, M., Servignat, G., Sevrin, A., Shaffer, T., Shah, U. S., Shahriar, M. S., Shaikh, M. A., Shao, L., Sharma, A. K., Sharma, P., Chaudhary, S. S., Shaw, M. R., Shawhan, P., Shcheblanov, N. S., Shikano, Y., Shikauchi, M., Shimode, K., Shinkai, H., Shiota, J., Shirke, S., Shoemaker, D. H., Shoemaker, D. M., Short, R. W., ShyamSundar, S., Sider, A., Siegel, H., Sigg, D., Silenzi, L., Simmonds, M., Singer, L. P., Singh, A., Singh, D., Singh, M. K., Singh, N., Singh, S., Singha, A., Sintes, A. M., Sipala, V., Skliris, V., Slagmolen, B. J. J., Slater, D. A., Slaven-Blair, T. J., Smetana, J., Smith, J. R., Smith, L., Smith, R. J. E., Smith, W. J., Somiya, K., Song, I., Soni, K., Soni, S., Sordini, V., Sorrentino, F., Sotani, H., Southgate, A., Spada, F., Spagnuolo, V., Spencer, A. P., Spera, M., Spinicelli, P., Sprague, C. A., Srivastava, A. K., Stachurski, F., Steer, D. A., Steinle, N., Steinlechner, J., Steinlechner, S., Stergioulas, N., Stevens, P., Stevenson, S. P., Stolzi, F., StPierre, M., Stratta, G., Strong, M. D., Strunk, A., Sturani, R., Stuver, A. L., Suchenek,

M., Sudhagar, S., Sueltmann, N., Suleiman, L., Sullivan, K. D., Sun, J., Sun, L., Sunil, S., Suresh, J., Sutton, B. J., Sutton, P. J., Suzuki, T., Suzuki, Y., Swinkels, B. L., Syx, A., Szczepańczyk, M. J., Szewczyk, P., Tacca, M., Tagoshi, H., Tait, S. C., Takahashi, H., Takahashi, R., Takamori, A., Takase, T., Takatani, K., Takeda, H., Takeshita, K., Talbot, C., Tamaki, M., Tamanini, N., Tanabe, D., Tanaka, K., Tanaka, S. J., Tanaka, T., Tang, D., Tanioka, S., Tanner, D. B., Tanner, W., Tao, L., Tapia, R. D., Martín, E. N. T. S., Tarafder, R., Taranto, C., Taruya, A., Tasson, J. D., Tau, J. G., Tenorio, R., Themann, H., Theodoropoulos, A., Thirugnanasambandam, M. P., Thomas, L. M., Thomas, M., Thomas, P., Thompson, J. E., Thondapu, S. R., Thorne, K. A., Thrane, E., Tissino, J., Tiwari, A., Tiwari, P., Tiwari, S., Tiwari, V., Todd, M. R., Toivonen, A. M., Toland, K., Tolley, A. E., Tomaru, T., Tomita, K., Tommasini, V., Tomura, T., Tong, H., Tong-Yu, C., Toriyama, A., Toropov, N., Torres-Forné, A., Torrie, C. I., Toscani, M., e Melo, I. T., Tournefier, E., Nery, M. T., Trapananti, A., Travasso, F., Traylor, G., Trejo, C., Trevor, M., Tringali, M. C., Tripathee, A., Troian, G., Trovato, A., Trozzo, L., Trudeau, R. J., Tsang, T. T. L., Tsuchida, S., Tsukada, L., Turbang, K., Turconi, M., Turski, C., Ubach, H., Uchikata, N., Uchiyama, T., Udall, R. P., Uehara, T., Uematsu, M., Ueno, S., Undheim, V., Ushiba, T., Vacatello, M., Vahlbruch, H., Vajente, G., Vajpeyi, A., Valdes, G., Valencia, J., Valentini, A. F., Valentini, M., Vallejo-Peña, S. A., Vallero, S., Valsan, V., van Bakel, N., van Beuzekom, M., van Dael, M., van den Brand, J. F. J., Broeck, C. V. D., Vander-Hyde, D. C., van der Sluys, M., de Walle, A. V., van Dongen, J., Vandra, K., van Haevermaet, H., van Heijningen, J. V., Hove, P. V., Vanier, J., VanKeuren, M., Vanosky, J., van Putten, M. H. P. M., Ranst, Z. V., van Remortel, N., Vardaro, M., Vargas, A. F., Varghese, J. J., Varma, V., Vazquez, A. N., Vecchio, A., Vedovato, G., Veitch, J., Veitch, P. J., Venikoudis, S., Venneberg, J., Verdier, P., Vereecken, M., Verkindt, D., Verma, B., Verma, P., Verma, Y., Vermeulen, S. M., Vetrano, F., Veutro, A., Vibhute, A. M., Viceré, A., Vidyant, S., Viets, A. D., Vijaykumar, A., Vilkha, A., Villa-Ortega, V., Vincent, E. T., Vinet, J. Y., Viret, S., Virtuoso, A., Vitale, S., Vives, A., Vocca, H., Voigt, D., von Reis,

E. R. G., von Wrangel, J. S. A., Vujeva, L., Vyatchanin, S. P., Wack, J., Wade, L. E., Wade, M., Wagner, K. J., Wajid, A., Walker, M., Wallace, G. S., Wallace, L., Wang, E. J., Wang, H., Wang, J. Z., Wang, W. H., Wang, Y. F., Wang, Z., Waratkar, G., Warner, J., Was, M., Washimi, T., Washington, N. Y., Watarai, D., Wayt, K. E., Weaver, B. R., Weaver, B., Weaving, C. R., Webster, S. A., Weickhardt, N. L., Weinert, M., Weinstein, A. J., Weiss, R., Wellmann, F., Wen, L., Weßels, P., Wette, K., Whelan, J. T., Whiting, B. F., Whittle, C., Wickens, E. G., Wildberger, J. B., Wilken, D., Willadsen, D. J., Willetts, K., Williams, D., Williams, M. J., Williams, N. S., Willis, J. L., Willke, B., Wils, M., Winborn, C. W., Winterflood, J., Wipf, C. C., Woan, G., Woehler, J., Wolfe, N. E., Wong, H. T., Wong, I. C. F., Wright, J. L., Wright, M., Wu, C., Wu, D. S., Wu, H., Wu, T. Y., Wuchner, E., Wysocki, D. M., Xu, V. A., Xu, Y., Yadav, N., Yamamoto, H., Yamamoto, K., Yamamoto, T. S., Yamamoto, T., Yamamura, S., Yamazaki, R., Yan, T., Yang, F. W., Yang, F., Yang, K. Z., Yang, Y., Yarbrough, Z., Yasui, H., Yeh, S. W., Yelikar, A. B., Yin, X., Yokoyama, J., Yokozawa, T., Yoo, J., Yu, H., Yuan, S., Yuzurihara, H., Zadrożny, A., Zanolin, M., Zeeshan, M., Zelenova, T., Zendri, J. P., Zeoli, M., Zerrad, M., Zevin, M., Zhang, A. C., Zhang, L., Zhang, R., Zhang, T., Zhang, Y., Zhao, C., Zhao, Y., Zhao, Y., Zheng, Y., Zhong, H., Zhou, R., Zhu, X. J., Zhu, Z. H., Zimmerman, A. B., Zucker, M. E., and Zweizig, J. (2025a). Gwtc-4.0: Population properties of merging compact binaries.

Collaboration, T. L. S., the Virgo Collaboration, the KAGRA Collaboration, Abac, A. G., Abouelfettouh, I., Acernese, F., Ackley, K., Adhicary, S., Adhikari, D., Adhikari, N., Adhikari, R. X., Adkins, V. K., Afroz, S., Agarwal, D., Agathos, M., Abchouyeh, M. A., Aguiar, O. D., Ahmadzadeh, S., Aiello, L., Ain, A., Ajith, P., Akcay, S., Akutsu, T., Albanesi, S., Alfaidi, R. A., Al-Jodah, A., Alléné, C., Allocca, A., Al-Shammari, S., Altin, P. A., Alvarez-Lopez, S., Amarasinghe, O., Amato, A., Amra, C., Ananyeva, A., Anderson, S. B., Anderson, W. G., Andia, M., Ando, M., Andrade, T., Andrés-Carcasona, M., Andrić, T., Anglin, J., Ansoldi, S., Antelis, J. M., Antier, S., Aoumi, M., Appavuravther, E. Z., Appert, S., Apple, S. K., Arai, K., Araya, A., Araya, M. C., Sedda, M. A., Areeda,

J. S., Argianas, L., Aritomi, N., Armato, F., Armstrong, S., Arnaud, N., Arogeti, M., Aronson, S. M., Ashton, G., Aso, Y., Assiduo, M., de Souza Melo, S. A., Aston, S. M., Astone, P., Attadio, F., Aubin, F., AultONeal, K., Avallone, G., Babak, S., Badaracco, F., Badger, C., Bae, S., Bagnasco, S., Bagui, E., Baiotti, L., Bajpai, R., Baka, T., Baker, T., Ball, M., Ballardin, G., Ballmer, S. W., Banagiri, S., Banerjee, B., Bankar, D., Baptiste, T. M., Baral, P., Barayoga, J. C., Barish, B. C., Barker, D., Barman, N., Barneo, P., Barone, F., Barr, B., Barsotti, L., Barsuglia, M., Barta, D., Bartoletti, A. M., Barton, M. A., Bartos, I., Basak, S., Basalaev, A., Bassiri, R., Basti, A., Bates, D. E., Bawaj, M., Baxi, P., Bayley, J. C., Baylor, A. C., II, P. A. B., Bazzan, M., Bedakihale, V. M., Beirnaert, F., Bejger, M., Belardinelli, D., Bell, A. S., Bellie, D. S., Bellizzi, L., Benoit, W., Bentara, I., Bentley, J. D., Yaala, M. B., Bera, S., Bergamin, F., Berger, B. K., Bernuzzi, S., Beroiz, M., Berry, C. P. L., Bersanetti, D., Bertolini, A., Betzwieser, J., Beveridge, D., Bevilacqua, G., Bevins, N., Bhandare, R., Bhat, S. A., Bhatt, R., Bhattacharjee, D., Bhaumik, S., Bhowmick, S., Biancalana, V., Bianchi, A., Bilenko, I. A., Billingsley, G., Binetti, A., Bini, S., Binu, C., Birnholtz, O., Biscoveanu, S., Bisht, A., Bitossi, M., Bizouard, M. A., Blaber, S., Blackburn, J. K., Blagg, L. A., Blair, C. D., Blair, D. G., Bobba, F., Bode, N., Boileau, G., Boldrini, M., Bolingbroke, G. N., Bolliand, A., Bonavena, L. D., Bondarescu, R., Bondu, F., Bonilla, E., Bonilla, M. S., Bonino, A., Bonnand, R., Booker, P., Borchers, A., Borhanian, S., Boschi, V., Bose, S., Bossilkov, V., Boudon, A., Bozzi, A., Bradaschia, C., Brady, P. R., Branch, A., Branchesi, M., Braun, I., Briant, T., Brillet, A., Brinkmann, M., Brockill, P., Brockmueller, E., Brooks, A. F., Brown, B. C., Brown, D. D., Brozzetti, M. L., Brunett, S., Bruno, G., Bruntz, R., Bryant, J., Bu, Y., Bucci, F., Buchanan, J., Bulashenko, O., Bulik, T., Bulten, H. J., Buonanno, A., Burtnyk, K., Buscicchio, R., Buskulic, D., Buy, C., Byer, R. L., Davies, G. S. C., Cabras, G., Cabrita, R., Cáceres-Barbosa, V., Cadonati, L., Cagnoli, G., Cahillane, C., Calafat, A., Bustillo, J. C., Callister, T. A., Calloni, E., Canepa, M., Santoro, G. C., Cannon, K. C., Cao, H., Capistran, L. A., Capocasa, E., Capote, E., Capurri, G., Cara-

pella, G., Carbognani, F., Carlassara, M., Carlin, J. B., Carlson, T. K., Carney, M. F., Carpinelli, M., Carrillo, G., Carter, J. J., Carullo, G., Diaz, J. C., Casentini, C., Castro-Lucas, S. Y., Caudill, S., Cavaglià, M., Cavalieri, R., Cella, G., Cerdá-Durán, P., Cesarini, E., Chaibi, W., Chakraborty, P., Chakraborty, S., Subrahmanya, S. C., Chan, J. C. L., Chan, M., Chang, R. J., Chao, S., Charlton, E. L., Charlton, P., Chassande-Mottin, E., Chatterjee, C., Chatterjee, D., Chatterjee, D., Chaturvedi, M., Chaty, S., Chatziioannou, K., Checchia, C., Chen, A., Chen, A. H. Y., Chen, D., Chen, H., Chen, H. Y., Chen, S., Chen, Y., Chen, Y., Chen, Y., Cheng, H. P., Chessa, P., Cheung, H. T., Cheung, S. Y., Chiadini, F., Chiarini, G., Chierici, R., Chincarini, A., Chiofalo, M. L., Chiummo, A., Chou, C., Choudhary, S., Christensen, N., Chua, S. S. Y., Chugh, P., Ciani, G., Ciecielag, P., Cieślar, M., Cifaldi, M., Ciolfi, R., Clara, F., Clark, J. A., Clarke, J., Clarke, T. A., Clearwater, P., Clesse, S., Clyne, S. M., Coccia, E., Codazzo, E., Cohadon, P. F., Colace, S., Colangeli, E., Colleoni, M., Collette, C. G., Collins, J., Colloms, S., Colombo, A., Compton, C. M., Connolly, G., Conti, L., Corbitt, T. R., Cordero-Carrión, I., Corezzi, S., Cornish, N. J., Corsi, A., Cortese, S., Cottingham, R., Coughlin, M. W., Couineaux, A., Coulon, J. P., Coupechoux, J. F., Couvares, P., Coward, D. M., Coyne, R., Craig, K., Creighton, J. D. E., Creighton, T. D., Cremonese, P., Criswell, A. W., Crook, S., Crouch, R., Csizmazia, J., Cudell, J. R., Cullen, T. J., Cumming, A., Cuoco, E., Cusinato, M., Dabadie, P., Conceição, L. V. D., Canton, T. D., Dall'Osso, S., Pra, S. D., Dálya, G., D'Angelo, B., Danilishin, S., D'Antonio, S., Danzmann, K., Darroch, K. E., Dartez, L. P., Dasgupta, A., Datta, S., Dattilo, V., Daumas, A., Davari, N., Dave, I., Davenport, A., Davier, M., Davies, T. F., Davis, D., Davis, L., Davis, M. C., Davis, P., Dax, M., Bolle, J. D., Deenadayalan, M., Degallaix, J., Deka, U., Laurentis, M. D., Deléglise, S., Lillo, F. D., Dell'Aquila, D., Valle, F. D., Pozzo, W. D., Marco, F. D., Demasi, G., Matteis, F. D., D'Emilio, V., Demos, N., Depasse, A., DePergola, N., Pietri, R. D., Rosa, R. D., Rossi, C. D., Desai, M., DeSalvo, R., DeSimone, A., Simone, R. D., Dhani, A., Diab, R., Díaz, M. C., Cesare, M. D., Dideron, G., Didio, N. A., Dietrich, T., Fiore, L. D., Fronzo,

C. D., Giovanni, M. D., Girolamo, T. D., Diksha, D., Michele, A. D., Ding, J., Pace, S. D., Palma, I. D., Renzo, F. D., Divyajyoti, Dmitriev, A., Doctor, Z., Doerksen, N., Dohmen, E., Dominguez, D., D'Onofrio, L., Donovan, F., Dooley, K. L., Dooney, T., Doravari, S., Dorosh, O., Drago, M., Driggers, J. C., Ducoin, J. G., Dunn, L., Dupletsa, U., D'Urso, D., Duval, H., Dwyer, S. E., Eassa, C., Ebersold, M., Eckhardt, T., Eddolls, G., Edelman, B., Edo, T. B., Edy, O., Effler, A., Eichholz, J., Einsle, H., Eisenmann, M., Eisenstein, R. A., Ejlli, A., Emma, M., Endo, K., Enficiaud, R., Engl, A. J., Errico, L., Espinosa, R., Esposito, M., Essick, R. C., Estellés, H., Etzel, T., Evans, M., Evstafyeva, T., Ewing, B. E., Ezquiaga, J. M., Fabrizi, F., Faedi, F., Fafone, V., Fairhurst, S., Farah, A. M., Farr, B., Farr, W. M., Favaro, G., Favata, M., Fays, M., Fazio, M., Feicht, J., Fejer, M. M., Felicetti, R., Fenyvesi, E., Ferguson, D. L., Fernandes, T., Fernando, D., Ferraiuolo, S., Ferrante, I., Ferreira, T. A., Fidecaro, F., Figura, P., Fiori, A., Fiori, I., Fishbach, M., Fisher, R. P., Fittipaldi, R., Fiumara, V., Flaminio, R., Fleischer, S. M., Fleming, L. S., Floden, E., Fong, H., Font, J. A., Foo, C., Fornal, B., Forsyth, P. W. F., Franceschetti, K., Franchini, N., Frasca, S., Frasconi, F., Mascioli, A. F., Frei, Z., Freise, A., Freitas, O., Frey, R., Frischhertz, W., Fritschel, P., Frolov, V. V., Fronzé, G. G., Fuentes-Garcia, M., Fujii, S., Fujimori, T., Fulda, P., Fyffe, M., Gadre, B., Gair, J. R., Galaudage, S., Galdi, V., Gallagher, H., Gallego, B., Gamba, R., Gamboa, A., Ganapathy, D., Ganguly, A., Garaventa, B., García-Bellido, J., Núñez, C. G., García-Quirós, C., Gardner, J. W., Gardner, K. A., Gargiulo, J., Garron, A., Garufi, F., Garver, P. A., Gasbarra, C., Gateley, B., Gautier, F., Gayathri, V., Gayer, T., Gemme, G., Gennai, A., Gennari, V., George, J., George, R., Gerberding, O., Gergely, L., Ghosh, A., Ghosh, S., Ghosh, S., Ghosh, S., Ghosh, S., Ghosh, T., Giaime, J. A., Giardina, K. D., Gibson, D. R., Gibson, D. T., Gier, C., Gkaitatzis, S., Glanzer, J., Glotin, F., Godfrey, J., Godwin, P., Goettel, A. S., Goetz, E., Golomb, J., Lopez, S. G., Goncharov, B., Gong, Y., González, G., Goodarzi, P., Goode, S., Goodwin-Jones, A. W., Gosselin, M., Gouaty, R., Gould, D. W., Govorkova, K., Goyal, S., Grace, B., Grado, A., Graham, V., Granados, A. E., Granata, M., Granata,

V., Gras, S., Grassia, P., Gray, A., Gray, C., Gray, R., Greco, G., Green, A. C., Green, S. M., Green, S. R., Gretarsson, A. M., Gretarsson, E. M., Griffith, D., Griffiths, W. L., Griggs, H. L., Grignani, G., Grimaud, C., Grote, H., Grunewald, S., Guerra, D., Guetta, D., Guidi, G. M., Guimaraes, A. R., Gulati, H. K., Gulminelli, F., Gunny, A. M., Guo, H., Guo, W., Guo, Y., Gupta, A., Gupta, A., Gupta, I., Gupta, N. C., Gupta, P., Gupta, S. K., Gupta, T., Gupta, V., Gupte, N., Gurs, J., Gutierrez, N., Guzman, F., Haba, D., Haberland, M., Haino, S., Hall, E. D., Hamburg, R., Hamilton, E. Z., Hammond, G., Han, W. B., Haney, M., Hanks, J., Hanna, C., Hannam, M. D., Hannuksela, O. A., Hanselman, A. G., Hansen, H., Hanson, J., Harada, R., Hardison, A. R., Harikumar, S., Haris, K., Harmark, T., Harms, J., Harry, G. M., Harry, I. W., Hart, J., Haskell, B., Haster, C. J., Haughian, K., Hayakawa, H., Hayama, K., Hayes, R., Heintze, M. C., Heinze, J., Heinzel, J., Heitmann, H., Heffernan, A., Hellman, F., Helmling-Cornell, A. F., Hemming, G., Henderson-Sapir, O., Hendry, M., Heng, I. S., Hennig, M. H., Henshaw, C., Heurs, M., Hewitt, A. L., Heyns, J., Higginbotham, S., Hild, S., Hill, S., Himemoto, Y., Hirata, N., Hirose, C., Hochheim, S., Hofman, D., Holland, N. A., Holz, D. E., Honet, L., Hong, C., Hoshino, S., Hough, J., Hourihane, S., Howard, N. T., Howell, E. J., Hoy, C. G., Hrishikesh, C. A., Hsieh, H. F., Hsieh, H. Y., Hsiung, C., Hsu, W. F., Hu, Q., Huang, H. Y., Huang, Y., Huang, Y. T., Huddart, A. D., Hughey, B., Hui, D. C. Y., Hui, V., Husa, S., Huxford, R., Iampieri, L., Iandolo, G. A., Ianni, M., Ierardi, A., Iess, A., Imafuku, H., Inayoshi, K., Inoue, Y., Iorio, G., Iosif, P., Iqbal, M. H., Irwin, J., Ishikawa, R., Isi, M., Itoh, Y., Iwanaga, H., Iwaya, M., Iyer, B. R., Jacquet, C., Jacquet, P. E., Jadhav, S. J., Jadhav, S. P., Jain, T., James, A. L., James, P. A., Jamshidi, R., Jan, A., Jani, K., Janquart, J., Janssens, K., Janthalur, N. N., Jaraba, S., Jaranowski, P., Jaume, R., Javed, W., Jennings, A., Jia, W., Jiang, J., Jin, S. J., Johanson, C., Johns, G. R., Johnson, N. A., Johnson-McDaniel, N. K., Johnston, M. C., Johnston, R., Johny, N., Jones, D. H., Jones, D. I., Jones, E. J., Jones, R., Jose, S., Joshi, P., Joshi, S. K., Ju, J., Ju, L., Jung, K., Junker, J., Juste, V., Kabagoz, H. B., Kajita, T., Kaku, I.,

Kalogera, V., Kalomenopoulos, M., Kamiizumi, M., Kanda, N., Kandhasamy, S., Kang, G., Kannachel, N. C., Kanner, J. B., Kapadia, S. J., Kapasi, D. P., Karat, S., Kashyap, R., Kasprzack, M., Kastaun, W., Kato, T., Katsavounidis, E., Katzman, W., Kaushik, R., Kawabe, K., Kawamoto, R., Kazemi, A., Keitel, D., Kennington, J., Kesharwani, R., Key, J. S., Khadela, R., Khadka, S., Khalili, F. Y., Khan, F., Khan, I., Khanam, T., Khursheed, M., Khusid, N. M., Kiendrebeogo, W., Kijbunchoo, N., Kim, C., Kim, J. C., Kim, K., Kim, M. H., Kim, S., Kim, Y. M., Kimball, C., Kinley-Hanlon, M., Kinnear, M., Kissel, J. S., Klimenko, S., Knee, A. M., Knust, N., Kobayashi, K., Koch, P., Koehlenbeck, S. M., Koekoek, G., Kohri, K., Kokeyama, K., Koley, S., Kolitsidou, P., Komori, K., Kong, A. K. H., Kontos, A., Korobko, M., Kossak, R. V., Kou, X., Koushik, A., Kouvatsos, N., Kovalam, M., Kozak, D. B., Kranzhoff, S. L., Kringel, V., Krishnendu, N. V., Królak, A., Kruska, K., Kubisz, J., Kuehn, G., Kulkarni, S., Ramamohan, A. K., Kumar, A., Kumar, P., Kumar, P., Kumar, R., Kumar, R., Kume, J., Kuns, K., Kuntimaddi, N., Kuroyanagi, S., Kuwahara, S., Kwak, K., Kwan, K., Kwok, J., Lacaille, G., Lagabbe, P., Laghi, D., Lai, S., Lalande, E., Lalleman, M., Lalremruati, P. C., Landry, M., Lane, B. B., Lang, R. N., Lange, J., Langgin, R., Lantz, B., Rana, A. L., Rosa, I. L., Larsen, J., Lartaux-Vollard, A., Lasky, P. D., Lawrence, J., Lawrence, M. N., Laxen, M., Lazarte, C., Lazzarini, A., Lazzaro, C., Leaci, P., Leali, L., Lecoeuche, Y. K., Lee, H. M., Lee, H. W., Lee, J., Lee, K., Lee, R. K., Lee, R., Lee, S., Lee, S., Lee, Y., Legred, I. N., Lehmann, J., Lehner, L., Jean, M. L., Lemaître, A., Lenti, M., Leonardi, M., Lequime, M., Leroy, N., Lesovsky, M., Letendre, N., Lethuillier, M., Levin, Y., Leyde, K., Li, A. K. Y., Li, K. L., Li, T. G. F., Li, X., Li, Y., Li, Z., Lihos, A., Lin, C.-Y., Lin, E. T., Lin, L. C. C., Lin, Y. C., Lindsay, C., Linker, S. D., Littenberg, T. B., Liu, A., Liu, G. C., Liu, J., Villarreal, F. L., Llobera-Querol, J., Lo, R. K. L., Locquet, J. P., Loizou, M. R., London, L. T., Longo, A., Lopez, D., Portilla, M. L., Lorenzo-Medina, A., Loriette, V., Lormand, M., Losurdo, G., Lotti, E., IV, T. P. L., Lough, J. D., Loughlin, H. A., Lousto, C. O., Low, N., Lowry, M. J., Lu, N., Lucchesi, L., Lück, H., Lumaca, D., Lundgren, A. P., Lussier, A. W., Ma, L. T.,

Ma, S., Macas, R., Macedo, A., MacInnis, M., Maciy, R. R., Macleod, D. M., MacMillan, I. A. O., Macquet, A., Macri, D., Maeda, K., Maenaut, S., Magare, S. S., Magee, R. M., Maggio, E., Maggiore, R., Magnozzi, M., Mahesh, M., Maini, M., Majhi, S., Majorana, E., Makarem, C. N., Malakar, D., Malaquias-Reis, J. A., Mali, U., Maliakal, S., Malik, A., Mallick, L., Malz, A., Man, N., Mandic, V., Mangano, V., Mannix, B., Mansell, G. L., Mansingh, G., Manske, M., Mantovani, M., Mapelli, M., Marchesoni, F., Marinelli, C., Pina, D. M., Marion, F., Márka, S., Márka, Z., Markosyan, A. S., Markowitz, A., Maros, E., Marsat, S., Martelli, F., Martin, I. W., Martin, R. M., Martinez, B. B., Martinez, M., Martinez, V., Martini, A., Martins, J. C., Martynov, D. V., Marx, E. J., Massaro, L., Masserot, A., Masso-Reid, M., Mastrodicasa, M., Mastrogiovanni, S., Matcovich, T., Matiushechkina, M., Matsuyama, M., Mavalvala, N., Maxwell, N., McCarrol, G., McCarthy, R., McClelland, D. E., McCormick, S., McCuller, L., McEachin, S., McElhenny, C., McGhee, G. I., McGinn, J., McGowan, K. B. M., McIver, J., McLeod, A., McRae, T., Meacher, D., Meijer, Q., Melatos, A., Melching, M., Mellaerts, S., Menoni, C. S., Mera, F., Mercer, R. A., Mereni, L., Merfeld, K., Merilh, E. L., Mérou, J. R., Merritt, J. D., Merzougui, M., Messenger, C., Messick, C., Mestichelli, B., Meyer-Conde, M., Meylahn, F., Mhaske, A., Miani, A., Miao, H., Michaloliakos, I., Michel, C., Michimura, Y., Middleton, H., Miller, S. J., Millhouse, M., Milotti, E., Milotti, V., Minenkov, Y., Mio, N., Mir, L. M., Mirasola, L., Miravet-Tenés, M., Miritescu, C. A., Mishra, A. K., Mishra, A., Mishra, C., Mishra, T., Mitchell, A. L., Mitchell, J. G., Mitra, S., Mitrofanov, V. P., Mittleman, R., Miyakawa, O., Miyamoto, S., Miyoki, S., Mo, G., Mobilia, L., Mohapatra, S. R. P., Mohite, S. R., Molina-Ruiz, M., Mondal, C., Mondin, M., Montani, M., Moore, C. J., Moraru, D., More, A., More, S., Moreno, E. A., Moreno, G., Morisaki, S., Moriwaki, Y., Morras, G., Moscatello, A., Mould, M., Mourier, P., Mours, B., Mow-Lowry, C. M., Muciaccia, F., Mukherjee, D., Mukherjee, S., Mukherjee, S., Mukherjee, S., Mukherjee, S., Mukund, N., Mullavey, A., Mullock, H., Munch, J., Mundi, J., Mungioli, C. L., Murakami, Y., Murakoshi, M., Murray, P. G., Muusse, S., Nabari, D., Nadji, S. L., Nagar,

A., Nagarajan, N., Nakagaki, K., Nakamura, K., Nakano, H., Nakano, M., Nanadoumgar-Lacroze, D., Nandi, D., Napolano, V., Narayan, P., Nardecchia, I., Narikawa, T., Narola, H., Naticchioni, L., Nayak, R. K., Nela, A., Nelson, A., Nelson, T. J. N., Nery, M., Neunzert, A., Ng, S., Quynh, L. N., Nichols, S. A., Nielsen, A. B., Nieradka, G., Nishino, Y., Nishizawa, A., Nissanke, S., Nitoglia, E., Niu, W., Nocera, F., Norman, M., North, C., Novak, J., Siles, J. F. N., Nuttall, L. K., Obayashi, K., Oberling, J., O'Dell, J., Oertel, M., Offermans, A., Oganesyan, G., Oh, J. J., Oh, K., O'Hanlon, T., Ohashi, M., Ohkawa, M., Ohme, F., Oliveri, R., Omer, R., O'Neal, B., Oohara, K., O'Reilly, B., Oram, R., Ormsby, N. D., Orselli, M., O'Shaughnessy, R., O'Shea, S., Oshima, Y., Oshino, S., Osthelder, C., Ota, I., Ottaway, D. J., Ouzriat, A., Overmier, H., Owen, B. J., Pace, A. E., Pagano, R., Page, M. A., Pai, A., Paiella, L., Pal, A., Pal, S., Palaia, M. A., Pálfi, M., Palma, P. P., Palomba, C., Palud, P., Pan, J., Pan, K. C., Panai, R., Panda, P. K., Pandey, S., Pandey, S., Pang, P. T. H., Pannarale, F., Pannone, K. A., Pant, B. C., Panther, F. H., Paoletti, F., Paolone, A., Papadopoulos, A., Papalexakis, E. E., Papalini, L., Papigkiotis, G., Paquis, A., Parisi, A., Park, B. J., Park, J., Parker, W., Pascale, G., Pascucci, D., Pasqualetti, A., Passaquieti, R., Passenger, L., Passuello, D., Patane, O., Pathak, D., Pathak, L., Patra, A., Patricelli, B., Patron, A. S., Patterson, B. G., Paul, K., Paul, S., Payne, E., Pearce, T., Pedraza, M., Pele, A., Arellano, F. E. P., Penn, S., Penuliar, M. D., Perego, A., Pereira, Z., Perez, J. J., Périgois, C., Perna, G., Perreca, A., Perret, J., Perriès, S., Perry, J. W., Pesios, D., Petracca, S., Petrillo, C., Pfeiffer, H. P., Pham, H., Pham, K. A., Phukon, K. S., Phurailatpam, H., Piarulli, M., Piccari, L., Piccinni, O. J., Pichot, M., Piendibene, M., Piergiovanni, F., Pierini, L., Pierra, G., Pierro, V., Pietrzak, M., Pillas, M., Pilo, F., Pinard, L., Pinto, I. M., Pinto, M., Piotrzkowski, B. J., Pirello, M., Pitkin, M. D., Placidi, A., Placidi, E., Planas, M. L., Plastino, W., Plunkett, C., Poggiani, R., Polini, E., Pompili, L., Poon, J., Porcelli, E., Porter, E. K., Posnansky, C., Poulton, R., Powell, J., Pracchia, M., Pradhan, B. K., Pradier, T., Prajapati, A. K., Prasai, K., Prasanna, R., Prasia, P., Pratten, G., Principe, G., Principe, M., Prodi, G. A., Prokhorov,

L., Prosperi, P., Prosposito, P., Providence, A. C., Puecher, A., Pullin, J., Punturo, M., Puppo, P., Pürrer, M., Qi, H., Qin, J., Quéméner, G., Quetschke, V., Quinonez, P. J., Raab, F. J., Rainho, I., Raja, S., Rajan, C., Rajbhandari, B., Ramirez, K. E., Vidal, F. A. R., Ramos-Buades, A., Rana, D., Ranjan, S., Ransom, K., Rapagnani, P., Ratto, B., Ray, A., Raymond, V., Razzano, M., Read, J., Payo, M. R., Regimbau, T., Rei, L., Reid, S., Reitze, D. H., Relton, P., Renzini, A. I., Revenu, B., Reyes, R., Rezaei, A. S., Ricci, F., Ricci, M., Ricciardone, A., Richardson, J. W., Richardson, M., Rijal, A., Riles, K., Riley, H. K., Rinaldi, S., Rittmeyer, J., Robertson, C., Robinet, F., Robinson, M., Rocchi, A., Rolland, L., Rollins, J. G., Romano, A. E., Romano, R., Romero, A., Romero-Shaw, I. M., Romie, J. H., Ronchini, S., Roocke, T. J., Rosa, L., Rosauer, T. J., Rose, C. A., Rosińska, D., Ross, M. P., Rossello-Sastre, M., Rowan, S., Roy, S., Roy, S. K., Rozza, D., Ruggi, P., Ruhama, N., Morales, E. R., Ruiz-Rocha, K., Sachdev, S., Sadecki, T., Sadiq, J., Saffarieh, P., Safi-Harb, S., Sah, M. R., Saha, S., Sainrat, T., Menon, S. S., Sakai, K., Sakellariadou, M., Sakon, S., Salafia, O. S., Salces-Carcoba, F., Salconi, L., Saleem, M., Salemi, F., Sallé, M., Salunkhe, S. U., Salvador, S., Samajdar, A., Sanchez, A., Sanchez, E. J., Sanchez, J. H., Sanchez, L. E., Sanchis-Gual, N., Sanders, J. R., Sänger, E. M., Santoliquido, F., Sarandrea, F., Saravanan, T. R., Sarin, N., Sarkar, P., Sasaoka, S., Sasli, A., Sassi, P., Sassolas, B., Sathyaprakash, B. S., Sato, R., Sato, Y., Sauter, O., Savage, R. L., Sawada, T., Sawant, H. L., Sayah, S., Scacco, V., Schaetzl, D., Scheel, M., Schiebelbein, A., Schiworski, M. G., Schmidt, P., Schmidt, S., Schnabel, R., Schneewind, M., Schofield, R. M. S., Schouteden, K., Schulte, B. W., Schutz, B. F., Schwartz, E., Scialpi, M., Scott, J., Scott, S. M., Sedas, R. M., Seetharamu, T. C., Seglar-Arroyo, M., Sekiguchi, Y., Sellers, D., Sengupta, A. S., Sentenac, D., Seo, E. G., Seo, J. W., Sequino, V., Serra, M., Servignat, G., Sevrin, A., Shaffer, T., Shah, U. S., Shahriar, M. S., Shaikh, M. A., Shao, L., Sharma, A., Sharma, A. K., Sharma, P., Chaudhary, S. S., Shaw, M. R., Shawhan, P., Shcheblanov, N. S., Shikano, Y., Shikauchi, M., Shimode, K., Shinkai, H., Shiota, J., Shirke, S., Shoemaker, D. H., Shoemaker, D. M., Short, R. W., ShyamSundar,

S., Sider, A., Siegel, H., Sigg, D., Silenzi, L., Simmonds, M., Singer, L. P., Singh, A., Singh, D., Singh, M. K., Singh, N., Singh, S., Singha, A., Sintes, A. M., Sipala, V., Skliris, V., Slagmolen, B. J. J., Slater, D. A., Slaven-Blair, T. J., Smetana, J., Smith, J. R., Smith, L., Smith, R. J. E., Smith, W. J., Somiya, K., Song, I., Soni, K., Soni, S., Sordini, V., Sorrentino, F., Sotani, H., Southgate, A., Spada, F., Spagnuolo, V., Spencer, A. P., Spera, M., Spinicelli, P., Sprague, C. A., Srivastava, A. K., Stachurski, F., Steer, D. A., Steinle, N., Steinlechner, J., Steinlechner, S., Stergioulas, N., Stevens, P., Stevenson, S. P., Stolzi, F., StPierre, M., Stratta, G., Strong, M. D., Strunk, A., Sturani, R., Stuver, A. L., Suchenek, M., Sudhagar, S., Sueltmann, N., Suleiman, L., Sullivan, J. M., Sullivan, K. D., Sun, J., Sun, L., Sunil, S., Suresh, J., Sutton, B. J., Sutton, P. J., Suzuki, T., Suzuki, Y., Swinkels, B. L., Syx, A., Szczepańczyk, M. J., Szewczyk, P., Tacca, M., Tagoshi, H., Tait, S. C., Takahashi, H., Takahashi, R., Takamori, A., Takase, T., Takatani, K., Takeda, H., Takeshita, K., Talbot, C., Tamaki, M., Tamanini, N., Tanabe, D., Tanaka, K., Tanaka, S. J., Tanaka, T., Tang, D., Tanioka, S., Tanner, D. B., Tanner, W., Tao, L., Tapia, R. D., Martín, E. N. T. S., Tarafder, R., Taranto, C., Taruya, A., Tasson, J. D., Tau, J. G., Tenorio, R., Themann, H., Theodoropoulos, A., Thirugnanasambandam, M. P., Thomas, L. M., Thomas, M., Thomas, P., Thompson, J. E., Thondapu, S. R., Thorne, K. A., Thrane, E., Tibrewal, S., Tissino, J., Tiwari, A., Tiwari, P., Tiwari, S., Tiwari, V., Todd, M. R., Toivonen, A. M., Toland, K., Tolley, A. E., Tomaru, T., Tomita, K., Tommasini, V., Tomura, T., Tong, H., Tong-Yu, C., Toriyama, A., Toropov, N., Torres-Forné, A., Torrie, C. I., Toscani, M., e Melo, I. T., Tournefier, E., Nery, M. T., Trapananti, A., Travasso, F., Traylor, G., Trejo, C., Trevor, M., Tringali, M. C., Tripathee, A., Troian, G., Trovato, A., Trozzo, L., Trudeau, R. J., Tsang, T. T. L., Tsuchida, S., Tsukada, L., Turbang, K., Turconi, M., Turski, C., Ubach, H., Uchikata, N., Uchiyama, T., Udall, R. P., Uehara, T., Uematsu, M., Ueno, S., Undheim, V., Ushiba, T., Vacatello, M., Vahlbruch, H., Vajente, G., Vajpeyi, A., Valdes, G., Valencia, J., Valentini, A. F., Valentini, M., Vallejo-Peña, S. A., Vallero, S., Valsan, V., van Bakel, N., van Beuzekom, M., van Dael,

M., van den Brand, J. F. J., Broeck, C. V. D., Vander-Hyde, D. C., van der Sluys, M., de Walle, A. V., van Dongen, J., Vandra, K., van Haevermaet, H., van Heijningen, J. V., Hove, P. V., Vanier, J., VanKeuren, M., Vanosky, J., van Putten, M. H. P. M., Ranst, Z. V., van Remortel, N., Vardaro, M., Vargas, A. F., Varghese, J. J., Varma, V., Vazquez, A. N., Vecchio, A., Vedovato, G., Veitch, J., Veitch, P. J., Venikoudis, S., Venneberg, J., Verdier, P., Vereecken, M., Verkindt, D., Verma, B., Verma, P., Verma, Y., Vermeulen, S. M., Vetrano, F., Veutro, A., Vibhute, A. M., Viceré, A., Vidyant, S., Viets, A. D., Vijaykumar, A., Vilkha, A., Villa-Ortega, V., Vincent, E. T., Vinet, J. Y., Viret, S., Virtuoso, A., Vitale, S., Vives, A., Vocca, H., Voigt, D., von Reis, E. R. G., von Wrangel, J. S. A., Vujeva, L., Vyatchanin, S. P., Wack, J., Wade, L. E., Wade, M., Wagner, K. J., Wajid, A., Walker, M., Wallace, G. S., Wallace, L., Wang, E. J., Wang, H., Wang, J. Z., Wang, W. H., Wang, Y. F., Wang, Z., Waratkar, G., Warner, J., Was, M., Washimi, T., Washington, N. Y., Watarai, D., Wayt, K. E., Weaver, B. R., Weaver, B., Weaving, C. R., Webster, S. A., Weickhardt, N. L., Weinert, M., Weinstein, A. J., Weiss, R., Wellmann, F., Wen, L., Weßels, P., Wette, K., Whelan, J. T., Whiting, B. F., Whittle, C., Wickens, E. G., Wildberger, J. B., Wilken, D., Willadsen, D. J., Willetts, K., Williams, D., Williams, M. J., Williams, N. S., Willis, J. L., Willke, B., Wils, M., Winborn, C. W., Winterflood, J., Wipf, C. C., Woan, G., Woehler, J., Wolfe, N. E., Wong, H. T., Wong, I. C. F., Wright, J. L., Wright, M., Wu, C., Wu, D. S., Wu, H., Wuchner, E., Wysocki, D. M., Xu, V. A., Xu, Y., Yadav, N., Yamamoto, H., Yamamoto, K., Yamamoto, T. S., Yamamoto, T., Yamamura, S., Yamazaki, R., Yan, T., Yang, F. W., Yang, F., Yang, K. Z., Yang, Y., Yarbrough, Z., Yasui, H., Yeh, S. W., Yelikar, A. B., Yin, X., Yokoyama, J., Yokozawa, T., Yoo, J., Yu, H., Yuan, S., Yuzurihara, H., Zadrożny, A., Zanolin, M., Zeeshan, M., Zelenova, T., Zendri, J. P., Zeoli, M., Zerrad, M., Zevin, M., Zhang, A. C., Zhang, L., Zhang, R., Zhang, T., Zhang, Y., Zhao, C., Zhao, Y., Zhao, Y., Zheng, Y., Zhong, H., Zhou, R., Zhu, X. J., Zhu, Z. H., Zimmerman, A. B., Zucker, M. E., and Zweizig, J. (2025b). Gwtc-4.0: An introduction to version 4.0 of the gravitational-wave

transient catalog.

Conselice, C. J., Blackburne, J. A., and Papovich, C. (2005). The luminosity, stellar mass, and number density evolution of field galaxies of known morphology from $z = 0.5$ to 3. *The Astrophysical Journal*, 620(2):564–583.

Cornish, N. and Robson, T. (2017). Galactic binary science with the new LISA design. In *Journal of Physics Conference Series*, volume 840 of *Journal of Physics Conference Series*, page 012024. IOP.

Cornish, N. J. and Larson, S. L. (2003). LISA data analysis: Source identification and subtraction. *Phys. Rev. D*, 67(10):103001.

Cornish, N. J. and Rubbo, L. J. (2003). Lisa response function. *Phys. Rev. D*, 67:022001.

Corral-Santana, J. M., Casares, J., Muñoz-Darias, T., Bauer, F. E., Martínez-Pais, I. G., and Russell, D. M. (2016). BlackCAT: A catalogue of stellar-mass black holes in X-ray transients. *A&A*, 587:A61.

Coughlin, M., Meyers, P., Thrane, E., Luo, J., and Christensen, N. (2015). Detectability of eccentric compact binary coalescences with advanced gravitational-wave detectors. *Physical Review D*, 91(6).

Cutler, C. (1998). Angular resolution of the LISA gravitational wave detector. *Phys. Rev. D*, 57(12):7089–7102.

Cutler, C. and Flanagan, É. E. (1994). Gravitational waves from merging compact binaries: How accurately can one extract the binary's parameters from the inspiral waveform? *Phys. Rev. D*, 49(6):2658–2697.

Cutler, C. and Vallisneri, M. (2007). LISA detections of massive black hole inspirals: Parameter extraction errors due to inaccurate template waveforms. *Phys. Rev. D*, 76(10):104018.

Damour, T. and Deruelle, N. (1985). General relativistic celestial mechanics of binary systems. I. The post-Newtonian motion. *Annales de L'Institut Henri Poincare Section (A) Physique Theorique*, 43(1):107–132.

Damour, T. and Deruelle, N. (1986). General relativistic celestial mechanics of binary systems. II. The post-Newtonian timing formula. *Annales de L'Institut Henri Poincare Section (A) Physique Theorique*, 44(3):263–292.

Danielski, C., Korol, V., Tamanini, N., and Rossi, E. M. (2019). Circumbinary exoplanets and brown dwarfs with the Laser Interferometer Space Antenna. *A&A*, 632:A113.

Dashwood Brown, C., Gandhi, P., and Zhao, Y. (2024). On the natal kick of the black hole X-ray binary H 1705-250. *MNRAS*, 527(1):L82–L87.

de Mink, S. E. and Belczynski, K. (2015). Merger Rates of Double Neutron Stars and Stellar Origin Black Holes: The Impact of Initial Conditions on Binary Evolution Predictions. *ApJ*, 814:58.

Deason, A. J., Belokurov, V., and Sanders, J. L. (2019). The total stellar halo mass of the milky way. *Monthly Notices of the Royal Astronomical Society*, 490(3):3426–3439.

Deloye, C. J. and Bildsten, L. (2003). White dwarf donors in ultracompact binaries: The stellar structure of finite-entropy objects. *The Astrophysical Journal*, 598(2):1217–1228.

Deme, B., Hoang, B.-M., Naoz, S., and Kocsis, B. (2020). Detecting kozai–lidov imprints on the gravitational waves of intermediate-mass black holes in galactic nuclei. *The Astrophysical Journal*, 901(2):125.

Digman, M. C. and Cornish, N. J. (2022). Lisa gravitational wave sources in a time-varying galactic stochastic background. *The Astrophysical Journal*, 940(1):10.

Do, T., Ghez, A. M., Morris, M. R., Lu, J. R., Matthews, K., Yelda, S., and Larkin, J. (2009).

High Angular Resolution Integral-Field Spectroscopy of the Galaxy's Nuclear Cluster: A Missing Stellar Cusp? *ApJ*, 703:1323–1337.

Do, T., Hees, A., Ghez, A., Martinez, G. D., Chu, D. S., Jia, S., Sakai, S., Lu, J. R., Gautam, A. K., O'Neil, K. K., Becklin, E. E., Morris, M. R., Matthews, K., Nishiyama, S., Campbell, R., Chappell, S., Chen, Z., Ciurlo, A., Dehghanfar, A., Gallego-Cano, E., Kerzendorf, W. E., Lyke, J. E., Naoz, S., Saida, H., Schödel, R., Takahashi, M., Takamori, Y., Witzel, G., and Wizinowich, P. (2019). Relativistic redshift of the star S0-2 orbiting the Galactic Center supermassive black hole. *Science*, 365(6454):664–668.

Do, T., Lu, J. R., Ghez, A. M., Morris, M. R., Yelda, S., Martinez, G. D., Wright, S. A., and Matthews, K. (2013). Stellar Populations in the Central 0.5 pc of the Galaxy. I. A New Method for Constructing Luminosity Functions and Surface-density Profiles. *ApJ*, 764:154.

Dominik, M., Berti, E., O'Shaughnessy, R., Mandel, I., Belczynski, K., Fryer, C., Holz, D. E., Bulik, T., and Pannarale, F. (2015). Double Compact Objects III: Gravitational-wave Detection Rates. *ApJ*, 806:263.

D'Orazio, D. J. and Samsing, J. (2018). Black hole mergers from globular clusters observable by LISA II. Resolved eccentric sources and the gravitational wave background. *MNRAS*, 481(4):4775–4785.

Downing, J. M. B., Benacquista, M. J., Giersz, M., and Spurzem, R. (2010). Compact binaries in star clusters - I. Black hole binaries inside globular clusters. *MNRAS*, 407:1946–1962.

East, W. E., McWilliams, S. T., Levin, J., and Pretorius, F. (2013). Observing complete gravitational wave signals from dynamical capture binaries. *Phys. Rev. D*, 87(4):043004.

El-Badry, K., Rix, H.-W., Cendes, Y., Rodriguez, A. C., Conroy, C., Quataert, E., Hawkins, K., Zari, E., Hobson, M., Breivik, K., Rau, A., Berger, E., Shahaf, S., Seeburger, R.,

Burdge, K. B., Latham, D. W., Buchhave, L. A., Bieryla, A., Bashi, D., Mazeh, T., and Faigler, S. (2023). A red giant orbiting a black hole. *MNRAS*, 521(3):4323–4348.

Eldridge, J. J., Stanway, E. R., and Tang, P. N. (2019). A consistent estimate for gravitational wave and electromagnetic transient rates. *MNRAS*, 482(1):870–880.

Eldridge, J. J., Stanway, E. R., Xiao, L., McClelland, L. A. S., Taylor, G., Ng, M., Greis, S. M. L., and Bray, J. C. (2017). Binary Population and Spectral Synthesis Version 2.1: Construction, Observational Verification, and New Results. *Publ. Astron. Soc. Aust.*, 34:e058.

Emami, R. and Loeb, A. (2020). Probingintermediate-mass black holes in M87 through multiwavelength gravitational wave observations. *MNRAS*, 495(1):536–543.

Fan, H.-M., Zhong, S., Liang, Z.-C., Wu, Z., Zhang, J.-d., and Hu, Y.-M. (2022). Extreme-mass-ratio burst detection with tianqin. *Phys. Rev. D*, 106:124028.

Fan, H.-M., Zhong, S., Liang, Z.-C., Wu, Z., Zhang, J.-d., and Hu, Y.-M. (2022). Extreme-mass-ratio burst detection with TianQin. *Phys. Rev. D*, 106(12):124028.

Fang, X., Thompson, T. A., and Hirata, C. M. (2019). The population of eccentric binary black holes: Implications for mHz gravitational-wave experiments. *The Astrophysical Journal*, 875(1):75.

Fang, X., Thompson, T. A., and Hirata, C. M. (2019a). The Population of Eccentric Binary Black Holes: Implications for mHz Gravitational Wave Experiments. *arXiv e-prints*, page arXiv:1901.05092.

Fang, Y., Chen, X., and Huang, Q.-G. (2019b). Impact of a Spinning Supermassive Black Hole on the Orbit and Gravitational Waves of a Nearby Compact Binary. *ApJ*, 887(2):210.

Finn, L. S. (1992). Detection, measurement, and gravitational radiation. *Phys. Rev. D*, 46:5236–5249.

Finn, L. S. and Chernoff, D. F. (1993). Observing binary inspiral in gravitational radiation: One interferometer. *Phys. Rev.*, D47:2198–2219.

Finn, L. S. and Thorne, K. S. (2000). Gravitational waves from a compact star in a circular, inspiral orbit, in the equatorial plane of a massive, spinning black hole, as observed by lisa. *Physical Review D*, 62(12).

Fishbach, M. and Fragione, G. (2023). Globular cluster formation histories, masses, and radii inferred from gravitational waves. *MNRAS*, 522(4):5546–5557.

Fragione, G., Antonini, F., and Gnedin, O. Y. (2018). Disrupted globular clusters and the gamma-ray excess in the Galactic Centre. *Monthly Notices of the Royal Astronomical Society*, 475(4):5313–5321.

Fragione, G. and Bromberg, O. (2019). Eccentric binary black hole mergers in globular clusters hosting intermediate-mass black holes. *MNRAS*, 488(3):4370–4377.

Fragione, G., Grishin, E., Leigh, N. W. C., Perets, H. B., and Perna, R. (2019). Black hole and neutron star mergers in galactic nuclei. *MNRAS*, 488(1):47–63.

Fragione, G. and Kocsis, B. (2018). Black Hole Mergers from an Evolving Population of Globular Clusters. *Phys. Rev. Lett.*, 121(16):161103.

Fragione, G., Kocsis, B., Rasio, F. A., and Silk, J. (2022). Repeated Mergers, Mass-gap Black Holes, and Formation of Intermediate-mass Black Holes in Dense Massive Star Clusters. *ApJ*, 927(2):231.

Fragione, G., Metzger, B. D., Perna, R., Leigh, N. W. C., and Kocsis, B. (2020). Electromagnetic transients and gravitational waves from white dwarf disruptions by stellar black holes in triple systems. *Monthly Notices of the Royal Astronomical Society*, 495(1):1061–1072.

Fragos, T., Andrews, J. J., Bavera, S. S., Berry, C. P. L., Coughlin, S., Dotter, A., Giri, P., Kalogera, V., Katsaggelos, A., Kovlakas, K., Lalvani, S., Misra, D., Srivastava, P. M.,

Qin, Y., Rocha, K. A., Román-Garza, J., Serra, J. G., Stahle, P., Sun, M., Teng, X., Trajcevski, G., Tran, N. H., Xing, Z., Zapartas, E., and Zevin, M. (2023). POSYDON: A General-purpose Population Synthesis Code with Detailed Binary-evolution Simulations. *ApJS*, 264(2):45.

Fragos, T., Willems, B., Kalogera, V., Ivanova, N., Rockefeller, G., Fryer, C. L., and Young, P. A. (2009). Understanding Compact Object Formation and Natal Kicks. II. The Case of XTE J1118 + 480. *ApJ*, 697(2):1057–1070.

Fryer, C. L., Woosley, S. E., and Heger, A. (2001). Pair-Instability Supernovae, Gravity Waves, and Gamma-Ray Transients. *ApJ*, 550(1):372–382.

Fuller, J. and Lai, D. (2012a). Dynamical tides in compact white dwarf binaries: tidal synchronization and dissipation. *MNRAS*, 421(1):426–445.

Fuller, J. and Lai, D. (2012b). Tidal Novae in Compact Binary White Dwarfs. *ApJ Lett.*, 756(1):L17.

Fuller, J. and Lai, D. (2013). Dynamical tides in compact white dwarf binaries: helium core white dwarfs, tidal heating and observational signatures. *MNRAS*, 430(1):274–287.

Gautam, A. K., Do, T., Ghez, A. M., Morris, M. R., Martinez, G. D., Hosek, Matthew W., J., Lu, J. R., Sakai, S., Witzel, G., Jia, S., Becklin, E. E., and Matthews, K. (2019). An Adaptive Optics Survey of Stellar Variability at the Galactic Center. *ApJ*, 871(1):103.

Gautham Bhaskar, H., Li, G., and Lin, D. (2023). Enhanced Blackhole mergers in AGN discs due to Precession induced resonances. *arXiv e-prints*, page arXiv:2303.12539.

Gayathri, V., Healy, J., Lange, J., O'Brien, B., Szczepanczyk, M., Bartos, I., Campanelli, M., Klimenko, S., Lousto, C., and O'Shaughnessy, R. (2022). Eccentricity estimate for black hole mergers with numerical relativity simulations.

Gerosa, D., Ma, S., Wong, K. W. K., Berti, E., O'Shaughnessy, R., Chen, Y., and Belczynski, K. (2019). Multiband gravitational-wave event rates and stellar physics. *arXiv e-prints*.

Ghez, A. M., Salim, S., Weinberg, N. N., Lu, J. R., Do, T., Dunn, J. K., Matthews, K., Morris, M. R., Yelda, S., Becklin, E. E., Kremenek, T., Milosavljevic, M., and Naiman, J. (2008). Measuring Distance and Properties of the Milky Way's Central Supermassive Black Hole with Stellar Orbits. *ApJ*, 689(2):1044–1062.

Giacobbo, N., Mapelli, M., and Spera, M. (2018). Merging black hole binaries: the effects of progenitor's metallicity, mass-loss rate and Eddington factor. *MNRAS*, 474(3):2959–2974.

Glampedakis, K. (2005). Extreme mass ratio inspirals: Lisa's unique probe of black hole gravity. *Classical and Quantum Gravity*, 22(15):S605.

Gnedin, O. Y., Ostriker, J. P., and Tremaine, S. (2014). Co-evolution of galactic nuclei and globular cluster systems. *The Astrophysical Journal*, 785(1):71.

Gondán, L. and Kocsis, B. (2021). High eccentricities and high masses characterize gravitational-wave captures in galactic nuclei as seen by Earth-based detectors. *MNRAS*, 506(2):1665–1696.

Gondán, L., Kocsis, B., Raffai, P., and Frei, Z. (2018a). Accuracy of estimating highly eccentric binary black hole parameters with gravitational-wave detections. *The Astrophysical Journal*, 855(1):34.

Gondán, L., Kocsis, B., Raffai, P., and Frei, Z. (2018b). Eccentric black hole gravitational-wave capture sources in galactic nuclei: Distribution of binary parameters. *The Astrophysical Journal*, 860(1):5.

Gopakumar, A. and Iyer, B. R. (2002). Second post-Newtonian gravitational wave polarizations for compact binaries in elliptical orbits. *Phys. Rev. D*, 65(8):084011.

Gould, A. (2011). Gravitational pulse astronomy. *The Astrophysical Journal Letters*, 729(2):L23.

GRAVITY Collaboration, Abuter, R., Amorim, A., Bauböck, M., Berger, J. P., Bonnet, H., Brandner, W., Cardoso, V., Clénet, Y., de Zeeuw, P. T., Dexter, J., Eckart, A., Eisenhauer, F., Förster Schreiber, N. M., Garcia, P., Gao, F., Gendron, E., Genzel, R., Gillessen, S., Habibi, M., Haubois, X., Henning, T., Hippler, S., Horrobin, M., Jiménez-Rosales, A., Jochum, L., Jocou, L., Kaufer, A., Kervella, P., Lacour, S., Lapeyrère, V., Le Bouquin, J. B., Léna, P., Nowak, M., Ott, T., Paumard, T., Perraut, K., Perrin, G., Pfuhl, O., Rodríguez-Coira, G., Shangguan, J., Scheithauer, S., Stadler, J., Straub, O., Straubmeier, C., Sturm, E., Tacconi, L. J., Vincent, F., von Fellenberg, S., Waisberg, I., Widmann, F., Wieprecht, E., Wiezorrek, E., Woillez, J., Yazici, S., and Zins, G. (2020). Detection of the Schwarzschild precession in the orbit of the star S2 near the Galactic centre massive black hole. *A&A*, 636:L5.

Grishin, E., Perets, H. B., Zenati, Y., and Michaely, E. (2017). Generalized Hill-stability criteria for hierarchical three-body systems at arbitrary inclinations. *MNRAS*, 466(1):276–285.

Grishin, E., Romero-Shaw, I. M., and Trani, A. A. (2026). Gravitational-wave signatures of highly eccentric stellar-mass binary black holes in galactic nuclei.

Gupta, P., Suzuki, H., Okawa, H., and Maeda, K.-i. (2020). Gravitational waves from hierarchical triple systems with Kozai-Lidov oscillation. *Phys. Rev. D*, 101(10):104053.

Hamers, A. S. (2018). Secular dynamics of hierarchical multiple systems composed of nested binaries, with an arbitrary number of bodies and arbitrary hierarchical structure - II. External perturbations: flybys and supernovae. *MNRAS*, 476(3):4139–4161.

Hamers, A. S. (2020). Secular dynamics of hierarchical multiple systems composed of nested binaries, with an arbitrary number of bodies and arbitrary hierarchical structure - III.

Suborbital effects: hybrid integration techniques and orbit-averaging corrections. *MNRAS*, 494(4):5492–5506.

Hamers, A. S. (2021). An Improved Numerical Fit to the Peak Harmonic Gravitational Wave Frequency Emitted by an Eccentric Binary. *Research Notes of the American Astronomical Society*, 5(11):275.

Hamers, A. S., Pols, O. R., Claeys, J. S. W., and Nelemans, G. (2013). Population synthesis of triple systems in the context of mergers of carbon-oxygen white dwarfs. *MNRAS*, 430(3):2262–2280.

Hamers, A. S. and Portegies Zwart, S. F. (2016). Secular dynamics of hierarchical multiple systems composed of nested binaries, with an arbitrary number of bodies and arbitrary hierarchical structure. First applications to multiplanet and multistar systems. *MNRAS*, 459(3):2827–2874.

Han, W.-B., Zhong, X.-Y., Chen, X., and Xin, S. (2020). Very extreme mass-ratio bursts in the Galaxy and neighbouring galaxies in relation to space-borne detectors. *MNRAS*, 498(1):L61–L65.

Hansen, B. M. S. and Phinney, E. S. (1997). The pulsar kick velocity distribution. *MNRAS*, 291(3):569–577.

Harris, W. E. (1996). A Catalog of Parameters for Globular Clusters in the Milky Way. *AJ*, 112:1487.

Harris, W. E. (2010). A New Catalog of Globular Clusters in the Milky Way. *arXiv e-prints*, page arXiv:1012.3224.

Heggie, D. C. (1975). Binary evolution in stellar dynamics. *MNRAS*, 173:729–787.

Heggie, D. C. (2001). The gravitational million-body problem.

Heinke, C. O., Ivanova, N., Engel, M. C., Pavlovskii, K., Sivakoff, G. R., Cartwright, T. F., and Gladstone, J. C. (2013). Galactic ultracompact x-ray binaries: Disk stability and evolution. *The Astrophysical Journal*, 768(2):184.

Helstrom, C. W. (2013). *Statistical theory of signal detection: international series of monographs in electronics and instrumentation*, volume 9. Elsevier.

Hills, J. G. (1983). The effects of sudden mass loss and a random kick velocity produced in a supernova explosion on the dynamics of a binary star of arbitrary orbital eccentricity. Applications to X-ray binaries and to the binarypulsars. *ApJ*, 267:322–333.

Hinder, I., Herrmann, F., Laguna, P., and Shoemaker, D. (2010). Comparisons of eccentric binary black hole simulations with post-Newtonian models. *Phys. Rev. D*, 82(2):024033.

Hinder, I., Vaishnav, B., Herrmann, F., Shoemaker, D. M., and Laguna, P. (2008). Circularization and final spin in eccentric binary-black-hole inspirals. *Phys. Rev. D*, 77(8):081502.

Hoang, B.-M., Naoz, S., Kocsis, B., Farr, W. M., and McIver, J. (2019). Detecting Supermassive Black Hole-induced Binary Eccentricity Oscillations with LISA. *ApJ Lett.*, 875(2):L31.

Hoang, B.-M., Naoz, S., Kocsis, B., Farr, W. M., and McIver, J. (2019). Detecting supermassive black hole–induced binary eccentricity oscillations with LISA. *The Astrophysical Journal*, 875(2):L31.

Hoang, B.-M., Naoz, S., Kocsis, B., Rasio, F. A., and Dosopoulou, F. (2018). Black Hole Mergers in Galactic Nuclei Induced by the Eccentric Kozai-Lidov Effect. *ApJ*, 856(2):140.

Hoang, B.-M., Naoz, S., and Kremer, K. (2020). Neutron Star-Black Hole Mergers from Gravitational-wave Captures. *ApJ*, 903(1):8.

Hobbs, G., Faulkner, A., Stairs, I. H., Camilo, F., Manchester, R. N., Lyne, A. G., Kramer, M., D'Amico, N., Kaspi, V. M., Possenti, A., McLaughlin, M. A., Lorimer, D. R., Burgay,

M., Joshi, B. C., and Crawford, F. (2004). The Parkes multibeam pulsar survey - IV. Discovery of 180 pulsars and parameters for 281 previously known pulsars. *MNRAS*, 352(4):1439–1472.

Hopman, C. and Alexander, T. (2006). The Effect of Mass Segregation on Gravitational Wave Sources near Massive Black Holes. *ApJ Lett.*, 645:L133–L136.

Hopman, C., Freitag, M., and Larson, S. L. (2007). Gravitational wave bursts from the galactic massive black hole. *Monthly Notices of the Royal Astronomical Society*, 378(1):129–136.

Huerta, E. A., Kumar, P., McWilliams, S. T., O'Shaughnessy, R., and Yunes, N. (2014). Accurate and efficient waveforms for compact binaries on eccentric orbits. *Phys. Rev. D*, 90(8):084016.

Hughes, S. A., Warburton, N., Khanna, G., Chua, A. J. K., and Katz, M. L. (2021). Adiabatic waveforms for extreme mass-ratio inspirals via multivoice decomposition in time and frequency. *Phys. Rev. D*, 103(10):104014.

in 't Zand, J. J. M., Jonker, P. G., and Markwardt, C. B. (2007). Six new candidate ultracompact x-ray binaries. *Astronomy and amp; Astrophysics*, 465(3):953–963.

Inayoshi, K., Tamanini, N., Caprini, C., and Haiman, Z. (2017). Probing stellar binary black hole formation in galactic nuclei via the imprint of their center of mass acceleration on their gravitational wave signal. *Phys. Rev. D*, 96(6):063014.

Ivanov, P. B., Polnarev, A. G., and Saha, P. (2005). The tidal disruption rate in dense galactic cusps containing a supermassive binary black hole. *MNRAS*, 358:1361–1378.

Ivanova, N. (2011). Common envelope: the progress and the pitfalls.

Ivanova, N., Chaichenets, S., Fregeau, J., Heinke, C. O., Lombardi, J. C., and Woods, T. E. (2010). Formation of black hole x-ray binaries in globular clusters. *The Astrophysical Journal*, 717(2):948–957.

Ivanova, N., Heinke, C. O., Rasio, F. A., Belczynski, K., and Fregeau, J. M. (2008). Formation and evolution of compact binaries in globular clusters - II. Binaries with neutron stars. *MNRAS*, 386(1):553–576.

Ivanova, N., Justham, S., and Podsiadlowski, P. (2015). On the role of recombination in common-envelope ejections. *Monthly Notices of the Royal Astronomical Society*, 447(3):2181–2197.

Ivanova, N., Rocha, C. A. d., Van, K. X., and Nandez, J. L. A. (2017). Formation of black hole x-ray binaries with non-degenerate donors in globular clusters. *The Astrophysical Journal Letters*, 843(2):L30.

Jurado, C., Naoz, S., Lam, C. Y., and Hoang, B.-M. (2023). Natal Kicks from the Galactic Center and Implications on their Environment and the Roman Space Telescope. *arXiv e-prints*, page arXiv:2310.17707.

Jurić, M., Ivezić, Ž., Brooks, A., Lupton, R. H., Schlegel, D., Finkbeiner, D., Padmanabhan, N., Bond, N., Sesar, B., Rockosi, C. M., Knapp, G. R., Gunn, J. E., Sumi, T., Schneider, D. P., Barentine, J. C., Brewington, H. J., Brinkmann, J., Fukugita, M., Harvanek, M., Kleinman, S. J., Krzesinski, J., Long, D., Neilsen, Jr., E. H., Nitta, A., Snedden, S. A., and York, D. G. (2008). The Milky Way Tomography with SDSS. I. Stellar Number Density Distribution. *ApJ*, 673(2):864–914.

Kaib, N. A. and Raymond, S. N. (2014). Very Wide Binary Stars as the Primary Source of Stellar Collisions in the Galaxy. *ApJ*, 782(2):60.

Kalogera, V. (2000). Spin-orbit misalignment in close binaries with two compact objects. *The Astrophysical Journal*, 541(1):319–328.

Katz, M. L., Chua, A. J. K., Speri, L., Warburton, N., and Hughes, S. A. (2021). Fast extreme-mass-ratio-inspiral waveforms: New tools for millihertz gravitational-wave data analysis. *Phys. Rev. D*, 104(6):064047.

Khalil, M., Buonanno, A., Steinhoff, J., and Vines, J. (2022). Energetics and scattering of gravitational two-body systems at fourth post-minkowskian order. *Physical Review D*, 106(2).

Kharchenko, N. V., Piskunov, A. E., Schilbach, E., Röser, S., and Scholz, R. D. (2012). Global survey of star clusters in the Milky Way. I. The pipeline and fundamental parameters in the second quadrant. *A&A*, 543:A156.

Kharchenko, N. V., Piskunov, A. E., Schilbach, E., Röser, S., and Scholz, R. D. (2013). Global survey of star clusters in the Milky Way. II. The catalogue of basic parameters. *A&A*, 558:A53.

Kim, M., Kim, D., Wilkes, B. J., Green, P. J., Kim, E., Anderson, C. S., Barkhouse, W. A., Evans, N. R., Ivezić, Z., Karovska, M., Kashyap, V. L., Lee, M. G., Maksym, P., Mossman, A. E., Silverman, J. D., and Tananbaum, H. D. (2007). Chandra multiwavelength project x-ray point source catalog. *The Astrophysical Journal Supplement Series*, 169(2):401–429.

Kimball, C., Imperato, S., Kalogera, V., Rocha, K. A., Doctor, Z., Andrews, J. J., Dotter, A., Zapartas, E., Bavera, S. S., Kovlakas, K., Fragos, T., Srivastava, P. M., Misra, D., Sun, M., and Xing, Z. (2023). A Black Hole Kicked at Birth: MAXI J1305-704. *ApJ Lett.*, 952(2):L34.

Klein, A., Barausse, E., Sesana, A., Petiteau, A., Berti, E., Babak, S., Gair, J., Aoudia, S., Hinder, I., Ohme, F., and Wardell, B. (2016a). Science with the space-based interferometer eLISA: Supermassive black hole binaries. *Phys. Rev. D*, 93(2):024003.

Klein, A., Barausse, E., Sesana, A., Petiteau, A., Berti, E., Babak, S., Gair, J., Aoudia, S., Hinder, I., Ohme, F., and Wardell, B. (2016b). Science with the space-based interferometer eLISA: Supermassive black hole binaries. *Phys. Rev. D*, 93(2):024003.

Klimenko, S. and Mitselmakher, G. (2004). A wavelet method for detection of gravitational wave bursts. *Classical and Quantum Gravity*, 21(20):S1819.

Knee, A. M., McIver, J., Naoz, S., Romero-Shaw, I. M., and Hoang, B.-M. (2024). Detecting gravitational-wave bursts from black hole binaries in the galactic center with lisa.

Knee, A. M., Romero-Shaw, I. M., Lasky, P. D., McIver, J., and Thrane, E. (2022). A Rosetta Stone for Eccentric Gravitational Waveform Models. *ApJ*, 936(2):172.

Kocsis, B. (2020). *Dynamical Formation of Merging Stellar-Mass Binary Black Holes*, pages 1–44. Springer Singapore, Singapore.

Kocsis, B., Gáspár, M. E., and Márka, S. (2006a). Detection Rate Estimates of Gravity Waves Emitted during Parabolic Encounters of Stellar Black Holes in Globular Clusters. *ApJ*, 648(1):411–429.

Kocsis, B., Gáspár, M. E., and Márka, S. (2006b). Detection Rate Estimates of Gravity Waves Emitted during Parabolic Encounters of Stellar Black Holes in Globular Clusters. *ApJ*, 648(1):411–429.

Kocsis, B., Gáspár, M. E., and Márka, S. (2006c). Detection Rate Estimates of Gravity Waves Emitted during Parabolic Encounters of Stellar Black Holes in Globular Clusters. *ApJ*, 648:411–429.

Kocsis, B., Haiman, Z., and Menou, K. (2008). Premerger localization of gravitational wave standard sirens withlisa: Triggered search for an electromagnetic counterpart. *The Astrophysical Journal*, 684(2):870–887.

Kocsis, B., Haiman, Z., Menou, K., and Frei, Z. (2007). Premerger localization of gravitational-wave standard sirens with LISA: Harmonic mode decomposition. *Phys. Rev. D*, 76(2):022003.

Kocsis, B. and Levin, J. (2012). Repeated bursts from relativistic scattering of compact objects in galactic nuclei. *Physical Review D*, 85(12).

Kocsis, B. and Levin, J. (2012). Repeated bursts from relativistic scattering of compact objects in galactic nuclei. *Phys. Rev. D*, 85(12):123005.

Kocsis, B., Ray, A., and Portegies Zwart, S. (2012). Mapping the Galactic Center with Gravitational Wave Measurements Using Pulsar Timing. *ApJ*, 752(1):67.

Kocsis, B., Ray, A., and Portegies Zwart, S. (2012). Mapping the galactic center with gravitational wave measurements using pulsar timing. *The Astrophysical Journal*, 752(1):67.

Kocsis, B. and Sesana, A. (2011). Gas-driven massive black hole binaries: signatures in the nHz gravitational wave background. *MNRAS*, 411(3):1467–1479.

Kormendy, J. and Ho, L. C. (2013). Coevolution (Or Not) of Supermassive Black Holes and Host Galaxies. *ARA&A*, 51(1):511–653.

Kozai, Y. (1962). Secular perturbations of asteroids with high inclination and eccentricity. *AJ*, 67:591.

Kremer, K. (2025). Compact objects in globular clusters.

Kremer, K., Chatterjee, S., Breivik, K., Rodriguez, C. L., Larson, S. L., and Rasio, F. A. (2018a). LISA Sources in Milky Way Globular Clusters. *Phys. Rev. Lett.*, 120(19):191103.

Kremer, K., Chatterjee, S., Ye, C. S., Rodriguez, C. L., and Rasio, F. A. (2019a). How Initial Size Governs Core Collapse in Globular Clusters. *ApJ*, 871(1):38.

Kremer, K., Rodriguez, C. L., Amaro-Seoane, P., Breivik, K., Chatterjee, S., Katz, M. L., Larson, S. L., Rasio, F. A., Samsing, J., Ye, C. S., and Zevin, M. (2019b). Post-Newtonian dynamics in dense star clusters: Binary black holes in the LISA band. *Phys. Rev. D*, 99(6):063003.

Kremer, K., Rui, N. Z., Weatherford, N. C., Chatterjee, S., Fragione, G., Rasio, F. A., Rodriguez, C. L., and Ye, C. S. (2021). White Dwarf Subsystems in Core-Collapsed Globular Clusters. *ApJ*, 917(1):28.

Kremer, K., Ye, C. S., Chatterjee, S., Rodriguez, C. L., and Rasio, F. A. (2018b). How Black Holes Shape Globular Clusters: Modeling NGC 3201. *ApJ Lett.*, 855(2):L15.

Kremer, K., Ye, C. S., Rui, N. Z., Weatherford, N. C., Chatterjee, S., Fragione, G., Rodriguez, C. L., Spera, M., and Rasio, F. A. (2020). Modeling dense star clusters in the milky way and beyond with the cmc cluster catalog. *The Astrophysical Journal Supplement Series*, 247(2):48.

Kroupa, P. (2001). On the variation of the initial mass function. *MNRAS*, 322(2):231–246.

Kulkarni, S. R., Hut, P., and McMillan, S. (1993). Stellar black holes in globular clusters. *Nature*, 364:421–423.

Kupfer, T., Korol, V., Shah, S., Nelemans, G., Marsh, T. R., Ramsay, G., Groot, P. J., Steeghs, D. T. H., and Rossi, E. M. (2018). Lisa verification binaries with updated distances from gaia data release 2. *Monthly Notices of the Royal Astronomical Society*, 480(1):302–309.

Lagos, F., Schreiber, M. R., Parsons, S. G., Gänsicke, B. T., and Godoy, N. (2020). Most EL CVn systems are inner binaries of hierarchical triples. *MNRAS*, 499(1):L121–L125.

Lamberts, A., Garrison-Kimmel, S., Hopkins, P. F., Quataert, E., Bullock, J. S., Faucher-Giguère, C. A., Wetzel, A., Kereš, D., Drango, K., and Sand erson, R. E. (2018). Predicting the binary black hole population of the Milky Way with cosmological simulations. *MNRAS*, 480(2):2704–2718.

Lang, R. N. and Hughes, S. A. (2006). Measuring coalescing massive binary black holes with gravitational waves: The impact of spin-induced precession. *Phys. Rev. D*, 74:122001.

Lau, S. Y., Yagi, K., and Arras, P. (2022). Periastron precession effect of <mml:math xmlns:mml="http://www.w3.org/1998/math/mathml" dis-

play="inline"><mml:mi>f</mml:mi></mml:math> -mode dynamical tides on gravitational waves from eccentric double white dwarfs. *Physical Review D*, 106(10).

Lau, S. Y., Yagi, K., and Arras, P. (2022). The effect of dynamical tides on gravitational waves from eccentric double white dwarfs. *arXiv e-prints*, page arXiv:2209.07009.

Lau, S. Y. and Yu, H. (2025). Gravitational radiation-driven chaotic tide in a white dwarf-massive black hole binary as a source of repeating x-ray transients.

Launhardt, R., Zylka, R., and Mezger, P. G. (2002). The nuclear bulge of the Galaxy. III. Large-scale physical characteristics of stars and interstellar matter. *A&A*, 384:112–139.

Lenon, A. K., Nitz, A. H., and Brown, D. A. (2020). Measuring the eccentricity of gw170817 and gw190425. *Monthly Notices of the Royal Astronomical Society*, 497(2):1966–1971.

Levesque, E. M., Massey, P., Olsen, K. A. G., Plez, B., Josselin, E., Maeder, A., and Meynet, G. (2005). The effective temperature scale of galactic red supergiants: Cool, but not as cool as we thought. *The Astrophysical Journal*, 628(2):973–985.

Li, A. K. Y., Lo, R. K. L., Sachdev, S., Chan, J. C. L., Lin, E. T., Li, T. G. F., and Weinstein, A. J. (2023). Targeted subthreshold search for strongly lensed gravitational-wave events. *Phys. Rev. D*, 107(12):123014.

Li, G., Naoz, S., Kocsis, B., and Loeb, A. (2015). Implications of the eccentric Kozai-Lidov mechanism for stars surrounding supermassive black hole binaries. *MNRAS*, 451(2):1341–1349.

Lidov, M. L. (1962). The evolution of orbits of artificial satellites of planets under the action of gravitational perturbations of external bodies. *Planetary and Space Sci.*, 9:719–759.

Lindblom, L., Owen, B. J., and Brown, D. A. (2008). Model waveform accuracy standards for gravitational wave data analysis. *Phys. Rev. D*, 78(12):124020.

Littenberg, T. B., Cornish, N. J., Lackeos, K., and Robson, T. (2020). Global analysis of the gravitational wave signal from Galactic binaries. *Phys. Rev. D*, 101(12):123021.

Lombardi, Jr., J. C., Proulx, Z. F., Dooley, K. L., Theriault, E. M., Ivanova, N., and Rasio, F. A. (2006). Stellar collisions and ultracompact x-ray binary formation. *The Astrophysical Journal*, 640(1):441–458.

Loutrel, N. (2020). Repeated Bursts: Gravitational Waves from Highly Eccentric Binaries. *arXiv e-prints*, page arXiv:2009.11332.

Loutrel, N. and Yunes, N. (2017). Eccentric gravitational wave bursts in the post-newtonian formalism. *Classical and Quantum Gravity*, 34(13):135011.

Lower, M. E., Thrane, E., Lasky, P. D., and Smith, R. (2018). Measuring eccentricity in binary black hole inspirals with gravitational waves. *Phys. Rev. D*, 98:083028.

Lu, C. X. and Naoz, S. (2019). Supernovae kicks in hierarchical triple systems. *Monthly Notices of the Royal Astronomical Society*.

Lu, J. R., Do, T., Ghez, A. M., Morris, M. R., Yelda, S., and Matthews, K. (2013). Stellar Populations in the Central 0.5 pc of the Galaxy. II. The Initial Mass Function. *ApJ*, 764:155.

Lu, J. R., Ghez, A. M., Hornstein, S. D., Morris, M., Matthews, K., Thompson, D. J., and Becklin, E. E. (2006). Galactic Center Youth: Orbits and Origins of the Young Stars in the Central Parsec. In *Journal of Physics Conference Series*, volume 54 of *Journal of Physics Conference Series*, pages 279–287.

Lu, J. R., Ghez, A. M., Hornstein, S. D., Morris, M. R., Becklin, E. E., and Matthews, K. (2008). A DISK OF YOUNG STARS AT THE GALACTIC CENTER AS DETERMINED BY INDIVIDUAL STELLAR ORBITS. *The Astrophysical Journal*, 690(2):1463–1487.

Luo, J., Chen, L.-S., Duan, H.-Z., Gong, Y.-G., Hu, S., Ji, J., Liu, Q., Mei, J., Milyukov, V., Sazhin, M., Shao, C.-G., Toth, V. T., Tu, H.-B., Wang, Y., Wang, Y., Yeh, H.-C., Zhan, M.-S., Zhang, Y., Zharov, V., and Zhou, Z.-B. (2016). TianQin: a space-borne gravitational wave detector. *CQG*, 33(3):035010.

Maccarone, T. J., Kundu, A., Zepf, S. E., and Rhode, K. L. (2007). A black hole in a globular cluster. *Nature*, 445(7124):183–185.

Mackey, A. D., Wilkinson, M. I., Davies, M. B., and Gilmore, G. F. (2007). The effect of stellar-mass black holes on the structural evolution of massive star clusters. *MNRAS*, 379(1):L40–L44.

Maggiore, M. (2000). Gravitational wave experiments and early universe cosmology. *Physics Reports*, 331(6):283–367.

Mandel, I. and Broekgaarden, F. S. (2022). Rates of compact object coalescences. *Living Reviews in Relativity*, 25(1).

Mandel, I. and de Mink, S. E. (2016). Merging binary black holes formed through chemically homogeneous evolution in short-period stellar binaries. *Monthly Notices of the Royal Astronomical Society*, 458(3):2634–2647.

Mardling, R. A. and Aarseth, S. J. (2001). Tidal interactions in star cluster simulations. *MNRAS*, 321:398–420.

Marks, M. and Kroupa, P. (2010). Initial conditions for globular clusters and assembly of the old globular cluster population of the milky way: Initial conditions and assembly of old mw gcs. *Monthly Notices of the Royal Astronomical Society*, pages no–no.

Marsat, S., Baker, J. G., and Canton, T. D. (2021). Exploring the bayesian parameter estimation of binary black holes with lisa. *Physical Review D*, 103(8).

Martinez, M. A. S., Fragione, G., Kremer, K., Chatterjee, S., Rodriguez, C. L., Samsing, J., Ye, C. S., Weatherford, N. C., Zevin, M., Naoz, S., and Rasio, F. A. (2020). Black Hole Mergers from Hierarchical Triples in Dense Star Clusters. *ApJ*, 903(1):67.

Martins, F., Trippe, S., Paumard, T., Ott, T., Genzel, R., Rauw, G., Eisenhauer, F., Gillessen, S., Maness, H., and Abuter, R. (2006). GCIRS 16SW: A Massive Eclipsing Binary in the Galactic Center. *ApJ Lett.*, 649(2):L103–L106.

Meiron, Y., Kocsis, B., and Loeb, A. (2017). Detecting Triple Systems with Gravitational Wave Observations. *ApJ*, 834(2):200.

Melchor, D., Mockler, B., Naoz, S., Rose, S. C., and Ramirez-Ruiz, E. (2024). Tidal Disruption Events from the Combined Effects of Two-body Relaxation and the Eccentric Kozai-Lidov Mechanism. *ApJ*, 960(1):39.

Merritt, D. (1999). Black holes and galaxy evolution.

Merritt, D. (2010). The Distribution of Stars and Stellar Remnants at the Galactic Center. *ApJ*, 718:739–761.

Merritt, D., Piatek, S., Portegies Zwart, S., and Hemsendorf, M. (2004). Core Formation by a Population of Massive Remnants. *ApJ Lett.*, 608(1):L25–L28.

Michaely, E. and Naoz, S. (2022). Ultrawide Black Hole-Neutron Star Binaries as a Possible Source for Gravitational Waves and Short Gamma-Ray Bursts. *ApJ*, 936(2):184.

Michaely, E. and Perets, H. B. (2019). Gravitational-wave Sources from Mergers of Binary Black Holes Catalyzed by Flyby Interactions in the Field. *ApJ Lett.*, 887(2):L36.

Michaely, E. and Perets, H. B. (2020). High rate of gravitational waves mergers from flyby perturbations of wide black hole triples in the field. *MNRAS*, 498(4):4924–4935.

Mikóczi, B., Kocsis, B., Forgács, P., and Vasúth, M. (2012a). Parameter estimation for inspiraling eccentric compact binaries including pericenter precession. *Phys. Rev. D*, 86(10):104027.

Mikóczi, B., Kocsis, B., Forgács, P., and Vasúth, M. (2012b). Parameter estimation for inspiraling eccentric compact binaries including pericenter precession. *Phys. Rev. D*, 86(10):104027.

Miller, M. C. and Hamilton, D. P. (2002). Four-Body Effects in Globular Cluster Black Hole Coalescence. *ApJ*, 576:894–898.

Miller-Jones, J. C. A., Strader, J., Heinke, C. O., Maccarone, T. J., van den Berg, M., Knigge, C., Chomiuk, L., Noyola, E., Russell, T. D., Seth, A. C., and Sivakoff, G. R. (2015). Deep radio imaging of 47 tuc identifies the peculiar x-ray source x9 as a new black hole candidate. *Monthly Notices of the Royal Astronomical Society*, 453(4):3919–3932.

Mirabel, I. F. (2017). Black holes formed by direct collapse: observational evidences. In Gomboc, A., editor, *New Frontiers in Black Hole Astrophysics*, volume 324 of *IAU Symposium*, pages 303–306.

Misner, C. W., Thorne, K. S., and Wheeler, J. A. (1973). *Gravitation*.

Mockler, B., Melchor, D., Naoz, S., and Ramirez-Ruiz, E. (2023). Uncovering Hidden Massive Black Hole Companions with Tidal Disruption Events. *ApJ*, 959(1):18.

Moe, M. and Di Stefano, R. (2017). Mind Your Ps and Qs: The Interrelation between Period (P) and Mass-ratio (Q) Distributions of Binary Stars. *ApJ*, 230(2):15.

Moe, M. and Kratter, K. M. (2021). Impact of binary stars on planet statistics - I. Planet occurrence rates and trends with stellar mass. *MNRAS*, 507(3):3593–3611.

Moore, B., Robson, T., Loutrel, N., and Yunes, N. (2018). Towards a Fourier domain

waveform for non-spinning binaries with arbitrary eccentricity. *Classical and Quantum Gravity*, 35(23):235006.

Moore, B. and Yunes, N. (2019a). A 3pn fourier domain waveform for non-spinning binaries with moderate eccentricity. *Classical and Quantum Gravity*, 36(18):185003.

Moore, B. and Yunes, N. (2019b). A 3pn fourier domain waveform for non-spinning binaries with moderate eccentricity. *Classical and Quantum Gravity*, 36(18):185003.

Moore, C. J., Cole, R. H., and Berry, C. P. L. (2014). Gravitational-wave sensitivity curves. *Classical and Quantum Gravity*, 32(1):015014.

Moore, C. J., Gerosa, D., and Klein, A. (2019). Are stellar-mass black-hole binaries too quiet for LISA? *MNRAS*, 488(1):L94–L98.

Moreno-Garrido, C., Mediavilla, E., and Buitrago, J. (1995). Gravitational radiation from point masses in elliptical orbits: spectral analysis and orbital parameters. *MNRAS*, 274(1):115–126.

Morscher, M., Pattabiraman, B., Rodriguez, C., Rasio, F. A., and Umbreit, S. (2015). The Dynamical Evolution of Stellar Black Holes in Globular Clusters. *ApJ*, 800(1):9.

Muñoz, D. J., Stone, N. C., Petrovich, C., and Rasio, F. A. (2022). Eccentric Mergers of Intermediate-Mass Black Holes from Evection Resonances in AGN Disks. *arXiv e-prints*, page arXiv:2204.06002.

Murray, C. D. and Dermott, S. F. (1999). *Solar System Dynamics*.

Mushkin, J. and Katz, B. (2020). A simple random walk model explains the disruption process of hierarchical, Eccentric three-body systems. *MNRAS*, 498(1):665–673.

Nagarajan, P. and El-Badry, K. (2025). Mixed origins: strong natal kicks for some black holes and none for others.

Naoz, S. (2016). The Eccentric Kozai-Lidov Effect and Its Applications. *ARA&A*, 54:441–489.

Naoz, S. and Fabrycky, D. C. (2014). Mergers and Obliquities in Stellar Triples. *ApJ*, 793(2):137.

Naoz, S., Farr, W. M., Lithwick, Y., Rasio, F. A., and Teyssandier, J. (2013a). Secular dynamics in hierarchical three-body systems. *MNRAS*, 431(3):2155–2171.

Naoz, S., Fragos, T., Geller, A., Stephan, A. P., and Rasio, F. A. (2016). Formation of Black Hole Low-mass X-Ray Binaries in Hierarchical Triple Systems. *ApJ Lett.*, 822(2):L24.

Naoz, S., Ghez, A. M., Hees, A., Do, T., Witzel, G., and Lu, J. R. (2018). Confusing Binaries: The Role of Stellar Binaries in Biasing Disk Properties in the Galactic Center. *ApJ Lett.*, 853(2):L24.

Naoz, S. and Haiman, Z. (2023). The Enhanced Population of Extreme Mass-Ratio Inspirals in the LISA Band from Supermassive Black Hole Binaries. *arXiv e-prints*, page arXiv:2307.11149.

Naoz, S., Kocsis, B., Loeb, A., and Yunes, N. (2013b). Resonant Post-Newtonian Eccentricity Excitation in Hierarchical Three-body Systems. *ApJ*, 773:187.

Naoz, S., Rose, S. C., Michaely, E., Melchor, D., Ramirez-Ruiz, E., Mockler, B., and Schnittman, J. D. (2022). The Combined Effects of Two-body Relaxation Processes and the Eccentric Kozai-Lidov Mechanism on the Extreme-mass-ratio Inspirals Rate. *ApJ Lett.*, 927(1):L18.

Naoz, S., Will, C. M., Ramirez-Ruiz, E., Hees, A., Ghez, A. M., and Do, T. (2020). A Hidden Friend for the Galactic Center Black Hole, Sgr A*. *ApJ Lett.*, 888(1):L8.

Nelemans, G., Yungelson, L. R., and Portegies Zwart, S. F. (2004). Short-period AM CVn

systems as optical, X-ray and gravitational-wave sources. *Monthly Notices of the Royal Astronomical Society*, 349(1):181–192.

Nelson, L. A., Rappaport, S. A., and Joss, P. C. (1986). The Evolution of Ultrashort Period Binary Systems. *ApJ*, 304:231.

Nishizawa, A., Berti, E., Klein, A., and Sesana, A. (2016). elisa eccentricity measurements as tracers of binary black hole formation. *Physical Review D*, 94(6).

Nishizawa, A., Berti, E., Klein, A., and Sesana, A. (2016). eLISA eccentricity measurements as tracers of binary black hole formation. *Phys. Rev. D*, 94(6):064020.

Nishizawa, A., Sesana, A., Berti, E., and Klein, A. (2017). Constraining stellar binary black hole formation scenarios with eLISA eccentricity measurements. *MNRAS*, 465:4375–4380.

Nissanke, S., Vallisneri, M., Nelemans, G., and Prince, T. A. (2012a). Gravitational-wave Emission from Compact Galactic Binaries. *ApJ*, 758(2):131.

Nissanke, S., Vallisneri, M., Nelemans, G., and Prince, T. A. (2012b). Gravitational-wave Emission from Compact Galactic Binaries. *ApJ*, 758(2):131.

Nitz, A., Harry, I., Brown, D., Biwer, C. M., Willis, J., Canton, T. D., Capano, C., Dent, T., Pekowsky, L., Davies, G. S. C., De, S., Cabero, M., Wu, S., Williamson, A. R., Machenschalk, B., Macleod, D., Pannarale, F., Kumar, P., Reyes, S., dfinstad, Kumar, S., Tápai, M., Singer, L., Kumar, P., veronica villa, maxtrevor, Gadre, B. U. V., Khan, S., Fairhurst, S., and Tolley, A. (2024). gwastro/pycbc: v2.3.3 release of pycbc.

Offner, S. S. R., Moe, M., Kratter, K. M., Sadavoy, S. I., Jensen, E. L. N., and Tobin, J. J. (2023). The Origin and Evolution of Multiple Star Systems. In Inutsuka, S., Aikawa, Y., Muto, T., Tomida, K., and Tamura, M., editors, *Protostars and Planets VII*, volume 534 of *Astronomical Society of the Pacific Conference Series*, page 275.

O'Leary, R. M., Kocsis, B., and Loeb, A. (2009a). Gravitational waves from scattering of stellar-mass black holes in galactic nuclei. *MNRAS*, 395(4):2127–2146.

O'Leary, R. M., Kocsis, B., and Loeb, A. (2009b). Gravitational waves from scattering of stellar-mass black holes in galactic nuclei. *MNRAS*, 395:2127–2146.

Olejak, A., Fishbach, M., Belczynski, K., Holz, D. E., Lasota, J. P., Miller, M. C., and Bulik, T. (2020). The Origin of Inequality: Isolated Formation of a 30+10 $M_\odot$ Binary Black Hole Merger. *ApJ Lett.*, 901(2):L39.

Oliver, D. J., Johnson, A. D., Berrier, J., Glampedakis, K., and Kennefick, D. (2023). Gravitational wave peeps from emris and their implication for lisa signal confusion noise.

Ott, T., Eckart, A., and Genzel, R. (1999). Variable and Embedded Stars in the Galactic Center. *ApJ*, 523:248–264.

Paumard, T., Genzel, R., Martins, F., Nayakshin, S., Beloborodov, A. M., Levin, Y., Trippe, S., Eisenhauer, F., Ott, T., Gillessen, S., Abuter, R., Cuadra, J., Alexander, T., and Sternberg, A. (2006). The Two Young Star Disks in the Central Parsec of the Galaxy: Properties, Dynamics, and Formation. *ApJ*, 643(2):1011–1035.

Paxton, B., Bildsten, L., Dotter, A., Herwig, F., Lesaffre, P., and Timmes, F. (2011). Modules for Experiments in Stellar Astrophysics (MESA). *ApJS*, 192(1):3.

Pelisoli, I. and Williams, J. (2025). An observational overview of white dwarf stars.

Peng, P. and Chen, X. (2021). The last migration trap of compact objects in AGN accretion disc. *MNRAS*, 505(1):1324–1333.

Peng, P. and Chen, X. (2023). Synchronizing the EMRIs and IMRIs in AGN Accretion Disks. *ApJ*, 950(1):3.

Perpinyà-Vallès, M., Rebassa-Mansergas, A., Gänsicke, B. T., Toonen, S., Hermes, J. J., Gentile Fusillo, N. P., and Tremblay, P. E. (2019). Discovery of the first resolved triple white dwarf. *MNRAS*, 483(1):901–907.

Peters, P. C. (1964). Gravitational Radiation and the Motion of Two Point Masses. *Physical Review*, 136:1224–1232.

Peters, P. C. and Mathews, J. (1963). Gravitational Radiation from Point Masses in a Keplerian Orbit. *Physical Review*, 131:435–440.

Petigura, E. A., Marcy, G. W., and Howard, A. W. (2013). A Plateau in the Planet Population below Twice the Size of Earth. *ApJ*, 770(1):69.

Peuten, M., Zocchi, A., Gieles, M., Gualandris, A., and Hénault-Brunet, V. (2016). A stellar-mass black hole population in the globular cluster NGC 6101? *MNRAS*, 462(3):2333–2342.

Pfuhl, O., Alexander, T., Gillessen, S., Martins, F., Genzel, R., Eisenhauer, F., Fritz, T. K., and Ott, T. (2014a). Massive Binaries in the Vicinity of Sgr A*. *ApJ*, 782(2):101.

Pfuhl, O., Alexander, T., Gillessen, S., Martins, F., Genzel, R., Eisenhauer, F., Fritz, T. K., and Ott, T. (2014b). Massive Binaries in the Vicinity of Sgr A*. *ApJ*, 782(2):101.

Pfuhl, O., Fritz, T. K., Zilka, M., Maness, H., Eisenhauer, F., Genzel, R., Gillessen, S., Ott, T., Dodds-Eden, K., and Sternberg, A. (2011). The Star Formation History of the Milky Way's Nuclear Star Cluster. *ApJ*, 741(2):108.

Phinney, E. S. (2001). A Practical Theorem on Gravitational Wave Backgrounds. *arXiv e-prints*, pages astro–ph/0108028.

Podsiadlowski, P., Ivanova, N., Justham, S., and Rappaport, S. (2010). Explosive common-envelope ejection: implications for gamma-ray bursts and low-mass black-hole binaries. *MNRAS*, 406(2):840–847.

Podsiadlowski, P., Rappaport, S., and Pfahl, E. D. (2002). Evolutionary Sequences for Low- and Intermediate-Mass X-Ray Binaries. *ApJ*, 565(2):1107–1133.

Portegies Zwart, S. F. and McMillan, S. L. W. (2002). The Runaway Growth of Intermediate-Mass Black Holes in Dense Star Clusters. *ApJ*, 576(2):899–907.

Porter, E. K. and Sesana, A. (2010). Eccentric massive black hole binaries in lisa i : The detection capabilities of circular templates.

Pretorius, F. (2005). Evolution of binary black-hole spacetimes. *Physical Review Letters*, 95(12).

Pribulla, T. and Rucinski, S. M. (2006). Contact Binaries with Additional Components. I. The Extant Data. *AJ*, 131(6):2986–3007.

Purohit, R. A., Fragione, G., Rasio, F. A., Petter, G. C., and Hickox, R. C. (2024). Binary black hole mergers and intermediate-mass black holes in dense star clusters with collisional runaways.

Qin, K., Jiang, L., and Chen, W.-C. (2023). Black hole ultracompact x-ray binaries: Galactic low-frequency gravitational wave sources. *The Astrophysical Journal*, 944(1):83.

Rafelski, M., Ghez, A. M., Hornstein, S. D., Lu, J. R., and Morris, M. (2007). Photometric Stellar Variability in the Galactic Center. *ApJ*, 659(2):1241–1256.

Raghavan, D., McAlister, H. A., Henry, T. J., Latham, D. W., Marcy, G. W., Mason, B. D., Gies, D. R., White, R. J., and ten Brummelaar, T. A. (2010). A Survey of Stellar Families: Multiplicity of Solar-type Stars. *ApJ*, 190(1):1–42.

Rahmani, S., Lianou, S., and Barmby, P. (2016). Star formation laws in the andromeda galaxy: gas, stars, metals and the surface density of star formation. *Monthly Notices of the Royal Astronomical Society*, 456(4):4128–4144.

Randall, L., Shelest, A., and Xianyu, Z.-Z. (2022). An efficient signal-to-noise approximation for eccentric inspiraling binaries. *The Astrophysical Journal*, 924(2):102.

Randall, L. and Xianyu, Z.-Z. (2019a). A Direct Probe of Mass Density near Inspiraling Binary Black Holes. *ApJ*, 878(2):75.

Randall, L. and Xianyu, Z.-Z. (2019b). Eccentricity Without Measuring Eccentricity: Discriminating Among Stellar Mass Black Hole Binary Formation Channels. *arXiv e-prints*, page arXiv:1907.02283.

Randall, L. and Xianyu, Z.-Z. (2019c). Observing Eccentricity Oscillations of Binary Black Holes in LISA. *arXiv e-prints*, page arXiv:1902.08604.

Rasio, F. A., Pfahl, E. D., and Rappaport, S. (2000). Formation of short-period binary pulsars in globular clusters. *The Astrophysical Journal*, 532(1):L47–L50.

Reid, M. J., McClintock, J. E., Steiner, J. F., Steeghs, D., Remillard, R. A., Dhawan, V., and Narayan, R. (2014). A Parallax Distance to the Microquasar GRS 1915+105 and a Revised Estimate of its Black Hole Mass. *ApJ*, 796(1):2.

Robson, T. and Cornish, N. J. (2019). Detecting gravitational wave bursts with lisa in the presence of instrumental glitches. *Physical Review D*, 99(2).

Robson, T., Cornish, N. J., and Liu, C. (2019a). The construction and use of LISA sensitivity curves. *Classical and Quantum Gravity*, 36(10):105011.

Robson, T., Cornish, N. J., and Liu, C. (2019b). The construction and use of LISA sensitivity curves. *Classical and Quantum Gravity*, 36(10):105011.

Robson, T., Cornish, N. J., Tamanini, N., and Toonen, S. (2018a). Detecting hierarchical stellar systems with LISA. *Phys. Rev. D*, 98(6):064012.

Robson, T., Cornish, N. J., Tamanini, N., and Toonen, S. (2018b). Detecting hierarchical stellar systems with LISA. *Phys. Rev. D*, 98(6):064012.

Rodriguez, C. L., Amaro-Seoane, P., Chatterjee, S., Kremer, K., Rasio, F. A., Samsing, J., Ye, C. S., and Zevin, M. (2018). Post-Newtonian dynamics in dense star clusters: Formation, masses, and merger rates of highly-eccentric black hole binaries. *Phys. Rev. D*, 98(12):123005.

Rodriguez, C. L., Chatterjee, S., and Rasio, F. A. (2016). Binary black hole mergers from globular clusters: Masses, merger rates, and the impact of stellar evolution. *Phys. Rev. D*, 93(8):084029.

Rodriguez, C. L., Chatterjee, S., and Rasio, F. A. (2016). Binary black hole mergers from globular clusters: Masses, merger rates, and the impact of stellar evolution. *Phys. Rev. D*, 93:084029.

Rodriguez, C. L., Haster, C.-J., Chatterjee, S., Kalogera, V., and Rasio, F. A. (2016). Dynamical Formation of the GW150914 Binary Black Hole. *ApJ Lett.*, 824:L8.

Rodriguez, C. L., Morscher, M., Pattabiraman, B., Chatterjee, S., Haster, C.-J., and Rasio, F. A. (2015). Binary black hole mergers from globular clusters: Implications for advanced ligo. *Phys. Rev. Lett.*, 115:051101.

Rodriguez, C. L., Morscher, M., Pattabiraman, B., Chatterjee, S., Haster, C.-J., and Rasio, F. A. (2015). Binary Black Hole Mergers from Globular Clusters: Implications for Advanced LIGO. *Physical Review Letters*, 115(5):051101.

Rodriguez, C. L., Weatherford, N. C., Coughlin, S. C., Amaro-Seoane, P., Breivik, K., Chatterjee, S., Fragione, G., Kıroğlu, F., Kremer, K., Rui, N. Z., Ye, C. S., Zevin, M., and Rasio, F. A. (2022). Modeling Dense Star Clusters in the Milky Way and beyond with the Cluster Monte Carlo Code. *ApJS*, 258(2):22.

Rom, B., Linial, I., Kaur, K., and Sari, R. (2024). Dynamics around supermassive black holes: Extreme mass-ratio inspirals as gravitational-wave sources.

Romagnolo, A., Belczynski, K., Klencki, J., Agrawal, P., Shenar, T., and Szécsi, D. (2023). The role of stellar expansion on the formation of gravitational wave sources. *Monthly Notices of the Royal Astronomical Society*, 525(1):706–720.

Romero-Shaw, I., Lasky, P. D., Thrane, E., and Bustillo, J. C. (2020). Gw190521: Orbital eccentricity and signatures of dynamical formation in a binary black hole merger signal. *The Astrophysical Journal Letters*, 903(1):L5.

Romero-Shaw, I., Loutrel, N., and Zevin, M. (2023). Inferring interference: Identifying a perturbing tertiary with eccentric gravitational wave burst timing. *Phys. Rev. D*, 107(12):122001.

Romero-Shaw, I. M., Lasky, P. D., and Thrane, E. (2019). Searching for eccentricity: signatures of dynamical formation in the first gravitational-wave transient catalogue of ligo and virgo. *Monthly Notices of the Royal Astronomical Society*, 490(4):5210–5216.

Rose, S. C., Naoz, S., Gautam, A. K., Ghez, A. M., Do, T., Chu, D., and Becklin, E. (2020). On Socially Distant Neighbors: Using Binaries to Constrain the Density of Objects in the Galactic Center. *ApJ*, 904(2):113.

Rose, S. C., Naoz, S., and Geller, A. M. (2019). Companion-driven evolution of massive stellar binaries. *MNRAS*, 488(2):2480–2492.

Rose, S. C., Naoz, S., Sari, R., and Linial, I. (2023). Stellar Collisions in the Galactic Center: Massive Stars, Collision Remnants, and Missing Red Giants. *ApJ*, 955(1):30.

Rowan, C., Boekholt, T., Kocsis, B., and Haiman, Z. (2023). Black hole binary formation in AGN discs: from isolation to merger. *MNRAS*, 524(2):2770–2796.

Ruan, W.-H., Liu, C., Guo, Z.-K., Wu, Y.-L., and Cai, R.-G. (2020). The lisa–taiji network. *Nature Astronomy*, 4(2):108–109.

Rubbo, L. J., Holley-Bockelmann, K., and Finn, L. S. (2006). Event Rate for Extreme Mass Ratio Burst Signals in the Laser Interferometer Space Antenna Band. *ApJ Lett.*, 649(1):L25–L28.

Rui, N. Z., Kremer, K., Weatherford, N. C., Chatterjee, S., Rasio, F. A., Rodriguez, C. L., and Ye, C. S. (2021). Matching Globular Cluster Models to Observations. *ApJ*, 912(2):102.

Samsing, J. (2018). Eccentric black hole mergers forming in globular clusters. *Phys. Rev. D*, 97(10):103014.

Samsing, J., Bartos, I., D'Orazio, D. J., Haiman, Z., Kocsis, B., Leigh, N. W. C., Liu, B., Pessah, M. E., and Tagawa, H. (2022). AGN as potential factories for eccentric black hole mergers. *Nature*, 603(7900):237–240.

Samsing, J. and D'Orazio, D. J. (2019a). How post-Newtonian dynamics shape the distribution of stationary binary black hole LISA sources in nearby globular clusters. *Phys. Rev. D*, 99(6):063006.

Samsing, J. and D'Orazio, D. J. (2019b). How post-Newtonian dynamics shape the distribution of stationary binary black hole LISA sources in nearby globular clusters. *Phys. Rev. D*, 99(6):063006.

Samsing, J., Hamers, A. S., and Tyles, J. G. (2019). Effect of distant encounters on black hole binaries in globular clusters: Systematic increase of in-cluster mergers in the LISA band. *Phys. Rev. D*, 100(4):043010.

Samsing, J., MacLeod, M., and Ramirez-Ruiz, E. (2014). The Formation of Eccentric Compact Binary Inspirals and the Role of Gravitational Wave Emission in Binary-Single Stellar Encounters. *ApJ*, 784:71.

Sana, H., de Mink, S. E., de Koter, A., Langer, N., Evans, C. J., Gieles, M., Gosset, E.,

Izzard, R. G., Le Bouquin, J. B., and Schneider, F. R. N. (2012). Binary Interaction Dominates the Evolution of Massive Stars. *Science*, 337(6093):444.

Sana, H. and Evans, C. J. (2011). The multiplicity of massive stars. In Neiner, C., Wade, G., Meynet, G., and Peters, G., editors, *Active OB Stars: Structure, Evolution, Mass Loss, and Critical Limits*, volume 272, pages 474–485.

Sana, H., Le Bouquin, J. B., Lacour, S., Berger, J. P., Duvert, G., Gauchet, L., Norris, B., Olofsson, J., Pickel, D., Zins, G., Absil, O., de Koter, A., Kratter, K., Schnurr, O., and Zinnecker, H. (2014). Southern Massive Stars at High Angular Resolution: Observational Campaign and Companion Detection. *ApJS*, 215(1):15.

Sari, R. and Fragione, G. (2019). Tidal Disruption Events, Main-sequence Extreme-mass Ratio Inspirals, and Binary Star Disruptions in Galactic Nuclei. *ApJ*, 885(1):24.

Sasaki, M., Suyama, T., Tanaka, T., and Yokoyama, S. (2016). Primordial black hole scenario for the gravitational-wave event gw150914. *Physical Review Letters*, 117(6).

Sathyaprakash, B. S. and Schutz, B. F. (2009). Physics, Astrophysics and Cosmology with Gravitational Waves. *Living Reviews in Relativity*, 12(1):2.

Savonije, G. J., de Kool, M., and van den Heuvel, E. P. J. (1986). The minimum orbital period for ultra-compact binaries with the helium burning secondaries. *A&A*, 155:51–57.

Schmeja, S., Kharchenko, N. V., Piskunov, A. E., Röser, S., Schilbach, E., Froebrich, D., and Scholz, R. D. (2014). Global survey of star clusters in the Milky Way. III. 139 new open clusters at high Galactic latitudes. *A&A*, 568:A51.

Scholz, R. D., Kharchenko, N. V., Piskunov, A. E., Röser, S., and Schilbach, E. (2015). Global survey of star clusters in the Milky Way. IV. 63 new open clusters detected by proper motions. *A&A*, 581:A39.

Sengar, R., Tauris, T. M., Langer, N., and Istrate, A. G. (2017). Novel modelling of ultra-compact x-ray binary evolution – stable mass transfer from white dwarfs to neutron stars. *Monthly Notices of the Royal Astronomical Society: Letters*, 470(1):L6–L10.

Sesana, A. (2016a). Prospects for Multiband Gravitational-Wave Astronomy after GW150914. *Physical Review Letters*, 116(23):231102.

Sesana, A. (2016b). Prospects for Multiband Gravitational-Wave Astronomy after GW150914. *Phys. Rev. Lett.*, 116(23):231102.

Sesana, A., Lamberts, A., and Petiteau, A. (2020). Finding binary black holes in the Milky Way with LISA. *Mon. Not. Roy. Astron. Soc.*, 494(1):L75–L80.

Seto, N. (2001). Proposal for Determining the Total Masses of Eccentric Binaries Using Signature of Periastron Advance in Gravitational Waves. *Phys. Rev. Lett.*, 87(25):251101.

Seto, N. (2002a). Long-term operation of the Laser Interferometer Space Antenna and Galactic close white dwarf binaries. *MNRAS*, 333(2):469–474.

Seto, N. (2002b). Long-term operation of the Laser Interferometer Space Antenna and Galactic close white dwarf binaries. *MNRAS*, 333:469–474.

Seto, N. (2008). Detecting Planets around Compact Binaries with Gravitational Wave Detectors in Space. *ApJ Lett.*, 677(1):L55.

Seto, N. (2013). Highly eccentric kozai mechanism and gravitational-wave observation for neutron-star binaries. *Physical Review Letters*, 111(6).

Shara, M. M. and Hurley, J. R. (2002). Star clusters as type ia supernova factories. *The Astrophysical Journal*, 571(2):830.

Shariat, C., El-Badry, K., and Naoz, S. (2025a). 10,000 Resolved Triples from Gaia: Empirical Constraints on Triple Star Populations. *PASP*, 137(9):094201.

Shariat, C., Naoz, S., El-Badry, K., Rocha, K. A., Kalogera, V., Stephan, A. P., Burdge, K. B., and Angelo, I. (2025b). Triple Evolution Pathways to Black Hole Low-mass X-Ray Binaries: Insights from V404 Cygni. *ApJ*, 983(2):115.

Shariat, C., Naoz, S., Hansen, B. M. S., Angelo, I., Michaely, E., and Stephan, A. P. (2023a). Dynamical Evolution of White Dwarfs in Triples in the Era of Gaia. *ApJ Lett.*, 955(1):L14.

Shariat, C., Naoz, S., Hansen, B. M. S., Angelo, I., Michaely, E., and Stephan, A. P. (2023b). Dynamical Evolution of White Dwarfs in Triples in the Era of Gaia. *ApJ Lett.*, 955(1):L14.

Sharpe, C., Ginat, Y. B., Xuan, Z., and Kocsis, B. (2026). Resonant locking between binary systems induced by gravitational waves. *Phys. Rev. D*, 113(2):023040.

Shenar, T., Sana, H., Mahy, L., El-Badry, K., Marchant, P., Langer, N., Hawcroft, C., Fabry, M., Sen, K., Almeida, L. A., Abdul-Masih, M., Bodensteiner, J., Crowther, P. A., Gieles, M., Gromadzki, M., Hénault-Brunet, V., Herrero, A., de Koter, A., Iwanek, P., Kozłowski, S., Lennon, D. J., Maíz Apellániz, J., Mróz, P., Moffat, A. F. J., Picco, A., Pietrukowicz, P., Poleski, R., Rybicki, K., Schneider, F. R. N., Skowron, D. M., Skowron, J., Soszyński, I., Szymański, M. K., Toonen, S., Udalski, A., Ulaczyk, K., Vink, J. S., and Wrona, M. (2022). An X-ray-quiet black hole born with a negligible kick in a massive binary within the Large Magellanic Cloud. *Nature Astronomy*, 6:1085–1092.

Sigurdsson, S. and Hernquist, L. (1993). Primordial black holes in globular clusters. *Nature*, 364:423–425.

Smith, G. P., Jauzac, M., Veitch, J., Farr, W. M., Massey, R., and Richard, J. (2018). What if LIGO's gravitational wave detections are strongly lensed by massive galaxy clusters? *MNRAS*, 475:3823–3828.

Spadaro, A., Buscicchio, R., Vetrugno, D., Klein, A., Gerosa, D., Vitale, S., Dolesi, R., Weber, W. J., and Colpi, M. (2023). Glitch systematics on the observation of massive black-hole binaries with lisa.

Spitzer, Lyman, J. (1969). Equipartition and the Formation of Compact Nuclei in Spherical Stellar Systems. *ApJ Lett.*, 158:L139.

Steffen, J. H., Wu, D.-H., and Larson, S. L. (2018). Detecting circumbinary exoplanets and hierarchical stellar triples with the LISA gravitational radiation mission. *arXiv e-prints*, page arXiv:1812.03438.

Stegmann, J. and Klencki, J. (2025). Spin-orbit misalignment and residual eccentricity are evidence that neutron star-black hole mergers form through triple star evolution.

Stegmann, J., Vigna-Gómez, A., Rantala, A., Wagg, T., Zwick, L., Renzo, M., van Son, L. A. C., de Mink, S. E., and White, S. D. M. (2024). Close Encounters of Wide Binaries Induced by the Galactic Tide: Implications for Stellar Mergers and Gravitational-Wave Sources. *arXiv e-prints*, page arXiv:2405.02912.

Stegmann, J., Vigna-Gómez, A., Rantala, A., Wagg, T., Zwick, L., Renzo, M., van Son, L. A. C., de Mink, S. E., and White, S. D. M. (2024). Close encounters of wide binaries induced by the galactic tide: Implications for stellar mergers and gravitational-wave sources. *The Astrophysical Journal Letters*, 972(2):L19.

Stephan, A. P., Naoz, S., Ghez, A. M., Morris, M. R., Ciurlo, A., Do, T., Breivik, K., Coughlin, S., and Rodriguez, C. L. (2019). The Fate of Binaries in the Galactic Center: The Mundane and the Exotic. *ApJ*, 878(1):58.

Stephan, A. P., Naoz, S., Ghez, A. M., Witzel, G., Sitarski, B. N., Do, T., and Kocsis, B. (2016a). Merging binaries in the Galactic Center: the eccentric Kozai-Lidov mechanism with stellar evolution. *MNRAS*, 460(4):3494–3504.

Stephan, A. P., Naoz, S., Ghez, A. M., Witzel, G., Sitarski, B. N., Do, T., and Kocsis, B. (2016b). Merging binaries in the Galactic Center: the eccentric Kozai-Lidov mechanism with stellar evolution. *MNRAS*, 460:3494–3504.

Stevenson, S., Vigna-Gómez, A., Mandel, I., Barrett, J. W., Neijssel, C. J., Perkins, D., and de Mink, S. E. (2017). Formation of the first three gravitational-wave observations through isolated binary evolution. *Nature Communications*, 8(1).

Storch, N. I. and Lai, D. (2013). Viscoelastic tidal dissipation in giant planets and formation of hot jupiters through high-eccentricity migration. *Monthly Notices of the Royal Astronomical Society*, 438(2):1526–1534.

Su, Y. and Lai, D. (2022). Dynamical tides in eccentric binaries containing massive main-sequence stars: analytical expressions. *MNRAS*, 510(4):4943–4951.

Sukhbold, T., Ertl, T., Woosley, S. E., Brown, J. M., and Janka, H. T. (2016). Core-collapse Supernovae from 9 to 120 Solar Masses Based on Neutrino-powered Explosions. *ApJ*, 821(1):38.

Suvorov, A. G. (2021). Ultra-compact x-ray binaries as dual-line gravitational-wave sources. *Monthly Notices of the Royal Astronomical Society*, 503(4):5495–5503.

Sylvestre, J. (2002). Time-frequency detection algorithm for gravitational wave bursts. *Phys. Rev. D*, 66:102004.

Tagawa, H., Haiman, Z., and Kocsis, B. (2020). Formation and Evolution of Compact-object Binaries in AGN Disks. *ApJ*, 898(1):25.

Tagawa, H., Kocsis, B., Haiman, Z., Bartos, I., Omukai, K., and Samsing, J. (2021). Eccentric Black Hole Mergers in Active Galactic Nuclei. *ApJ Lett.*, 907(1):L20.

Tai, K. S., McWilliams, S. T., and Pretorius, F. (2014). Detecting gravitational waves from highly eccentric compact binaries. *Physical Review D*, 90(10).

Tai, K. S., McWilliams, S. T., and Pretorius, F. (2014). Detecting gravitational waves from highly eccentric compact binaries. *Phys. Rev. D*, 90(10):103001.

Takahashi, R. and Seto, N. (2002a). Parameter Estimation for Galactic Binaries by the Laser Interferometer Space Antenna. *ApJ*, 575:1030–1036.

Takahashi, R. and Seto, N. (2002b). Parameter Estimation for Galactic Binaries by the Laser Interferometer Space Antenna. *ApJ*, 575(2):1030–1036.

Tamanini, N. and Danielski, C. (2019). The gravitational-wave detection of exoplanets orbiting white dwarf binaries using LISA. *Nature Astronomy*, 3:858–866.

Tamanini, N., Klein, A., Bonvin, C., Barausse, E., and Caprini, C. (2020a). Peculiar acceleration of stellar-origin black hole binaries: Measurement and biases with LISA. *Phys. Rev. D*, 101(6):063002.

Tamanini, N., Klein, A., Bonvin, C., Barausse, E., and Caprini, C. (2020b). Peculiar acceleration of stellar-origin black hole binaries: Measurement and biases with LISA. *Phys. Rev. D*, 101(6):063002.

Tang, P., Eldridge, J. J., Meyer, R., Lamberts, A., Boileau, G., and van Zeist, W. G. J. (2024). Predicting gravitational wave signals from BPASS white dwarf binary and black hole binary populations of a Milky Way-like galaxy model for LISA. *MNRAS*, 534(3):1707–1728.

Tauris, T. M. (2018). Disentangling coalescing neutron-star–white-dwarf binaries for lisa. *Physical Review Letters*, 121(13).

The LIGO Scientific Collaboration, the Virgo Collaboration, the KAGRA Collaboration, et al. (2021). The population of merging compact binaries inferred using gravitational waves through GWTC-3. *arXiv e-prints*.

Thompson, T. A. (2011). Accelerating Compact Object Mergers in Triple Systems with the Kozai Resonance: A Mechanism for "Prompt" Type Ia Supernovae, Gamma-Ray Bursts, and Other Exotica. *ApJ*, 741(2):82.

Thorne, K. S. (1987). *Gravitational radiation.* Cambridge University Press.

Thorne, K. S., Hawking, S., and Israel, W. (1987). 300 years of gravitation.

Tinto, M. and Dhurandhar, S. V. (2021). Time-delay interferometry. *Living Reviews in Relativity*, 24(1):1.

Tinto, M., Estabrook, F. B., and Armstrong, J. W. (2002). Time-delay interferometry for LISA. *Phys. Rev. D*, 65(8):082003.

Tokovinin, A. (2014). From Binaries to Multiples. II. Hierarchical Multiplicity of F and G Dwarfs. *AJ*, 147(4):87.

Tokovinin, A. (2022). Resolved Gaia Triples. *ApJ*, 926(1):1.

Tokovinin, A., Thomas, S., Sterzik, M., and Udry, S. (2008). Tertiary Companions to Close Spectroscopic Binaries. In Hubrig, S., Petr-Gotzens, M., and Tokovinin, A., editors, *Multiple Stars Across the H-R Diagram*, page 129.

Toonen, S., Boekholt, T. C. N., and Portegies Zwart, S. (2022). Stellar triples on the edge. Comprehensive overview of the evolution of destabilised triples leading to stellar and binary exotica. *A&A*, 661:A61.

Toonen, S., Hamers, A., and Portegies Zwart, S. (2016). The evolution of hierarchical triple star-systems. *Computational Astrophysics and Cosmology*, 3(1):6.

Toonen, S., Hollands, M., Gänsicke, B. T., and Boekholt, T. (2017). The binarity of the local white dwarf population. *A&A*, 602:A16.

Toonen, S., Perets, H. B., and Hamers, A. S. (2018). Rate of WD-WD head-on collisions in isolated triples is too low to explain standard type Ia supernovae. *A&A*, 610:A22.

Toonen, S., Perets, H. B., Igoshev, A. P., Michaely, E., and Zenati, Y. (2018). The demographics of neutron star – white dwarf mergers: Rates, delay-time distributions, and progenitors. *Astronomy and amp; Astrophysics*, 619:A53.

Torres-Orjuela, A., Amaro Seoane, P., Xuan, Z., Chua, A. J. K., Rosell, M. J. B., and Chen, X. (2021). Exciting Modes due to the Aberration of Gravitational Waves: Measurability for Extreme-Mass-Ratio Inspirals. *Phys. Rev. Lett.*, 127(4):041102.

Toubiana, A., Marsat, S., Babak, S., Barausse, E., and Baker, J. (2020). Tests of general relativity with stellar-mass black hole binaries observed by lisa. *Physical Review D*, 101(10).

Trani, A. A., Spera, M., Leigh, N. W. C., and Fujii, M. S. (2019). The Keplerian Three-body Encounter. II. Comparisons with Isolated Encounters and Impact on Gravitational Wave Merger Timescales. *ApJ*, 885(2):135.

Tudor, V., Miller-Jones, J. C. A., Knigge, C., Maccarone, T. J., Tauris, T. M., Bahramian, A., Chomiuk, L., Heinke, C. O., Sivakoff, G. R., Strader, J., Plotkin, R. M., Soria, R., Albrow, M. D., Anderson, G. E., van den Berg, M., Bernardini, F., Bogdanov, S., Britt, C. T., Russell, D. M., and Zurek, D. R. (2018). HST spectrum and timing of the ultracompact X-ray binary candidate 47 Tuc X9. *MNRAS*, 476(2):1889–1908.

Vallisneri, M. (2008). Use and abuse of the fisher information matrix in the assessment of gravitational-wave parameter-estimation prospects. *Physical Review D*, 77(4).

van Dokkum, P. G., Leja, J., Nelson, E. J., Patel, S., Skelton, R. E., Momcheva, I., Brammer, G., Whitaker, K. E., Lundgren, B., Fumagalli, M., Conroy, C., Förster Schreiber, N., Franx, M., Kriek, M., Labbé, I., Marchesini, D., Rix, H.-W., van der Wel, A., and Wuyts, S. (2013). The assembly of milky-way-like galaxies since z 2.5. *The Astrophysical Journal*, 771(2):L35.

van Haaften, L. M., Nelemans, G., Voss, R., Wood, M. A., and Kuijpers, J. (2012). The evolution of ultracompact x-ray binaries. *Astronomy and amp; Astrophysics*, 537:A104.

Vick, M., Lai, D., and Fuller, J. (2017). Tidal dissipation and evolution of white dwarfs around massive black holes: an eccentric path to tidal disruption. *MNRAS*, 468(2):2296–2310.

Vitale, S. (2016). Multiband Gravitational-Wave Astronomy: Parameter Estimation and Tests of General Relativity with Space- and Ground-Based Detectors. *Physical Review Letters*, 117(5):051102.

Vitale, S. (2021). The first 5 years of gravitational-wave astrophysics. *Science*, 372(6546):eabc7397.

Vitale, S. and Whittle, C. (2018). Characterization of binary black holes by heterogeneous gravitational-wave networks. *Physical Review D*, 98(2).

Wagg, T., Broekgaarden, F. S., de Mink, S. E., Frankel, N., van Son, L. A. C., and Justham, S. (2022). Gravitational Wave Sources in Our Galactic Backyard: Predictions for BHBH, BHNS, and NSNS Binaries Detectable with LISA. *ApJ*, 937(2):118.

Wang, H., Stephan, A. P., Naoz, S., Hoang, B.-M., and Breivik, K. (2021). Gravitational-wave Signatures from Compact Object Binaries in the Galactic Center. *ApJ*, 917(2):76.

Wang, L., Spurzem, R., Aarseth, S., Giersz, M., Askar, A., Berczik, P., Naab, T., Schadow, R., and Kouwenhoven, M. B. N. (2016). The DRAGON simulations: globular cluster evolution with a million stars. *MNRAS*, 458(2):1450–1465.

Wen, L. (2003). On the Eccentricity Distribution of Coalescing Black Hole Binaries Driven by the Kozai Mechanism in Globular Clusters. *ApJ*, 598(1):419–430.

Wette, K. (2020). Swiglal: Python and octave interfaces to the lalsuite gravitational-wave data analysis libraries. *SoftwareX*, 12:100634.

Whitehead, H., Rowan, C., Boekholt, T., and Kocsis, B. (2024). Gas assisted binary black hole formation in AGN discs. *MNRAS*, 531(4):4656–4680.

Will, C. M., Naoz, S., Hees, A., Tucker, A., Zhang, E., Do, T., and Ghez, A. (2023). Constraining a companion of the galactic center black hole, Sgr A*. *arXiv e-prints*, page arXiv:2307.16646.

Willems, B., Kalogera, V., Vecchio, A., Ivanova, N., Rasio, F. A., Fregeau, J. M., and Belczynski, K. (2007). Eccentric double white dwarfs as lisa sources in globular clusters. *The Astrophysical Journal*, 665(1):L59–L62.

Winter-Granić, M., Petrovich, C., and Peña-Donaire, V. (2023). Binary mergers in the centers of galaxies: synergy between stellar flybys and tidal fields.

Winters, J. G., Henry, T. J., Jao, W.-C., Subasavage, J. P., Chatelain, J. P., Slatten, K., Riedel, A. R., Silverstein, M. L., and Payne, M. J. (2019). The Solar Neighborhood. XLV. The Stellar Multiplicity Rate of M Dwarfs Within 25 pc. *AJ*, 157(6):216.

Wong, K. W. K., Baibhav, V., and Berti, E. (2019). Binary radial velocity measurements with space-based gravitational-wave detectors. *MNRAS*, 488(4):5665–5670.

Woosley, S. E., Heger, A., and Weaver, T. A. (2002). The evolution and explosion of massive stars. *Reviews of Modern Physics*, 74:1015–1071.

Woosley, S. E. and Weaver, T. A. (1995). The Evolution and Explosion of Massive Stars. II. Explosive Hydrodynamics and Nucleosynthesis. *ApJS*, 101:181.

Wu, Z., Fan, H.-M., Hu, Y.-M., and Heng, I. S. (2023). Searching gravitational-wave bursts with space-borne detectors.

Xuan, Z., Kremer, K., and Naoz, S. (2025a). Localizing Dynamically Formed Black Hole Binaries in Milky Way Globular Clusters with LISA. *ApJ Lett.*, 985(2):L42.

Xuan, Z., Naoz, S., and Chen, X. (2023). Detecting accelerating eccentric binaries in the LISA band. *Phys. Rev. D*, 107(4):043009.

Xuan, Z., Naoz, S., Kocsis, B., and Michaely, E. (2024a). Detecting Gravitational Wave Bursts from Stellar-mass Binaries in the mHz Band. *ApJ*, 965(2):148.

Xuan, Z., Naoz, S., Kocsis, B., and Michaely, E. (2024b). Stochastic gravitational wave background from highly-eccentric stellar-mass binaries in the millihertz band. *Phys. Rev. D*, 110(2):023020.

Xuan, Z., Naoz, S., Kremer, K., Katz, M. L., Kocsis, B., and Michaely, E. (2026). Eccentric Stellar-mass Binary Black Holes: Population, Detectability, and Waveform Analysis in the LISA and LIGO Era. *arXiv:2605.15265*.

Xuan, Z., Naoz, S., Li, A. K. Y., Kocsis, B., Petigura, E., Knee, A. M., McIver, J., Kremer, K., and Farr, W. M. (2025b). Extracting astrophysical information of highly eccentric binaries in the millihertz gravitational wave band. *Phys. Rev. D*, 111(4):043018.

Xuan, Z., Peng, P., and Chen, X. (2021). Degeneracy between mass and peculiar acceleration for the double white dwarfs in the LISA band. *MNRAS*, 502(3):4199–4209.

Xuan, Z., Shariat, C., and Naoz, S. (2025c). From Wide Triples to Ultracompact X-ray Binaries: Multimessenger Signatures of Dynamically Formed Black Hole-White Dwarf Systems in the LISA Band. *ApJ*, 995(1):27.

Yan, H., Chen, X., and Torres-Orjuela, A. (2023). Calculating the gravitational waves emitted from high-speed sources. *Phys. Rev. D*, 107(10):103044.

Yang, X.-P., Xu, K., Gao, Z.-F., Jiang, L., and Chen, W.-C. (2025). Formation of a possible black-hole ultracompact x-ray binary with the shortest orbital period.

Ye, C. S., Fragione, G., and Perna, R. (2023). On the tidal capture of white dwarfs by

intermediate-mass black holes in dense stellar environments. *The Astrophysical Journal*, 953(2):141.

Ye, C. S., Kremer, K., Chatterjee, S., Rodriguez, C. L., and Rasio, F. A. (2019). Millisecond Pulsars and Black Holes in Globular Clusters. *ApJ*, 877(2):122.

Ye, C. S., Kremer, K., Ransom, S. M., and Rasio, F. A. (2024). Lower-mass-gap Black Holes in Dense Star Clusters. *ApJ*, 975(1):77.

Ye, C. S., Kremer, K., Rodriguez, C. L., Rui, N. Z., Weatherford, N. C., Chatterjee, S., Fragione, G., and Rasio, F. A. (2022). Compact Object Modeling in the Globular Cluster 47 Tucanae. *ApJ*, 931(2):84.

Yunes, N., Sopuerta, C. F., Rubbo, L. J., and Holley-Bockelmann, K. (2008). Relativistic effects in extreme mass ratio gravitational wave bursts. *The Astrophysical Journal*, 675(1):604–613.

Zevin, M., Bavera, S. S., Berry, C. P. L., Kalogera, V., Fragos, T., Marchant, P., Rodriguez, C. L., Antonini, F., Holz, D. E., and Pankow, C. (2021). One Channel to Rule Them All? Constraining the Origins of Binary Black Holes Using Multiple Formation Pathways. *ApJ*, 910(2):152.

Zevin, M., Pankow, C., Rodriguez, C. L., Sampson, L., Chase, E., Kalogera, V., and Rasio, F. A. (2017). Constraining Formation Models of Binary Black Holes with Gravitational-wave Observations. *ApJ*, 846(1):82.

Zevin, M., Romero-Shaw, I. M., Kremer, K., Thrane, E., and Lasky, P. D. (2021). Implications of eccentric observations on binary black hole formation channels. *The Astrophysical Journal Letters*, 921(2):L43.

Zevin, M., Samsing, J., Rodriguez, C., Haster, C.-J., and Ramirez-Ruiz, E. (2019). Eccentric

black hole mergers in dense star clusters: The role of binary–binary encounters. *The Astrophysical Journal*, 871(1):91.

Zhang, E., Naoz, S., and Will, C. M. (2023a). A Stability Timescale for Non-Hierarchical Three-Body Systems. *arXiv e-prints*, page arXiv:2301.08271.

Zhang, E., Naoz, S., and Will, C. M. (2023b). A Stability Timescale for Nonhierarchical Three-body Systems. *ApJ*, 952(2):103.

Zhang, F., Chen, X., Shao, L., and Inayoshi, K. (2021). The eccentric and accelerating stellar binary black hole mergers in galactic nuclei: Observing in ground and space gravitational-wave observatories. *The Astrophysical Journal*, 923(2):139.

Zhang, F., Chen, X., Shao, L., and Inayoshi, K. (2021). The Eccentric and Accelerating Stellar Binary Black Hole Mergers in Galactic Nuclei: Observing in Ground and Space Gravitational-wave Observatories. *ApJ*, 923(2):139.

Zhang, J., Bao, T., and Li, Z. (2024). A Chandra search for periodic X-ray sources in the bulge of M31. *MNRAS*, 530(2):2096–2113.

Zhang, J., Bao, T., and Li, Z. (2024). A chandra search for periodic x-ray sources in the bulge of m31.

Zhang, Z. and Chen, X. (2024a). The dynamics and gravitational-wave signal of a binary flying closely by a Kerr supermassive black hole. *arXiv e-prints*, page arXiv:2402.02178.

Zhang, Z. and Chen, X. (2024b). The Dynamics and Gravitational-wave Signal of a Binary Flying Closely by a Kerr Supermassive Black Hole. *ApJ*, 968(2):122.

Zhu, L.-G. and Chen, X. (2024). Unveiling the Solution to the Final-parsec Problem by Combining Millihertz Gravitational-wave Observation and Active Galactic Nucleus Survey. *ApJ*, 960(1):43.

Zocchi, A., Gieles, M., and Hénault-Brunet, V. (2019). The effect of stellar-mass black holes on the central kinematics of ω Cen: a cautionary tale for IMBH interpretations. *MNRAS*, 482(4):4713–4725.

Zwart, S. F. P. and McMillan, S. L. W. (1999). Black hole mergers in the universe. *The Astrophysical Journal*, 528(1):L17.

Zwick, L., Capelo, P. R., Bortolas, E., Mayer, L., and Amaro-Seoane, P. (2020). Improved gravitational radiation time-scales: significance for LISA and LIGO-Virgo sources. *MNRAS*, 495(2):2321–2331.